LOS ANGELES PUBLIC LIBRARY

SCIENCE & TECHNOLOGY

ARS JOURNAL

A PUBLICATION OF THE AMERICAN ROCKET SOCIETY

VOLUME 31 NUMBER 12 DECEMBER 1961

BIND

SURVEY ARTICLE

Recent Advances in Magnetohydrodynamic Propulsion . . . Meredith C. Gourdine 1670

CONTRIBUTED ARTICLES

Approximate Analysis of Thrust Vector Control by Fluid Injection . . . Jain-Ming Wu, Robert L. Chapkis, and Artur Mager 1677

Theoretical Performance of Propellants Suitable for Electrothermal Jet Engines . . . John R. Jack 1685

Dynamic Response of Liquid Fueled Rocket Engines on Flexible Stands . . . V. Chobotov 1690

Representation of Fuel Sloshing in Cylindrical Tanks by an Equivalent Mechanical Model . . . H. Norman Abramson, Wen-Hwa Chu, and Guido E. Ransleben Jr. 1697

Stability of a Cylinder Under Dynamic Radial Pressure . . . John C. Yao 1705

Hot Wire Measurements in Low Reynolds Number Hypersonic Flows . . . C. Forbes Dewey Jr. 1709

Plasma Propulsion With a Pulsed Transmission Line . . . Allan Schaffer 1718

Three-Dimensional Optimum Thrust Trajectories for Power Limited Propulsion Systems . . . William G. Melbourne 1723

Preliminary Orbit Determination of a Nontransmitting Satellite Using the DOPLOC Tracking System . . . Paul B. Richards 1729

Attenuated Intercept Satellite Rendezvous System . . . M. Shapiro 1733

Nuclear Safety Analysis of Snap III for Space Missions . . . W. Hagis, T. Dobry, and G. Dix 1744

Water Impact of Manned Spacecraft . . . William H. Mueller and James L. Malokoff 1751

TECHNICAL NOTES

Configuration Efficiency: a New Measure of Ballistic Quality for a Grain Design . . . R. A. Rossini, J. S. Billheimer, and T. R. Threewit 1761

Design Criteria for Space Vehicles to Resist Wind Induced Oscillations . . . A. A. Ezra and S. Birnbaum 1764

Error Analysis for Doppler Determined Satellite Orbits of Other Planets . . . Paula L. Cohen and Armin J. Deutsch 1767

Influences of Solid Propellant Burning Rate Exponents on Performance of Engines With Large Back Pressure Variations . . . Robert C. Brumfield 1769

Mass Spectrometer for Upper Air Measurements . . . E. J. Schaefer and M. H. Nichols 1773

Momentum Dumping Using Magnetic Torques . . . J. W. Barrow 1776

Approximate Method of Predicting Hypersonic Pressure Distribution on Nonlifting Near Power Law Bodies Using Similar Flow Theory Results . . . N. R. Augustine 1778

Gaseous Detonation Wave Intersections With Nonrigid Boundaries . . . William P. Sommers 1780

Theory of Liquid Atomization in High Velocity Gas Streams . . . Ernest Mayer 1783

Interdependence of Base Pressure and Base Heat Transfer . . . R. J. Dixon and R. H. Page 1785

Solutions for Satellite Motion Under Low Acceleration Using the Method of Variation of Parameters . . . Stephen J. Citron 1786

Thrust Vector Determination of an Ion Engine by Differential Comparison With an Unthrusted Orbit . . . James N. Hanson 1787

Consumable Case Solid Rocket . . . A. N. Baxter 1790

DEPARTMENTS

Patents . . . 1793

Book Notes . . . 1794

Technical Literature Digest . . . 1795

1961 INDEX OF PAPERS PUBLISHED IN ARS JOURNAL . . . 1803

PROGRESS IN ASTRONAUTICS AND ROCKETRY

Series Editor
MARTIN SUMMERFIELD
Princeton University

SPONSORED BY THE AMERICAN ROCKET SOCIETY

Forthcoming volumes, 1962:

Volume 8 Guidance and Control

Edited by
ROBERT E. ROBERSON
Consultant
JAMES S. FARRIOR
Lockheed Missiles and Space Company

A Selection of Technical Papers based mainly on a Symposium of the American Rocket Society held at Stanford, California, August 7–9, 1961

Volume 7 Hypersonics

Edited by
FREDERICK R. RIDDELL
AVCO Corporation

A Selection of Technical Papers based mainly on a Symposium of the American Rocket Society held at Cambridge, Massachusetts, August 16–18, 1961

Volume 6 Detonation and Two-Phase Flow

Edited by
S. S. PENNER
California Institute of Technology
F. A. WILLIAMS
Harvard University

A Selection of Technical Papers based mainly on a Symposium of the American Rocket Society held at Palm Beach, Florida, April 26–28, 1961

Previously published:

Volume 5 Electrostatic Propulsion

Edited by
DAVID B. LANGMUIR
ERNST STUHLINGER
J. M. SELLEN, JR.

A Selection of Technical Papers based mainly on a Symposium of the American Rocket Society held at Monterey, California, November 3, 4, 1960

May 1961, 579 pp., $5.75

Volume 4 Space Power Systems

Edited by
NATHAN W. SNYDER

A Selection of Technical Papers based mainly on a Symposium of the American Rocket Society held at Santa Monica, California, September 27–30, 1960

May 1961, 632 pp., $6.00

Volume 3 Energy Conversion for Space Power

Edited by
NATHAN W. SNYDER

A Selection of Technical Papers based mainly on a Symposium of the American Rocket Society held at Santa Monica, California, September 27–30, 1960

March 1961, 779 pp., $7.25

Volume 2 Liquid Rockets and Propellants

Edited by
LOREN E. BOLLINGER
MARTIN GOLDSMITH
ALEXIS W. LEMMON, JR.

A Selection of Technical Papers based mainly on a Symposium of the American Rocket Society held at The Ohio State University, Columbus, Ohio, July 18, 19, 1960

December 1960, 682 pp., $6.50

Volume 1 Solid Propellant Rocket Research

Edited by
MARTIN SUMMERFIELD

A Selection of Technical Papers based mainly on a Symposium of the American Rocket Society held at Princeton University, Princeton, New Jersey, January 28, 29, 1960

November 1960, 692 pp., $6.50

ACADEMIC PRESS | **New York and London**

111 Fifth Avenue, New York 3, New York Berkeley Square House, London, W. 1

ARS JOURNAL

A PUBLICATION OF THE AMERICAN ROCKET SOCIETY

EDITOR — Martin Summerfield

ASSOCIATE TECHNICAL EDITOR — Irvin Glassman

MANAGING EDITOR — Margaret Sherman

STAFF EDITOR — Barbara Nowak

ART EDITOR — John Culin

ASSOCIATE EDITORS

Igor Jurkevich, *G. E. Space Sciences Laboratory, Russian Supplement;* George F. McLaughlin, *Patents;* Charles J. Mundo, Jr., *Raytheon Co., Guidance;* Bernard H. Paiewonsky, *Aeronautical Research Associates of Princeton, Flight Mechanics;* M. H. Smith, *Princeton University, Technical Literature Digest*

ASSISTANT EDITORS

Carol Falcetti, Norma Herrin, Carol Rubenstein

DIRECTOR OF MARKETING

Owen A. Kean

ADVERTISING PRODUCTION MANAGER

Walter Brunke

ADVERTISING REPRESENTATIVES

New York
D. C. Emery and Thomas Harford
400 Madison Ave., New York, N. Y.
Telephone: Plaza 9-7460

Los Angeles
James C. Galloway and Co.
6335 Wilshire Blvd., Los Angeles, Calif.
Telephone: Olive 3-3223

London
B. C. Nichols
151 Fleet St.
London E. C. 4, England

American Rocket Society

500 FIFTH AVE., NEW YORK 36, NEW YORK, AREA CODE 212 PE 6-6845

Founded 1930

OFFICERS

President	Harold W. Ritchey
Vice-President	William H. Pickering
Executive Secretary	James J. Harford
Treasurer	Robert M. Lawrence
General Counsel	Andrew G. Haley
Director of Publications	Irwin Hersey

BOARD OF DIRECTORS

(Terms expire on dates indicated)

Ali B. Cambel	1962	Samuel Herrick	1963
Richard B. Canright	1962	Arthur Kantrowitz	1963
William J. Cecka, Jr.	1963	A. K. Oppenheim	1961
James R. Dempsey	1961	Simon Ramo	1963
Herbert Friedman	1962	David G. Simons	1961
George Gerard	1961	John L. Sloop	1961
Robert A. Gross	1962	Martin Summerfield	1962
Abe M. Zarem	1963		

TECHNICAL COMMITTEES AND CHAIRMEN

Astrodynamics, Robert M. L. Baker, Jr.
Communications and Instrumentation, Frank W. Lehan
Electric Propulsion, Ernst Stuhlinger
Guidance and Control, James S. Farrior
Human Factors and Bioastronautics, Eugene B. Konecci
Hypersonics, William H. Dorrance
Liquid Rockets, Martin Goldsmith
Magnetohydrodynamics, Milton M. Slawsky
Missiles and Space Vehicles, William M. Duke
Nuclear Propulsion, Robert W. Bussard
Physics of the Atmosphere and Space, Herbert Friedman
Power Systems, John H. Huth
Propellants and Combustion, Peter L. Nichols, Jr.
Ramjets, William H. Avery
Solid Propellant Rockets, G. Daniel Brewer
Space Law and Sociology, Andrew G. Haley
Structures and Materials, George Gerard
Test, Operations, and Support, Bernhardt L. Dorman
Underwater Propulsion, Herman E. Sheets

Scope of ARS JOURNAL

This Journal is devoted to the advancement of astronautics through the dissemination of original papers disclosing new scientific knowledge and basic applications of such knowledge. The sciences of astronautics are understood here to embrace selected aspects of jet and rocket propulsion spaceflight mechanics, high speed aerodynamics, flight guidance, space communications, atmospheric and outer space physics, materials and structures, human engineering, overall system analysis and possibly certain other scientific areas. The selection of papers to be printed will be governed by the pertinence of the topic to the field of astronautics, by the current or probable future significance of the research, and by the importance of distributing the information to the members of the Society and to the profession at large.

Information for Authors

Manuscripts must be as brief as the proper presentation of the ideas will allow. Exclusion of dispensable material and conciseness of expression will influence the Editors' acceptance of a manuscript. In terms of standard-size double-spaced typed pages, a typical maximum length is 22 pages of text (including equations), 1 page of references, 1 page of abstract and 12 illustrations. Fewer illustrations permit more text, and vice versa. Greater length will be acceptable only in exceptional cases.

Short manuscripts, not more than one quarter of the maximum length stated for full articles, may qualify for publication as Technical Notes or Technical Comments. They may be devoted to new developments requiring prompt disclosure or to comments on previously published papers. Such manuscripts are published within a few months of the date of receipt.

Sponsored manuscripts are published occasionally as an ARS service to the industry. A manuscript that does not qualify for publication according to the above-stated requirements as to subject, scope or length, but which nevertheless deserves widespread distribution among jet propulsion engineers, may be printed as an extra part of the Journal or as a special supplement, if the author or his sponsor will reimburse the Society for actual publication costs. Estimates are available on request. Acknowledgment of such financial sponsorship appears as a footnote on the first page of the article. Publication is prompt, since such papers are not in the ordinary backlog.

Manuscripts must be double spaced on one side of paper only with wide margins to allow for instructions to printer. Include a 100 to 200 word abstract. State the authors' positions and affiliations in a footnote on the first page. Equations and symbols may be handwritten or typewritten; clarity for the printer is essential. Greek letters and unusual symbols should be identified in the margin. If handwritten, distinguish between capital and lower case letters, and indicate subscripts and superscripts. References are to be grouped at the end of the manuscript and are to be given as follows. For journal articles: Authors first, then title, journal, volume, year, page numbers; for books: Authors first, then title, publisher, city, edition and page or chapter numbers. Line drawings must be clear and sharp to make clear engravings. Use black ink on white paper or tracing cloth. Lettering should be large enough to be legible after reduction. Photographs should be glossy prints, not matte or semi-matte. Each illustration must have a legend; legends should be listed in order on a separate sheet.

Manuscripts must be accompanied by written assurance as to security clearance in the event the subject matter lies in a classified area or if the paper originates under government sponsorship. Full responsibility rests with the author.

Preprints of papers presented at ARS meetings are automatically considered for publication.

Submit manuscripts in duplicate (original plus first carbon, with two sets of illustrations) to the Managing Editor, ARS JOURNAL, 500 Fifth Avenue, New York 36, N.Y.

ARS JOURNAL is published monthly by the American Rocket Society Inc. and the American Interplanetary Society at 20th & Northampton Sts., Easton, Pa., U. S. A. Editorial offices: 500 Fifth Ave., New York 36, N. Y. Price: $18.00 per year, $3.00 per single copy. Second-class postage paid at Easton, Pa., with additional entry at New York, N. Y. This publication is authorized to be mailed at the special rates of postage prescribed by Section 132.122. Notice of change of address should be sent to the Secretary, ARS, at least 30 days prior to publication. Opinions expressed herein are the authors' and do not necessarily reflect the views of the editors or of the Society.

© Copyright 1961 by the American Rocket Society, Inc.

Recent Advances in Magnetohydrodynamic Propulsion

MEREDITH C. GOURDINE

Plasmadyne Corp.
Santa Ana, Calif.

MAN'S desire to explore space has led to the development of the chemical rocket. It is quite capable of overcoming the pull of gravity and the resistance of Earth's atmosphere; however, it can now be shown that electrical propulsion is superior to chemical propulsion for missions starting from low altitude Earth orbits. Furthermore, for certain missions in the Earth-Moon gravitational field, magnetohydrodynamic (MHD) propulsion is superior to other types of electrical propulsion, i.e., electro-thermal or ion propulsion. This fact gives impetus to those scientists and engineers striving to develop MHD propulsion systems.

Although there are a great variety of MHD propulsion devices, they all accelerate plasma (a neutral ionized gas) using the Lorentz force, which is the force exerted on a current element by a magnetic field. It is convenient to classify these devices under the following major categories: 1) series MHD propulsors; 2) shunt MHD propulsors; and 3) induction MHD propulsors. These classifications are based on an analogy with electric motors in which the plasma replaces the armature. Thus, in series MHD propulsors (sometimes called pulse or pinch engines) the current that produces the magnetic field is the same current that flows through the plasma. In shunt MHD propulsors (sometimes called J × B accelerators or crossed field accelerators) the magnet current and the plasma current are separately excited. In induction MHD propulsors, there are no electrodes in contact with the plasma (electrodeless); currents are induced in the plasma by time varying magnetic fields, which in turn interact with the applied magnetic field to produce acceleration. These three types of MHD propulsors are discussed separately in this article.

Missions for MHD Propulsors

There are many excellent articles on space missions requiring electrical propulsion, and a few references are cited that show why there is such intense interest in developing MHD propulsion in particular (1–7).[1]

Space vehicles are often described in terms of the velocity of the vehicle v, e.g., escape velocity, satellite velocity. It can be shown from simple rocket dynamics that the velocity of the rocket is proportional to the exhaust velocity of the fuel v_e. Let $\dot{M}$ be the rate at which fuel is thrown away; then the thrust is $F = \dot{M}v_e$. Applying Newton's second law $F = Mv = \dot{M}v_e$ and integrating, the following expression for velocity is obtained:

$$v = v_e \ln (M_i/M_f) \qquad [1]$$

where M_i and M_f are the initial and final masses of the rocket respectively. The rocket equation, Eq. 1, shows vividly the incentive for high exhaust velocities.

The exhaust velocity of chemical rockets is limited by the energy content of the fuel and oxidizer, but the exhaust velocity of electrical propulsion systems is limited only by the electrical power available. The power required to produce an exit velocity v_e at a thrust level F is $P = Fv_e/2$.

Electrothermal propulsors develop thrust by ejecting the electrically heated gases through a mechanical nozzle. Since the exhaust velocity is proportional to the square root of the temperature, maintaining the integrity of the nozzle becomes an almost insurmountable problem for exhaust velocities above 15,000 m/sec, or a specific impulse of 1500 sec. The specific impulse I_{sp} is the ratio of pounds of thrust to the rate of flow of gas in pounds per sec; therefore, $I_{sp} = F/Mg = v_e/g$ in seconds. Hence, for high specific impulses, it is desirable to convert the electrical power directly into kinetic energy by means of a body-force and thereby reduce the heat transfer problem. In the MHD propulsor, the Lorentz force is used, and in ion propulsors, the electrostatic force is used. Kash (44) has shown that the specific thrust T_{sp} of ion engines

Received Oct. 27, 1961.

[1] Numbers in parentheses indicate References at end of paper.

Dr. Gourdine received his B.S. in engineering physics from Cornell University in 1953 and his Ph. D. in engineering sciences from the California Institute of Technology. His doctoral thesis was a theoretical study, "Magnetohydrodynamic Flow Over Solids." He did theoretical and experimental work in magnetogasdynamics and electrogasdynamics for one year at the Ramo-Wooldridge Corp. and for two years at the Jet Propulsion Laboratory. He is presently director of the Electro and Magneto Fluid Dynamics Laboratory at Plasmadyne Corp. and is also a Senior Member of ARS.

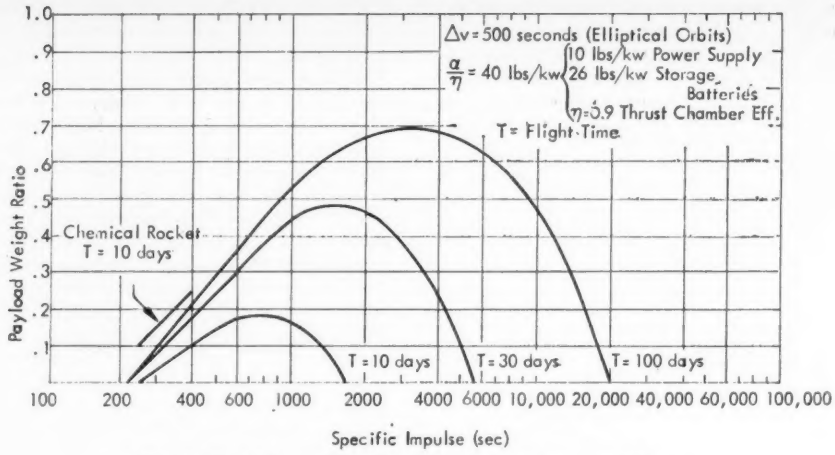

Fig. 1 Payload capability for a round trip to a lunar orbit as a function of specific impulse and flight time

will be of the order $\epsilon_0 E^2/2$, the electric pressure at the cathode, with $E \approx 10^6$ volts/m at the cathode, $T_{sp} \approx 4.4$ newtons/m^2 or 0.16 psf. The specific thrust for MHD propulsors can be of the order $B^2/2\mu$—the magnetic pressure on the plasma, with $B \approx 1$ weber/m^2, $T_{sp} \approx 5 \times 10^5$ newtons/m^2. Therefore, the T_{sp} of MHD propulsors is expected to be as much as 10^5 times as large as the T_{sp} for ion engines. The pulsed MHD propulsors may have their magnetic fields on as little as one thousandth of the total operating time; in this case the T_{sp} would still be 100 times that of the ion engine. Furthermore, the ion engine must operate with voltages high enough to draw saturation current; otherwise its efficiency is severely reduced. Since v_e is proportional to the square root of the applied voltage, there is a minimum practical specific impulse of around 7000 sec for ion rockets. It may be concluded then that electrothermal propulsors will be useful for missions requiring an I_{sp} less than 1500 sec, and ion propulsors for missions requiring an I_{sp} greater than 7000 sec. This leaves MHD propulsors as the only electrical propulsion devices capable of delivering specific impulses in the range 1500 to 7000 sec.

Camac, Kantrowitz, and Petschek (1) show that, for missions in the gravitational field of Earth and moon, the optimum specific impulses for electrical propulsors lie between 1500 and 5000 sec. This is made clear by their plot given in Fig. 1, which shows the payload capability for a roundtrip to a lunar orbit from a 150-mile Earth orbit. It shows that chemical rockets should strive for the highest I_{sp} possible in order to achieve high payload capability. However, this is not the case for electrical propulsors. Since the source of power is separate from the propellant, there is always an optimum I_{sp} for a given flight time and total weight, because, if the I_{sp} is too high, the power plant is too heavy, and if the I_{sp} is too low, the propellant is too heavy. The payload ratio is maximized when the propellant and power supply weight are minimized. This occurs when the payload and power supply weights are equal. The following simple analysis demonstrates these facts and yields the formula for optimum specific impulse vs. flight time T. Let W_T be the total weight, W_L the payload weight, W_P the weight of the power supply, and W_F the weight of the propellant; then

$$W_T = W_L + W_P + W_F \qquad [2]$$

But $W_P = \alpha F V_e/2\eta$, where α is the specific weight of the power supply and η the propulsion efficiency. Also, $W_F = MT = gTF/v_e$. Therefore

$$W_L = W_T - \frac{\alpha F v_e}{2\eta} - \frac{gTF}{v_e} \qquad [3]$$

Differentiating with respect to v_e to find the condition for maximum W_L yields the condition $W_P = W_F$ and the formula for optimum specific impulse

$$I_{sp}^* = \sqrt{(2\eta/\alpha)gT} \qquad [4]$$

Camac, Kantrowitz, and Petschek (1) also show that the use of electrical propulsion reduces the initial weight required in the 150-mile orbit by a factor of 2 or 3 below the weight required for chemical propulsion. This affects the economy by a factor of 2 or 3 in booster costs and makes electrical propulsion, in particular MHD propulsion, look very attractive for space missions in the Earth-Moon gravitational field.

Series MHD Propulsors

The propulsion devices in this category are all analogous to the series wound d-c motor in that the current through the plasma (armature) is the same current that provides the

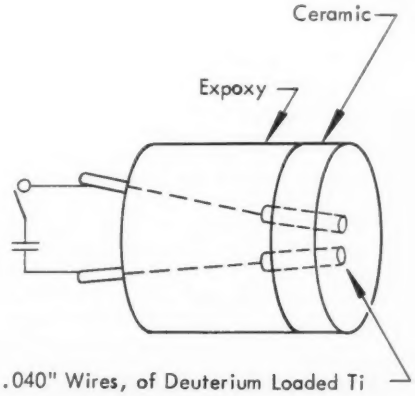

Fig. 2 Button plasma gun or source

magnetic field for acceleration. Various types of accelerators in this class have been proposed: to name a few, the Bostick button gun (8, 11), the rail gun (8, 11), the AVCO coaxial gun (8, 11, 13), the Kolb *T*-tube (8, 12), and the Republic pinch accelerator (9). The main difference between these devices is geometry, as shown by Figs. 2–6. The characteristic feature of all of these accelerators is that the magnetic field is self-induced by the current with which it interacts to produce thrust.

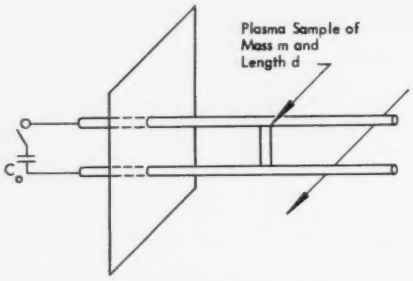

Fig. 3 Rail-type plasma accelerator or gun

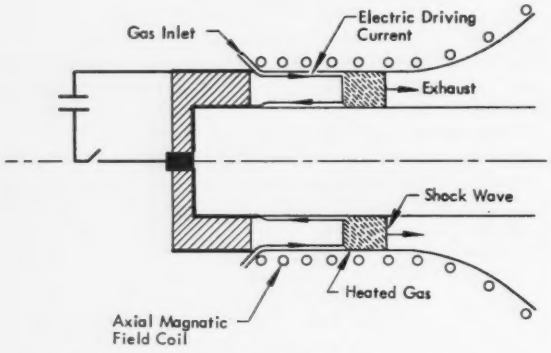

Fig. 4 Magnetic annular shock tube accelerator

Perhaps the simplest arrangement is the Bostick button gun (Fig. 2), in which the terminals of a capacitor are shorted by a fine wire. The capacitor dumps its charge through this wire, vaporizing it to form a plasma. The plasma is blown out by the magnetic pressure induced within the loop formed by the plasma, and the return leads to the capacitor bank. Bostick calls the ejected plasma loop a *plasmoid*. A slight modification is called the *rail accelerator* (Fig. 3). In this arrangement, the electrodes extend beyond the point at which they are shorted. The result is that the plasma formed out of the shorting element continues to be fed with current as it travels along the rails. In an attempt to better confine the plasma and the fields, a third modification led to the coaxial gun, in which a central and a coaxial cylinder are used as electrodes. Patrick (13) has used one version of this design to produce strong shock waves in a gas filled device (Fig. 4). The Kolb *T*-tube (Fig. 5) is another method of generating strong shock waves in a gas filled device. Other attempts to better confine the plasma and fields led Kunen (9) to a configuration called the pulsed pinch plasma accelerator (Fig. 6).

Analytical Investigations

The operation of some of these devices has been investigated analytically by Bostick (14, 15), Morozov (16), and Artsimovitch et al. (17). The differential equations describing the operation are nonlinear and do not lend themselves to analytic solutions. However, both Bostick and Morozov made certain reasonable assumptions that permit analytic solutions to the equations, and their results serve as a guide to the general behavior of these devices and in the design of experiments. Thourson (8) uses solutions of these equations generated by an analog computer to design an experimental rail gun. Kantrowitz and Janes (18) in their analysis show the importance of recovering the electromagnetic energy in the field that drives the plasma. They also derive a formula relating the minimum instantaneous power, the efficiency, and the specific impulse of devices of this type.

Experimental Investigations

The velocities reported for these devices are of the order

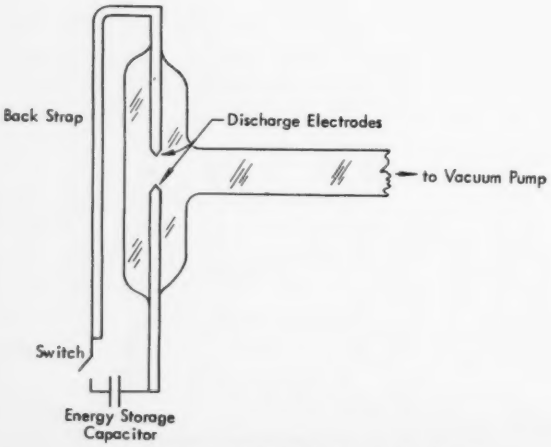

Fig. 5 Schematic drawing of Kolb's tube

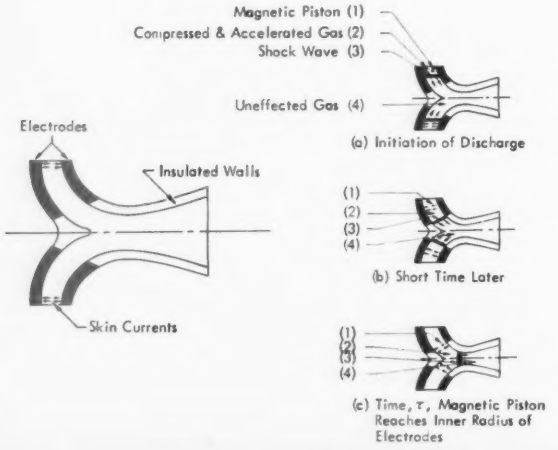

Fig. 6 Curved nozzle-electrodes

10^7 cm/sec, or a specific impulse of 10^5 sec (8, 11, 19). However, in some cases, it is the speed of the fastest particles in the discharge that is measured, and this leads to an overestimate of the specific impulse. Also, some of the ballistic pendulum measurements, designed to measure one-shot impulse and mass of propellant, may not reach the pendulum. Perhaps the best way to determine the propulsion characteristics is the method employed by Cavalaconte et al. (20). They mounted the entire pulsed pinch plasma engine on a thrust stand and measured thrust directly; the mass of propellant used was determined by weighing. Some of their performance figures on a prototype model are an average thrust of 0.01 lb at a repetition rate of 2 pulses/sec, with specific impulses above 8000 sec. The operating time logged on this engine was over 35 hr with continuous periods ranging from 15 min to more than 7 hr (20).

The devices in which the plasma is physically or magnetically contained (*T*-tube, coaxial, pinch) perform more efficiently. The button and rail guns are less efficient because the plasma expands, and the fields are less effective in producing acceleration. For example, in the Borg-Warner work (8, 21) with exploded wires and a parallel rail accelerator, the measured efficiency was less than 1%. In addition to the transverse spread of plasma, it was also suspected that the degree of ionization was small because the wire melts without vaporizing.

The main advantage of series-type MHD propulsors is the simplicity of construction (bulky magnets are not required) and inherent reliability of the accelerator components. Some of the difficulties are introducing the propellant, producing the plasma, and converting the electromagnetic energy of the fields into kinetic energy of the plasma before it leaves the device. Other problems lie in the capacitor banks and energy transfer system, and these are formidable. Pulse rates of 10^3 and 10^4 per sec are desired in order to get high thrust and to keep the weight of energy storage capacitors low; however, the highest pulse rate reported in the literature is 20 pps (10).

Undoubtedly, intensive work will continue on the development of series MHD propulsors, because they have the potential for delivering specific impulses as high as ion rockets at much higher specific thrust levels. Future developments depend strongly on advances in the development of storage capacitors and energy transfer systems.

Shunt MHD Propulsors

This type of MHD propulsion is analagous to the d-c shunt motor; the current through the plasma (armature) and the current through the magnet are separately excited. These accelerators are usually called crossed field accelerators, or J × B pumps, and are designed to run continuously. The current flowing between electrodes interacts with the perpendicular magnetic field and causes the plasma to be accelerated along the electrodes. Such a crossed field accelerator can also be constructed with cylindrical symmetry, where the electrodes are concentric cylinders and the magnetic field is coaxial. This is called the *Homopolar Device*, where the Lorentz force is tangential and the plasma is forced to rotate. The rotational kinetic energy can partially be converted into axial kinetic energy by directing the flow through a nozzle, as shown in Fig. 7 (22).

Analytical Work

The steady crossed field accelerator lends itself more easily to analytical study than the other types. Hartmann and Lazarus (23) were the first to provide theoretical and experimental results on magnetohydrodynamic channel flow of a viscous incompressible fluid. Sears and Resler (24) treated the case of compressible inviscid channel flow assuming uniform and scalar electrical conductivity. C. C. Chang (25) provided a theory for the Homopolar Device, assuming an incompressible viscous fluid with uniform scalar conductivity. Janes and Fay generalized the analysis by including the effects of temperature and seeding on conductivity (Fig. 8) and the effects of the Hall current and ion slip (26).

An appreciable Hall current flows at right angles to both the applied magnetic and electric field when $\omega_e \tau_e > 1$, because electrons actually follow curved paths between collisions. Here ω_e is the electron cyclotron angular frequency and τ_e the mean electron collision time. The flow of Hall current may be prevented by using segmented electrodes; in this case, a Hall voltage is generated instead. Some researchers consider segmented electrodes a means of reducing the losses associated with Hall currents (30, 42).

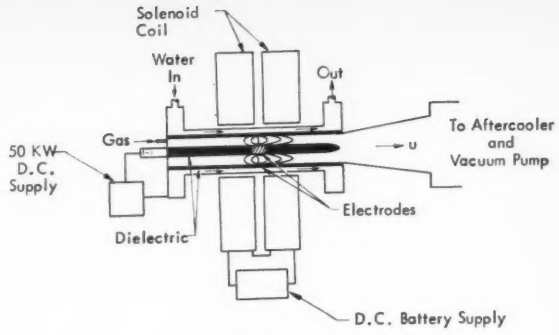

Fig. 7 Magnetic annular arc

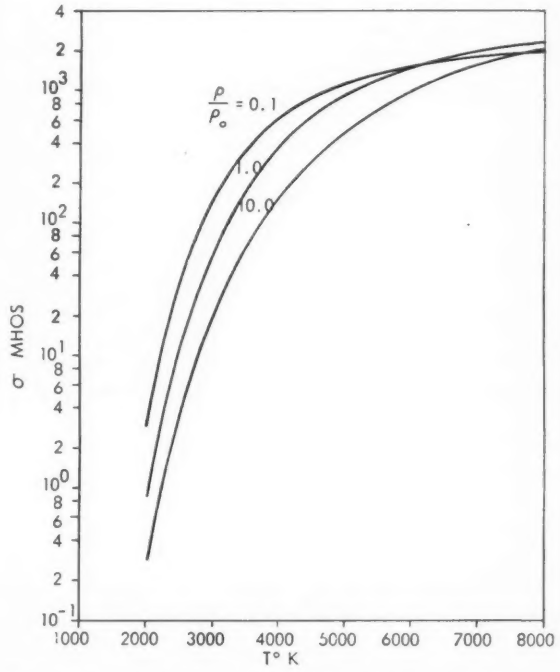

Fig. 8 Typical plot of electrical conductivity vs. temperature for a gas with 1% potassium which has a neutral atomic collision cross section, Q_a equal to 6×10^{-16} cm². The quantity ρ/ρ refers to the density relative to the density existing at °NTP

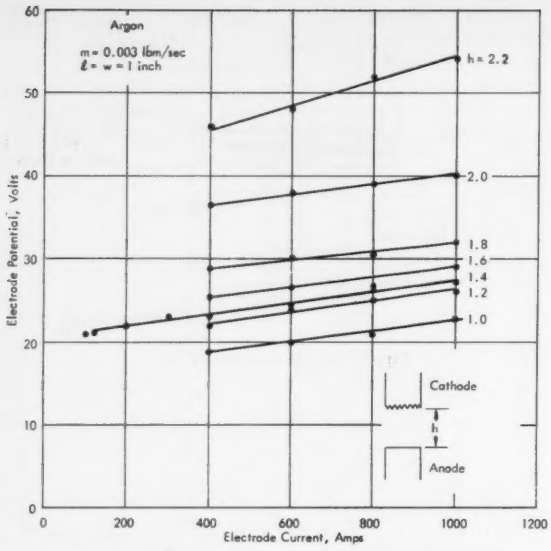

Fig. 9 Current-voltage plots for various electrode spacings across an argon thermal arc jet

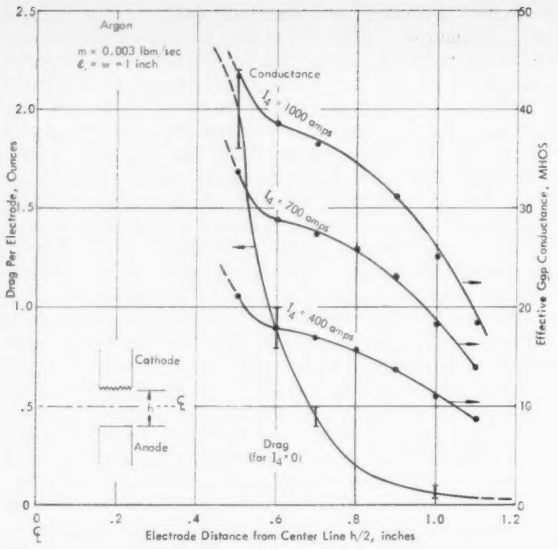

Fig. 10 Gap conductance for various electrode spacings across an argon thermal arc jet. Electrode drag is also plotted

Ion slip refers to the fact that the J × B force primarily accelerates the electrons; then, due to a slight charge separation, electrostatic fields are generated which transmit the force to the ions. The ions must then make sufficient collisions with the neutrals to accelerate the predominantly neutral gas. In certain cases of interest, the ions can acquire an appreciable velocity relative to the neutrals, and this is known as ion slip (26, 27).

Janes and Fay (26) have also derived an approximate formula for the length of a constant temperature constant area J × B accelerator

$$L = \frac{\rho_e u_e}{\sigma B^2} \frac{l}{4(\gamma M_e^2 - 1)} \qquad [5]$$

where the subscript e refers to exit conditions. They also show that there is a minimum power below which the total losses (viscous, ohmic, frozen flow, etc.) are comparable with the ideal power, and efficient operation is marginal.

Experimental Work

Although the theory leads to the correct qualitative picture, quantitatively the results can be misleading. One criticism of the theory is the assumption that the conductivity, as determined by the thermodynamic state of the gas, can be used in a simple Ohm's law. This is certainly not the case in the experimental results reported by Demetriades. He has measured the current that can be drawn across a plasma jet with various voltages and electrode spacings (Fig. 9).[2] From the slopes of these curves, he has calculated the mean conductance for various electrode gaps (Fig. 10). This plot clearly shows the strong dependence of conductance on current, which indicates that the electrical properties of the gas in the discharge depend not only on the thermodynamic state of the hot plasma jet, but also on the applied voltage or current, the nature of the electrodes, the effects of convection, and the magnetic field, when it is applied. For a spacing of 1 in. and a current of 1000 amp, Fig. 10 indicates a mean conductivity of around 800 mhos/m, without seeding. Referring to Fig. 8, this high a conductivity in an equilibrium plasma could only be achieved at temperatures above 5000°K with seeding. Demetriades did not use seeding, but the temperature of the jet was estimated to be 6400°K.

The radial distribution of momentum in the plasma jet was also determined by measuring the thrust on the electrodes for various gap widths. Fig. 10 shows the boundary of the free jet to be about 0.7-in. radius, yet the conductance of the gap remains high at 1.0 in. Thus, the electrodes can

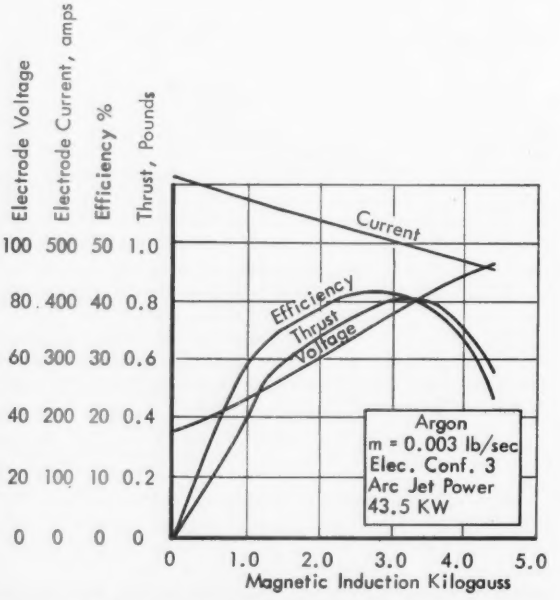

Fig. 11 Typical experimental performance of the MGD driver with argon plasma

[2] Article to be published in *Phys. of Fluids*, December 1961.

operate in the cool boundary layer and exert much less drag on the flow. Since the electrodes are observed to remain cool, it is believed that field emission is partially responsible for the large currents. This is qualitatively consistent with the results of a theoretical problem solved by J. J. Thompson (43). In this problem, current is drawn from an ionized layer analogous to the arc jet by applying a voltage between electrodes that are not in contact with the layer. The electric field in the ionized layer is found to be small, whereas the electric field at the cathode is very large. For large currents, the electric field at the cathode, due to the space charge of the ions drawn out of the ionized layer, can become high enough to cause cathode field emission. Perhaps an analysis based on this model, with generalizations to include convection and magnetic field, would shed more light on the nature of the discharge in Demetriades' experiments.

By taking advantage of these effects and others, Demetriades and Zeimer (28) have achieved the laboratory results summarized in Fig. 11. The curves represent the performance of the J × B section alone, because it is electrically and mechanically isolated from the thermal arc jet and mounted on its own thrust stand (Fig. 12). Other noteworthy experimental work is being done by Ragusa and Baker (29), who have demonstrated the importance of choosing proper electrode design in obtaining a stable discharge, and Carter, Wood, et al. (30), one of the first teams to successfully demonstrate J × B thrust. In order to maintain the Lorentz force parallel to the axis, they apply an auxiliary electric field in the axial direction. Also, by using a long array of segmented electrodes and tailoring the applied electric field, they have had some success in producing a constant temperature flow according to theoretical predictions.

With the experimental attainment of specific thrusts in the 1-psi range, at specific impulses around 1500 sec and efficiencies around 40%, there is increased interest in continuing the development of the shunt-type MHD propulsor. The next step is to increase the specific impulse by decreasing mass flow. This may have a serious effect on the characteristics of the discharge and alter the propulsion performance considerably. Since the discharge in Demetriades' work is neither an arc nor a glow, the discharge itself deserves further study.

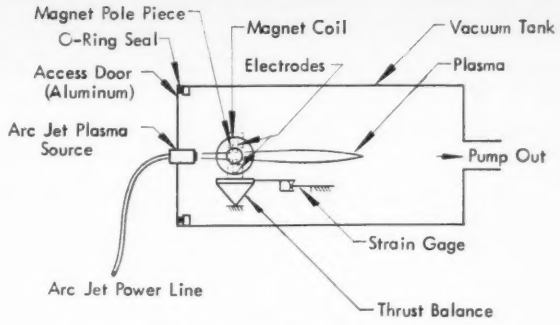

Fig. 12 Schematic diagram of experimental apparatus

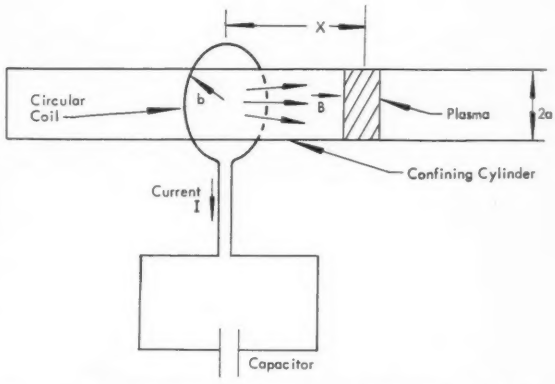

Fig. 13 Schematic diagram of system for plasma propulsion by a magnetic field

Induction MHD Propulsors

Just as the brushes of series and shunt wound motors are eroded, so are the electrodes of series- and shunt-type MHD propulsors. These effects represent a loss in efficiency, so attempts to avoid these losses have led to the investigation of electrodeless plasma accelerators. They are analogous to induction motors, because the applied time-varying magnetic fields induce currents in the plasma (armature) that in turn interact with the magnetic field to produce acceleration.

Perhaps the simplest form of an MHD induction propulsor is the one shown in Fig. 13. Here the capacitor is discharged through a single loop, and the transient magnetic field associated with this current loop induces an azimuthal electric field strong enough to ionize the gas. The azimuthal current induced in the gas interacts with the magnetic field to produce a Lorentz force radially inward and axially away from the disturbance. Thus, the plasma is compressed and propelled away from the coil. Waniek (36) uses a one-turn sheet conductor, which is conically shaped in order to drive the plasma in one direction. Other investigators use several single-turn coils timed so the discharges give the plasma several kicks as it travels down the tube. It is also possible to generate a traveling wave or magnetic piston that steadily drives the plasma down the tube (Fig. 14). In this case, the shock wave preceding the magnetic piston ionizes the gas. There are other schemes for propelling plasma bunches in which the plasma is contained by the magnetic field and does not contact the wall, e.g., Fig. 15 (38).

Analytical Work

Klein and Breuckner (39) have made a theoretical study of a plasma driven by a rapidly varying magnetic field from a single-turn coil like the one in Fig. 13. They consider the diamagnetic case (ionization process ignored) and the more complicated nondiamagnetic case, in which the processes of ionization must be considered. They show that velocities of 10^7 cm/sec may be obtained, but at low efficiencies around 5 to 10% for practical applications. Furthermore, the efficiency is affected only slightly by changes in the degree of ionization and physical parameters. The important processes occurring in the initial stages of ionization in the electrodeless discharge are described by Treat (37). Pennfold (41) provides a theoretical analysis of the problem of inductively accelerating plasma toroids along their axes. Other theoretical studies have been performed by Clauser (32), Schaffer (33), and Meyer (34, 35).

Experimental Work

Waniek (36) has measured speeds around 10^7 cm/sec of plasma blobs shot out of a conically shaped one-turn coil. He reports efficiencies on the order of 1%. A weak coupling of a continuous traveling magnetic field with a plasma has been demonstrated in the preliminary experiments of Covert and Haldeman (31). Pennfold (40) is experimenting with a pulsed approximation to a continuous traveling wave accelerator that propels pinched plasma rings along their axes.

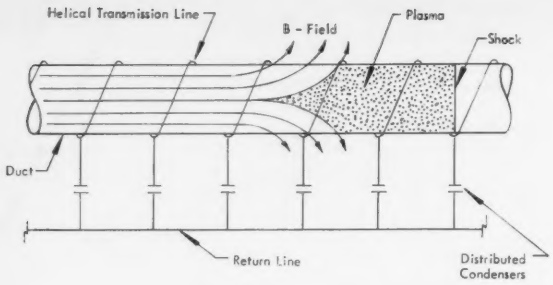

1a

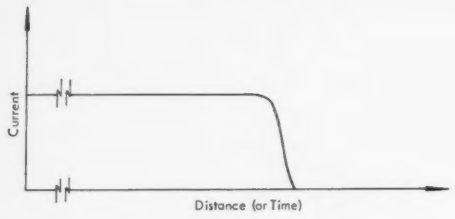

1b

Fig. 14 Magnetic piston apparatus

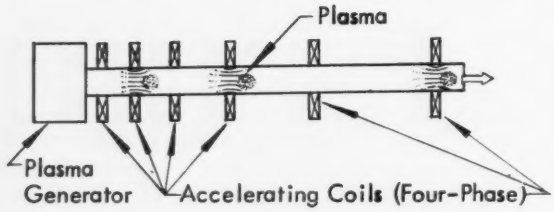

Fig. 15 A traveling wave plasma accelerator

There are 19 single-turn coils, 6-in. diam, spaced 1 in. apart on a glass tube, each of them energized at the proper time by discharging individual capacitors through individual spark gaps. His experiments are too preliminary to give propulsion possibilities, but they clearly demonstrate the possibility of forming, containing, and accelerating plasmas in a traveling electromagnetic field without electrodes or plasma contact with physical walls. Rayle (38) and S. Janes[3] of AVCO also report success in their preliminary experiments on induction-type MHD propulsors.

Conclusions

For missions in the gravitational field of Earth and moon, specific impulses in the range 1500 to 5000 sec are desired for maximum payload. The only electrical propulsion system capable of operating efficiently in this range appears to be an MHD propulsor. Furthermore, of the three types of MHD propulsors—series, shunt, and induction—the shunt-type seems most suitable. Both series and induction MHD propulsors are transient devices, and their performance to date indicates they will probably operate at specific impulses greater than 10,000 sec. On the other hand, the shunt, or crossed field MHD propulsor, provides much higher specific thrusts (1 psi) and has been operated experimentally at a specific impulse of approximately 1500 sec. Therefore, it seems that the shunt-type MHD propulsor is the ideal choice for missions in the Earth-Moon system.

For missions beyond the moon, the series- and induction-type MHD propulsors can become serious competition for the ion rocket because they also operate with specific impulses beyond 10,000 sec. However, they have one important advantage: they can potentially develop specific thrusts 100 to 1000 times as high as present day ion rockets. At present, the series-type MHD propulsor is more developed than induction-type MHD propulsors; it is almost ready for flight testing. The induction-type MHD propulsor is still undergoing intensive laboratory study, and it is too early to prognosticate on its future in electrical propulsion.

There are missions for which electrical propulsion will be needed outside of the ones mentioned here. There may be a need for small precision thrustors for vehicle control and alignment, for orbit sustainment or transfer, etc. The propulsion requirements will be different in each case; therefore, it is desirable to continue research and development on all three types of MHD propulsors. They may all prove useful.

One final question should be of concern to us all. During the preparation of this survey article, the paucity of Russian papers on this subject became quite apparent. Could this mean that in the near future a Russian satellite will be the first to successfully use electrical propulsion?

[3] Article to be published in *Phys. of Fluids*, December 1961.

References

Mission Studies and General References

1 Camac, M., Kantrowitz, A. and Petschek, H. E., "Plasma Propulsion Devices for Space Flight," *IRE Trans. on Military Electronics*, vol. MIL 3, no. 2, April 1959.

2 Elliott, D. G. and Molitov, J. H., "Thrust-Unit Requirements for Electrically Propelled Spacecraft," *Tech. Rep. no. 32-117*, Cal. Tech. Jet Propulsion Laboratory, Pasadena, Calif., June 1961.

3 Demetriades, S. T., "Magnetohydrodynamic Orbit Control for Satellites," *Electrical Engng.*, December 1960.

4 Demetriades, S. T., "Orbital Propulsion System for Space Maneuvering (PROFAC)," *Astronaut. Scien. Review*, October–December 1959.

5 Camac, M., "Plasma Propulsion of Spacecraft," ASTRONAUTICS, vol. 4, October 1959.

6 Giannini, G., "Electrical Propulsion in Space," *Scien. Amer.*, vol. 204, March 1961.

7 Slawsky, M. M., "Plasma Accelerators," *IRE Trans.*, Fifth National Symposium on Space Electronics and Telemetry, September 1960.

Series MHD Propulsors

8 Thourson, T. L., "Pulsed Plasma Accelerator," *2nd Symposium on Advanced Propulsion Concepts*, Vol. 1 (Unpublished, Confidential), Boston, Mass., October 1959.

9 Kunen, Granet, and Guman, "The Plasma Pinch Engine," *2nd Symposium on Advanced Propulsion Concepts*, Vol. 1 (Unpublished, Confidential), Boston, Mass., October 1959.

10 Kovits, B., "Plasma Accelerator for Spacecraft Control," *Space Aeronaut.*, vol. 31, March 1959, p. 57.

11 Bostick, W., "Plasma Motors," *J. Astronaut. Sci.*, vol. 5, no. 2, Summer 1958.

12 Kolb, A. C., "Production of High Energy Plasmas by Magnetically Driven Shock Waves," *Physical Review*, vol. 107, no. 2, July 15, 1957, pp. 345–350.

13 Patrick, R. M., "A Description of a Propulsion Device Employing a Magnetic Field as a Driving Force," *ASTIA No. AD 159 614*, May 1958.

14 Bostick, W., "Plasma Motors," *Conf. on Extremely High Temperatures*, May 1, 1959, John Wiley & Sons Inc., New York, pp. 404–412.

15 Bostick, W., "Plasma Motors: The Propulsion of Plasma by Magnetic Means," *IXth International Astronautical Congress*, Amsterdam, 1958, Springer-Verlag, Wein, 1959, p. 794 ff.

16 Morozov, A. I., "On the Acceleration of Plasma by a Magnetic Field," *Zh. eksper. teor, Fiz.*, vol. 32, no. 2, 1952, pp. 305–310.

17 Artsimovitch, La., Luk'ianov, S. Iu., Podgonyi, I. M. and Chuvatin, S. A., "Electrodynamic Acceleration of Plasma Bunches," *Soviet Physics-JETP*, vol. 6, no. 1, January 1958, pp. 1–5.

18 Kantrowitz, A. and Janes, G. S., "On Magnetohydrodynamic Propulsion: Electrical Characteristics of Plasma Accelerators Employing Electrodes," presented at the ARS 14th Annual Meeting, Washington, D. C., November 1959 (*ARS preprint no.* 1009-59).

19 Starr, W. C., "A Propulsive Device Using an Exploding Wire Plasma Accelerator," *Exploding Wires*, Plenum Press Inc., New York, 1959.

20 Cavalaconte, C. C., Guman, W. and Granet, I., "Experimental Studies of a Pulsed Pinch Space Engine," paper delivered at the 1961 SAE National Aeronautic Meeting on Magnetohydrodynamics, New York, Univ. of Pennsylvania, 1961.

21 Borg Warner Corp., "Pulsed Plasma Propulsion—An Advanced

Reaction Propulsion System," WADC Contract AF 33(616)6036, Final Rep., *WADC TR 59-321*, June 1959 (Secret Restricted Data).

Shunt MHD Propulsor

22 Powers, W. E. and Patrick, R. M., "A Magnetic Annular Arc," *2nd Symposium on the Engineering Aspects of Magnetohydrodynamics*, Univ. of Pennsylvania, March 1961.

23 Hartmann, J. and Lazarus, F., *Kgl. Danske Videnskab. Selskab, Mat.-fys Medd.*, vol. 15, nos. 6 and 7, 1937.

24 Resler, E. L. and Sears, W. R., "Magneto-Gasdynamic Channel Flow," *J. Appl. Math. and Phys.*, March 1958.

25 Chang, C. C. and Lundgren, T. S., "A Theory on a Homopolar Device," *UCRL-8877*, Controlled Thermonuclear Process, *TID-04500*, 15th ed., September 1959.

26 Janes, G. S. and Fay, J. A., "Magnetohydrodynamic Acceleration of Slightly Ionized, Viscously Contained Gases," *2nd Symposium on Advanced Propulsion Concepts*, Vol. 1 (Unpublished, Confidential), Boston, Mass. , October 1959.

27 Demetriades, S. T., "Operating Characteristics of Continuous MGD Engines," Part I, *ASG-TM-61-6 Tech. Mem. Astro Scien. Group*, Northrop Corp., Norair Div., Hawthorne, Calif., February 1961.

28 Demetriades, S. T. and Zeimer, R. W., "Energy Transfer to Plasmas by Continuous Lorentz Forces," paper presented at the 4th Biennial Gasdynamics Symposium on Magnetohydrodynamics, Aug. 23–25, 1961, Northwestern Univ.

29 Ragusa, D. and Baker, J., "Experimental Results with a DC Electromagnetic Plasma Accelerator," *2nd Symposium on the Engineering Aspects of Magnetohydrodynamics*, Univ. of Pennsylvania, March 1961.

30 Carter, A. F., Wood, G. P., Sabol, A. P. and Weinstein, R. H., "Experiments in Steady-state, High-Density Plasma Acceleration," *2nd Symposium on the Engineering Aspects of Magnetohydrodynamics*, Univ. of Pennsylvania, March 1961.

Induction MHD Propulsors

31 Covert, E. E. and Haldeman, C. W., "The Traveling Wave Pump," ARS JOURNAL, vol. 31, no. 9, pp. 1252–1260.

32 Clauser, M. V., "The Magnetic Induction Plasma Engine," *STL/TR-60-0000-00263*, Physical Research Laboratory, Space Technology Laboratories Inc., Los Angeles, Calif., August 1960.

33 Schaffer, A. B., "Hardness of the Axially-Symmetric Magnetic Piston," *STL/TR-60-0000-09011*, Physical Research Laboratory, Space Technology Laboratories Inc., Los Angeles, Calif., January 1960.

34 Meyer, R. X., "A Magnetohydrodynamic Model for a Two-Dimensional Magnetic Piston," *STL/TR-59-0000-0617*, Physical Research Laboratory, Space Technology Laboratories Inc., Los Angeles, Calif., March 1959.

35 Meyer, R. X., "Magnetic Plasma Propulsion by Means of a Traveling Sinusoidal Field," *STL/TR-60-0000-09114*, Physical Research Laboratory, Space Technology Laboratories Inc. Los Angeles, Calif., April 1960.

36 Waniek, R. W., "Problems of Magnetic Propulsion of Plasma," *2nd Symposium on Advanced Propulsion Concepts*, Vol. 1 (Unpublished, Confidential), Boston, Mass., October 1959.

37 Treat, R. P., "Ionization in an Electrodeless Discharge," *TN-031-655*, Contract AF 49(638)-655, ASTIA no. AD-256-216, March 15, 1961.

38 Rayle, W., "Plasma Propulsion Possibilities," *IRE Trans. on Military Electronics*, vol. MIL-3, no. 2, April 1959.

39 Klein, M. M. and Brueckner, K. A., "Plasma Propulsion by a Rapidly Varying Magnetic Field," *R59SD453*, Aerosciences Laboratory, General Electric, MSVD, December 1959.

40 Penfold, A. S., "Experimental Results Concerning the Electro-Magnetic Acceleration of Plasma Toroids," *4th Annual AFOSR Contractors Meeting on Ion and Plasma Acceleration*, Beverly Hills, Calif., April 1961.

41 Penfold, A. S., "Two-Fluid Model for the Motion of a Rarefied Plasma Accelerated by Induction," presented at the ARS 15th Annual Meeting, Washington, D. C., December 1960 (*ARS preprint no.* 1533-60).

42 Wood, G. P., Carter, A. F., Lintz, H. K. and Pennington, J. B., "A Theoretical Treatment of the Steady Flow, Linear Crossed-Field, Direct-Current Plasma Accelerator for Inviscid, Adiabatic, Isothermal Constant-Area Flow," *Tech. Rep. R-114*, Langley Research Center, Langley AFB, Va., 1961.

43 Thompson, J. J., *Conduction of Electricity through Gases*, Chap. 4, Cambridge Press, New York, 1959.

44 Kash, S. W., "A Comparison of the Specific Thrust of Ion and Plasma Drive Accelerators," *2nd Symposium on Advanced Propulsion Concepts*, Vol. 1, (Unpublished, Confidential), Boston, Mass., October 1959.

Approximate Analysis of Thrust Vector Control by Fluid Injection[1]

JAIN-MING WU[2]
ROBERT L. CHAPKIS[3]
ARTUR MAGER[4]

National Engineering Science Co.
Pasadena, Calif.

A study has been made of the side force generated by injection of secondary material into the main stream of a rocket nozzle. Two cases have been analyzed: gas injection and liquid injection. For the gas injection case, it is assumed that the turbulent boundary layer ahead of the injection point separates from the wall. The pressure in the separated region and the extent of the separated region are determined by a consideration of turbulent boundary layer-shock wave interaction and the accommodation height of the injected gas stream. Equations are derived for calculating the side force, and the side forces predicted by the theory are compared with experimental data. The agreement between theory and experiment is fair. For the case of liquid injection, it is assumed that the liquid flows along the nozzle wall and evaporates into the main stream. The resulting side force on the nozzle wall is determined on the basis of linearized theory, thus restricting the analysis to small rates of liquid injection. The effects of small rates of heat addition are also included in the analysis. A very simple equation for calculating the side force is obtained.

Presented at the ARS Solid Propellant Rocket Conference, Salt Lake City, Utah, Feb. 1–3, 1961; revision received Oct. 2, 1961.

[1] This work has been carried out for the Aerojet-General Corp., Sacramento, Calif., under Contract No. PO S-409721-OP.

[2] Member of the Technical Staff.

[3] Member of the Technical Staff. Member ARS.

[4] Assistant Director of Spacecraft Sciences, Aerospace Corp., El Segundo, Calif.; formerly Director of Sciences, National Engineering Science Co. Member ARS.

THE CURRENT demands that rocket propelled vehicles fly more precise trajectories has stimulated a search for better and more effective means of attitude control than provided by simple external aerodynamic surfaces. This is because such surfaces are effective only during the relatively short periods of time when the rocket is moving at high speed through the atmosphere. At liftoff and during much of the flight, the ineffectiveness of aerodynamic surfaces requires that control be provided by some other, more positive means.

To accomplish this, control devices that affect the direction of the exhaust jet, such as jet vanes, jetavators, and swiveling or pivoting nozzles, have been tried and proved fairly successful. Unfortunately, all such devices are subject to failures due to erosion, ablation, melting, thermal deformation, and deposits from propellants which cause interference and binding. To provide control reliability, overprotective designs are often used, resulting in heavy weight penalties.

Another method of control depends on the use of small vernier rockets to make flight path corrections. These are quite effective and have been used extensively. However, early in 1952, United Aircraft Corp. (1)[5] showed that the injection of a secondary gas stream into the exhaust cone of a supersonic nozzle resulted in the production of a side thrust. This thrust was larger than the thrust that would be developed by a comparable, simple vernier rocket using the same amount of mass flow. Hence the ratio of these thrusts was called the *magnification factor*, and its value, which was approximately two, became a convenient measure of the effectiveness of thrust vectoring by gas injection. Later tests by NOTS and Aerojet-General have shown that similar effects could also be obtained by the injection of liquids.

It should be noted here that, whereas there is a ready supply of gaseous injectant available in the primary combustion chamber (which could be tapped for the thrust vectoring), such a scheme presents considerable practical difficulties in connection with the containment and valving of the hot gas. For these reasons the injection of liquids appears considerably more attractive from the standpoint of design and reliability. Furthermore, liquids are easier to contain and distribute, and their higher densities permit smaller component parts that should result in a lighter control system. On the other hand, the forces and the specific impulse which thus far have been obtained by the injection of liquids are appreciably smaller than those attained with gas injection.

This analytical study was made to evaluate the ultimate potential and effectiveness of thrust vectoring by fluid injection.

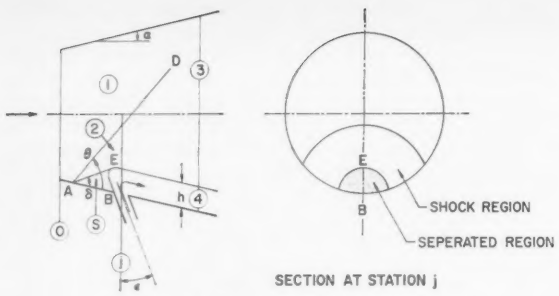

Fig. 1 Sketch of the model for gas injection

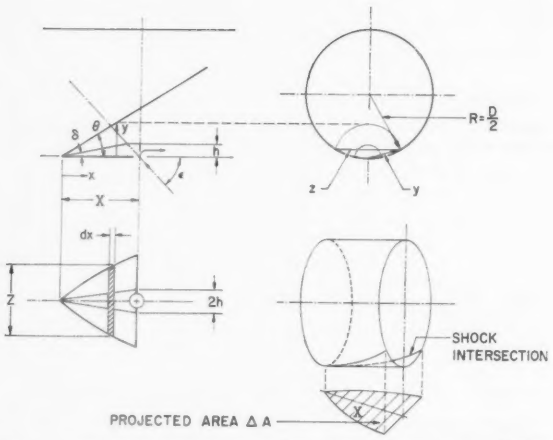

Fig. 2 Projected area of a conical shock wave in a cylinder

Gas Injection Analysis

Model Description

Gas injected from the side into a supersonic stream flowing in a three-dimensional nozzle will deflect the main stream. Thrust control by this means requires a knowledge of the interaction of the primary and secondary streams. The model postulated to describe the observed effects is shown in Fig. 1.

The primary gas stream is assumed to be flowing supersonically at station 0. It encounters the secondary stream injected through a port in the wall at station 1. As a result, the turbulent boundary layer of the primary stream is forced to separate from the nozzle wall causing shock AD to form. The shock is assumed to be conical, and the position of the vertex A depends on the main stream conditions, the injected flow rate, and the physical properties of the secondary stream.

The shock angle, separation angle, and conditions behind the shock and in the separated flow region can be determined from the upstream Mach number by the method described in (2) and extended in the Appendix. The side force results from the higher pressure behind the shock acting on the projected area of the shock and the separated region. Since the separation angle is known, the vertex A of the conical shock can be determined once the accommodation height EB is known. To determine the accommodation height it is assumed that after injection the gas makes a sharp turn and flows parallel to the wall without mixing with the main stream. Assuming for simplicity that within the region considered for the separation the nozzle is cylindrical, i.e., $\alpha = 0$, it is possible to write the following eight equations with eight unknowns:

Conservation of Mass in Primary Flow

$$\dot{m}_0 = \sqrt{\frac{\gamma_0}{R_0}}\, M_0 A_0 \frac{P_0}{\sqrt{T_{t_0}}} \left(1 + \frac{\gamma_0 - 1}{2} M_0^2\right)^{1/2} =$$

$$\dot{m}_3 = \sqrt{\frac{\gamma_0}{R_0}}\, M_3 A_3 \frac{P_3}{\sqrt{T_{t_3}}} \left(1 + \frac{\gamma_0 - 1}{2} M_3^2\right)^{1/2} \quad [1]$$

Conservation of Energy in Primary Flow

$$T_{t_0} = T_{t_3} \quad [2]$$

Streamwise Momentum Balance Between Stations 0 and 3

$$P_0 A_0 (1 + \gamma_0 M_0^2) = P_3 A_3 (1 + \gamma_0 M_3^2) + \bar{P}_s A_4 \quad [3]$$

[5] Numbers in parentheses indicate References at end of paper.

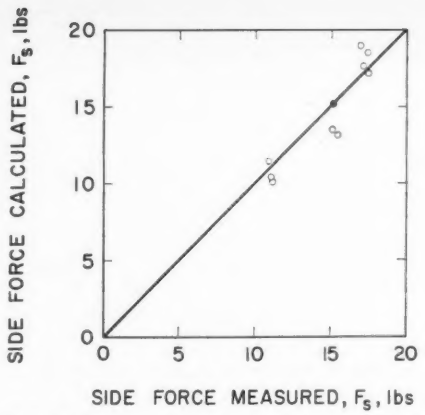

Fig. 3 Calculated vs. measured side forces for gas injection

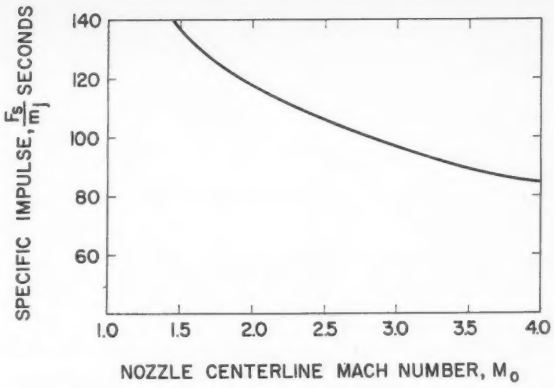

Fig. 4 Specific impulse vs. main stream Mach number holding other parameters constant for gas injection

Conservation of Mass in Secondary Flow

$$\dot{m}_j = \sqrt{\frac{\gamma_j}{R_j}}\, M_j A_j \frac{P_j}{\sqrt{T_{t_j}}} \left(1 + \frac{\gamma_j - 1}{2} M_j^2\right)^{1/2} = \sqrt{\frac{\gamma_j}{R_j}}\, M_4 A_4 \frac{P_4}{\sqrt{T_{t_4}}} \left(1 + \frac{\gamma_j - 1}{2} M_4^2\right)^{1/2} \quad [4]$$

Conservation of Energy in Secondary Flow

$$T_{t_j} = T_{t_4} \quad [5]$$

Momentum Balance of Secondary Flow in Streamwise Direction

$$\bar{P}_s A_4 = P_4 A_4 (1 + \gamma_j M_4^2) \quad [6]$$

Boundary Condition

$$P_3 = P_4 \quad [7]$$

Geometrical Relationships

$$A_0 = A_3 + A_4 \quad [8]$$

As will be shown in the next section, the average pressure $\bar{P}_s$ acting on the area A_4 behind the separated flow region can be determined once the main stream flow conditions are known. Thus, there are eight equations with the eight unknowns P_3, P_4, A_3, A_4, M_3, M_4, T_{t_3}, and T_{t_4}. The accommodation height EB on Fig. 1 can be determined once the area A_4 is solved.

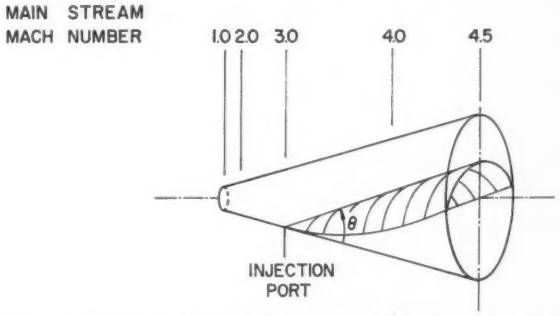

Fig. 5 Sketch of optimum location for gas injection for 15° exit cone and $\gamma = 1.2$

Derivation of Accommodation Height

After making the turn the secondary flow is assumed to take a hemi-cylindrical shape. Thus, once the cross-sectional area for the secondary flow is determined, the accommodation height h is known.

As part of the solution for the area, the average static pressure acting on area A_4 at station j must be estimated. It is known that the injected gas expands rapidly, so it is assumed that the pressure varies parabolically from the injected pressure to the separation pressure.[6] The average pressure acting on A_4 is then

$$\bar{P}_s = P_j - (2/3)(P_j - P_s) = (1/3)(P_j + 2P_s) \quad [9]$$

To solve for the area A_4, Eqs. 1, 2, 7, and 8 are employed to obtain the following equation:

$$\gamma_0^2 M_0^2 \left(1 + \frac{\gamma_0 - 1}{2} M_0^2\right) = \left[(1 + \gamma_0 M_0^2) + \left(\frac{A_4}{A_0} - 1\right)\frac{P_4}{P_0} - \frac{\bar{P}_s}{P_0}\frac{A_4}{A_0}\right] \cdot \left[\frac{\gamma_0 + 1}{2}\left(\frac{P_4}{P_0}\right)\left(1 - \frac{A_4}{A_0}\right) + \frac{\gamma_0 - 1}{2}\left(1 + \gamma_0 M_0^2 - \frac{\bar{P}_s}{P_0}\frac{A_4}{A_0}\right)\right] \quad [10]$$

As part of the solution for the area, the average static pressure acting on area A_4 at station j must be estimated. It is known that the injected gas expands rapidly, so it is assumed that the pressure varies parabolically from the injected pressure to the separation pressure.[6] The average pressure acting on A_4 is then

$$\bar{P}_s = P_j - (2/3)(P_j - P_s) = (1/3)(P_j + 2P_s) \quad [9]$$

To solve for the area A_4, Eqs. 1, 2, 7, and 8 are employed to obtain the following equation:

$$\gamma_0^2 M_0^2 \left(1 + \frac{\gamma_0 - 1}{2} M_0^2\right) = \left[(1 + \gamma_0 M_0^2) + \left(\frac{A_4}{A_0} - 1\right)\frac{P_4}{P_0} - \frac{\bar{P}_s}{P_0}\frac{A_4}{A_0}\right] \cdot \left[\frac{\gamma_0 + 1}{2}\left(\frac{P_4}{P_0}\right)\left(1 - \frac{A_4}{A_0}\right) + \frac{\gamma_0 - 1}{2}\left(1 + \gamma_0 M_0^2 - \frac{\bar{P}_s}{P_0}\frac{A_4}{A_0}\right)\right] \quad [10]$$

After making the turn the secondary flow is assumed to take a hemi-cylindrical shape. Thus, once the cross-sectional area for the secondary flow is determined, the accommodation height h is known.

As part of the solution for the area, the average static pressure acting on area A_4 at station j must be estimated. It is known that the injected gas expands rapidly, so it is assumed that the pressure varies parabolically from the injected pressure to the separation pressure.[6] The average pressure acting on A_4 is then

$$\bar{P}_s = P_j - (2/3)(P_j - P_s) = (1/3)(P_j + 2P_s) \quad [9]$$

To solve for the area A_4, Eqs. 1, 2, 7, and 8 are employed to obtain the following equation:

$$\gamma_0^2 M_0^2 \left(1 + \frac{\gamma_0 - 1}{2} M_0^2\right) = \left[(1 + \gamma_0 M_0^2) + \left(\frac{A_4}{A_0} - 1\right)\frac{P_4}{P_0} - \frac{\bar{P}_s}{P_0}\frac{A_4}{A_0}\right] \cdot \left[\frac{\gamma_0 + 1}{2}\left(\frac{P_4}{P_0}\right)\left(1 - \frac{A_4}{A_0}\right) + \frac{\gamma_0 - 1}{2}\left(1 + \gamma_0 M_0^2 - \frac{\bar{P}_s}{P_0}\frac{A_4}{A_0}\right)\right] \quad [10]$$

and Eqs. 4–6 are used to obtain

$$2\gamma_j^2 M_j^2 \left(1 + \frac{\gamma_j - 1}{2} M_j^2\right) = \left(\frac{A_4}{A_0}\right)^2 \left(\frac{A_0}{A_j}\right)^2 \left(\frac{P_0}{P_j}\right)^2 \left(\frac{\bar{P}_s}{P_0} - \frac{P_4}{P_0}\right) \cdot \left[(\gamma_j + 1)\frac{P_4}{P_0} + (\gamma_j - 1)\frac{\bar{P}_s}{P_0}\right] \quad [11]$$

Eqs. 10 and 11 may be solved graphically or numerically for the two unknowns P_4/P_0 and A_4/A_0. However, results of

[6] The form of the assumed pressure distribution is not critical; thus a linear variation could also be used. However, the parabolic variation seems more reasonable.

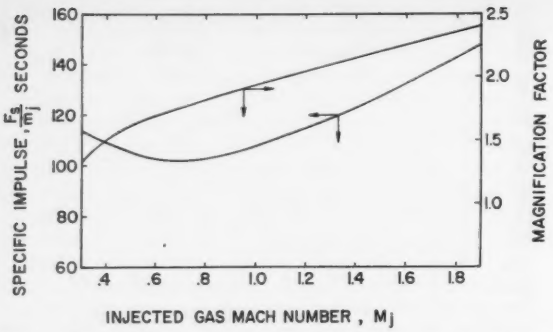

Fig. 6 Specific impulse and magnification factor vs. secondary stream Mach number for constant mass flow ratio $\dot{m}_j/\dot{m}_0$

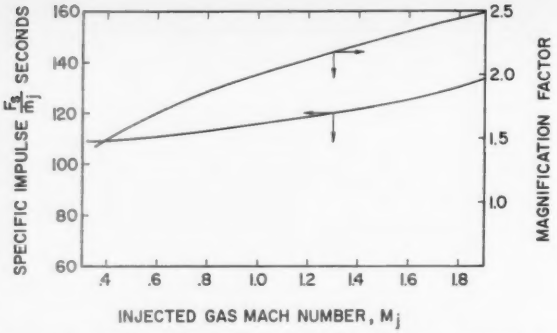

Fig. 7 Specific impulse and magnification factor vs. secondary stream Mach number for constant injection area A_j

graphical solutions show that the ratio P_4/P_0 is very nearly one, as would be expected. Thus, a good approximation for the ratio A_4/A_0 can be made by setting the ratio $P_4/P_0 = 1$ in Eq. 11. With this approximation, the accommodation height h can be solved directly

$$h = \left[\frac{2A_4}{\pi}\right]^{1/2} = \left[\frac{2A_0}{\pi}\right]^{1/2} \times \left\{\frac{2\gamma_j^2 M_j^2\left(1 + \frac{\gamma_j - 1}{2} M_j^2\right)}{\left(\frac{A_0}{A_j}\right)^2\left(\frac{P_0}{P_j}\right)^2\left(\frac{\bar{P}_s}{P_0} - 1\right)\left[(\gamma_j + 1) + (\gamma_j - 1)\frac{\bar{P}_s}{P_0}\right]}\right\}^{1/4} \quad [12]$$

Derivation of Projected Area

The area on which the pressure difference acts to cause the side force is bounded by the intersection of a shock cone with the conical wall of the nozzle. For simplicity and consistency with our ideal model, the projected area bounded by a shock cone and a cylinder has been used in this analysis. This simplification is valid as long as the nozzle cone angle is small.

The centerline through the injection port was selected as the reference for calculating the projected area, as is shown in Fig. 2. The distance X is the distance from the vortex of the shock to the center of the injection port and depends not only on the separation angle and the accommodation height, but also on the angle of injection ϵ

$$X = h[\cot\delta + \tan(\alpha + \epsilon)] \quad [13]$$

The dimension z is the common chord between the cone and cylinder needed to calculate the projected area. The radius of the shock cone is y and the radius of the cylinder $R = D/2$.

From the geometry and some trigonometric manipulation, the expression for z may be written in the following form:

$$z = y\sqrt{4 - (y/R)^2} \quad [14]$$

Thus the projected area can be calculated by integration as

$$\Delta A = \int_0^X z\,dx = \int_0^{X\tan\theta} \frac{z}{\tan\theta}\,dy = \frac{2D^2}{3\tan\theta}\left\{1 - \left[1 - \frac{X^2\tan\theta}{D^2}\right]^{3/2}\right\} \quad [15]$$

Since $(y/D)^2 = (X^2\tan^2\theta/D^2) \ll 1$, further simplification is possible by expanding Eq. 15 into a series and omitting the higher order terms

$$\Delta A = X^2\tan\theta[1 - (1/4)(X^2\tan^2\theta/D^2) + \ldots] \cong X^2\tan\theta = h^2[\cot\delta + \tan(\alpha + \epsilon)]^2\tan\theta \quad [16]$$

Once this projected area is determined, the side force can be computed.

Equation for Side Force

It is assumed for this model that downstream of the injection port there is no contribution to the side force, as any forces present in this region balance one another. Obviously this is an oversimplification. The interaction of the conical shock with the nozzle wall will certainly result in a reflection of the shock. The flow patterns and pressure distributions in this region are very complex and difficult to predict. It is known, however, from limited experimental data (3) that the secondary gas tends to overexpand. This overexpansion tends to cancel any pressure increases due to shock reflection from the walls, and thus the above assumption is made.

An exception to this cancellation occurs once the intersection of the conical shock wave and the nozzle wall passes above the centerline of the nozzle. Beyond this point the shock reflection from the nozzle walls may be expected to reduce the net side force. The present analysis does not include such situations.

Within these limitations, then, it is assumed for this model that the side force produced by the injection of gas is the sum of three components. The first results from the pressure increase in the separated region. The second is due to a similar increase occurring between the shock and the separated region. The pressure in this region is assumed to vary parabolically between the pressure in the separated region P_s and the pressure just behind the shock P_2. As shown in the Appendix, the average pressure can be calculated by

$$\bar{P}_2 = P_s - (1/3)(P_s - P_2) \quad [17]$$

Finally, the third component is due to the momentum of the injected gas.

The equation for the side force perpendicular to the axis of the nozzle can now be written as

$$F_s = [(P_s - P_0)(Xh - A_j/2)\cos\alpha] + [(\bar{P}_2 - P_0)(\Delta A - Xh)\cos\alpha] + [(P_j - P_0)A_j\cos\epsilon + m_j v_j]$$

where V_j is perpendicular to the axis of the nozzle. Or rewriting

$$F_s = [(\bar{P}_2/P_0 - 1)(\Delta A - Xh) + (P_s/P_0 - 1)(Xh - A_j/2)]P_0\cos\alpha + P_0A_j\cos\epsilon(P_j/P_0 - 1) + \dot{m}_j v_j \quad [18]$$

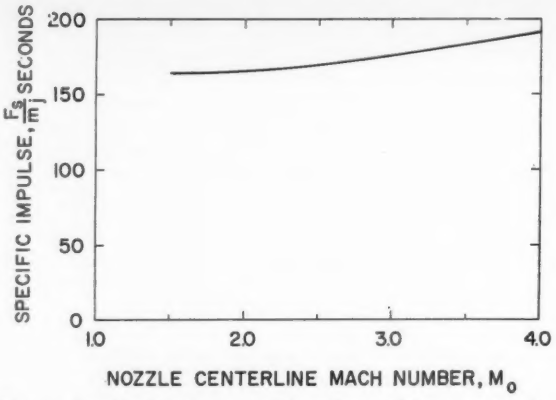

Fig. 8 Specific impulse vs. main stream Mach number for limiting condition $P_j = P_s$

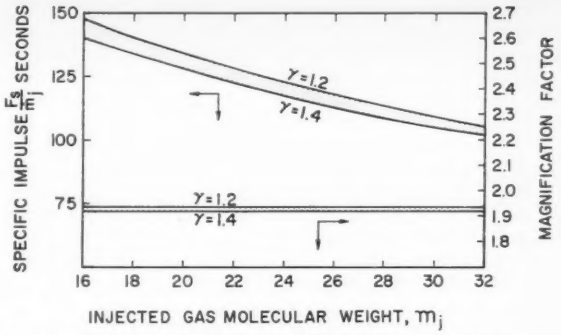

Fig. 9 Specific impulse and magnification factor vs. injected gas molecular weight m_j

Thus the side force can be calculated using Eqs. 12, 13, 16, and 18.

Comparison With Tests

The analytical model has been compared with the results of tests conducted by the U.S. Naval Ordnance Test Station at China Lake. The NOTS data (4) used here are corrected and were obtained by correspondence with the author.

Using the conditions of the tests, side forces have been calculated using the equations developed by the analysis. The available data are in part incomplete, for not all of the variables have been measured. Also, the tests are for a limited range of some of the variables, and so the role of these variables in the equations could not be thoroughly verified.

Calculated side forces have been plotted against the measured side forces in Fig. 3, and, as can be seen, the agreement between the experiment and theory is good. The experimental magnification factor for these tests is about 1.6.

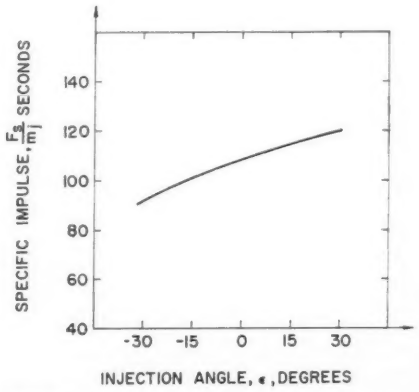

Fig. 10 Effect of injection angle on specific impulse for gas injection

Effect of Parameters

In order to determine the optimum conditions for thrust vectoring by gas injection, a controlled variation of the various parameters entering into the analysis has been made. The first parameter studied was the main stream Mach number M_0, corresponding to different injection stations downstream of the throat. Holding all other parameters constant, the specific impulse $F_s/\dot{m}_j$ for the injected gas is plotted vs. M_0 in Fig. 4. Note that the specific impulse decreases as M_0 increases. This is because the static pressure decreases faster with increasing Mach number than the projected area ΔA increases. Thus it would seem that the gas should be injected at as low a M_0 as possible.

However, as mentioned in the model description previously, once the conical shock wave starts reflecting above the centerline of the nozzle wall, an unbalanced negative side force will result. Therefore, it may be expected that under these conditions there exists an optimum location for gas injection such that the conical shock wave just reaches the centerline of the nozzle wall. A sketch of such a situation showing the optimum location of the injection port for a nozzle that expands to $M_0 = 4.5$ is given in Fig. 5. Observe that for this nozzle the injection should be made at about $M_0 = 3.0$.

On the other hand, if all the parameters except the injected stream Mach number M_j are held constant, the specific impulse is found to increase as M_j increases. There are two ways M_j can be varied. Either the mass flow ratio $\dot{m}_j/\dot{m}_0$ or the port area A_j can be varied while holding the other constant. Both ways give the same trends shown in Figs. 6 and 7. Both ways then suggest injecting the gas supersonically at the highest possible M_j to get the best performance.

There is an interrelation between M_j and M_0 that must be considered. The M_j can only be increased to the point where the static pressure of the injected stream equals the separation pressure. Using the maximum values of M_j thus obtained, the specific impulse was found to increase for increasing M_0. This is shown in Fig. 8. Consequently it appears that, if the injection Mach number is properly adjusted, the best location for injection occurs as far downstream as possible.

The third parameter investigated was the variation of molecular weight of the injected gas. In Fig. 9, it can be seen that neither the molecular weight nor the specific heat ratio appreciably alter the magnification factor. On the other hand, the lighter the molecular weight, the higher will be the specific impulse. This suggests that the injection gas should have a low molecular weight.

The final parameter investigated was the angle with which the gas is injected into the main stream. The analytical model supposes two opposing effects to exist. The first causes the side force to decrease as the angle increases, due to the reduced momentum perpendicular to the nozzle axis.

The second causes the side force to increase, due to an increased projected area over which the separation pressure acts. The model assumes that the accommodation height h remains unchanged by the injection angle, whereas the vertex of the shock moves forward by an amount determined by $h \tan (\alpha + \epsilon)$. The effect on the specific impulse of varying the injection angle is shown in Fig. 10. As can be seen, the greater the injection angle, the higher will be the side force. It must be cautioned that the steeper the injection angle, the greater the viscous effects are apt to be, causing the flow to be considerably different from the assumed model. The trends indicated in Fig. 10 still show that the injection in the upstream direction is desirable. It should be noted that the purpose of Figs. 3–10 is to indicate the trend of the effects of the various parameters. By no means should these figures be taken as representative of the best performance achievable.

Discussion of Port Geometry

The assumed model uses a circular port for the injection of the gas. It might be asked whether or not this is the best geometry to obtain optimum performance. As a crude attempt to answer this, it was assumed that a slot sufficiently long to minimize edge effects is used. The problem can then be treated as two-dimensional, and it was found that such a change results in an improvement of the side force.

Due to structural problems, it might be easier to arrange a series of holes perpendicular to the nozzle axis to simulate a slot. The analysis of the interaction produced by injection from several holes is extremely complex and was not undertaken.

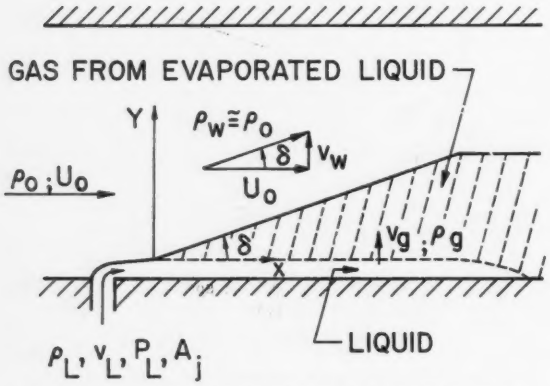

Fig. 11 Two-dimensional flow model for liquid injection

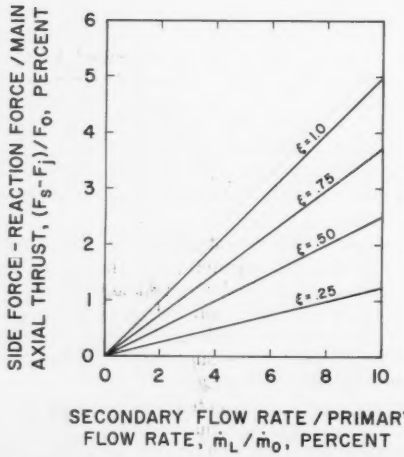

Fig. 12 Computed side force vs. mass flow rate and evaporation ratio for a typical case

Liquid Injection Analysis

Model Description

Injecting a liquid rather than a gas into the main stream of a supersonic nozzle also creates a side force. However, the physical mechanism causing the side force is different, and so a different model has been proposed. Fig. 11 is a sketch of the model indicating the symbols used.

The model assumes that, upon injection, the liquid immediately makes a turn and flows along the nozzle wall. Mass enters the main stream as the liquid evaporates. Thus, a uniform distribution of sources can be imagined to exist along the length of the liquid-gas surface. The mass addition from these sources is

$$\dot{m}_g = \rho_g V_g A_g \qquad [19]$$

where v_g is assumed to be a constant velocity, ρ_g the density, and A_g the area of the gas-liquid interface. It is assumed that the mass addition rate is low enough for supersonic linear small perturbation theory to be valid.

Derivation of Side Force

The linearized theory indicates that the assumed uniformly distributed sources are equivalent to a wedge of half angle $\delta = V_w/U_0$. The pressure coefficient for the wedge is given by

$$C_p = \frac{P - P_0}{(1/2)\rho_0 U_0^2} = \frac{2\delta}{\sqrt{M_0^2 - 1}} = \frac{2}{\sqrt{M_0^2 - 1}} \left(\frac{V_w}{U_0}\right) \qquad [20]$$

The velocity V_w can be found by expanding ρV in a Taylor series about $y = 0$

$$(\rho V)_{y=y_w} = (\rho V)_{y=0} + \left(\frac{\partial \rho V}{\partial Y}\right)_{y=0} Y_w + \ldots \qquad [21]$$

Since the value ρU does not depend on x, the continuity equation says

$$\left(\frac{\partial \rho V}{\partial y}\right)_{y=0} = -\left(\frac{\partial \rho U}{\partial x}\right)_{y=0} = 0 \qquad [22]$$

Thus

$$(\rho V)_{y=y_w} \cong (\rho V)_{y=0} \qquad [23]$$

and

$$V_w \cong \frac{\rho_g}{\rho_w} V_g \cong \frac{\rho_g}{\rho_0} V_g \qquad [24]$$

Substituting back for the pressure coefficient

$$C_p = \frac{P - P_0}{(1/2)\rho_0 U_0^2} \cong \frac{2}{\sqrt{M_0^2 - 1}} \left(\frac{\rho_g}{\rho_0}\right) \frac{V_g}{U_0} = \frac{2}{\sqrt{M_0^2 - 1}} \cdot \frac{\dot{m}_g}{\rho_0 U_0 A_g} \qquad [25]$$

Thus the force perpendicular to the nozzle wall due to gas vaporizing is

$$F = (P - P_0) A_g = \dot{m}_g U_0 / \sqrt{M_0^2 - 1}$$

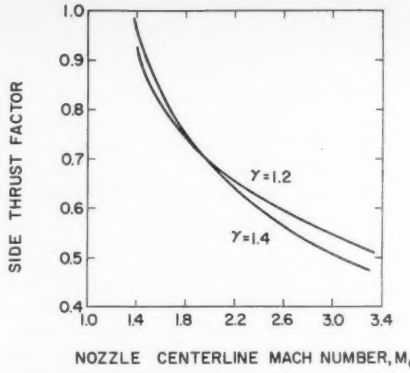

Fig. 13 Side thrust factor for liquid injection vs. nozzle centerline Mach number

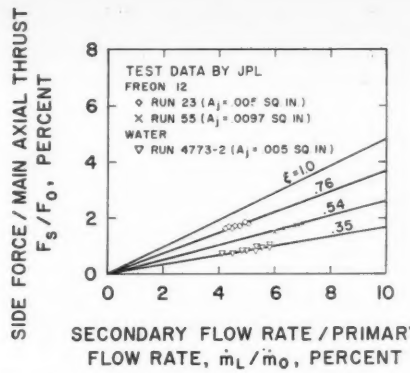
SIDE FORCE / MAIN AXIAL THRUST
Fs / F0, PERCENT
TEST DATA BY JPL
FREON 12
◇ RUN 23 (Aj = .007 SQ IN.)
× RUN 55 (Aj = .0097 SQ IN.)
WATER
▽ RUN 4773-2 (Aj = .005 SQ IN.)
ξ=1.0
.76
.54
.35
0 2 4 6 8 10
SECONDARY FLOW RATE / PRIMARY FLOW RATE, ṁL / ṁ0, PERCENT

Fig. 14 Comparison of theory with test data of (5)

and the component of this force perpendicular to the nozzle centerline is

$$(P - P_0)A_g \cos \alpha = \frac{\dot{m}_g U_0}{\sqrt{M_0^2 - 1}} \cos \alpha \qquad [26]$$

where α is the nozzle half angle.

In addition to the force produced by the vaporization of the liquid, there is the force due to the momentum of the liquid jet

$$F_j = [\dot{m}_L V_L + (P_L - P_0)A_j] \cos \epsilon \qquad [27]$$

where ϵ is the injection angle measured from the perpendicular to the nozzle centerline. The expression for the side force is the sum of these forces

$$F_s = \frac{\dot{m}_g U_0}{\sqrt{M_0^2 - 1}} \cos \alpha + F_j \qquad [28]$$

Thus, for the range of conditions that meet the limits of the linearized theory, the side force can be determined directly.

It is convenient to express side force in terms of mass flow ratios and the fraction of the fluid vaporized ξ

$$F_s = \frac{2}{\sqrt{M_0^2 - 1}} q_0 A_0 \frac{\xi \dot{m}_L}{\dot{m}_0} \cos \alpha + F_j \qquad [29]$$

where $q_0 = (1/2)\rho_0 U_0^2$. A typical plot of the above computed side force as a function of the amount of liquid injected and for various values of evaporation ratio is shown in Fig. 12. A side force factor can be defined that is a function of γ and M_0 only

$$\left(\frac{F_s - F_j}{P_{t_0} A_0^*}\right)\left(\frac{\dot{m}_0}{\xi \dot{m}_L}\right) \sec \alpha = \frac{2}{\sqrt{M_0^2 - 1}} \left(\frac{q_0}{P_{t_0}}\right)\left(\frac{A_0}{A_0^*}\right) \qquad [30]$$

Curves of the side force factor vs. M_0 for $\gamma = 1.2$ and $\gamma = 1.4$ have been plotted in Fig. 13. Notice that the side force factor decreases as the main stream Mach number increases.

The side force factor defined in Eq. 30 can also be written for $\xi = 1$, that is, for complete vaporization, as

$$\frac{F_s - F_j}{P_{t_0} A_0^*}\left(\frac{\dot{m}_0}{\dot{m}_j}\right) \sec \alpha = \frac{\dot{m}_0}{P_{t_0} A_0^*}\left(\frac{F_s}{\dot{m}_j} - \frac{F_j}{\dot{m}_j}\right) \sec \alpha = \frac{\dot{m}_0}{P_{t_0} A_0^*} (I_{sp} - I_{spj}) \sec \alpha \qquad [31]$$

For the injection of liquids, $F_j \ll F_s$, so $I_{spj} \ll I_{sp}$ resulting in F_s being proportional to I_{sp} for constant free stream conditions.

Comparison With Experimental Tests

The side force computed by use of Eq. 29 was compared with some of the applicable experimental data of (5) in Figs. 14 and 15. These experiments, which were carried out in two different nozzles and for Freon 12 as well as for water, offer only a very limited confirmation of the present results. This is because the amount of the liquid that is evaporated in each case cannot be ascertained with any degree of confidence. Still, as the comparison shows, the general trends of the experimental data are nearly linear, thus lending strong support to the validity of the present approach. Furthermore, Freon 12, which has the lower heat of evaporation (and is thus more likely to have ξ values near unity), shows a performance which is much better than that for water.

Effect of Parameters

The analytical model for liquid injection has been studied in order to determine the optimum conditions within the limits of the linearized theory. If the total pressure, the mass flow ratio, and the force contributed by the momentum of the jet are held constant, the side force decreases as the main stream Mach number increases. This would suggest that liquid should be injected as near the throat as practical. From Fig. 13 it can further be seen that the specific heat ratio γ does not materially affect the side thrust. Although not directly indicated by the model, it is implied by the assumption of complete vaporization that the heat of vaporization should be low.

Effect of Heat Addition

The linearized theory can be extended to include the added effect of low rates of heat addition. Willmarth (6) has shown the existence of an analogy between heat sources and fluid sources, and he has used this to determine the aerodynamic forces produced by distributed heat sources on the external surfaces of aircraft.

The analogy states that the effect of a heat source is equivalent to that of a fluid source when

$$\frac{(\gamma - 1)\dot{Q}}{a_0^2 A} = \frac{\dot{m}}{A} \qquad [32]$$

where $\dot{Q}$ is the rate of heat addition, and a_0 is the speed of sound.

Thus the additional upwash due to a uniform distribution of heat sources is given by

$$\left(\frac{V}{U_0}\right)_{heat} = (\gamma - 1)\frac{Q}{\rho_0 a_0^2 U_0 A} \quad [33]$$

so that the pressure coefficient is

$$(C_p)_{heat} = \frac{2}{\sqrt{M_0^2 - 1}}\left(\frac{V}{U_0}\right)_{heat} = \frac{2(\gamma - 1)}{\rho_0 U_0 A \sqrt{M_0^2 - 1}}\frac{Q}{a_0^2} \quad [34]$$

and the added side force due to heat addition is

$$(F_s)_{heat} = [(P - P_0)A]_{heat}\cos\alpha = \frac{\gamma - 1}{U_0}\frac{M_0^2}{\sqrt{M_0^2 - 1}}\dot{Q}\cos\alpha \quad [35]$$

Discussion and Conclusions

1 Two analytical models have been developed for the analysis of the side force generated by injection of secondary material into the main stream of a rocket nozzle. The first model is applicable to the case of gas injection and the second to low rates of liquid injection.

2 For the gas injection case, the magnification factor and side force predicted by the model agree fairly well with available experimental data, although more data are needed to verify in detail the individual parameters contained in the model. The analysis showed that for maximum specific impulse, the injection port should be located as far downstream as possible, with the Mach number of the injected gas as high as possible. In addition, the gas should be injected in an upstream direction. The magnification factor is practically independent of the injected gas specific heat ratio or molecular weight, but the specific impulse does go up as the molecular weight is decreased.

3 For the liquid injection case, the postulated model should be valid only for low mass flow rates, as linearized theory was used. For maximum specific impulse with liquid injection, the fluid should be injected as far upstream as possible, and the heat of vaporization of the liquid should be low enough to insure complete and even evaporation. Additional side force can be obtained if an exothermic reaction occurs between the injected liquid and the primary gas.

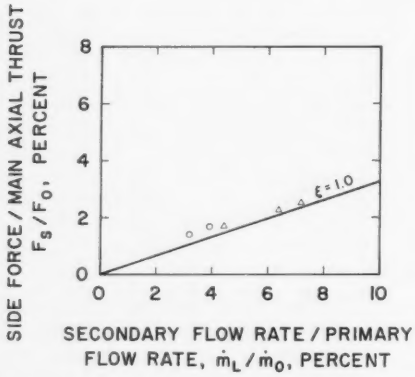

Fig. 15 Comparison of theory with test data of (5)

Appendix

Conical Shock Separation Analysis

The model used for the analysis to predict thrust by gas injection depends on a knowledge of the required pressure ratio across the shock to cause the boundary layer to separate. For two-dimensional flow, it has been shown that this pressure ratio is mostly a function of the upstream Mach number (2) for a given value of the specific heat ratio. The analysis has been extended for three-dimensional conical shocks with $\gamma = 1.2$ and $\gamma = 1.4$.

The basic assumption for the extension is that the pressure ratio at the outer boundary of a conical separated region required for separation is the same as that for the two-dimensional case. With this assumption, it is possible to determine the angles for the conical shock from charts and tables given in (7). To determine conical shock angles for other γ, it is necessary to make correction of the above solution by methods presented in (8).

The results are shown in Figs. 16 and 17 for $\gamma = 1.2$ and $\gamma = 1.4$ respectively. The pressure ratio for separation P_s/P_0 increases as the main stream Mach number increases. In addition, an estimate of the average pressure ratio $\bar{P}_2/P_0$ is shown. The average pressure $\bar{P}_2$ that acts between the shock and the separated region is calculated by assuming that the pressure varies parabolically in this region.

$$\bar{P}_2 = P_s - (1/3)(P_s - P_2)$$

The shock angle θ and the angle of separation δ are also plotted on the figures.

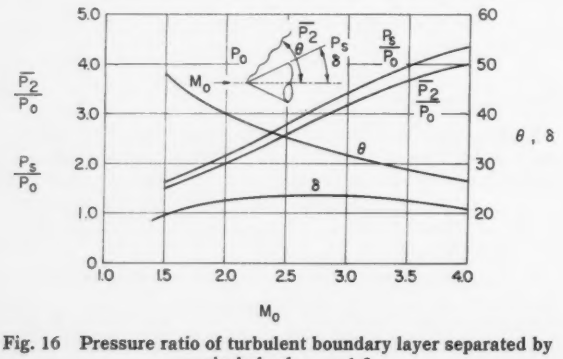

Fig. 16 Pressure ratio of turbulent boundary layer separated by conical shock $\gamma = 1.2$

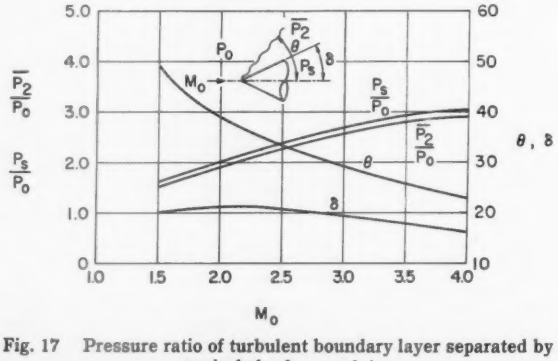

Fig. 17 Pressure ratio of turbulent boundary layer separated by conical shock, $\gamma = 1.4$

Acknowledgment

The authors would like to express their appreciation to F. E. Marble, J. M. Chenoweth, O. J. Demuth, and S. A. Lorenc for their valuable criticism and stimulating discussions.

Nomenclature

A_0^* = throat area of main nozzle
a = speed of sound
D = diameter of nozzle at injection station
I_{sp} = specific impulse of injected fluid
M = Mach number
m = molecular weight
P = pressure

Subscripts

0 = primary flow before separation
1 = primary flow at injection port station
2 = region behind shock wave
3 = primary flow downstream of injection port
4 = secondary flow downstream of injection port
g = gas from evaporated liquid
j = secondary flow at injection port
L = liquid
s = separated region
t = stagnation or total condition
w = surface of wedge in linearized theory

References

1 Hausmann, G. F., "Thrust Axis Control of Supersonic Nozzles by Airjet Shock Interference," *United Aircraft Corp. Dept. Rep. R-63143-24*, May 2, 1952.
2 Mager, A., "On the Model of the Free, Shock-Separated, Turbulent Boundary Layer," *J. Aeronaut. Sci.*, February 1956, vol. 23, pp. 181–184.
3 Bankston, L. T. and Barnes, G. G., "Gas Injection Thrust Vectoring," *NOTS Rep. IDP 662*, China Lake, July 23, 1959.
4 Bankston, L. T. and Larsen, H. M., "Thrust Vectoring Experiments with Gas Injection," *NAVORD Rep. 6548*, China Lake, May 1959.
5 Newton, J., "Secondary Injection for Thrust Vector Control," *Research Summary no. 36-9*, Vol. I, JPL, Pasadena, Calif., July 1961, pp. 90–96.
6 Willmarth, W. W., "The Production of Aerodynamic Forces by Heat Addition on External Surfaces of Aircraft," *Rand Corp. Research Mem. RM-2078*, Dec. 30, 1957.
7 Ames Research Staff, "Equations, Tables, and Charts for Compressible Flow," *NACA TR 1135*, 1953.
8 Hammitt, A. G. and Murthy, K. R. A., "Approximate Solutions for Supersonic Flow over Wedges and Cones," *AFOSR TN 59-304, Rep. 449*, Princeton Univ., April 1959.

Theoretical Performance of Propellants Suitable for Electrothermal Jet Engines

JOHN R. JACK[1]

NASA Lewis Research Center
Cleveland, Ohio

The performance of eight possible propellants for electrothermal jet engines has been evaluated theoretically. Performance characteristics are presented for enthalpies up to 200,000 Btu/lb, temperatures as high as 45,000° R, pressures ranging from 0.01 to 100 atm, and specific impulses from 500 to 2000 sec. Of the propellants studied, hydrogen and helium appear to be the best for specific impulse in the vicinity of 1000 sec. At specific impulses greater than 1600 sec, lithium becomes more efficient.

RECENT analyses of some of the more immediate space missions have indicated that a large increase in payload may be achieved by using an electrical propulsion system instead of the conventional chemical system. For missions in the gravitational field of Earth and Moon, the optimum specific impulse I_{opt} for an electric propulsion device ranges from approximately 1000 to 5000 sec, depending on the specific power plant weight α and on the desired trip time τ in days (1).[2]

$$I_{opt} = 1990\sqrt{\tau/\alpha}$$

It has been demonstrated that adequate payloads may be handled for a mission, such as the 24-hr communications satellite, with specific impulses ranging from 800 to 1500 sec (2), whereas faster trip times are obtained at the lower specific impulses. An electrothermal propulsion device that operates well over the specific impulse range from 800 to 2000 sec is the thermal arc jet. Another electrothermal device, which shows promise in the 800 to 1100 sec specific impulse range, is an engine using a resistance heated refractory metal heat exchanger.

With this interest in electrothermal propulsion devices, it is desirable to obtain the performance characteristics of potential propellants for this type of propulsion device. Some of the prime factors to be considered in the selection of a propellant are the desired specific impulse, the associated stagnation enthalpies and temperatures, and the overall engine efficiency. Of course there are other important problem areas to be considered, such as arc heating limitations and propellant storage; however, these problems are beyond the scope

Presented at the ARS 15th Annual Meeting, Washington, D. C., Dec. 5–8, 1960; revision received Sept. 18, 1961.
[1] Head, Electrothermal Section.
[2] Numbers in parentheses indicate References at end of paper.

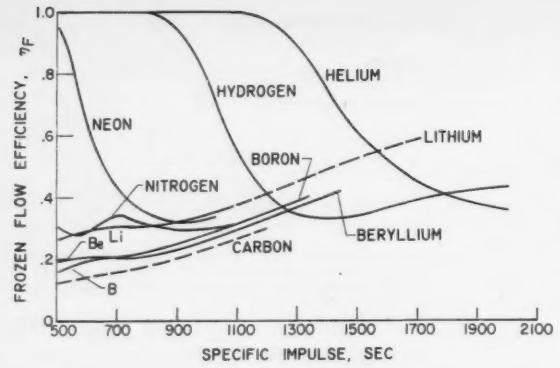

Fig. 1 Frozen flow efficiencies for various propellants; pressure, 1 atm

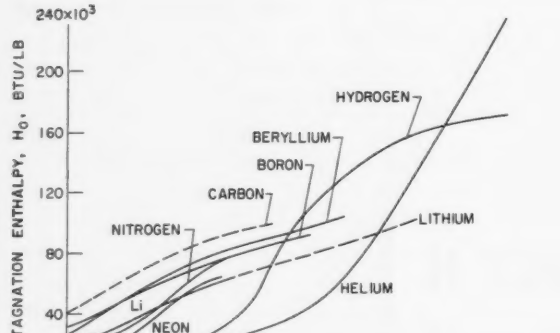

Fig. 2 Stagnation enthalpies for various propellants; pressure, 1 atm

of this paper and will not be discussed.

In this paper an analysis is given for a number of possible propellants, comparing them on the basis of the three factors mentioned in the previous paragraph.

Analysis

An electrothermal thrust generator heats the propellant electrically to a very high temperature and then expands it in a convergent-divergent nozzle. Propulsion is thus obtained by a thermodynamic process. As a result, a great deal of insight may be obtained for the selection of an appropriate propellant by considering the thermodynamics involved.

Some of the pertinent parameters that govern the efficiency of the thermodynamic propulsion process will now be considered.

Specific Impulse

The exhaust velocity of any thermodynamic propulsion system is given by

$$V_e = \sqrt{2Jg(H_0 - H_e)} \qquad [1]$$

The static enthalpy in the exit plane of the nozzle H_e is made up of the thermal energy H_T remaining in the flow because of the finite expansion ratio and the energy unavailable or frozen H_F in dissociation or ionization. With this definition, the exhaust velocity becomes

$$V_e/g = 6.95\sqrt{H_0 - H_T - H_F} \quad \text{sec} \qquad [2]$$

At this point, a simplifying assumption will be made regarding the nozzle expansion ratio. For a space environment any pressure or expansion ratio is obtainable; therefore, it will be assumed that it is large enough to make $H_T \ll H_0$. With this assumption, the specific impulse is given by

$$I_s = 6.95\sqrt{H_0 - H_F} \quad \text{sec} \qquad [3]$$

Thus, if the energy input is large, the propulsion fluid will become dissociated or ionized, and, as a result, the specific impulse will become dependent on the particular working fluid even though the stagnation enthalpy is constant (Eq. 3). That is, the energy put into the propellant goes partly into useful enthalpy and partly into ionization or dissociation, which energy may or may not be recoverable.

Considering the small thrusts and, consequently, the small nozzles associated with some of our more immediate space missions, it is unlikely that much recombination will take place. For example, exact calculations of the chemical nonequilibrium effects on a hydrogen rocket have been made (3), and the results indicate that the flow is essentially frozen. Therefore it will be assumed in this paper that the flow is frozen at the stagnation conditions, and as a result a frozen flow efficiency may be defined.

Frozen Flow Efficiency

The frozen flow efficiency η_F is defined as the ratio of the available thermal power to the total power put into the propellant

$$\eta_F = \dot{w}(H_0 - H_F)/\dot{w}H_0 = 1 - H_F/H_0 \qquad [4]$$

wherein $\dot{w}$ is the propellant flow rate. Combining Eqs. 3 and 4 yields the relation

$$I_s = 6.95\sqrt{\eta_F H_0} = 6.95\sqrt{H_a} \qquad [5]$$

To calculate the available enthalpy, the degree of dissociation or ionization is required. For the polyatomic propellants considered, the required data have been obtained from Mollier charts (4–6).

For monatomic gases, for which Mollier charts are not available, the relation between the degree of ionization, the temperature, and the pressure may be obtained from the Saha equation (7)

$$\log K_p = \log \frac{\alpha^2}{1 - \alpha^2} p_0 = -\frac{9072E_i}{T_0} + (5/2)\log\frac{T_0}{1.8} + \log\frac{2Q^+}{Q} - 6.491 \qquad [6]$$

The partition functions Q, Q^+ required in the Saha equation may be found tabulated in (8).

Having found the degree of ionization, the stagnation enthalpy and the frozen enthalpy may be derived. The enthalpy invested in ionization is

$$H_i = 41526\alpha E_i/M \quad \text{Btu/lb} \qquad [7]$$

The dissociation energy per unit weight for the diatomic gases considered is found from the same equation, except that in this case α represents the degree of dissociation and E_i the dissociation potential of the molecule.

The stagnation enthalpy for an ideal monatomic gas becomes

$$H_0 = [(5/2)(1 + \alpha)][(R/M)(T_0 - T_e)] + H_e + H_i \quad \text{Btu/lb} \qquad [8]$$

However, Eq. 8 includes the total heat required to vaporize a

propellant, and most of this heat could be recovered only if the expansion process cooled the propellant considerably below its vaporization temperature. Expansion below the vaporization temperature is not feasible, for a condensation shock could be produced which would lower the exhaust velocity. Consequently, this energy will also be assumed frozen, so that the available enthalpy becomes

$$H_a = [(5/2)(1 + \alpha)][(R/M)(T_0 - T_v) = H_0 - H_i - H_v \quad [9]$$

Eq. 5 then reduces to

$$I_s = 6.95\sqrt{(5/2)(1 + \alpha)(R/M)(T_0 - T_v)} = 6.95\sqrt{H_0 - H_i - H_v} \quad [10]$$

Or using Eq. 6

$$\alpha = \sqrt{K_p/(K_p + p)} \quad [11]$$

so that Eq. 10 becomes

$$I_s = 6.95\sqrt{\frac{5}{2}\left(1 + \sqrt{\frac{K_p}{K_p + p}}\right)\frac{R}{M}(T_0 - T_v)}$$

$$= 6.95\sqrt{H_0 - \frac{41526E_i}{M}\sqrt{\frac{K_p}{K_p + p}} - H_v} \quad [12]$$

In general, the latter form of Eq. 12 should be used to evaluate a propellant, since the heat transfer losses are governed by H_0. However, for an engine using a resistance heated refractory-metal heat exchanger, the temperature form of Eq. 12 should be used, because the heat exchanger operating temperature must be at least as high as the stagnation temperature.

Eq. 12 shows that, for operation at a given temperature, the highest specific impulse is obtained by operating at a low pressure with a low molecular weight propellant. There is no effect of K_p, since it is solely a function of temperature. On the other hand, operation at a given stagnation enthalpy requires a high pressure and a low ratio of ionization potential to molecular weight to obtain the highest specific impulse.

Overall Engine Efficiency

A parameter of particular interest is the overall engine efficiency, since it sizes the electric powerplant and determines the transit time for a space mission.

The overall engine efficiency η is defined as the ratio of jet power P_j to input power P. It may be derived immediately from its definition

$$\eta = \frac{P_j}{P} = \frac{P_j}{P_p}\frac{P_p}{P} \quad [13]$$

With the assumptions used herein the ratio P_j/P_p is equal to $H_a/H_0 = \eta_F$, and the ratio P_p/P is nothing more than a propellant heater efficiency η_p. Therefore

$$\eta = \eta_F\eta_p \quad [14]$$

Incorporated in the derivation of Eq. 14 are two assumptions: 1) the nozzle efficiency is 1; and 2) the heat transfer losses to the engine walls occur before the expansion process and are contained in the propellant heater efficiency. If the heat transfer losses are recovered through the use of a regenerative cooling system, the propellant heater efficiency becomes 1, and the overall engine efficiency approaches the frozen flow efficiency.

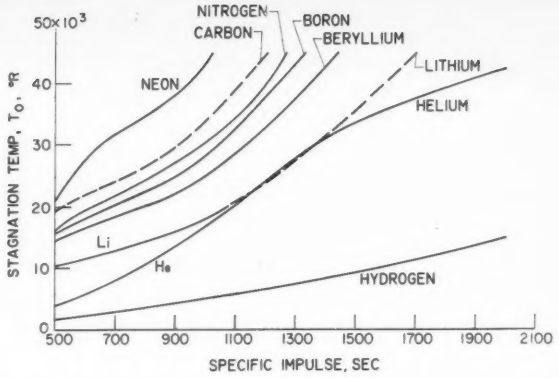

Fig. 3 Stagnation temperature for various propellants; pressure, 1 atm

Results and Discussion

The propellants to be studied are in the first part of the periodic table. Both gaseous and solid materials are considered, since a solid may be vaporized and then used as a

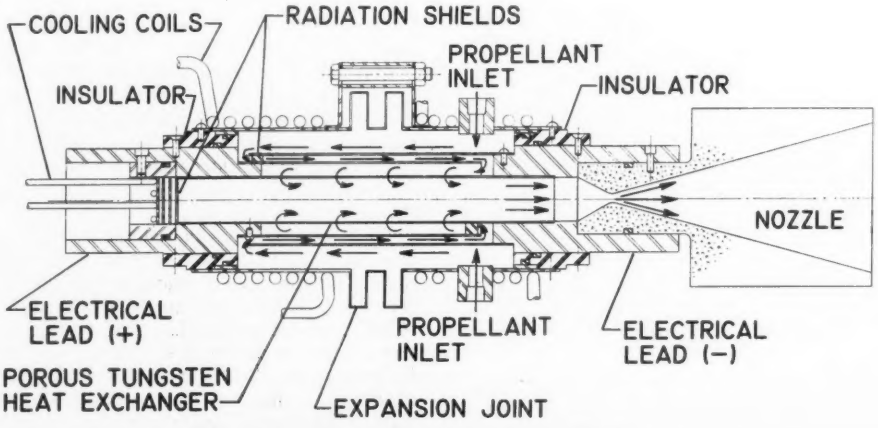

Fig. 4 Resistance heated hydrogen engine

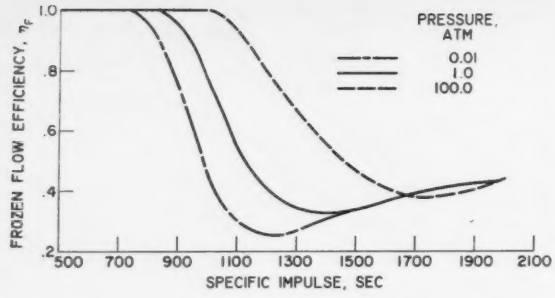

Fig. 5a Effect of pressure on frozen flow efficiency, hydrogen

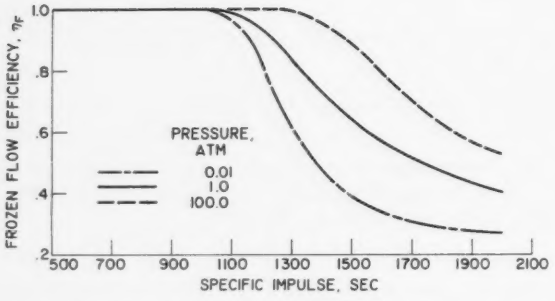

Fig. 5b Effect of pressure on frozen flow efficiency, helium

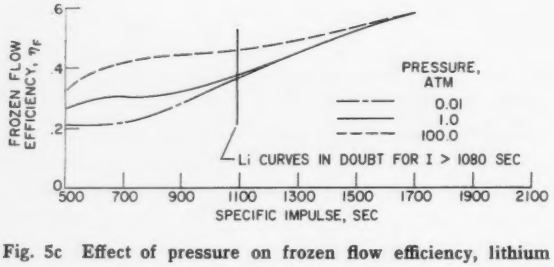

Fig. 5c Effect of pressure on frozen flow efficiency, lithium

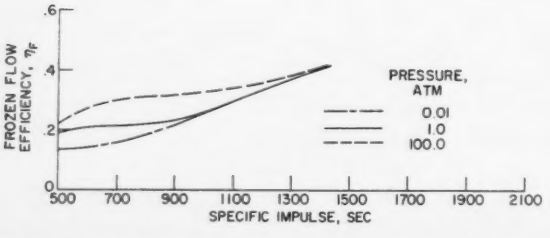

Fig. 5d Effect of pressure on frozen flow efficiency, beryllium

propellant. For example, a possible solid propellant often referred to in the literature is lithium. With this possibility in mind an arc jet could be designed having consumable electrodes, and this design would eliminate the severe electrode erosion problem of conventional arc jets.

The results of the propellant analysis to be presented cover enthalpies as high as 200,000 Btu/lb, temperatures up to 45,000° R, pressures from 0.01 to 100 atm, and specific impulses from 500 to 2000 sec.

Frozen Flow Efficiencies

The frozen flow efficiencies for the various propellants are presented in Fig. 1 as a function of specific impulse for a pressure level of 1 atm. It should be noted at this point that the curves for lithium and carbon are in doubt above a temperature level of 20,000° R ($I > 500$ and 1080 sec, respectively) because their partition functions are in doubt. As the specific impulse increases, the frozen flow efficiency decreases, because more and more energy is invested in ionization and dissociation. Finally a point is reached where the fluid is completely ionized or dissociated, and then the frozen flow efficiency begins to increase.

At a specific impulse in the neighborhood of 1000 sec, helium and hydrogen have considerably better efficiencies than any of the other fluids. At specific impulses greater than about 1600 sec, lithium appears to be more efficient than either helium or hydrogen. For example, at a specific impulse of 1700 sec, lithium has an efficiency of 0.58, whereas hydrogen has the lowest value, 0.39.

Stagnation Enthalpies and Temperatures

Unlike other electric propulsion systems, the efficiency and performance of electrothermal rockets is limited by the convective heat transfer loss from the hot propellant to the engine walls. (The assumption is made here that the radiation loss from the hot propellant is small compared to the convective heat loss. Based on current knowledge, this appears to be reasonable.) This means that ultimately engine stagnation conditions are limited by the cooling system employed; however, the final limiting factor varies with the choice of cooling system. For example, if a convective cooling scheme is used, the final limiting factor is either the maximum local heating rate or the propellant heat capacity. If radiation cooling is employed, the final limiting factor is the maximum wall temperature that can be tolerated by the engine wall material. (A detailed discussion of these limitations may be found in Ref. 9.) However, regardless of the cooling system chosen, the driving potential for the convective heat losses is at all times essentially governed by the difference between the propellant stagnation enthalpy and the enthalpy based on engine wall conditions. Therefore, because of their importance in determining convective heat losses and cooling system limitations, the stagnation enthalpies required to produce a given specific impulse are presented in Fig. 2 for the various propellants. This figure, together with Fig. 1, indicates clearly that hydrogen and helium are the best propellants for specific impulses around 1000 sec. Both propellants have high frozen flow efficiencies and low stagnation enthalpies. For specific impulses around 1700 sec, lithium again seems to be the best choice.

The equilibrium stagnation temperatures needed for the propellants considered are presented in Fig. 3 as a function of specific impulse. Note that the hydrogen stagnation temperature is at least a factor of 3 lower than any other for specific impulses greater than 1000 sec. In fact, the temperature required to produce a specific impulse of 1000 sec (5000° R) could be supplied by using a resistance heated refractory-metal heat exchanger. This approach is within the present state of the art and should result in an engine having a long reliable operating life. A specific design now being investigated

at the Lewis Research Center is shown in Fig. 4.

Effect of Pressure Level

The effect of pressure on the frozen flow efficiencies of four promising propellants is shown in Figs. 5a–5d. An increase in pressure yields an increase in frozen flow efficiency. This is expected, since an increase in pressure inhibits dissociation or ionization and thereby reduces the amount of energy tied up in the process. Even though an increase in pressure yields a better frozen flow efficiency, it should be kept in mind that the increased operating pressure may contribute greatly to increased heat transfer, which may in turn reduce the propellant heater efficiency.

The change in stagnation enthalpy due to a change in operating pressure may be obtained by referring to Fig. 1 and Eq. 5. Eq. 5 shows that the stagnation enthalpy varies inversely with the frozen flow efficiency for a given specific impulse. Therefore, increasing the operating pressure will cause a decrease in stagnation enthalpy, or, for a given stagnation enthalpy, operation at a high pressure level yields the highest specific impulse.

The change in the stagnation temperature of hydrogen with a change in operating pressure is shown in Fig. 6. Here it is noted that, for a given temperature level, operation at a low pressure produces the highest specific impulse. This variation is readily surmised from Eq. 12. Also included in Fig. 6 is the maximum specific impulse achievable at a 1-atm operating pressure level. A comparison of this curve with that obtained using the frozen flow assumption indicates the great gains possible in specific impulse if hydrogen recombination takes place in the nozzle.

Overall Engine Efficiency

The variation of the maximum overall engine efficiency with specific impulse may be obtained by referring to Fig. 1 and Figs. 5a–5d. The assumption has been made here that the engine may be regeneratively cooled so that the propellant heater efficiency becomes 1 and the overall engine efficiency equals the frozen flow efficiency. If the heat transfer losses cannot be handled by a regenerative cooling system, the propellant heater efficiency is less than 1, and the maximum overall efficiency is reduced by η_p.

Concluding Remarks

An analysis of several monatomic and diatomic materials suitable as propellants for plasma jet engines has been presented. The parameters used in the analysis were pressures from 0.01 to 100 atm, enthalpies as high as 200,000 Btu/lb, and specific impulses ranging from 500 to 2000 sec.

Of the eight possible propellants considered, there are three that are outstanding based on high frozen flow efficiencies: hydrogen, helium, and lithium. At the lower values of specific impulse (1000 sec), hydrogen and helium require the least amount of power to produce a pound of thrust. At specific impulses greater than about 1600 sec, lithium becomes more efficient.

An increase in operating pressure level improves the frozen flow performance of all the propellants considered. However, this increase in efficiency may be accompanied by an increase in heat transfer, so that a decrease in the propellant heater efficiency may occur.

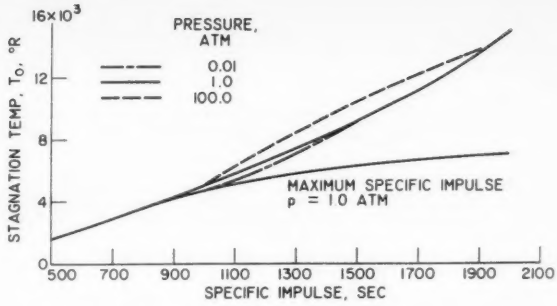

Fig. 6 Effect of pressure on hydrogen stagnation temperature

Nomenclature

g = gravitational constant
J = Joule's constant, 778 ft-lb/Btu
K_p = equilibrium constant, atm
M = molecular weight, lb
P_p = power in propellant
p = pressure, atm
R = universal gas constant
T = temperature, °R

Subscripts

a = available
e = nozzle exit
F = frozen
i = ionization
T = thermal
v = vaporization
0 = stagnation

References

1 Moeckel, W. E., Baldwin, L. V., English, R. E., Lubarsky, B. and Maslen, S. H., "Satellite and Space Propulsion Systems," *NASA TN D-285*, 1960.

2 Moeckel, W. E. and Rayle, W. D., "NASA Research on Plasma Accelerators for Space Propulsion," presented at the ARS 14th Annual Meeting, Washington, D. C., Nov. 16–20, 1959 (*ARS preprint no. 1005-59*).

3 Hall, J. G., Eschenroeder, A. Q. and Klein, J. J., "Chemical Non-Equilibrium Effects on Hydrogen Rocket Impulse at Low Pressure," ARS JOURNAL, vol. 30, no. 2, February 1960, pp. 188–189.

4 Woolley, H. W., "Effect of Dissociation on Thermodynamic Properties of Pure Diatomic Gases," *NACA TN 3270*, 1955.

5 Altman, D., "Thermodynamic Properties and Calculated Rocket Performance of Hydrogen to 20,000° K," *JPL Rep. 20-106*, September 1956.

6 Kanter, I. E., Martinek, F. and Ghai, M. L., "High Temperature Heat Transfer from Gases to Cylinders and Nozzles," *AFOSR TN 59-488*, General Electric Co., February 1958–February 1959, Contract AF 49(638)-243.

7 Zemansky, M. W., *Heat and Thermodynamics*, 4th ed., McGraw-Hill Book Co. Inc., New York, 1957, p. 439.

8 Allen, C. W., *Astrophysical Quantities*, The Athlone Press, Univ. of London, 1955.

9 Jack, J. R., "Regenerative and Radiation Cooling of Electrothermal Thrust Generators," presented at the ARS Semi-Annual Meeting, Los Angeles, Calif., June 13–16, 1961 (*ARS preprint no. 61-97-1791*).

Dynamic Response of Liquid Fueled Rocket Engines on Flexible Stands

V. CHOBOTOV[1]

Space Technology Laboratories Inc.
Los Angeles, Calif.

The equations of motion for the free and forced vibrations of a liquid fueled rocket engine on a typical test stand are derived. Treated is a four degree of freedom system that considers rotation and translation of the engine as well as the effects of nozzle flexibility. The cubic and quadratic frequency equations resulting from simpler cases involving only three and two degrees of freedom, respectively, are solved by graphical or analytical methods, which are unique and valuable for their simplicity. The report concludes with a frequency response analysis of an engine driven by a hydraulic actuator as a demonstration of the applicability of the methods discussed.

THE PURPOSE of the subject analytical investigation was to develop methods of analysis for the treatment of rocket engines on flexible test stands. More specifically, the mode shapes and frequency equations for several stand configurations were required to facilitate vibration data reduction and analysis.

In the course of the investigation, graphical methods were developed and used for the solution of cubic and quadratic frequency equations. These methods are simple and can be of value to designers of engine frames or to test engineers requiring quick but fairly accurate estimates of the effects of the many parameters involved.

The report is divided into two parts: free vibration and forced vibration. In the first part equations of motion are derived for the four, three, and two degrees of freedom of a typical test stand installation. These are presented in the form most useful for determination of natural frequencies and mode shapes of free vibration. In the second part of the report the effect of a forcing function is considered. It can result from an electrodynamic shaker or a hydraulic actuator; both cases are investigated and the results discussed.

The models for the analysis, however, consist only of springs and masses; no damping is used except in the form of cylinder leakages in the frequency response analysis.

Free Vibration

Three cases of free vibration are considered: four degrees of freedom—flexible engine, frame, and stand; three degrees of freedom—rigid engine, flexible frame, and stand; and two degrees of freedom—rigid engine, and flexible frame.

Four Degrees of Freedom: Flexible Engine, Frame, and Stand

Fig. 1 illustrates a liquid rocket engine on a flexible test stand. In this case the stiffness of the frame corresponds to that in the missile in which the engine will be used. However, the stiffness of the stand is preferably as high as possible so that its motion is minimized.

In the general case indicated in Fig. 2, which is an idealization of Fig. 1, the mass m_1 and the spring k_1 represent the mass and rigidity of the stand. The rigidities of the frame are represented by springs k_0, k_2, and k_3.

The engine combustion chamber and the nozzle may be considered as rigid bodies connected by a torsional spring k_t. For practical purposes the flexing of the nozzle on the combustion chamber is a simplified but good approximation of an engine modal analysis where only the first bending mode is considered.

As shown in Fig. 2, only the lateral motions will be considered. Let q_0 and q_1 represent the lateral displacements of the frame and stand, and q_2 and q_3 the angular displacements of the combustion chamber and nozzle. All angles will be assumed small, and no friction or bending of the arm l_1 is allowed. All other applicable symbols are as indicated in the schematic diagram.

Equations of motion

In terms of the generalized coordinates, the velocities of the mass m_1, the combustion chamber, and the nozzle respectively are

$$\dot{q}_1$$

$$\dot{q}_0 + \dot{q}_1 + y_2\dot{q}_2$$

$$\dot{q}_0 + \dot{q}_1 + l_{23}\dot{q}_2 + y_3\dot{q}_3$$

where y_2, y_3, and l_{23} are defined in Fig. 2, and q_2 and q_3 are assumed to be small, i.e., $\sin q_2 = q_2$, $\cos q_2 = 1$, etc.

Respectively, the kinetic and potential energies are

$$2T = m_1\dot{q}_1^2 + \int_0^{l_2} \rho A(\dot{q}_0 + \dot{q}_1 + y_2\dot{q}_2)^2\, dy_2 + \int_0^{l_3} \rho A(\dot{q}_0 + \dot{q}_1 + l_{23}\dot{q}_2 + y_3\dot{q}_3)^2 dy_3 \quad [1]$$

$$2V = k_0q_0^2 + k_1q_1^2 + \frac{k_2k_3}{k_2 + k_3}(l_1q_2)^2 + k_t(q_2 - q_3)^2 \quad [2]$$

Define as follows:

Combustion Chamber

$$\int_0^{l_2} \rho A dy_2 = m_2 \qquad (\sim\text{mass}) \quad [3a]$$

$$\int_0^{l_2} \rho A y_2^2 dy_2 = I_2$$

$$(\sim\text{moment of inertia about the gimbal}) \quad [3b]$$

Received April 20, 1961.

[1] Member Technical Staff.

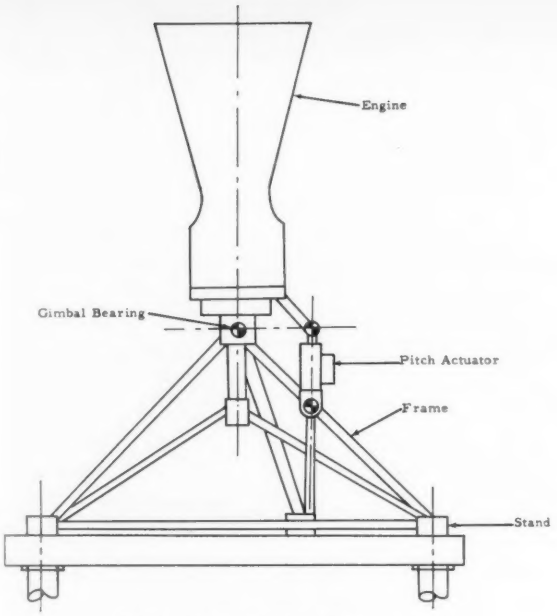

Fig. 1 Rocket engine test assembly

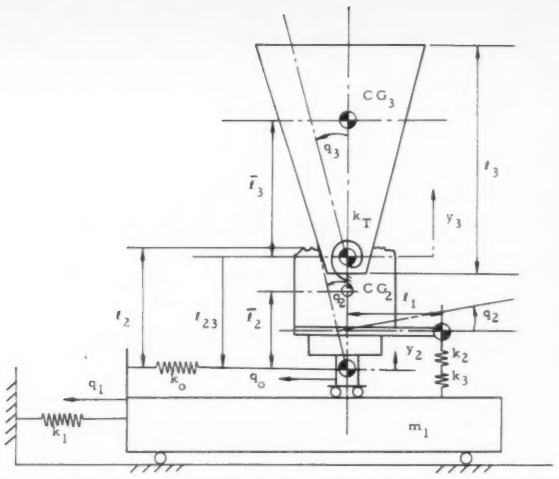

Fig. 2 Schematic diagram of engine on a test stand: four degrees of freedom

$$\int_0^{l_2} \rho A y_2 dy_2 = l_2 m_2 \qquad (\sim\text{centroidal location}) \qquad [3c]$$

Nozzle

$$\int_0^{l_3} \rho A dy_3 = m_3 \qquad (\sim\text{mass}) \qquad [4a]$$

$$\int_0^{l} \rho A y_3 dy_3 = l_3 m_3 \qquad (\sim\text{centroidal location}) \qquad [4b]$$

$$\int_0^{l_3} \rho A y_3^2 dy_3 = I_3$$

$$(\sim\text{moment of inertia about the pivot of the nozzle}) \qquad [4c]$$

and substitute these definitions into the Lagrange equation

$$\frac{d}{dt}\left[\frac{\partial}{\partial \dot{q}_n}(T - V)\right] - \frac{\partial}{\partial q_n}(T - V) = 0 \qquad [5]$$

With q_n the generalized coordinate of the nth mode, the equation of motion is

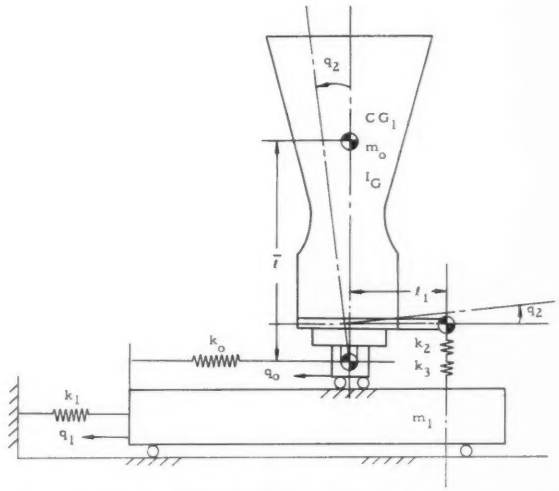

Fig. 3 Schematic diagram of simplified test setup: three degrees of freedom

$$(m_2 + m_3)\ddot{q}_0 + (m_2 + m_3)\ddot{q}_1 + (\bar{l}_2 m_2 + l_{23} m_3)\ddot{q}_2 + \bar{l}_3 m_3 \ddot{q}_3 + k_0 q_0 = 0 \qquad [6a]$$

$$(m_2 + m_3)\ddot{q}_0 + (m_1 + m_2 + m_3)\ddot{q}_1 + (\bar{l}_2 m_2 + l_{23} m_3)\ddot{q}_2 + \bar{l}_3 m_3 \ddot{q}_3 + k_1 q_1 = 0 \qquad [6b]$$

$$(\bar{l}_2 m_2 + l_{23} m_3)\ddot{q}_0 + (\bar{l}_2 m_2 + l_{23} m_3)\ddot{q}_1 + (I_2 + l_{23}^2 m_3)\ddot{q}_2 + m_3 l_{23}\ddot{q}_3 + \frac{k_2 k_3}{k_2 + k_3} l_1^2 q_2 + (q_2 - q_3)k_t = 0 \qquad [6c]$$

$$\bar{l}_3 m_3 \ddot{q}_0 + \bar{l}_3 m_3 \ddot{q}_1 + \bar{l}_3 l_{23} m_3 \ddot{q}_2 + I_3 \ddot{q}_3 + k_t(q_3 - q_2) = 0 \qquad [6d]$$

Frequency determinant

Define

$$\alpha = \sqrt{k_t/I_3} \qquad \sim\text{rotational frequency of the nozzle with the combustion chamber held fixed} \qquad [7a]$$

$$\beta = \sqrt{k_0/(m_2 + m_3)} \qquad \sim\text{translational frequency of the engine with the stand held fixed} \qquad [7b]$$

$$\gamma = \sqrt{k_1/m_1} \qquad \sim\text{translational frequency of the stand} \qquad [7c]$$

and assume that

$$q_0 = Ae^{i\omega t} \qquad [8a]$$

$$q_1 = Be^{i\omega t} \qquad [8b]$$

$$q_2 = Ce^{i\omega t} \qquad [8c]$$

$$q_3 = De^{i\omega t} \qquad [8d]$$

The natural frequencies and modes of vibration then can be obtained in terms of the definitions by substituting Eqs. 7 and 8 into Eqs. 6 and solving the resultant set of equations. In determinant form the characteristic equation becomes

$$\begin{vmatrix} \left[1-\left(\frac{\beta}{\omega}\right)^2\right]A & B & \left(\frac{l_2m_2-l_{23}m_3}{m_2+m_3}\right)C & \left(\frac{l_3m_3}{m_2+m_3}\right)D \\ A & \left\{1+\frac{m_1}{m_2+m_3}\left[1-\left(\frac{\gamma}{\omega}\right)^2\right]\right\}B & \left(\frac{l_2m_2-l_{23}m_3}{m_2+m_3}\right)C & \left(\frac{l_3m_3}{m_2+m_3}\right)D \\ \frac{\bar{l}_2m_2+l_{23}m_3}{I_3}A & \frac{\bar{l}_2m_2+l_{23}m_3}{I_3}B & & \\ & & \left\{\frac{1}{I_3}\left[(I_2+l_{23}{}^2m_3)-\frac{k_2k_3l_1{}^2}{(k_2+k_3)\omega^2}\right]-\left(\frac{\alpha}{\omega}\right)^2\right\}C & \left[\frac{m_3\bar{l}_3l_{23}}{I_3}+\left(\frac{\alpha}{\omega}\right)^2\right]D \\ \bar{l}_3\frac{m_3}{I_3}A & \frac{\bar{l}_2m_3}{I_3}B & \left[\frac{\bar{l}_3l_{23}m_3}{I_3}+\left(\frac{\alpha}{\omega}\right)^2\right]C & \left[1-\left(\frac{\alpha}{\omega}\right)^2\right]D \end{vmatrix} = 0 \quad [9]$$

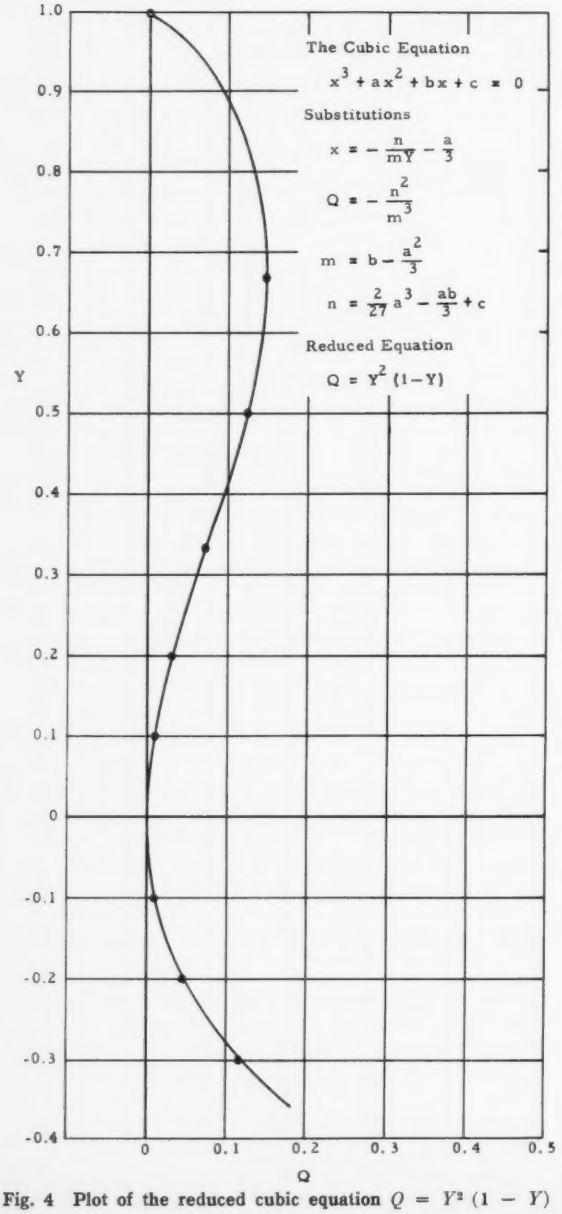

Fig. 4 Plot of the reduced cubic equation $Q = Y^2(1 - Y)$

Three Degrees of Freedom: Rigid Engine, Flexible Frame, and Stand

This case of the rigid engine on the flexible frame and stand is a special case of the previous problem. Fig. 3 is a schematic diagram for this problem. It is seen from the diagram that the engine is allowed to rotate with an angle q_2 and translate in the q_0 and q_1 directions. Such representation of a test setup is justified where the engine is considered quite rigid or where a simplified analysis of the previous problem is more desirable.

Equations of motion

The equations of motion for the system shown in Fig. 3 can be obtained readily from the equations of motion for the previous case. Thus, in Eqs. 6, letting

$$q_3 = k_t = m_3 = 0$$

and

$m_2 = m_0$ (~total mass of engine)

$\bar{l}_2 = \bar{l}$ (~engine CG location)

$I_2 = I_G$ (~engine moment of inertia about the gimbal)

the equations of motion become

$$m_0\ddot{q}_0 + m_0\ddot{q}_1 + \bar{l}m_0\ddot{q}_2 + k_0q_0 = 0 \quad [10a]$$

$$m_0\ddot{q}_0 + (m_1 + m_0)\ddot{q}_1 + \bar{l}m_0\ddot{q}_2 + k_1q_1 = 0 \quad [10b]$$

$$\bar{l}m_0\ddot{q}_0 + \bar{l}m_0q_1 + I_G\ddot{q}_2 + k_2k_3l_1{}^2/(k_2 + k_3)q_2 = 0 \quad [10c]$$

Frequency determinant

The frequency determinant is obtained as before, by letting

$$q_0 = Ae^{i\omega t} \quad [11a]$$

$$q_1 = Be^{i\omega t} \quad [11b]$$

$$q_2 = Ce^{i\omega t} \quad [11c]$$

and substituting into the equations of motion. Thus, defining

$$\mu = m_0\bar{l}^2/I_G \quad [12a]$$

$$\lambda = \frac{k_2k_3}{k_2 + k_3}\frac{l_1{}^2}{I_G} \quad [12b]$$

and, as before

$$\beta^2 = k_0/m_0$$

$$\gamma^2 = k_1/m_1$$

the frequency determinant is

$$\begin{vmatrix} \left[1-\left(\frac{\beta}{\omega}\right)^2\right]A & B & \bar{l}\,C \\ A & \left\{1+\frac{m_1}{m_0}\left[1-\left(\frac{\gamma}{\omega}\right)^2\right]\right\}B & \bar{l}\,C \\ \mu A & \mu B & \left[1-\left(\frac{\lambda}{\omega}\right)^2\right]-\bar{l}\,C \end{vmatrix} = 0 \qquad [13]$$

By expanding Eq. 13 the frequency or characteristic equation is obtained, i.e.

$$\left(\frac{\omega}{\lambda}\right)^6(1-\mu)+\left(\frac{\omega}{\lambda}\right)^4\left\{\mu\left[\left(\frac{\gamma}{\lambda}\right)^2+\frac{m_0}{m_1}\left(\frac{\beta}{\lambda}\right)^2\right]-\left(\frac{\beta}{\lambda}\right)^2\frac{m_0}{m_1}+1-\left(\frac{\gamma}{\lambda}\right)^2-1\right\}+$$

$$\left(\frac{\omega}{\lambda}\right)^2\left\{\left(\frac{\gamma}{\lambda}\right)^2\left[1+\left(\frac{\beta}{\lambda}\right)^2\right]+\left(\frac{\beta}{\lambda}\right)^2\left(1+\frac{m_0}{m_1}\right)\right\}-\left(\frac{\gamma}{\lambda}\right)^2\left(\frac{\beta}{\lambda}\right)^2=0 \qquad [14]$$

Solving the frequency determinant for the mode shapes gives

$$\frac{B}{A}=\frac{\frac{m_0}{m_1}\left(\frac{\beta}{\omega}\right)^2}{\left(\frac{\gamma}{\omega}\right)^2-1} \qquad [15]$$

$$\frac{\bar{l}C}{A}=\frac{\left(\frac{\beta}{\omega}\right)^2}{\frac{1}{\mu}\left[\left(\frac{\lambda}{\omega}\right)^2-1\right]+1} \qquad [16]$$

$$\frac{\bar{l}C}{B}=\frac{-\mu\left(\frac{\beta}{\omega}\right)^2}{\left[1-\left(\frac{\lambda}{\omega}\right)^2\right]\left[\left(\frac{\beta}{\omega}\right)^2-1\right]+\mu} \qquad [17]$$

Solution of the frequency equation

By means of Fig. 4 (1),[2] the cubic frequency Eq. 14 can be solved analytically for the three real roots $(\omega/\lambda)_{1,2,3}^2$, as follows:

Fig. 4 is a plot of the reduced cubic equation $Q = Y^2(1 - Y)$ which can be used to solve for the three real roots of the equation

$$x^3+ax^2+bx+c=0 \qquad [18]$$

1 From Fig. 4 read off the three roots Y_1, Y_2, Y_3 for a given

$$Q=-n^2/m^3$$

where

$$n=(2/27)a^3-ab/3+c$$

$$m=b-a^2/3$$

and a, b, c are constants in Eq. 18.

2 The roots x_1, x_2, and x_3 are then obtained from equation

$$x_{1,2,3}=n/mY-a/3 \qquad [19]$$

and, since in the vibration problem discussed here all roots are real, the limits of Q are $0 < Q < 4/27$; consequently, no imaginary solutions exist.

Note, however, that an approximation can be obtained if in Eq. 14 the ratio $\mu = m_0l^2/I_G$ is close to unity. In this case the coefficient of $(\omega/\lambda)^6$ becomes zero, and the equation is reduced to a quadratic in $(\omega/\lambda)^2$

$$\left(\frac{\omega}{\lambda}\right)^4-\left[\left(\frac{\gamma}{\lambda}\right)^2+\frac{1+\frac{m_0}{m_1}}{1+\left(\frac{\lambda}{\beta}\right)^2}\right]\left(\frac{\omega}{\lambda}\right)^2+\frac{\left(\frac{\gamma}{\lambda}\right)^2}{1+\left(\frac{\lambda}{\beta}\right)^2}=0 \qquad [20]$$

After completing the squares, Eq. 20 can be easily plotted or

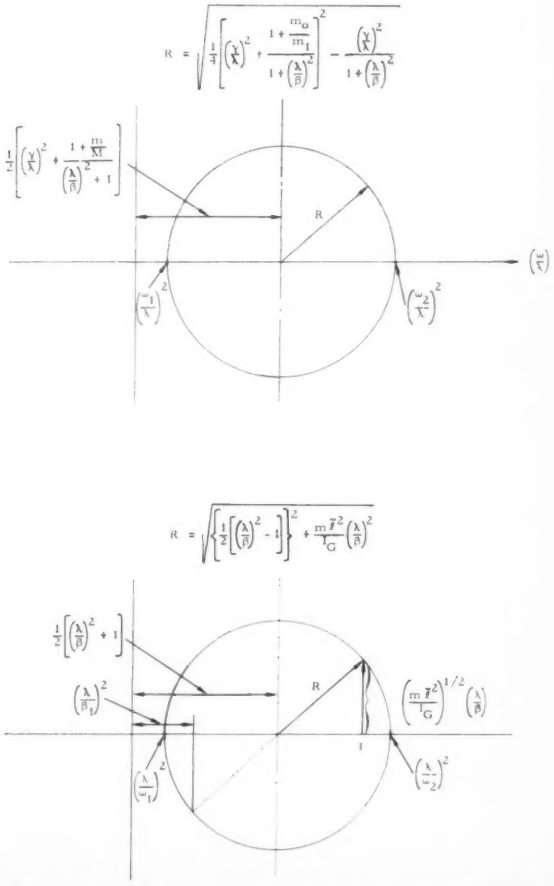

Fig. 5 Graphic solutions of quadratic frequency equations

[2] Numbers in parentheses indicate References at end of paper.

solved analytically. For example, as shown in Fig. 5, Eq. 20 can be written as

$$\left\{\left(\frac{\omega}{\lambda}\right)^2 - \frac{1}{2}\left[\left(\frac{\gamma}{\lambda}\right)^2 + \frac{1+\frac{m_0}{m_1}}{1+\left(\frac{\lambda}{\beta}\right)^2}\right]\right\}^2 = \frac{1}{4}\left[\left(\frac{\gamma}{\lambda}\right)^2 + \frac{1+\frac{m_0}{m_1}}{1+\left(\frac{\lambda}{\beta}\right)^2}\right] - \frac{\left(\frac{\gamma}{\lambda}\right)^2}{1+\left(\frac{\lambda}{\beta}\right)^2}$$

where the two solutions $(\omega/\lambda)_{1,\,2}{}^2$ are given by the intersections of a circle of radius

$$R = \sqrt{\frac{1}{4}\left[\left(\frac{\gamma}{\lambda}\right)^2 + \frac{1+\frac{m_0}{m_1}}{1+\left(\frac{\lambda}{\beta}\right)^2}\right]^2 - \frac{\left(\frac{\gamma}{\lambda}\right)^2}{1+\left(\frac{\lambda}{\beta}\right)^2}}$$

at the center located

$$\frac{1}{2}\left[(\gamma/\lambda)^2 + \frac{1+m_0/m_1}{1+(\lambda/\beta)^2}\right]$$

units away from zero on the $(\omega/\lambda)^2$-axis.

Two Degrees of Freedom: Rigid Engine, Flexible Frame

The two degrees of freedom system is the simplest, yet in practice often the most significant, case. Fig. 6 schematically illustrates a two degree of freedom system.

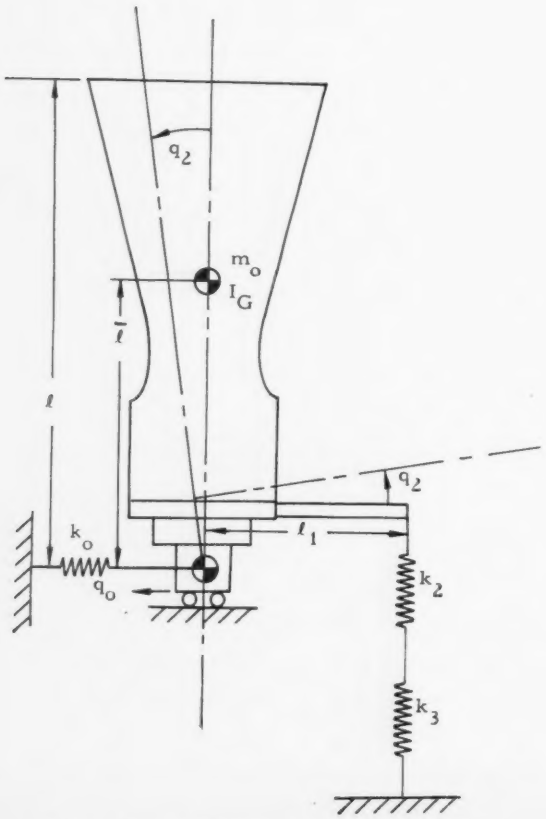

Fig. 6 Schematic diagram: two degrees of freedom

Equation of motion

In this problem the equations of motion can be obtained immediately from Eqs. 10 by letting $q_1 = 0$. Hence, the equations of motion are

$$\begin{aligned} m_0\ddot{q}_0 + m_0\bar{l}\ddot{q}_2 + k_0 q_0 &= 0 \\ \bar{l}m_0\ddot{q}_0 + I_G\ddot{q}_2 + \frac{l_1{}^2 k_2 k_3}{k_2 + k_3}\, q_2 &= 0 \end{aligned} \qquad [21]$$

Frequency equation and mode shape

The frequency equation of the two degrees of freedom system is

$$\left(\frac{\omega}{\lambda}\right)^4\left[1 - \frac{m_0\bar{l}^2}{I_G}\right] - \left(\frac{\omega}{\lambda}\right)^2\left[\left(\frac{\beta}{\lambda}\right)^2 + 1\right] + \left(\frac{\beta}{\lambda}\right)^2 = 0 \qquad [22]$$

and the mode shape is

$$\bar{l}C/A = (\beta/\omega)^2 - 1 \qquad [23]$$

where as before

$$\beta^2 = \frac{k_0}{m_0} \qquad \lambda^2 = \frac{l_1{}^2}{I_G}\left(\frac{k_2 k_3}{k_2 + k_3}\right)$$

Solution of frequency equation

Frequency Eq. 22 can be solved analytically or graphically for the two natural frequencies of the system. As before, the graphical solution can be obtained by rewriting Eq. 22 and completing squares. Thus

$$\left(\frac{\lambda}{\omega}\right)^4 - \left(\frac{\lambda}{\omega}\right)^2\left[1 + \left(\frac{\lambda}{\beta}\right)^2\right] + \left(\frac{\lambda}{\beta}\right)^2\left[1 - \frac{m_0\bar{l}^2}{I_G}\right] = 0 \qquad [24]$$

$$\left\{\left(\frac{\lambda}{\omega}\right)^2 - \frac{1}{2}\left[\left(\frac{\lambda}{\beta}\right)^2 + 1\right]\right\}^2 = \left\{\frac{1}{2}\left[\left(\frac{\lambda}{\beta}\right)^2 - 1\right]\right\}^2 + \frac{m_0\bar{l}^2}{I_G}\left(\frac{\lambda}{\beta}\right)^2 \qquad [25]$$

As plotted in Fig. 5, Eq. 25 is a circle whose radius is

$$R = \sqrt{\left\{\frac{1}{2}\left[\left(\frac{\lambda}{\beta}\right)^2 - 1\right]\right\}^2 + \frac{m_0\bar{l}^2}{I_G}\left(\frac{\lambda}{\beta}\right)^2}$$

and whose center is at $(1/2)[(\lambda/\beta)^2 + 1]$ on the $(\lambda/\omega)^2$-axis.

The roots $(\lambda/\omega_1)^2$ and $(\lambda/\omega_2)^2$ are located on the intersection of the circle with the abscissa of the graph. The construction in Fig. 5 then illustrates the behavior of the roots (λ/ω_1) and (λ/ω_2) as the ratio $m_0\bar{l}^2/I_G$ is varied. This allows for quick determination of the roots.

Thus, from either Eq. 25 or Fig. 5 it is seen that the two roots are

$$\left(\frac{\lambda}{\omega_1}\right)^2 = \frac{1}{2}\left[\left(\frac{\lambda}{\beta}\right)^2 + 1\right] - \sqrt{\left\{\frac{1}{2}\left[\left(\frac{\lambda}{\beta}\right)^2 - 1\right]\right\}^2 + \frac{m_0\bar{l}^2}{I_G}\left(\frac{\lambda}{\beta}\right)^2} \qquad [26]$$

and

$$\left(\frac{\lambda}{\omega_2}\right)^2 = \frac{1}{2}\left[\left(\frac{\lambda}{\beta}\right)^2 + 1\right] + \sqrt{\left\{\frac{1}{2}\left[\left(\frac{\lambda}{\beta}\right)^2 - 1\right]\right\}^2 + \frac{m_0\bar{l}^2}{I_G}\left(\frac{\lambda}{\beta}\right)^2} \qquad [27]$$

The coupled frequencies ω_1 and ω_2 are functions of the uncoupled frequencies λ and β and of the factor $\mu = m_0\bar{l}^2/I_G$. This dependence on the ratio μ is shown in Fig. 7, where the ratios of ω/ω_1 and ω/ω_2 are plotted against the ratio λ/β, and ω is defined as the frequency of the system when $\mu = 1$. It is seen in the illustration that the higher frequency ω_1

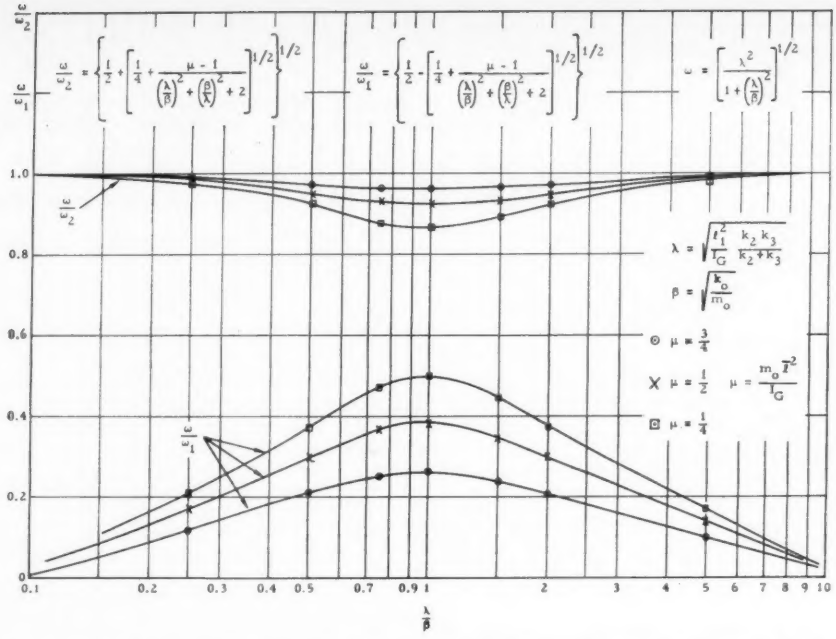

Fig. 7 Plot of the coupled frequencies as functions of the uncoupled frequencies and of the factor μ

appears to be more affected by the ratio $\mu = m_0\bar{l}^2/I_G$ than the lower frequency. Furthermore, the effect of μ seems largest when λ/β is close to unity. Therefore, when μ and λ/β are known, the coupled frequencies ω_1 and ω_2 can be estimated from Fig. 7.

Forced Vibration

In the previous sections only the free vibrations of the various test setups were considered. How the dynamic response of systems is affected by forcing functions will now be discussed. Fig. 8 shows a schematic representation of a system using an electrodynamic shaker for excitation. Fig. 9 is a system in which a hydraulic actuator is used. The Lagrange equations for such systems now contain the generalized force term Q_n, and the q_2 is a generalized coordinate. For example

$$\frac{d}{dt}\left[\frac{\partial}{\partial \dot{q}_n}(T - V)\right] - \frac{\partial}{\partial q_n}(T - V) = Q_n \qquad [28]$$

Electrodynamic Shaker Excitation

The generalized force Q_2 (Fig. 8) will now be determined. From physics, the generalized work W is

$$W = Q_2\Delta q_2 = F_2 l_1 \Delta q_2 \qquad [29]$$

where $l_1\Delta q_2$ is a virtual displacement, and F_2 is the force on the actuator arm of the length l_1.
However, since

$$F_2 = \Delta\delta k_2$$

$$F_1 = \Delta\delta k_3$$

$$F = F_1 + F_2$$

$$= \Delta\delta(k_2 + k_3)$$

$$\Delta\delta = \frac{F}{k_2 + k_3}$$

therefore

$$F_2 = k_2\Delta\delta$$

$$= \frac{Fk_2}{k_2 + k_3} \qquad [30]$$

where F is shaker force, $\Delta\delta$ is shaker displacement, and k_2, k_3 are spring constants (as in Fig. 8).

The generalized force in terms of the shaker force F becomes

$$Q_2 = F_2 l_1$$

$$= Fl_1\frac{k_2}{k_2 + k_3} \qquad [31]$$

The generalized force Q_2 can now be inserted in the proper equation of motion. For example, in the two degrees of freedom case Eq. 21 gives

$$m_0\ddot{q}_0 + m_0\bar{l}\ddot{q}_2 + k_0 q_0 = 0 \qquad [32a]$$

$$\bar{l}m_0\ddot{q}_0 + I_G\ddot{q}_2 + \frac{l_1^2 k_2 k_3}{k_2 + k_3}q_2 = Fl_1\frac{k_2}{k_2 + k_3} \qquad [32b]$$

Eqs. 32 can be solved by standard methods.

Excitation by a Hydraulic Actuator

Fig. 9 shows a typical test stand installation using a hydraulic actuator for vibration excitation. The spring constants of the frame and the hydraulic actuator itself actually may be identical with those used in the missile for which the engine is intended. Such a test setup can, therefore, be used to make frequency response studies in order to determine the dynamic characteristics of the missile-installed engine.

Frequency response analysis

A simplified frequency response analysis for the system in Fig. 9 can be made as follows:

Suppose it is desired to obtain an expression for the closed loop frequency response δ_A/δ_C, where $\delta_A = \delta_{P_a} + \delta_S$, and δ_C is the command signal in degrees of engine rotation.

The equations of motion for the system can be obtained from Eq. 21 by including the generalized force $F_2 l_1$ and letting

$$\lambda^2 = k_e l_1^2 / I_G$$

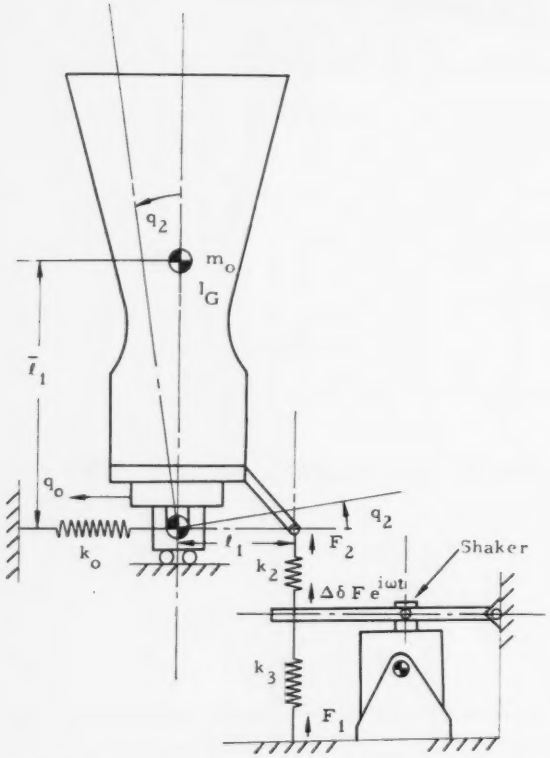

Fig. 8 Electrodynamic excitation of an engine on test stand

Fig. 9 Hydraulic excitation of an engine on test stand

where

$$k_s = \frac{k_2 k_3 k_4}{k_1 k_3 + k_2 k_4 + k_3 k_2}$$

and k_4 is the spring constant of the oil under compression.

Thus, with λ defined as above, and $\beta^2 = k_0/m_0$

$$\ddot{q}_0 + \bar{l}\ddot{q}_2 + \beta^2 q_0 = 0 \qquad [33a]$$

$$\bar{l} m_0 \ddot{q}_0 + I_G \ddot{q}_2 + I_G \lambda^2 q_2 = F_2 l_1 \qquad [33b]$$

To write F_2 in terms of δ_A and δ_C, the equations for the actuator (2) are written

$$A_1 \dot{\delta}_A = k_v A_1 (l_1 \delta_C - \delta_A) - P_a L \qquad [34]$$

$$A_1 P_a = k_e (\delta_A - l_1 q_2) \qquad [35]$$

$$\delta_A = \delta_{P_a} + \delta_S \qquad [36]$$

$$F_2 = k_s \delta_A \qquad [37]$$

where

k_v = valve constant
A_1 = area of the actuator piston
P_a = working pressure in actuator
L = coefficient of leakage in the actuator

Combining Eqs. 33 through 37 and applying the Laplace transformation gives

$$\frac{\delta_C}{\delta_A} = \frac{1 + \left(\frac{S}{\lambda}\right)^2 \left(1 - \frac{\mu S^2}{S^2 + \beta^2}\right)}{\frac{L k_e}{l_1 k_v A_1^2}\left(1 - \frac{\mu S^2}{S^2 + \beta^2}\right)\left(\frac{S}{\lambda}\right)^2 + \frac{(S + k_v)}{l_1 k_v}\left[1 + \left(\frac{S}{\lambda}\right)^2 \left(1 - \frac{\mu S^2}{S^2 + \beta^2}\right)\right]} \qquad [38]$$

where $\mu = m_0 \bar{l}^2 / I_G$, as before, and $S = i\omega$.

Discussion

The transfer function Eq. 38 approaches zero when its numerator, or frequency equation, approaches zero, or when the denominator goes to infinity. Thus, setting the numerator of Eq. 38 to zero and solving for the frequencies at which this occurs gives

$$\omega_{1,2}^2 = \frac{\left(\frac{\beta}{\lambda}\right)^2 + 1 \pm \left\{\left[\left(\frac{\beta}{\lambda}\right)^2 + 1\right]^2 - 4\left(\frac{\beta}{\lambda}\right)^2 (1 - \mu)\right\}^{1/2}}{2\left(\frac{1 - \mu}{\lambda^2}\right)} \qquad [39]$$

when the correct β, λ, and μ are used, frequencies ω_1 and ω_2 in Eq. 39 are the same as those that can be obtained from Fig. 5 or Fig. 7.

If $k_0 \to \infty$, then $\beta \to \infty$ and $\delta_A/\delta_C \to 0$ at $\omega_1^2 \to \lambda^2$, as would be expected. The special case when $\mu = 1$ yields

$$\omega_1^2 = \frac{\beta^2}{1 + \left(\frac{\beta}{\lambda}\right)^2}$$

Therefore from this discussion it can be seen that if $k_0 \neq \infty$, two frequencies ω_1 and ω_2 are obtained, for which $\delta_A/\delta_G = 0$. These frequencies can be obtained exactly from Eq. 39 or estimated from Fig. 7.

References

1 Christensen, B., "Discussion and Solution of the Cubic Equation," *Acta Polytechnica*, vol. 238, 1957, or "Applied Mathematics and Computing Machinery Series," vol. 1, no. 4.

2 Martin, D. C., "Generalized Missile Dynamics Analysis VI—Control System Equations," *GM-TR-0165-00430*, Rep. no. EM 8-14, April 7, 1958.

Representation of Fuel Sloshing in Cylindrical Tanks by an Equivalent Mechanical Model[1]

H. NORMAN ABRAMSON[2]
WEN-HWA CHU[3]
GUIDO E. RANSLEBEN Jr.[4]

Southwest Research Institute
San Antonio, Texas

A mechanical model for representation of linear fuel sloshing with damping is derived by comparison and extension of available theoretical results in both translation and pitching without damping. Available experimental data indicates that the mechanical model representation is satisfactory for predicting total force response. A simple interpretation of the formulation also makes it possible to apply the mechanical model to the case of axial thrust acting in addition to the vertical gravitational field.

THE OSCILLATORY motion of fuel in a large rocket tank, or even an airplane, may be near resonance with the motion or control system of the vehicle and thus can lead to dynamic instabilities or even to structural failure. For small oscillations the complete dynamic system is linear, but even so, for analysis sake, it may often be desirable to replace the liquid, which has a free surface, with a simpler mechanical system that is dynamically equivalent to the sloshing liquid. This equivalence is taken in the sense of equal resultant force and moment acting on the tank wall. By properly accounting for the equivalent mechanical system representation for sloshing, the problem of overall dynamic system behavior can be formulated more simply and can then be investigated by employing an analog or digital computer (1).[5] For rectangular fuel tanks, both the force and moment resulting from sloshing and an appropriate equivalent mechanical system or model, without damping, have been given in (2). The equivalent mechanical model suggested for such rectangular tanks is a series of spring-mass elements suspended at various heights in the tank.

In many large rockets, however, the fuel tanks are cylindrical; the equations for force and moment resulting from fuel sloshing in such tanks, without damping, have been derived in (3–5). The equivalent mechanical model suggested in (3, 4) is a series of pendulum-mass elements of various arm lengths attached to the centerline in the plane of symmetry. For sloshing in a cylindrical tank with damping, in an Earth-fixed vertical gravitational (inertial) field a, the equations for force and moment are given in (6). This analysis is based on consideration of a single element spring mass dashpot; however, no explicit mechanical system is described. The suggested procedure (6) is to introduce an imaginary damping coefficient g into the resonance terms of the theoretical force, moment, pressure, and surface amplitude equations derived for the undamped case (5). These equations are then transformed so that they reduce to those of the undamped case for $g = 0$ and to those of a rigid mass for $g = \infty$.

A somewhat different but still simple equivalent mechanical system (model), consisting of a series of spring mass dashpot elements attached at various specified heights in the plane of of symmetry, is suggested in this paper. Since it is probable, when large damping exists, that the only substantial change in the system is in the damping coefficient, the new formulation is based on derived equations for small damping with the assumption that the parameters of the equivalent mechanical system, in a fixed gravitational field, are frequency independent and are the same as those for zero damping. This makes the height of each of the spring mass dashpot elements independent of frequency. The resulting equations for force and moment in translation and the force in pitching oscillation reduce to the same as those given by Bauer (6); however, a new expression for the moment resulting from pitching oscillations is required. The resulting equivalent mechanical system appears to be satisfactory for practical applications. It is also found that the same system is valid even if there is axial[6] thrust, provided that proper interpretation of the results is made.

Development of the Equivalent Mechanical Model

Force and Moment Resulting From Sloshing With Zero Damping

The equations for force and moment resulting from sloshing in a cylindrical tank with zero damping have been given in (5) and elsewhere[7] as follows:

$$F_H^{(1)} = Ae^{i\omega t} \cdot \omega^2 M_F \left\{ 1 + \sum_{n=1}^{\infty} \frac{2 \operatorname{Tanh}\left(\xi_n \frac{2h}{d}\right)}{\xi_n \left(\frac{2h}{d}(\xi_n^2 - 1)\right)} \cdot \frac{1}{\left(\frac{\omega_n^2}{\omega^2} - 1\right)} \right\} \quad [1]$$

Received Sept. 22, 1960.

[1] The results presented in this paper were obtained during the course of research carried out under Contract No. DA-23-072-ORD-1251 and sponsored by the Army Ballistic Missile Agency, U. S. Army Ordnance Missile Command. Appreciation is expressed to the ABMA for permission to publish this paper, and Helmut Bauer for valuable discussions.

[2] Director, Department of Mechanical Sciences. Member ARS.

[3] Senior Research Engineer, Department of Mechanical Sciences.

[4] Senior Research Engineer, Department of Mechanical Sciences.

[5] Numbers in parentheses indicate References at end of paper.

[6] In this paper the word *axial* is not to be taken as necessarily synonymous with the word *vertical* since, even though the flight path is assumed to be vertical, the vehicle may be oscillating about the flight path.

[7] Equivalent analyses are given, for example, in (3, 4, 7).

$$M_y^{(1)} = Ae^{i\omega t} \cdot \omega^2 M_F h \left\{ \frac{1}{4\left(\frac{2h}{d}\right)^2} + \sum_{n=1}^{\infty} \frac{\xi_n \operatorname{Tanh}\left(\xi_n \frac{2h}{d}\right) + \frac{4}{\left(\frac{2h}{d}\right)\operatorname{Cosh}\left(\xi_n \frac{2h}{d}\right)} - \frac{2}{\left(\frac{2h}{d}\right)}}{\left(\xi_n \frac{2h}{d}\right) \xi_n (\xi_n^2 - 1)\left(\frac{\omega_n^2}{\omega^2} - 1\right)} \right\} \quad [2]$$

where

$$\omega_n^2 = \frac{2a}{d} \xi_n \operatorname{Tanh}\left(\xi_n \frac{2h}{d}\right)$$

$$F_H^{(2)} = F_b - M_F a \cdot Be^{i\omega t}$$

$$= 2Be^{i\omega t} \cdot \omega^2 M_F \frac{d}{2} \sum_{n=1}^{\infty} \frac{\frac{2}{\left(\frac{2h}{d}\right)}\left(\frac{1}{\operatorname{Cosh}\left(\xi_n \frac{2h}{d}\right)} - 1\right) + \left(\frac{2a}{d} \cdot \frac{\xi_n}{\omega^2} \cdot \frac{1}{\frac{2h}{d}} + \frac{\xi_n}{2}\right) \operatorname{Tanh}\left(\xi_n \frac{2h}{d}\right)}{\xi_n^2 (\xi_n^2 - 1)\left(\frac{\omega_n^2}{\omega^2} - 1\right)}$$

$$= Be^{i\omega t} \cdot \omega^2 M_F h \left\{ \frac{1}{4\left(\frac{2h}{d}\right)^2} + \sum_{n=1}^{\infty} \frac{\xi_n \operatorname{Tanh}\left(\xi_n \frac{2h}{d}\right) + \frac{4}{\left(\frac{2h}{d}\right)\operatorname{Cosh}\left(\xi_n \frac{2h}{d}\right)} - \frac{2}{\left(\frac{2h}{d}\right)}}{\left(\xi_n \frac{2h}{d}\right) \xi_n (\xi_n^2 - 1)\left(\frac{\omega_n^2}{\omega^2} - 1\right)} \right\} \quad [3]$$

$$M_y^{(2)} = Be^{i\omega t} \cdot \omega^2 M_F h^2 \left\{ \frac{1}{12} - \frac{1}{8\left(\frac{2h}{d}\right)^2} + \frac{ad^2}{16h^3\omega^2} + \frac{2}{\left(\frac{2h}{d}\right)^2} \sum_{n=1}^{\infty} \frac{1}{\xi_n^2(\xi_n^2 - 1)\left(\frac{\omega_n^2}{\omega^2} - 1\right)} \cdot \right.$$

$$\left. \left[\frac{2 - \frac{8a}{d\omega^2} \cdot \frac{1}{\left(\frac{2h}{d}\right)}}{\operatorname{Cosh}\left(\xi_n \frac{2h}{d}\right)} + \frac{10a}{d\omega^2} \cdot \frac{1}{\left(\frac{2h}{d}\right)} + \frac{1}{2} + \left(\frac{1}{4} \cdot \xi_n \cdot \frac{2h}{d} - \frac{3}{2} \cdot \frac{2a\xi_n}{d\omega^2} - \frac{4}{\xi_n \frac{2h}{d}}\right) \operatorname{Tanh}\left(\xi_n \frac{2h}{d}\right) \right] \right\}$$

$$= Be^{i\omega t} \cdot \omega^2 M_F h^2 \left\{ \left\{ \frac{I_F}{M_F h^2} + \frac{1}{\left(\frac{2h}{d}\right)^2} \sum_{n=1}^{\infty} \left[\frac{-8}{\operatorname{Sinh}\left(\xi_n \frac{2h}{d}\right)\left(\xi_n \frac{2h}{d}\right)} - 6 + \frac{10}{\left(\xi_n \frac{2h}{d}\right) \operatorname{Tanh}\left(\xi_n \frac{2h}{d}\right)} \right] \frac{1}{\xi_n^2(\xi_n^2 - 1)} + \right. \right.$$

$$\left. \left. \sum_{n=1}^{\infty} \frac{1}{\left[\frac{2 \operatorname{Tanh}\left(\xi_n \frac{2h}{d}\right)}{\left(\xi_n \frac{2h}{d}\right)(\xi_n^2 - 1)} \right] \left(\frac{\omega_n^2}{\omega^2} - 1\right)} \left[\frac{\xi_n \operatorname{Tanh}\left(\xi_n \frac{2h}{d}\right) + \frac{4}{\left(\frac{2h}{d}\right)\operatorname{Cosh}\left(\xi_n \frac{2h}{d}\right)} - \frac{2}{\left(\frac{2h}{d}\right)}}{\left(\xi_n \frac{2h}{d}\right) \xi_n (\xi_n^2 - 1)} \right]^2 \right\} + \right.$$

$$Be^{i\omega t} (M_F a h) \left[\frac{1}{4\left(\frac{2h}{d}\right)^2} \right] \quad [4]$$

where

$$I_F = M_F h^2 \left\{ \frac{1}{12} + \frac{1}{4\left(\frac{2h}{d}\right)^2} \right\}$$

Equivalent Mechanical Model for Representation of Sloshing With Damping

The equivalent mechanical system with damping is shown in Fig. 1. The sloshing liquid is replaced by a series of spring

mass dashpot elements, in addition to a rigid mass M_0 having a moment of inertia I_0. The other masses are all point masses, each of which has zero inertia about its center, and each spring is compressible along its axis but infinitely stiff in the direction normal to its axis. The equivalent system is supposed to be moving in an effective Earth-fixed vertical gravitational field (total acceleration = a). The equivalent system in an effective gravitational field provides a complete analogy to the sloshing liquid without damping. The introduction of dashpots may provide a good approximation to the sloshing liquid with damping, but this will have to be examined in more detail by comparison with experimental data.

Let the tank undergo a translational oscillation $x = Ae^{i\omega t}$ and a pitching oscillation $\theta = Be^{i\omega t}$. The forces and moments exerted by the equivalent system are

$$F_H^{(1)} = Ae^{i\omega t}\cdot\omega^2 M_F \left\{\frac{m_0}{M_F} + \sum_{n=1}^{\infty}\frac{m_n}{M_F}\sum_{n=1}^{\infty}\frac{m_n}{M_F}\cdot \frac{1}{\left(\frac{\omega_n^2}{\omega^2}-1\right)+ig_n\frac{\omega_n}{\omega}}\right\} \quad [5a]$$

$$\lim_{g_n's\to 0} F_H^{(1)} = Ae^{i\omega t}\cdot\omega^2 M_F \times \left\{\frac{m_0}{M_F} + \sum_{n=1}^{\infty}\frac{m_n}{M_F} + \sum_{n=1}^{\infty}\frac{m_n}{M_F\left(\frac{\omega_n^2}{\omega^2}-1\right)}\right\} \quad [5b]$$

$$M_y^{(1)} = Ae^{i\omega t}\cdot\omega^2 M_F h\left\{\frac{m_0}{M_F}\cdot\frac{Z_0}{h} + \sum_{n=1}^{\infty}\frac{m_n}{M_F}\cdot\frac{z_n}{h} + \sum_{n=1}^{\infty}\frac{m_n}{M_F}\left(\frac{z_n}{h}+\frac{a}{h\omega^2}\right)\frac{1}{\left(\frac{\omega_n^2}{\omega^2}-1\right)+ig_n\frac{\omega_n}{\omega}}\right\} \quad [6a]$$

$$\lim_{g_n's\to 0} M_y^{(1)} = Ae^{i\omega t}\cdot\omega^2 M_F h\left\{\frac{m_0}{M_F}\cdot\frac{Z_0}{h} + \sum_{n=1}^{\infty}\frac{m_n}{M_F}\left(\frac{z_n}{h}+\frac{a}{\omega_n^2 h}\right)\sum_{n=1}^{\infty}\frac{m_n}{M_F}\left(\frac{z_n}{h}+\frac{a}{\omega_n^2 h}\right)\frac{1}{\frac{\omega_n^2}{\omega^2}-1}\right\} \quad [6b]$$

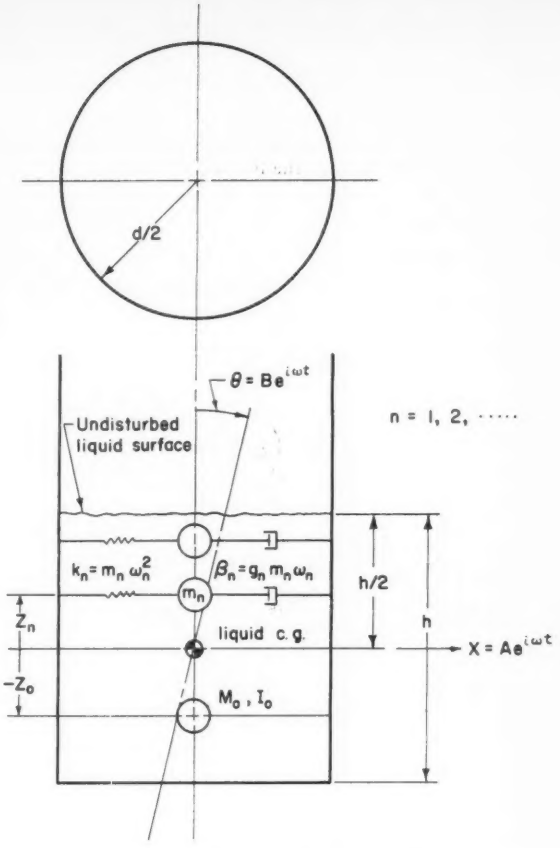

Fig. 1 Equivalent mechanical systen

$$F_H^{(2)} = Be^{i\omega t}\cdot\omega^2 h M_F\left\{\frac{m_0}{M_F}\cdot\frac{Z_0}{h} + \sum_{n=1}^{\infty}\frac{z_n}{h}\cdot\frac{m_n}{M_F} + \sum_{n=1}^{\infty}\left(\frac{z_n}{h}\right)\frac{m_n}{M_F}\cdot\frac{1}{\left(\frac{\omega_n^2}{\omega^2}-1\right)+ig_n\frac{\omega_n}{\omega}}\right\} + M_F B a e^{i\omega t}\sum_{n=1}^{\infty}\frac{m_n}{M_F}\left[\frac{1}{\left(\frac{\omega_n^2}{\omega^2}-1\right)+ig_n\frac{\omega_n}{\omega}}\right] = \frac{B}{A}M_y^{(1)} \quad [7a]$$

$$\lim_{g_n's\to 0} F_H^{(2)} = Be^{i\omega t}\cdot\omega^2 h M_F\left\{\frac{m_0}{M_F}\frac{Z_0}{h} + \sum_{n=1}^{\infty}\left(\frac{z_n}{h}+\frac{a}{\omega_n^2 h}\right)\frac{m_n}{M_F} + \sum_{n=1}^{\infty}\frac{m_n}{M_F}\left(\frac{z_n}{h}+\frac{a}{\omega_n^2 h}\right)\frac{1}{\frac{\omega_n^2}{\omega^2}-1}\right\} \quad [7b]$$

$$M_y^{(2)} = M_F h^2 Be^{i\omega t}\cdot\omega^2\left\{\frac{I_0}{M_F h^2} + \frac{m_0}{M_F}\cdot\frac{z_0^2}{h^2} + \sum_{n=1}^{\infty}\frac{m_n}{M_F}\cdot\frac{z_n^2}{h^2} + \sum_{n=1}^{\infty}\frac{m_n}{M_F}\left(\frac{z_n}{h}+\frac{a}{\omega^2 h}\right)^2\frac{1}{\left(\frac{\omega_n^2}{\omega^2}-1\right)+ig_n\frac{\omega_n}{\omega}}\right\} + Be^{i\omega t}\cdot M_F a h\left[\frac{m_0}{M_F}\cdot\frac{z_0}{h} + \sum_{n=1}^{\infty}\frac{m_n}{M_F}\cdot\frac{z_n}{h}\right] \quad [8a]$$

$$\lim_{g_n's\to 0} M_y^{(2)} = Be^{i\omega t}\cdot\omega^2 M_F h^2\left\{\frac{I_0}{M_F h^2} + \frac{m_0}{M_F}\cdot\frac{z_0^2}{h} + \sum_{n=1}^{\infty}\frac{m_n}{M_F}\left(\frac{z_n}{h}+\frac{a}{\omega_n^2 h}\right)^2 + \sum_{n=1}^{\infty}\frac{m_n}{M_F}\left(\frac{z_n}{h}+\frac{\alpha}{\omega_n^2 h}\right)^2\frac{1}{\frac{\omega_n^2}{\omega_n^2}-1}\right\} + Be^{i\omega t}\cdot M_F a h\left[\frac{m_0}{M_F}\cdot\frac{z_0}{h} + \sum_{n=1}^{\infty}\frac{m_n}{M_F}\left(\frac{z_n}{h}+\frac{a}{\omega_n^2 h}\right)\right] \quad [8b]$$

The derivations of these equations, although lengthy, are not difficult; the derivation of $M_y^{(2)}$ (Eq. 8) is given in the Appendix by way of illustration. Eqs. 5b, 6b, 7b, and 8b agree with the results given in (2).

Equivalent Mechanical Model for Representation of Sloshing With Small Damping

In many practical applications, the damping coefficients are small. For zero damping, the equivalent system may be given by a series of spring-mass combinations, the positions of which are frequency independent. The essential characteristics of the model are given by the following equations:

$$\frac{m_n}{M_F} = \frac{d \operatorname{Tanh}\left(\xi_n \frac{2h}{d}\right)}{\xi_n h(\xi_n^2 - 1)} \geq 0 \qquad n = 1, 2 \ldots \tag{9}$$

$$\frac{m_0}{M_F} = 1 - \sum_{n=1}^{\infty} \frac{d \operatorname{Tanh}\left(\xi_n \frac{2h}{d}\right)}{\xi_n h(\xi_n^2 - 1)} \geq 0 \tag{10}$$

$$\frac{Z_n}{h} = \frac{1}{2} + \frac{2}{\left(\xi_n \frac{2h}{d}\right) \operatorname{Sinh}\left(\xi_n \frac{2h}{d}\right)} - \frac{2}{\left(\xi_n \frac{2h}{d}\right) \operatorname{Tanh}\left(\xi_n \frac{2h}{d}\right)} \geq 0 \qquad \text{for } n \geq 1 \tag{11}$$

$$\frac{Z_0}{h} = \frac{+1}{1 - \sum_{n=1}^{\infty} \frac{d \operatorname{Tanh}\left(\xi_n \frac{2h}{d}\right)}{\xi_n h(\xi_n^2 - 1)}} \left[\frac{1}{4\left(\frac{2h}{d}\right)^2} - \sum_{n=1}^{\infty} \frac{\xi_n \operatorname{Tanh}\left(\xi_n \frac{2h}{d}\right) + \frac{4}{\left(\frac{2h}{d}\right) \operatorname{Cosh}\left(\xi_n \frac{2h}{d}\right)} - \frac{2}{\left(\frac{2h}{d}\right)}}{\xi_n \left(\xi_n \frac{2h}{d}\right)(\xi_n^2 - 1)} \right] \leq 0 \tag{12}$$

$$\frac{I_0}{M_F h^2} = \frac{I_F}{M_F h^2} + \frac{1}{\left(\frac{2h}{d}\right)^2} \sum_{n=1}^{\infty} \left[\frac{-8}{\operatorname{Sinh}\left(\xi_n \frac{2h}{d}\right)\left(\xi_n \frac{2h}{d}\right)} - 6 + \frac{10}{\left(\xi_n \frac{2h}{d}\right) \operatorname{Tanh}\left(\xi_n \frac{2h}{d}\right)} \right] \frac{1}{\xi_n^2(\xi_n^2 - 1)} -$$

$$\frac{1}{1 - \sum_{n=1}^{\infty} \frac{d \operatorname{Tanh}\left(\xi_n \frac{2h}{d}\right)}{\xi_n h(\xi_n^2 - 1)}} \left\{ \frac{1}{4\left(\frac{2h}{d}\right)^2} - \sum_{n=1}^{\infty} \frac{\xi_n \operatorname{Tanh}\left(\xi_n \frac{2h}{d}\right) + \frac{4}{\left(\frac{2h}{d}\right) \operatorname{Cosh}\left(\xi_n \frac{2h}{d}\right)} - \frac{2}{\left(\frac{2h}{d}\right)}}{\xi_n \left(\xi_n \frac{2h}{d}\right)(\xi_n^2 - 1)} \right\}^2 -$$

$$\sum_{n=1}^{\infty} \frac{\xi_n \left(\frac{2h}{d}\right)(\xi_n^2 - 1)}{2 \operatorname{Tanh}\left(\xi_n \frac{2h}{d}\right)} \left\{ \frac{\xi_n \operatorname{Tanh}\left(\xi_n \frac{2h}{d}\right) + \frac{4}{\left(\frac{2h}{d}\right) \operatorname{Cosh}\left(\xi_n \frac{2h}{d}\right)} - \frac{2}{\left(\frac{2h}{d}\right)}}{\left(\xi_n \frac{2h}{d}\right) \xi_n(\xi_n^2 - 1)} \right\}^2 \tag{13}$$

where

$$\frac{I_F}{M_F h^2} = \frac{1}{12} + \frac{1}{4} \frac{1}{\left(\frac{2h}{d}\right)^2}$$

For small damping, it is assumed that the mass distribution remains approximately unaltered, and therefore the force and moment are given by Eq. 5–13, i.e.

$$F_B^{(1)} = Ae^{i\omega t} \cdot \omega^2 M_F \left\{ 1 + \sum_{n=1}^{\infty} \frac{2 \operatorname{Tanh}\left(\xi_n \frac{2h}{d}\right)}{\left(\xi_n \frac{2h}{d}\right)(\xi_n^2 - 1)\left[\frac{\omega_n^2}{\omega^2} - 1 + ig_n \frac{\omega_n}{\omega}\right]} \right\} \tag{14}$$

$$M_y^{(1)} = Ae^{i\omega t} \cdot \omega^2 M_F h \left\{ \frac{1}{4\left(\frac{2h}{d}\right)^2} - \sum_{n=1}^{\infty} \frac{2}{\left(\xi_n \frac{2h}{d}\right)^2(\xi_n^2 - 1)} + \sum_{n=1}^{\infty} \frac{2 \operatorname{Tanh}\left(\xi_n \frac{2h}{d}\right)}{\left(\xi_n \frac{2h}{d}\right)(\xi_n^2 - 1)} \left[\frac{1}{2} + \frac{2}{\left(\xi_n \frac{2h}{d}\right) \operatorname{Sinh}\left(\xi_n \frac{2h}{d}\right)} - \right. \right.$$

$$\left. \left. \frac{2}{\left(\xi_n \frac{2h}{d}\right) \operatorname{Tanh}\left(\xi_n \frac{2h}{d}\right)} + \frac{a}{h\omega^2} \right] \cdot \frac{1}{\left(\frac{\omega_n^2}{\omega^2} - 1\right) + ig_n \frac{\omega_n}{\omega}} \right\} \tag{15}$$

$$F_H^{(2)} = Be^{i\omega t}\cdot\omega^2 h M_F \left\{\frac{M_y^{(1)}}{Ae^{i\omega t}\cdot\omega^2 M_F h}\right\} = \frac{B}{A}\,M_y^{(1)} \qquad [16]$$

$$M_y^{(2)} = M_F h^2 Be^{i\omega t}\cdot\omega^2 \left\{\frac{1}{12} - \frac{1}{2\left(\frac{2h}{d}\right)^2} + \sum_{n=1}^{\infty}\left[\frac{-8}{\mathrm{Sinh}\left(\xi_n\frac{2h}{d}\right)\left(\xi_n\frac{2h}{d}\right)} + \frac{10}{\left(\xi_n\frac{2h}{d}\right)\mathrm{Tanh}\left(\xi_n\frac{2h}{d}\right)}\right]\cdot\frac{1}{\xi_n^2(\xi_n^2-1)}\cdot\right.$$

$$\frac{1}{\left(\frac{2h}{d}\right)^2} + \sum_{n=1}^{\infty}\frac{d\,\mathrm{Tanh}\left(\xi_n\frac{2h}{d}\right)}{\xi_n h(\xi_n^2-1)}\left[\frac{1}{2} + \frac{2}{\left(\xi_n\frac{2h}{d}\right)\mathrm{Sinh}\left(\xi_n\frac{2h}{d}\right)} - \frac{2}{\left(\xi_n\frac{2h}{d}\right)\mathrm{Tanh}\left(\xi_n\frac{2h}{d}\right)}\right]^2 -$$

$$\sum_{n=1}^{\infty}\frac{d\,\mathrm{Tanh}\left(\xi_n\frac{2h}{d}\right)}{\xi_n h(\xi_n^2-1)}\left[\frac{1}{2} + \frac{2}{\left(\xi_n\frac{2h}{d}\right)\mathrm{Sinh}\left(\xi_n\frac{2h}{d}\right)} - \frac{1}{\left(\xi_n\frac{2h}{d}\right)\mathrm{Tanh}\left(\xi_n\frac{2h}{d}\right)}\right]^2 +$$

$$\left.\sum_{n=1}^{\infty}\frac{2\,\mathrm{Tanh}\left(\xi_n\frac{2h}{d}\right)}{\left(\xi_n\frac{2h}{d}\right)(\xi_n^2-1)}\left[\frac{1}{2} + \frac{2}{\left(\xi_n\frac{2h}{d}\right)\mathrm{Sinh}\left(\xi_n\frac{2h}{d}\right)} - \frac{2}{\left(\xi_n\frac{2h}{d}\right)\mathrm{Tanh}\left(\xi_n\frac{2h}{d}\right)} + \frac{a}{h\omega^2}\right]^2\cdot\frac{1}{\frac{\omega_n^2}{\omega^2} - 1 + ig_n\frac{\omega_n}{\omega}}\right\} +$$

$$Be^{i\omega t}\cdot M_F a h\left\{\frac{1}{4\left(\xi_n\frac{2h}{d}\right)^2} - \sum_{n=1}^{\infty}\frac{2}{\left(\xi_n\frac{2h}{d}\right)^2(\xi_n^2-1)}\right\} \qquad [17]$$

$$M_y^{(2)} = M_F h^2 Be^{i\omega t}\cdot\omega^2\left\{\frac{1}{12} + \frac{2}{4\left(\frac{2h}{d}\right)^2} + \frac{2}{\left(\frac{2h}{d}\right)^2}\sum_{n=1}^{\infty}\frac{1}{\xi_n(\xi_n^2-1)}\left[-4 - \frac{8}{\left(\xi_n\frac{2h}{d}\right)\mathrm{Sinh}\left(\xi_n\frac{2h}{d}\right)} + \frac{8}{\left(\xi_n\frac{2h}{d}\right)\mathrm{Tanh}\left(\xi_n\frac{2h}{d}\right)}\right] +\right.$$

$$\left.\sum_{n=1}^{\infty}\frac{2\,\mathrm{Tanh}\left(\xi_n\frac{2h}{d}\right)}{\xi_n\frac{2h}{d}(\xi_n^2-1)}\left[\frac{1}{2} + \frac{2}{\left(\xi_n\frac{2h}{d}\right)\mathrm{Sinh}\left(\xi_n\frac{2h}{d}\right)} - \frac{2}{\left(\xi_n\frac{2h}{d}\right)\mathrm{Tanh}\left(\xi_n\frac{2h}{d}\right)} + \frac{a}{h\omega^2}\right]^2\frac{1}{\frac{\omega_n^2}{\omega^2} - 1 + ig\frac{\omega_n}{\omega}}\right\} \qquad [18]$$

where the identity $^1/_3 = \sum_{n=1}^{\infty} 1/\xi_n^2(\xi_n^2-1)$ has been used.

In Eqs. 15 and 17 the term $\dfrac{1}{4(2h/d)^2} - \sum_{n=1}^{\infty}\dfrac{2}{(\xi_n 2h/d)^2(\xi_n^2-1)}$ is automatically zero.

When $g_n \to 0$, the effective moment of inertia is the same as that with a frozen free surface, i.e., the moment of inertia of a completely filled tank (8), and the effective mass is the total mass of the fluid M_F.

It should be noted that the total force on the tank wall is given by

$$F_X = F_H + M_F a\vartheta$$

Comparison With Bauer's Theory (6)

The only difference between Bauer's results (6) and those of this paper is the moment resulting from pitching oscillations. For infinite damping, the forces and moments reduce to those corresponding to a frozen free surface, whereas Bauer's theory requires them to reduce to those of a frozen (rigid) body. The difference between the two analyses is large near the first resonant frequency.[8] In many practical applications, however, the center of rotation is about one diameter or more from the c.g. of the liquid, and in such cases the moment about the c.g. contributes only a small percentage of the total moment. For this reason, the discrepancy between the theories may be of little practical importance.

Interpretation of Model for Case of Axial Thrust

During vertical launching of a rocket, there is an axial thrust producing an upward axial acceleration α_T'.[9] If the gravitational acceleration is G, the resultant acceleration is $\alpha_T' + G$. The inertia force $-\rho(\alpha_T' + G)$ plus the gravitational force ρG results in the total body force $-\rho\alpha_T'$, which oscillates with the tank when the tank itself undergoes pitching oscillations. From studies of a more general case it can be easily shown that the same equivalent system as derived in the foregoing is valid here, provided that the natural frequencies[10] are calculated with a replaced by the total downward axial acceleration due to body forces, which is equal to α_T' in this important case. These two quantities coincide in the case of pure translational oscillations.

[8] The results of some computations will be given later in this paper.

[9] The important point to note here is that the axial thrust and corresponding axial acceleration need not be vertical in the Earth-fixed sense; see also (9) for further discussion.

[10] See just following Eq. 2.

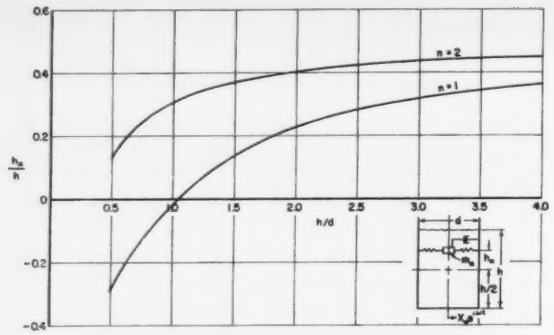

Fig. 2 Height of sloshing mass vs. liquid height

Experimental Evaluation of the Equivalent Mechanical Model

General

In order to examine the ability of the equivalent mechanical model to represent the actual force and moment response of a tank containing sloshing liquid, it is necessary first to have knowledge of, or to determine, appropriate values for damping factors. The mechanical model can then be employed to predict the response that is to be compared with that actually measured during some test program. Earlier work during this program of research has resulted in the accumulation of a rather substantial amount of experimental data for model tanks in translation and in pitching and with different types of suppression devices (10,11). This experimental data can therefore serve as the basis for evaluation of the equivalent mechanical model. The two types of suppression devices to be considered are floating cans and conical (or long single) rings (10).

Damping Factors

The damping factors were obtained directly from the experimental response data by an iterative procedure based on the half band-width technique, as given and described in (6). The damping factors thus obtained depend, of course, on excitation amplitude and equivalent Reynolds number. It is necessary to correlate the damping factors obtained from pitching tests with those obtained from translational tests to insure that the values are in sufficiently close agreement for the two types of motion to allow the use of a single value for a given suppression device. A basis must therefore be established for determining equivalent excitation amplitudes in pitching and translation at which damping factors may be correlated. The equivalent mechanical system consists of a fixed mass and a series of sloshing masses connected to the tank through springs and dashpots; each mass corresponds to one of the natural resonant modes, and the height location of the various masses depends on the liquid height being represented. Since the measured damping factors are obtained at the first mode ($n = 1$), the effects of higher modes being relatively unimportant, the amplitude of motion of the mass corresponding to this mode may be used for comparison between translation and pitching. Fig. 2 shows the height of the $n = 1$ and $n = 2$ masses as a function of liquid height. Fig. 3 shows the variation of the pitching angle required to displace the $n = 1$ mass by an equivalent translational displacement, where h_1/h is obtained from Fig. 2. The pitching excitation amplitudes of the various test data were therefore converted into the equivalent translational excitation amplitudes by use of Fig. 3. The resulting plots of damping factors for the conical rings are given in Fig. 4 and for the floating cans in Fig. 5, expressed in terms of dimensionless excitation

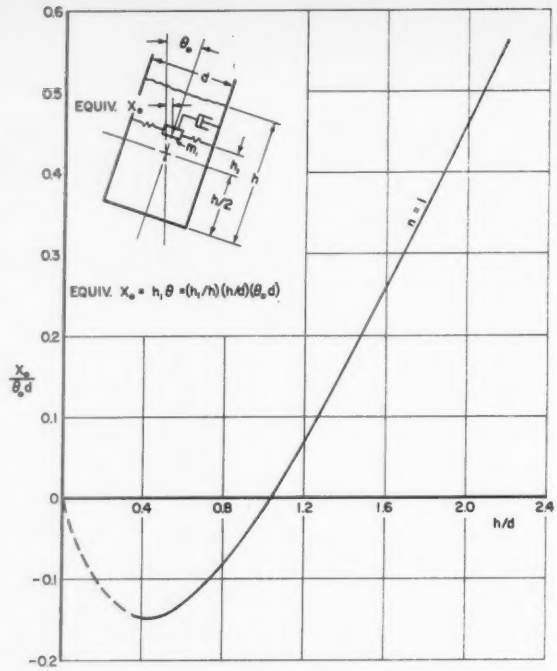

Fig. 3 Equivalence of translation and pitching amplitudes of sloshing mass

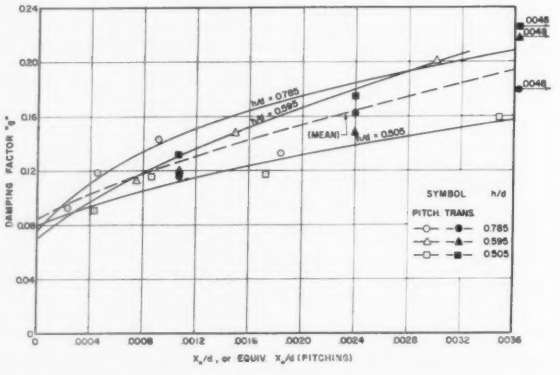

Fig. 4 Comparison of damping factors in pitching and translation: conical rings, $\rho\, d^{3/2}\, a^{1/2}/\mu = 1.680 \times 10^6$

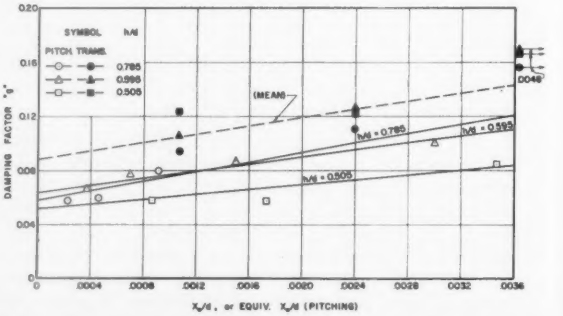

Fig. 5 Comparison of damping factors in pitching and translation: 90 floating cans, $\rho\, d^{3/2}\, a^{1/2}/\mu = 1.680 \times 10^6$

amplitude X_0/d at one value of the effective Reynolds number (10,11).

Comparison of damping factors due to the conical rings (Fig. 4) shows rather good agreement between pitching and translation. Comparison of damping factors due to the 90 floating cans (Fig. 5) shows fair agreement, the damping factors in pitching being lower than those in translation. A possible explanation of this discrepancy may be the different manner in which the cans introduce damping into the liquid system. Whereas the rings are distributed through most of the liquid height and thus impart a distributed form of damping, the cans introduce damping at the surface only. A slightly more accurate equivalent mechanical model for floating can suppressors might therefore be obtained by the introduction of some appropriate empirical correction factor that would tend to shift the damping curves in pitching in Fig. 5 nearer those in translation. It is shown in the following section that the calculated response curves are sufficiently accurate, for practical applications, so that the introduction of such an empirical correction is not considered necessary.

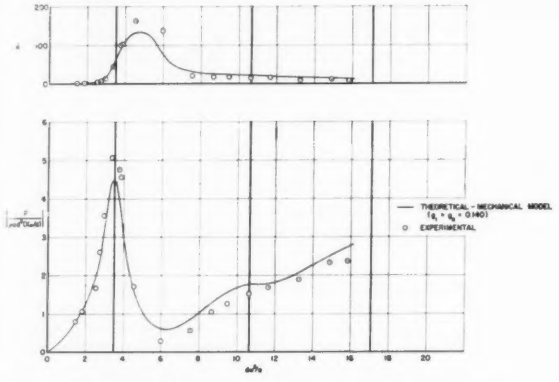

Fig. 6 Translational force response: 90 floating cans, $h/d = 0.505$, $x_0/d = 0.00480$

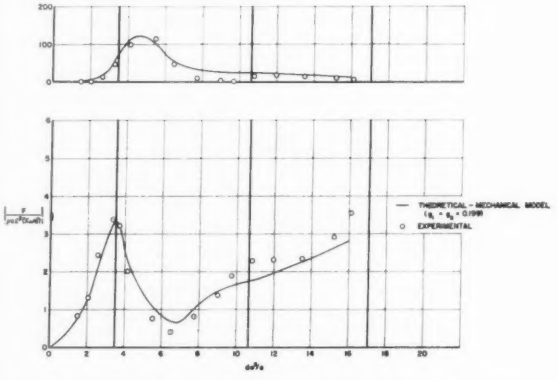

Fig. 7 Translational force response: long single rings, $h/d = 0.505$, $x_0/d = 0.00480$

Comparison of Measured and Calculated Force Response

The values of the damping factors obtained as described above have been employed in the relevant equations of the equivalent mechanical model to calculate the total force response in translation and in pitching, and these are then compared directly with the original experimental data. The calculations carried through with the mechanical model generally involved three spring mass dashpot elements, although a few examples did involve four or five elements.

Examples of the results of the comparisons in translation are shown in Fig. 6 for the floating cans and in Fig. 7 for the conical rings.[11] The agreement between calculated and measured force response is generally very good in both amplitude and phase, and is somewhat better for the rings than for the cans. The slightly poorer agreement for the cans is probably attributable to the fact that part of the damping is provided by mechanical friction between cans, and this damping cannot be represented well by an equivalent dashpot in the mechanical system, as mentioned previously.

Similar results of the comparisons in pitching are shown in Fig. 8 for the floating cans and in Fig. 9 for the conical rings. The agreement between calculated and measured force response is generally very good in both amplitude and phase for both rings and cans.

Unfortunately, no reliable experimental data has yet been obtained for moment response in either translation or pitching, because of certain instrumentation problems, and therefore no comparisons are possible. However, it was noted earlier in this paper that the moment resulting from pitching oscillations as given by the present mechanical model is slightly different from that given by Bauer (6), and therefore it is of some interest to compare the moment due to pitching given by the two analyses. This is done in the following section.

[11] Because of space limitations, only a few examples of a large series of comparisons can be given here. The comparisons are equally good, or better, at other liquid depths and excitation amplitudes.

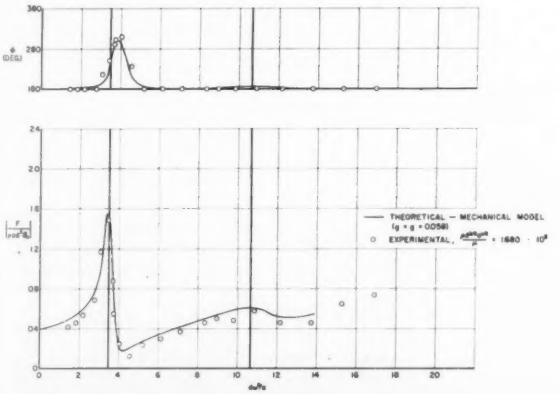

Fig. 8 Pitching force response: 90 floating cans, $h/d = 0.505$, $\theta_0 = 0.01191$

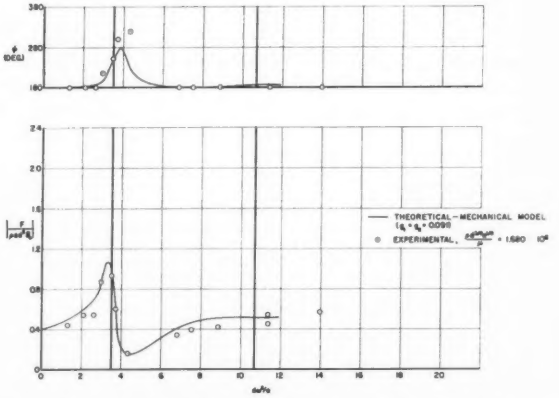

Fig. 9 Pitching force response: long single rings, $h/d = 0.505$, $\theta_0 = 0.00298$

Calculated Moment Response in Pitching

Examples of the calculated response curves for the moment resulting from pitching oscillations are shown in Fig. 10 for the floating cans and in Fig. 11 for the conical rings. It is noted that the present analysis gives response amplitudes consistently less than those obtained from Bauer's analysis (6). Again, the moment about the c.g. contributes only slightly to the total moment so that this difference between the two analyses may not be of great practical importance.

Conclusion

It would appear that the equivalent mechanical model for the representation of linear fuel sloshing with damping in cylindrical tanks proposed in this paper is fairly well established. This is evidenced by its analytical foundations and by the rather good agreement obtained between measured force response and that computed by means of the model. The appropriate values of damping factors to be employed in the model must, of course, be determined in advance by some experimental or analytical program.

Appendix

Derivation of Eq. 8

The derivation of Eqs. 5–8, although lengthy, is not difficult; by way of illustration, the derivation of $M_y^{(2)}$, the moment due to sloshing in pitching (Eq. 8), will be given here.

Assume that there is no axial thrust ($a = G$) and let x_n be the horizontal displacement of the mass m_n from the vertical axis, due to pitching. The balance of force on the mass m_n yields

$$m_n\ddot{x}_n \cong -k_n(x_n - \theta z) - \beta_n(\dot{x}_n - z_n\dot{\theta}) + m_n a\theta \quad \text{[A-1]}$$

for $\theta = Be^{i\omega t}$

$$X_n = Be^{i\omega t}\, z_n\left[1 + \frac{\omega^2}{{\omega_n}^2 - \omega^2 + ig_n\omega_n\omega}\right] + Be^{i\omega t}\left[\frac{a}{{\omega_n}^2 - \omega^2 + ig_n\omega_n\omega}\right] \quad \text{[A-2]}$$

provided that

$$m_n = k_n{\omega_n}^2$$

$$\beta_n = m_n g_n \omega_n$$

$$\omega_0 \text{ and } g_0 \to \infty$$

The force perpendicular to the wall is

$$F_x^{(2)} = \sum_{n=1}^{\infty}[-m_n\ddot{x}_n + m_n a\theta]$$

$$= Be^{i\omega t}\cdot\omega^2 M_F h\left\{\frac{M_0}{M_F}\frac{Z_0}{h} + \sum_{n=1}^{\infty}\frac{m_n}{M_F}\frac{Z_n}{h} + \sum_{n=0}^{\infty}\frac{m_n}{M_F}\frac{Z_n}{h}\frac{1}{\dfrac{{\omega_n}^2}{\omega^2} - 1 + ig_n\dfrac{\omega_n}{\omega}}\right\} + Be^{i\omega t}M_F a\sum_{n=1}^{\infty}\frac{m_n}{M_F}\left[\frac{1}{\dfrac{{\omega^2}_n}{\omega^2} - 1 + ig_n\dfrac{\omega_n}{\omega}}\right] + aBe^{i\omega t}M_F\sum_{n=0}^{\infty}\frac{m_n}{M_F} \quad \text{[A-3]}$$

The moment exerted on the tank is

$$M_y^{(2)} \cong \sum_{n=0}^{\infty} F_x^{(2)}\cdot Z_n + \sum_{n=1}^{\infty} m_n\, a\,[x_n - Z_n\theta] + (-I_0\ddot{\theta})$$

By direct substitution, this leads immediately to Eq. 8 of the main text.

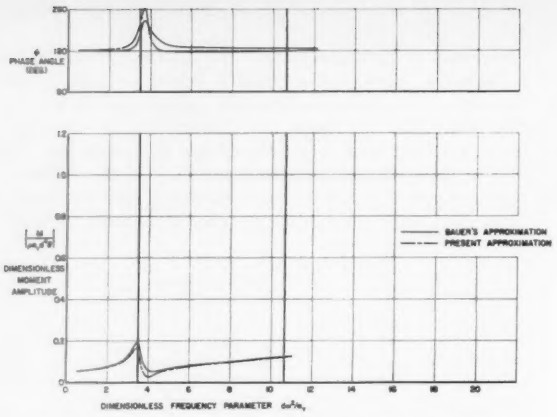

Fig. 10 Pitching moment response: 90° floating cans, $h/d = 0.505$, $g = 0.058$

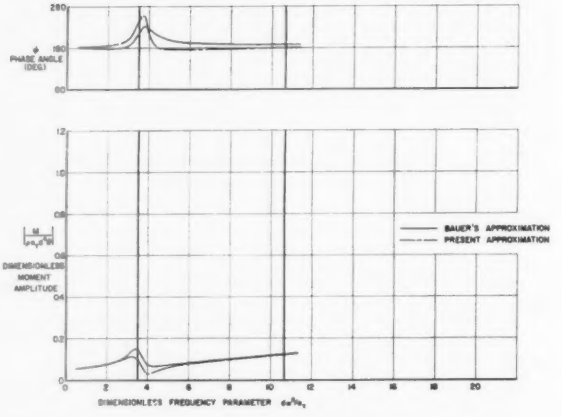

Fig. 11 Pitching moment response: long single rings, $h/d = 0.505$, $g = 0.091$

Nomenclature

d	= diameter of cylindrical tank
F_H	= horizontal force
g_n	= nth damping coefficient
h	= height of undisturbed liquid
k_n	= spring constant of the nth spring
M_y	= moment about y-axis normal to the plane of symmetry through c.g.
m_n	= mass of the nth point mass
X_0	= translational displacement

$Z_n = z_n$ = vertical position of the nth point mass from a horizontal plane through c.g. (tank undisturbed)

α = downward axial acceleration field acting in addition to gravity

α_T = $\alpha + G \operatorname{Cos} \theta \cong \alpha + G$

β_n = $m_n \omega_n g_n$

θ = angular displacement, positive clockwise (Fig. 1)

μ = fluid viscosity

ξ_n = nth zero of the first derivative of the Bessel function of the first kind of the order one, i.e., $J_1'(\xi_n) = 0$

ρ = fluid density

ω_n = $\sqrt{k_n/m_n}$, nth natural frequency

Superscripts

$(\ )^{(1)} - (\ )$ = associated with translational motion

$(\ )^{(2)} - (\ )$ = associated with pitching motion

References

1 Luskin, L. and Lapin, E., "An Analytical Approach to the Fuel Sloshing and Buffeting Problems of Aircraft," *J. Aeronaut. Sci.*, vol. 19, no. 4, April 1952, pp. 217–228.

2 Graham, E. W. and Rodriquez, A. M., "The Characteristics of Fuel Motion Which Affect Airplane Dynamics," *J. Appl. Mech.*, vol. 19, no. 3, September 1952, pp. 381–388 (see also *Douglas Aircraft Co. Rep. No. SM-14212*).

3 Kachigan, K., "Forced Oscillations of a Fluid in a Cylindrical Tank," *Convair Rep. ZU-7-046*, October 1955.

4 Schmitt, A. F., "Forced Oscillations of a Fluid in a Cylindrical Tank Undergoing Translation and Rotation," *Convair Rep. ZU-7-069*, October 1956.

5 Bauer, H. F., "Fluid Oscillations in a Circular Cylindrical Tank," *ABMA Rep. DA-TR-1-58*, April 1958.

6 Bauer, H. F., "Fluid Oscillations in a Cylindrical Tank With Damping," *ABMA Rep. DA-TR-4-58*, April 1958.

7 Miles, J. W., "On the Sloshing of Liquid in a Cylindrical Tank," *Ramo-Wooldridge Rep. AM6-5*, April 1956.

8 Bauer, H. F., "The Moment of Inertia of a Liquid in a Circular Cylindrical Tank," *ACMA DA-TR-5-58*, April 1958.

9 Chu, W. H., "Free Surface Condition for Sloshing Resulting From Pitching and Some Corrections," ARS JOURNAL, vol. 30, no. 11, November 1960, pp. 1093–1094.

10 Abramson, H. N. and Ransleben, G. E., Jr., "Simulation of Fuel Sloshing Characteristics in Missile Tanks by Use of Small Models," ARS JOURNAL, vol. 30, no. 7, July 1960, pp. 603–612.

11 Abramson, H. N. and Ransleben, G. E., Jr., "Liquid Sloshing in Rigid Cylindrical Tanks Undergoing Pitching Motion," *Tech. Rep. no. 11*, Contract no. DA 23-072-ORD-1251, Southwest Research Inst., May 1961.

Stability of a Cylinder Under Dynamic Radial Pressure[1]

JOHN C. YAO[2]

Aerospace Corp.
El Segundo, Calif.

A study is made of the stability of a long cylinder under radial pressure of short duration. The equilibrium equations are reduced to a mass-spring system in a single degree of freedom. It is shown that if the magnitude of the pressure is greater than the static buckling pressure, the displacement will increase monotonically as loading duration becomes long. The cylinder can withstand an impulsive loading greater than the static buckling pressure if the loading duration is very short compared with the free vibration period of the cylinder in the first mode. Numerical results are obtained for the radial displacement amplitudes for various load intensities and loading durations.

THIS investigation is concerned with the buckling resistance of a cylinder under radial pressure with a rather short loading duration, i.e., impulsive loading. It is well known that a structure can withstand a dynamic load greater than the static buckling load if the loading is impulsive rather than static.

Received May 28, 1961.

[1] This work was carried out in the Research and Development Group, Structures Section, Missiles and Space Systems Engineering Div., Douglas Aircraft Co.

[2] Member of Technical Staff; formerly with Douglas Aircraft Co.

Equations of Motion

The motion of a long cylinder due to radial pressure will be independent of the axial coordinate. The motion is asymmetric, and the equilibrium equations (1)[3] can easily be

[3] Numbers in parentheses indicate References at end of paper.

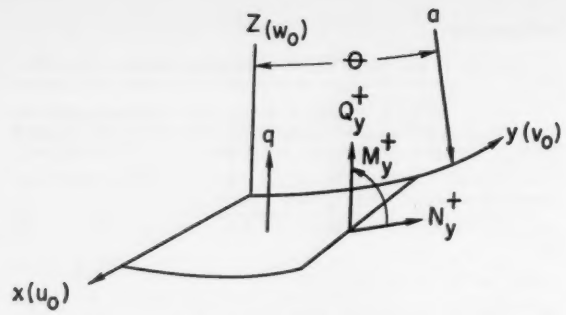

Fig. 1 Shell element

written down with the aid of the notation given in Fig. 1

$$a \cdot \frac{\partial N_y}{\partial y} - \frac{\partial M_y}{\partial y} = ma \frac{\partial^2 v_0}{\partial t^2} \quad [1]$$

$$N_y \left(1 + a \frac{\partial^2 w_0}{\partial y^2}\right) + a \frac{\partial^2 M_y}{\partial y^2} + qa = ma \frac{\partial^2 w_0}{\partial t^2} \quad [2]$$

The circumferential force N_y and moment M_y are given in terms of the displacements by

$$N_y = \frac{Eh}{1-\mu^2}\left(\frac{\partial v_0}{\partial y} - \frac{w_0}{a}\right) \quad [3a]$$

$$M_y = -\frac{Eh^3}{12(1-\mu^2)} \cdot \frac{\partial^2 w_0}{\partial y^2} \quad [3b]$$

Substituting these displacement expressions in Eqs. 1 and 2 yields

$$a \frac{\partial^2 v_0}{\partial y^2} - \frac{\partial w_0}{\partial y} + \frac{1}{12}\left(\frac{h}{a}\right)^2 \cdot a^2 \frac{\partial^3 w_0}{\partial y^3} = \frac{1-\mu^2}{Eh} ma \frac{\partial^2 v_0}{\partial t^2} \quad [4]$$

$$\left(\frac{\partial v_0}{\partial y} - \frac{w_0}{a}\right)\left(1 + a \frac{\partial^2 w_0}{\partial y^2}\right) - \frac{1}{12}\left(\frac{h}{a}\right)^2 \cdot a^3 \frac{\partial^4 w_0}{\partial y^4} + \frac{1-\mu^2}{Eh} qa = \frac{1-\mu^2}{Eh} ma \frac{\partial^2 w_0}{\partial t^2} \quad [5]$$

Next, decompose the displacement into two parts so that

$$w_0 = w + w_1 \quad [6a]$$

$$v_0 = v + v_1 \quad [6b]$$

where w_1 and v_1 are displacement components producing membrane stress only, and w and v are the remaining displacement components. In membrane shell theory, w_1 and v_1 satisfy the equations of equilibrium (2)

$$a \frac{\partial}{\partial y}\left(\frac{\partial v_1}{\partial y} - \frac{w_1}{a}\right) = \frac{1-\mu^2}{Eh} ma \frac{\partial^2 v_1}{\partial t^2} \quad [7]$$

$$\frac{\partial v_1}{\partial y} - \frac{w_1}{a} + \frac{1-\mu^2}{Eh} qa = \frac{1-\mu^2}{Eh} ma \frac{\partial^2 w_1}{\partial t^2} \quad [8]$$

Subtracting Eqs. 7 and 8 from Eqs. 4 and 5 respectively after omitting the contribution to the bending terms by the membrane displacement and observing that $(\partial v_1/\partial y) - (w_1/a) \approx -(1-\mu^2/Eh)\, qa$ is the dominant part in the expression $[(\partial v_0/\partial y) - (w_0/a)]$, the final equilibrium equation may be given in terms of v and w:

$$a \frac{\partial^2 v}{\partial y^2} - \frac{\partial w}{\partial y} + \frac{1}{12}\left(\frac{h}{a}\right)^2 a^2 \frac{\partial^3 w}{\partial y^3} = \frac{1-\mu^2}{Eh} ma \frac{\partial^2 v}{\partial t^2} \quad [9]$$

$$\frac{\partial v}{\partial y} - \frac{w}{a} - \frac{1-\mu^2}{Eh}\left(qa^2\right)\frac{\partial^2 w}{\partial y^2} - \frac{1}{12}\left(\frac{h}{a}\right)^2 a^3 \frac{\partial^4 w}{\partial y^4} = \frac{1-\mu^2}{Eh} ma \frac{\partial^2 w}{\partial t^2} \quad [10]$$

The inertia term in Eq. 9 may be ignored since the magnitude v is small compared with w (3). The basic equation of motion in terms of w is obtained only by combining Eqs. 9 and 10

$$\frac{1-\mu^2}{Eh} ma^3 \frac{\partial^3 w}{\partial y \partial t^2} + \left[\left(\frac{1}{12}\frac{h^2}{a^2} + \frac{1-\mu^2}{Eh} qa\right) \cdot a^3 \frac{\partial^3}{\partial y^3} + \frac{h^2}{12a^2} a^5 \frac{\partial^5}{\partial y^5}\right] w = 0 \quad [11]$$

Solution of Problem

Eq. 11 will be satisfied by the following expression:

$$w = W(t) \cos n(y/a) \quad [12]$$

where n is an integer ≥ 2. $W(t)$ is a function of time only. Substitution in Eq. 11 yields

$$\frac{d^2W(t)}{dt^2} + \frac{n^4 - n^2(1 + 3\, q/q_{cr})}{3(ma/q_{cr})} W(t) = 0 \quad [13]$$

where

$$q_{cr} = \frac{E}{4(1-\mu^2)}\left(\frac{h}{a}\right)^3 \quad [14]$$

is the classical buckling pressure acting uniformly on the external surface of a long cylinder.

Denote

$$p^2 = \frac{n^4 - n^2(1 + 3\, q/q_{cr})}{3(ma/q_{cr})} \quad [15]$$

and rewrite Eq. 13 in the form

$$\frac{d^2W}{dt^2} + p^2 W = 0 \quad [16]$$

Eq. 16 is recognized as the motion equation of a mass-spring system. The first term represents the inertia force and the second the restoring force of the spring. The nature of the solution will depend on the sign of p^2. Note from Eq. 15 that p will be zero if

$$q/q_{cr} = (1/3)(n^2 - 1) \quad [17]$$

In this case, the restoring force of the spring is destroyed, and the system is unstable. As the cylinder offers the least resistance possible, the minimum q required to satisfy Eq. 17 will be given for $n = 2$. So

$$q = q_{cr} \quad [18]$$

Notice from Eq. 12 that for $n = 2$ the displaced position of the cylinder is an oval. Call this vibration the fundamental mode. From now on only this mode, i.e., the case of $n = 2$, will be considered, as it gives the lowest unstable q. Hence, Eq. 15 may be rewritten

$$p^2 = \frac{16 - 4(1 + 3\, q/q_{cr})}{3(ma/q_{cr})} \quad [15a]$$

Accordingly, p^2 will be positive for $q < q_{cr}$ and negative for $q > q_{cr}$. The case of $q \gtrless q_{cr}$ and the one in which q approaches

q_{cr} as a limit will be investigated separately.

Case 1: Subcritical Condition ($q/q_{cr} = \alpha < 1$)

As previously stated, impulse type loading is under consideration. Assume, for the present, that the loading is given as shown in Fig. 2, i.e.

$$\begin{aligned} q/q_{cr} &= \alpha & 0 \le t \le \tau \\ &= 0 & t > \tau \end{aligned} \quad [19]$$

According to Eq. 19, the well-known solution for Eq. 16 takes the form (Ref. 4, pp. 4 and 104)

$$W(t) = \int_0^t \frac{1}{p}\left(\frac{\alpha q_{cr}}{m}\right) \sin p(t - t^*)dt^*$$

$$= \frac{\alpha q_{cr}}{p^2 m}(1 - \cos pt) \qquad 0 \le t \le \tau \quad [20]$$

and

$$W(t) = W(\tau)\cos p_0 t + \frac{1}{p_0}\left(\frac{dW}{dt}\right)_{t=\tau} \cdot \sin p_0 t \qquad t > \tau \quad [21]$$

In Eq. 21, p_0 is the natural angular frequency of the long cylinder at its fundamental mode, i.e.

$$p_0 = 2\sqrt{q_{cr}/ma} \quad [22]$$

Its period of vibration is equal to

$$T_0 = 2\pi/p_0 = \pi\sqrt{ma/q_{cr}} \quad [23]$$

Also note that Eq. 20 satisfies the initial condition

$$W(0) = \left(\frac{dW}{dt}\right)_{t=0} = 0 \quad [24]$$

The cylinder will undergo a periodic motion in the presence of the impulse load and will continue to vibrate after the loading period terminates simply by changing its angular frequency from p to p_0 (cf. Eqs. 20 and 21). Therefore, it may be said that the motion is always stable under the subcritical condition.

Case 2: Supercritical Condition($q/q_{cr} = \alpha > 1$)

The loading character will be assumed the same as that given by Eq. 19. It is found that with p imaginary this time, the solution of Eq. 16 is as follows:

$$W(t) = \int_0^t \frac{1}{(-ip)}\left(\frac{\alpha q_{cr}}{m}\right) \sinh(-ip)(t - t^*)\, dt^*$$

$$= \frac{\alpha q_{cr}}{-p^2 m}[\cosh(-ipt) - 1] \qquad 0 \le t \le \tau \quad [25]$$

and

$$W(t) = W(\tau)\cos p_0 t + \frac{1}{p_0}\left(\frac{dW}{dt}\right)_{t=\tau} \cdot \sin p_0 t \qquad t > \tau \quad [26]$$

Eq. 25 again satisfies the initial conditions of Eq. 24.

The amplitude of the motion will increase monotomically as long as the load is acting. The cylinder will certainly collapse if the loading period is long enough. If, however, the loading period is short enough not to cause buckling (amplitude approaches infinity), the cylinder will then undergo periodic motion with natural angular frequency p_0 as soon as the load is removed (see dotted curve in Fig. 2). Here then, the stability of the motion depends on the duration of the impulse.

Case 3: Near-Critical Condition

This case shall be investigated by referring to Eq. 15a

$$\lim_{\epsilon \to 0} \frac{q}{q_{cr}} = \frac{q_{cr} + \epsilon}{q_{cr}} = 1 \qquad \lim_{\epsilon \to 0} p = 0 \quad [27]$$

The solution may be derived from Eq. 25 by applying L'Hospital Rule. Thereby

$$W(t) = \lim_{\epsilon \to 0} \frac{\alpha}{-p^2}\frac{q_{cr}}{m}[\cosh(-ipt) - 1]$$

$$= \frac{1}{2}\left(\frac{q_{cr}}{m}\right)t^2 \qquad 0 \le t \le \tau \quad [28]$$

$$\frac{dW(t)}{dt} = \lim_{\epsilon \to 0} \frac{i\alpha}{p}\left(\frac{q_{cr}}{m}\right) \sinh(-ipt)$$

$$= \left(\frac{q_{cr}}{m}\right)t \qquad 0 \le t \le \tau \quad [29]$$

The equation of motion for $t > \tau$ is seen equal to

$$\lim_{\epsilon \to 0} W(t) = \frac{1}{2}\left(\frac{q_{cr}}{m}\right)\tau^2 \cos p_0 t + \frac{\tau}{p_0}\left(\frac{q_{cr}}{m}\right) \sin p_0 t \quad [30]$$

The physical phenomenon displayed by Eqs. 28 and 30 are comparable to Eqs. 25 and 26 in case 2.

Numerical Results

The ranges of load intensity and duration for which the cylinder responds to loading without causing buckling are interesting from the viewpoint of design. The amplitude of vibration caused by a given impulse shall be found in terms of thickness of the shell. It can be judged from the amplitude whether the vibrating motion is greater than allowable. The amplitude W_m (Fig. 2) is readily found by the following expression (Ref. 4, p. 5):

$$W_m = \sqrt{[W(\tau)]^2 + \left[\frac{1}{p_0}\left(\frac{dW}{dt}\right)_{t=\tau}\right]^2} \quad [31]$$

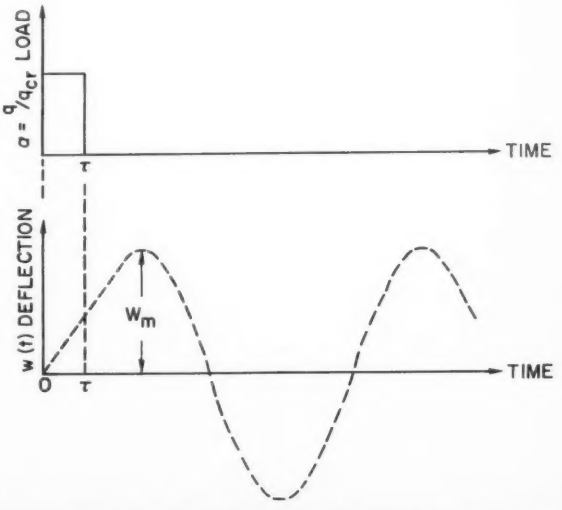

Fig. 2 Load and radial displacement vs. time

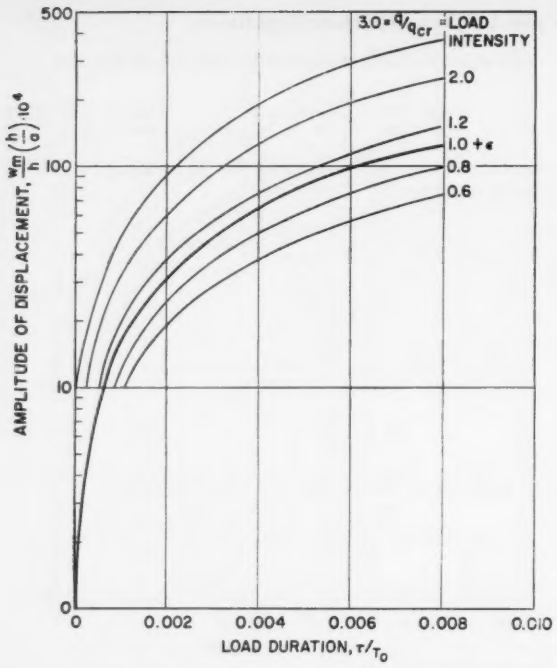

Fig. 3 Amplitude of radial displacement vs. load duration for various load intensity

where $W(\tau)$ and $(dW/dt)_{t=\tau}$ are obtained from Eq. 20 for the subcritical condition, from Eq. 25 for the supercritical condition, and from Eqs. 28 and 29 for the near-critical condition. The results for all cases discussed are plotted in Fig. 3 with $(W_m/h)(h/a)$ as ordinate and nondimensional loading duration τ/T_0 as the abscissa. The following conclusions may be drawn by studying Fig. 3:

1 The cylinder can withstand radial pressure greater than the classical (static) buckling pressure if the loading duration is short enough in the supercritical condition.

2 In the static case, as long as $q < q_{cr}$, the cylinder simply undergoes membrane strain due to hoop compression, which is negligibly small. In the case where the load is the impulse type, even under the subcritical condition, the amplitude of vibration is the same order of magnitude as that under the supercritical condition.

3 It is shown from Fig. 3 that the allowable loading duration, without causing the cylinder to buckle, is rather short.

The buckling resistance can be substantially increased if sandwich construction is used. The sandwich cylinder has a much higher bending stiffness, which contributes substantially to buckling resistance, than the monocoque shell. Also, a sandwich cylinder can actually be made lighter than a monocoque cylinder, reducing the inertia force.

Nomenclature

t	=	time
y	=	a θ, arc length, Fig. 1
u_0, v_0, w_0	=	x, y, z displacement components
m	=	mass per unit area of middle surface
a, h	=	radius of the middle surface, shell thickness
$E\mu$	=	Young's modulus, Poisson's ratio
N_y	=	membrane force in the y direction
M_y	=	moment, Fig. 1
q	=	radial pressure
k_y	=	curvature
τ	=	impulse loading duration
T_0	=	period of the first mode of a long cylinder in free vibration
q_a	=	classical buckling pressure
W_m	=	maximum amplitude of vibration
α	=	q/q_{cr}
n	=	number of waves around circumference
p	=	natural frequency, see Eq. 15

References

1 Timoshenko, S., *Theory of Plates and Shells*, McGraw-Hill Book Co. Inc., New York, 1940, p. 440.

2 Bolotin, V. V., "Dynamic Stability of Elastic Systems," *Gos. Izdat. Tekh.-Teor. Lit.*, Moscow, 1956, p. 573.

3 Markov, A. N., *Prikladnaia Mathmatika i Mekhnika*, Vol. 13, 1949, pp. 145–150.

4 Timoshenko, S., *Vibration Problems in Engineering*, 2nd. ed., D. Van Nostrand Co. Inc., New York, 1937 pp. 4. 5. 104.

Hot Wire Measurements in Low Reynolds Number Hypersonic Flows[1]

C. FORBES DEWEY Jr.[2]

Guggenheim Aeronautical Laboratory
California Institute of Technology
Pasadena, Calif.

Measurements were made of the heat loss and recovery temperature of a fine hot wire at a nominal Mach number of 5.8. Data were obtained over an eightfold range of Reynolds numbers in the transitional regime between continuum and free molecule flow. At high Reynolds numbers, the heat transfer data agree well with the results of Laufer and McClellan, which were obtained at lower Mach numbers. At lower Reynolds numbers, the results indicate a monotonic transition between continuum and free molecule heat transfer laws. The slope of the heat transfer correlation was found to vary monotonically, with $Nu \sim \sqrt{Re}$ at high Reynolds numbers and $Nu \sim Re$ for $Re \ll 1$. Data on the wire recovery temperature, corresponding to zero net heat transfer, were obtained for free stream Knudsen numbers between 0.4 and 3.0. Comparison with previous data suggests that for Mach numbers greater than about two the normalized variation of recovery temperature in the transitional regime is a unique function of the free stream Knudsen number. The steady-state hot wire may be used as a quantitative instrument to obtain two thermodynamic measurements: the rate of heat transfer from the wire and the wire recovery temperature. Hot wire and pressure measurements in the wake of a transverse cylinder show that good accuracy may be obtained, even when the Reynolds number based on wire diameter is small.

HOT WIRE probes have been used for a number of years to measure the mean properties of a fluid stream. The hot wire is capable of providing two thermodynamic measurements: the rate at which heat is transferred from the wire to the stream and the wire recovery temperature for zero heat transfer. If sufficiently accurate relations are known for the heat loss and recovery temperature as a function of the properties of the flow, only one additional thermodynamic measurement is necessary to specify the flow field uniquely.

The present investigation was undertaken with two purposes in mind. First, in using the hot wire to measure mean quantities in low density compressible flow, it is necessary to have an accurate calibration of the wire heat loss and recovery temperature as a function of Mach number and Reynolds number. For high Reynolds number flows, these relations are well represented by the data of Laufer and McClellan (1).[3] Often, however, it is necessary to use the hot wire in regions where the Reynolds number based on wire diameter is small. Previous investigations (3, 4, 6, 7) have illustrated the general qualitative features of the Nu-Re relation at small Reynolds numbers, but the experimental uncertainties are too large for calibration purposes. The first objective, therefore, was to obtain an accurate hot wire calibration at high Mach number in the transition regime between continuum and free molecule flow.

The second purpose of this investigation was to provide further information on two features of low Reynolds number flow which are important from a theoretical point of view. One of these is the recovery temperature phenomenon which was theoretically and experimentally investigated by Stalder, Goodwin, and Creager (8). It was found by these authors that the equilibrium, or recovery, temperature of an unheated cylinder in free molecule flow is greater than the stagnation temperature of the stream. In the present investigation, measurements were made of the wire recovery temperature in the range of Knudsen numbers between 0.4 and 3.0. These and previous data (1, 2) provide an accurate high Mach number relation between the recovery ratio (T_{aw}/T_0) and Kn over the complete range from continuum to free molecule flow.

At high Reynolds numbers, the heat transfer to the stagnation point of a blunt body may be accurately predicted using boundary layer theory. Recently, a considerable amount of attention has been given to the problem of determining appropriate corrections to the high Reynolds number, high Mach number boundary layer solutions which would extend their validity to lower Reynolds numbers. The data obtained in this investigation, when combined with the results of Laufer and McClellan (1), show the departure of the Nu-Re relation from the high Reynolds number correlation and the approach to free molecule flow for an infinite, conducting cylinder.

In many physical situations, it is difficult to obtain precise data using standard pitot probes. Particularly in regions of low density, instrumentation sufficiently large to obtain reliable results may introduce appreciable disturbances into the flow. Total temperature, mass flow, and velocity profiles in the wake of a transverse cylinder are reported to illustrate the use of the hot wire in such regions. By using both hot wire

Presented at the ARS 15th Annual Meeting, Washington, D. C., Dec. 5–8, 1960; revision received Oct. 27, 1961.

[1] A portion of this work was conducted under Army Ordnance Contracts DA-04-495-Ord-1960 and DA-04-495-Ord-3231.

[2] National Science Foundation Fellow in Aeronautics. Student Member ARS.

[3] Numbers in parentheses indicate References at end of paper.

and pressure measurements, the flow field was overdetermined, and this redundancy permitted an estimate of the accuracy of the hot wire measurements.

Experimental Method

The measurements were performed in Leg 1 of the GALCIT hypersonic wind tunnel at a nominal Mach number of 5.8. This tunnel has a 3-in. × 3-in. core of uniform flow. Other features of this facility are described in (9). The stagnation pressure was varied between 0 and 95 psig at a nominal stagnation temperature of 226°F. Because of the tunnel wall boundary layer, the actual test section Mach number was a function of stagnation pressure. Using a 0.063-in. ID stainless steel pitot probe, the Mach number was found to vary between 5.64 and 5.83, with a repeatability of ±0.3%. The stagnation temperature was maintained between 223.5° and 227.2°F and for each run was known to an accuracy of ±1.5°F.

Under certain conditions, free stream turbulence may affect the heat transfer rate measured by a hot wire. Demetriades (10) found that the free stream integrated rms mass-flux and temperature fluctuations in Leg 1 were on the order of 0.4%. The dominant turbulence scale, given by the velocity divided by the frequency, was on the order of 10^3 to 10^5 times the wire diameter, and by the criteria of (12) should have caused no measurable effect on the heat loss. Additional quantitative turbulence measurements are necessary before a similar statement can be made about the wake results.

The detachable hot wire holders consisted of a conical brass body, a thin double wedge brass support blade, and two sewing needles to hold the wire. The needles were attached to and electrically insulated from the brass blade by epoxy resin; Fig. 1a illustrates the holder configuration. The complete hot wire assembly, including holder, sting support, and total pressure tube, is shown in Fig. 1b. The hot wire was soft soldered to the needle supports within 0.002 in. of the tips; a typical installation is shown in Fig. 2. Details of the electrical connectors and head assembly may be found in (10).

A calibration oven was used to determine the temperature-resistance relation of the wires. Heat was supplied by a helically wound nichrome ribbon, and sufficient thermal lagging was used to make the temperature gradients within the oven negligible. An iron-constantan thermocouple placed 0.25 in. from the wire gave the oven temperature. Measurements were made only when the oven had reached thermal equilibrium (temperature changes less than 0.2°F/min).

The electrical instrumentation consisted of a precision Leeds and Northrup K-2 potentiometer accurate to one part in 5000, five 45-v dry cells to supply the wire current, and a variable series resistance for current control. Measurements of the potential drop across the wire and the standard 1-ohm resistor were made with the K-2 potentiometer, giving the wire current and resistance. All readings were corrected for the small line resistance between the hot wire and the potentiometer. During each series of measurements, the current was constant within 0.02%.

To determine the Nusselt number and recovery temperature of the wire, the voltage drop across the wire and across a standard 1-ohm resistor was measured for several values of wire current. The resistance was then plotted against i^2 to determine the slope and intercept at zero current (e.g., Fig. 9). Extreme care had to be exercised in achieving constant tunnel stagnation temperature, since a change of 1°F was easily detectable in the R vs. i^2 plot.

In performing the wake test, a continuous curve of wire temperature vs. position in the wake was desired for a fixed wire current, and a Mosely Autograph x-y plotter was used for this purpose. The traverse mechanism was geared to a linear resistance coil, and a small constant current through this resistance created a voltage drop proportional to the transverse position. This signal and the voltage drop across the hot wire were the two electrical inputs for the plotter. Scale factors were obtained by measuring the voltage drop across the wire with the K-2 potentiometer at two known values of y/D.

Wire Calibration and Annealing

All data were obtained using 0.00010-in. diam Pt-10% Rh wire from a single spool. No attempt was made to measure the wire diameter directly, since it was felt that the manufacturer's[4] drawing procedures were of greater accuracy than any available optical measurement technique. However, each wire was examined visually under a microscope to detect any macroscopic irregularities. The resistance of each wire was measured at several temperatures in the calibration oven. At the end of each series of runs, the wire resistance at room temperature was again measured; if the resistance had changed more than a few tenths of a per cent, the data were discarded. The mounted wire resistance and length were also carefully measured and checked against the manufacturers quoted resistance of 11,580 ohms/ft at 68°F. The mean

[4] Sigmund Cohn, Mt. Vernon, N. Y.

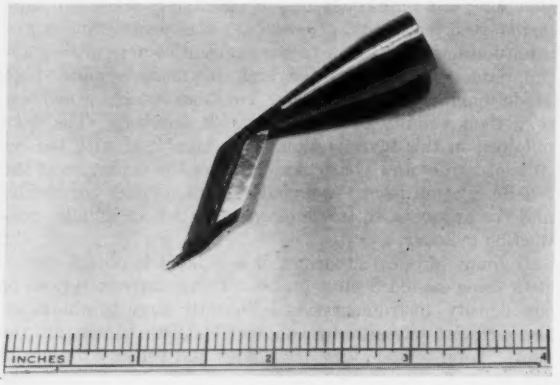

Fig. 1a Hot wire holder

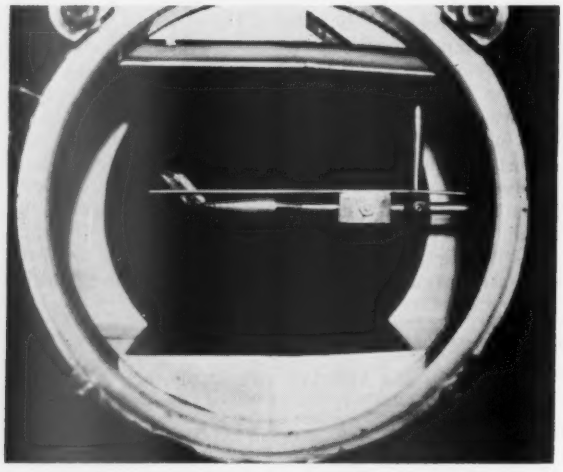

Fig. 1b Hot wire probe installed in tunnel

deviation of the unannealed, installed resistance from this reference value was less than 1.0%, indicating high uniformity of the wire.

Through prolonged use, the wire resistance increased between 2 and 8%. Since it was necessary to limit the increase between successive calibrations to a few tenths of a per cent, several tests were conducted to determine the major factors involved. It was found that a large part of the resistance shift could be eliminated by heating the wire to a dull glow for several minutes prior to tunnel use.

The largest wire resistance changes are associated with exposure to free stream pressure loads while the wire is at an elevated temperature; the wires experienced 1) large stepwise increases in resistance if the previous maximum temperature and pressure of operation were exceeded (*deformation* phenomenon); and 2) a much smaller increase, which was a function of time (*creep* phenomenon). Fig. 2 shows a typical deformation caused by an overheat τ of about 0.8 at 90 psig stagnation pressure. The creep phenomenon was negligible after the first few hours of tunnel exposure.

Two factors limited the aspect ratio of the wires. First, it was found that wire curvature increased with aspect ratio. Second, for aspect ratios greater than 375, wires of 0.00010-in. diam were easily broken during the tunnel starting process. Since it was desired to keep the end loss corrections as low as possible, the range $320 \leqq l/d \leqq 360$ was chosen as an acceptable compromise.

The temperature coefficient of resistivity α_r varied between 0.88 and 0.93 $(°F)^{-1}$ at 0°F, with a mean value of 0.91. The measured resistivity coefficient α_r was accurate to about 1.5% for each wire. Several tests indicated that the resistivity coefficient was not affected by tunnel exposure, provided that the wire had been initially annealed to a dull glow in still air.

In (32), the correction factors for heat loss to the wire supports are derived. This analysis is carried through the support temperature as a free parameter and shows that for large end loss correction the support temperature has an important effect on both the Nusselt number and recovery factor. Depending on the tip shape, thermal conduction, and free stream Reynolds number, the effective value of $\eta_s = (T_s/T_0)$ should lie between 0.85 and 1.0 and should vary with the wire attachment location. Since the recovery temperature correction was quite sensitive to η_s, a special test was conducted to measure this parameter (32). The value of η_s was found to be constant over the complete range of tunnel conditions encountered and equal to 0.903 ± 0.005. This value is approximately equal to the calculated laminar boundary layer recovery factor for flow along the support needle downstream of the stagnation region.

Data Reduction

The largest portion of heat transferred from a blunt body is in the vicinity of the forward stagnation point. At high Reynolds numbers and Mach numbers, the appropriate temperature for evaluating viscosity and thermal conductivity is that existing behind a normal shock at the free stream Mach number. At low Reynolds numbers, a distinct shock wave does not appear; under these conditions, the results of free molecule theory (8) may be conveniently expressed using fluid properties evaluated at the stagnation temperature. In this paper, the heat transfer data are correlated using the Nusselt and Reynolds numbers

$$\mathrm{Nu}_0 = (hd/k_0) \qquad [1a]$$

$$\mathrm{Re}_0 = (\rho_\infty U_\infty d)/\mu_0 \qquad [1b]$$

where μ_0 and k_0 are the air viscosity and thermal conductivity evaluated at stagnation temperature. This form offers distinct advantages when the hot wire is used as a measuring instrument in nonuniform flow fields.[5]

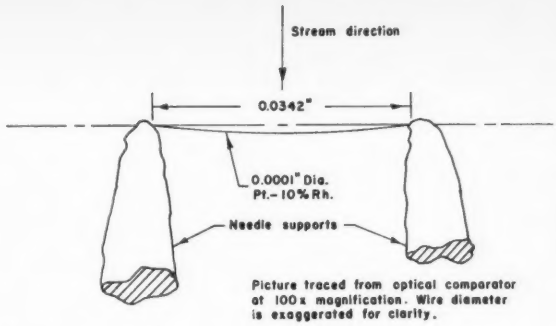
Stream direction
0.0342"
0.0001" Dia.
Pt.- 10% Rh.
Needle supports
Picture traced from optical comparator at 100 x magnification. Wire diameter is exaggerated for clarity.

Fig. 2 Typical hot wire installation after tunnel exposure

All hot wires of finite length lose a certain amount of heat to their supports. The quantity Nu_0 represents the heat transfer rate for a wire of infinite length and is related to the measured Nusselt number Nu_m by the relation

$$\mathrm{Nu}_0 = \Psi_N \mathrm{Nu}_m = \Psi_N \left[\frac{i^2 R_m}{\pi l k_0 (T_w - T_{awm})}\right] \qquad [2]$$

where Ψ_N is the Nusselt number end loss correction factor, i^2R_m the measured Joule heating, and $(T_w - T_{awm})$ the measured temperature potential. Similarly, the recovery ratio η_* for an infinitely long wire may be written

$$\eta_* = (T_{aw*}/T_0) = \Psi_R \eta_m = \Psi_R (T_{awm}/T_0) \qquad [3]$$

where Ψ_R is the recovery ratio end loss correction factor.

For high Reynolds numbers, the recovery ratio $\eta_c = (T_c/T_0)$ has been shown experimentally to be a function only of Mach number (11); η_c decreases from 1.0 at M = 0 to 0.95 for Mach numbers greater than about two. This behavior is explained by the well-known hypersonic freeze or Mach number independence principle, which recognizes that the viscous and inviscid flow fields become independent of Mach number if the Mach number is sufficiently large. For blunt bodies such as the cylindrical wire considered here, changes in the flow field are small beyond a Mach number of three (14, 15). A value $\eta_c = 0.950$ was used as a reference for the present experiments and the data of Laufer and McClellan (1) and Sherman (2). Stalder et al. (5) found $\eta_c = 0.96$, and this value was used in interpreting their results.

For free molecular flow, the heat loss and recovery temperature of an infinite, perfectly conducting cylinder with no radiative cooling are given in (8):

$$\mathrm{Nu}_0 = \frac{(\gamma - 1)}{2(\pi)^{3/2}} \alpha \, \mathrm{Re}_0 \, \mathrm{Pr}_0 \left(\frac{g(s_1)}{s_1}\right) \qquad [4]$$

$$\eta_f = T_{aw}/T_0 = \left(1 + \frac{\gamma + 1}{2} \mathrm{M}^2\right) \frac{f(s_1)}{g(s_1)} \qquad [5]$$

$$s_1 = \sqrt{\gamma/2}\, \mathrm{M} \qquad [6]$$

where $f(s_1)$ and $g(s_1)$ depend only on the molecular speed ratio s_1 and the number of excited degrees of freedom of the medium. These functions have been tabulated (8) for both monatomic and diatomic perfect gases. As $\mathrm{M} \to \infty$, Eqs. 4 and 5 approach the limiting forms

$$\mathrm{Nu}_0 = \left(\frac{\gamma + 1}{2\pi}\right) \alpha \, \mathrm{Re}_0 \mathrm{Pr}_0 \qquad [4a]$$

[5] Morkovin (11) and Collis and Williams (13) discuss this problem in more detail.

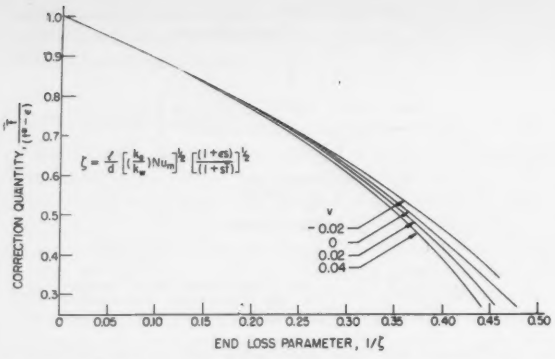

Fig. 3 End loss relations for Nusselt number correction

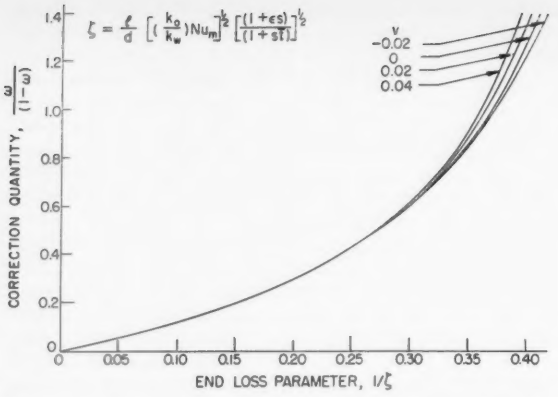

Fig. 4 End loss relations for recovery temperature correction

and

$$\eta_s = \frac{2\gamma}{\gamma + 1} \qquad [5a]$$

As in the case of continuum flow, the Nusselt number and recovery ratio become independent of Mach number as the Mach number increases. The fact that the recovery ratio in continuum and free molecule flow obeys the Mach number independence principle suggests that the normalized recovery ratio

$$\tilde{\eta}_* = \frac{\eta_* - \eta_c}{\eta_f - \eta_c} \qquad [7]$$

is a unique function of the Knudsen number for M sufficiently large.

All computations of flow properties were made using $\gamma = {}^7/_5$ and the Sutherland viscosity formula. Values of air thermal conductivity were obtained from Hilsenrath and Beckett (16), and the wire thermal conductivity was taken from (17), with the data linearly extrapolated to the measured mean wire temperature.

A derivation of the end loss corrections appropriate to transitional flow is given in (32). This analysis assumes that the wire temperature is radially uniform, wire resistance is a linear function of temperature, and the heat transfer coefficient $h = \mathrm{Nu}_0(k_0/d)$ is constant over the wire length. For convenience, the supports are taken to be equal in temperature, although this restriction is not essential. The Nusselt number correction factor may be written

$$\Psi_N = \left(\frac{\bar{l}}{t_* - \epsilon}\right)\frac{(1 + st_*)}{(1 + s\bar{l})} \qquad [8]$$

whereas the recovery ratio end loss correction factor is given approximately by[6]

$$\Psi_R = \frac{\eta_*}{\eta_m} = \left[1 - \omega\left(\frac{\eta_s}{\eta_m}\right)\right](1 - \omega)^{-1} \qquad [9]$$

Here η_s is the normalized support temperature, η_m the measured recovery ratio, and ω a parameter that depends primarily on the wire aspect ratio and Nusselt number. The quantities $[\bar{l}/(t_* - \epsilon)]$ and $[\omega/(1 - \omega)]$ are given in Figs. 3 and 4 as functions of two parameters

$$\zeta = (l/d)\left[(k_0/k_w)\ \mathrm{Nu}_m\frac{(1 + \epsilon s)}{(1 + s\bar{l})}\right]^{1/2} \qquad [10]$$

and

$$v = -(1/2)t_s s \qquad [11]$$

[6] The quantity ω is a weak function of overheat; this refinement is included in the analysis of (32).

The normalized quantity $\bar{l}$ represents the length-average wire temperature

$$\bar{l} = \frac{1}{l}\int_{-l/2}^{l/2}\left(\frac{T - T_{aw}}{T_0}\right)dz$$

and t_* is the value of $\bar{l}$ as $l/d \to \infty$. The quantities ϵ and t_s are defined by

$$\epsilon = \eta_* - \eta_m \ll 1$$
$$t_s = \eta_s - \eta_m \ll 1$$

and s is a constant of order 1 (see Nomenclature). Since ζ involves ϵ, which in turn depends on ζ, an iterative method of solution is required (32). Even for large corrections, the iteration scheme rapidly converges to a unique value, irrespective of the initial choice of ϵ; one iteration on ϵ will usually give values of Ψ_N and Ψ_R correct to three significant figures.

The correction factor Ψ_N does not depend strongly on overheat. As ζ decreases, both Ψ_N and Ψ_R depart from unity; from Figs. 3 and 4, it may be seen that the support temperature parameter v plays a minor role in determining the end loss correction, although it must be considered if the corrections are large.

For the present data, the measured value $\eta_s = 0.903$ was used with the measured values of η_m and Nu_m to compute the end loss correction. A slightly more complicated procedure was required in interpreting the results of Laufer and McClellan (1). In that investigation, the wire supports were equivalent to a two-dimensional wedge of 7° included angle. Using the observation that the support temperature is equal to the laminar boundary layer adiabatic wall temperature, η_s could be calculated explicitly. Since Nu_m was not known, an iterative computation process was adopted which used as input the known quantities η_s, η_m, and the wire Reynolds number Re_0. With Re_0 known, Nu_0 was taken from the heat loss correlation, and the value of Nu_m was computed. The procedure for obtaining Nu_m and η_* with Nu_0 and η_m known is analogous to the determination of Nu_0 and η_* with Nu_m and η_m given.

No correction was made to the data for radiation effects, since calculation showed that the error in both Nu_0 and $\tilde{\eta}_*$ was less than one tenth of one per cent. The correction is roughly proportional to (T_w^4/Nu) and may become appreciable for high overheats or extremely low Reynolds numbers.

The raw data from the wake traverse consisted of a series of continuous curves of wire voltage vs. voltage output from the traverse mechanism. The voltage scale was established by

two calibration measurements with the K-2 potentiometer at known values of y/D. Using this calibration, the wire resistance was computed for several representative stations within the wake. Fig. 9 shows the measured wire resistance as a function of wire current.

Two thermodynamic measurements were obtained with the hot wire; these were $[dR/d(i^2)]_{i=0}$ and the zero current intercept R_{aw}. Pitot pressure and static pressure across the wake were also measured separately. Thus, the measured thermodynamic quantities were more than sufficient to specify the flow completely, and this redundancy permitted an estimate of the accuracy of the combined measurements.

The static and pitot pressure measurements were obtained by John F. McCarthy Jr. of GALCIT. Free stream conditions for the hot wire and pressure traverses were

	M_∞	x/D	$Re_{\infty,D}$
Hot wire	5.74	9.0	1.75×10^4
Pressure	5.74	9.0	2.60×10^4

Hot wire fluctuation measurements showed that the wake was laminar in both cases, and the assumption was made that the local pressure profiles were similar for the two tests. The Reynolds number effect is discussed more fully in a subsequent section.[7]

Heat Transfer Measurements

Fig. 5 has been prepared as a guide to the experimental variation of Nusselt number as a function of Reynolds number and Mach number in the range $0.2 \leqq Re_0 \leqq 100$. In preparing the figure, particular weight was given to the correlation of McAdams (20) at $M = 0$ and the results of Laufer and McClellan (1) and the present investigation of Mach numbers greater than two. Within the Reynolds number range $1 \leqq Re_0 \leqq 100$, the data of Baldwin (21) and Cybulski and Baldwin (7) are representative of the information available at subsonic velocity. Spangenberg's data (Ref. 19, Fig. 17c) show a similar Mach number variation for Reynolds numbers greater than one and far better agreement with (1,20) than the work of Baldwin. The cold wire data of Christiansen (22) at low Reynolds numbers are also included. These transonic measurements agree well with the hot wire results for $Re_0 < 1$ and provide a consistent set of measurements in the near free molecule flow regime. At low Reynolds numbers, the correlation would be changed considerably if incomplete accommodation were present.

[7] Details of the computation procedure may be found in (32).

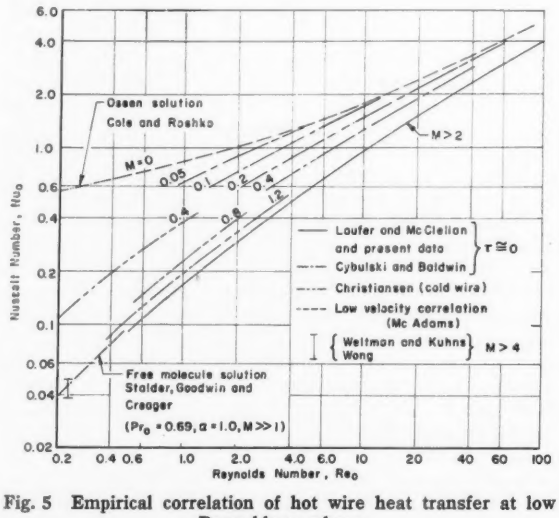

Fig. 5 Empirical correlation of hot wire heat transfer at low Reynolds numbers

Theoretical studies are of limited use in preparing a heat transfer correlation. The solution of Cole and Roshko (23) for continuum Oseen flow agrees well with the experiments of Collis and Williams (24) at low Reynolds numbers. Levy (25) has considered the Oseen flow problem with temperature-jump boundary conditions, and the results agree qualitatively with the experiments of Cybulski and Baldwin (7). However, the velocities and Reynolds numbers covered by Oseen theory are quite small. Free molecule analysis has provided what appears from Eq. 4 to be a straightforward calibration for all flows where the Knudsen number is sufficiently high. The fact that the accommodation coefficient α is an arbitrary parameter has been a major weakness in all attempts to apply this theory to a given set of data.

The heat transfer data obtained in this investigation are presented in Fig. 6. These data agree well with the measurements of Laufer and McClellan (1) at Reynolds numbers Re_0 greater than three. One may infer from this agreement and the Mach number independence principle that the solid line shown in Fig. 6 represents the Nu_0-Re_0 relation for Mach numbers greater than about two.

For comparative purposes, the results of free molecule theory (Eq. 4) and the extrapolated slope of the high Reynolds number data are shown in Fig. 6. At high Reynolds numbers, the Nusselt number becomes proportional to $(Re_0)^{1/2}$, whereas $Nu_0 \sim Re_0$ for $Re_0 \ll 1$. The present measurements asymptotically approach the free molecule result with an accommodation coefficient α near unity. For the heat transfer tests in air and argon by Christiansen (22), Weltman and Kuhns (6), and Wong (3), an accommodation coefficient of unity represents the data within the experimental error. Experimentally, it has been found that surface conditions are of primary importance in determining the degree of energy accommodation (26); the presence of adsorbed gases on the body surface increases the accommodation coefficient.

All data shown in Fig. 6 are based on the measured Nusselt number at zero overheat; the effects of overheat are discussed in detail elsewhere (30, 32). In free molecule flow, the surface temperature enters the heat transfer relation only through its effect on the accommodation coefficient. If the accommodation coefficient were unaffected by surface temperature, the cold wire results of Christiansen (22) and the present measurements should agree closely, except for the small Mach number variation given by $f(s_1)/s_1$ in Eq. 4. Fig. 5 indicates that the hot wire and cold wire data agree well up to a Reynolds number Re_0 of about one.

For high Reynolds number flows, a large part of the heat transfer to the body occurs in the vicinity of the forward stagnation point. For a perfect gas, the heat transfer at the stagnation point of a cylinder in supersonic flow is closely represented by (27)

$$Nu_0 \cong 0.50 \sqrt{Re_0} \left(\frac{Pr_0}{Pr_w}\right)\left(\frac{T_0}{T_w}\frac{\mu_w}{\mu_0}\right)^{0.06} \qquad [12]$$

Eq. 12 indicates that the effects of overheat at high Reynolds numbers should be small over the range of conditions encountered in the laboratory.

Although no complete solutions are available for a cylinder in high speed flow because of the lack of an adequate theory covering the region of separation, many analyses are available for heat transfer near the stagnation point of a blunt body. It has been pointed out that both the hot wire data and the stagnation point boundary layer solutions exhibit heat transfer coefficients proportional to $\sqrt{Re_0}$ at high Reynolds numbers, and the behavior of the stagnation point solutions with decreasing Reynolds number should agree well with the hot wire measurements.

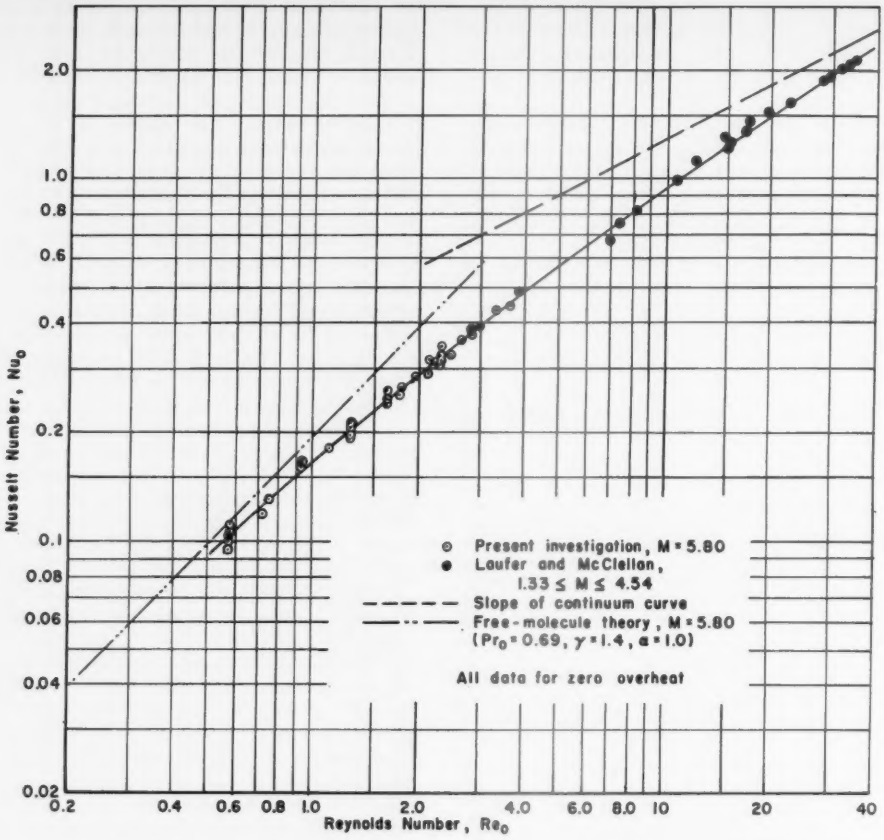

Fig. 6 **Nusselt number-Reynolds number relation for supersonic and hypersonic flow**

Two recent investigations by Probstein and Kemp (28) and Van Dyke (33) have used the Navier-Stokes equations to describe the flow field near the stagnation point of a blunt body in hypersonic flow. These analyses show that conventional high Reynolds number boundary layer theory must be modified as the body Reynolds number is decreased. First order corrections may be present due to external vorticity, boundary layer displacement, surface velocity and temperature jump, and body curvature. For a cylinder, the vorticity along the zero streamline is zero in the inviscid flow, so the vorticity effect on heat transfer is of second order. However, the boundary layer displacement and curvature effects both produce a first-order decrease in surface heat transfer, compared with the conventional high Reynolds number value. Slip effects would also decrease the heat transfer rate. Probstein and Kemp (28) have proposed a merged layer analysis based on continuum relations for the range $30 \lesssim Re_0 \lesssim 100$. The results agree qualitatively with the present measurements.

The slope of the Nu_0-Re_0 relation is a quantity of considerable interest. The exponent n in the relation

$$Nu_0 \sim Re_0^n \qquad [13]$$

correlates the results of several independent investigations better than the absolute magnitudes of the observed quantities. In Fig. 7, the exponent n is shown as a function of Reynolds number and Mach number for several investigations. The present measurements and those of Laufer and McClellan (1) were used for $M > 2$, whereas selected results of Christiansen (22), Cybulski (7), and Baldwin (21) are shown for $M < 1$. At high Reynolds numbers, the exponent n is $1/2$; in the limit of $Kn \to \infty$, the free molecule relation, Eq. 4, shows that $n = 1$. A third relation, derived from the Oseen solution of Cole and Roshko (23), is applicable when $M/Re \ll 1$ and $Re_0 \ll 1$; in this instance, the exponent is of the form

$$n = \frac{1}{\log (8/Re_0 Pr_0)} \qquad [14]$$

Collis and Williams' (24) experiments agree very well with Eq. 14 for $0.01 < Re_0 < 0.3$.

At high Mach numbers, the exponent n is seen to vary monotonically between the continuum and free molecule values of $1/2$ and 1. The measured slope begins to depart from the continuum value at a Reynolds number Re_0 of about 200 for an insulated wire. A comparison between Christiansen's data (22) and the present measurements indicates that the departure from the continuum heat transfer law occurs at a slightly lower value of Re_0 if the wall is highly cooled; this may be explained by the fact that a cool wall decreases the boundary layer displacement effect at a given Reynolds number. From boundary layer theory, $q \sim (D/2)^{-1/2}$, where D is the diameter of the cylinder. If the boundary layer displacement thickness is not negligibly small, then $q \sim [(D/2)(1 + 2\delta^*/D)]^{-1/2}$, and an increase in the displacement thickness (i.e., an increase in the wire temperature) would tend to decrease the heat transfer rate to the body.

Willis (29) has treated several problems in the near free molecule regime using an iterative solution to the integral

form of the Boltzmann equations. This approach is equivalent to the so-called first collision theory if only the first iterate is considered. Willis' results for a two-dimensional strip normal to a rarefied flow should be identical in form to the solution for a cylinder normal to the flow. By writing a heat balance for the body, the resulting equations may be solved for the departure of the Nusselt number and recovery temperature from the free molecule values as a function of the free stream Knudsen number. The results may be expressed as ($\alpha = 1$)

$$\frac{\mathrm{Nu}_0}{(\mathrm{Nu}_0)_{\text{free molelule}}} = 1 + \mu\chi \qquad [15]$$

$$\frac{T_{aw}}{(T_{aw})_{\text{free molecule}}} = \frac{1 + \mu\psi}{1 + \mu\chi} \qquad [16]$$

where

$$\mu = \frac{2}{\sqrt{\pi}} \frac{1}{\mathrm{Kn}} \log\left(\frac{1}{\mathrm{Kn}}\right) \qquad [17]$$

$$\chi = \frac{N_i - N_{if}}{N_{if}} \qquad [18]$$

$$\psi = \frac{Q_i - Q_{if}}{Q_{if}} \qquad [19]$$

Here N_i is the incident molecular flux, Q_i the incident energy flux, and $(\ )_f$ indicates the value for $\mu \to 0$. Willis has tabulated values of ψ and χ for a two-dimensional strip and a monatomic gas. The value of these quantities would be slightly different for a cylinder.

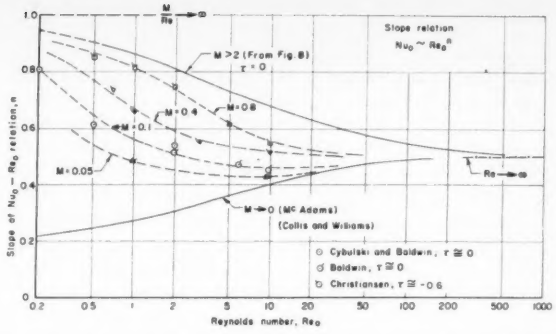

Fig. 7 Slope of Nusselt number-Reynolds number relation

Willis (29) found that ψ and χ depend on the molecular speed ratio, the body temperature, the molecular model, and the number of degrees of freedom of the gas. ψ and χ are weak functions of the body temperature if the overheat τ is small; the results are more sensitive to body temperature at higher values of the molecular speed ratio s_1. For an insulated strip and $s_1 \to \infty$, $\psi = 0.42$ and $\chi = 0.11$ for the modified Krook molecular model, whereas $\psi = 0.78$ and $\chi = 0.48$ if the hard sphere model is used. From Eq. 15 it may be seen that the departure of the Nusselt number from the free molecule result is a strong function of the molecular model employed. Eqs. 15 and 16 agree qualitatively with the present experiments if $\psi > \chi > 0$.

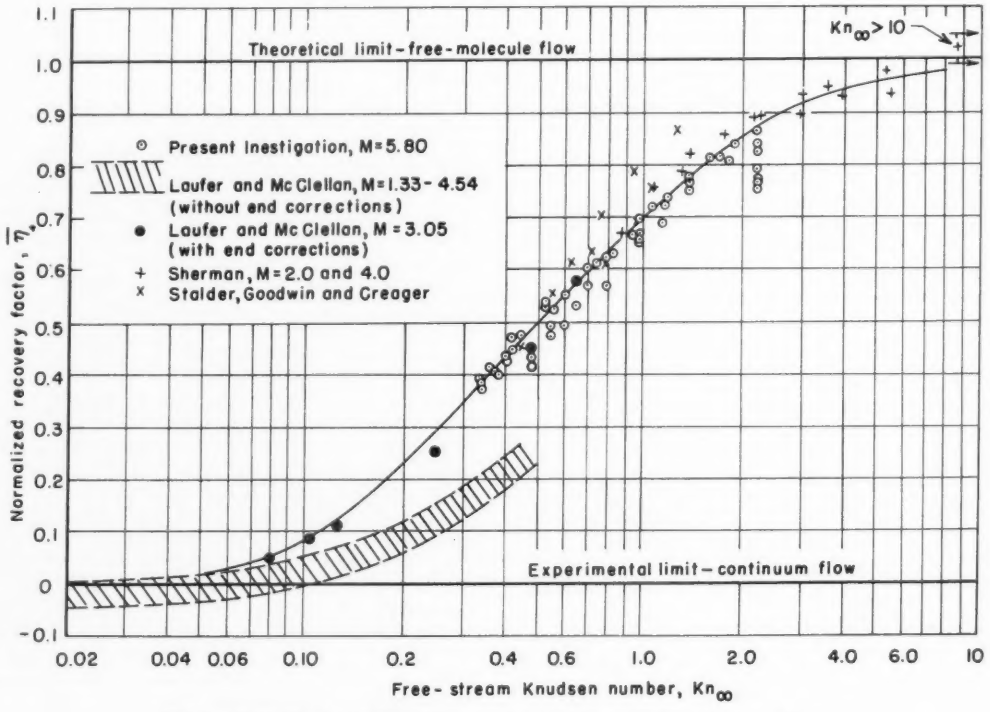

Fig. 8 Normalized variation of recovery temperature with Knudsen number

Several interesting conclusions may be drawn from the above analysis. First, the small parameter in near free molecule flow for a two-dimensional body is (1/Kn) log (1/Kn) rather than the quantity 1/Kn, which pertains to axisymmetric bodies. Thus, the range of validity of the two-dimensional analysis is restricted to Knudsen numbers higher than the axisymmetric counterpart. Second, for viscosity proportional to $(T)^{1/2}$, Kn $\sim$ $(1/\mathrm{Re}_0)$ at high Mach number, and the analysis predicts that the Nu_0-Re_0 relation at high Knudsen numbers should, as expected, become independent of Mach number.

Recovery Temperature Measurements

In the transitional regime, the measurements reported in (1, 2) indicated that at Knudsen numbers of about 0.1 the recovery temperature begins to rise above the high Reynolds number value, whereas at Knudsen numbers greater than 10, the full temperature rise predicted by Eq. 5 is attained. However, at Knudsen numbers of about one and at roughly the same Mach number, the two investigations reported significant differences in the recovery factor.

The present investigation was undertaken in an attempt to resolve this apparent discrepancy and at the same time provide additional recovery temperature data for use in steady-state hot wire work. The results are shown in Fig. 8, using the normalized recovery ratio $\bar{\eta}_*$ and the free stream Knudsen number as parameters. Fortunately, the recovery temperature for a cylinder is independent of the accommodation coefficient (provided that the wire is infinitely long) and rapidly approaches an asymptote as the Mach number increases. Therefore, since $\bar{\eta}_* = 0$ for $\eta_* = \eta_c$ and $\bar{\eta}_* = 1$ for $\eta_* = \eta_f$, all investigations should agree at least in these two limits.

The shaded area representing the data of Laufer and McClellan defines the limits of experimental scatter of nearly 100 separate measurements made over a large range of Mach and Reynolds numbers. Considering the range of parameters studied, the data are extremely consistent. However, the aspect ratios of the wires used in their recovery temperature study were on the order of 200, and at the highest Knudsen numbers these wires were subject to significant end losses. Several representative data points were corrected for support conduction and plotted in Fig. 8.

By combining the corrected data of (1), the results of Sherman (2), and the present measurements, a continuous transition of the normalized recovery factor is obtained between continuum and free molecule flow. From a consideration of the Mach number independence principle, this curve should be valid for all Mach numbers above approximately two. Considering the sensitivity of the normalized recovery ratio to experimental error, the correlation appears to be very good. At lower Mach numbers, the $\bar{\eta}_*$(Kn) correlation should show a dependence on Mach number.

The behavior of the $\bar{\eta}_*$(Kn) relation at small Knudsen numbers agrees qualitatively with the results of Probstein and Kemp (28). In the incipient merged layer analysis, they find that the gas temperature at the stagnation point of a blunt body becomes greater than the free stream stagnation temperature in the low Reynolds number continuum range. For large Knudsen numbers, Eq. 16 predicts that the recovery temperature will fall below the free molecule value if $\psi > \chi$; the experimental data shown in Fig. 8 indicate that for a circular cylinder and a diatomic gas, ψ and χ are nearly equal.

Application of the Steady-State Hot Wire to Wake Measurements

The number of investigations using the hot wire in a redundant measurement scheme is quite small, and consequently it was decided to perform an illustrative experiment involving four measured quantities, two of which were obtained from a hot wire operated in the transitional regime. The wake of a cylinder traverse to a hypersonic flow was chosen both because its flow field was amenable to hot wire and pressure measurements and because of current interest in the thermal wakes of hypersonic blunt bodies.

The wire used in this experiment had an aspect ratio of 311 and $\alpha_r = 0.93$. The measured variation of wire resistance with i^2 is shown in Fig. 9. It may be seen that the instrument sensitivity was quite sufficient to pick out small differences in the R vs. i^2 relation. This property is absolutely essential for quantitative interpretation.

The following groups of variables were chosen to represent the data:

Group I: $\left[\dfrac{dR}{d(i^2)}\right]_{i=0}$, R_{awm}, p

Group II: p_{t2}, p, R_{awm}

The distributions of flow quantities across the wake were computed (32) using the measurements of Group I and Group II in independent calculations. Thus the agreement between the results of Group I and Group II provides a measure of the accuracy of the combined measurements.

Fig. 10a shows the results of the stagnation temperature calculation. T_0' is the measured stagnation temperature at the outer edge of the mixing layer.[8] Results for the several representative stations are shown first as *uncorrected* data, i.e., the temperature one would calculate using only the zero current intercept of Fig. 9 and the wire resistivity coefficient. The wire was subject to end loss effects, and by using Figs. 6 and 8 and the derived end loss corrections, an iteration was performed to find the true value of T_0. Only three iterations were required to obtain convergence.

Qualitatively, the behavior of (T_0/T_0') is similar to that obtained in a high speed boundary layer (1) with Prandtl number less than one. Because of laminar shear and heat conduction processes, the centerline Mach number for this particular streamwise station was about $^3/_4$ of M', and the centerline stagnation temperature was about 0.96 of T_0'. The two values of T_0' agreed within 0.14% and were 2% lower than the free stream stagnation temperature. This result agrees well with the postulate of isoenergetic flow everywhere outside the viscous mixing region.

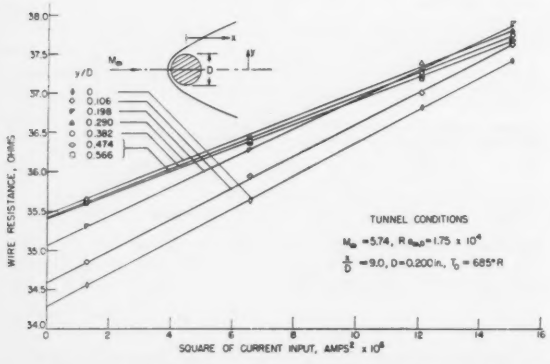

Fig. 9 Data obtained from cylinder wake traverse

[8] Quantities without superscripts are functions of distance from the wake centerline, whereas ( )′ signifies the measured value at the edge of the mixing region.

The local mass flow in the wake is shown in Fig. 10b. For purposes of comparison, the uncorrected hot wire data are also shown; the quantity $R_{aw}(dR/di^2)^{-1}$ is directly proportional to the local mass flow (ρu) if end losses are negligible. Since the end loss correction increases with decreasing (ρu), the uncorrected mass flow is higher than the final corrected value based on the measurements of Group I.

The agreement between the two values of $(\rho u/\rho' u')$ computed using Group I and Group II is good. The differences between the two curves are primarily due to the different cylinder Reynolds numbers for the hot wire and pressure tests. Subsequent pitot pressure data have indicated that the higher value of $(\rho u/\rho' u')$ at the wake centerline obtained with Group II is caused by the higher value of $\mathrm{Re}_{\infty,D}$ for the pressure measurements. At the edge of the wake, $(\rho' u')$ for Group I was 0.85 of $(\rho' u')$ for Group II. Taking this Reynolds number effect into account, the absolute values of (ρu) from Group I and Group II were found to agree within 7% throughout the mixing region. The small differences between the two values of (T_0/T_0') shown in Fig. 10a are also attributable to the differences in $\mathrm{Re}_{\infty,D}$.

The velocity defect in the wake mixing region is shown in Fig. 10c. The agreement between the hot wire and pressure measurements is seen to be excellent and verifies the fact that the differences shown in Figs. 10a and 10b are due to differences in $\mathrm{Re}_{\infty,D}$; for $x/D = 9$ and these Reynolds numbers, the wake is laminar and the velocity defect $[(u - u_{\mathfrak{L}})/(u' - u_{\mathfrak{L}})]$ should show little dependence on $\mathrm{Re}_{\infty,D}$.

Acknowledgment

The author would like to express his deep gratitude to Lester Lees for suggesting this investigation and supervising the research program. Anthony Demetriades and Toshi Kubota contributed many important suggestions and criticisms to the investigation. The cooperation of John Laufer and Thomas Vrebalovich of the Jet Propulsion Laboratory is also gratefully acknowledged.

Additional Nomenclature

c_p = specific heat
d = hot wire diameter
i = wire current
k_w = wire thermal conductivity at temperature T_w
l = wire length
p = static pressure
p_{t_2} = pitot pressure
q = heat transfer rate per unit area
R = wire resistance
s = resistance parameter, $\dfrac{\alpha_r T_0}{1 + \alpha_r(T_{awm} - T_r)}$
t = nondimensional temperature, $\dfrac{T - T_{awm}}{T_0}$
U_∞ = free stream velocity
x = distance from cylinder axis in streamwise direction
y = distance from cylinder axis in transverse direction
z = distance along wire
δ^* = boundary layer displacement thickness
ϵ = recovery ratio parameter, $\eta_* - \eta_m$
ζ = end loss correction parameter, Eq. 10
η_c = experimental recovery ratio for continuum flow
η_f = theoretical recovery ratio for free molecule flow, Eq. 5
μ = viscosity; also $(2/\sqrt{\pi})(1/\mathrm{Kn})\log(1/\mathrm{Kn})$ in near free molecule flow analysis
ρ = density
χ = dimensionless quantity in near free molecule flow analysis, Eq. 18
ψ = dimensionless quantity in near free molecule flow analysis, Eq. 19
$(\ )_r$ = reference temperature T_r
$(\ )_s$ = support temperature T_s
$(\ )_w$ = wire temperature T_w

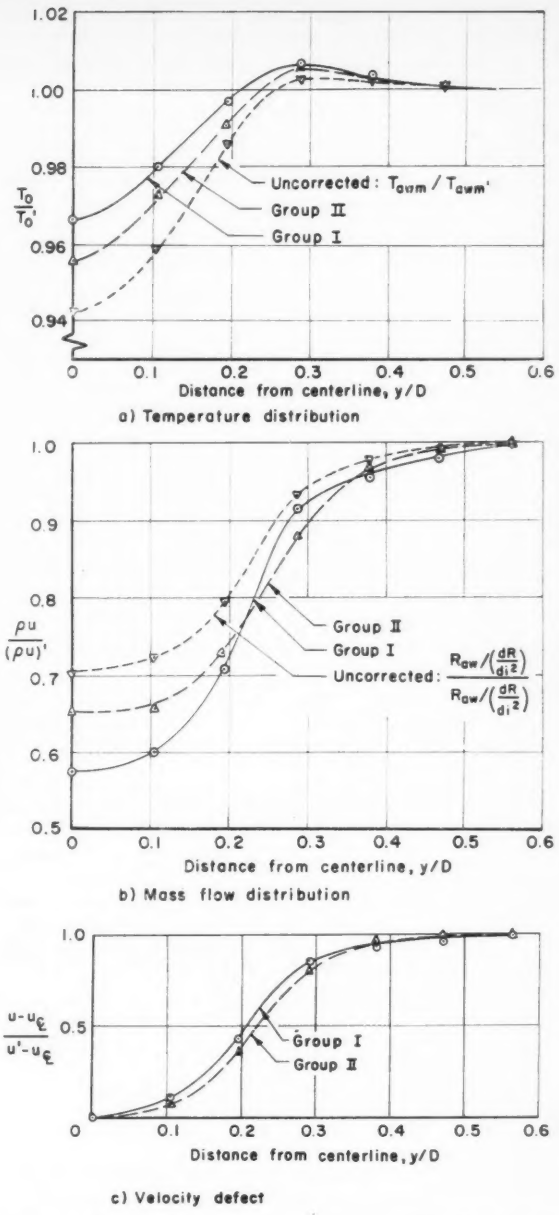

Fig. 10 Variation of flow quantities across the cylinder wake

$(\ )_*$ = infinitely long wire
$(\ )_\infty$ = free stream
$(\ )_2$ = behind a normal shock

References

1 Laufer, J. and McClellan, R., "Measurements of Heat Transfer from Fine Wires in Supersonic Flows," *J. Fluid Mech.*, vol. 1, no. 3, 1956, pp. 276–289.

2 Sherman, F. S., "A Low-Density Wind-Tunnel Study of Shock-Wave Structure and Relaxation Phenomena in Gases," *NACA TN 3298*, 1955.

3 Wong, H., "Design and Development of a Free-Molecule Heat Transfer Probe," Univ. of Calif., Berkeley, Calif., *Rep. HE-150-145*, 1956.

4 Laurman, J. A. and Ipsen, D. C., "Use of a Free-Molecule Probe in High Speed Rarefied Gas Flow Studies," Univ. of Calif., Berkeley, Calif., *Rep. HE-150-146*, 1957.

5 Stalder, J. R., Goodwin, G. and Creager, M. O., "Heat Transfer to Bodies in a High-Speed Rarefied-Gas Stream," *NACA Rep. 1093*, 1952.

6 Weltmann, R. N. and Kuhns, P. W., "Heat Transfer to Cylinders in Crossflow in Hypersonic Rarefied Gas Streams," *NASA TN D-267*, 1960.

7 Cybulski, R. J. and Baldwin, L. V., "Heat Transfer from Cylinders in Transition from Slip Flow to Free-Molecule Flow," *NASA Mem. 4-27-59E*, 1959.

8 Stalder, J. R., Goodwin, G. and Creager, M. O., "A Comparison of Theory and Experiment for High-Speed Free-Molecule Flow," *NACA Rep. 1032*, 1951.

9 Eimer, M., "Direct Measurements of Laminar Skin Friction at Hypersonic Speeds," *GALCIT Hypersonic Wind Tunnel, Mem. no. 16*, 1953.

10 Demetriades, A., "An Experimental Investigation of the Stability of the Hypersonic Laminar Boundary Layer," *GALCIT Hypersonic Research Project, Mem. no. 43*, 1958, also *J. Fluid Mech.*, vol. 7, no. 3, 1960, pp. 385–396.

11 Morkovin, M. V., "Fluctuations and Hot-Wire Anemometry in Compressible Flows," *AGARDograph 24*, 1956.

12 Van Der Hegge Zijnen, B. G., "Heat Transfer from Horizontal Cylinders to a Turbulent Air Flow," *Appl. Sci. Res.*, vol. 7, sect. A, 1958, pp. 205–223.

13 Collis, D. C. and Williams, M. J., "Molecular and Compressibility Effects on Forced Convection of Heat from Cylinders," *Australian Aero. Res. Lab. Rep. ARL/A. 110*, 1958.

14 Tewfik, O. K. and Geidt, W. H., "Local Heat Transfer, Recovery Factor, Pressure Distribution Around a Circular Cylinder Normal to a Rarefied Supersonic Air Stream," *Proc.* of the 1959 Heat Transfer and Fluid Mech. Inst., Stanford University Press, Stanford, Calif., 1959, pp. 15–26.

15 Hayes, W. D. and Probstein, R. F., *Hypersonic Flow Theory*, Academic Press, New York, 1959.

16 Hilsenrath, J., Beckett, W. S., et al., "Tables of Thermal Properties of Gases," *N.B.S. Circular 564*, 1955.

17 *Handbook of Chemistry and Physics*, 35th ed., C. D. Hodgman, ed., Chemical Rubber Publishing Co., Cleveland, Ohio, 1953, p. 2433.

18 Kovasznay, L. S. G. and Törmarck, S. I. A., "Heat Loss of Hot-Wires in Supersonic Flow," *Bumblebee Rep. no. 127*, Johns Hopkins Univ., 1950.

19 Spangenberg, W. G., "Heat Loss Characteristics of Hot-Wire Anemometers at Various Densities in Transonic and Supersonic Flow," *NACA TN 3381*, 1955.

20 McAdams, W. H., *Heat Transmission*, 3rd ed., McGraw-Hill Book Co. Inc., New York, 1954, p. 259.

21 Baldwin, L. V., "Slip-Flow Heat Transfer from Cylinders in Subsonic Airstreams," *NACA TN 4369*, 1958.

22 Christiansen, W. H., "Development and Calibration of a Cold Wire Probe for Use in Shock Tubes," *GALCIT Hypersonic Research Project, Mem. no. 62*, July 1, 1961.

23 Cole, J. D. and Roshko, A., "Heat-Transfer from Wires at Reynolds Numbers in the Oseen Range," *Proc.* of the 1954 Heat Transfer and Fluid Mech. Inst., Stanford University Press, Stanford, Calif., 1954, pp. 13–24.

24 Collis, D. C. and Williams, M. J., "Two-Dimensional Convection from Heated Wires at Low Reynolds Numbers," *J. Fluid Mech.*, vol. 6, 1959, pp. 357–384.

25 Levy, H. C., "Heat Transfer in Slip Flow at Low Reynolds Number," *J. Fluid Mech.*, vol. 6, 1959, pp. 385–391.

26 Hurlbut, F. C., "Notes on Surface Interaction and Satellite Drag," Symposium on Aerodynamics of the Upper Atmosphere, *RAND R-339*, June 1959.

27 Beckwith, I. E., "Similar Solutions for the Compressible Boundary Layer on a Yawed Cylinder with Transpiration Cooling," *NASA TR R-42*, 1959.

28 Probstein, R. F. and Kemp, N. H., "Viscous Aerodynamic Characteristics in Hypersonic Rarefied Gas Flow," *J. Aerospace Sci.*, vol. 27, no. 3, 1960, pp. 174–192.

29 Willis, D. R., "On the Flow of Gases under Nearly Free Molecular Conditions," Princeton Univ., Dept. of Aero. Eng., *Rep. no. 442*, December 1958.

30 McClellan, R., "Equilibrium Temperature and Heat Transfer Characteristics of Hot Wires in Supersonic Flow," Ae. E. Thesis, Calif. Inst. of Tech., Pasadena, Calif., 1955.

31 Winovich, W. and Stine, H. A., "Measurements of the Non-Linear Variation with Temperature of Heat-Transfer Rate from Hot Wires in Transonic and Supersonic Flow," *NACA TN 3965*, 1957.

32 Dewey, C. F., Jr., "Hot-Wire Measurements in Low Reynolds Number Hypersonic Flows," *GALCIT Hypersonic Research Project, Mem. no. 65*, Sept. 15, 1961.

33 Van Dyke, M., "Second-Order Boundary-Layer Theory for Blunt Bodies in Hypersonic Flow," presented at the International Hypersonics Conference, Cambridge, Mass., Aug. 16–18, 1961 (*ARS paper no. 1966-61*).

Plasma Propulsion With a Pulsed Transmission Line

ALLAN SCHAFFER[1]

Aerospace Corp.
Los Angeles, Calif.

When a current pulse is sent down a helical transmission line, the radial component of the fringing magnetic field acts like a piston on plasma ahead. This study leads to expressions for the resulting velocity and pressure of the plasma. The principal assumption is that leakage of the plasma through the magnetic piston is negligible. The analysis is based on the simultaneous solution of the transmission line equations, the conservation of energy, and the normal shock relationships. The analysis involves only algebraic equations, even though the usual simplifying assumption that the magnetic pressure equals the plasma pressure is not made. It is shown that the piston is always slowed down by the presence of the plasma. The distribution of the energy supplied to the device is traced. The results of the analysis are applied to a typical design problem.

THE MAGNETIC induction plasma engine (MIPE) is receiving increased attention as a plasma propulsion device (1, 2).[2] Its principal advantage is that electrodes need not be in contact with the hot gas, since the propulsive force arises from currents induced in the plasma.

Conceptually one of the simplest methods for producing a MIPE is by means of a pulsed transmission line. A helical conductor is wrapped around a plasma duct, and capacitors are distributed along the turns of the helix (Fig. 1). A current pulse is sent down the line. The radial component of the fringing magnetic field associated with the pulse acts like a

Presented at the ARS 15th Annual Meeting, Washington, D. C., Dec. 5–8, 1960; revision received Oct. 20, 1961.

[1] Presently Senior Scientist with Clauser Technology Corp., Torrance, Calif.

[2] Numbers in parentheses indicate References at end of paper.

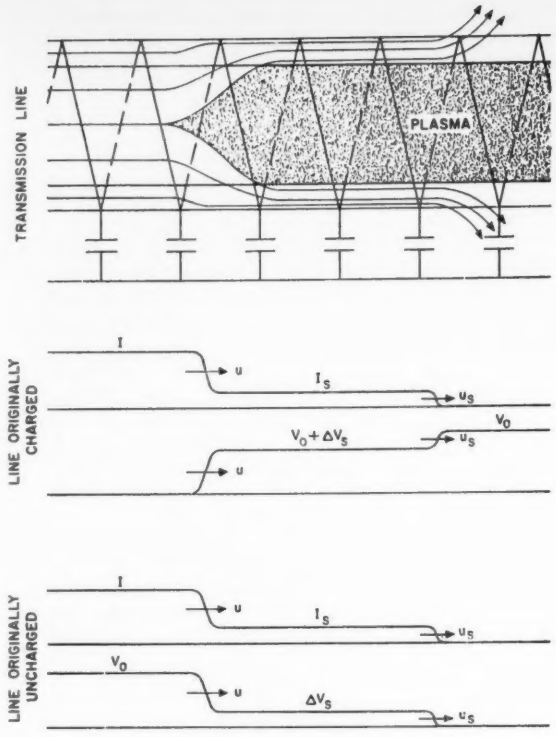

Fig. 1 Transmission line and wave forms

piston, since ring currents are induced in the plasma when it tries to slip through the fringing field. If the magnetic piston is reasonably hard to leakage, the device acts like a mechanical piston driving a shock ahead of it. The speed of the piston is matched to the desired plasma velocity by distributing the appropriate capacitance per unit length along the line. The device can be operated either with the distributed capacitors originally charged (pulse initiated by shorting the input end) or with the capacitors originally uncharged (pulse initiated by applying a voltage to the input end).

The shock wave that the piston drives in the gas is not shown in Fig. 1. There are two current fronts, one moving behind the plasma with velocity u and the other traveling with velocity u_s in the annular sheath between the plasma and the coil. The front moving behind the plasma provides the piston action. The sheath front, which corresponds to a refracted wave in the initial transient establishment of the piston, must always be present, even if the cross-sectional area of the sheath approaches zero.

This paper is a study of the interaction between the transmission line and the plasma. The interaction can be separated into two problems: 1) leakage of the plasma through the fringing field; and 2) effect of the plasma loading on the piston velocity. In the present analysis only problem 2 is studied. Problem 1 is obviated by assuming that leakage is negligible, i.e., that the piston velocity equals the plasma velocity, an assumption that could be reasonable considering the high magnetic Reynolds numbers involved (1, 3). The true leakiness of the piston is being determined by other theoretical and experimental programs that are now in progress.

Other assumptions in the analysis are that the transmission line is infinitely long, that the slug of shocked gas is infinitely long,[3] and that ohmic dissipation losses in the plasma and coil are negligible. The helix of the transmission line is allowed to have an arbitrary number of identical strands in parallel, and, whereas mutual inductance effects between the various strands are included, the mutual inductance between the turns of any one strand is assumed to be negligible. The transmission line is permitted to have any diameter equal to or greater than that of the plasma.

The analysis involves the simultaneous solution of four basic equations: 1) the conservation of current across a wave front in a transmission line; 2) Faraday's law of induction applied to such a wave front; 3) the conservation of energy for the transmission line pushing on the plasma; and 4) the normal shock relationships. The two methods of operation previously mentioned, i.e., capacitors originally charged and capacitors originally uncharged, are both treated.

The principal aim of the analysis is to determine the velocity that results when the transmission line pushes on the plasma. Once the velocity is known, other useful parameters, such as the plasma pressure and the distribution of the energy supplied to the device, are readily computed. The results of the analysis can be applied to design problems of interest. One such numerical calculation is performed. For a particular choice of design parameters, i.e., for a particular gas, tube diameter, capacitance per unit length, and charging voltage, calculations are performed to find the pressure, velocity, fraction of the energy imparted to the plasma, fraction of the energy converted to magnetic energy, etc.

Line Originally Charged

The helix of the transmission line is allowed to have λ identical strands in parallel. In the analysis, a bar under a quantity will indicate the value for a single strand of the λ strands. For example, C is the total capacitance per unit length of the transmission line, whereas $\underline{C} = C/\lambda$ is the capacitance per unit length per strand.

The conservation of current across an arbitrary right-running wave front moving at constant velocity u in a transmission line gives

$$\Delta \underline{I}_{\text{front}} = -\underline{C} u \Delta V_{\text{front}} \qquad [1]$$

As seen from Fig. 1, Eq. 1, when applied to each of the two wave fronts for the case of line originally charged, gives

$$\underline{I}_s - \underline{I} = -\underline{C} u (V_0 + \Delta V_s) \qquad [2]$$

and

$$-\underline{I}_s = \underline{C} u_s \Delta V_s \qquad [3]$$

Faraday's Law of Induction specialized for right-running constant velocity wave fronts of arbitrary shape yields[4]

$$\Delta V_{\text{front}} = -u_n \Delta \phi_{\text{front}} \qquad [4]$$

Applying Eq. 4 to the two wave fronts gives

[3] This is a nontrivial assumption, since it guarantees that the wave traveling in the sheath will never catch the shock front. If the sheath wave passes the shock front, magnetic field will then fill the tube ahead of the plasma with the catastrophic result that there is now no net force on the plasma. It is possible to make the sheath velocity less than the shock velocity, but only at the expense of large energy loss into the magnetic field of the sheath.

[4] Eq. 4 follows from Faraday's Law written in the form

$$\oint_{\text{circuit}} \boldsymbol{E} \cdot \boldsymbol{dl} = \frac{\partial}{\partial t} \int_{\text{front}} \phi(x - ut) \underline{n} \, dx$$

and the relationship

$$\frac{\partial}{\partial t} [\phi(x - ut)] = -u \frac{\partial \phi}{\partial x}$$

where l is distance along a closed electrical path that encompasses the wave front, i.e., along a single strand plus its return, and $\phi(x - ut)$ is an arbitrary wave function representing the total magnetic flux due to all λ strands.

$$V_0 + \Delta V_s = -u\underline{n}\Delta\phi_{\text{front 1}} = u\underline{n}(\phi - \phi_s) \quad [5]$$

and

$$\Delta V_s = u_s\underline{n}\Delta\phi_{\text{front 2}} = -u_s n\phi_s \quad [6]$$

Since ϕ and ϕ_s are uniform, $\phi = AB$ and $\phi_s = A_sB_s$, where A is the cross-sectional area of the coil, B the uniform magnetic field strength behind the piston, A_s the cross-sectional area of the sheath between the plasma and the coil, and B_s the uniform magnetic field strength in the sheath.[5] Eqs. 5 and 6 combined thus yield

$$V_0 = u\underline{n}AB + (u_s - u)nA_sB_s \quad [7]$$

The uniform magnetic fields are related to their respective currents by the solenoid relations

$$B = \mu\lambda\underline{n}\underline{I} \quad [8]$$

$$B_s = \mu\lambda\underline{n}\underline{I}_s \quad [9]$$

Since ohmic dissipation losses are being ignored, the energy equation for the case of capacitors originally charged will simply relate to net change of stored electrical energy in the condensers, the production of magnetic energy, and the work done on the plasma. Application of the control volume technique to Fig. 1 yields

$$(1/2)\,CV_0^2u_s = (1/2)C(V_0 + \Delta V_s)^2(u_s - u) + (B^2A/2\mu)u + (B_s^2A_s/2\mu)(u_s - u) + pAu[1 - (A_s/A)] \quad [10]$$

where p is the plasma pressure behind the shock and u the particle and piston velocity.

It is assumed that the gas is singly ionizable. Moreover, the shock velocities of interest in plasma propulsion are sufficiently high so that the shocked gas can be considered completely ionized. The normal shock equations then yield to better than 0.1% accuracy a linear relationship between p and u^2 of the form

$$p = \alpha u^2 - \beta \quad [11]$$

where if the unshocked gas is monatomic

$$\alpha = \frac{20p_1}{9a_1^2}$$

$$\beta = \frac{2\chi p_1}{3RT_1}$$

and if the unshocked gas is diatomic

$$\alpha = \frac{28p_1}{15a_1^2}$$

$$\beta = \frac{p_1}{3}\left[-6 + \frac{2}{T_1}\left(\frac{\psi}{R} + 2\,\frac{\chi}{R}\right)\right]$$

Eqs. 2, 3, 7–11 are seven equations among the seven unknowns: $\underline{I}_s$, $\underline{I}$, u, ΔV_s, B, B_s, and p. The first six equations will be combined to give an electrodynamic relationship between p and u^2 which can be solved simultaneously with the hydrodynamic relationship, Eq. 11.

Combination of Eqs. 2, 3, 7–9 together with the definitions

$$\underline{u}_0 = [\mu\underline{n}^2A\underline{C}]^{-1/2}$$

$$\underline{u}_s = [\mu\underline{n}^2A_s\underline{C}]^{-1/2}$$

gives

$$\Delta V_s = \frac{-[1 - \lambda\,(u^2/\underline{u}_0^2)]\,V_0}{\lambda(u_s - u)\,[u/\underline{u}_0^2 + u_s/\underline{u}_s^2]} \quad [12]$$

[5] Consistent with the high magnetic Reynolds number assumption, the skin depth in the plasma along the sheath is taken to be negligibly small.

The velocities $\underline{u}_0$ and $\underline{u}_s$ are the regular transmission line phase velocities for a single stranded helix, without and with a perfectly conducting core. These velocities are related to the corresponding phase velocities for a multistranded helix, u_0 and u_s, by $\underline{u}_0^2 = \lambda u_0^2$ and $\underline{u}_s^2 = \lambda u_s^2$. Eq. 12 thus becomes

$$\Delta V_s = \frac{-\left(1 - \dfrac{u^2}{u_0^2}\right)V_0}{\left(\dfrac{u_s}{u} - 1\right)\left(\dfrac{u^2}{u_0^2} + \dfrac{u}{u_s}\right)} \quad [13]$$

Eq. 13 can be used with Eqs. 2, 3, 8, and 9 to obtain expressions for I, I_s, B, and B_s in terms of u. When all of these are substituted into Eq. 10, the electrodynamic relationship between p and u^2 is obtained as

$$\frac{pA}{W_0} = \left[\frac{1 - \dfrac{u^2}{u_0^2}}{1 - \dfrac{u_0^2}{u_s^2}}\right]\left[1 + \frac{\left(1 - \dfrac{u^2}{u_0^2}\right)\left(\dfrac{u^2}{u_0^2} + 2\,\dfrac{u}{u_s} - \dfrac{2}{\dfrac{u_s}{u} - 1}\right)}{\left(\dfrac{u^2}{u_0^2} + \dfrac{u}{u_s}\right)^2}\right] \quad [14]$$

It is interesting that λ does not appear explicitly in Eq. 14, the form of the relationship thus being the same as for the single-stranded transmission line. Of course, the equation is not independent of λ since

$$u_0 = [\lambda\mu\underline{n}^2A\underline{C}]^{-1/2}$$

$$u_s = [\lambda\mu\underline{n}^2A_s\underline{C}]^{-1/2}$$

A special case worth noting occurs when the internal diameter of the duct coincides with the diameter of the coil; that is, when the sheath area A_s approaches zero. For this case we obtain a much simpler equation, letting $u_s \to \infty$ in Eq. 14, viz.

$$\frac{pA}{W_0} = \frac{u_0^2}{u^2} - 1 \quad [15]$$

Eq. 14, the electrodynamical relationship between p and u^2, is solved simultaneously with the hydrodynamic relationship Eq. 11 to complete the solution. The resulting equation is somewhat cumbersome and will be omitted.

It is interesting to trace the energy transfers in the device. The net rate of energy disappearance from the capacitors P_c divides as power to the plasma P_p, to the pushing magnetic field P_m, and to the sheath magnetic field P_s. The nondimensionalized expressions for these powers become

$$\frac{P_c}{W_0u} = 1 + \frac{1 - \dfrac{u^2}{u_0^2}}{\dfrac{u^2}{u_0^2} + \dfrac{u}{u_s}}\left[2 - \frac{1 - \dfrac{u^2}{u_0^2}}{\left(\dfrac{u_s}{u} - 1\right)\left(\dfrac{u^2}{u_0^2} + \dfrac{u}{u_s}\right)}\right] \quad [16]$$

$$\frac{P_p}{W_0u} = \frac{pA}{W_0}\left(1 - \frac{u_0^2}{u_s^2}\right) \quad [17]$$

$$\frac{P_m}{W_0u} = \frac{u^2}{u_0^2}\left(\frac{1 + \dfrac{u}{u_s}}{\dfrac{u}{u_s} + \dfrac{u^2}{u_0^2}}\right)^2 \quad [18]$$

$$\frac{P_s}{W_0u} = \frac{\left(1 - \dfrac{u^2}{u_0^2}\right)^2}{\left(\dfrac{u_s}{u} - 1\right)\left(\dfrac{u}{u_s} + \dfrac{u^2}{u_0^2}\right)^2} \quad [19]$$

Eq. 16 equals the sum of Eqs. 17–19. Thus division of each of the latter three equations by Eq. 16 give the fractional distribution of the energy.

Line Originally Uncharged

Analogous expressions exist for the mode of operation in which the capacitors are originally uncharged and the pulse is initiated by applying a voltage to the input end.

Eq. 1 is unchanged. Eq. 2 becomes

$$\underline{I}_s - \underline{I} = -\underline{C}u(\Delta V_s - V_0) \qquad [20]$$

Eqs. 3 and 4 are unchanged. Eq. 7 becomes

$$V_0 = -u\underline{n}AB - (u_s - u)nA_sB_s \qquad [21]$$

Eq. 8 and 9 are unchanged. The energy balance, Eq. 10, is considerably altered, since now external power is being supplied to the device. The appropriate expression is

$$-V_0I = (1/2)CV_0^2u + (1/2)C\Delta V_s^2(u_s - u) + \frac{B^2A}{2\mu}u + \frac{B_s^2A_s}{2\mu}(u_s - u) + pAu\left(1 - \frac{u_0^2}{u_s^2}\right) \qquad [22]$$

Eq. 11 is unchanged. Eq. 13 becomes

$$\Delta V_s = \frac{V_0\left(1 - \frac{u^2}{u_0^2}\right)}{\left(\frac{u_s}{u} - 1\right)\left(\frac{u}{u_s} + \frac{u^2}{u_0^2}\right)} \qquad [23]$$

The final result i that Eqs. 14 and 15 are unchanged. Thus the plasma velocity and pressure are the same with either mode of operation.

In computing the power distribution, an additional term for the case of line originally uncharged must now be considered: namely, the external power supplied, $P_s = -V_0I$. The following expressions are obtained:

$$\frac{P_c}{W_0u} = 2\left(\frac{1 + \frac{u}{u_s}}{\frac{u}{u_s} + \frac{u^2}{u_0^2}}\right) \qquad [24]$$

$$\frac{P_c}{W_0u} = 1 + \frac{\left(1 - \frac{u^2}{u_0^2}\right)^2}{\left(\frac{u_s}{u} - 1\right)\left(\frac{u}{u_s} + \frac{u^2}{u_0^2}\right)^2} \qquad [25]$$

$$\frac{P_p}{W_0u} = \frac{pA}{W_0}\left(1 - \frac{u_0^2}{u_s^2}\right) \qquad [26]$$

$$\frac{P_m}{W_0u} = \frac{u^2}{u_0^2}\left(\frac{1 + \frac{u}{u_s}}{\frac{u}{u_s} + \frac{u^2}{u_0^2}}\right)^2 \qquad [27]$$

$$\frac{P_s}{W_0u} = \frac{\left(1 - \frac{u^2}{u_0^2}\right)^2}{\left(\frac{u_s}{u} - 1\right)\left(\frac{u}{u_s} + \frac{u^2}{u_0^2}\right)^2} \qquad [28]$$

Eq. 24 equals the sum of Eqs. 25–28. The energy fraction transferred to the plasma per shot equals P_p/P_s. For the special case of $A_s = 0$, this ratio is particularly simple, viz.

$$\frac{P_p}{P_s} = \frac{1}{2}\left(1 - \frac{u^2}{u_0^2}\right) \qquad [29]$$

It follows that, in this case, at most 50% of the energy can be transferred to the plasma per shot.

Required Velocity Inequalities

There are three velocities in the problem: the plasma and piston velocity u, the unloaded transmission line velocity u_0, and the velocity of wave propagation along the sheath u_s. Since $A > A_s$, it is evident that $u_0 < u_s$. It remains to be shown that $u < u_0$.

With either mode of operation, Eq. 14 shows that for $p > 0$ it is necessary that the following inequality be satisfied:

$$\frac{\left(1 - \frac{u^2}{u_0^2}\right)\left(\frac{u^2}{u_0^2} + 2\frac{u}{u_s} - \frac{2}{\frac{u_s}{u} - 1}\right)}{\left(\frac{u^2}{u_0^2} + \frac{u}{u_s}\right)^2} \gtrless -1$$

where the top inequality sign is applicable if $u < u_0$ and the bottom inequality sign is applicable if $u > u_0$.

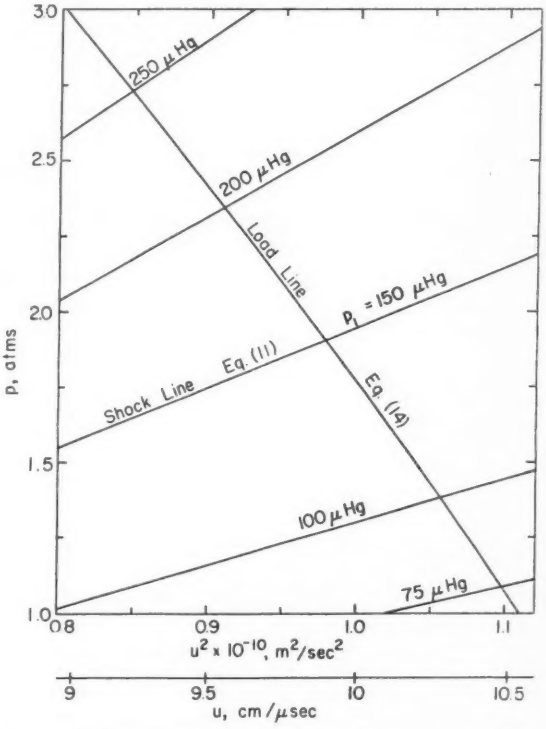

Fig. 2 Simultaneous plots of Eqs. 11 and 14 for a typical design

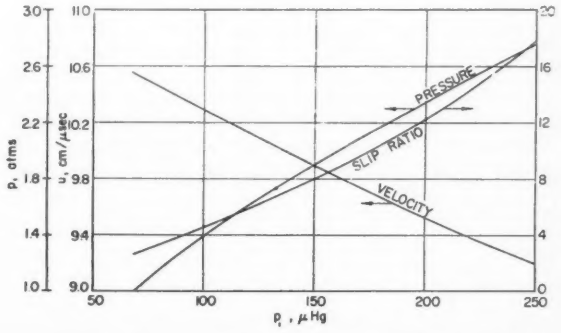

Fig. 3 Computed performance for a typical design

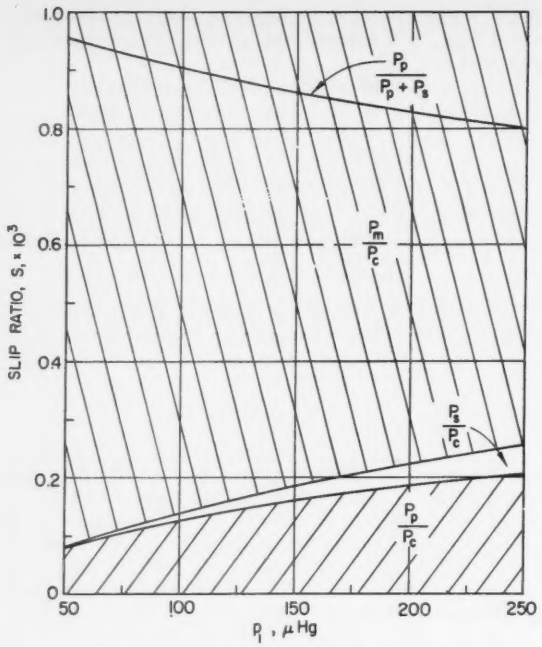

Fig. 4 Distribution of energy for a typical design

The above inequality reduces to the simple relationship

$$u_0 \lesseqgtr u_s$$

Since the top inequality is true and the bottom one false, it follows that $u < u_0$. This means that the piston always travels slower when plasma is present than when no plasma is present.

Numerical Example

The results of the analysis will be applied to a typical design problem of interest. Select the following values for the electrical design parameters, using MKS units:

$$\begin{aligned} \lambda &= 1 \\ C &= 13.1 \times 10^{-6}\ \text{farad/m} \\ A &= 7.1 \times 10^{-3}\ \text{m}^2 \\ A_s &= 2.56 \times 10^{-3}\ \text{m}^2 \\ n &= 26.2\ \text{m}^{-1} \\ V_0 &= 2.5 \times 10^4\ \text{v} \end{aligned}$$

It follows that

$$\begin{aligned} W_0 &= 4.09 \times 10^3\ \text{joules/m} \\ u_0 &= 1.12 \times 10^5\ \text{m/sec} \\ u_s &= 1.86 \times 10^6\ \text{m/sec} \end{aligned}$$

In addition, choose H_2 gas with $T_1 = 300°\text{K}$. Let p_1 vary through the range $75\mu\ \text{Hg} < p_1 < 250\mu\ \text{Hg}$. The parameters α and β are given by $\alpha = 1.41 \times 10^{-7}\, p_1$ and $\beta = 1.08 \times 10^2\, p_1$, where p_1 is in μ Hg. Finally, specify the mode of operation to be the one for which the capacitors are originally charged.

The results are given in Figs. 2, 3, and 4. Graphs of Eqs. 11 and 14 are shown in Fig. 2. Eq. 14 is labeled the load line, whereas the solutions of Eq. 11, corresponding to various initial pressures, are labeled as shock lines. The intersection of the load line and a shock line gives the solution for the particular initial pressure.

The resulting solutions for p and u as a function of p_1 are given in Fig. 3. The slip ratio, also plotted in Fig. 3, is a rough measure of the piston hardness to leakage across magnetic field lines. It is defined as the mean velocity of the plasma relative to the piston divided by the absolute piston velocity, and it has been computed by means of the order of magnitude analysis described in (3). The slip ratio used here is not necessarily indicative of the true piston hardness, since only one form of leakage has been considered.

The distribution of the energy is shown by the cumulative diagram, Fig. 4. The fraction of the energy going into the sheath field is seen to be very small. On the other hand, a large fraction of the energy goes into the pushing magnetic field. Evidently if the pulsed MIPE is to be practical, a way must be found to recover this energy. On the assumption that it is recoverable, an efficiency for the device can be defined to equal $P_p/(P_p + P_s)$. A plot of this variable is also shown in Fig. 4.

It is worth noting in Figs. 3 and 4 that decreasing the pressure has a favorable influence on both the slip ratio and the efficiency.

Acknowledgments

The author is indebted to R. H. Huddlestone and R. X. Meyer of the Physical Research Laboratory, Aerospace Corp., for considerable contributions to the present analysis.

Nomenclature

a	=	speed of sound
d	=	internal diameter of plasma duct
E	=	electric field strength
I	=	current
l	=	circuit length coordinate
n	=	coil turns per unit axial length
p	=	gas pressure
R	=	universal gas constant
T	=	temperature
t	=	time
V	=	voltage
x	=	axial length coordinate
W_0	=	$(1/2)CV_0^2$ = condenser energy per unit length
α	=	parameter
β	=	parameter
μ	=	permeability
ϕ	=	magnetic flux
χ	=	ionization energy
ψ	=	dissociation energy
$(\ )_1$	=	property of the unshocked gas
$(\ )_s$	=	property associated with the sheath
$(\underline{\ })$	=	property associated with a single strand or with a single stranded coil

References

1 Clauser, M. U., "The Magnetic Induction Plasma Engine," Space Technology Laboratories, *Rep. No. STL/TR-60-0000-00263*, August 1960 (presented at the AGARD Meeting on Advanced Propulsion Techniques, Pasadena, Calif., August 1960).

2 Covert, E. E. and Haldemann, C. W., "The Traveling-Wave Pump," ARS Journal, vol. 31, no. 9, September 1961, pp. 1252–1260.

3 Schaffer, A. B., "Hardness of the Axially-Symmetric Magnetic Piston," Space Technology Laboratories, *Rep. No. STL/TR-60-0000-09011*, January 1960.

Three-Dimensional Optimum Thrust Trajectories for Power Limited Propulsion Systems

WILLIAM G. MELBOURNE[1]

Jet Propulsion Laboratory
Pasadena, Calif.

The three-dimensional equations for optimum variable thrust with power limited propulsion systems are presented. An iterative routine for solving the two-point boundary value problem has been coupled with these equations to obtain numerical solutions for specified end conditions. A set of interplanetary rendezvous trajectories to Venus and Mars is presented, and the effects of orbital inclination and eccentricity are assessed.

FOR THE past few years mission feasibility studies and trajectory analyses have been conducted to assess the payload capabilities of power limited advanced propulsion vehicles for various interplanetary missions. This paper describes one type of optimum thrust program for power limited propulsion systems which is currently being used in these studies.

The power limited propulsion system is constrained in the amount of kinetic power contained in the exhaust propellant. By a consideration of the energy and momentum equations, a rocket equation suitable for such a system is obtained. This is given by

$$\frac{1}{m_1} = \frac{1}{m_0} + \int_0^{t_1} \frac{a^2}{2P}\, dt \qquad [1]$$

where m_0 and m_1 are the vehicle masses at the beginning and end, respectively, of the flight, a is the thrust acceleration, and P the power expended in the rocket exhaust. The exhaust power is determined by the power rating of the power plant carried by the vehicle and by the efficiency of conversion by the propulsion system, which is generally dependent on the exhaust velocity. The final vehicle mass depends on the value of this integral, which in turn depends on the flight time, the mission involved (namely, the specification of the kinematic conditions of the vehicle initially and terminally), the force field in which the vehicle travels, the nature of the thrust program used to accomplish this mission, and finally, the engineering design of the propulsion system. This integral is analogous to the concept of incremental velocity in a chemical rocket and is useful in payload optimization studies.

For the preliminary mission feasibility studies, it is desirable to employ optimum thrust programs which exclude the complexity imposed by the engineering design but which bracket or isolate that class of trajectories and vehicle performances which an actual vehicle would be capable of achieving.

One such thrust program, which partially fulfills this need, is obtained by satisfying the criterion that the quantity $\int_0^{t_1} a^2 dt$ is a minimum using an unconstrained thrust magnitude and direction. The justification of this program is based on the fact that over a wide range of specific impulse, but excluding lower values, the power conversion efficiency of the propulsion system is nearly constant, thus allowing the removal of P from the integral. Since the thrust is unconstrained, this program yields the absolute minimum that $\int_0^{t_1} a^2 dt$ may have for a given mission and therefore leads to a somewhat optimistic estimate of vehicle payload.[2]

The equations of motion of a vehicle in a conservative force field may be written in vectorial form as

$$\ddot{\mathbf{r}} + \nabla V - \mathbf{a} = 0 \qquad [2]$$

where $\mathbf{r}$ is the position vector and V the potential in this force field. The minimization of $\int_0^{t_1} a^2 dt$ may be accomplished by calculus of variations methods in which this integral is minimized subject to certain constraints, namely, the equations of motion and the initial and terminal kinematic conditions specified by the mission.

For the variable thrust program, it may be shown (1–3)[3] that the thrust acceleration equations that must be satisfied as necessary conditions for minimum $\int_0^{t_1} a^2 dt$ are the Euler-Lagrange equations

$$\ddot{\mathbf{a}} + (\mathbf{a}\cdot\nabla)\nabla V = 0 \qquad [3]$$

Since V is not an explicit function of time, these equations admit a first integral in scalar form which may be expressed as

$$\dot{\mathbf{a}}\cdot\dot{\mathbf{r}} - (1/2)a^2 + \mathbf{a}\cdot\nabla V = \text{const} \qquad [4]$$

The present studies employ an inverse-square central force field model in three dimensions. Because of the spherical symmetry of this problem, it is advantageous to express these equations in spherical coordinates. This coordinate system and the direction of the basis vectors are illustrated in Fig. 1. The state variables for this formulation are r, θ, ϕ, u, h_θ, and h_ϕ, where u is radial velocity, and h_θ and h_ϕ are the components of angular momentum per unit mass. The control variables are a_r, a_θ, and a_ϕ. After some manipulation it may be shown that Eqs. 2 and 3 may be expressed as

$$\dot{u} - (h^2/r^3) + (\mu/r^2) - a_r = 0 \qquad [5]$$

Received April 26, 1961.

[1] Research Group Supervisor. Member ARS.

[2] For a comparison of this program with a constant thrust program, consult Ref. 3.

[3] Numbers in parentheses indicate References at end of paper.

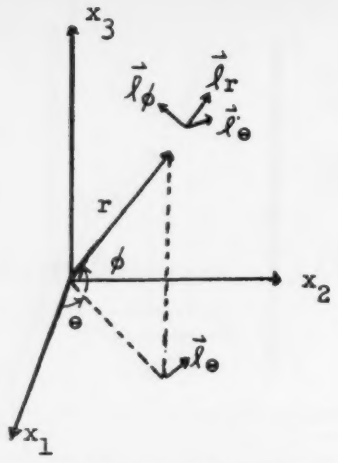

Fig. 1 Spherical coordinate system

$$u - \dot{r} = 0 \quad [6]$$

$$\dot{h}_\theta - (h_\phi{}^2 \tan\phi/r^2) + ra_\phi = 0 \quad [7]$$

$$\dot{h}_\phi + (h_\theta h_\phi \tan\phi/r^2) - r\,a_\theta = 0 \quad [8]$$

$$h_\vartheta + r^2\dot{\phi} = 0 \quad [9]$$

$$h_\phi - r^2\dot{\theta}\cos\phi = 0 \quad [10]$$

$$h^2 = h_\phi{}^2 + h_\theta{}^2 \quad [11]$$

$$\dot{a}_r + \frac{3a_r}{r^4}\left[h^2 - \frac{2\mu r}{3}\right] - \frac{1}{r}\,[a_\theta{}^2 + a_\phi{}^2] - \frac{2h_\phi \tan\phi}{r^4}\,(\mathbf{h}\cdot\mathbf{a}) - \frac{h_\theta F(t)}{r^3} - \frac{K_1 h_\phi}{r^3\cos\phi} = 0 \quad [12]$$

$$F(t) + 2r^2\frac{d}{dt}\left[\frac{a_\phi}{r}\right] - \frac{4h_\theta a_r}{r} + \frac{2h_\phi a_\theta \tan\phi}{r} = 0 \quad [13]$$

$$\dot{F}(t) - \frac{2h_\phi}{r^3\cos^2\phi}\,(\mathbf{h}\cdot\mathbf{a}) - \frac{K_1 h_\phi \sin\phi}{r^2\cos^2\phi} = 0 \quad [14]$$

$$r^2\frac{d}{dt}\left[\frac{a_\theta}{r}\right] + \frac{h_\phi}{r}\,(2a_r - a_\phi\tan\phi) - \frac{\tan\phi}{r}\,(\mathbf{h}\cdot\mathbf{a}) - \frac{K_1}{2\cos\phi} = 0 \quad [15]$$

where h is the angular momentum per unit mass of the vehicle and μ the gravitational constant of the central body. The quantity $F(t)$ is an auxiliary variable, essentially one of the Lagrange multipliers that could not easily be eliminated. The constant K_1 is a constant of integration resulting from the cyclic nature of the variable θ. Eq. 4 becomes

$$a^2 - 2\dot{a}_r\dot{r} + \frac{2a_r}{r^3}\,[h^2 - \mu r] - \frac{K_1 h_\phi}{r^2\cos\phi} - \frac{h_\theta F(t)}{r^2} - \frac{2h_\phi\tan\phi}{r^3}\,(\mathbf{h}\cdot\mathbf{a}) = K_2 \quad [16]$$

The quantities K_1 and K_2 are the only constants of motion which have been found. Eq. 16 is not used in numerical integrations because of the $\dot{a}_r\dot{r}$ term, but it is useful in checking the accuracy of the numerical integrations of Eqs. 5–15. It may be easily verified that these equations reduce to those contained in (1) upon reduction to two dimensions.

Missions and Terminal Conditions

The kinematic variables in most missions are specified at the initial point of a trajectory, and in a final trajectory design the terminal values are usually specified. In a preliminary study, however, it is advantageous to let certain terminal variables be free in order to optimize the trajectory with respect to certain criteria such as payload capability, communication distance, and error sensitivity.

In planetary rendezvous missions, six terminal quantities must be specified. It is convenient to group these into five quantities that determine the shape and orientation of the terminal orbit and one quantity indicating the rendezvous position on the orbit. These quantities are the energy per unit mass E, the angular momentum per unit mass h, the orbital inclination i, the argument of perigee ω, the longitude

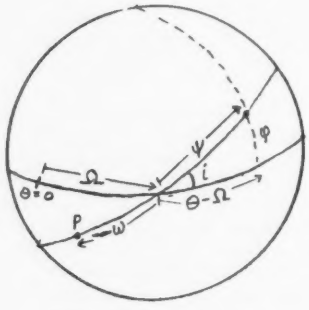

Fig. 2 Orbital elements

Table 1 Useful combinations of rendezvous terminal conditions and corresponding transversality relations[a]

	I	II	III	IV	V	VI
1	$E = E_s$	$E = E_s$	$E = E_s$	$E = E_s$	$E = E_s$	$E = E_s$
2	$h = h_s$	$h = h_s$	$h = h_s$	$h = h_s$	$h = h_s$	$h = h_s$
3	$i = i_s$	$i = i_s$	$i = i_s$	$i = i_s$	$i = i_s$	$K_1 = 0$
4	$\omega = \omega_s$	$\omega = \omega_s$	$\omega = \omega_s$	$\Omega = \Omega_s$	$K_1 = 0$	$M = 0$
5	$\Omega = \Omega_s$	$\Omega = \Omega_s$	$K_1 = 0$	$M = 0$	$M = 0$	$\mathbf{a}\cdot\mathbf{h} = 0$
6	$\psi = \psi_s$	$M + N + \frac{K_1 h_\phi}{r^2\cos\phi} = 0$	$M + N = 0$	$N + \frac{K_1 h_\phi}{r^2\cos\phi} = 0$	$N = 0$	$F = 0$

[a] The subscript s denotes a specified terminal value. The functions M and N are given by

$$M(t) = 2\dot{a}_r\dot{r} + (2a_r/r^3)(\mu r - h^2)$$

$$N(t) = [2h_\phi(\mathbf{a}\cdot\mathbf{h})/r^3]\tan\phi + (h_\theta F(t)/r^2)$$

and will be recognized as components of Eq. 16.

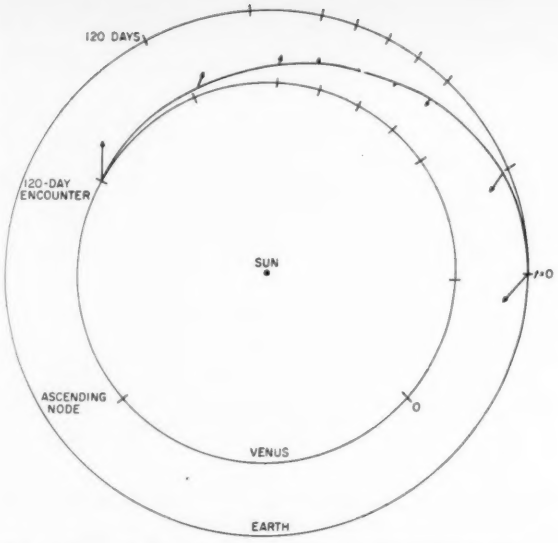

Fig. 3 Venus three-dimensional optimum rendezvous trajectory, ecliptic projection

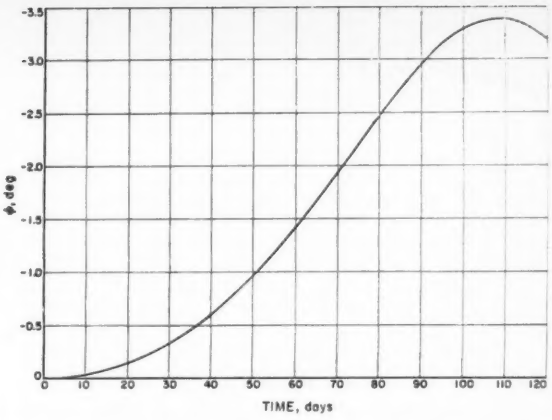

Fig. 4 Venus three-dimensional optimum rendezvous trajectory, celestial latitude

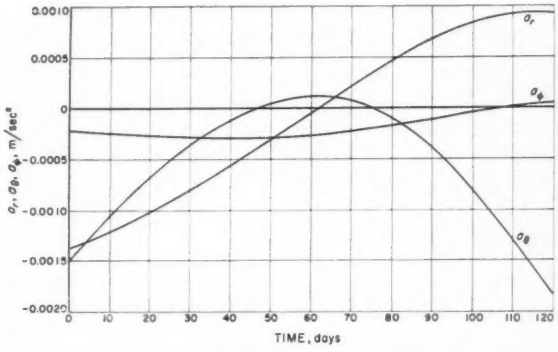

Fig. 5 Venus three-dimensional optimum rendezvous trajectory, thrust program

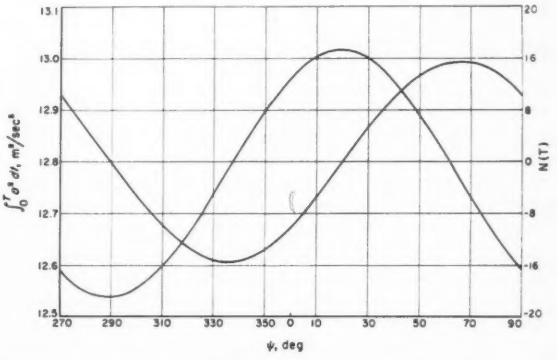

Fig. 6 Venus three-dimensional rendezvous trajectories, 120-day flight time

of the ascending node Ω, and the angle from the line of nodes to the rendezvous point ψ. The angular quantities are exhibited in Fig. 2. These quantities are expressed in terms of the six kinematic variables through the relations

$$E = (1/2)[\dot{r}^2 + (h^2/r^2)] - \mu/r \quad [17]$$

$$h^2 = h_\theta^2 + h_\phi^2 \quad [18]$$

$$\cos i = h_\phi \cos \phi / h \qquad 0 \le i \le \pi \quad [19]$$

$$\omega = \psi - \sin^{-1}(h\dot{r}/\mu e) \qquad 0 \le \omega \le 2\pi \quad [20a]$$

$$\omega = \psi - \cos^{-1}\left[\frac{1}{e}\frac{h^2}{\mu r} - 1\right] \qquad 0 \le \omega \le 2\pi \quad [20b]$$

$$\sin \Omega = \frac{-h_\theta \sin \theta - h_\phi \sin \phi \cos \theta}{h \sin i} \qquad 0 \le \Omega \le 2\pi \quad [21a]$$

$$\cos \Omega = \frac{-h_\theta \cos \theta + h_\phi \sin \phi \sin \theta}{h \sin i} \qquad 0 \le \Omega \le 2\pi \quad [21b]$$

$$\sin \psi = \sin \phi / \sin i \qquad 0 \le \psi \le 2\pi \quad [22a]$$

$$\cos \psi = -h_\theta \cos \phi / h \sin i \qquad 0 \le \psi \le 2\pi \quad [22b]$$

where e is the eccentricity of the ellipse. These six expressions may serve as boundary conditions at the terminal point of the trajectory. For each one of these conditions that is left unspecified, there is, from the calculus of variations, a corresponding transversality expression to be satisfied at the terminal point. Satisfying these transversality expressions yields extremals in the quantity to be optimized with respect to the unspecified boundary conditions. Both relative maxima and minima result from satisfying these conditions. The general formulation of transversality conditions may be found in treatises on calculus of variations; in (3) a formulation that is directly applicable to this problem is presented.

Table 1 lists several useful combinations of rendezvous terminal conditions and corresponding transversality relations obtained from an application of this formulation for a fixed final time. Combination I is, of course, the case where all six terminal conditions are specified. In combination II the position on the terminal orbit ψ is left unspecified, and the corresponding transversality condition appears. In combination III both ψ and Ω are unspecified, and two transversality conditions result. This combination is most useful when the trajectory commences from a circular orbit, thus relaxing the necessity of specifying $\Omega(t_1)$. Combinations IV and V apply to circular terminal orbits and to the case of orbital inclination changes. Combination VI also applies to the two-dimensional case where $\mathbf{a} \cdot \mathbf{h}$ and $F(t)$ are zero over the trajectory. This

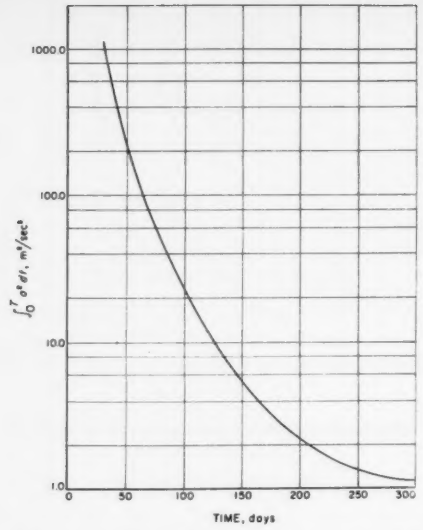

Fig. 7 Venus two-dimensional rendezvous trajectories

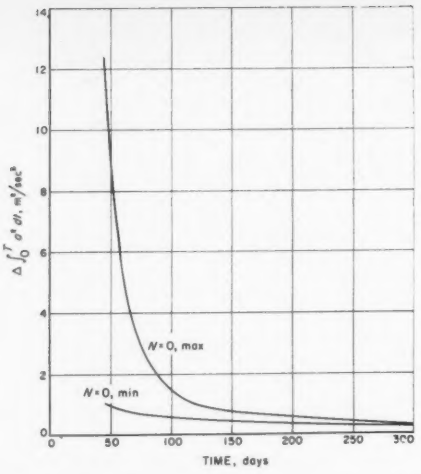

Fig. 8 Venus three-dimensional rendezvous trajectories, the effect of orbital inclination

particular case has, in effect, been noted by Blum (1). The quantity K_1 is zero when neither θ nor any quantity explicitly dependent on θ, e.g., Ω, is specified.

Interplanetary Trajectories

In three dimensions, the set of equations to be solved requires the specification of 12 constants of integration. The specification of the six state variables initially and the six terminal and transversality conditions define the system.

D. E. Richardson of Jet Propulsion Laboratory has programmed these equations in an inverse-square force field for numerical solution on an IBM 7090 digital computer. To overcome the two-point boundary value problem associated with this type of equations, an iterative routine designed to efficiently conduct parametric analyses has been developed. Eqs. 5–15 are used to obtain a search matrix by a direct perturbation procedure. From this matrix a set of corrections to the initial conditions is obtained yielding a trajectory whose terminal conditions converge toward the specified values. The validity of this procedure is predicated on the assumption of a near-linear behavior of the variables in the small. Several devices are used to minimize computer time. If successive iterations are required, the original matrix is used as long as the process converges and the number of iterations is less than some specified value. To use this computer efficiently, a family of converged trajectories (for different terminal conditions and/or flight times, for example), is obtained in one machine run. This allows the accumulation of information about previously converged trajectories, which is used to predict initial conditions and search matrix elements for the succeeding case. This routine has been remarkably successful in the large-scale production of interplanetary rendezvous and flyby trajectories to nearly all the planets, with flight times ranging from 30 days to 3 years (2,3).

The numerical examples presented consist of sets of interplanetary rendezvous trajectories commencing from Earth's heliocentric position and terminating at Venus and at Mars. The orbits of Earth and Venus were assumed circular with the latter possessing an inclination of 3.°394 to the ecliptic plane. The orbit of Mars possesses an eccentricity of 0.09337 and an inclination of 1.°850; the argument of perigee is

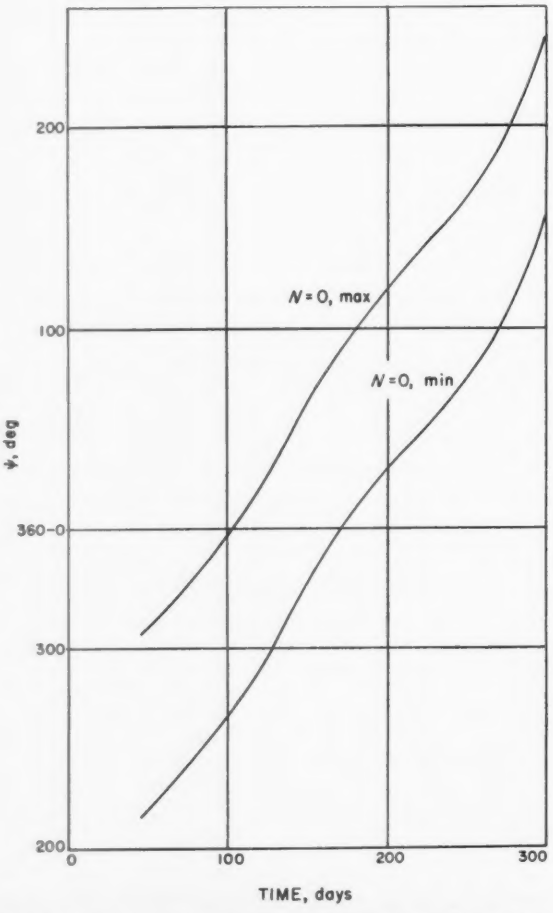

Fig. 9 Venus three-dimensional rendezvous trajectories, variation of positions of extremal points with flight time

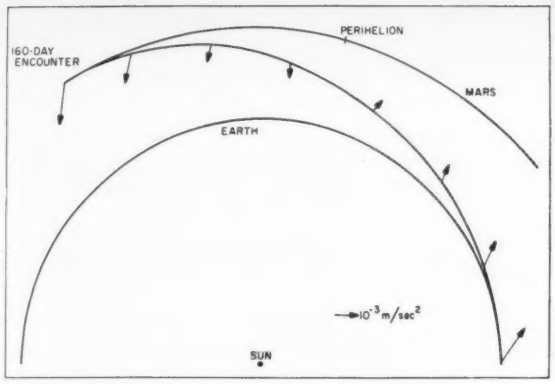

Fig. 10 Mars three-dimensional optimum rendezvous trajectory, ecliptic projection

$-73.°93$. The planets themselves were assumed massless, and only the mass of the sun was used in the calculations.

Fig. 3 illustrates an ecliptic projection of an interplanetary trajectory which will rendezvous Venus in 120 days. The terminal conditions in combination V were used. The arrows represent the ecliptic projection of **a** at various points along the trajectory. Fig. 4 shows the variation of celestial latitude of the vehicle along this trajectory; the thrust program is presented in Fig. 5. The rendezvous of this particular trajectory is at the optimum point on Venus's orbit, which for this flight time is $\phi = -3.°189$ on the ascending branch. Because of symmetry, the point $\phi = +3.°189$ on the descending branch is also optimum. Fig. 6 exhibits the variation in the value of $\int_0^{t_1} a^2 dt$ and the transversality quantity $N(t_1)$, with rendezvous at different points along the orbit of Venus. $M(t_1)$ is zero at all rendezvous points in the case of Venus because of the circular terminal orbit. For this case the terminal conditions are given by combination V with condition 6 replaced by ψ_s. It is observed that the zero crossings of N mark the minimum and maximum values of $\int_0^{t_1} a^2 dt$ with respect to ψ. The amplitude of the variation is only a small percentage of the average value.

The iterative routine mentioned above was used to generate a series of two- and three-dimensional Venus trajectories for a wide range of flight times. Fig. 7 shows the variation in $\int_0^{t_1} a^2 dt$ for a two-dimensional model. The effect of the third dimension due to the inclination of Venus's orbit is exhibited by Fig. 8, in which the increment in $\int_0^{t_1} a^2 dt$ over the two-dimensional value has been plotted. Both the upper and lower bounds of this increment are included. The variation in ψ for both of these cases is shown in Fig. 9.

In ballistic interplanetary trajectories where velocity impulses are made at the terminal points, it is known that the effects of planetary inclinations on the required velocity increment to perform a mission can be quite severe. It will be observed, however, that this is not the case for advanced propulsion trajectories in which thrust is applied over an extended range. The reason for the comparatively slight effects of inclination is partly due to the small planetary inclinations involved and the relative efficiency with which the advanced system is capable of generating these required inclinations at the terminal point.

Orbital eccentricity has a considerably more prominent effect on $\int_0^{t_1} a^2 dt$, particularly for nearby planets such as Mercury and Mars. As a second example, a similar series of

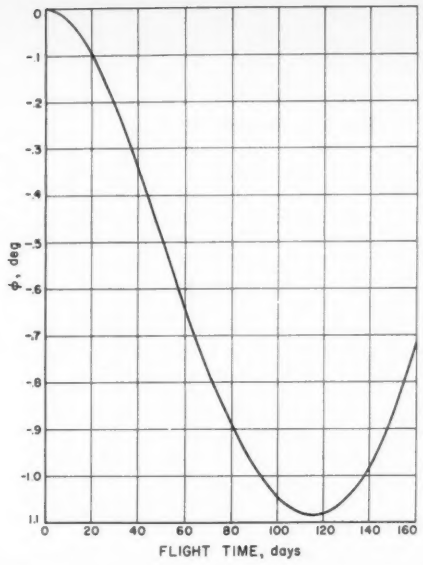

Fig. 11 Mars three-dimensional optimum rendezvous trajectory, celestial latitude

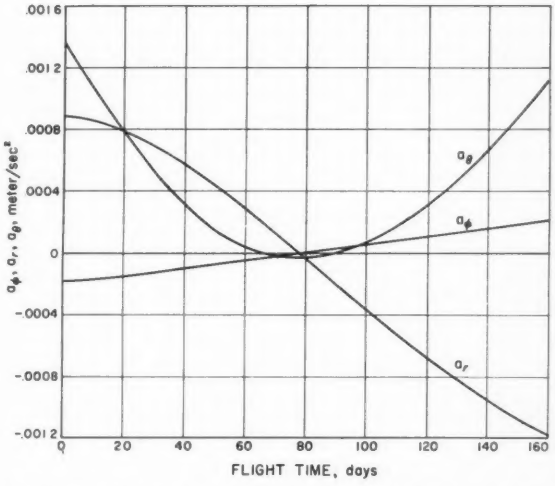

Fig. 12 Mars three-dimensional optimum rendezvous trajectory, thrust program

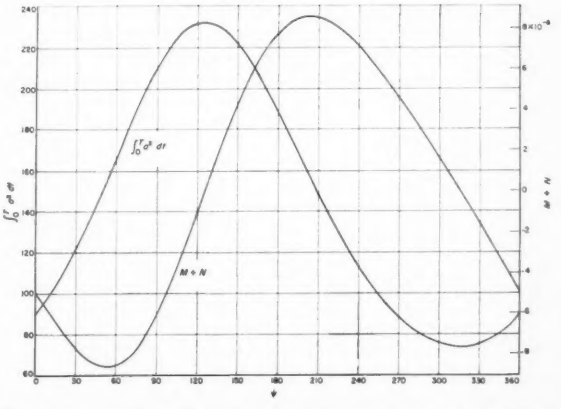

Fig. 13 Mars three-dimensional rendezvous trajectories, 90-day flight time

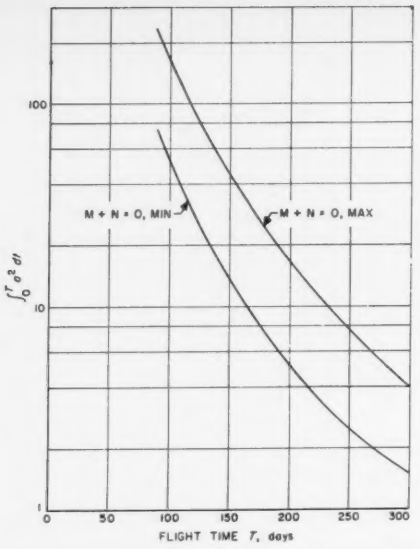

Fig. 14 Mars three-dimensional trajectories, rendezvous at extremal points

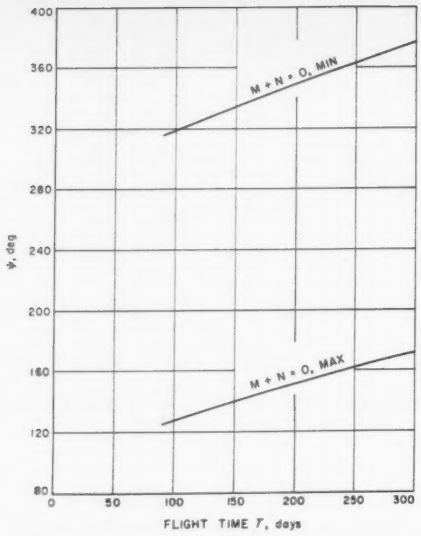

Fig. 15 Mars three-dimensional rendezvous trajectories, variations of positions of extremal points with flight time

results for rendezvous trajectories to Mars is presented. Figs. 10, 11, and 12 exhibit the characteristics of a 160-day trajectory which, for this flight time, will rendezvous at the optimum point on the orbit of Mars. The terminal conditions in combination III were used. Fig. 13 shows the effect of orbital eccentricity for a set of 90-day rendezvous trajectories to Mars. The magnitude of the variation of $\int_0^{t_1} a^2 dt$ with ψ is about 50% of the average value. The transversality expression $M(t_1) + N(t_1)$ is included, and its zero crossings coincide with the maximum and the minimum values of $\int_0^{t_1} a^2 dt$ with respect to ψ.

Fig. 14 shows the variation of $\int_0^{t_1} a^2 dt$ with flight time for both extremal points. The variation of these extremal points with flight time is shown in Fig. 15. As in the case of Venus, the effect of the inclination of the orbit of Mars is quite small. The contribution of inclination to the variation, $\int_0^{t_1} a^2 dt$ in Fig. 13, is less than 1% of the mean value. This was confirmed by a comparison with an analogous set of two-dimensional trajectories.

For interplanetary mission studies with advanced propulsion systems, it appears that planetary inclinations are negligible in payload capability studies. Even for the planet Mercury, with its 7° inclination, the effect is small. On the other hand, the effect of orbital eccentricities warrants the use of the appropriate eccentric orbits for Mercury and Mars. In (2) a comparison of results obtained from using both circular and eccentric terminal orbits will be found.

Acknowledgment

The author wishes to express his sincere appreciation to D. E. Richardson (JPL), who collaborated in the development of the computer program for these calculations, and to G. C. Sauer (JPL), who made valuable contributions to discussions concerning the analysis.

This paper presents the results of one phase of research carried out at the Jet Propulsion Laboratory, California Institute of Technology, under Contract No. NASw-6, sponsored by NASA.

References

1 Irving, J., *Space Technology*, John Wiley and Sons Inc., New York, 1959, Chap. 10.

2 Melbourne, W. G., "Interplanetary Trajectories and Payload Capabilities of Advanced Propulsion Vehicles," *Tech. Rep. no. 32-68*, Jet Propulsion Laboratory, Pasadena, Calif., 1961.

3 Melbourne, W. G. and Sauer, C. G., Jr., "Optimum Thrust Programs for Power-Limited Propulsion Systems," *Tech. Rep. no. 32-118*, Jet Propulsion Laboratory, Pasadena, Calif., 1961.

Preliminary Orbit Determination of a Nontransmitting Satellite Using the DOPLOC Tracking System[1]

PAUL B. RICHARDS[2]

General Electric Co.
Missile and Space Vehicle Dept.
Valley Forge Space
Technology Center
King of Prussia, Pa.

A method is presented for predicting a preliminary orbit of a passive (nontransmitting) satellite, using tracking data collected during one passage of the satellite by a tracking system consisting of only one transmitter and one receiver of the DOPLOC network. Equations are derived which relate passive satellite Doppler tracking data to range, speed, and time parameters at closest approach. These determine an ellipsoid whose foci are the transmitter and receiver stations. The satellite lies on this ellipsoid, and its trajectory is tangent to the surface. This ellipsoid can be completely determined without using any angle information. The satellite position and velocity components at closest approach are then calculated on a digital computer using Doppler and limited angle information provided by the DOPLOC tracking system. Preliminary orbits determined in this way agree favorably with the refined orbits of Ballistic Research Laboratories and Space Track.

THE EQUATION that describes the Doppler shift of radio signals transmitted from a station on Earth, reflected from the passive (nontransmitting) satellite, and received at another station on Earth is

$$\dot{\rho}_T + \dot{\rho}_R = (c/f_T)(f_T - f_R)$$

where

$\dot{\rho}_T$, $\dot{\rho}_R$ = range rates of the satellite relative to the transmitter and receiver stations, respectively
f_T, f_R = transmitter and receiver frequencies, respectively
c = speed of light

A typical continuous Doppler curve is shown in Fig. 1.

The measured Doppler data ($f_T - f_R$) is related to the solution $x(t_0)$, $y(t_0)$, $z(t_0)$, $\dot{x}(t_0)$, $\dot{y}(t_0)$, $\dot{z}(t_0)$ of the orbit determination problem by the expressions relating the time-dependent range rates to the time-dependent solution $x(t)$, $y(t)$, $z(t)$, $\dot{x}(t)$, $\dot{y}(t)$, $\dot{z}(t)$ of the equation of motion of the satellite, $\ddot{\mathbf{r}} + \mu \mathbf{r}/r^3 = 0$, since the solution of the equation of motion is unique, corresponding to a particular set of initial conditions $x(t_0)$, $y(t_0)$, $z(t_0)$, $\dot{x}(t_0)$, $\dot{y}(t_0)$, $\dot{z}(t_0)$. The desired expression for $\dot{\rho}_T$ is

$$\dot{\rho}_T(t) = \frac{[x(t) - X_T(t)][\dot{x}(t) - \dot{X}_T(t)] + [y(t) - Y_T(t)][\dot{y}(t) - \dot{Y}_T(t)] + [z(t) - Z_T(t)][\dot{z}(t) - \dot{Z}_T(t)]}{\{[x(t) - X_T(t)]^2 + [y(t) - Y_T(t)]^2 + [z(t) - Z_T(t)]^2\}^{1/2}}$$

where

X_T, Y_T, Z_T = position components of transmitter
$\dot{X}_T$, $\dot{Y}_T$, $\dot{Z}_T$ = velocity components of transmitter

In the same manner $\dot{\rho}_R(t)$ may be derived.

Having obtained Doppler data from one or more transmitter-receiver stations, the procedure for arriving at a solution to the orbit determination problem is as follows:

1 Select preliminary values of the initial conditions $x(t_0)$, $y(t_0)$, $z(t_0)$, $\dot{x}(t_0)$, $\dot{y}(t_0)$, $\dot{z}(t_0)$, i.e., establish a preliminary orbit.

2 Solve the equation of motion for the time-dependent position and velocity components.

3 Compute values of $\dot{\rho}_T + \dot{\rho}_R$ for each transmitter-receiver pair at times corresponding to measured Doppler data.

4 Compare computed values of $\dot{\rho}_T + \dot{\rho}_R$ with data.

5 Select an improved set of initial conditions and repeat the process until the computed values agree with the data. Items 2 through 5 constitute the determination of the refined or final orbit.

The Ballistic Research Laboratories has a numerical technique (1)[3] for establishing the final orbit that will converge using information provided by one transmitter and one receiver of the ARPA-BRL DOPLOC[4] system, provided the preliminary values of the initial conditions are sufficiently accurate.

Doppler tracking of active (transmitting) satellites has

Received March 15, 1961.
[1] Research performed under the auspices of the Ballistic Research Laboratories, Aberdeen Proving Ground, Md., Contract No. DA-36-034-509-ORD-3159-RD.
[2] Consultant Mathematician.

[3] Numbers in parentheses indicate References at end of paper.
[4] The word DOPLOC is a combination of the first three letters of Doppler and lock and implies a phase-locked Doppler measuring system. The DOPLOC system is described in detail in (1).

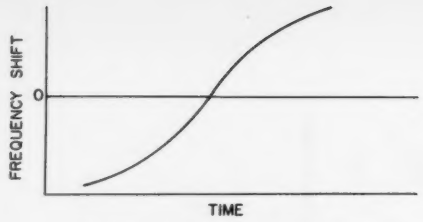

Fig. 1 Continuous Doppler curve

received considerable attention (2–7), but little has been found in the literature regarding the problem of establishing preliminary orbits.

The object of the present paper is to show that it is possible to determine a preliminary orbit of a passive satellite during a single pass of the vehicle, using the combination of Doppler data and limited angle information provided by one transmitter and one receiver of the DOPLOC system. The method is formulated in this report and applied to actual DOPLOC data.

The angle information supplied by the DOPLOC system consists not of actual measured angles, but of computed angles based on the geometry of the DOPLOC transmitter beams, which are so oriented that data are recorded only during three widely separated time intervals. For low satellites, these intervals can be as short as 5 sec.

Parametric Representation of Doppler Curve

Integration of the Doppler equation for a single transmitter-receiver pair

$$\dot{\rho}_T + \dot{\rho}_R = \lambda_T \Delta f \qquad [1]$$

where

$$\lambda_T = c/f_T$$
$$\Delta f = f_T - f_R$$

yields

$$\rho_T + \rho_R = \int_{t_0}^{t} \lambda_T \Delta f \, dt + (\rho_T + \rho_R)_{t_0} = 2a(t) \qquad [2]$$

which indicates that at a given time t the satellite lies on an ellipsoid of semimajor axis $a(t)$ with foci at T and R, the sites of the transmitter and receiver. Since T and R are known locations, the eccentricity of the ellipsoid is obtained from the expression $ae = \overline{TR}/2$. Thus the ellipsoid is completely determined once the constant of integration $(\varrho_T + \rho_R)_{t_0}$ is known. This is determined in the following manner: The Doppler Eq. 1 may be written in vector form as

$$\varrho_T \cdot \dot{\varrho}_T/\rho_T + \varrho_R \cdot \dot{\varrho}_R/\rho_R = \lambda_T \Delta f \qquad [3]$$

In a geocentric inertial coordinate system, neglecting Earth's rotation[5] $\dot{\varrho}_T = \dot{\varrho}_R = \mathbf{v}$, where $\mathbf{v}$ is the satellite velocity, and Eq. 3 becomes

$$\mathbf{v} \cdot \left(\frac{\varrho_T}{\rho_T} + \frac{\varrho_R}{\rho_R} \right) = \lambda_T \Delta f \qquad [4]$$

Define the vector

$$\mathbf{p}(t) = \frac{1}{2} \left[\frac{\rho_T \rho_R}{1 - (\overline{TR}/[\rho_T + \rho_R])^2} \right]^{1/2} \left(\frac{\varrho_T}{\rho_T} + \frac{\varrho_R}{\rho_R} \right) \qquad [5]$$

[5] For a low Earth satellite, the error incurred by this assumption will be small.

Then

$$|\mathbf{p}(t)| = p(t) = (1/2)(\rho_T + \rho_R) \qquad [6]$$

and the Doppler Eq. 1 becomes

$$\dot{p}(t) = \lambda_T \Delta f/2 \qquad [7]$$

or

$$\mathbf{p} \cdot \dot{\mathbf{p}}/p = \lambda_T \Delta f/2 \qquad [8]$$

Define the time of closest approach as the time at which $\rho_T + \rho_R$ is minimum ($\Delta f = 0$), and let t_0 in Eq. 2 be this time. Then the constant of integration in Eq. 2 is the major axis of the smallest ellipsoid upon which the satellite will lie, the ellipsoid at closest approach. From Eqs. 2 and 6

$$p_0 = p(t_0) = (1/2)(\rho_T + \rho_R)_{t_0} = a(t_0)$$

Using zero subscripts to denote values at t_0, the time of closest approach, it follows from Eqs. 4, 5, and 8 that

$$\mathbf{v}_0 \perp \mathbf{p}_0 \qquad [9a]$$

$$\dot{\mathbf{p}}_0 \perp \mathbf{p}_0 \qquad [9b]$$

Further, the vector $\mathbf{p}(t)$ is perpendicular to the tangent plane of the ellipsoid at the location of the satellite. Hence, both vectors $\mathbf{v}_0$ and $\dot{\mathbf{p}}_0$ lie in the plane that is tangent to the ellipsoid at closest approach, at the location of the satellite.

Thus, the following conclusions have been established: at the time of closest approach t_0 the satellite lies on the surface of the ellipsoid of semimajor axis p_0, having foci at the transmitter T and receiver R; further, the satellite trajectory is tangent to this ellipsoid. The location of the satellite on this ellipsoid, together with its associated velocity and the time t_0, will determine a preliminary orbit of the satellite.

Now assume that $\ddot{\mathbf{p}}$ is constant[6] ($= \dot{\mathbf{p}}_0$) in the neighborhood of closest approach t_0. Then, in this neighborhood

$$\mathbf{p}(t) = \mathbf{p}_0 + \dot{\mathbf{p}}_0(t - t_0)$$

Then, using Eq. 9b

$$p^2(t) = p_0^2 + |\dot{\mathbf{p}}_0|^2(t - t_0)^2$$

and

$$\dot{p}(t) = \frac{|\dot{\mathbf{p}}_0|^2(t - t_0)}{[p_0^2 + |\dot{\mathbf{p}}_0|^2(t - t_0)^2]^{1/2}} \qquad [10]$$

Thus the parameters t_0, p_0, $|\dot{\mathbf{p}}_0|$ are related to the Doppler data Δf by Eqs. 10 and 7.

Before proceeding to determine p_0 and the satellite position and velocity components at t_0, an interpretation of $\mathbf{p}(t)$ is in order. This vector can be expressed in the form

$$\dot{\mathbf{p}}(t) = a\varrho_T + b\varrho_R + c\mathbf{v}$$

where a, b, c are time-dependent scalars, for the vectors ϱ_T, ϱ_R, $\mathbf{v}$ constitute a basis in three-dimensional space. The vector $\dot{\mathbf{p}}(t)$ may be interpreted as a fictitious velocity, for if the base of $\mathbf{p}(t)$ is held fixed at the origin of a three-dimensional vector space, the locus of the end point of $\mathbf{p}(t)$ will be a fictitious trajectory. The base of $\mathbf{p}_0$ is taken as origin of this vector space, i.e., $\mathbf{p}$ at closest approach. This point will be in plane of ϱ_T and ϱ_R on the normal to the actual trajectory at the point of the trajectory where $\rho_T + \rho_R$ is a minimum, and at a distance along this normal equal to $\frac{1}{2}$ this minimum value of $\rho_T + \rho_R$. In the vector space there will be a sphere of radius $p_0 = (1/2)(\rho_T + \rho_R)_{\min}$ such that the fictitious trajectory and the true trajectory are both

[6] This assumption implies that the Doppler curve has an inflection point at t_0, a characteristic observable in most Doppler data.

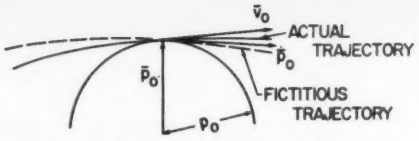

Fig. 2 Actual and fictitious trajectories

tangent to this sphere at the point of closest approach. Elsewhere both trajectories are exterior to the sphere (Fig. 2).

Determination of Closest Approach Ellipsoid and Time

The process of fitting Eq. 10 to the recorded Doppler data in order to determine t_0, p_0, $|\dot{\mathbf{p}}_0|$ is complicated when these data are obtained by the DOPLOC system because of the DOPLOC transmitter beam geometry. These beams are so oriented that data are recorded only during three widely separated time intervals, which can be as short as 5 sec for low satellites.

A brief description of this system will illustrate the advantages and disadvantages of this geometry. The DOPLOC transmitter station, located at Fort Sill, Okla., consists of a 50-kw transmitter and three high gain antennas. All of the antennas can be excited separately from the transmitter but not simultaneously. Each antenna is capable of radiating a thick fan-shaped beam having dimensions of approximately 8×76 deg. The beam from the center antenna is directed vertically with the 76° dimension in the direction of the receiver. The north and south antennas are identical to the center antenna except that they are tilted to radiate fan-shaped beams 20° above the north and south horizons respectively. This arrangement of beams is intended to detect a satellite as it rises over the horizon, track through the beam width, switch to the center antenna, track through its beam, and then switch to the third antenna to obtain three segments of data from the characteristic S-curve.

The DOPLOC system has two receiving stations, one at the White Sands Missile Range and the other at Forrest City, Ark. Both stations lie on the great circle that passes through the transmitter station.

At each receiving station three high gain antennas, which are identical to the transmitting antennas except in power handling capability, are tilted to see the same volumetric space that is illuminated by the transmitting antennas. The receiving antennas are switched synchronously with the transmitting antennas.

In the following analysis, only one transmitter-receiver pair will be considered. Without loss of generality, the technique for the transmitter at Fort Sill, Okla. and the receiver at Forrest City, Ark. will be described. These stations are separated by a base line of 435 statute miles and, of course, are the foci of the ellipsoid of closest approach for each satellite observed.

A typical DOPLOC data plot for this transmitter-receiver pair is shown in Fig. 3. Here the time of closest approach occurs while the satellite is in the center beam, which means that the satellite lies on the associated ellipsoid of closest approach in the strip intersected by the center beam of the transmitter. In all cases, the ellipsoid of closest approach associated with a particular transmitter-receiver pair will be intersected by the three transmitter beams, and at time of closest approach, the location of the satellite relative to these beams gives a good indication of where the satellite lies on the ellipsoid. Further, the time of appearance in the beams indicates the general direction of the satellite. For example,

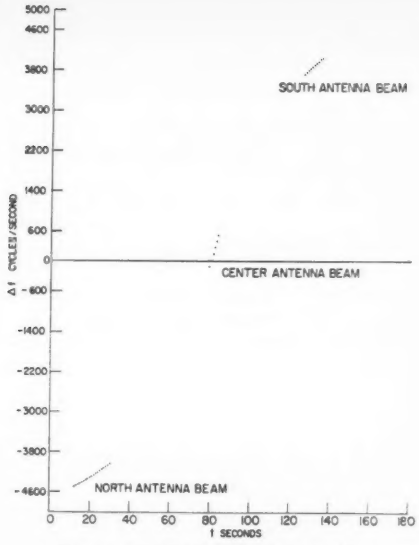

Fig. 3 Typical DOPLOC data plot

the satellite of Fig. 3 is clearly going south as it passes over the stations. This information can be expressed analytically, in a form easily programmed for a digital computer, in order to calculate the approximate position and velocity components of the satellite at the time of closest approach.

Before this can be done, however, the ellipsoid at closest approach must be determined by fitting Eq. 10 to the DOPLOC data in the neighborhood of closest approach, where data are very meager (Fig. 3). Further, the data appear to be nearly linear in this neighborhood. Therefore, if the nonlinear expression, Eq. 10, is fitted directly to the recorded data in this center interval, the parameters so determined will be inaccurate. This was verified by actual computation.

Details of different techniques that were attempted are described elsewhere (8). Here the procedure that proved most successful will be outlined.

1 First determine t_0 by fitting the cubic in t

$$\dot{p} = A + Bt + Ct^2 + Dt^3 \qquad [11]$$

to the measured data in the neighborhood of t_0, with the time origin for t fairly close to t_0 so that roundoff errors will not be significant. Once the coefficients are determined, t_0 is computed as the single root of the equation $\dot{p} = 0$ that lies in this neighborhood. The cubic was used because it was found that accuracy in t_0 improved as the degree of the approximating polynomial increased from one to three, and remained unchanged thereafter.

2 Using t_0, fit the cubic

$$\dot{p} = \alpha\tau + \beta\tau^2 + \gamma\tau \qquad \tau = t - t_0 \qquad [12]$$

to all the recorded data.

3 After writing Eq. 10 as

$$\tau^2/\dot{p}^2 = a + b\tau^2 \qquad [13]$$

where

$$a = p_0^2/|\dot{\mathbf{p}}_0|^4$$
$$b = 1/|\dot{\mathbf{p}}_0|^2$$
$$\tau = t - t_0$$

a linear expression in a and b, determine a, b, and p_0 by fitting Eq. 13 to values of $\dot{p}$ given by Eq. 12 over a sufficiently large

Table 1 Discoverer XI oribital elements

Rev. no. 30, April 17, 1960

	a	e	$M(t)$, t = 18:39:21.5	i	Ω	ω
General Electric Co. (preliminary orbit)	4090 mile	0.0106	342.48°	76.41°	217.7°	144.18
Ballistic Research Laboratories (final solution)	4186 mile	0.0295	345.23°	80.15°	215.93°	154.97°
Space Track (final solution)	4188 mile	0.0291	—	80.01°	215.84°	146.28°

Rev. no. 172, April 26, 1960

	a	e	$M(t)$ t = 16:53:58	i	Ω	ω
General Electric Co. (preliminary orbit)	4045 mile	0.0147	41.21°	74.5°	204.8°	59.31°
Ballistic Research Laboratories (final solution)	4093 mile	0.0189	43.01°	80.44°	203.18°	96.08°
Space Track (final solution)	4090 mile	0.0111	—	80.10°	202.84°	114.23°

neighborhood of t_0. The interval $t_0 \pm 30\%$ of the time interval between t_0 and the side beams has been found adequate.

Determination of Position and Velocity at Closest Approach

Once p_0 is determined, the ellipsoid at the time of closest approach is known, since the eccentricity is $e = \overline{TR}/2p_0$, where $\overline{TR}$ is the length of the base line between the transmitter and receiver, the foci of the ellipsoid. It remains now to determine the location of the satellite on this ellipsoid, as well as its velocity components. To do this, the transmitter beam geometry described in the preceding section is used.

At the time of closest approach, a horizontal plane at the altitude h of the satellite above the transmitter will intersect the transmitter beams, as shown in Fig. 4. If it is assumed that the satellite remains in this plane during its flight through the three beams and that its speed v is that corresponding to a circular orbit at this altitude h, then the satellite path length Δs between the center and north beams is given by

$$\Delta s = v\Delta t \qquad [14]$$

where Δt is the time interval corresponding to the gap in the data between the center and north beams. The acute angle θ between the path and the vertical plane of the transmitter center beam is obtained from

$$\Delta s = \Delta N/\sin\theta \qquad 0 < \theta \leq \pi/2 \qquad [15]$$

where ΔN is the perpendicular distance between these beams at the given altitude h.

It will be convenient to use a topocentric coordinate system, originating at T and having an x-axis vertical, a z-axis in the horizontal plane at the elevation of the transmitter and in the direction of the ellipsoid base line TR extended westward, and a y-axis in the same horizontal plane and normal to TR (Fig. 4).

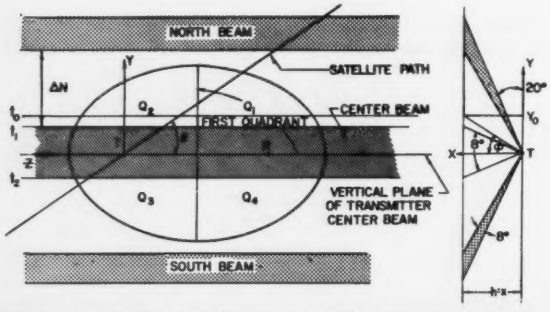

Fig. 4 Orientation of ellipsoid and DOPLOC antenna beams

Then, corresponding to a given altitude h (or x), Eqs. 14 and 15 give

$$\sin\theta = A\,x\sqrt{r+x}/\Delta t\sqrt{k^2M}$$

where

A = cot 28° − tan 4°
r = radius of Earth at transmitter
k^2 = Newton's gravitational constant
M = mass of Earth

Clearly the altitude x of the satellite will be restricted by the upper bound of sin θ. This restriction can be seen intuitively: the higher the satellite, the greater must be its speed to traverse the wider distance between beams in the fixed time interval; on the other hand, the speed in a circular orbit reduces with increased altitude. There will thus be an upper bound on permissible altitudes.

In the horizontal plane at some altitude x, the satellite will lie on the ellipse

$$\frac{(z+ae)^2}{(a^2/b^2)(b^2-x^2)} + \frac{y^2}{b^2-x^2} = 1$$

where a, b are the semimajor axis p_0 and semiminor axis respectively of the ellipsoid at closest approach. Since the satellite path is tangent to this ellipse at the location of the satellite, this point is to be determined from the expressions

$$y^2 = \frac{(b^2/a^2)(b^2-x^2)}{(b^2/a^2)+\tan^2\theta}$$

$$(z+ae)^2 = \frac{(a^2/b^2)(b^2-x^2)\tan^2\theta}{(b^2/a^2)+\tan^2\theta}$$

The velocity components of the satellite are to be determined from the expressions

$$\dot{x} = 0$$
$$\dot{y}^2 = v^2\sin^2\theta$$
$$\dot{z}^2 = v^2\cos^2\theta$$

where

$$v^2 = k^2M/(r+x)$$

A given value of θ will determine four possible points on the ellipse, one in each quadrant. A unique velocity is associated with each pair of opposing quadrants. The sign of $\dot{y}$ is determined from the data by observing which beam the satellite crosses first; hence the sign of $\dot{z}$ is known for each point.

There is still the problem of selecting the correct altitude

x and the correct point (y, z) at this altitude out of four possible values of (y, z). It has been shown that the possible values of x are already restricted by the upper bound of sin θ. For a chosen x, the four possible values of (y, z) just defined are not all acceptable. The data tell where the satellite is at t_0 relative to the center beam. That is, the satellite is either in the beam or on one side of it and proceeding toward it or away from it. This information, expressed analytically, imposes severe restrictions on the possible values of (y, z) that are to be accepted.

Denote by t_1 and t_2 the times at which the satellite crosses the edges of the center beam (Fig. 4). The distance travelled by the satellite along its path in the horizontal plane at altitude x between the time of closest approach t_0 and the time it crosses the vertical plane xz is given by

$$\Delta s = v|(t_1 + t_2)/2 - t_0|$$

Then, for the case where $\dot{y} > 0$ (satellite travelling north), the y coordinate of the satellite at t_0 is given by

$$y_0 = v \sin \theta(t_0 - [t_1 + t_2]/2)$$

and for $\dot{y} < 0$ (satellite moving south), the y coordinate at t_0 is given by

$$y_0 = v \sin \theta([t_1 + t_2]/2 - t_0)$$

The appropriate formula can be used as a criterion for selection of permissible points (y, z) at a given altitude x, from the four points previously computed. To allow for possible inaccuracy in the precise location of the satellite at times t_1, t_2, and t_0, values of the y coordinate that lie in the range $y_0 - \epsilon < y < y_0 + \epsilon$, $\epsilon > 0$ can be accepted. To select this range, define the angle ϕ in the xy plane by the relation

$$\tan \phi = y_0/x$$

Then, assigning the small angle $\Delta\phi > 0$, the x, y, z coordinates of the satellite must satisfy the inequality

$$\tan (\phi - \Delta\phi) < y/x < \tan (\phi + \Delta\phi)$$

Application to DOPLOC Field Data

Using the methods just described, preliminary orbits were established for two revolutions of the Discoverer XI satellite. The data were obtained from the ARPA-BRL DOPLOC system, using the transmitter at Fort Sill, Okla. and the receiver at Forrest City, Ark.

The preliminary orbits obtained, expressed in terms of the usual orbital elements, are compared in Table 1 with the final solutions obtained by BRL and NSSCC (Space Track).[7] BRL uses an analog procedure to determine a preliminary orbit from the DOPLOC data, whereas at Space Track all available data are compiled over a period of time to compute the orbit.

References

1 Patton, R. B., Jr. and Richard, V. W., "Determination of Orbital Elements and Refraction Effects from Single Pass Doppler Observations," Committee on Space Research Meeting and Symposium, Florence, Italy, April 1961.

2 Guier, W. H. and Weiffenbach, G. C., "Theoretical Analysis of Doppler Radio Signals from Earth Satellites," John Hopkins Univ., Applied Physics Lab., *Bumblebee Series Rep. No. 276*, April 1958.

3 Skinner, T., "Tracking of a Moving Transmitter by the Doppler Effect," *AFCRC-TR-58-364*, (*ASTIA Document AD208699*), December 1958.

4 Kotelnikov, V. A., "Determination of the Elements of the Orbit of a Satellite Using Doppler Effect," translated from *Radiotekhnika Elektrickestvo*, vol. 7, pp. 875–881, 1958; reproduced by the National Academy of Sciences.

5 Burt, E. G. C., "The Computation of Orbit Parameters from Interferometer and Doppler Data," *Proc. of the Royal Society*, Series A, Vol. 248, Oct. 28, 1958.

6 Newton, R. R., "Tracking Objects within the Solar System Using Only Doppler Measurements," *Proc. 10th Internatl. Astronaut. Congress*, Vol. 1, 1959.

7 Carrara, N., Checcacci, P. F. and Ronchi, L., "Sulla Determinazione della Traiettoria dei Satelliti Artificiali," *La Ricerca Scientifica*, Anno 28, N. 7, July 1958.

8 Richards, P. B., "Orbit Determination of a Non-Transmitting Satellite using Doppler Tracking Data," Shepherd Program, *ARPA Order 8-58*, BRL DOPLOC Satellite Fence Series, *Rep. No. 12*, October 1960.

[7] Space Track results were furnished to the author by BRL.

Attenuated Intercept Satellite Rendezvous System

M. SHAPIRO[1]

Applied Research and Development
Republic Aviation Corp.
Farmingdale, N. Y.

An automatic terminal guidance logic is presented for rendezvous of two space vehicles in orbit. Specifically, that phase between terminal acquisition and final docking is treated. The system, termed *attenuated intercept*, initiates an intercept orbit that is successively softened by dilating the time to intercept. This leads to a succession of revised intercept commands which, in the limit, results in zero relative velocity at intercept. The characteristics of this system have been evaluated by means of analog computer simulations for noncoplanar elliptic relative orbits. Propellant consumption comparisons between this system and optimum impulsive transfers are made. Attitude rates of 2 deg/sec consistent with single engine operation are found adequate for system implementation. The ability of the system to accommodate a wide range of thrust levels is demonstrated. Multiple start nonthrottleable engines appear adequate for the task.

Presented at the ARS-IAS Joint Meeting, Los Angeles, Calif., June 13–16, 1961.

[1] Specialist Research Engineer.

AUTOMATIC terminal rendezvous systems can be categorized under three broad headings: 1) proportional navigation; 2) Keplerian transfer; and 3) combinations of 1 and 2. System 1 has received attention by numerous investigators (1–6).[2] System commands are based on either suppressing or maintaining constant sensor look angle rates of change between the ferry and target vehicles. Additional range and range rate commands control relative acceleration along the line of sight. The fundamental advantage of this system is the ability to force rendezvous when target orbital characteristics are unknown. Propellant requirements for such a terminal maneuver are relatively large.

Guidance logic using impulsive Keplerian orbit transfers are treated in (7–11) and can result in a minimization of the number of thrust pulses and propellant payload. Target and ferry orbital characteristics must be accurately known—the former possibly from ground tracking, the latter from integrating accelerometers or from radar range and range rate data aboard the ferry. However, errors result because of equipment limitations. These errors distort the terminal transfer orbit and, if uncorrected, will prevent rendezvous. An additional computation scheme that supplies corrective thrust pulses is needed. Thus, steering equation complexities increase.

Modification of the above transfer schemes usually leads to some sort of combination transfer line of sight system. One such system successfully employed as part of the subject study is termed *attenuated intercept*. Control equations are based on differences between a desired and actual ferry orbit intercept path relative to a target in a circular orbit (12, 13). Rendezvous rather than intercept occurs, however, because of dilating the time scale. It is demonstrated that rendezvous is insured even for elliptic target orbits. This scheme is attractive because the control equations are relatively simple and depend only on an accurate estimate of the target period rather than on a complete set of orbital elements.

Analog Computer Equations: Relative Motion Synthesis

Equations of relative motion between a ferry vehicle and its objective were simulated on an analog computer and are given below. The rectangular triad is target-centered, wherein Z denotes the local vertical, X the local horizon, and $\overline{Y} = \overline{X} \times \overline{Z}$ (see Fig. 1).

$$\ddot{\rho} = \frac{H^2}{\rho^3} - \frac{K^2M}{\rho^2} \qquad [1a]$$

$$\overline{H} = \text{const} = \overline{\rho} \times \overline{V} \qquad [1b]$$

$$\ddot{X} = \frac{T_X}{m} + \frac{XH^2}{\rho^4} - \frac{2\dot{Z}H}{\rho^2} + \frac{2Z\dot{\rho}H}{\rho^3} - \frac{K^2MX}{r^3} \qquad [2a]$$

$$\ddot{Y} = \frac{T_Y}{m} - \frac{K^2MY}{r^3} \qquad [2b]$$

$$\ddot{Z} = \frac{T_Z}{m} + \frac{ZH^2}{\rho^4} + \frac{2\dot{X}H}{\rho^2} - \frac{2X\dot{\rho}H}{\rho^3} + K^2M\left[\frac{(\rho - Z)}{r^3} - \frac{1}{\rho^2}\right] \qquad [2c]$$

Expanding the gravitational accelerations and deleting third-order terms gives

$$\frac{X}{r^3} \cong \frac{X}{\rho^3} + \frac{3XZ}{\rho^4} \qquad [3a]$$

[2] Numbers in parentheses indicate References at end of paper.

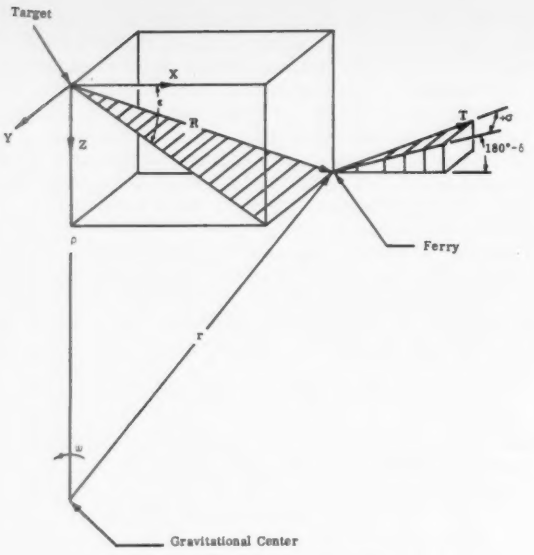

Fig. 1 Coordinate schematic

$$\frac{Y}{r^3} \cong \frac{Y}{\rho^3} + \frac{3YZ}{\rho^4} \qquad [3b]$$

$$\frac{\rho - Z}{r^3} - \frac{1}{\rho^2} \cong \frac{2Z}{\rho^3} - \frac{3X^2}{2\rho^4} + \frac{3Z^2}{\rho^4} - \frac{3Y^2}{2\rho^4} \qquad [3c]$$

Consider a target orbit whose semimajor axis and eccentricity are 5000 statute miles and 0.1, respectively. To compute ρ directly from Eq. 1 implies that less than 20% of the amplifier voltage is used, since ρ varies from 4500 to 5500 miles. Ensuing computer errors would therefore be larger than second-order gravitational accelerations. Maximum permissible simulator precision is maintained, however, by referring target radius variations to a base value of 5000 miles. Necessary manipulations relating $\Delta\rho$ to ρ are given below. Define

$$\rho = \Delta\rho + \frac{10^4}{2} \qquad [4]$$

$$\frac{1}{\rho} = \Delta\frac{1}{\rho} + \frac{2}{10^4} \qquad [5]$$

$$\frac{1}{\rho^2} = \Delta\frac{1}{\rho^2} + \frac{4}{10^8} \qquad [6]$$

$$\frac{1}{\rho^3} = \Delta\frac{1}{\rho^3} + \frac{8}{10^{12}} \qquad [7]$$

Target radius is eliminated by substituting Eq. 4 into Eq. 5, Eq. 5 into Eq. 6, and Eqs. 5 and 6 into Eq. 7. Now

$$\Delta\frac{1}{\rho} = -\frac{2}{10^4}\Delta\rho\left(\frac{2}{10^4} + \Delta\frac{1}{\rho}\right) \qquad [8a]$$

$$\Delta\frac{1}{\rho^2} = \Delta^2\frac{1}{\rho} + \frac{4}{10^4}\Delta\frac{1}{\rho} \qquad [8b]$$

$$\Delta\frac{1}{\rho^3} = \Delta\frac{1}{\rho}\left(\Delta\frac{1}{\rho^2} + \frac{4}{10^8}\right) + \frac{2}{10^4}\Delta\frac{1}{\rho^2} \qquad [8c]$$

$\dot{\delta}_{max}$ = ± 3 deg/sec

η = ± 14 deg

a_T = 4500 Miles

e_T = 0

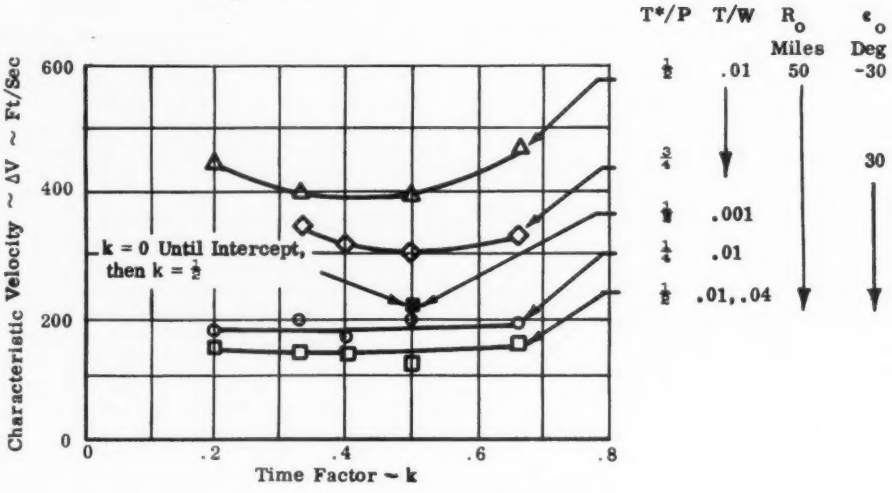

Fig. 2a Dependence of characteristic velocity on k and T^*

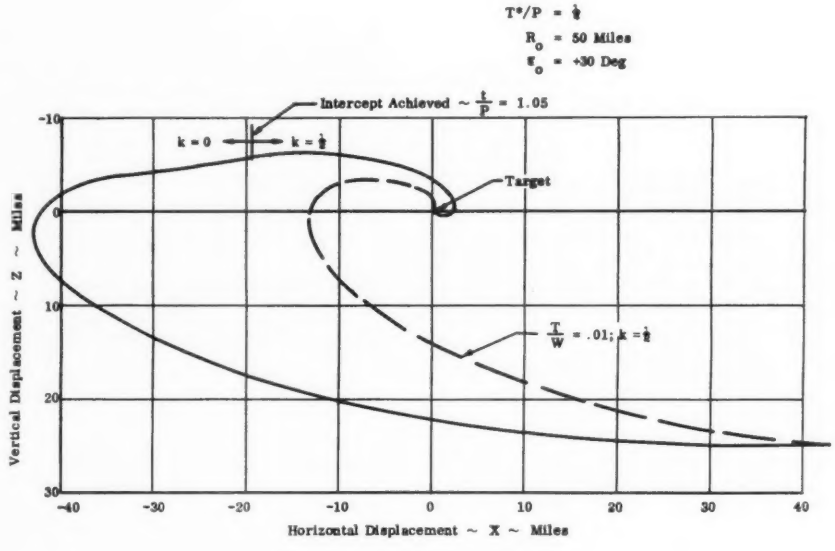

Fig. 2b Trajectory comparison

Substituting Eqs. 6 and 7 into Eq. 1 completes the amplifier equation for target radius variations, since $\Delta(1/\rho^3)$ and $\Delta(1/\rho^2)$ are given by Eqs. 8.

$$\ddot{\rho} = H^2\left(\Delta\frac{1}{\rho^3} + \frac{8}{10^{12}}\right) - K^2M\left(\Delta\frac{1}{\rho^2} + \frac{4}{10^8}\right) \qquad [9]$$

Employing the preceeding difference method, the horizontal acceleration becomes

$$\ddot{X} = \rho^2\left(\ddot{X} - \frac{T_X}{m}\right)\Delta\frac{1}{\rho^2} + \frac{4}{10^8}\rho^2\left(\ddot{X} - \frac{T_X}{m}\right) + \frac{T_X}{m} \qquad [10]$$

where

$$\rho^2\left(\ddot{X} - \frac{T_X}{m}\right) = \frac{XH^2}{\rho^2} - 2\dot{Z}H + \frac{2Z\dot{\rho}H}{\rho} - \frac{K^2MX}{\rho} - \frac{3K^2MXZ}{\rho^2}$$

and

$$\frac{X}{\rho} = X\left(\Delta\frac{1}{\rho} + \frac{2}{10^4}\right) \qquad [11a]$$

$$\frac{X}{\rho^2} = X\left(\Delta\frac{1}{\rho^2} + \frac{4}{10^8}\right) \quad [11b]$$

$$\frac{Z}{\rho} = Z\left(\Delta\frac{1}{\rho} + \frac{2}{10^4}\right) \quad [11c]$$

A similar technique yields Y and Z.

Under the premise of single engine operation, thrust allocations along each reference axis become.

$$\frac{T_X}{m} = -\frac{T}{m}\cos\sigma\cos\delta \quad [12a]$$

$$\frac{T_Y}{m} = -\frac{T}{m}\sin\sigma \quad [12b]$$

$$\frac{T_Z}{m} = -\frac{T}{m}\cos\sigma\sin\delta \quad [12c]$$

Angle δ is the angle between the local target horizon and the thrust vector projection onto the target plane. Angle σ is the out of plane angle described by the thrust vector and is restricted to $\pm 90°$ rotations.

Control System Equations

Intercept Attenuation

Homing guidance rendezvous schemes are based on error signals generated by comparing parameter differences between a desired trajectory and an actual trajectory. A rendezvous path is ultimately forced by translating these error signals into vehicle orientation and thrust firing commands. Desired trajectory velocities computed herein are based on the following equations wherein the coordinate system is target centered:

$$\dot{X}_D = \frac{(6Z\omega\tau - X)\sin\omega\tau - 14Z(1-\cos\omega\tau)}{8(1-\cos\omega\tau) - 3\omega\tau\sin\omega\tau}\cdot\omega \quad [13a]$$

$$\dot{Z}_D = \frac{Z(3\omega\tau\cos\omega\tau - 4\sin\omega\tau) + 2X(1-\cos\omega\tau)}{8(1-\cos\omega\tau) - 3\omega\tau\sin\omega\tau}\cdot\omega \quad [13b]$$

This set, derived in (12), defines approximate coplanar impulsive transfer requirements necessary to achieve an intercept path between a ferry vehicle in any initial orbit and a target vehicle in a circular orbit. Eqs. 13 are approximate since, in the derivation, the relative gravitational acceleration had been linearized. Relative motion discrepancies must therefore exist and, if uncorrected, will increase with intercept time and/or initial separation distance (7).

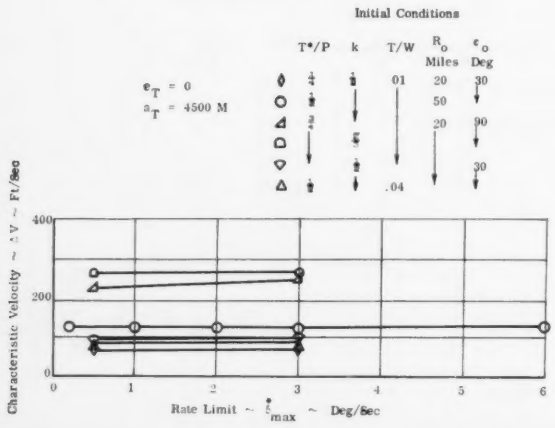

Fig. 3 Dependence of characteristic velocity on attitude response

Let the ferry velocity at maneuver initiation be $\dot{X}_D$ and $\dot{Z}_D$. On this basis intercept will occur τ seconds later. However, intercept is nothing more than a hard rendezvous, and, consequently, Eqs. 13 must be modified to soften the intercept. Barring an impulsive correction prior to collision, this softening may be induced as follows. Assume initially that the target is at a higher energy level than the ferry. Eqs. 13 will demand an increase in ferry velocity to produce intercept path 1. After some elapsed time along path 1, let a new transfer be made based on an extended intercept time. Accordingly, control Eqs. 13 will command a new trajectory formed essentially by retroaction. Subsequent velocity additions will generally be less than those required for preceeding intercept paths. As shown later, extending this process to the limit forces both vehicles on identical orbits with identical epochs. Thus, in principle, by modifying intercept time a series of orbit transfers is achieved which tends to moderate the initial intercept and, in the limit, command rendezvous.

Maneuver time is modified by simply replacing τ by $T^* - kt$. Parameter T^* is a fictitious intercept time ($0 < T^* < P$), parameter k an appropriate time factor ($0 < k < 1$), and t is time elapsed since problem initiation. At each instant of real time, therefore, an intercept path is computed based on the original intercept time T^* minus some percentage of the actual time elapsed. Desired velocity magnitudes, associated with each new orbit computed, continually decrease because of the dilated time scale. The proof that desired velocities and corresponding distances are in fact zero when time approaches T^*/k follows. Since the area of concern is in the vicinity of T^*/k, replace $\sin\omega(T^* - kt)$ and $\cos\omega(T^* - kt)$ (Eqs. 13) by $\omega(T^* - kt)$ and $1 - \omega^2(T^* - kt)^2/2$. Then

$$\frac{\dot{X}}{\omega} = -\frac{X}{\omega(T^* - kt)} - Z \quad [14a]$$

$$\frac{\dot{Z}}{\omega} = -\frac{Z}{\omega(T^* - kt)} + X \quad [14b]$$

The general solution of Eqs. 14 is

$$X = \left[\omega(T^* - kt)\right]^{1/k}\left[A\sin\frac{\omega(T^* - kt)}{k} + B\cos\frac{\omega(T^* - kt)}{k}\right] \quad [15a]$$

$$Z = \left[\omega(T^* - kt)\right]^{1/k}\left[-B\sin\frac{\omega(T^* - kt)}{k} + A\cos\frac{\omega(T^* - kt)}{k}\right] \quad [15b]$$

A and B are arbitrary constants that depend on initial conditions. Again, within the rendezvous sphere of interest, these equations become

$$X = \omega^{1/k}(T^* - kt)^{1/k}\left(\frac{A\omega}{k}(T^* - kt) + B\left[1 - \left(\frac{\omega}{k}(T^* - kt)\right)^2/2\right]\right) \quad [16a]$$

$$Z = \omega^{1/k}(T^* + - kt)^{1/k}\left(-\frac{B\omega}{k}(T^* - kt) + A\left[1 - \left(\frac{\omega}{k}(T^* + kt)\right)^2/2\right]\right) \quad [16b]$$

$e_T = 0$
$a_T = 4500$ M
R = 50 M
$\epsilon = -30$ Deg
T/W = .01
T*/P = ½
k = ½

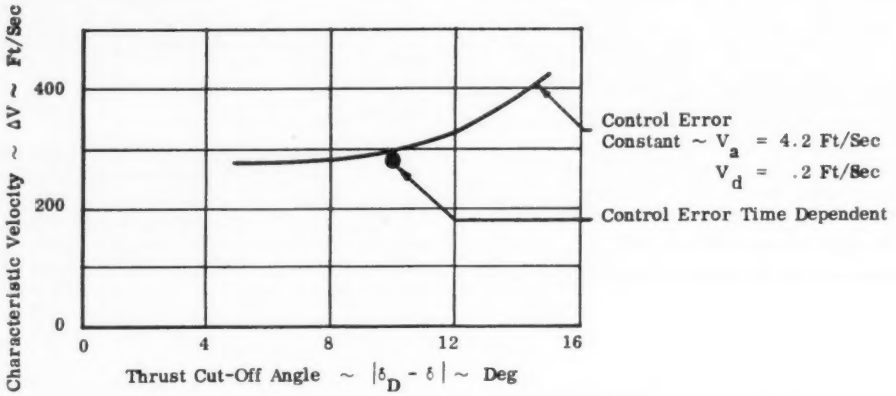

Fig. 4 Effect on ΔV due to attitude firing tolerance

Since X and Z expressions are similar, only horizontal motions will be considered. Differentiation of Eqs. 16 yields

$$\dot{X} = \omega^{1/k}(T^* - kt)^{(1/k)-1}\left(-\alpha(T^* - kt) - B + \beta\frac{(T^* - kt)^2}{2}\right) \quad [17]$$

where

$$\alpha = (A\omega/k)(k+1)$$
$$\beta = B(\omega/k)^2(1+2k)$$

The acceleration $\ddot{X}$ becomes

$$\ddot{X} = \omega^{1/k}(T^* - kt)^{(1/k)-2}\{\alpha(T^* - kt) - \beta[(T^* - kt)^2/2](k+1) + B(1-k)\} \quad [18]$$

Now, consider the following cases:

1 When $k > 1$ the exponent $(1/k) - 2$ preceding the parenthesized term in Eq. 18 becomes negative. Therefore, as $t \to T^*/k$

$$\ddot{X} \to \infty$$
$$\dot{X} \to \infty$$
$$X \to 0$$

Infinite accelerations and velocities are required to superimpose ferry and target vehicles.

2 When $k = 1$ the term $B(1-k) = 0$ and, as $t \to T^*/k$

$$\ddot{X} \to \omega\alpha$$
$$\dot{X} \to -B\omega$$
$$X \to 0$$

Note that these conditions correspond identically to the intercept problem. For intercept ($X = 0$) a finite thrust produces a finite velocity.

3 When $\frac{1}{2} < k < 1$ and, as $t \to T^*/k$, inspection of foregoing equations reveals that

$$\ddot{X} \to \infty$$
$$\dot{X} \to 0$$
$$X \to 0$$

The implication here is that rendezvous can be achieved, at least theoretically, if infinite thrust is available.

4 When $0 < k < \frac{1}{2}$ the term $(T^* - kt)^{(1/k)-2}$ remains in the numerator. Now, as $t \to T^*/k$

$$\ddot{X} \to 0$$
$$\dot{X} \to 0$$
$$X \to 0$$

This can be classified as a true rendezvous condition. Notice that limit accelerations, velocities, and distances are unaltered even if ω varies about some nominal value. Attention to this fact will be made when elliptic target orbits are discussed.

Control System Synthesis

Control provisions regarding thrusting intervals and direction must be included to monitor desired velocities. Thrusting intervals are defined with respect to error signals generated by continually comparing desired velocities to actual relative ferry velocities available from the equations of motion. These differences then specify a coplanar velocity error

$$V_\delta = +\sqrt{(\dot{X}_D - \dot{X})^2 + (\dot{Z}_D - \dot{Z})^2} \quad [19]$$

Should V_δ be greater[3] than an assigned control error V_a, thrust is activated; should V_δ be less than an assigned control error V_d, thrust is deactivated. Resolution of the velocity control

[3] For the three-dimensional case, V_δ is replaced by V_σ.

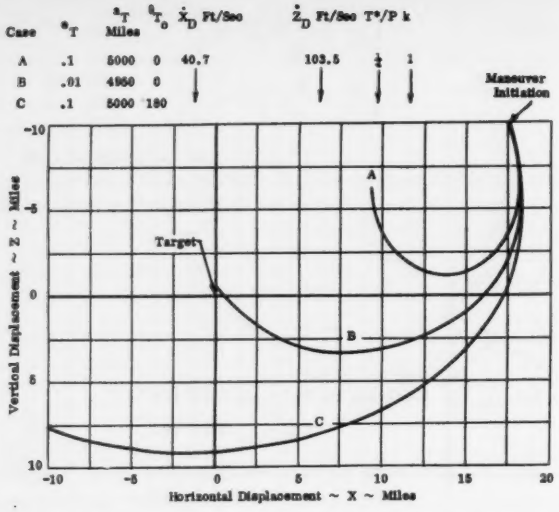

Fig. 5 Miss distance based on impulsive velocity for intercept

error vector yields a coplanar command thrust direction[4]

$$\delta_D = \cos^{-1}\left(-\frac{\dot{X}_D - \dot{X}}{V_\delta}\right) = \sin^{-1}\left(-\frac{\dot{Z}_D - \dot{Z}}{V_\delta}\right) \quad [20]$$

Any difference between command and actual deflection $K(\delta_D - \delta)$ generates a rate signal error that drives the vehicle toward the command firing direction. Maximum pitch rate $\dot{\delta}$ is generally limited. Furthermore, firing is prohibited if the thrust axis does not lie within $\pm\eta$ deg of the command direction ($|\delta_D - \delta| > \eta$). This latter limit is obvious because of the undesirability of applying thrust in a direction contrary to that commanded.

Errors in the knowledge of the target orbit, deviations in planned launch conditions, and system inaccuracies all contribute to preclude a two-dimensional rendezvous problem. Admittedly, relative target-ferry orbital inclinations will be small; nevertheless, a realistic system must include provisions to nullify noncoplanar motion. Relative out of plane motion is sinusoidal and uncoupled from planar motion. In this case the desired lateral motion $\dot{Y}_D$ is simply selected as a linear function of nonplanar displacement

$$\dot{Y}_D = -k_Y Y \quad [21]$$

The total velocity error now becomes

$$V_\sigma = \sqrt{(\dot{X}_D - \dot{X})^2 + (\dot{Y}_D - \dot{Y})^2 + (\dot{Z}_D - \dot{Z})^2} \quad [22]$$

Thrust must be applied such that $\dot{Y}_D - \dot{Y} \rightarrow 0$. This is accomplished by defining a yaw angle σ_D where

$$\sigma_D = \tan^{-1}\frac{\dot{Y}_D - \dot{Y}}{V_\delta} \quad [23]$$

Attitude and attitude rate limits applicable to the pitch mode are also applicable to the yaw mode.

Discussion

The basic system operation has been outlined in the foregoing section. The intent here is to discuss related effects on the path, thrusting schedule, and propellant consumption due to variations in allowable pitch rate, thrust angle cutoff commands, velocity control errors, and degree of engine throttleability. First circular, then elliptic target orbits are considered. Prior to any performance assessment, however, some criterion for selecting T^* and k need be established (since desired velocities depend on these parameters). In essence, T^* determines characteristic velocity which includes velocity to be gained for intercept and velocity expended for rendezvous. Attainment of an intercept path comprises the initial phase of rendezvous and is defined when actual and desired velocities are first matched. Factor k dilates the time scale, thereby providing sufficient time to fulfill velocity commands within available vehicle thrust limitations. An interdependence between available thrust and parameters T^* and k exists, particularly for low thrust levels.

T^* Selection

Rendezvous propellant expenditure has a direct dependence on T^*. Minimum propellant paths compatible with this system can be approached by selecting that unique T^* that denotes minimum characteristic impulsive velocity requirements (13). The primary purpose of this study is to demonstrate system feasibility. Consequently T^* was chosen arbitrarily.

k Selection

If ΔV_G represents initial impulsive velocity to be gained for intercept lock-on, then for a constant thrust engine the time required to generate this velocity increment is approximately

$$t' = \frac{\Delta V_G}{T/Wg}$$

When $k \neq 0$ rendezvous time becomes T^*/k. It follows, therefore, that t' must be less than T^*/k to ensure sufficient time for retrothrust after an intercept path is attained. Based on a series of initial conditions investigated, it was empirically found that rendezvous is ensured if intercept lock-on time t' is less than $0.2T^*/k$. A possible k selection criterion is thus established.

A particlarly attractive alternate k selection criterion was also considered. At maneuver initiation let $k = 0$. This corresponds to terminal phase initiation based on infinite time to go. Eqs. 13, however, continually compute desired velocities while command equations attempt to correlate actual and desired velocities, thereby forcing the ferry toward the target. When $V_\delta = V_d$ time is started with k equivalent to $1/2$. This k switching program yields the simplest method for ensuring rendezvous regardless of initial conditions or available thrust level (analog scaling limits and drift precluded accurate representations of thrust levels much less than 10^{-3} g).

Fig. 2a relates characteristic velocity to time factor k for a variety of intercept times and initial conditions. In each instance both ferry and target vehicles are on coplanar circular orbits. Only constant thrust engines are considered. With the exception of the solid symbol, which is characterized by the alternate k selection criterion, all data comply with $t < 0.2T^*/k$. Factor k therefore remains constant throughout each run. The dependence of characteristic velocity on T^* and k is seen. Extending k beyond the maximum value shown results in large propellant expenditures. Should available thrust be reduced from 10^{-2}g to 10^{-3}g, rendezvous is unattainable for those conditions shown, since the low thrust engine is not capable of forcing a rendezvous path within the time restrictions imposed. Rendezvous is feasible, however, if the k switching technique is used (refer to solid symbol). Additional propellant is spent when this run is compared to the open symboled data, primarily because of the differences in rendezvous time. Rendezvous time for the 0.01g engine is slightly less than a target period, whereas nearly 1.8 target revolutions transpire when $T/W = 0.001$ (refer to Fig. 2b for the trajectories).

[4] Anticipating changes in desired velocities (i.e. $\ddot{X}_D$, $\ddot{Z}_D$) and processing this information in the command thrust equation could possibly produce a more efficient thrust schedule.

Thrust Deflection Rate $\dot{\delta}$

Rate limits have no effect on characteristic velocity, as evidenced from Fig. 3. The remainder of the data are based on $\dot{\delta}_{max} = \pm 1$ deg/sec.

Thrust Cutoff Angle ($\delta_D - \delta$)

The consequence of firing in an undesirable direction is clearly indicated in Fig. 4. A 55% propellant increase results due to varying the cutout angle from 5° to 15°. All subsequent runs were limited to $|\delta_D - \delta| = 10°$ since the major propellant disparity exists beyond a cutout angle of 10°.

Velocity Control Error

Velocity control errors are necessary to prevent hunting of constant thrust on-off signals. Parameter V_a activates corrective thrust, whereas parameter[5] V_d deactivates thrust. The data presented in Figs. 2 and 3 used a constant deadband defined by $V_a = 4.2$ fps and $V_d = 0.2$ fps. Reducing this deadband an order of magnitude nearly doubles the characteristic velocity due to the addition of on-off thrust pulse requirements. Increasing the deadband diminishes thrust correction requirements and propellant payload, but rendezvous accuracy is compromised. In an effort to reduce corrective thrust applications without sacrificing accuracy, the following time dependent deadband was introduced

$$V_a = \frac{T^* - kt}{T^*} (42.2) \text{ fps} \qquad [24a]$$

$$V_d = \frac{T^* - kt}{T^*} (2.1) \text{ fps} \qquad [24b]$$

Velocity control errors are initially increased tenfold and then forced to diminish with time until the base value is reached. Characteristic velocity allied with this technique is illustrated by the solid symbol in Fig. 4. Propellant expenditure remained substantially constant; however, the number of thrust pulses sustained was reduced from 25 (V_a = const) to 14. Rendezvous trajectories and rendezvous time were unaltered.

Based on the foregoing, rendezvous occurs when relative velocities are within a 4 fps deadband. This is unsatisfactory for docking purposes, because relative distances can oscillate within a few hundred feet without generating corrective commands. Rectification demands a problem rescaling. It will be shown later that the steering equations, when modified slightly, provide docking trajectories along a predetermined direction relative to the target.

Elliptic Target Orbits

Eqs. 13 were derived based on circular target orbits. Fig. 5 demonstrates the equation's open loop inability to define an intercept trajectory with a target in an elliptic orbit (a_T = 5000 miles, $e_T = 0.1$). Impulsive transfer velocity magnitude and direction were selected by nulling V_δ. With the target initially located at perigee, an extreme undershoot prevails (ΔV too small); whereas, with target initially situated at apogee, a large overshoot exists (ΔV too large). As expected, a tenfold reduction in eccentricity favorably alters the path from A to B. Alternatively, path A indicates that ω is initially too small, whereas path C indicates the reverse. Attempts to empirically ascertain some functional relationship for angular velocity proved fruitless. Throughout the remainder of the study w represents mean angular motion.

Closing the loop and applying a succession of thrust pulses rectifies the highly unfavorable condition examined above. Effectively, Eqs. 13 process information defined by the exact

[5] Ideally, V_d should be zero. A residual voltage was mandatory to maintain servo stability.

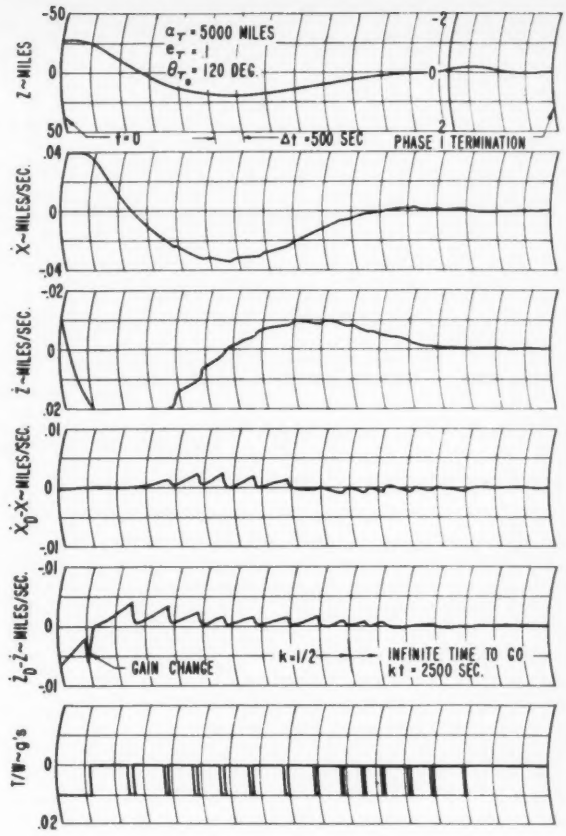

Fig. 6a Terminal phase time history

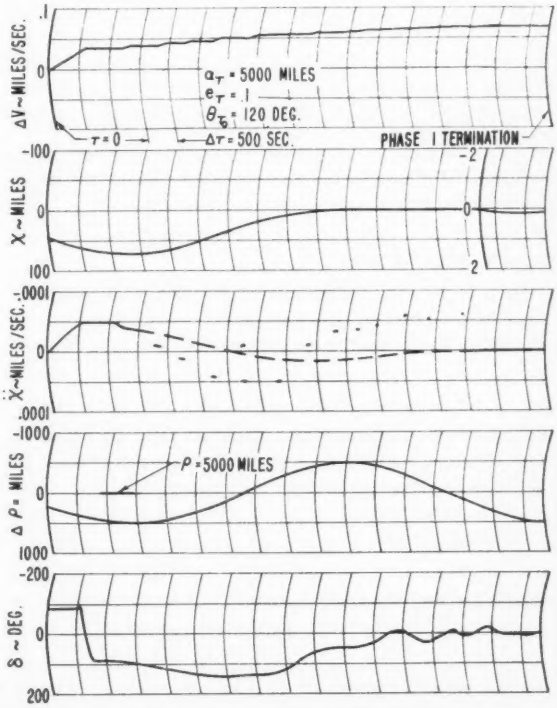

Fig. 6b Terminal phase time history

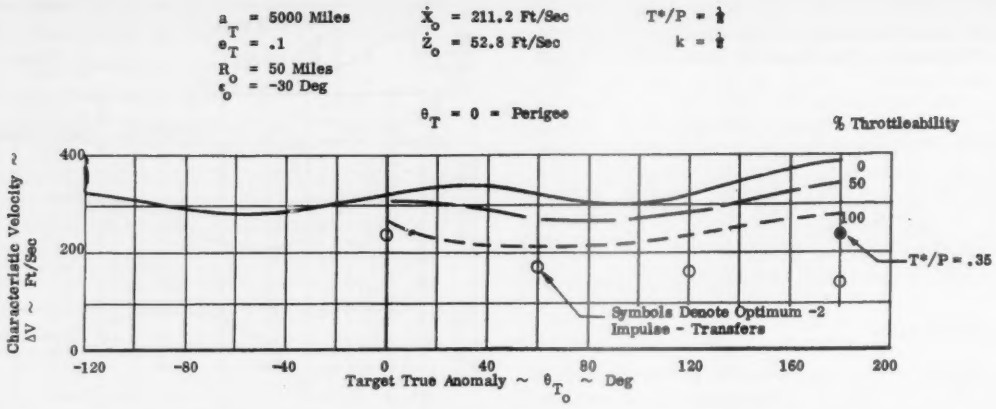

Fig. 7 Propellant assessment based on degree of engine throttleability

equations of motion and interpret the information as a succession of new initial conditions for rendezvous with a series of circular target orbits. The condition imposed that $\dot{\theta}$ of the target remain constant, when in fact it varies, implies a variation in rendezvous time. However, previous data has shown that a variation in rendezvous time, through T^* and k, does not hinder rendezvous. Moreover, equations in the section on control system equations indicate that rendezvous end conditions are unaffected, regardless of ω.

An elliptic orbit ($e_T = 0.1$) with a semimajor axis of 5000 miles was chosen to demonstrate rendezvous feasibility employing Eqs. 13 without modifications. Initially the target true anomaly is 120°. The single engine ferry vehicle is prepositioned 50 miles from the target at an associated look angle of −30° and a relative velocity of 217 fps. Other pertinent conditions are specified on the time history given in Figs. 6a and 6b. Note the allowable error decay with time and subsequent diminishing of thrusting intervals. At the outset the thrust vector is oriented toward Earth ($\delta = -83°$). Upon intercept lock-on the vehicle rotates approximately 180° ($\delta_{max} = 1$ deg/sec), whereon a slow rotation persists until the engine orients itself along the horizon ($\delta = 0$) at rendezvous completion. Notice that time is stopped (kt = const) just prior to rendezvous. This technique is similar to imposing an infinite time to go and was used to prevent voltage overloads. Ultimately the ferry oscillates about the target within the velocity control deadband provided.

Throttleable Engines

The velocity control error and firing logic employed for each engine investigated are given in Table 1.

Variable thrust commands depend on the total velocity error V_σ. Thrust activation control V_a for the 50% throttleable engine is time dependent. A time dependent gain $[100(T^* - kt)/T^*]^{-1}$ was required to ensure a 0.01g thrust output during each initial thrusting period. When V_a diminished to 4.2 fps, kt remained constant. Engine 3 thrust (100% throttleable) is never deactivated. Instead a small fraction of thrust output is maintained to counterbalance a steady-state error within 1.5 fps.

Propellant costs in terms of characteristic velocity spent when using engines 1, 2, and 3 are supplied in Fig. 7 for a variety of initial target locations. Pertinent initial conditions are given in the figure. The constant thrust engine consumes propellant equivalent to a characteristic velocity of approximately 317 fps. Propellant disparities between engines 1 and 2 are small (48 fps). Further, propellant savings are evident when a fully throttleable (engine 3) rather than a constant thrust engine is used. Nevertheless, constant thrust engines appear attractive because the modest propellant benefits derived from throttleable engines may not compensate for their additional weight, extended burning times, and general complexity.

As mentioned previously, T^*/P was arbitrarily selected. The data represented by the 0, 50, and 100% throttleable engines are therefore nonoptimum. For the 50% throttleable case, however, one optimized run was performed and is indicated by the solid symbol ($T^*/P = 0.35$). In this instance a propellant saving of 30% is noted. The final decision to either optimize T^*/P or simply to preload an intercept time equivalent to $P/2$ must be based on the results of a tradeoff study wherein propellant savings are weighed against additional computer capacity. It is conjectured that preloading T^*/P at ½ will be satisfactory for most terminal guidance maneuvers performed within 100 miles.

Table 1

Engine	If	Then	Comment
Constant thrust	$V_\sigma \geq V_a$	$T/m = 0.01g$	V_a and V_d are time dependent. See Eqs. 24.
	$V_d < V_\sigma < V_a$		
	$V_\sigma \leq V_d$	$T/m = 0$	
50% variable thrust	$V_\sigma \geq V_a$	$T/m = 0.01g$	V_a is time dependent. At $t = 0$, $V_a = 32.2$ fps. When V_a becomes equal to 4.2 fps, kt remains constant.
	$0.5\,V_a \leq V_\sigma < V_a$	$\frac{T}{m} = \frac{V_\sigma}{100(T^* - kt)/T^*}$	
	$V_\sigma < 0.5\,V_a$	$T/m = 0$	
100% variable thrust	$V_\sigma \geq V_a$	$T/m = 0.01g$	$V_a = 32.2$ fps.
	$V_\sigma < V_a$	$T/m = V_\sigma/100$	

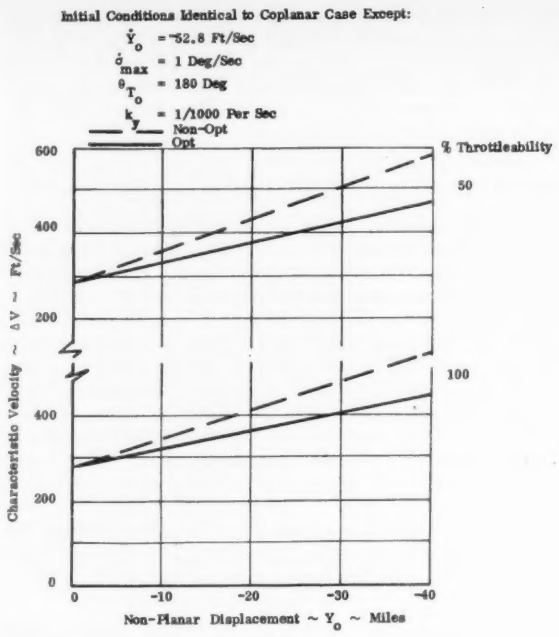

Fig. 8 Optimum vs. nonoptimum lateral correction

Some basis must be made available for evaluating overall system performance. For this reason a series of data points representing the absolute minimum propellant boundary consistent with a two-impulse orbit transfer path is included in Fig. 7. These data were digitally computed (11). In terms of vehicle mass ratio from launch or from parking orbit departure, the propellant differences between the data shown are small. Proportional navigation schemes require characteristic velocities that are approximately an order of magnitude larger than the optimum double impulse data shown. On this basis the subject system appears attractive.

Nonplanar Ferry Motion

It is well known that propellant is minimized when small orbital corrections are made at a node. The nonplanar control system described in the section on control system equations attempts to correct orbital inclination regardless of nodal position. This situation is ameliorated by taking advantage of the sinusoidal motion; that is, fire only in the vicinity of a node and only when actual velocity and displacement differ in sign. Necessary computer logic for autopilot implementation takes the following simple form:

If	Then
$\dot{Y} > -k_Y Y < 0$	$\dot{Y}_\delta = O$ ($\sigma_D = 0$ thrust direction parallel to target plane)
$\dot{Y} < -k_Y Y > 0$	
$\dot{Y} > -k_Y Y > 0$	$\dot{Y}_\delta = \dot{Y}_D - \dot{Y}$
$\dot{Y} < -k_Y Y < 0$	

Fig. 8 depicts propellant saving when an optimum rather than a nonoptimum, noncoplanar command system is used. Coplanar initial conditions were unaltered from those previously investigated. Propellant savings increase linearly with nonplanar displacement. A time history, based on the optimum lateral mode, is given in Figs. 9a and 9b. The 100% throttleable engine rapidly reduces and then maintains nearly zero velocity control errors. Smooth parameter variations are noted.

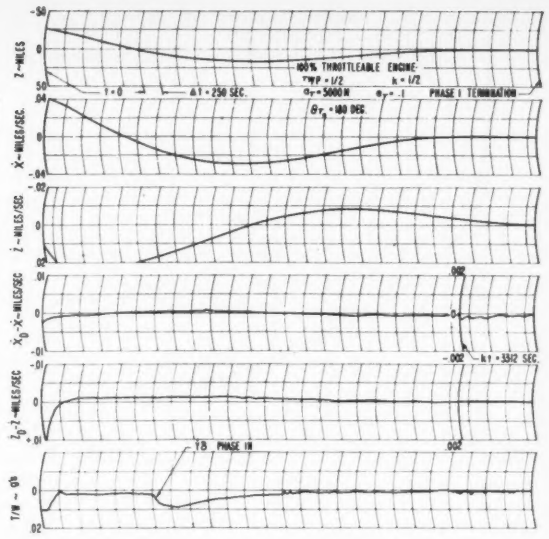

Fig. 9a Three-dimensional time history; optimum lateral mode

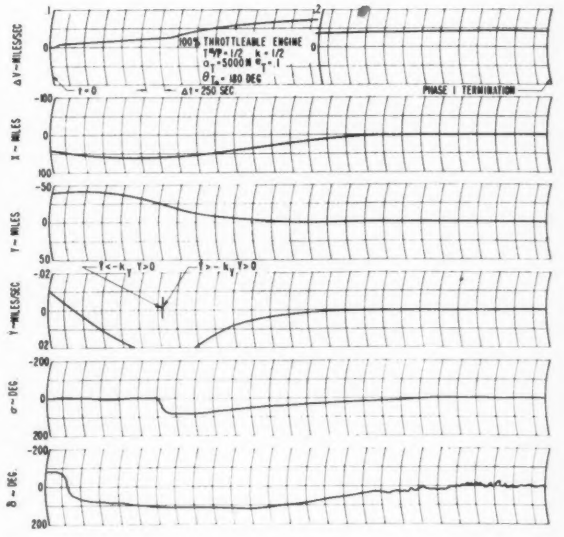

Fig. 9b Three-dimensional time history; optimum lateral mode

Rendezvous Offset

As mentioned earlier, a distinction exists between terminal phase initiation and docking lock-on. Mechanical considerations will generally require that final docking be unidirectional with respect to the target. A correct directional approach can be ensured by instructing the control equations to command rendezvous at a point removed from the target so as to

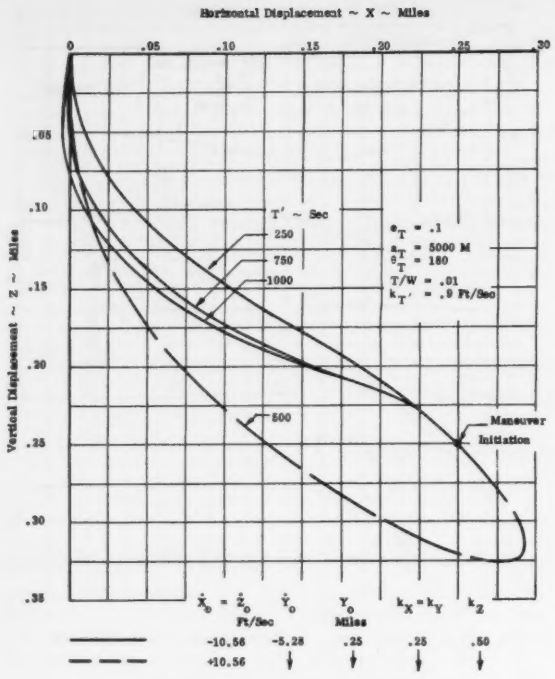

Fig. 10 Docking trajectories

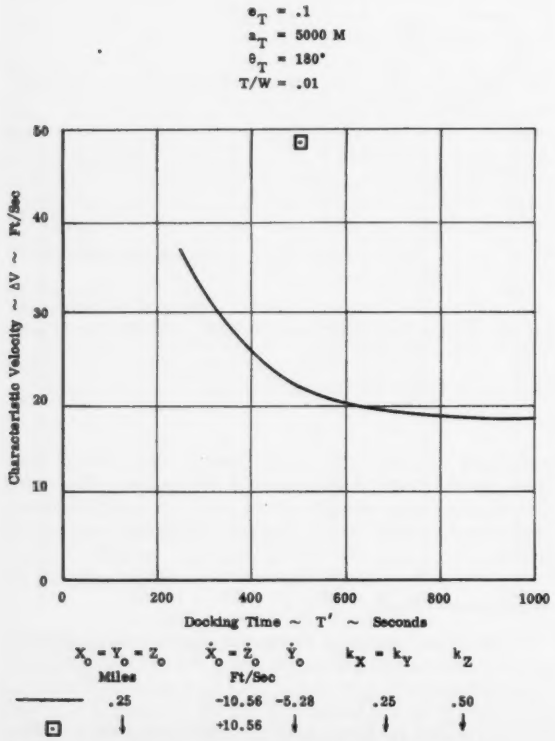

Fig. 11 Docking propellant consumption

define favorable docking initial conditions. Mechanization simply requires that X, Y, and Z appearing in Eqs. 13 and 21 be replaced by X-X_{off}, Y-Y_{off}, and Z-Z_{off}. If the mission requirement dictates inspection rather than rendezvous, then a corkscrew motion of the ferry about the target can be achieved by properly offsetting X, Y, and Z.

Docking

Docking as defined herein is that portion of the terminal guidance maneuver wherein the ferry is brought from close target proximity to actual target contact. For purposes of this study a unidirectional docking requirement is imposed, since addition of propellant modules or transfer of men and material necessitates a particular mating of target and ferry structure. Two assumptions made are that the friendly target vehicle is oriented to the local vertical and that previous steering loops have placed the ferry in a favorable spacial position with respect to a predetermined lock-on direction (offset). Initial conditions for switching to this phase depend on initial terminal guidance sensitivities and sensing acuity. They are arbitrarily selected as $R < 1/2$ mile and $\dot{R} < 20$ fps.

Computer rescaling was mandatory to ensure accurate distance representations within a few feet. The following steering equations, based on Eqs. 14, were employed:

$$\dot{X}_D = -\frac{X}{k_X(T'-t)} - Z\omega \qquad [25a]$$

$$\dot{Y}_D = -\frac{Y}{k_Y(T'-t)} \qquad [25b]$$

$$\dot{Z}_D = -\frac{Z}{k_Z(T'-t)} + X\omega \qquad [25c]$$

Parameter T' represents a predetermined docking time (T' = const = $T^*/k_X = T^*/k_Y = T^*/k_Z$). Gain constants ($k_X$, k_Y, k_Z) define response speed along any desired axis. Parameters $Z\omega$ and $X\omega$ partially compensate for coriolis forces tending to curve the ferry trajectory relative to the target.

Time dependent velocity control errors, Eqs. 24, must be altered to comply with docking requirements. Therefore let

$$V_a = K_T'(T' - t)/T' + \dot{R}_R$$

Residual velocity $\dot{R}_R$ (0.1 fps) is again defined as a servo compensating factor. Vehicle rotation rates for this phase were not limited, because angular response dictated by $K(\delta_D - \delta)$ was generally within 2 deg/sec.

Typical trajectories are displayed in Fig. 10. Final docking along the target's vertical axis was effectively accomplished by increasing sensitivities with respect to X and Y displacements. Appropriate choice of gains will drive the ferry along any desired docking axis. Related propellant costs are presented in Fig. 11. As expected, rapid docking and/or response demands increased propellant loads.

Approximately 80% of the docking propellant is consumed during the first 200 sec, due to the initial rapid succession of firing pulses required to shape the distance-velocity domain in accordance with Eqs. 25 (see Figs. 12a and 12b). For the remainder of the run (T' = 750 sec) propellant equivalent to 4 fps is expended. This small characteristic represents a series of final retrothrust bursts which could be generated by very low thrust engines.

Conclusions

The following conclusions are based on the preceding investigation:

1 The intercept attenuation scheme assures rendezvous for low or high thrust weight ratios. Relative distances, velocities, and target mean motion are required inputs.

2 A reduction in the number of constant thrust corrections

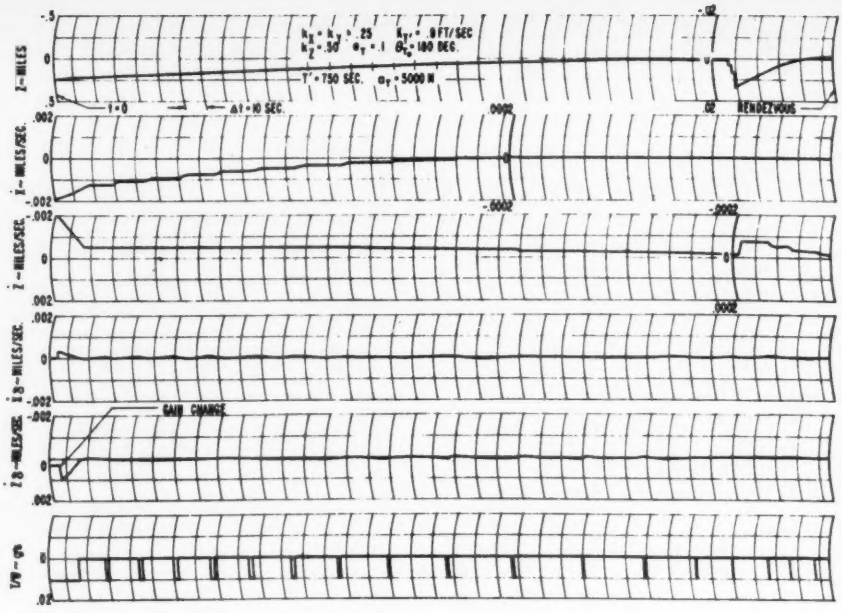

Fig. 12a Docking time history

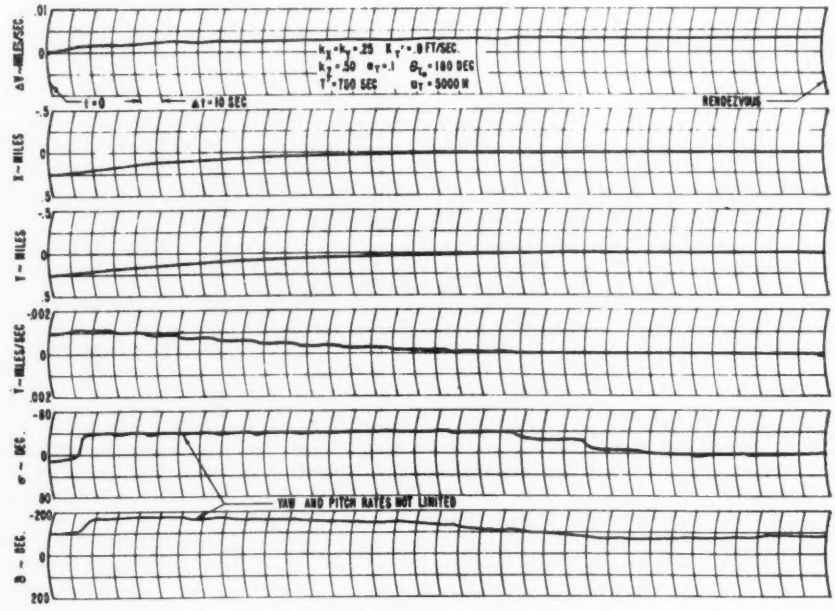

Fig. 12b Docking time history

can effectively be accomplished by inclusion of a time dependent velocity control error.

3 Single engine operation requires attitude rate changes that are less than 2 deg/sec.

4 Propellant costs are not prohibitive even when compared to optimum, two impulse, characteristic velocity requirements.

5 Small propellant reductions offered by a variable thrust engine do not appear to offset the desirability of using a constant thrust engine.

6 Offset constants inserted into the control equations ensure a final approach to the target from any desired direction.

7 A simplified control set can force docking along any predetermined docking axis.

Acknowledgment

Acknowledgment is due to the Analog Computing Group of Republic Aviation Corp. and in particular to Robert Croco for his assistance during all phases of the subject study.

Nomenclature

a	=	semimajor axis
e	=	eccentricity
g	=	sea level acceleration (32.2 ft/sec^2)
H	=	angular momentum
k	=	time dilation factor
K, k	=	gain constants
K^2M	=	gravitation constant
m	=	mass
P	=	period
r	=	ferry radius
R	=	relative distance
t	=	time
T	=	thrust
T^*	=	intercept time
T'	=	docking time
V_δ	=	coplanar velocity error
V_σ	=	total velocity error
V_a, V_d	=	control velocity errors
ΔV	=	characteristic velocity
W	=	weight
X, Y, Z	=	reference coordinates
δ	=	pitch angle
ϵ	=	look angle
η	=	angular restriction
θ	=	true anomaly
ρ	=	target radius
σ	=	equivalent yaw angle
τ	=	time to go
ω	=	mean angular motion

Subscripts

D	=	desired
0	=	initial
T	=	target

References

1 Sears, N. E., Jr. and Felleman, P. G., "Terminal Guidance for Satellite Rendezvous," presented at the ARS Controllable Satellite Conf., Cambridge, Mass., April 30–May 1, 1959 (*ARS preprint no. 778-59*).

2 Sears, N. E., Jr. and Felleman, P. G., "A Guidance Technique for Achieving Rendezvous," IAS Manned Space Stations Symposium, April 20–22, 1960.

3 Harrison, E., "Some Considerations of Guidance and Control Techniques for Coplanar Orbital Rendezvous," IAS National Specialists Meeting on Guidance of Aerospace Vehicles, May 25–27, 1960.

4 Simon, E., "A Proposed Control System to Facilitate the Terminal Stages of Manned Rendezvous," presented at the ARS 15th Annual Meeting, Washington, D. C., Dec. 5–8, 1960 (*ARS preprint no. 1480-60*).

5 Steffan, K. F., "A Satellite Rendezvous Terminal Guidance System," presented at the ARS 15th Annual Meeting, Washington, D. C., Dec. 5–8, 1960 (*ARS preprint no. 1494-60*).

6 Nason, M. L., "A Terminal Guidance Law Which Achieves Collision Based on Coriolis Balance Techniques," *AAS paper no. 61-40*, January 1961.

7 Eggleston, J. M., "The Trajectories and Some Practical Guidance Considerations for Rendezvous and Return," *IAS Paper No. 61-36*, January 1961.

8 Nelson, A. W., "Manned Orbital Rendezvous," presented at the ARS 15th Annual Meeting, Washington, D. C., Dec. 5–8, 1960 (*ARS preprint no. 1493-60*).

9 Stenihoff, E. A., "Orbital Rendezvous and Guidance," IAS Manned Space Stations Symposium, April 20–22, 1960.

10 Houbolt, J. C., "Considerations of the Rendezvous Problems for Space Vehicles," *SAE paper*, April 5–8, 1960.

11 Shapiro, M., "Requirements for Rendezvous," *Republic Aviation Corp. Rep. RAC-702-100*, Jan. 22, 1960.

12 Clohessey, W. H. and Wiltshire, R. S., "Terminal Guidance System for Satellite Rendezvous," *IAS Paper no. 59-93*, June 16–19, 1959.

13 Spalding, L. W., "The Long-Time Satellite Rendezvous Trajectory," IAS National Specialists Meeting on Guidance of Aerospace Vehicles, May 25–27, 1960.

Nuclear Safety Analysis of Snap III for Space Missions

W. HAGIS[1]
T. DOBRY[2]
G. DIX[3]

The Martin Co.
Baltimore, Md.

Snap III is an auxiliary power source using thermoelectric elements to convert decay heat from a radioisotope directly into electrical energy. The fate of the radioisotope fuel in the event of post orbital re-entry after a successful satellite mission or an abort during a launch attempt was investigated. The objective was to determine the locations of impact or the locations and altitudes of the radioisotopic fuel capsule during burnup that could result from all possible combinations of final stage booster thrust, misalignments, or failures. Burnup altitude for a post orbital re-entry was also determined for a 275-mile circular orbit. The safety of the mission was appraised with respect to the fate of the radiopolonium fuel for successful missions and for the spectrum of potential aborted missions. Seven general cases resulted from the 65 abort cases examined. Concurrent with the theoretical investigation, a safety experimental program was conducted. These tests involved both missile failure and aerodynamic forces. They included plasma jet, impact, shock, fire, and fallout tests. The results indicate that the Snap III would be acceptable for operational missions. The deposits resulting from dispersing the radioactive fuel during re-entries, from either successful or aborted missions, would be completely masked by the Po^{210} that is naturally present in soils all over the world.

Presented at the ARS 15th Annual Meeting, Washington, D. C., Dec. 5–8, 1960; revision received Oct. 25, 1961.

[1] Group Leader, Space Systems, Nuclear Safety Analysis Unit. Member ARS.

[2] Group Leader, Extraterrestrial Systems, Nuclear Safety Analysis Unit.

[3] Formerly Chief, Nuclear Safety Analysis Unit, Nuclear Div.; now Assistant Safety Officer, Space Nuclear Propulsion Office, NASA-AEC.

THE SNAP III thermoelectric generator[4] has been integrated with a vehicle consisting of a conventional booster mated to a final stage injection vehicle (2).[5]

Polonium-210, an alpha emitter with a half life of 138 days, produces the thermal energy. This isotope occurs in nature as one of the daughter products of the uranium disintegration series.

The successful mission results in the decay of the initial 2200-curie inventory of Po^{210} to 356 curies before the satellite re-enters Earth's atmosphere. The aerothermodynamic history of the generator during its postorbital re-entry was considered. The definitions of aborted missions and the forces imposed by them were determined. An evaluation of the thermal, mechanical, and chemical forces imposed by launch, ascent, and final stage failures was completed. A cartographic summary of the fate of the polonium fuel for both successful and aborted missions has been made. Sixty-five specific cases of successful and aborted missions are resolved into seven general cases.

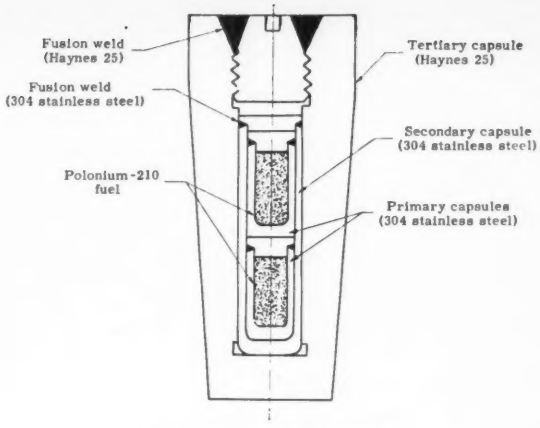
Fusion weld (Haynes 25)
Fusion weld (304 stainless steel)
Polonium-210 fuel
Tertiary capsule (Haynes 25)
Secondary capsule (304 stainless steel)
Primary capsules (304 stainless steel)

Fig. 1 Snap III fuel capsule

Thermoelectric Generator

Snap III (3) produces power from the heat evolved in the radioactive decay of Po^{210}. When launched into orbit, the generator contains about 0.489 gm of Po^{210} fuel, with an activity of 2200 curies. This provides 69 w of thermal power which, at a conversion efficiency of about 5%, will result in a 3.5-w electrical power output. The activity of Po^{210} falls off exponentially to half its original value in 138.4 days.

In the Snap III, the fuel is divided equally between two capsules. Both capsules are made of Type 304 SS. The two fuel capsules are placed in an SS canister, which is closed by welding. A heavy vessel made of the cobalt-base alloy, Haynes 25, contains the primary capsules and canister (Fig. 1). Haynes 25 provides the mechanical strength and corrosion resistance necessary to insure containment of the fuel under any condition encountered during manufacture, transportation, and installation of the generator. The outer surface of the Haynes 25 vessel has a temperature of about 1100°F (593°C). The interior temperature is slightly higher and well above the melting point of polonium.

The hot junctions of the 27 pairs of lead telluride thermoelectric elements are placed against the Haynes 25 vessel. The cold junctions are held in contact shoes that extend to the surface of the generator. The massive Haynes 25 vessel and the assembly of thermoelectric elements are held in place by rigid heat-insulating material, and voids are filled with powdered insulation.

The generator is encased in a nearly spherical shell of copper (Fig. 2). This shell is composed of segments soldered together so the seams will open and allow the insulation and thermoelectric elements to fall away, exposing the core. This procedure promotes burnup upon re-entry after an aborted satellite mission or after orbital decay following a successful mission.

At the time of encapsulation, each fuel capsule will contain 0.2446 gm, or 1.165×10^{-3} mole of Po^{210}. The Po^{210} occupies a volume of 0.027 cm^3, leaving a void in each capsule of 0.252 cm^3. The void is provided for the helium produced by the radioactive decay of the fuel. The evolution of helium tends to increase the pressure within the capsule, but the decrease in temperature has the opposite effect. At 290 days, the temperature is 160°C and the pressure is 126 atm, or 1850 psi.

The Haynes 25 containment vessel is able to withstand many times this internal pressure. When tested at temperatures from 1100° to 1700°F, there was no failure under a pressure of 30,000 psi after 640 hr (4).

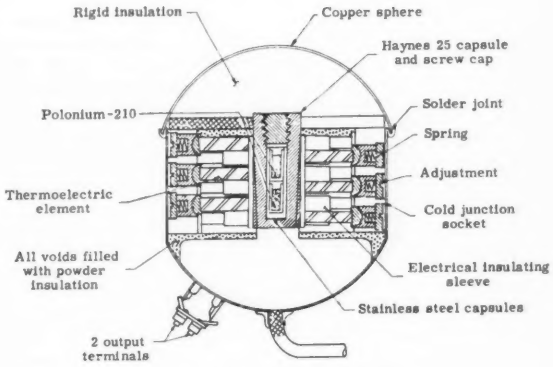

Fig. 2 Snap III generator

Systems Integration

Vehicle

The Snap III generator would be carried on a satellite mission by a vehicle consisting of a conventional ICBM or IRBM booster stage wedded to a final injection stage that also serves as the satellite. Typical boosters are fueled with RP-1 and liquid oxygen, and the injection stage is fueled with unsymmetrical dimethylhydrazine (UDMH) and inhibited red fuming nitric acid (IRFNA).

The booster for this study was assumed to be a single-stage system that places the final stage to an altitude of 500,000 ft and a velocity of about 13,000 fps. At this point, Vernier rockets fire for several seconds to adjust the flight attitude of the vehicle. The final stage separates from the exhausted booster stage and coasts to an altitude of 1,380,000 ft when it ignites and thrusts for about 120 sec to accelerate the satellite to orbital velocity.

The satellite consists of the final stage engine, empty propellant tanks, and the payload, which is located in the forward equipment compartment. Because of inherent system weight limitations, the satellite structure is relatively light, consisting of structural members up to 0.25-in. thickness and skins up to 0.1 in., generally made of magnesium and aluminum.

[4] Fueled at the Martin Co.

[5] Numbers in parentheses indicate References at end of paper.

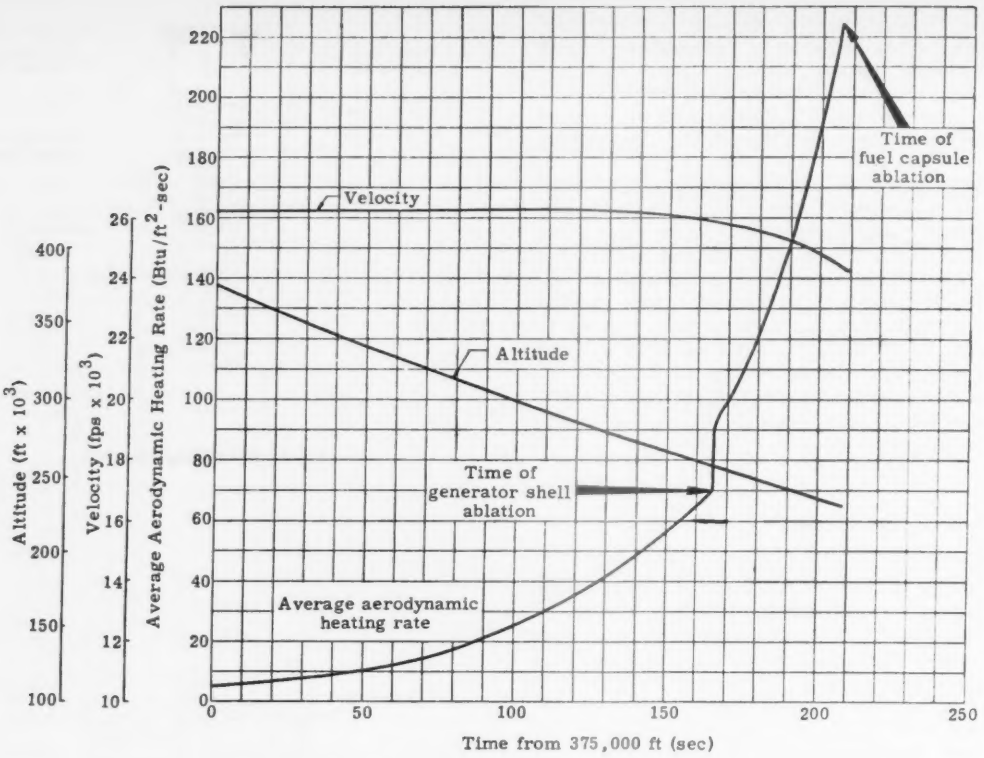

Fig. 3 Snap III postorbital re-entry

Properties of Polonium-210

Polonium-210 has aroused interest as a source of thermal energy because of its high power density. This isotope is a member of the naturally occurring uranium series and was first designated Radium F. The equilibrium ratio of natural uranium to natural polonium is 1.10×10^{-10}. Polonium occurs in Earth's crust at the rate of 3×10^{-10} gm/metric ton.

Physical Properties

Polonium is a metal that melts between 252° and 262°C and boils at about 962°C. It has a high vapor pressure at temperatures well below its boiling point. Its heat of vaporization is about 25,600 cal/mole.

Chemical Properties

Polonium usually exhibits a valence of four but forms a few compounds in which its valence is two. The known oxide is PoO_2. Both the dichloride and the tetrachloride have been prepared. Polonium enters into complex ions, in several cases, as a constituent of the cation. The solubility of polonium oxide in common solvents varies widely, and the results found by various experiments do not always agree.

Radiochemical Properties

Polonium-210, the principal isotope of the element, is a member of the naturally occurring uranium, or $4n + 2$, radioactive series, which includes U^{238} and Ra^{226}, the principal isotopes of these elements. The end of the series is stable Pb^{206}.

Polonium-210 has a half life of 138.39 days and decays by the emission of alpha particles. In 99.9988% of the disintegrations, the alpha particle has an energy of 5.3 mev. In the remaining 0.0012% of the disintegrations, a 4.5-mev alpha is accompanied by a 0.8-mev gamma photon. This is the most nearly pure alpha radiation given by any radionuclide that is useful for power purposes. The radiation due to the gamma photons is about 0.006 mr/hr at 1 m from a bare unshielded source of 1-curie activity. The radiation level 2 in. from the generator surface is 400 mr/hr for a gamma source and 10.6 mrem/hr for a neutron source.

Polonium-210 is now produced artificially by neutron irradiation of bismuth in a nuclear reactor. The isotope $_{83}Bi^{209}$, which constitutes practically 100% of natural bismuth, undergoes a neutron-gamma reaction to produce $_{83}Bi^{209}$. This nuclide, with a 5-day half life, decays by beta emission, forming $_{84}Po^{210}$.

$$_{83}Bi^{209} + O^{n1} \xrightarrow{\gamma} {}_{83}Bi^{210} \xrightarrow[5\text{ days}]{\beta^-} {}_{84}Po^{210}$$

While this reaction does not produce large amounts of Po^{210}, it is more feasible economically than the separation of the isotope from natural sources.

One curie of activity is produced by 2.225×10^{-4} gm of pure Po^{210}, and 3.15×10^{-2} w of thermal energy is released; the specific power is about 141 w/gm. Because it is almost exclusively an alpha emitter, requiring little shielding, and because it produces power at a high rate, Po^{210} is an excellent source of radioisotopic power.

Radiobiological Properties

The gamma radiation from Po^{210} is so small that the thermoelectric elements and supporting structure attenuate its effect to tolerable levels in the Snap III generator. Alpha

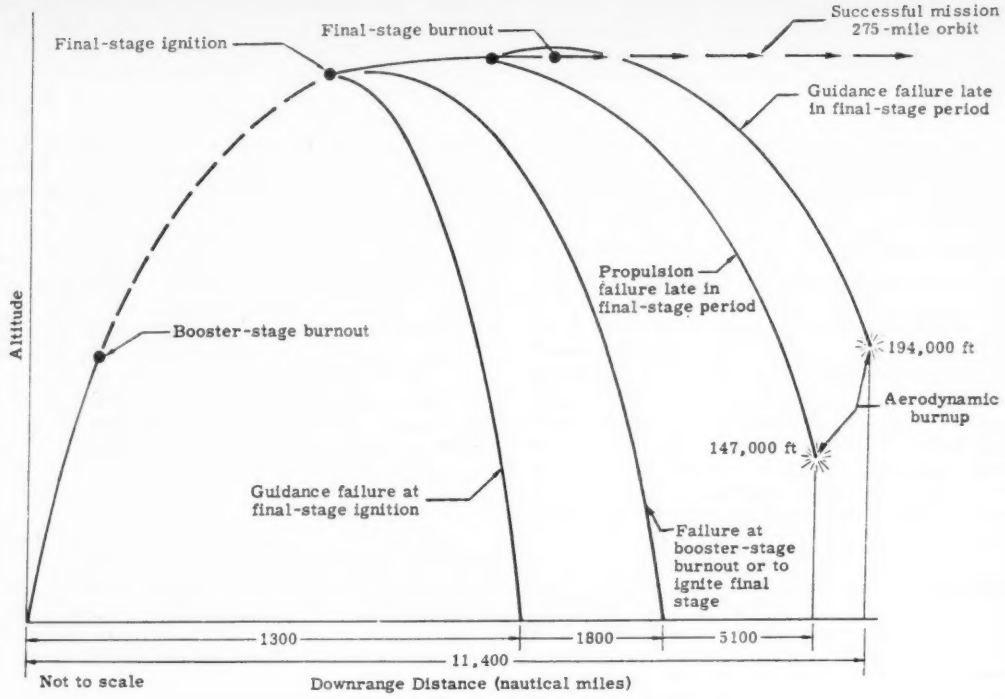

Fig. 4 Snap III aborted mission

radiation is almost entirely absorbed in less than a thousandth inch of the inner container. Consequently, potential radiobiological hazards can arise only if the fuel is released in a form in which it can enter the body by inhalation or by ingestion with food or water.

Successful Missions

For purposes of analyses, a successful mission was assumed to be a circular polar orbit at 275 statute miles altitude. Thus, launch was considered to be from the Point Arguello complex of the Pacific Missile Range. Satellite lifetime is a function of type of orbit and the shape of the satellite body. Using present day satellites capable of using Snap III generators, a lifetime of 365 days is expected. Thus, at the time of the satellite's re-entry, radioactive decay would have reduced the activity level of the fuel to 16% (356 curies) of the original amount.

Re-Entry From Orbit

Orbital altitude reduction is a continuous process because aerodynamic forces are acting on the body from the time it is injected into orbit. The lifetime of the orbit is a function of the eccentricity and altitude of the orbit and the shape of the satellite vehicle. The altitude of the orbit will be slowly reduced; when an altitude of 375,000 ft is reached, aerodynamic heating and dynamic pressure forces become significant. At this altitude, the fuel can be dispersed as aerosols by the eject-destruct system (1). The fuel would be completely dispersed above 100,000 ft, resulting in world-wide dispersion of the polonium.

Aerodynamic Analysis

In the aerothermodynamic analysis, it was assumed that the satellite structure was destroyed by aerodynamic and mechanical forces, releasing the generator to the air stream.

Fig. 3 shows the re-entry trajectory and the aerodynamic heating rate experienced by the generator shell and fuel capsule. The generator and fuel capsule were assumed to be spinning, and the developed stagnation heating was integrated over the entire surface of the unit. A point on the surface of the spinning body heats at a rate approximately 35% of the stagnation heating rate. The generator shell was ablated at an altitude of 256,000 ft. The aerodynamic heating rate is inversely proportional to the square root of the radius of curvature of the re-entering body. There is, therefore, a steep increase in the heating rate for the smaller fuel capsule at the time of its exposure. The Haynes 25 capsule will be heated and completely ablated at an altitude of 228,000 ft. The polonium, whose boiling point of 962°C is lower than the melting point of the surrounding capsule, will be dispersed as a vapor of molecular particle size.

The satellite will have a lifetime of approximately 365 days at the design orbital altitude. Failure of the launching vehicle to yield nominal performance will make it possible for the satellite to enter into orbits having shorter life times. Sixty-five re-entry trajectories resulting from malfunction of the launching vehicle have been determined. Of these trajectories, 10 will produce short-term orbits and not re-enter until after several or many orbital cycles have elapsed. Though the re-entry trajectories and the aerodynamic heating rates resulting from these postulated launch aborts are similar to those shown in Fig. 3, the polonium inventory will vary.

Aborted Missions

It is desired that during any re-entry the fuel capsule will either remain intact or be aerothermodynamically consumed at high altitude. In some aborts occurring during a

limited period of the final-stage operation, however, the capsule is only partially consumed because of insufficient aerodynamic heating. An analysis has been performed to determine the fate of the fuel and fuel capsule after malfunction of the booster vehicle or the orbital injection stage. A typical launching vehicle, capable of injecting several hundred pounds of payload into a low altitude orbit, has been considered for this study. The vehicle has one stage of boost and a coasting period followed by an orbital injection stage.

Definition of Aborted Mission

Potential malfunctions of the launching vehicle have been defined by analytical comparison of the failures of past missile and satellite vehicles with the characteristics of the assumed vehicle (Fig. 4). A series of tests simulating launch vehicle failures has been used to determine the destructive forces to be experienced by the Snap III generator. Additional tests were conducted to determine the integrity of the fuel capsule under the loads that would result from impact of the capsule against Earth at high velocities (simulating the terminal velocity of the capsule during re-entry) and to determine the validity of the aerothermodynamic calculations (plasma jet experimentation).

Launch failures

Launch failures are broadly defined as those that occur either on or directly above the launch pad. They are timed several minutes prior to liftoff and end approximately 15 sec after the vehicle is airborne. This specifically excludes minor electronic and mechanical failures that interrupt the countdown. The maximum height considered for launch failures is 1000 ft. The trajectory calculations and the location of the dispersion area of vehicle remnants in case of abort are greatly simplified, as the velocity of the vehicle has no horizontal component throughout this period. Launch failures are subdivided into propellant tank, propulsion, and/or guidance failures.

Ascent failures

The ascent portion of the trajectory is that segment between the end of launch and ignition of the orbital injection stage. For the vehicle under consideration, this will extend from 15 to approximately 500 sec after liftoff, the time of final stage ignition. This portion of the trajectory has several critical phases where failures should be considered.

Maximum dynamic pressure occurs at an altitude of approximately 40,000 ft and a velocity of about 1500 fps. Aerodynamic loads subject the control surfaces to the most severe loading at this time. Several past missile firings have failed during this period, and their points of impact were within a distance of less than 5 miles from the point of launch.

The point of booster separation is a major area of trajectory malfunction. The danger of interaction between the two stages is great and could result in damage to the second-stage engine, propellant tankage, and/or guidance system. A severe bump between stages can damage the nozzle of the second-stage rocket or cause the attitude of this stage to be misaligned so that large control moments may be necessary to return the vehicle to the programmed course. A failure at booster separation will cause the complete vehicle to impact downrange at approximately 2000 miles.

Final stage failure

Failure during final stage ignition and during its thrusting period is critical because of the generation of aerodynamic heating on the re-entering bodies. Failures are generally restricted to: 1) propulsion failure—either failure to ignite or failure after ignition; and 2) guidance failure. The probability of these malfunctions occurring is discussed in the next section.

A complex sequence of events must occur for final stage ignition. Thrust terminations were assumed at various times after ignition of the final stage. They were at 0, 28, 58, 88, 98, 108, and 113 sec after final stage ignition.

Failures in the guidance system during final stage operation will produce the greatest deviation from the planned trajectory. Though most large final stage rocket systems include redundant destruct systems with highly reliable operation, all possible re-entries resulting from this failure were investigated. As there is a possibility of such failures, this analysis must be conducted.

The final stage was analyzed for both pitch and yaw misalignments during stage operation, as a means of duplicating actual re-entry trajectories. Misalignment was simulated by instantaneous deflection of the vehicle in the pitch and yaw directions at various times from ignition, with continuous thrusting of the rocket after the misalignment. Thus, the widest possible impact area for this vehicle was achieved.

Table 1 Fate of fuel

Category	Type of failure	Fate of fuel	Fuel recovery
Impact on land	launch, ascent	contained	yes
Impact in shallow water	ascent	contained	yes
Impact in deep water	ascent, final stage	contained effectively	no
Partial ablation of fuel core impact on surface of ocean and fracture, releasing fuel	final stage	hydrospheric dissemination	no
Partial ablation of fuel core fracture at high altitude due to internal gas pressures	final stage	stratospheric dissemination	no
Prompt re-entry, burnup	final stage	stratospheric dissemination	no
Into orbit	final stage	stratospheric dissemination	no

Forces Imposed on Generator by Aborted Missions

The forces imposed on the generator by aborts along the launching trajectory result from three sources. They are thermal, mechanical, or chemical reactions. The degree to which they affect the generator depends on the time when the vehicle malfunctions.

Launch failures

A failure during launch will result in spilling propellant on the launch pad and the surrounding area. Present day large boosters use liquid oxygen and RP-1 (kerosene) as propellant. Upon detonation, sufficient thermal and mechanical energy is released to create a possible Po^{210} release mechanism (5).

The oxidizer from the basement booster will quickly vaporize, but the fuel will cause a severe fire. A distinct fireball will form and will be aggravated by the release and combustion of the final stage fuel. After a short period of time, the structural members of the vehicle may ignite and burn at a much higher temperature than the fuel fire. If the Snap III generator is located in the center of the wreckage,

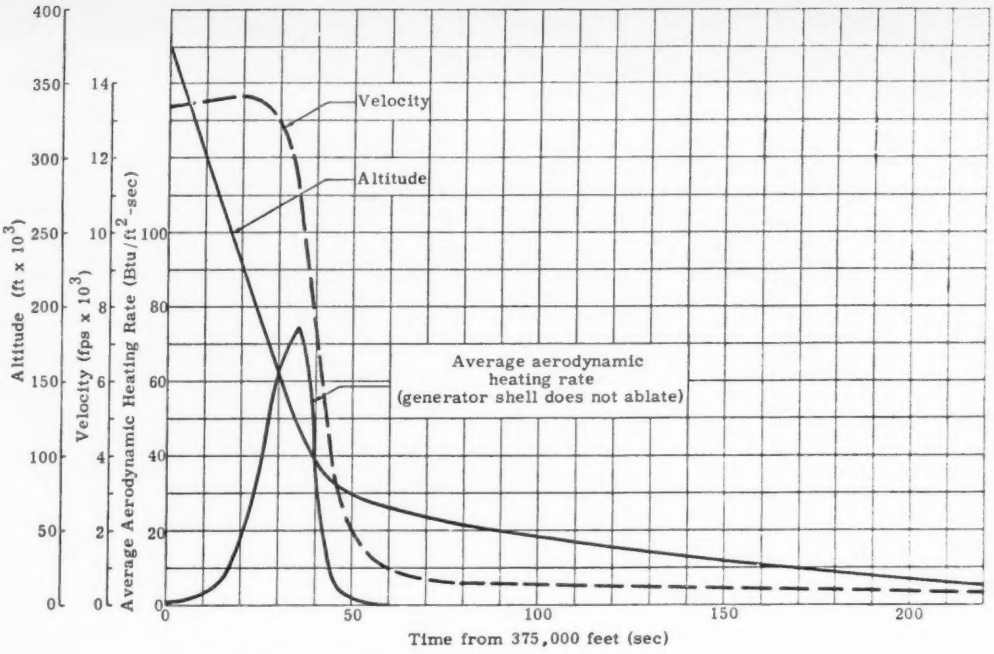
Velocity
Altitude
Average aerodynamic heating rate (generator shell does not ablate)
Altitude (ft x 10^3)
Velocity (fps x 10^3)
Average Aerodynamic Heating Rate (Btu/ft^2-sec)
Time from 375,000 feet (sec)

Fig. 5 Snap III re-entry trajectory after failure to ignite final stage

it will experience the thermal effects of the fire for a period of 20 min. A test program was conducted to determine the effects of thermal and mechanical forces on the thermo-electric generator and fuel capsule in the event of launch aborts. Five generator assemblies and three fuel cores were exposed to a thermal environment equivalent to a ICBM booster burning on the launch pad. In all cases, the fuel element was contained within the designed structure.

The impulsive force resulting from shock-pressure waves originating from the igniting of the liquid oxygen and RP-1 has been determined analytically by methods derived from tests involving TNT. Initial analysis showed that shock loads from these fuels will produce forces equivalent to 77% TNT. Later studies by STL developed empirical relations for the prediction of shock overpressures from LOX-RP-1 at radial distances from the point of origin.

The Snap III generator was tested under simulated vehicle-abort conditions at Aberdeen Proving Grounds. In these tests, fuel cores and generators were subjected to a shock overpressure of 1020 psi at an appropriately scaled distance from a 1650-lb TNT charge. The core material was Haynes 25 alloy, but similar cores were also constructed from graded aluminum for use in this test. Even the lowest grade aluminum core maintained its mechanical integrity.

A malfunction during the launch portion of the trajectory would cause the vehicle and thermoelectric generator to impact downrange at a distance of less than 5 miles from the launch point. This would cause impact of the fuel capsule in ground within the PMR range safety zone. During the fire test previously summarized, the fuel capsule was exposed to nitric acid and liquid oxygen; it withstood these attacks with no noticeable damage. Concentrated nitric acid will corrode Hayues 25 at the rate of 0.046 in./yr, but it is inconceivable that the capsule will be immersed in the acid for a period longer than a few days. Therefore, it is not expected that ground impact could result in significant corrosion damage to the fuel capsule.

Ascent failures

The types of failures that occur during the ascent period are very similar to the launch failures described prior and to the final stage failures described later. The amount of propellant available for thermal energy during abort is rapidly decreasing, and the effect of the high velocity at the time of abort will cause dissemination of the fire from the capsule. The fuel cores will impact at their terminal velocities at distances up to 2000 miles from the point of launch.

The effect of thermal energy released by the detonation of the launch boosters during the ascent portion of the trajectory is not so severe as the same effect during an on-pad abort. This results because the booster is continuously expending its propellant during ascent, and the effects of the velocity and aerodynamic forces would aid in the separation of the generator unit from the resulting fireball.

The aerothermodynamic effect on the generator increases during re-entries following aborts in the latter portion of the ascent phase of the trajectory but never damages the outer shell.

The impulse loads arising from impact against rigid targets have been determined analytically and proof tested by high speed rocket sled tests. The purpose of the tests was to determine the degree of damage and the mode of failure of the specimens. Four target materials were chosen to simulate actual targets on Earth's surface: granite, consolidated and unconsolidated rock, and water. In impact against granite, which is a rigid material, all of the energy is absorbed by the specimen. If the specimens can survive granite impact, the other target media will not cause damage.

Chemical forces exerted on the generator would result from the red fuming nitric acid (IRFNA) used as a fuel for the final stage rocket. The fuel cores could be exposed to the acid upon ground impact after a malfunction during pitch-over or at maximum dynamic pressure. It is inconceivable, however, that the core would lie immersed in a pool of acid

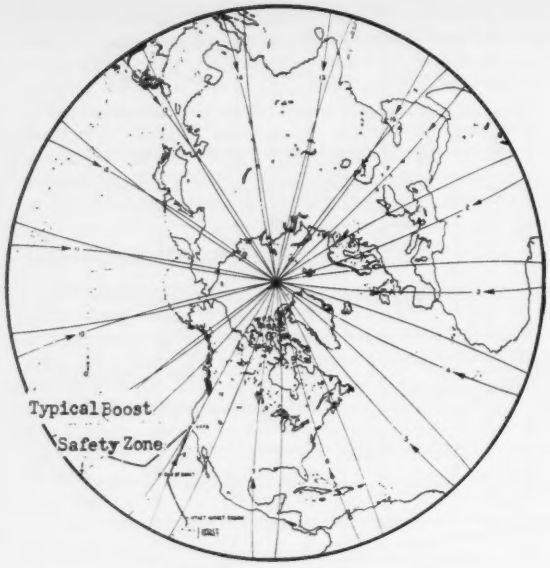

Fig. 6a Snap III impact areas

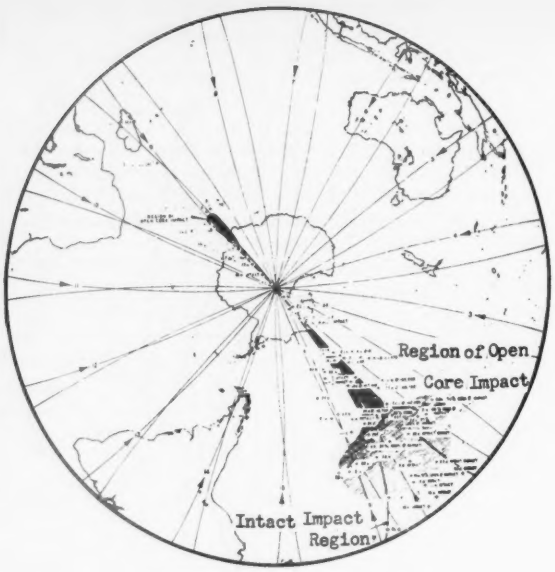

Fig. 6b Snap III impact areas

for any great length of time. In the event of a later abort during ascent, the fuel core would impact on the Pacific Ocean and sink to the bottom. The Haynes 25 outer vessel has a thickness of 0.1875 in. Since the sea water corrosion rate of Haynes 25 is 14.0 mils/yr, more than 13 years will be required for penetration of the first wall. At this time, the activity level of the enclosed fuel will have decreased to a negligible amount. If the penetration of the other two walls is considered, then the time required for fuel release by sea water corrosion is of the order of 25 years.

Final stage failures

Forces imposed on the thermoelectric generator by final stage failure originate from either aerodynamic heating during re-entry or core impact on the surface of Earth. The core is designed to burn up during re-entry from a successful orbit. It is also desired that the core sustain an abort during the launching period and re-enter intact. These design features are not compatible, as there are some re-entries following final stage aborts in which the capsule is completely or partially ablated by aerodynamic heat. Ablation occurs in an area that is far downrange of the launch complex and has essentially a zero population density. The thermal, mechanical, and chemical forces experienced by the generator during this abort period are discussed here. Table 1 summarizes the analytical study of the final stage rocket failures.

The fire resulting from the final stage abort will cause no damage to the fuel core. Thermal forces from propellant fires are most severe during on-pad failure, and it has been shown that the fuel capsule can survive this excursion.

Aerodynamic heating during final stage failure has a wide range of effects on the core material. It is assumed that the generator is released at 375,000 ft during its re-entry. Failure of the final stage to ignite results in an undamaged generator impact near the Equator. The re-entry trajectory and the resulting aerodynamic heating are shown in Fig. 5. This type of failure has the highest probability of occurrence. The fate of the fuel core is dependent on the programmed velocity contribution of the final stage. The initial velocity at final stage is 10,990 fps, too low to induce sufficient aerodynamic heating.

A propulsion failure after 98 sec of final stage thrusting, 83% of the scheduled thrusting period, results in generator melting and partial fuel core ablation. The core is 18% consumed, and the remnant impacts in the South Pacific Ocean, fracturing on contact. A propulsion failure very late in the final stage period, after 96% of the total scheduled thrusting time, results in the complete melting of the fuel core and the initial dispersion of the fuel at an altitude of 147,000 ft.

Guidance failures that cause deflection of the vehicle and/or the rocket line of thrust axis with respect to the velocity vector result in a complete spectrum of conditions. Thirty-two cases of pitch-deflection failure were considered. The time of guidance failure was considered from the point of final stage ignition to near the end of the thrusting period. Of the failures studies, four enter into a short-lived orbit, 10 are completely melted at altitudes above 100,000 ft, two impact after partial burnup, and the remaining 16 impact before any melting occurs.

Failures in the yaw direction result in the widest lateral displacement of the fuel cores or their remnants. Twenty-six cases of such aborts were considered. Of these, six enter into short-lived orbits, 11 are completely melted at altitudes above 100,000 ft, four are partially consumed, and five land intact.

The fuel cores that re-enter intact do not lose their integrity in impact on rigid media at terminal velocity. No aborts occurring during the final stage period result in land impacts. Of the 65 aborts considered, 33 impact on sea water; of these, 25 are not affected by aerodynamic heating. Only eight are partially melted when impact occurs.

The only chemical reaction experienced by the fuel core from a final stage abort is sea water corrosion. It has been described for the aborts that occur during the ascent portion of the trajectory. It was shown that more than 13 years of corrosion will be necessary to completely penetrate the capsule. If the capsule is partially ablated by aerodynamic heating at the time of impact, it either will sink and begin to corrode or will fracture at impact.

Fate of Fuel

Generally, for any mission, the fate of the fuel can be categorized as shown in Table 1.

The re-entry from a successful mission would result in the fuel being ablated and dispersed as molecular particles in the upper atmosphere at an altitude of 228,000 ft. The activity of the Po^{210} would be 356 curies at this time, and 75% of it would be deposited in the Temperate Zone of the hemisphere in which it is released with an 8-month mean residence time; the resultant peak ground concentration would be 0.63 $\mu\mu c/m^2$, and it would occur 146 days after re-entry (6–8). The gamma dose rate in the fallout field corresponding to the peak concentration is 1.3×10^{-7} millirad/hr.

During an aborted mission, the fuel would be: 1) contained after impacting on Earth's surface; 2) dispersed due to partial ablation of the fuel core; or 3) dispersed at high altitudes as aerosols.

Generally, those aborts resulting during the launch or the early part of the ascent trajectory would probably be entangled in the partially breached generator shell. The core would be intact in all cases, precluding contamination of the launch complex and environs.

The design philosophy, requiring either that the fuel core be completely melted and dispersed at high altitude for a postorbital re-entry or that the core return intact following an abort, creates a condition in which the core may be only partially melted at the end of the heating period (at approximately 100,000 ft). This occurs in eight of the cases considered. The fate of the fuel will depend on the degree of damage to the core. A core that has been only slightly affected by ablation will impact and probably fracture on the surface of Earth. In all of these cases, the core lands only on water areas. Local contamination of the sea will result but will be negligible because of the vast amount of water available. A core that is severely but not completely ablated will fail at altitude because of the internal pressure exerted by the encapsulated gases (Po^{210}, He) produced during the natural decay of the element. Fracturing of the core will result in the release of the fuel at the base of the stratosphere. It will disperse throughout the world, but mainly in the hemisphere in which it is released.

Most of the propulsion failures that occur in the final stage thrusting period and the guidance malfunctions result in aerothermodynamic consumption of the core at high altitude. Of the cases considered, 22 are so consumed. The resultant peak ground concentration for an aborted mission and complete burnup at high altitude is 3.86 $\mu\mu c/m^2$. This again assumes an 8-month mean residence time.

These malfunctions are shown on the polar projection map of Fig. 6. Two distinct boundaries are outlined. The first, labeled Intact Impact Zone, is the area in which the generator and/or fuel core will impact and retain the integrity of the core. Superimposed on this zone, and overlapping it just south of the Equator, is the region of Open Core Landing, an area where the fuel core will be partially consumed at impact and will release some of the fuel.

Conclusions

The fate of the polonium fuel for the mission analyzed is clearly defined. The fuel core will maintain its integrity for all launch and ascent failures. Those failures where the generator lands on Earth or in shallow water would be recovered. Impact in deep water would be an ideal resting place for radioactive materials during their decay.

Failures during final stage operation would result in all spectrum of cases. Of 65 cases analyzed, 25 of these resulted in an intact landing, 8 in partial ablation, 22 in complete ablation, and 10 entered in a low altitude orbit. In the latter three categories, the polonium release was shown to be negligible.

It is concluded that the consequences of the use of Snap III generators for space missions would present a tolerable radiological safety program and thus be acceptable for operational use.

References

1 Hagis, W., "Final Safety Analysis Report for Snap III Generator," The Martin Co., *MND-P-2364*, June 1960.

2 Dix, G. P., "Preliminary Operational Hazards Summary Report for the Task 2 Generator," The Martin Co., *MND-P-2184*, December 1959.

3 Dix, G. P., Dobry, T. J. and Guinn, P., "Snap III Thermoelectric Generator Radiological Safety Analysis," The Martin Co., *MND-P-2515*, February 1959.

4 Dobry, T. J. and Guinn, P., "Snap III Thermoelectric Generator Safe Handling Procedures," The Martin Co., *MND-P-2514*, April 1959.

5 Broadview Research Corp., "An Investigation of the Integrity of Certain Test Assemblies Under Missile Failure Forces—Explosive Shock, Temperature and Oxidation Test Program," *RD-58-2, 1035-9*, July 1958.

6 Joint Committee on Atomic Energy, *Fallout from Nuclear Weapons Tests*, August 1959.

7 Arnold, J. R. and Martell, E. A., "The Circulation of Isotopes," *Scien. Amer.*, vol. 201, no. 3, September 1959.

8 Eisenbud, M., private communication, New York Univ., Inst. of Industrial Medicine, May 16, 1960.

Water Impact of Manned Spacecraft

WILLIAM H. MUELLER[1]
JAMES L. MALAKOFF[2]

Grumman Aircraft Engineering Corp.
Bethpage, N. Y.

A state of the art study of the rough water impact of manned spacecraft is presented. The theoretical NASA approach for rotationally constrained, prismatic bodies impacting smooth water is expanded to account for the behavior of a pitching, nonprismatic vehicle penetrating rough water. Two re-entry vehicles are considered. With one, the final descent is by parachute, whereas the second impacts after a subsonic glide. Results are shown for both impacting in a sea state 4 environment. For each, normal load factors and rotational accelerations are presented for variations in speed, descent path, and initial attitude. The trends indicated by this approximate method show the parachute vehicle better suited for rough water landings. Comments are made on the feasibility of alleviating the glider impact by precontact maneuvers or additional landing devices.

Presented at the ARS Lifting Reentry Vehicles: Structures, Materials and Design Conf., Palm Springs, Calif., April 4–6, 1961.

[1] Structural Methods Engineer.

[2] Structural Methods Engineer.

SUCCESSFUL completion of manned missions into space, of necessity, require safe re-entry and landing. There is a great possibility, whether through design or mishap, that the landing may occur in water. Of prime consideration in this final phase of the re-entry operation is the absolute need for a humanly tolerable environment. Such an environment cannot be assured without adequate knowledge of the consequences of water impact. In order to obtain a first approximation of these consequences, an analysis was undertaken using presently available state of the art methods. These methods were originally developed for smooth water landing of seaplanes with rotationally constrained, prismatic hulls. Certain broad assumptions were required in order to use these methods in the investigation of rough water impact of a tapered, nonprismatic, pitching re-entry vehicle. These are discussed in the Appendix. As test data become available, the effects of these assumptions will be appraised.

Basically, two modes of water impact can occur, both different in the body shape presented to the water and the depth of the subsequent penetration. In one mode, penetration similar to seaplane impact is made with a long knifelike body. The other is a spearlike, plunging penetration that results in deep immersion. In the latter case, any forward motion of the body relative to the water caused by surface wind or wave motion can initiate a tumbling action. This tumbling instability at the initial impact could cause a subsequent impact to occur at an unfavorable body attitude. In this paper only the seaplane type of approach is considered.

The spacecraft's impacting surface may be clean or may include landing aids, such as skis. Since any aid would increase mechanical complexity, add weight, and introduce still another design requirement for the ablation shield, it would be advantageous to land the vehicle on the ablation shield itself. This analysis considers the case of a lifting re-entry vehicle impacting the water directly on the heat shield.

The final stage of flight may be either by parachute, which induces a high angle descent path with little or no directional controllability, or by a lifting glider, with a low angle descent path and limited directional control. Impact of both configurations is investigated for a variety of flight paths and initial trim attitudes.

A feature considered essential in this investigation is the inclusion of sea wave effects. Except for a few smooth water cases, all results are for impacts into a wave environment.

Table 1 Assumed body parameters

Item	Parachute descent vehicle	Lifting glider vehicle	
W, lb	10,000	10,000	
I, slug-sq ft	1,400	3,000	
a, ft	2.333	2.25	
b, ft	3.917	4.00	
Overall length, ft	11.415	13.11	
Beam at step, ft	10.00	8.5	
$C_{L_{max}}$	0	1.0	at 20°
C_M	0	0	
β, deg	15	10	

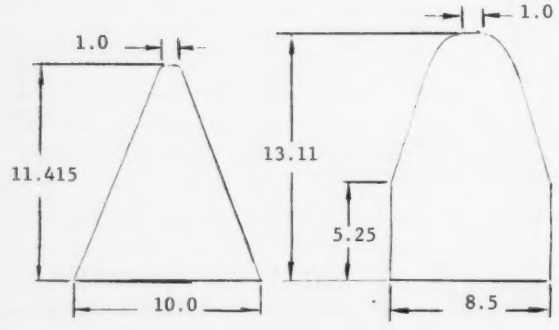

Fig. 1 Vehicle planforms; dimensions, ft. Left: parachute descent vehicle. Right: lifting glider vehicle

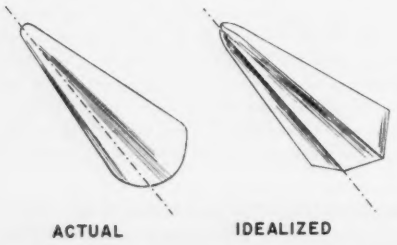

Fig. 2 Conical lifting re-entry vehicle

Analysis

Most published hydrodynamic impact theories consider penetration into initially undisturbed water. As displacement occurs, water is assumed to flow in a two-dimensional fashion within transverse planes. Since these methods were generated to accommodate seaplane hulls, where little change in shape occurs at the impact section, the impacting body is normally considered prismatic. For this type of hull, with large inertial resistance to rotation and short elapsed time to peak impact loads, the common assumption is that trim attitude remains fixed during impact.

Consistent with these assumptions, the water flow planes were oriented normal to the keel and fixed in space. As these planes are penetrated by the impacting body, a momentum exchange occurs between the displaced water and the body. The force between the water and the body was assumed dependent on the rate of change of the water momentum. A modification, based on aspect ratio, is normally made for the three-dimensional flow effects. This correction is required to account for the momentum contained in flow planes that have become part of the wake.

The assumption that attitude change does not occur is quite permissible in seaplane landings, whereas the compact design and size of lifting re-entry vehicles introduces a very small mass rotational inertia and necessitates the consideration of rotational freedom.

To obtain a consistent definition of that portion of water to which the body momentum is transferred (water virtual mass), most methods resort to assumptions that are functions of body shape. A large amount of published data is available for V-shaped prismatic hulls. Although the spacecraft envisioned will actually have conical or slightly curved ablation shields, these shapes were approximated in the transverse direction by V-wedges. Fair correlation with test of such an approach is shown in (5).[3] The use of a prismatic shape longitudinally is unrealistic for short stubby spacecraft. The longitudinal characteristics of the impacting surface are therefore accounted for by finite changes in curvature and tapering

[3] Numbers in parentheses indicate References at end of paper.

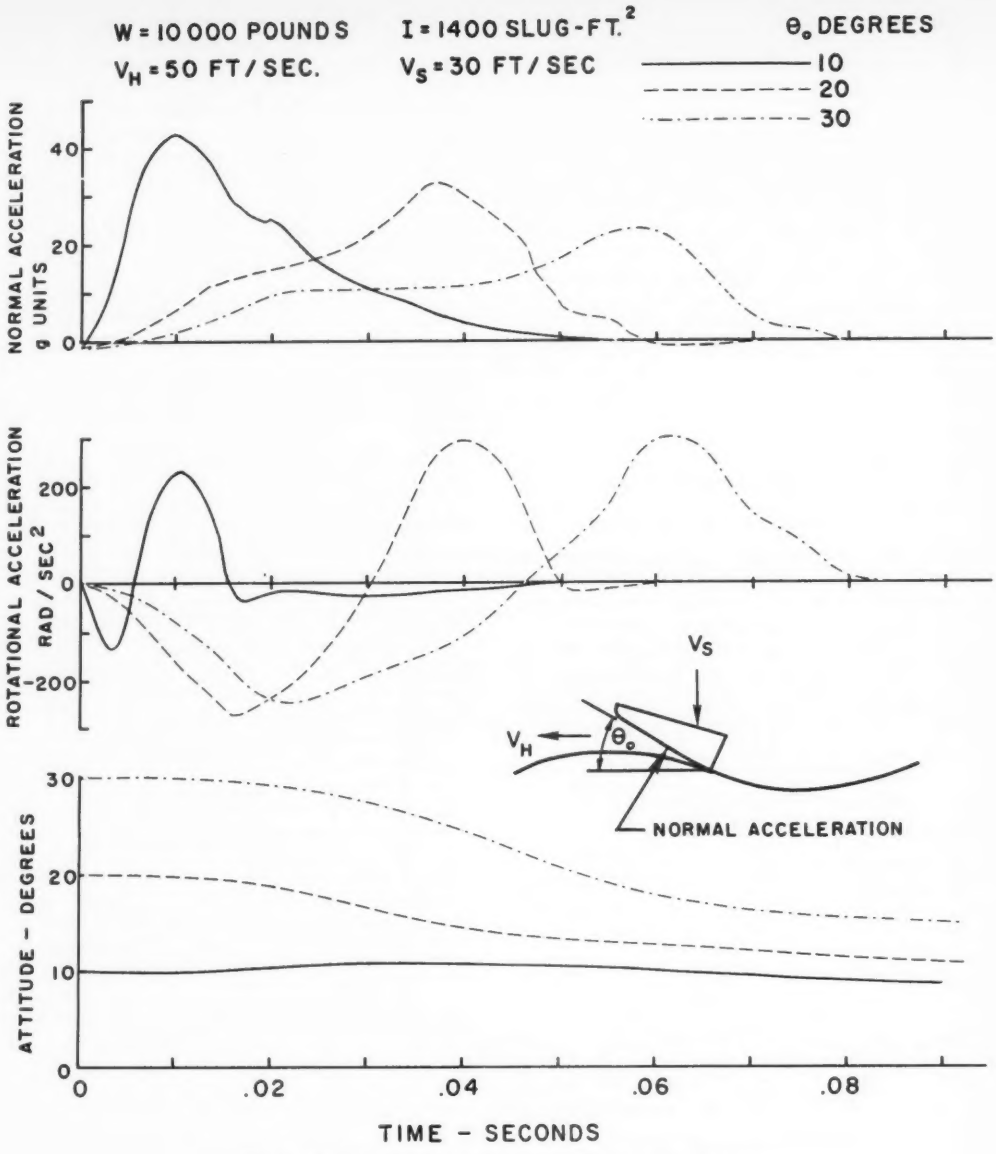

Fig. 3 Sample time histories for parachute descent impact

planform.

Sea state effects were introduced by allowing the normally smooth surface of water to assume a distance and time-dependent shape. For simplicity, sinusoidal waves with water particle motion were chosen, the characterizing parameters being crest to trough height and wavelength.

Aerodynamic lift and moment forces are included to represent adequately the lifting glider configuration. The omission of the aerodynamic drag force is consistent with the assumption that the water load includes no viscous effect.

A consistent set of results may be obtained for rough water impact of a variety of re-entry vehicles by applying the method presented in the Appendix. As shown, the method modifies existing approaches such that finite length, curved keels, and rotational motion are accounted for during impact in waves. The analysis shows excellent agreement with smooth water theories for both fixed and free to trim methods (2, 4). However, the results to be presented use models for which no experimental verification is presently available.

The applicable detailed description of the tractable mathematical model defining the body shape, virtual mass, and wave motion is shown in the Appendix. Also found in this section are the equations of motion, the solution of which provides the results to be presented.

Results

All results shown, unless otherwise noted, are for sinusoidal waves of trough to crest height of 8 ft. This height represents the average height of the one third highest waves of an environment classified as sea state 4 (6). To obtain comparable values for wave impact, the wavelength to height was maintained at 20 to 1. This was altered only when wavelength effect on load factor was desired. Although it is severe, all

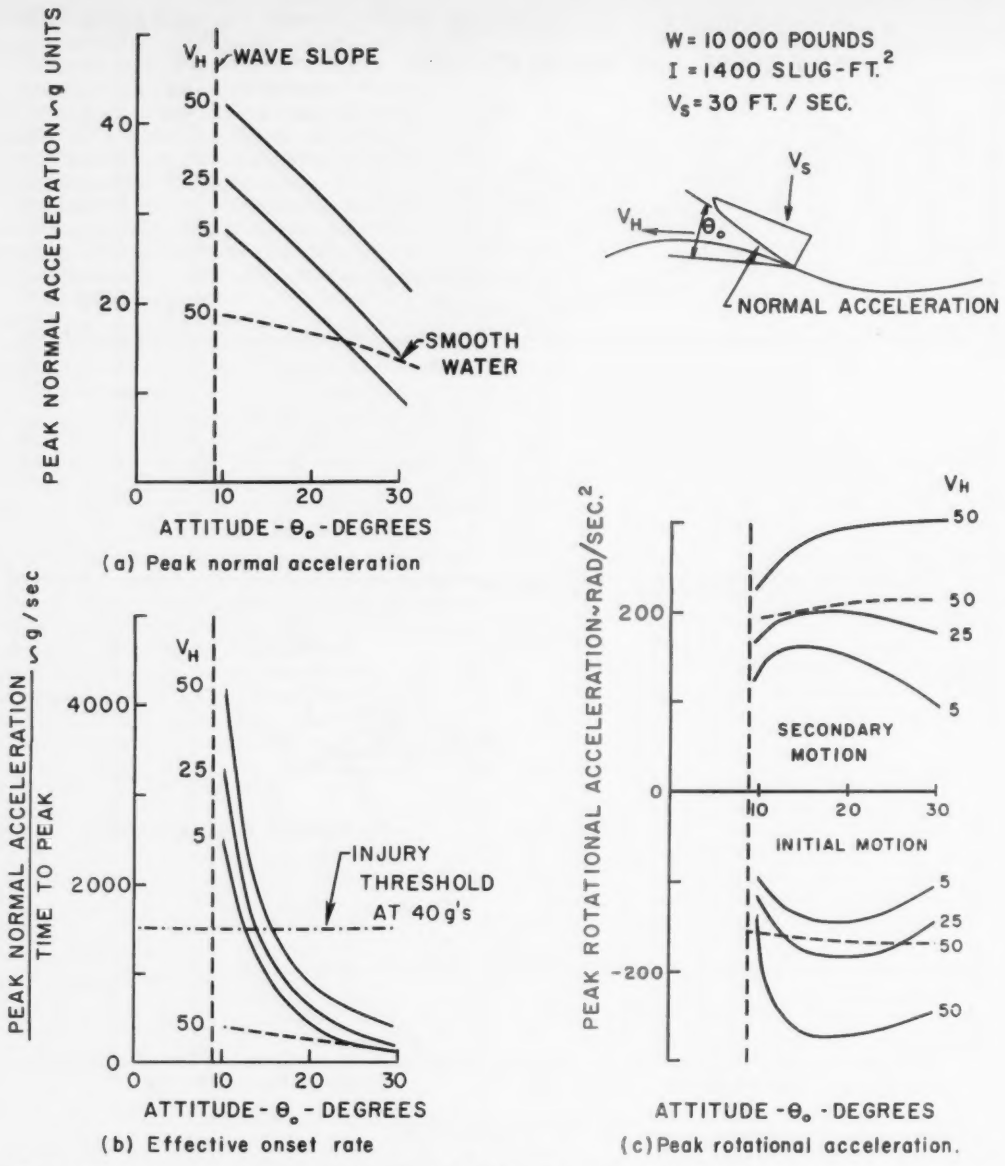

Fig. 4 Effects on parachute descent vehicle accelerations for variations in impact attitude and horizontal velocity

impacts, for which curves are presented, consider that vehicle contact occurs at the midpoint of the flank of an oncoming wave.

Two configurations are involved in the present analysis. A comparison of some of their assumed body parameters is shown in Table 1 and Fig. 1. For each, a series of results was obtained for various initial conditions at water contact that essentially describes the descent path and attitude of the vehicle.

Parachute Descent Vehicle

The parachute type of vehicle investigated was representative of the conical capsule variety. An idealization was made of the M2 shape (Fig. 2), which was consistent with the required mathematical model. As shown, the conical lower surface was considered to be a V-bottom with a 15° deadrise angle (angle between surface and horizontal). Except for longitudinal curvature at the nose, the keel remained straight. In order that the idealized width of the re-entry vehicle not exceed the actual width, the V-bottom was terminated at the actual width. The locus of the V-bottom termination produced the chine line.

The results for this modified M2 re-entry vehicle are shown in Figs. 3–5. In all instances, the initial trim was not allowed to decrease to the point where the nose portion was the first to impact the water, and no aerodynamic forces were considered to be acting after contact.

Typical time histories of normal load factor, rotational acceleration, and attitude are shown in Fig. 3. These results are for a constant flight path with variations in initial trim attitude. The horizontal velocity of 50 fps is representative of severe surface winds. The curves indicate that at low trim,

where the greatest portion of the body contacts the water in the shortest time, the largest normal load occurs. However, at greater initial attitudes, although a reduction of peak impact occurs, the larger time to peak causes greater rotational effects, as the lower grids of Fig. 3 indicate. These rotational effects ultimately cause the body to pitch nose down, and thus a greater surface contacts the water. Since this contact occurs at a lesser body sink speed, a much reduced normal acceleration results.

Fig. 4 presents the trends indicated by a series of parachute descent impacts at a constant sink speed. The variations considered were in forward speed and contact attitude. Pendulum action, while suspended from the parachute, could induce attitude and forward velocity changes prior to contact. Additional velocity effects can be caused by surface wind. On each curve of Fig. 4, impacts into smooth water at the highest forward speed are shown for comparative purposes. This type of impact is equivalent to landing parallel to a wave crest.

The variation in peak normal acceleration is shown in Fig. 4a. The curves indicate that an increase in load factor will accompany an increase in forward speed and a decrease in initial attitude. Note the large increase over the smooth water trends caused by impacting a wave. It must be remembered that these loads act on the vehicle primary structure, and the effects on the occupants may be attenuated by cushioning. However, to insure that attenuation occurs, structural integrity for these loads must exist.

Along with the magnitude of load a human can tolerate, the duration and rate of buildup of this load are also of extreme importance. As seen in Fig. 3, the duration of the load is no more than 10 millisec. Fig. 4b presents an effective buildup or onset rate which accompanies the accelerations shown in Fig. 4a. The variation of this rate with forward speed and contact attitude is similar to that of the peak accelerations. One startling difference is evident, that is, the rapid increase in this rate as trim decreases below 20°. At contact attitudes above 20° the predominant effect is produced by changing forward speed. For reference purposes, a commonly quoted injury threshold rate is shown (11). For the vehicle in question, indications are that for contact attitudes above 15° this configuration does not undergo rates beyond human tolerance.

Accompanying the translational effects discussed above are the rotational accelerations shown in Fig. 4c. These large accelerations are caused by the small inertial resistance to rotation. It is evident that an increase in forward speed causes an increase in both the initial nose-over rate (negative acceleration) and subsequent dynamic nose-up motion due to slamming. As can be seen in this figure, the peak accelerations maximize at an intermediate value of initial attitude. For the low trim condition, the rate of buildup of the hydrodynamic load is rapid, and it is distributed along a greater length of keel, inducing low rotational rates. However, at the intermediate trim attitudes, wave size and speed apparently caused the greatest rotational acceleration for this particular configuration. This is evident when compared with the smooth water results, where a decrease in initial attitude decreased the peak rotational acceleration. It is understood that these rotational rates can be tolerated by humans, since they are not accompanied by large angular displacements (in the order of complete revolutions). They would undoubtedly cause portions of the body to undergo intense local translational accelerations.

All the results shown in Figs. 3 and 4 were for a single wave height, length, and point of impact. In any sea state, the wavelength and waveheight are independent. The assumed characteristic wave of sea state 4 was varied in wavelength, and Fig. 5 presents the effect on peak normal acceleration of this variation. As the crest to crest distance decreases, the impact becomes more severe. This is primarily due to the increase in wave slope at the point of impact. The effect becomes pronounced at less than 20 to 1 length to height ratios. A ratio of 7 to 1 is a commonly accepted minimum, below which wave crests cannot be maintained.

Although the most adverse conditions for wave landing were considered, several impacts were made to note the effects of landing in a following sea or at various locations in an oncoming sea. For an impact with the initial conditions of the severest case shown in Fig. 4 (V_H = 50 fps, θ_0 = 10°), but occurring in a following sea, a reduction of peak normal acceleration from 43 to 25 g was realized. An even greater reduction occurred when the vehicle impacted an oncoming wave on a retreating flank. The wave slope and vehicle trim produce the greatest angular difference for this condition. Such an impact produced only 10 g compared with the previously mentioned values.

Lifting Glider Vehicle

The second re-entry vehicle investigated was a lifting glider that achieved a low, flat descent because of its subsonic aerodynamic capabilities. This type of descent is possible, as shown in the power-off landing techniques of (7). Fig. 6 shows a typical model of such a glider and the idealization used for water impact. Because of the very noticeable lack of transverse curvature, only 10° of deadrise was considered for this idealized V-bottom. However, in contrast to the conically shaped vehicle, almost the entire keel length was given longitudinal curvature. Once again a chine line was established to control the extent of the body width. The results of water impact of this vehicle are shown in Figs. 7 and 8. Notice that on both figures impacts occurred where initial trim was

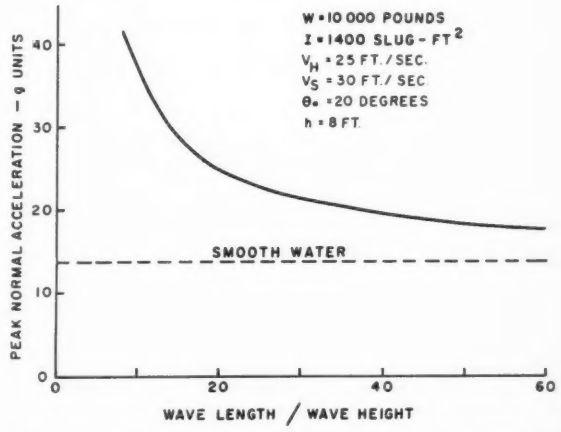

Fig. 5 Variation of peak normal acceleration with wavelength for parachute descent vehicle

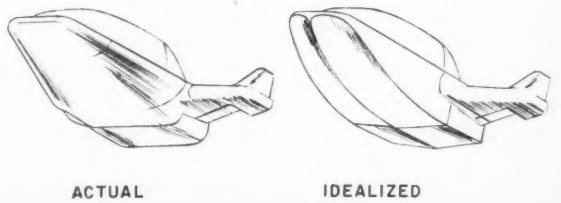

Fig. 6 Lifting re-entry glider

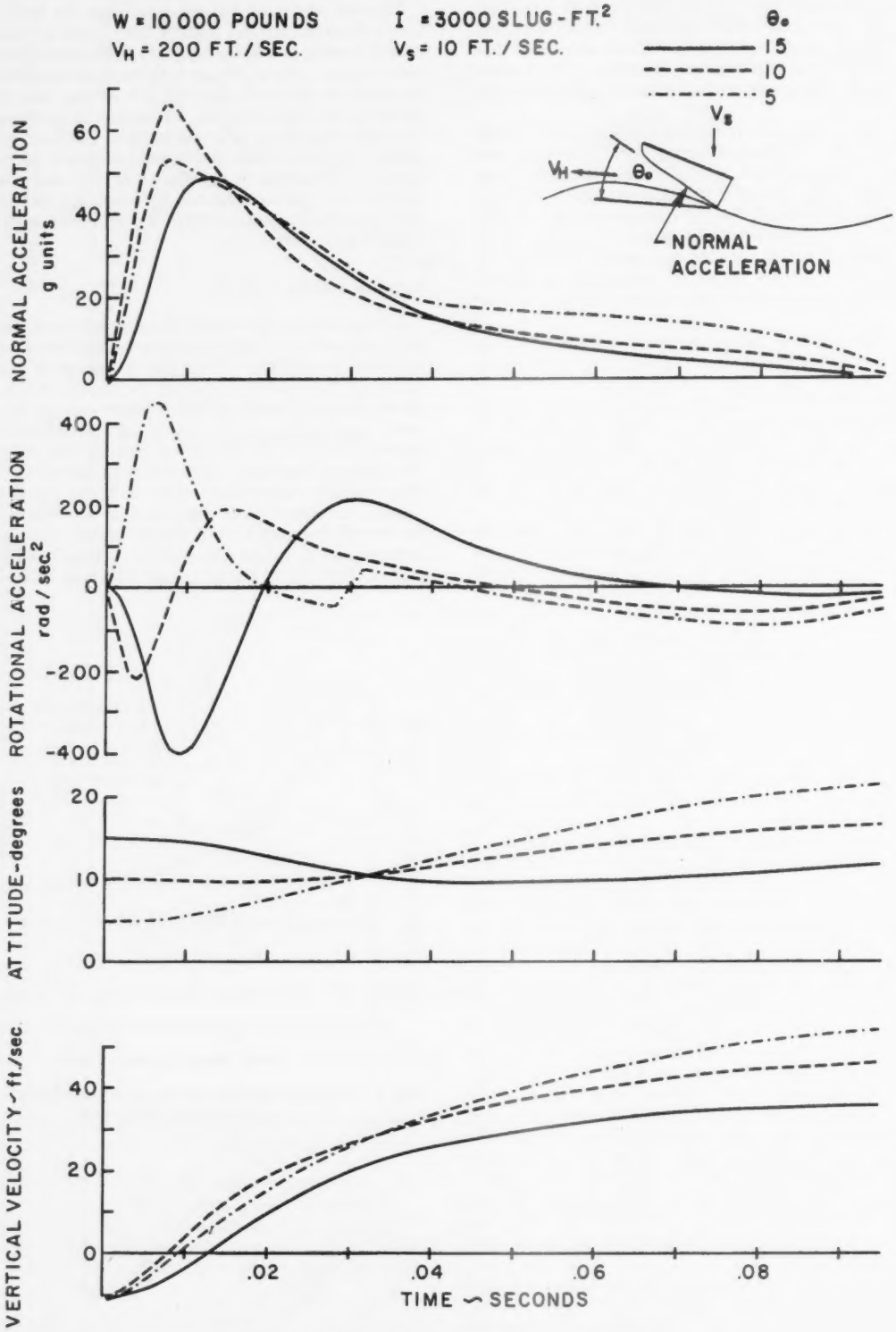

Fig. 7 Sample time histories for glider descent impact

less than the wave slope, since the keel longitudinal curvature prevented nose-first plunging. For each impact, aerodynamic lift acted throughout the period of water contact. The aerodynamic characteristic used was modeled after studies shown in (8).

Time histories of a series of typical impacts for the glider vehicle are shown in Fig. 7. These results are for three landings with different initial attitudes and a constant glide path. Besides presenting normal and rotational acceleration and attitude, vertical translational velocity is shown. It is apparent that at some low angle of initial trim the greatest normal acceleration occurs. In contrast to the trends indicated in Fig. 3, an increase in attitude does not appreciably increase the time to peak. This is directly attributable to immersing with severe forward velocity. Except for the low angle impact where bow contact occurred first, the initial tendency is for severe nose-down rotational accelerations with nose-up righting accelerations subsequently occurring. On the third grid of Fig. 7, attitude changes with time are shown. In each case, the initial effect of impact was to cause rotation towards the wave slope angle, 8.9°, followed by a subsequent increase from this position to a higher angle as the hull progresses up the wave flank. The translational vertical velocity is shown in the lowest grid of Fig. 7. The trends in all instances indicate the large rebound tendencies of a high forward speed impact. This may be attributed to the vertical force generated on the body by forward motion through the water. This force greatly exceeds that required to stop the initial sinking speed.

The effects of variations in initial trim attitudes and sink speeds on peak normal, longitudinal, and rotational accelerations for the constant forward speed lifting re-entry glider are shown in Fig. 8. These variations are caused by vehicle pitch control. For comparative purposes, impacts into smooth water at a 10-fps sink rate are shown.

Fig. 8a, peak normal accelerations, shows a definite increase for increased sink speeds. Decreasing trim has this effect also, until severe bow impact occurs at very low trim angles. In the bow impact range, a decrease in load for a decrease in trim is evident. However, regardless of the attitude or sink speed, the magnitudes of these rigid body accelerations are awesome.

The corresponding longitudinal acceleration caused by penetration of the curved keel is shown in Fig. 8b. An increase in sink speed and a decrease in initial trim cause an increase in the peak longitudinal acceleration. The more severe rate of increase at the lower attitudes is caused by the earlier immersion of the bow.

The rotational effects, in the form of accelerations, are presented in Fig. 8c. For the anticipated glide paths of this vehicle, decreases in trim angle result in a decrease in peak negative rotational accelerations if the attitude is above that of the wave slope. However, at smaller trim angles the acceleration is positive as bow impact occurs; trim reduction at these low angles causes an increase in positive acceleration. Depending on the attitude at contact, the initial acceleration is positive nose-up or negative nose-down. Secondary rotational accelerations that occur are opposite in direction to those of the initial accelerations and exhibit essentially the same variations with trim at reduced magnitudes.

Concluding Remarks

This investigation of the consequences of water landing of a lifting re-entry vehicle indicates that the sea is a hostile environment. However, for vehicles with no auxiliary landing devices, rough water landings following a parachute descent appear to be humanly tolerable. If, either by chance or control, impact occurs in a following sea, at a better position in an oncoming sea, or parallel to a wave crest (smooth water), the impact load factors and onset rates are reduced.

This type of control seems more possible in the lifting glider configuration. However, two basic items concerning the water impact of such a vehicle in rough seas must be overcome. First, landing devices must be used to minimize the impact load factor, and second, some stabilizing components must be found to restrict or preferably eliminate rebound.

The consequences of the assumptions made to use presently available hydrodynamic theory to obtain a first approximation of impact effects have not been appraised. This evaluation will be made as experimental data become available. In any event, the load factors and accelerations as shown throughout this paper are for a rigid vehicle. These would undoubtedly be reduced by energy absorbing structure between the impacting ablation shield and the inner stucture. Further attenuation of the loads and motions felt by the occupants could occur by means of their support system.

Since the possibility of water impact exists for manned re-entry vehicles, the investigation should be continued using other approaches to the problem. In this regard, impacts with deep plunging penetrations or with auxiliary landing devices should be examined.

Of prime importance in any re-entry landing is the safety of the occupants. To provide this safety, internal support systems must be considered. Analysis of these more complex configurations should be developed until the severity of water impact is reduced to tolerable levels.

Appendix

The analytic model for water impact is shown in Fig. 9. The forces considered in this three degree of freedom system are indicated in Fig. 9a.

Aerodynamic Forces

With the aerodynamic parameters C_L and C_M assumed measured at the body center of gravity and functions of the angle of attack, the aerodynamic forces become

$$L = (1/2)\rho_A[(\dot{X} - V_{SW})^2 + \dot{Z}^2]S_L C_L$$

$$M_a = (1/2)\rho_A[(\dot{X} - V_{SW})^2 + \dot{Z}^2]S_L C_M C$$

where

$$\alpha = \theta + \alpha_W - \gamma_W$$

and

$$\tan \gamma_W = \dot{Z}/(\dot{X} - V_{SW})$$

Aerodynamic drag is considered negligible during impact.

Hydrodynamic Forces

The theory discussed in (1–3) is based on the concept that flow occurs in transverse planes that are fixed in space and oriented normal to a straight keel. Fluid motion in each plane is treated separately, independent of other planes. This two-dimensional effect, when summed over the entire immersed surface and corrected for end losses, yields the total penetration resistance. For this type of fluid motion, all viscosity effects are assumed negligible.

In the analysis which follows, the same general concepts are considered with several exceptions:

1 Flow planes are allowed to rotate about instant centers, located at the intersection of the flow plane and the keel. These planes remain normal to the keel while it rotates but do not translate in space along the line of the keel. This assumption is the basis of the method outlined in (4).

2 In contrast to (4), the present analysis does not consider all flow planes parallel, since longitudinal curvature of the keel exists. It has been assumed that this overlap of planes causes no loss or increase in the reaction within a plane. Such an approach has been used in an impact investigation of boat hulls (10).

3 Although the transverse body plane is considered V-

shaped, as in the above references, it is not prismatic; the effect of the additional three-dimensional flow caused by taper has been neglected.

4 The undisturbed water surface is considered to be sinusoidal in shape with fluid particle motion.

The body and spacial geometry for a single idealized flow plane is shown in Fig. 9b.

Virtual mass concept

The hydrodynamic impact force exerted by a single flow plane is considered to be dependent on the rate of change of momentum of an associated virtual water mass (1-3)

$$F_{\text{imp}i} = \Phi(A) S_i \frac{d}{dt} [m_{wi} \dot{\xi}_i]$$

The associated water mass m_{wi} for V-bottom shapes is (2)

$$m_{wi} = (\pi/2)\rho_w[(\pi/2\beta_i) - 1]^2 \xi_i^2$$

This expression is considered applicable until the chines be-

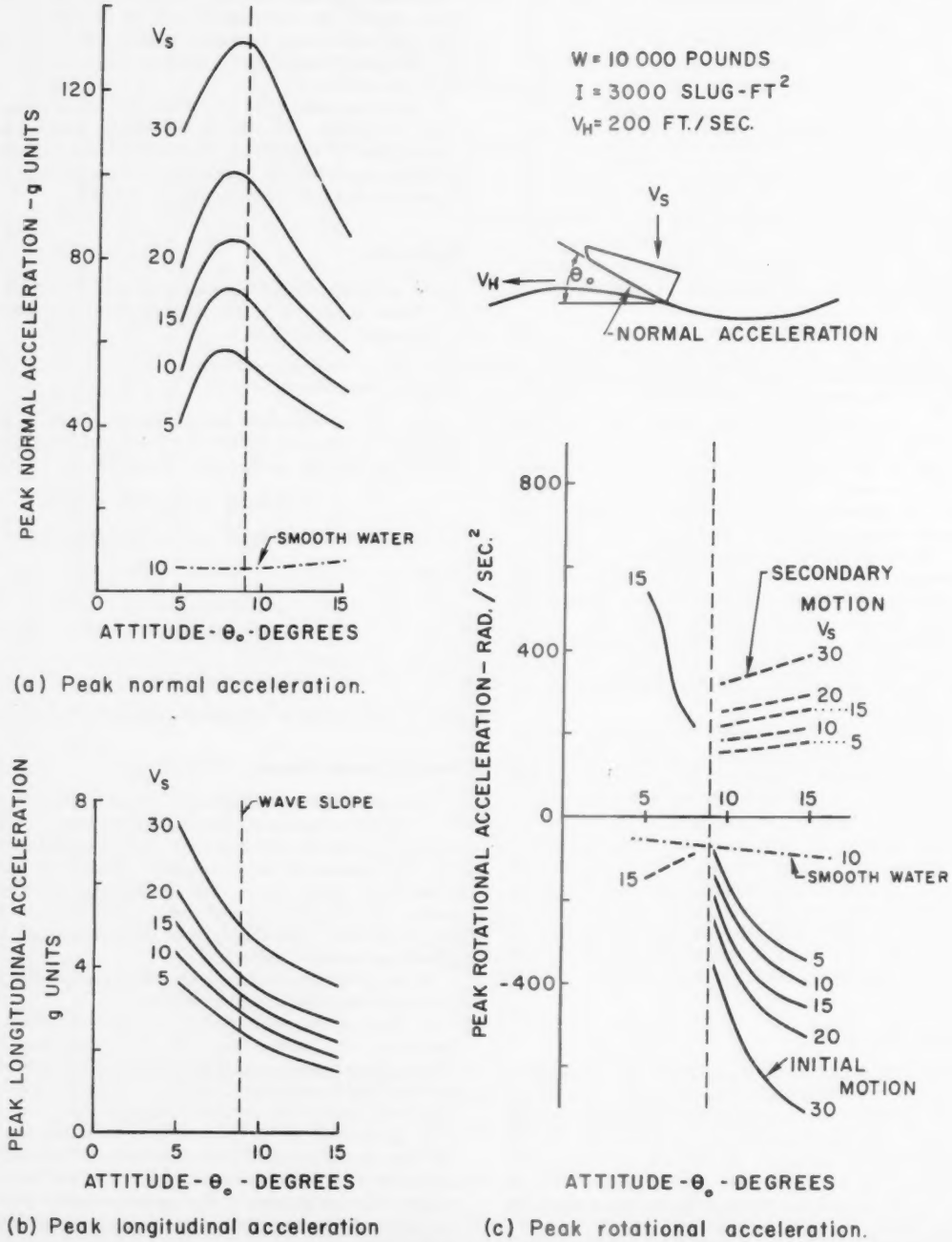

Fig. 8 Effects on glider descent vehicle accelerations for variations in impact attitude and vertical velocity

come immersed, i.e.

$$\xi_i = z_{CH_i}$$

At greater immersions the virtual mass is altered to account for chine immersion (3)

$$m_{w_i} = B_i \rho_w z_{CH_i}(\xi_i - z_{CH_i})/\tan \beta_i + (\pi/2)\rho_w[(\pi/2\beta_i) - 1]^2 z_{CH_i}^2$$

The three-dimensional correction factor $\Phi(A)$, required because the immersing body passes through the flow planes, is based on aspect ratio and is attributed to Pabst (3). Where

$$A = \frac{[\sum S_i]^2}{\sum l_i S_i}$$

and

$$l_i = 2K_i/\tan \beta_i$$

Depth K_i is dependent on the degree of immersion. The water rise factor used to obtain this depth is based on that used in (2). For $0 \leq \xi_i \leq z_{CH_i}{}^*$

$$K_i = \xi_i \tan \beta_i[(\pi/2\beta_i) - 1]$$

and for $z_{CH_i}{}^* < \xi_i$

$$K_i = z_{CH_i}$$

Waves

The undisturbed free water surface is assumed to be sinusoidal. The time-dependent space coordinate, velocity, and acceleration characteristics of the wave are as follows:

$$z_{w_i} = -(h/2) \sin \Omega_i$$

$$\dot{z}_{w_i} = -v \cos \Omega_i$$

$$\ddot{z}_{w_i} = (2\pi/\lambda)vc \sin \Omega_i$$

$$\dot{x}_{w_i} = v \sin \Omega_i$$

$$\ddot{x}_{w_i} = (2\pi/\lambda)vc \cos \Omega_i$$

where

$$v = \pi hc/\lambda$$

$$\Omega_i = (2\pi/\lambda)(x_i + ct)$$

$$c = \sqrt{g\lambda/2\pi}$$

with the local wave slope

$$\epsilon_i = \tan^{-1}[-(h\pi/\lambda) \cos \Omega_i]$$

Immersion depth, velocity, and acceleration

The net immersed depth, as shown in Fig. 9b, is dependent on hull and wave position.

$$\xi_i = (z_{w_i} - z_i)[\cos \epsilon_i/\cos [(\tau_i + \theta) - \epsilon_i]]$$

The velocity of immersion is

$$\dot{\xi}_i = (\dot{X} - \dot{x}_{w_i}) \sin (\tau_i + \theta) - (\dot{Z} - \dot{z}_{w_i}) \cos (\tau_i + \theta) + \dot{\theta}[(a - z'_i) \sin \tau_i + (b - x'_i) \cos \tau_i]$$

with a corresponding acceleration

$$\ddot{\xi}_i = \ddot{X} \sin (\tau_i + \theta) - \ddot{Z} \cos (\tau_i + \theta) + \ddot{\theta}[(b - x'_i) \cos \tau_i + (a - z'_i) \sin \tau_i] + \dot{\theta}^2[(b - x'_i) \sin \tau_i - (a - z'_i) \cos \tau_i] - (2\pi/\lambda)vc \sin [(\tau_i + \theta) - \Omega_i]$$

Equations of motion

As indicated in Fig. 9a, only three degrees of freedom exist, and the force equilibrium for these motions may be written

$$(W/g)\ddot{X} + L \sin \gamma_w + F_{hydX} = 0$$

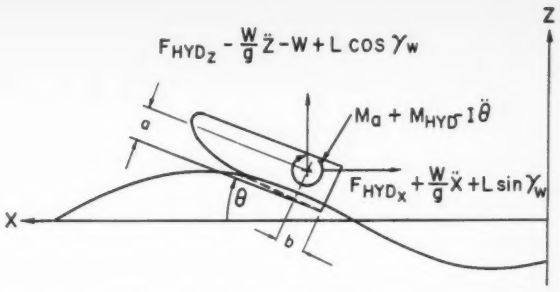

Fig. 9a Analytic model for water impact; external forces

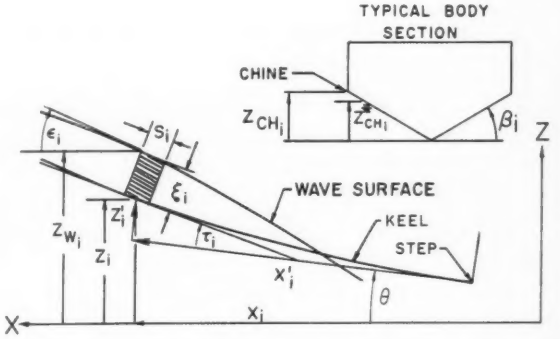

Fig. 9b Analytic model for water impact; idealized flow plane

$$(W/g)\ddot{Z} - L \cos \gamma_W + W - F_{hydZ} = 0$$

$$I\ddot{\theta} - M_a - M_{hyd} = 0$$

Eliminating F_{hydX}, F_{hydZ}, and M_{hyd} by incorporating the expression for virtual water mass, the equations of motion can be written as follows:

$$\begin{bmatrix} A_{ij} \end{bmatrix} \begin{bmatrix} \ddot{X} \\ \ddot{Z} \\ \ddot{\theta} \end{bmatrix} = \begin{bmatrix} F_i \end{bmatrix}$$

where

$$A_{11} = W/g + \Phi(A) \sum m_{w_i} \sin^2 (\tau_i + \theta)$$

$$A_{12} = A_{21} = -\Phi(A) \sum m_{w_i} \sin (\tau_i + \theta) \cos (\tau_i + \theta)$$

$$A_{13} = A_{31} = \Phi(A) \sum m_{w_i} d_i \sin (\tau_i + \theta)$$

$$A_{22} = W/g + \Phi(A) \sum m_{w_i} \cos^2 (\tau_i + \theta)$$

$$A_{23} = A_{32} = -\Phi(A) \sum m_{w_i} d_i \cos (\tau_i + \theta)$$

$$A_{33} = I + \Phi(A) \sum m_{w_i} d_i^2$$

and

$$F_1 = -L \sin \gamma_W - \Phi(A) \sum Q_i \sin (\tau_i + \theta) + \sum f_{bi} \sin (\tau_i + \theta)$$

$$F_2 = -W + L \cos \gamma_W + \Phi(A) \sum Q_i \cos (\tau_i + \theta) + \sum f_{bi} \cos (\tau_i + \theta)$$

$$F_3 = M_a - \Phi(A) \sum Q_i d_i - \sum f_{bi} d_i$$

where

$$Q_i = m_{wi}\{-(2\pi/\lambda)vc \sin (\tau_i + \theta - \Omega_i) + \dot{\theta}^2[(b - x'_i) \sin \tau_i - (a - z'_i) \cos \tau_i]\} + \dot{\xi}_i(dm_{wi}/dt)$$

$$d_i = [(b - x'_i) \cos \tau_i + (a - z'_i) \sin \tau_i]$$

The terms m_{wi} and dm_{wi}/dt must be the appropriate expression concerning each body station i with regard to chine immersion. The buoyant force f_{bi} in each plane is assumed to act at and normal to the keel and may be expressed as

$$f_{bi} = \rho_w g S_i \xi_i^3/\tan \beta_i \qquad 0 \leq \xi_i \leq z_{CHi}$$

or

$$f_{bi} = \rho_w g S_i[(2\xi_i - z_{CHi})z_{CHi}/\tan \beta_i] \qquad z_{CHi} < \xi_i$$

For these equations, the following criteria are used concerning water load:

1 If ξ_i is negative, $F_{hydi} = 0$.

2 If ξ_i is positive, but $\dot{\xi}_i$ is negative, $F_{hydi} = f_{bi}$.

3 If ξ_i is positive, $\dot{\xi}_i$ is positive, F_{hydi} is as appears in the equations of motion.

Nomenclature

W = weight
I = mass rotational inertia
x' = position on keel forward of step in body reference system
z' = position on keel above step in body reference system
x = forward position in space reference system
z = vertical position in space reference system
β = deadrise angle
τ = local keel angle relative to keel at step
z_{CH} = height above keel of chine, normal to local keel
z_{CH}^* = depth of penetration at which chines become wet due to water rise
a = distance between step and center of gravity, normal to keel at step
b = distance between step and center of gravity, parallel to keel at step
S = thickness of hull increment
C_L = aerodynamic lift coefficient
C_M = aerodynamic moment coefficient
C = mean aerodynamic chord
S_L = effective aerodynamic area
α_W = wing incidence angle to body reference axis
γ_W = angle of relative wind
α = angle of attack
ξ = immersion normal to keel
ρ_A = mass density of air
ρ_W = mass density of water
h = wave height, trough to crest
λ = wavelength, crest to crest
X = forward displacement of vehicle center of gravity
Z = vertical displacement of vehicle center of gravity
m_w = virtual water mass per unit length
ϵ = local wave slope
F_{imp} = water impact force
f_b = bouyant force
θ = angular displacement of vehicle
L = aerodynamic lift force
M_a = aerodynamic moment
F_{hyd} = total water force, $F_{imp} + f_b$
M_{hyd} = total water moment
V_H = horizontal velocity of vehicle
V_S = sink velocity of vehicle
V_{SW} = surface wind velocity
B = Bobyleff coefficient (3)
$\Phi(A)$ = Pabst three-dimensioal flow, aspect ratio correction
$\sum$ = $\sum_n$, where n is the number of flow planes penetrated by the body

Subscripts

i = the ith keel station
X = space axis direction
Z = space axis direction
w = wave

References

1 Mayo, W. L., "Analysis and Modification of Theory for Impact of Seaplanes on Water," *NACA Rep. 810*, 1945.

2 Milwitzky, B., "Generalized Theory for Seaplane Impact," *NACA Rep. 1103*, 1952.

3 Schnitzer, E., "Theory and Procedure for Determining Loads and Motions in Chine—Immersed Hydrodynamic Impacts of Prismatic Bodies," *NACA Rep. 1152*, 1953.

4 Miller, R. W., "Theoretical Analysis of Hydrodynamic Impact of a Prismatic Float Having Freedom in Trim," *NACA TN 2698*, 1952.

5 Edge, P. M., Jr., "Impact-Loads Investigation of Chine-Immersed Model Having a Circular-Arc Transverse Shape," *NACA TN 4103*, 1957.

6 Pierson, W. J., Jr., Neumann, G. and Jones, R. W., "Practical Methods for Observing and Forecasting Ocean Waves by Means of Wave Spectra and Statistics," *U. S. Navy Hydrographic Office Pub. No. 603*, 1955.

7 Bray, R. S., Drinkwater, F. J. III and White, M. D., "A Flight Study of a Power-Off Landing Technique Applicable to Reentry Vehicles," *NASA D-323*, 1960.

8 Ladson, C. L., Johnston, P. J. and Trescot, C. D., Jr., "Effects of Wing Plan-Form Geometry on the Aerodynamic Characteristics of Hypersonic Glider at Mach Numbers up to 9.6," *NASA TM X-286*, 1960.

9 Jagger, D. H., Notess, C. B. and Segel, L., "The Alleviation of Rough-Water Loads on Seaplanes Using Automatic Control Techniques," *Rep. No. TB-1315-F-1*, Cornell Aeronautical Laboratory Inc., June 1960.

10 Jensen, W. R., "Hydrofoil Boat Hull-Wave Impact Loads," *ASME Paper 60-WA-326*, 1960.

11 O'Bryan, T. C. and Hatch, H. G., Jr., "Limited Investigation of Crushable Structures for Acceleration Protection of Occupants of Vehicles at Low Impact Speeds," *NASA TN D-158*, 1959.

Technical Notes

Configuration Efficiency: a New Measure of Ballistic Quality for a Grain Design

R. A. ROSSINI,[1] J. S. BILLHEIMER,[2] and T. R. THREEWIT[3]

Aerojet-General Corp., Solid Rocket Plant
Sacramento, Calif.

The concept of configuration efficiency is introduced as an aid in determining optimum solid rocket propellant grain design. Several applications of this concept illustrate how configuration efficiency is used to evaluate variations in grain design. A correlation between configuration efficiency and propellant loading factor is indicated, although the quantity of available data is insufficient to establish a reliable relationship.

SELECTION of the optimum grain design for a given mission is extremely difficult because of the interaction between many important design parameters. In fact, the interaction of these parameters makes design optimization almost a theoretical goal.

Although many grain characteristics are adaptable to individual consideration, neutrality and minimum sliver (the two characteristics most influential to maximum impulse production) are interdependent. Unfortunately, these parameters have never been quantitatively related; thus there is no way to measure the degree that one parameter could be relaxed to improve the other to obtain the best possible performance for the specific mission and environment of operation. Qualitative evaluation of performance data without a correlation between neutrality and sliver cannot lead to an effective method of grain design optimization. This paper proposes a new grain parameter to satisfy this need.

Configuration Efficiency: Definition and Analytical Development

Configuration efficiency is defined as the ratio of actual total delivered impulse at action time to the ideal impulse produced if all of the original propellant is burned to deliver a constant maximum pressure, equivalent to the maximum pressure actually experienced, and expended through a nozzle with an optimum expansion ratio. By means of this definition, configuration efficiency becomes a measure of the losses that accrue as a result of deviations from a neutral, maximum pressure performance with sliverless exhaustion. Moreover, configuration efficiency is a weighted measure in that it reveals increases or decreases of these deviation losses due to operational environment.

The steady-state mass flow relationship is expressed as

$$A_t C_w P = A_p C P^n \rho \qquad [1]$$

from which the following expression is obtained:

$$P = \left(\frac{A_p \rho C}{A_T C_w}\right)^{1/(1-n)} = K_0 A_p^{\,1/(1-n)} \qquad [2]$$

where

$$K_0 = \left(\frac{\rho C}{A_T C_w}\right)^{1/(1-n)} \qquad [3]$$

can be assumed constant for a given propellant and nozzle.[4]

When a grain configuration is considered that is linearly progressive in accordance with the following expression

$$A = A_0(1 + \alpha t/T_b) \qquad [4]$$

the average burning area is

$$A = A_0(1 + \alpha/2) \qquad [5]$$

and the average pressure is

$$P = \frac{K_0}{T_b}\int_0^{T_b} A^{1/(1-n)}\,dt = K_0 A_0^{\,1/(1-n)} \int_0^{T_b} (1 + \alpha t/T_b)^{1/(1-n)} \frac{dt}{T_b} \qquad [6a]$$

$$P = \frac{K_0 A_0^{\,1/(1-n)}\,(1-n)}{\alpha(2-n)}\left[(1+\alpha)^{(2-n)/(1-n)} - 1\right] \qquad [6b]$$

When the instantaneous burning area equals the average burning area, the pressure is

$$P_{\bar{A}} = K_0 \bar{A}^{1/(1-n)} = K_0 A_0^{\,1/(1-n)} (1 + \alpha/2)^{1/(1-n)} \qquad [7]$$

The ratio of the average pressure to the pressure when the burning area equals the average burning area is

$$\frac{\bar{P}}{P_{\bar{A}}} = \frac{(1-n)\left[(1+\alpha)^{(2-n)/(1-n)} - 1\right]}{\alpha(2-n)\left(1 + \frac{\alpha}{2}\right)^{1/(1-n)}} \qquad [8]$$

Presented at the ARS Solid Propellant Rocket Conference, Salt Lake City, Utah, Feb. 1–3, 1961; revision received Oct. 12, 1961.

[1] Physicist, Performance Analysis Section, Interior Ballistics Dept.

[2] Head, Interior Ballistics Dept., Applied Mechanics Div. Member ARS.

[3] Supervisor, Performance Analysis Section, Interior Ballistics Dept.

[4] Effects of erosive burning and internal pressure drop on burning rate, erosion on throat area, and residence time on mass flow coefficient are neglected in this derivation.

EDITOR'S NOTE: The Technical Notes and Technical Comments sections of ARS JOURNAL are open to short manuscripts describing new developments or offering comments on papers previously published. Such manuscripts are usually published without editorial review within a few months of the date of receipt. Requirements as to style are the same as for regular contributions (see masthead page).

When Eq. 8 is expanded, the following power series results:

$$\frac{\bar{P}}{P_{\bar{A}}} = 1 + \frac{n\alpha^2}{24(1-n)^2} - \frac{n\alpha^3}{24(1-n)^2} + \dots \quad [9]$$

When a typical value for the burning rate exponent, $n = 0.25$, is substituted in the power series of Eq. 9, the result becomes

$$\bar{P}/P_{\bar{A}} = 1 + 0.0185\alpha^2 - 0.0185\alpha^3 + \dots \quad [10]$$

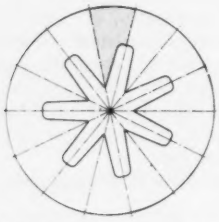

Fig. 1 Star grain design

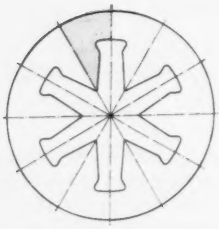

Fig. 2 Wagonwheel grain design

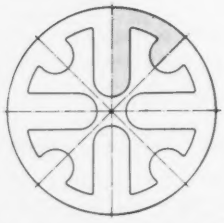

Fig. 3 Dendrite grain design

The value of Eq. 10 indicates that $\bar{P}$ differs from $P_{\bar{A}}$ by only about 0.3%, even in the case of a 50% progressive grain.

A similar relationship can be demonstrated between the average specific impulse and the specific impulse when the burning area is equal to the average burning area. Accordingly

$$I = w_p \overline{I_{sp}} = \frac{\lambda w_p}{C_w} \frac{\sqrt{2\gamma}}{\sqrt{\gamma-1}} \left(\frac{2}{\gamma+1}\right)^{(\gamma+1)/(2\gamma-2)} \times \left[1 - \left(\frac{P_a}{\bar{P}}\right)^{(\gamma-1)/\gamma}\right]^{1/2} \quad [11a]$$

$$= \frac{\lambda w_p}{C_w} \frac{\sqrt{2\gamma}}{\sqrt{\gamma-1}} \left(\frac{2}{\gamma+1}\right)^{(\gamma+1)/(2\gamma-2)} \times \left[1 - \left(\frac{P_a}{P_{\bar{A}}}\right)^{(\gamma-1)/\gamma}\right]^{1/2} \quad [11b]$$

when the losses due to nonoptimum nozzle expansion are neglected. The ideal delivered impulse, which would be obtained by expending propellant at maximum pressure or at maximum burning area of propellant, in equation form becomes

$$I_{\text{ideal}} = w_p I_{sp_{\max}} = \frac{\lambda w_p}{C_w} \frac{\sqrt{2\gamma}}{\sqrt{\gamma-1}} \left(\frac{2}{\gamma+1}\right)^{(\gamma+1)/(2\gamma-2)} \times \left[1 - \left(\frac{P_a}{P_{\max}}\right)^{(\gamma-1)/\gamma}\right]^{1/2} \quad [12]$$

Denoting configuration efficiency as ξ, then the fundamental configuration efficiency expression is

$$\xi = \frac{I}{I_{\text{ideal}}} \cong \left[\frac{1 - \left[\frac{P_a}{\bar{P}}\right]^{(\gamma-1)/\gamma}}{1 - \left[\frac{P_a}{P_{\max}}\right]^{(\gamma-1)/\gamma}}\right]^{1/2} \cong \left[\frac{1 - \left[\frac{P_a}{P_{\bar{A}}}\right]^{(\gamma-1)/\gamma}}{1 - \left[\frac{P_a}{P_{\max}}\right]^{(\gamma-1)/\gamma}}\right]^{1/2} \quad [13]$$

The second two forms of the basic expression (Eq. 13) neglect any losses in actual delivered impulse due to nonoptimum expansion of the nozzle. Through additional expansion this expression can be altered to define ξ as a function of grain parameters by expressing $P_{\bar{A}}$ and $P_{\max}$ in terms of burning areas of propellant or, in the case of grains with constant grain length L, in terms of peripheries.

DESIGN	CONFIGURATION EFFICIENCY	LOADING FACTOR
a	.9429	.887
b	.9556	.844
c	.9464	.810

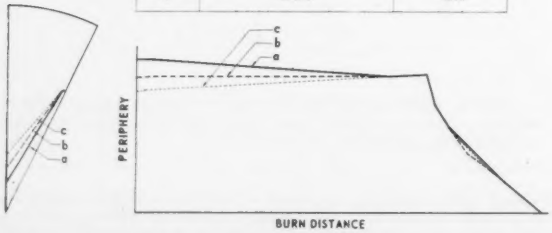

Fig. 4 Star grain variation

DESIGN	CONFIGURATION EFFICIENCY	LOADING FACTOR
a	.9370	.857
b	.9332	.778
c	.9411	.708

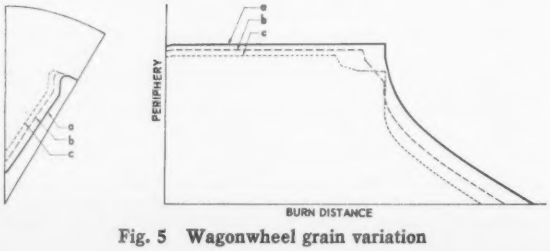

Fig. 5 Wagonwheel grain variation

Through proper substitution

$$P_{\overline{A}} = \left(\frac{C\rho}{A_T C_w}\right)^{1/(1-n)} \overline{A}_p{}^{1/(1-n)} = \left(\frac{C\rho L}{A_T C_w}\right)^{1/(1-n)} \times$$

$$\overline{Q}^{1/(1-n)} = K_1 \overline{Q}^{1/(1-n)} \quad [14]$$

where

$$K_1 = \left(\frac{C\rho L}{A_T C_w}\right)^{1/(1-n)}$$

$$P_{max} = \left(\frac{C\rho}{A_T C_w}\right)^{1/(1-n)} A_{p_{max}}{}^{1/(1-n)}$$

$$= \left(\frac{C\rho L}{A_T C_w}\right)^{1/(1-n)} Q_{max}{}^{1/(1-n)}$$

$$= K_1 Q_{max}{}^{1/(1-n)} \quad [15]$$

Then, a second equation for configuration efficiency ξ in terms of two-dimensional grain parameters is derived as a two-dimensional configuration efficiency expression

$$\xi = \left[\frac{1 - \left[\frac{P_a}{K_1 \overline{Q}^{1/(1-n)}}\right]^{(\gamma-1)/\gamma}}{1 - \left[\frac{P_a}{K_1 Q_{max}{}^{1/(1-n)}}\right]^{(\gamma-1)/\gamma}}\right]^{1/2} =$$

$$\left[\frac{K_2 - \overline{Q}^{(\gamma-1)/[\gamma(n-1)]}}{K_2 - Q_{max}{}^{(\gamma-1)/[\gamma(n-1)]}}\right]^{1/2} \quad [16]$$

where

$$K_2 = \left(\frac{K_1}{P_a}\right)^{(\gamma-1)/\gamma} \quad [17]$$

Eqs. 16 and 17 show configuration efficiency to be a function of atmospheric pressure P_a, altitude of operation, propellant ballistic properties, and nozzle parameters. The final expression for configuration efficiency depends only on the average and maximum peripheries $\overline{Q}$ and Q_{max} respectively, on the burning rate pressure exponent n, and on the combustion gas ratio of specific heats γ.

Configuration efficiency shows that conclusions about the appropriateness of any grain configuration for a specific motor cannot be generalized. Instead, careful calculations are required to determine the degree of optimization.

Application of Configuration Efficiency

The preceding section establishes expressions for configuration efficiency. Eq. 13, which defines configuration efficiency, can be used directly to evaluate all motors having actual or predicted pressure-time data available. Eq. 16, with additional assumptions, can be used for a practical evaluation of two-dimensional configurations and for screening of preliminary motor grain designs with large length to diameter ratios, in which head effects have only a secondary influence. Eq. 16 can also be used to relate configuration efficiency with changes in cross-sectional design for some typical internal burning charges such as is done in later analyses.

The effects of cross-sectional design parameter changes on the configuration efficiency for standard star, wagonwheel, and dendrite designs are illustrated in the following examples. The approach has been simplified somewhat to facilitate correlation of configuration efficiency with the parameter changes by assuming a grain of constant length and nominal ballistic parameter values. These assumptions permit replacement of the pressure functions of the basic configuration efficiency equation (Eq. 13) by the functions of cross-sectional periphery shown in Eq. 16. Figs. 1, 2, and 3 illustrate the example designs. For these examples, the curves of periphery-burn distance were evaluated and plotted as shown in Figs. 4, 5, and 6.

DESIGN	CONFIGURATION EFFICIENCY	LOADING FACTOR
a	.9246	.662
b	.9174	.581
c	.8965	.562
d	.8804	.517

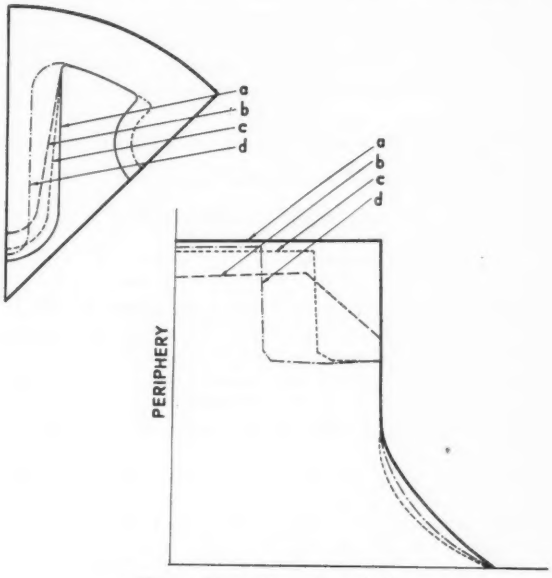

Fig. 6 Dendrite grain variation

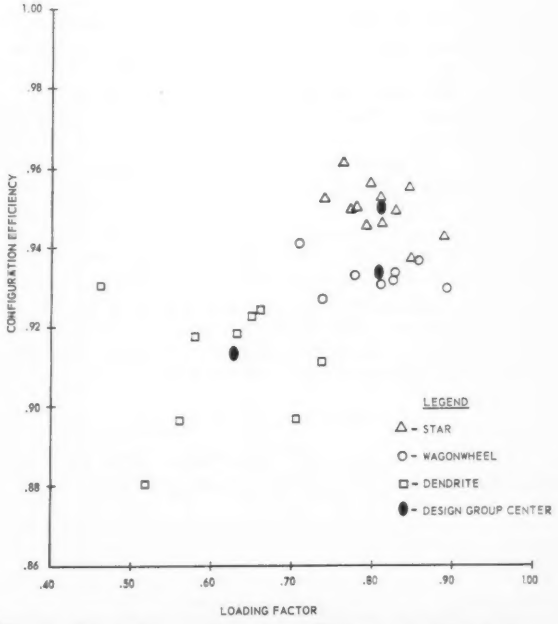

Fig. 7 Data plot, configuration efficiency vs. loading factor

Correlation

A total of 30 example grain designs were evaluated, including the example designs discussed in the preceding paragraph, to obtain a relationship between configuration efficiency, cross-sectional loading, and the geometrical parameters of the design. Twelve of these example designs had star perforated grains, eight had wagonwheel perforated grains, and ten had dendrite perforated grains.

Generalizations about design trends cannot be made at this time, since the purpose of this paper is to introduce the concept of configuration efficiency and determine its analytical validity before promoting its general use as a design parameter for grain design optimization. Nevertheless, Fig. 7 has been prepared to summarize results of the study thus far. The configuration efficiencies of the 30 cases that ranged from 88 to 96% were plotted as a function of the corresponding cross-sectional loading factor, which ranged from 46 to 90%. These figures represent only the examples selected for analysis in this paper. A much larger sample would be needed to establish limiting performance values for each design category. The design points obtained from the example designs of this paper have been used to establish a center for each design group.

Design Criteria for Space Vehicles to Resist Wind Induced Oscillations

A. A. EZRA[1] and S. BIRNBAUM[2]

The Martin Co., Denver, Colo.

SEVERAL investigators (1–4)[3] have noted that for supercritical Reynold's numbers ($R_n > 3 \times 10^5$) the vortex shedding about a cylinder is a random rather than a periodic phenomenon. The present note presents, in nondimensional form, the results of a series of wind tunnel investigations concerning wind induced oscillations at supercritical Reynold's numbers.

Also presented is a method for using these results to predict loads due to wind induced oscillations for cylindrical space vehicles with diameters large enough so that the flow is supercritical ($R_n > 3 \times 10^5$). The model used was a three-dimensional aeroelastic model of a large liquid fuelled ballistic missile. Details of the dimensional analysis may be found in (3), whereas the test procedure and results are reported in (2).

Fig. 1 shows some of the test results, presenting a nondimensional maximum moment at the base as a function of wind velocity, or Reynolds number, for several different nose shapes. It is clear that the phenomenon is three-dimensional and that a proper selection of nose shape can significantly reduce internal loads caused by wind induced oscillations.

Measurements of the bending moments in the drag direction were also made. In addition to the steady state drag, an oscillatory drag moment was observed. This oscillatory moment varied from 9 to 15% of the steady state drag moment. Fig. 2. shows the steady state coefficient as a function of Reynolds number. For design purposes, 15% should be added to these values to provide for oscillations in the drag direction.

It was noted in the course of testing that the response of the model was almost entirely in the first mode. The reason for this behavior lies in the fact that there was a relatively large separation between the model's first and second modes, and the power spectral density of the lateral aerodynamic forces decreases with increasing frequency in this region.

In order to deduce the power spectral density of the lateral aerodynamic forces, assume that the behavior of the model is described by the Euler-Bernoulli theory of beam vibrations and that the aerodynamic forces are given by

$$G(x, t) = F(x)\xi(t) \qquad [1]$$

where $\xi(t)$ is a random function of time. Then using the method outlined in (5), obtain for the mean-squared displacement, shear, and bending moment response

$$\overline{u(x)^2} = \sum_n \frac{\pi f(\omega_n) W_n^2 [\phi_n(x)]^2}{4\zeta_n M_n^2 \omega_n^3} \qquad [2]$$

$$\overline{V(x)^2} = \sum_n \frac{\pi f(\omega_n) W_n^2 [V_n'(x)]^2}{4\zeta_n M_n^2 \omega_n^3} \qquad [3]$$

$$\overline{M(x)^2} = \sum_n \frac{\pi f(\omega_n) W_n^2 [M_n'(x)]^2}{4\zeta_n M_n^2 \omega_n^3} \qquad [4]$$

where $f(\omega)$ is the power spectral density of the input, i.e.

$$\overline{\xi(t)^2} = \int_0^\infty f(\omega) d\omega \qquad [5]$$

The quantities $M_n'(x)$, M_n, ω_n, determined by a conventional vibration analysis, are properties of the model. The structural damping ratio in the nth mode ζ_n is determined by test. To determine W_n, it must be assumed that

$$F(x) = CqD(x) \qquad [6]$$

where C is a constant similar to a dimensionless coefficient of lift, q ($= (1/2)\rho V^2$) the dynamic pressure, and $D(x)$ the diameter of the cylindrical cantilever at any station x. Therefore

$$W_n = \frac{1}{A} \int_0^L D(x)\varphi_n(x) dx \qquad [7]$$

where A is the projected area of the space vehicle.

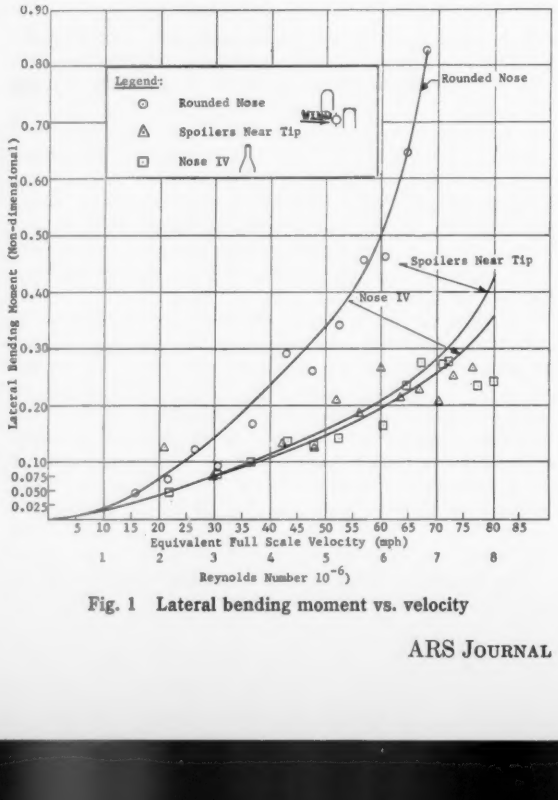

Fig. 1 Lateral bending moment vs. velocity

Presented at the Structural Design of Space Vehicles Conference, Santa Barbara, Calif., April 6–8, 1960; revision received Oct. 27, 1961.

[1] Chief, Technical Development Section, Aeronautics Dept. Member ARS.

[2] Design Engineer, Research Dept.

[3] Numbers in parentheses indicate References at end of paper.

At any station x, the maximum bending moment at a given wind velocity is some multiple p of the root mean square moment, say

$$[M(x)_{\max}]^2 = p^2 \overline{M(x)^2} = \sum_n \frac{\pi p^2 f(\omega_n) W_n^2 [M_n'(x)]^2}{4 M_n^2 \omega_n^3 \zeta_n} \quad [8]$$

Experimental evidence shows that the value of p is approximately 3; i.e., the maximum bending moment is approximately three times the root mean square value. However, the value of the total quantity $p^2 f(\omega)$ was determined experimentally in the following manner. Since the model response was primarily in the first mode, Eq. 8 could be approximated by using the first term only in the series expansion; that is

$$[M(x)_{\max}]^2 = \frac{\pi p^2 f(\omega_1) W_1^2 [M'(x)]^2}{4 M_1^2 \omega_1^3 \zeta_1} \quad [9]$$

It follows from Eq. 9 that

$$p^2 f(\omega) = \frac{4 M_1^2 \omega_1^3 \zeta_1}{\pi W_1^2} \left[\frac{M(x)_{\max}}{M_1'(x)}\right]^2 \quad [10]$$

where the right-hand side contains known quantities determined from wind tunnel tests or from computed model properties. A nondimensional power spectral density can be determined from Eq. 10 by

$$\Phi = p^2 f(\omega) \frac{2\pi V}{q^2 A^2 D} \quad [11]$$

where V is the wind velocity, q the wind dynamic pressure, and D a reference diameter.

Limited experimental evidence (4) does not show any appreciable dependence of the power spectral density of the lateral aerodynamic forces on Reynolds number for values above 1×10^6. For design purposes, therefore, φ is considered as a function only of the nondimensional frequency S when the Reynolds number exceeds this level. S is defined by

$$S = \frac{fd}{V} \quad [12]$$

$\Phi(S)$ in this paper is equal to $9C_L^2 F(S)$ where C_L and $F(S)$ are given in (4), according to which C_L is a constant and $F(S)$ a function of S.

The value of S was varied experimentally by changing the air velocity in the wind tunnel; the corresponding value of $\Phi(S)$ was obtained by substituting model properties and observed maximum bending moments into the following relationship

$$\Phi(S) = \frac{2\pi V}{q^2 A^2 D} \frac{4 M_1^2 \omega_1^3 \zeta_1}{\pi W_1^2} \left[\frac{M(x)_{\max}}{M_1'(x)}\right]^2 \quad [13]$$

The results of this procedure are shown (Fig. 3) for the several nose cone configurations and spoiler arrangements tested. Note that with a properly shaped nose, the response to wind induced oscillations can be drastically lowered.

The existence of this phenomenon was first observed in wind tunnel tests conducted for The Martin Co. at the Ames Aeronautical Laboratory in August 1958. Although this discovery was not classified, it was first reported in a classified paper (3) by the senior author. Data points on which Fig. 3 is based were obtained for values of S between 0.07 and 0.22. The curves presented in Fig. 4 are envelope curves for design purposes and give values for $\Phi(S)$ higher than those actually measured for $S > 0.15$. Between $S = 0.15$ and $S = 0.22$, the trend of the actual data points is towards decreasing $\Phi(S)$. The envelope curves, however, have been made horizontal in this range of S values. Extrapolating the curves beyond $S = 0.22$ will give increasingly conservative estimates of design bending moment.

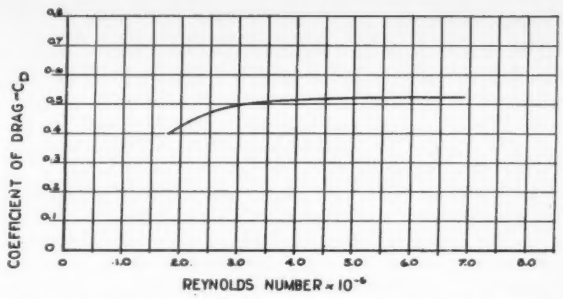

Fig. 2 Coefficient of static drag vs. Reynolds number for smooth cylinders

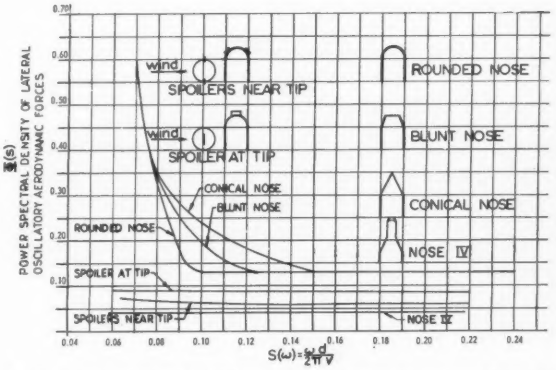

Fig. 3 Power spectral density of lateral oscillatory aerodynamic forces

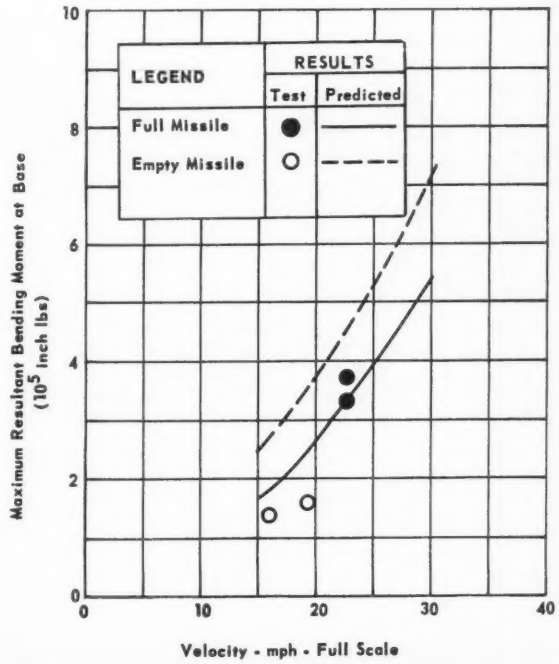

Fig. 4 Comparison of full-scale predictions with measurements

Design Procedure

Since the function $\Phi(S)$ is nondimensional, it may be used to determine loads on full-scale missiles. For an actual missile, wind loads are computed in the following manner:

1 From a vibration analysis determine the quantities ω_n, M_n, W_n, and the functions $M_n'(x)$, $V_n(x)$, and use an appropriate value of ζ_n.

2 Select the $\Phi(S)$ curve that most nearly corresponds to the nose shape.

3 By using the design wind velocity, compute the nondimensional frequency $S_n = \omega_n D/2\pi V$ for each mode, and from the $\Phi(S)$ curve determine the corresponding values of $\Phi(S_n)$.

4 Using Eq. 13, compute $p^2 f(\omega_n) = \Phi(S_n)\ q^2 A^2 D/2\pi V$.

5 From Eq. 16, the maximum moment at any station x in the lift plane is given by

$$[M(x)_{max}]^2 = \sum_n \frac{\pi p^2 f(\omega_n) W_n^2 [M_n'(x)]^2}{4 M_n^2 \omega_n^3 \zeta_n}$$

6 The moment at any station due to drag $M(x)_{drag}$ is computed in the usual manner.

7 The total bending moment at any station x is now given by

$$M(x)^2_{total} = M(x)^2_{max} + M(x)^2_{drag}$$

Verification of Full-Scale Response With Predictions

A comparison of predictions with full-scale observations of a large missile is shown in Fig. 4. The predictions of maximum resultant bending moment (drag and wind induced oscillations combined) are based on the power spectral density curves of Fig. 3 and include the effect of sloshing fuel for the fully fueled missile.

Bending moments were measured at the base of the missile by means of strain gage transducers that are an integral part of the missile launch system. Wind velocity was measured by anemometers located at four points equally spaced along the height of the missile. The average value of the wind velocity was used in calculating the predicted maximum bending moment. It will be noted that for the full missile, two different maximum bending moments were obtained in observations at the same wind velocity. The explanation for this anomaly is that the wind velocity profiles were nonuniform, as is to be expected of winds encountered in practice, and different from each other. On the whole, though, agreement between prediction and observation is rather good for the fully loaded missile.

For the empty missile the combination of increased natural frequencies and relatively lower wind velocities resulted in a nondimensional frequency of about 0.6, far above the range for which wind tunnel data are available. As previously explained, analytical predictions in these circumstances will be conservative. This is confirmed by the results shown in Fig. 4 for the empty missile.

Conclusions

When applying this method, certain limitations should be considered. The power spectral densities for lateral aerodynamic forces given in Fig. 3 are relatively independent of Reynolds number for values above 1×10^6. Nothing is known as yet about how the power spectral density of the lateral aerodynamic forces varies along the length of the cylindrical cantilever. An approximate compensation has been made by using an average value obtained experimentally from the response of the structure as a whole. Whereas no theoretical explanation exists for the tip effect, this has been provided for by experimentally determining a different power spectral density for each shape of tip. If the space vehicle is standing unsupported in the wake of another structure, the response cannot be predicted by the above method. No reliable quantitative information is available as yet about the effect of surface roughness. The design curves given in this paper should therefore be considered only as representative of typical surface roughness common to a machined aluminum cylinder.

The method should not take the place of a wind tunnel test using a dynamically similar model of the final design configuration of the space vehicle. Its greatest usefulness is in preliminary design work when the final configuration of a space vehicle has not been determined; comparative studies are in progress. This paper does provide a way of evaluating quantitatively the effect of different nose shapes or spoilers to reduce wind induced oscillations. The use of the curves of power spectral density in Fig. 3 will also reveal situations where the addition of spoilers or changes of nose shape will not produce any appreciable advantage, and the final solution will have to rely on increasing either the damping or the bending strength.

Nomenclature

$EI(x)$ = bending stiffness at station x
$G(x, t)$ = external force
$M(x, t)$ = beam bending moment at station x, time t
$M_n = \int_0^L m(x)[\varphi_n(x)]^2 dx$ generalized mass in the nth mode
$M_n'(x) = EI\partial^2\varphi_n/\partial x^2$
S = Strouhal number; nondimensional frequency
$V(x, t)$ = beam shear at station x, time t
$V_n'(x) = \frac{\partial}{\partial x}\left[EI\frac{\partial^2\varphi_n}{\partial x}\right]$
f = frequency, cps
p = ratio of maximum bending moment to rms bending moment
t = time
$u(x, t)$ = lateral displacement of station x, time t
x = coordinate measuring length along the space vehicle
$\Phi(S)$ = nondimensional power spectral density of the lateral aerodynamic forces; defined by Eq. 13
$\varphi_n(x)$ = nth modal shape
ω = frequency, radians per second
ω_n = natural frequency of the nth mode

References

1 Price, P. and Thompson, R. W., "Suppression of the Fluid Induced Vibration of Circular Cylinders," Stanford University Thesis, 1953.

2 Buell, D. A. and Kenyon, G. C., "The Wind Induced Loads on a Dynamically Scaled Model of a Large Missile in Launching Position," *NASA TMX109*, December 1959 (confidential).

3 Ezra, A. A., "Wind Induced Oscillations of a Flexible Cylindrical Cantilever at Supercritical Reynolds Numbers" (classified), Fourth Symposium on Ballistic Missile and Space Technology, Los Angeles, Calif., Aug. 24–27, 1959.

4 Fung, Y. C., "Fluctuating Lift and Drag Acting on a Cylinder in a Flow at Supercritical Reynolds Numbers," *J. Aerospace Sci.*, vol. 27, November 1960.

5 Thompson, W. T. and Barton, M. V., "Response of Mechanical Systems to Random Excitation," *J. Appl. Mech.*, vol. 24, June 1957.

Error Analysis for Doppler Determined Satellite Orbits of Other Planets

PAULA L. COHEN[1] and ARMIN J. DEUTSCH[2]
Douglas Aircraft Co., Santa Monica, Calif.

IT HAS recently been shown that if the Doppler effect is employed to establish the radial velocity of a satellite in a Kepler ellipse around another planet, then, in principle, all the orbital elements can be determined from these data alone (1).[3] In this paper the propagation of errors in this determination is investigated to discover the order of precision with which this technique can yield the orbital elements.

As in (1), it is assumed that the satellite orbit is a Kepler ellipse defined by six orbital elements and the planetary mass and that all these elements remain constant in time. As the planet and Earth describe their own orbits around the sun, the observer will then view the (constant) satellite orbit in different aspects. At any one epoch, Doppler observations of the satellite over a few hours will define a velocity curve, and from this curve the six intermediate elements are obtained. These are the period P, the eccentricity e, the time of periplanet T, the mean radial velocity γ, the angle ω at the planet from the orbital point of maximum radical velocity to periplanet, and the velocity-amplitude

$$K = 2\pi a \sin i/P(1 - e^2)^{1/2} \qquad [1]$$

Here a is the semimajor axis of the orbit and i the angle between the direction of the orbit pole and the line of sight from Earth to planet. The method of obtaining these parameters from the velocity curve is the classical astronomical procedure used for the determination of the orbits of spectroscopic binary stars (2). Observations at later epochs will yield similar sets of intermediate elements γ_j, e_j, ω_j, T_j, K_j, and P_j. These sets will be constrained by the condition that they all refer to the same Kepler ellipse. Suppose that three sets of intermediate elements are available; this is the minimum number that will determine all the Kepler elements.

A full-scale error analysis, with due regard to all the relevant constraints, represents a formidable computational task. However, from a somewhat less elaborate program, the error estimates for a representative case involving hypothetical data will be obtained. The numerical and analytical approximations introduced will always have the effect of yielding upper limits to the probable errors of the Kepler elements which are sought.

First, expressions for the probable errors of the intermediate elements at one epoch in terms of the probable error of the Doppler measurements themselves at that epoch will be obtained. Similar results will be obtained for the compatible intermediate elements at two other epochs. Neglecting the added precision that is conferred by the constraints on these 15 intermediate elements, the probable errors of the resulting Kepler elements will be computed, the latter being referred, as usual, to the plane of the ecliptic. In a later paper, the investigation will be completed by taking full account of the constraints on the intermediate elements.

The radial velocity $\dot{z}$ attributable to motion in the satellite orbit is

$$\dot{z} = K[e \cos \omega + \cos (\omega + v)] \qquad [2]$$

where v is the true anomaly, which is related to the time through Kepler's equation. Since some of the intermediate elements enter into this expression in a highly nonlinear way, the method of differential corrections will have to be used to obtain them from the measured quantity $\dot{z}$. Write

$$\dot{z}_p = z(K, e, \omega, P, T; t_p) = f(X_1, X_2, X_3, X_4, X_5; t_p) = f_p \qquad [3]$$

where

$$X_1 = K \qquad X_2 = eK' \qquad X_3 = \omega K'$$
$$X_4 = (K'/P')P \qquad X_5 = (K'/P')T \qquad [4]$$

Primes designate approximate values; these can be obtained by a graphical discussion of the velocity curve. If f_p' is written

$$f_p' = f(X_1', X_2', X_3', X_4', X_5'; t_p) \qquad [5]$$

then from the first-order Taylor expansion of f_p the relation

$$\sum_{n=1}^{5} a_{pn} x_n = \delta_p \qquad p = 1, 2, 3, \ldots s \qquad [6]$$

is obtained, where the δ_p are the residual radial velocities

$$\delta_p = f_p - f_p' \qquad [7]$$

the a_{pn} are the differential coefficients

$$a_{pn} = (\partial f_p/\partial X_n)_{X n'} \qquad [8]$$

and the x_n are the differential corrections, which will give the required constants

$$X_n = X_n' + x_n \qquad [9]$$

Suppose that an independent measure of $\dot{z}$ is made at each of s discrete instants t_p near one epoch. In Eq. 6 a system of s linear condition equations is then obtained for the five differential corrections x_n. Forming the normal equations according to the method of least squares (3)

$$[A][x] = [\Delta] \qquad [10]$$

is obtained, where $[A]$ is the square symmetric matrix of fifth order with elements

$$A_{kn} = \sum_{p=1}^{5} a_{pk}\, a_{pn} \qquad [11]$$

and where $[x]$ and $[\Delta]$ are column vectors of fifth order with elements, respectively, x_n and

$$\Delta_n = \sum_{p=1}^{5} a_{pn} \delta_p \qquad [12]$$

As is shown, e.g., by Whittaker and Robinson (3), the standard deviation of the element X_n will be given by the relation

$$\sigma_n^2 = \sigma_\delta^2 A_{nn}^{-1} \qquad [13]$$

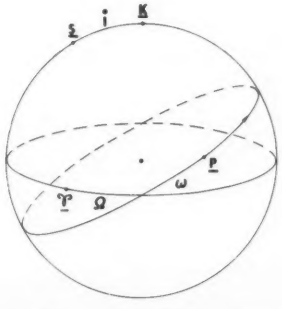

Fig. 1 Relation of the angular Kepler elements to S and P

Received Jan. 18, 1961.
[1] Research Analyst. Member ARS.
[2] Consultant.
[3] Numbers in parentheses indicate References at end of paper.

Table 1 Intermediate elements and their probable errors for a probable error of 10 fps in radial velocity (period = 173.4 min.)

Date	e	P.E.	K, fps	P.E., fps	ω, deg	P.E., deg	T, U.T.	P.E., sec
Dec. 1, 1959	0.3	0.00015	18,358.5	3.2	0	0.030	Dec. 1959 1.683	0.74
June 1, 1960	0.3	0.00016	17,510.8	3.0	134	0.032	June 1960 1.592	0.81
Dec. 1, 1960	0.3	0.00014	18,918.7	2.9	267	0.030	Dec. 1960 1.501	0.74

where σ_s is the standard deviation of the observed radial velocities and A_{nn}^{-1} the diagonal element in the matrix $[A^{-1}]$ reciprocal to $[A]$.

Having found the standard deviations σ_n of the intermediate elements, the corresponding quantities for the Kepler elements may be computed. According to the theory of propagation of errors, if F is any function of n independent variables $X_1, X_2, \ldots X_n$, then the standard deviation of F is related to the standard deviations σ_j of the respective X_j by the equation

$$\sigma^2(F) = \sum_{j=1}^{n} \left(\frac{\partial F}{\partial X_j} \sigma_j \right)^2 \qquad [14]$$

In particular, when F is any one of the Kepler elements, this relation may be used to find its standard deviation if the constraints upon the X_j can be neglected.

The three angular Kepler elements will be expressed in terms of the intermediate elements. In (1), the orientation of the orbit plane relative to inertial axes by means of a unit vector **S** directed toward the orbit pole and a unit vector **P** directed toward periplanet has been defined.

$$\mathbf{S} = \sum_{j=1}^{3} \alpha_j \mathbf{E}_j \qquad [15]$$

where the $\mathbf{E}_j$ are the noncoplanar unit vectors in the directions from Venus to Earth at the three epochs of observation. It is also shown that

$$\alpha_1 = \frac{\sin(\omega_2 - \omega_3) \sin i_2 \sin i_3}{\mathbf{E}_1 \cdot (\mathbf{E}_2 \times \mathbf{E}_3)} \qquad [16]$$

with similar expressions for α_2 and α_3 and that

$$\mathbf{P} = \mathbf{S} \times \mathbf{E}_j \frac{\cos \omega_j}{\sin i_j} + \mathbf{S} \times (\mathbf{S} \times \mathbf{E}_j) \frac{\sin \omega_j}{\sin i_j} \qquad [17]$$

Fig. 1 shows the conventional angular elements referred to the plane of the ecliptic: the inclination i, the longitude Ω of the ascending node, and the longitude ω of periplanet. To find these Kepler elements from **S** and **P**, define a unit vector **K** toward the pole of the ecliptic and a unit vector $\vec{\mathbf{T}}$ towards the vernal equinox. Then

$$\cos i = \mathbf{K} \cdot \mathbf{S} \qquad [18]$$

$$\cos \Omega = \vec{\mathbf{T}} \cdot \frac{(\mathbf{K} \times \mathbf{S})}{\sin i}; \quad \sin \Omega = \mathbf{K} \cdot \left[\frac{\vec{\mathbf{T}} \times (\mathbf{K} \times \mathbf{S})}{\sin i} \right] \qquad [19]$$

$$\cos \omega = \frac{(\mathbf{K} \times \mathbf{S}) \cdot \mathbf{P}}{\sin i}; \quad \sin \omega = \mathbf{S} \cdot \left[\frac{(\mathbf{K} \times \mathbf{S}) \times \mathbf{P}}{\sin i} \right] \qquad [20]$$

Table 2 Kepler elements and their probable errors derived from the intermediate elements

Kepler element	Probable error
a = 5200 n miles	.....
e = 0.3	0.00016
i = 29°59′	0°.329
Ω = 142°11′	11°.065
ω = 325°32′	5°.325
T = 1959 Dec. 1.683 U. T.	0.8 sec

In the example of (1), the velocity curves of a Venerian satellite observed on Dec. 1, 1959, June 1, 1960, and Dec. 1, 1960 have been considered. Suppose $s = 12$ for each curve, so that there are 12 equally spaced, independent observations of radial velocity at each epoch. Further, suppose that the probable error of each observation is ± 10 fps; as shown in (1), this requires that the frequency-stability of the transmitter be of the order of one part in 10^8 during an interval of 1 cycle of the satellite.

Although it is not necessary, assume for simplicity that the mass m of the planet is known a priori. It is also appropriate to assume that the period will be established with a fractional error much smaller than those of the other intermediate elements, for the three epochs of observation will span a large number of cycles. Accordingly, the error of P will be neglected, and it will be assumed that a can be found with negligible error from the harmonic law

$$\frac{P^2}{a^3} = \frac{4\pi^2}{Gm} \qquad [21]$$

Table 1 gives the intermediate elements derived from the curves of (1), together with their approximate probable errors as computed according to the precepts of this paper. Since no account has been taken of the constraints on the intermediate elements, the actual probable errors will be somewhat smaller than the tabulated results. Table 2 gives the corresponding set of Kepler elements, as derived from the intermediate elements of Table 1. It also gives the approximate probable errors of the Kepler elements.

In this example, where the constraints have been neglected, the tabular values represent conservative estimates. It can be seen that the Kepler elements are determined with a precision of the order of 1% or better—a precision entirely adequate for many important applications.

References

1 Deutsch, A. J., "Orbits for Planetary Satellites From Doppler Data Alone," ARS JOURNAL, vol. 30, no. 6, June 1960, pp. 536–542.

2 Aitkin, R. G., *Binary Stars*, McGraw-Hill Book Co. Inc., New York, 1935, pp. 151–180.

3 Whittaker, E. T. and Robinson, G., *Calculus of Observations*, Blackie and Son Ltd., London, 1924 pp. 209–258.

Influences of Solid Propellant Burning Rate Exponents on Performance of Engines With Large Back Pressure Variations

ROBERT C. BRUMFIELD[1]

M H D Research Inc., Newport Beach, Calif.

The idealized performance of external combustion engines driven by solid propellants with various burning rate pressure exponents is studied. Consideration is given to bypass requirements for a propulsion application with wide variations in back pressure and to the limiting values of the exponent for stable performance.

THIS analysis concerns a mathematical model of solid propellant gas generators and reciprocating engines for operation at high variable back pressures. The influence of burning rates pressure exponent on bypass requirements is studied. The engine is assumed to carry a load with mean effective pressure (average torques) and power proportional to second and third power of the speed respectively, as for an equilibrium hydrodynamic propulsion application.

The Engine

The basic engine model studied has formalized pressure-volume diagrams as shown in Fig. 1. Although the analysis is given in general algebraic form, it is applied numerically to an engine with 10% clearance volume and 30% cutoff. The work output is assumed proportional, in all cases, to the net area of the p-v diagram. The absolute value of the rotative speed and the size of the engine are not relevant to the present analysis. For example, the polytropic expansion exponent is assumed to be 1.276. Back pressure variations corresponding to 50 to 1500 ft depth in sea water (37 to 682 psia) at two distinct rotative speeds corresponding to full speed (full power) and half speed (one eighth full power) are involved.

Presented at the National ARS-IAS Joint Meeting, Los Angeles, Calif., June 13–16, 1961.

[1] Director of Engineering. Member ARS.

Work and Pressure Analysis

A requirement for full expansion at full speed and 1500 ft depth is assumed. This criterion, together with the assumptions outlined previously, determines the shapes of all p-v diagrams, e.g., Fig 1, as follows:

1 The volume coordinates are all determined by the clearance (10%) and cutoff (30%) in relation to displacement.

2 The depth-pressure levels p_d are determined by the hydrostatic pressure (pressure drop in exhaust manifolding is neglected).

3 The shape of all expansion curves is determined by a polytropic process equation

$$pV^k = \text{const} \qquad [1]$$

In the numerical examples given, $k = 1.276$ and

$$\frac{V_3}{V_2} = \frac{1.1}{0.4} = 2.75$$

Thus

$$p_2 = p_3(V_3/V_2)^k = 3.63\ p_3 \qquad [2]$$

or

$$p_s = 3.63\ p_e$$

4 The inlet pressure p_s for full depth operation at full power is determined by the assumption of full expansion (Fig. 1, Diagram F - 3). Thus

$$p_2 = 3.63 \times 682 = 2470 \text{ psia}$$

5 Since the power requirements are the same at all

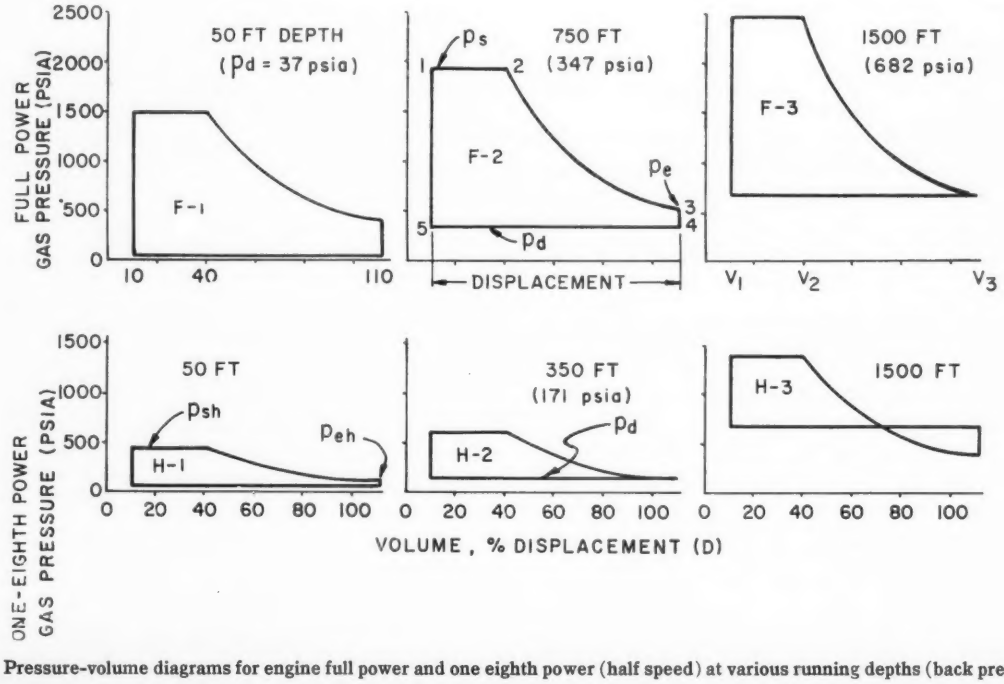

Fig. 1 Pressure-volume diagrams for engine full power and one eighth power (half speed) at various running depths (back pressures)

depths for a given running speed, the other full speed expansion curves and values of p_s and p_e are determined on the basis of equal areas in the p-v diagrams

$$\text{Area} = p_m \cdot D$$

$$= (p_e - p_d)V_3 - (p_s - p_d)V_1 + \frac{k}{k-1} p_s V_2 \left[1 - \left(\frac{V_2}{V_3}\right)^{k-1}\right] \quad [3]$$

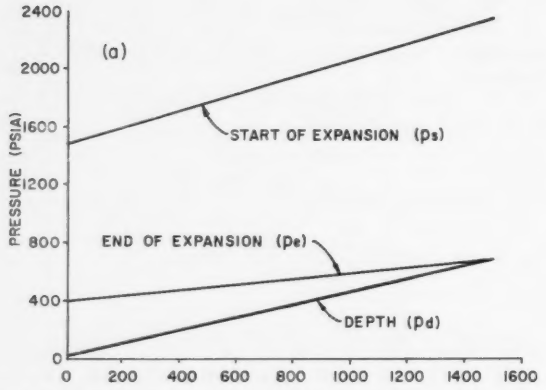

Fig. 2a Engine pressure vs. depth in sea water, full power (full speed)

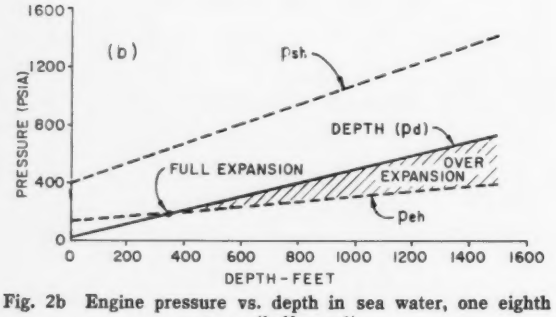

Fig. 2b Engine pressure vs. depth in sea water, one eighth power (half speed)

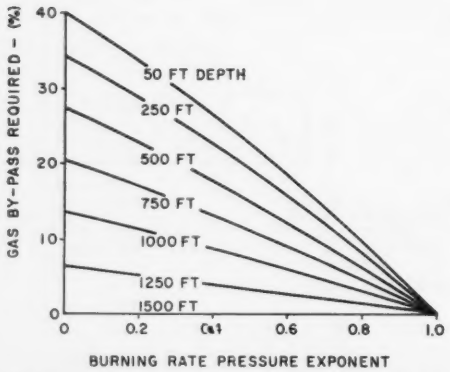

Fig. 3 Bypass required at full power and speed vs. operating depths vs. burning rate pressure exponent

which simplifies, for this engine, to

$$p_m = 1.1(p_e - p_d) - 0.1(p_s - p_d) + \frac{0.4k}{k-1} p_s \left[1 - \frac{1}{(2.75)^{k-1}}\right] \quad [4]$$

or

$$p_m = 0.651\, p_s - p_d \quad [5]$$

for

$k = 1.276$
$V_1 = 0.1D$
$V_2 = 0.4D$
$V_3 = 1.1D$

Three diagrams for full speed operation (F-1, F-2, and F-3) are shown in Fig. 1. For full speed at full depth, P_m can be calculated

$$p_m = 0.651 \times 2470 - 682 = 926 \text{ psi}$$

For operation at half speed, the expansion curves and the values of p_s and p_e are determined on the basis that the p-v areas and mean effective pressure be one quarter as large as for full speed. Thus $p_{mh} = (1/4)p_m = 232$ psia. The corresponding p-v diagrams (H-1, H-2, and H-3) are shown in Fig. 1.

The pressure levels involved in the above analysis are summarized in Fig. 2. Full expansion for full speed and 1500 ft depth is indicated by $p_e = p_d$.

Note that, for half speed operation, the engine expands fully at 350 ft and overexpands for depths greater than 350 ft. Overexpansion requires recompression. It is an inefficient process involving a negative area work loop on the p-v diagram (e.g., Fig. 1, H-3), and in applications it should be avoided where practical, if energy conservation is important.

So far, it has not been necessary to discuss the source of the working fluid or the method of control to be employed, except that k is taken to be 1.276. The source could be from gas, a boiler, a liquid propellant gas generator or a solid propellant gas generator with an appropriate bypass, or none, if the burning characteristics are proper.

Solid Propellant Gas Generator for Working Fluid

For the remainder of the mathematical model, it will be assumed that

1 A solid propellant gas generator is used as a gas source for driving the engine.

2 The burning rate is proportional to some power of the absolute chamber pressure

$$b = ap_c^n \quad [6]$$

as is true of many types of solid propellants.

3 The excess gas generated, if any, is bypassed around the engine.

4 All propulsion systems are designed to run with no bypass when at full speed and full depth (1500 ft).

For purposes of this study, it is not necessary to specify gas temperature, molecular weight, absolute burning rate of the propellant, engine running speed, size, etc. A polytropic exponent of $k = 1.276$ is used as before, and consideration is given to what happens at various values of the burning rate pressure exponent n as the operating depth is changed. Both full speed and half speed operations are analyzed.

Bypass Required for Full Speed Operation on Solid Propellants

The fraction of the total gases bypassed is

$$BP = \frac{b - b_w}{b} = 1 - \frac{b_w}{b} \quad [7]$$

where

b = actual burning rate
b_w = wanted (usable) burning rate
b_0 = standard design burning rate for full speed operation at full depth (1500 ft) and no bypass (a design criterion)

From the burning rate law (Eq. 6)

$$b = ap_s^n \qquad b_0 = ap_{s0}^n \qquad [8]$$

Since it is only desired to fill the cylinders at the pressure p_s

$$b_w = b_0(p_s/p_{s0}) \qquad [9]$$

if the gas density and mass are directly proportional to pressure. This follows from the equation of state and a need for a constant volume rate of gas consumption at constant speed. Thus $b_w \sim p_s$ is required, and a burning rate pressure exponent of unity($n = 1$) is most desirable, apart from stability considerations. Thus

$$b_w = a\frac{p_s}{p_{s0}^{(1-n)}} \qquad [10]$$

and

$$BP = 1 - \left(\frac{p_s}{p_{s0}}\right)^{(1-n)} \qquad [11]$$

giving zero bypass for $n = 1$. For the present analysis $p_{s0} =$ 2470 psi (Eq. 2). From Eq. 5.

$$p_s = 1.538\,(p_m + p_d) \qquad [12]$$

or

$$p_s = 1427 + 1.538\,p_d \qquad [13]$$

for

$$p_m = 926 \text{ psi (full speed)}$$

Thus

$$BP = 1 - \left(\frac{1427 + 1.538p_d}{2470}\right)^{(1-n)} \qquad [14]$$

Curves of this type are shown in Fig. 3. This indicates a considerable reduction in the bypass requirements for the higher values of the burning rate pressure exponent n.

Operation at Half Speed

As indicated in the section on work and pressure analysis, the mean effective pressure should be one quarter as large as for full speed, since the torque requirement is proportional to the square on the rotative speed. Thus $p_{mh} = 232$ psi, and from Eq. 5

$$P_{sh} = (p_{mh} + p_d)/0.651 = 357 + 1.538\,p_d \qquad [15]$$

From Eq. 2

$$p_{eh} = 0.275p_{sh} \qquad [16]$$

The p-v diagrams and pressure conditions are shown in Figs. 1 and 2 respectively.

Bypass Required for Half Speed Operation on Solid Propellants

Following the argument of the section on bypass required for full speed operation on solid propellants

$$(BP)_h = 1 - b_{wh}/b_h \qquad [17]$$

where

$$b_h = ap_{sh}^n \qquad [18]$$

and

$$b_{wh} = b_0\frac{N_h}{N}\frac{p_{sh}}{p_{s0}} \qquad [19]$$

and

$$b_0 = ap_{s0}^n \qquad [20]$$

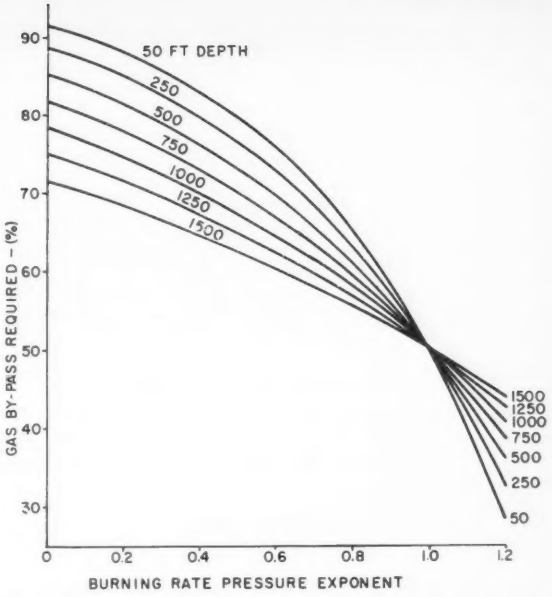

Fig. 4 Bypass required for operation at half speed (one eighth power) vs. operating depth in sea water vs. burning rate pressure exponent

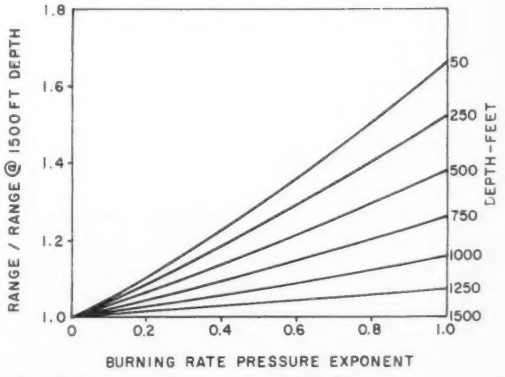

Fig. 5 Relative running range vs. burning rate pressure exponent at various operating depths in sea water

Eq. 19 derives from the equation of state and the requirements for just filling the engine at the lower speed. Thus

$$b_{wh} = a\frac{N_h}{N}\frac{p_{sh}}{p_{s0}^{(1-n)}} \qquad [21]$$

and

$$(BP)_h = 1 - \frac{N_h}{N}\left(\frac{p_{sh}}{p_{s0}}\right)^{(1-n)} \qquad [22]$$

where p_{s0} is the chamber pressure corresponding to full speed and full depth or $p_{s0} = 2470$ for the present case.

With $N_h/N = 1/2$

$$(BP)_h = 1 - \frac{1}{2}\left(\frac{p_{sh}}{2470}\right)^{(1-n)} \qquad [23]$$

combining with Eq. 15

$$(BP)_h = 1 - \frac{1}{2}\left(\frac{357 + 1.53p_d}{2470}\right)^{(1-n)} \quad [24]$$

for $n = 1$

$$(BP)_h = 1/2$$

for $n > 1$

$$(BP) < 1/2$$

but the full design speed could not be maintained above 1500 ft without a supplementary gas generator.

Eq. 24 is plotted in Fig. 4. Note that very high bypass percentages are required with low values of n, particularly at shallow depths.

Relative Running Range at Constant Depth

The standard running range is measured at full depth. The total running range R_t for any other constant depth is inversely proportional to the propellant burning rate at that depth. Thus

$$\frac{R_t}{R_0} = \left(\frac{p_{s0}}{p_s}\right)^n \quad [25]$$

or

$$\frac{R_t}{R_0} = \left(\frac{2470}{1427 + 1.538p_d}\right)^n \quad [26]$$

for the present conditions.

For variable depth operation, the total range can be approximately calculated from the following summation:

$$\sum\left(\frac{\Delta R}{R_t}\right)_m = 1 \quad [27]$$

where each m represents a discreet running depth, and ΔR is the range used at that depth. In differential form

$$\int_0^R \frac{dR}{R_t} = 1 \quad [28]$$

This can be integrated graphically by using Eq. 26 and noting that, for the entire run, $p_d = \phi(R)$, a curve which can be easily drawn.

Relative Running Range at Half Speed

Following the argument of the previous section

$$\frac{R_{th}}{R_{1500}} = \frac{1}{2}\left(\frac{p_{s0}}{p_{sh}}\right)^n \quad [29]$$

For variable depth operation, the total range can be approximately calculated from the summation

$$\sum\left(\frac{\Delta R}{R_{th}}\right)_{mh} + \sum\left(\frac{\Delta R}{R_t}\right)_m = 1 \quad [30]$$

including full and half speed operation, where h denotes the half speed condition.

Stability Considerations

Evidently relatively high burning rate exponents n are desirable for ease of speed regulation with changes in depth. Values as high as unity ($n = 1$) would lead to unstable behavior in rocket motors with fixed nozzle throat areas. An engine, however, presents an effective orifice area that is proportional to rotative speed. The approximate influence of this variable effective orifice area can be studied if the mathematical model is further simplified as follows:

1 A very low inertia system is assumed. The mean effective pressure required for a simple hydrodynamic propulsion application is then proportional to the square on the rotative speed of the engine. Thus $p_m \sim N^2$ or $N \sim p_m^{1/2}$.

2 The mean effective pressure is assumed proportional to the propellant chamber pressure or $p_m \sim p_c$. (In the initial model, p_m does not increase so rapidly with p_c.)

The mass flow rate $\dot{m}$ to the engine is related to the gas density ρ and the rotative speed N by

$$\dot{m} \sim \rho N \quad [31]$$

For an ideal gas $\rho \sim p_c$, thus

$$\dot{m} \sim p_c \cdot p_m^{1/2} \sim p_c^{3/2} \quad [32]$$

Since $b \sim p_c^n$, the above mathematical model would be neutrally stable with a burning rate exponent $n = 1.5$.

For use in rocket motors, burning rate pressure exponents above $n = 0.6$ to 0.7 are undesirable from a stability standpoint. On the basis of the above arguments, namely fuel economy, bypass control and safety, somewhat higher values of n are desirable and worthy of further study.

Acknowledgment

H. E. Karig, Consultant, made the first numerical calculations on bypass requirements. W. B. McLean, Technical Director at the Naval Ordnance Test Station, first suggested that, from a stability standpoint, an engine can tolerate high burning rate pressure exponents because the effective orifice size is proportional to rotative speed.

Additional Nomenclature

a	= burning rate pressure coefficient
BP	= relative bypass of propellant gases
D	= engine piston displacement volume
h	= subscript denotes half speed operation
k	= polytropic exponent for gas expansion process
m	= general label for interval at constant conditions
0	= subscript for reference condition
p	= pressure
p_c	= propellant chamber pressure
p_d	= ambient pressure corresponding to depth of operation in sea water
p_e	= pressure at end of expansion
p_m	= mean effective pressure
p_s	= pressure at start of expansion
p_1, p_2, p_3, p_4	= pressure at points 1, 2, 3, and 4 respectively on p-v diagram
R	= running range of underwater vehicle
R_t	= total running range
V_1, V_2, V_3, V_4	= cylinder volume at points 1, 2, 3, and 4 respectively on p-v diagram

Mass Spectrometer for Upper Air Measurements

E. J. SCHAEFER[1] and M. H. NICHOLS[2]

University of Michigan, Ann Arbor, Mich.

The need for synoptic measurements of atmospheric composition as a function of altitude, latitude, and time is becoming increasingly critical. The Paul "massenfilter" is light, rugged, and simple and, therefore, easily adaptable to rocket borne composition measurements. A model tailored to these requirements was successfully designed, built, and tested in the laboratory. The complete instrumentation package includes supporting circuitry and telemeter transmitter. Contamination by occluded rocket gases is avoided by ejecting the instrumentation canister from an evacuated chamber at altitude. Surface recombination of nascent oxygen is minimized by immersing the fine grids that compose the ion source in the ambient gas. Two flights were attempted in November 1960 without result, apparently due to a failure of the canister to eject. A new, improved version is under construction for flight test in the near future.

THE NEED for synoptic measurements of atmospheric composition as a function of altitude, latitude and time is becoming increasingly critical. Above about 100 km variations in composition are known to exist. Diffusive separation of the lighter gases modifies composition with altitude. Dissociation of molecular oxygen by the sun's radiation results in variations with time, altitude, and latitude. Recombination processes yield oxides of nitrogen which further modify composition (1–3).[3]

The problem has been investigated by a variety of methods (4–6). Techniques have varied from postflight analysis of upper air samples to mass spectrometer in-flight measurements. The available data thus far, however, must be greatly extended to satisfy the requirements. In particular, variations with altitude, time, and latitude must be investigated on a synoptic basis.

This paper describes the development of an instrumentation package with which to accomplish a synoptic investigation. Support for the work has been furnished by NASA.

Mass Spectrometer

The instrument which was selected for in-flight composition analysis is a mass spectrometer first described by Paul, Reinhard, and von Zahn (7). Briefly, its principle of operation is as follows:

The analyzing section of the massenfilter, also known as the *Paul tube* and *quadrupole mass filter*, consists of four circular rods positioned 90° apart and connected as shown in Fig. 1. The applied potentials are given by the equations

$$V_{0x} = U + V \cos \omega t \qquad [1]$$

$$V_{0y} = -V_{0x} \qquad [2]$$

where V is the peak value of an RF sine wave upon which is superimposed the d-c voltage U. Ideally the rods have a hyperbolic cross section, in which case the potential at any point in the field is given by

$$V_{x,y} = (U + V \cos \omega t) \frac{x^2 - y^2}{R_0^2} \qquad [3]$$

Received June 22, 1961.

[1] Research Engineer, Department of Aeronautical and Astronautical Engineering.

[2] Professor of Aeronautical and Astronautical Engineering; now at San Diego State College, San Diego, Calif.

[3] Numbers in parentheses indicate References at end of paper.

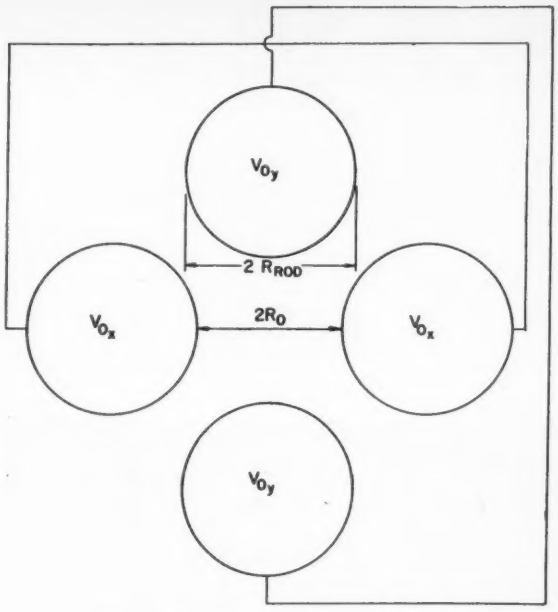

Fig. 1 Circular electrode arrangement

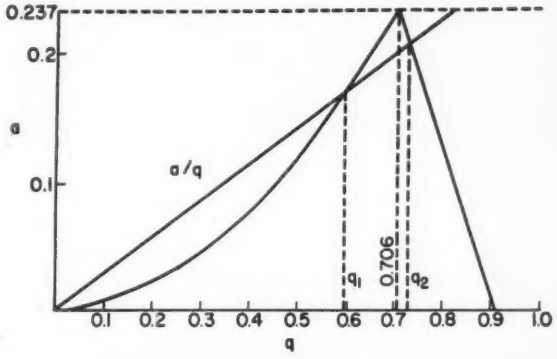

Fig. 2 Massenfilter stability diagram

Fig. 3 Laboratory massenfilter

In practice circular rods of radius 1.16 R_0 closely approximate the ideal field out to about 0.8 R_0.

The equations of motion of a singly charged ion in such a field are

$$m\ddot{x} + 2e(U + V \cos \omega t)x/R_0^2 = 0 \qquad [4]$$

$$m\ddot{x} - 2e(U + V \cos \omega t)y/R_0^2 = 0 \qquad [5]$$

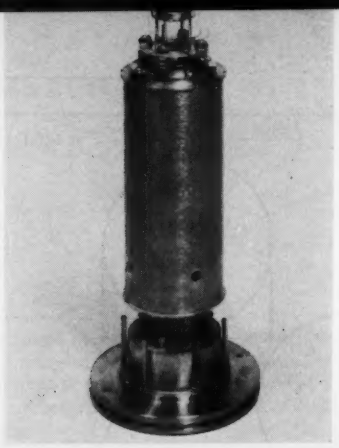

Fig. 4 Flight model

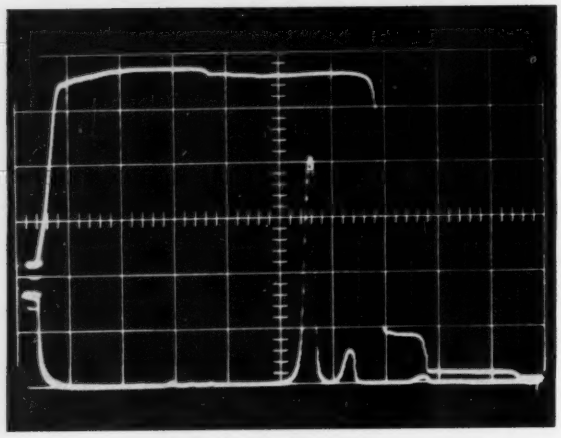

Fig. 5 Spectrum of air

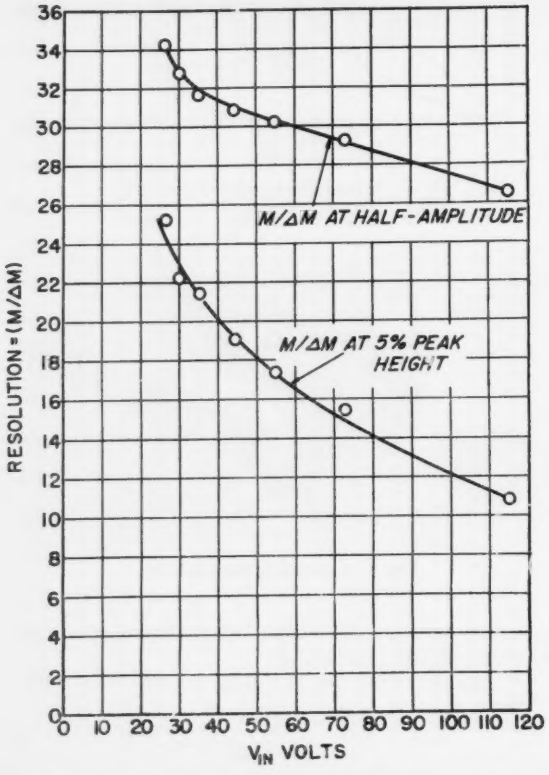

Fig. 6 Resolution of nitrogen as a function of injection voltage

Making the substitutions

$$p = \omega t/2 \quad [6]$$

$$a = 8eU/mR_0^2\omega^2 \quad [7]$$

$$q = 4eV/mR_0^2\omega^2 \quad [8]$$

Eqs. 4 and 5 become

$$d^2x/dp^2 + (a + 2q \cos 2p)\, x = 0 \quad [9]$$

$$d^2y/dp^2 - (a + 2q \cos 2p)\, y = 0 \quad [10]$$

These are Mathieu differential equations. Their solutions in terms of a and q yield regions wherein the ionic trajectories are stable and regions where they are unstable. A stable trajectory is defined as one which remains finite in amplitude as p grows infinite. For an ion to be stable in both axes, Eqs. 9 and 10 must each yield a stable solution. The values of a and q in which this condition occurs are given in Fig. 2. From Eqs. 7 and 8

$$a/q = 2U/V \quad [11]$$

Thus if the ratio of d-c to RF voltages is held constant, a/q plots as a straight line on Fig. 2. This line is the locus of the working points of all ions. Heavy ions plot close to the origin, and lighter ions plot progressively toward the upper right. If the voltages are increased from zero, the working points will move away from the origin. The lightest ion passes through the stable region first, followed by the heavy ions in order of their mass. Ideally, if a stream of ions is injected at one end of the field, unstable ions are removed by collision with the rods. Stable ions negotiate the length of the field and are detected when they deliver their charge to a collector placed at the other end. In practice, however, there is a minimum number of cycles of the applied RF voltage for which an unstable ion must remain in the field to insure removal. Further, initial conditions of radial velocity and displacement must be restricted to insure collection of a stable ion. Both restrictions increase in severity with resolution. A complete discussion of inlet conditions is beyond the scope of this paper. One appears in (7).

From Fig. 2 it will be noted that if U, and therefore a, is made zero, the locus of all working points lies on the q-axis. At low RF voltages, all ions are in the stable region. As the RF voltage is increased, the working points move away from the origin so that the ions become unstable in order of increasing mass. This mode of operation and the conventional method each offer their own unique advantage. Both are employed in the application described herein.

The massenfilter was selected for upper atmosphere measurements because of the following advantages:

1 It requires no magnetic field; hence it is inherently light in weight.

2 Its construction is simple and rugged.

3 Initial conditions affect only percentage transmission and resolution. They have no effect on the indicated mass of the ion.

4 Supporting circuitry is simple. A constant voltage ratio is maintained by rectifying a portion of the RF voltage to obtain the d-c voltage.

5 A linear mass spectrum is obtained from a linear voltage sweep.

Flight Design

For design purposes, four parameters may be independently selected. These, in turn, fix the remainder of the design. The parameters which were selected were resolution, peak RF voltage, rod length, and ion injection voltage. Resolution is here defined as the mass of the ion divided by the width, expressed in mass units, of its spectral peak at half amplitude. A resolution of 40 for mass 46 was considered

adequate to separate the gases that can reasonably be expected in the upper atmosphere. Due to the shorter residence times of the lighter ions, resolution will become less as mass is reduced, but less resolution is required as mass decreases. The peak RF voltage was selected to be 500 v as conveniently obtainable in a miniaturized flight package. Rod length was set at 5 in. (12.75 cm) as a reasonable size for small rocket borne experiments. Finally, an injection ion energy of 45 v was selected as a compromise between a low ion velocity that reduces RF power requirements and a high ionic energy that avoids the difficulties inherent in controlling low energy particles. The important design parameters are:

Quantity	Symbol	Value
Mass number	A	46 amu
Resolution	$m/\Delta m$	40
Peak RF voltage	V	500 v
Length of field	L	12.75 cm
Ion injection voltage	V_{in}	45 v
Frequency	f	2.39 Mc
Field radius	R_0	0.522 cm
Rod radius	R_{rod}	0.609 cm
Injection port diameter	D_{in}	0.081 cm
Maximum injection angle	θ	5.25°

A laboratory model is shown in Fig. 3. The collector is positioned with respect to the rods and ion source when assembled into the vacuum container seen in the picture. A completely assembled flight model is seen in Fig. 4. With the exception of insulators, the rhenium filament, and platinum grid, stainless steel is used throughout its construction. An analysis of a calibrated air leak is seen in Fig. 5. Here, the "staircase" sweep illustrates the type of response obtained when the d-c voltage is zero and the working points lie along the q-axis of Fig. 2. In flight use, the type of spectrum is alternated. Complete transmission is assured in the zero d-c sweep. Hence the height of the major steps serves as a calibration of the heights of the corresponding peaks. The conventional spectrum provides a sensitive method of detecting the rarer species. Resolution of the nitrogen peak as a function of ion accelerating voltage is presented in Fig. 6.

Instrumentation

Perhaps the largest uncertainty in past measurements is the error in analysis due to recombination of atomic oxygen on the walls of the gage. Another uncertainty is the contribution of occluded gases on the rocket to the analysis.

Contamination by rocket gases is avoided by ejecting the entire pressurized instrument package from an evacuated volume when altitude is reached. A sketch of the separation technique is shown in Fig. 7. Emerging from a vacuum, the surface of the instrumentation cylinder is clean of occluded gases. Use of "O" rings limits the attainable vacuum to approximately 1 μ of pressure. A continuing goal is to develop techniques to maintain harder vacuums in a system of this type.

Recombination is minimized by an ion source composed of fine grid structure directly immersed in the ambient gas. This increases the probability that an ambient molecule will enter the ionization volume without first encountering a solid surface where recombination can occur. Future design will attempt to realize an efficient ion source farther removed from the head end of the canister to further reduce the probability of surface recombination.

Fig. 8 is a photograph of instrumentation flown November 1960. The massenfilter is at the forward end followed by the electrometer amplifier to detect ion currents. The next chassis is the source of rod potential. Below that is the emission regulator chassis. Following that is a section containing timer and power supply including batteries. Finally, the telemeter transmitter is located at the bottom surmounted by four subcarrier oscillators devoted to the four channels of

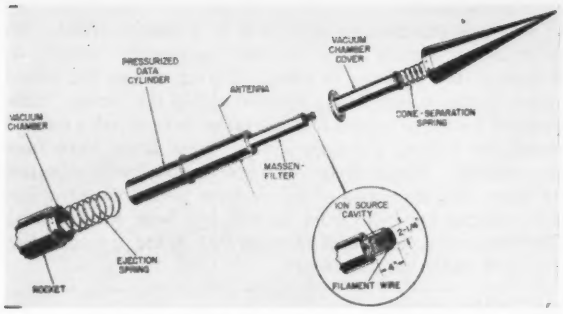

Fig. 7 Data cylinder separation

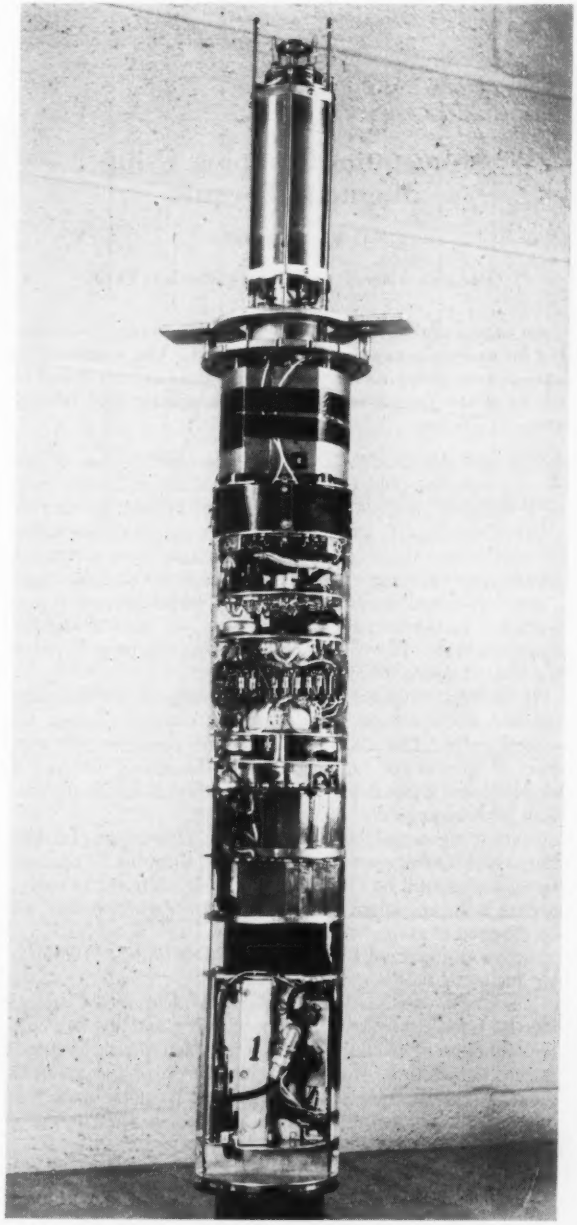

Fig. 8 Flight instrumentation

signal information.

Two instrumentations were fired in November 1960. No telemetering signals were received, apparently because of failure of the package to eject. During ascent the folded dipole is almost completely shielded within the rocket. Subsequent testing of a third unit has failed to establish a definite cause for failure, although several possibilities have been ascertained. Minor design changes directed to elimination of these possible causes of failure have been completed, and telemetering coverage from takeoff has been incorporated. Four improved versions of instrumentation are in preparation for flight test in the near future.

Acknowledgments

We wish to acknowledge the able assistance of our colleague, D. R. Glass, in the development of the flight massenfilter. J. Brown and E. A. Wenzel made valuable contributions in the development of the flight equipment.

References

1 Chapman, S., "The Earth in the Sun's Atmosphere," *Scien. Amer.*, vol. 201, no. 4, October 1959, pp. 64–71.

2 Nicolet, M., "High Atmosphere Densities," *Science*, vol. 127, no. 3310, June 1958, pp. 1317–1320.

3 Nicolet, M., "Atmospheric Models and Thermospheric Gradients," *Proc.* Fourth Meeting of COSPAR, Florence, Italy, April 1961 (to be published).

4 Meadows, E. B. and Townsend, J W., "IGY Rocket Measurements of Arctic Atmospheric Composition Above 100 Km," Space Research, *Proc. First Int. Space Science Symp.*, COSPAR, 1960, pp. 175–198.

5 Pukhunov, A. A., ibid, p. 101.

6 Wenzel, E. A., Loh, L. T., Nichols, M. H. and Jones, L. M. "The Measurement of Diffusive Separation in the Upper Atmosphere," *Annals of the IGY*, Vol. 12, Part 1, 1960, pp. 407–421.

7 Paul, W., Reinhard, H. P. and von Zahn, U., "Das Elektrische Massenfilter als Massenspektrometer und Isotopentrenner," *Zeitschrift fur Physik*, vol. 152, 1958, pp. 143–182.

Momentum Dumping Using Magnetic Torques

J. W. BURROW[1]

Douglas Aircraft Co., Santa Monica, Calif.

An aspect of reaction wheel design with magnetic torquing for momentum removal is discussed. The momentum storage requirements for the wheel system are developed in terms of the torque input and the magnetic field history along the orbit.

IN A RECENT article Kamm (1)[2] discussed the use of current carrying coils, which, in the presence of Earth's magnetic field, will produce a torque that may be used for satellite attitude control. It was suggested that such a device might be used to remove accumulated momentum from a reaction wheel control system. A problem arises in the design of such a system because of the fact that the generated torque is proportional to the vector product of the coil current and the magnetic field. Therefore, no momentum can be removed in the instantaneous field direction.

However, for an orbit not in the plane of the magnetic equator, there will be a change in field direction along the orbital path. The maximum change in direction will vary from 0° to over 90° for polar orbits. Therefore, except in a singular case, there is no constant direction in which momentum is nonremovable.

Some of the consequences of this fact in the design of a reaction wheel control system with magnetic torquing for momentum removal will be examined. Of major interest in such a system is the maximum momentum that the wheel system will be required to store. As will be shown, this is a function of steady-state external torque and the directional variation of the magnetic field.

The angle between Earth's magnetic field vector and an inertial reference system moving with the satellite is a complex function of orbital inclination, position of the satellite in its orbit, and time (due to the inclination of the magnetic polar axis with respect to the geographic polar axis). In order to have a simple example to illustrate the concept of

Received Sept. 11, 1961.

[1] Group Engineer, Guidance and Control Section. Member ARS.

[2] Numbers in parentheses indicate Reference at end of paper.

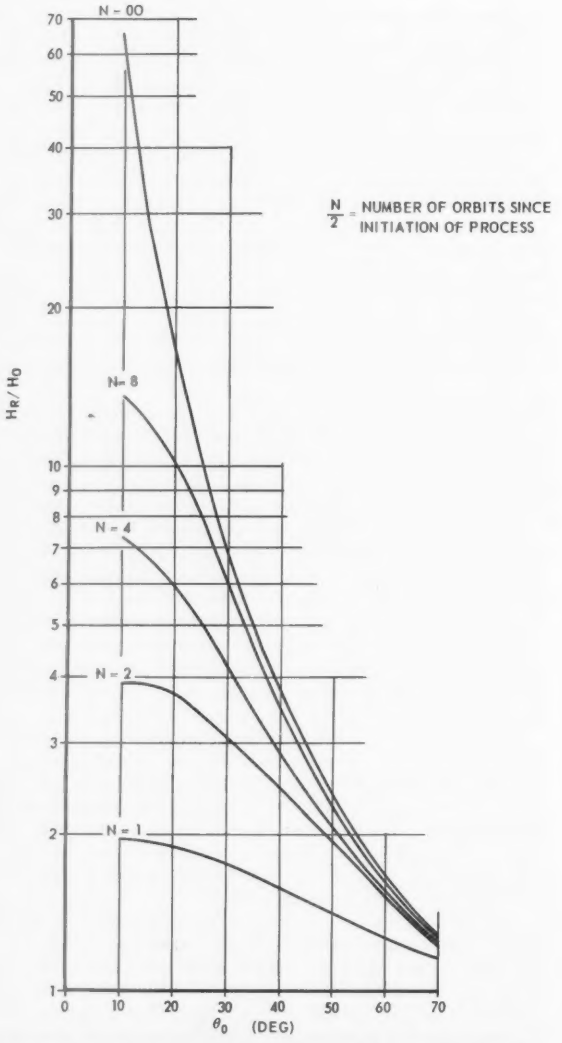

Fig. 1 Ratio of residual to input momentum vs. field direction variation angle θ_0

magnetic torquing for momentum removal, assume that the angle between Earth's magnetic field and some inertial reference θ may be expressed as

$$\theta = \theta_0 \cos (2\pi/T)t$$

where T is the orbital period.

If at $t = 0$ an initial momentum H_0 is present in the same direction as the instantaneous field vector, it will be nonremovable at this time. One quarter orbit later the field direction will have changed by an amount θ_0, and a quantity $H_0 \sin \theta_0$ of the initial momentum may be removed, leaving $H_0 \cos \theta_0$ as residual momentum. As this process is repeated, the residual momentum will be $H_{r_n} = H_0 \cos^n \theta_0$, where $n/4$ is the number of complete orbits since the beginning of the process. In this case the maximum momentum that must be stored is simply H_0.

Next, examine the case where there is a steady-state constant direction momentum input into the system. Assume that the momentum input is parallel to the field vector at $t = 0$. Let it have a magnitude

$$\dot{H} = 4H_0/T$$

so that every quarter orbit an amount H_0 is delivered to the system in the original field direction. If, as before, the torquing coils are energized every quarter orbit, which corresponds to the maximum change in field direction, the momentum remaining in the system can be expressed as

$$H_{r_2} = \left(\sum_{n=0}^{N} 2H_0 \cos^{2n} \theta_0 \right) - \left(H_0(1 + \cos^{2N} \theta_0) \right)$$

where N is the number of half orbits since the initiation of the process. The ratio H_{r_2}/H_0 is shown in Fig. 1 as a function of θ_0 and N.

As N becomes large, H_{r_2} approaches a limiting value

$$\lim_{N \to \infty} H_{r_2} = H_0 \left[(2/\sin^2 \theta_0) - 1 \right]$$

which is the maximum momentum storage requirement for a continuous torque input.

If the momentum input and the field direction are predictable for some portion of the orbit in advance, the above momentum storage requirement may be reduced. Referring to Fig. 2, if $\mathbf{B}_0$ is the instantaneous field direction, $\mathbf{B}_1$ is the field direction displaced by θ_0 some predictable time later. Let $\mathbf{H}_0$ be the momentum input expected in this time period. If a momentum $\mathbf{H}_a$ is generated by the torquing coils such that the resultant momentum $\mathbf{H}_r$ forms an angle α with $\mathbf{B}_0$, where $\alpha + \theta_0 = \pi/2$, then when $\mathbf{B} = \mathbf{B}_1$ the total momentum $\mathbf{H}_r$ may be removed.

The maximum momentum that must be stored in this mode is

$$H_{r_3} = \frac{H_0}{\sin \theta_0}$$

Comparing H_{r_3} with H_{r_2}, it is seen that

$$\frac{H_{r_3}}{H_{r_2}} = \frac{H_0/\sin \theta_0}{H_0(2/\sin^2 \theta_0 - 1)} = \frac{\sin \theta_0}{2 - \sin^2 \theta_0} \qquad H_{r_3}/H_{r_2} \leqslant 1$$

H_{r_3}/H_{r_2} is shown in Fig. 3 as a function of θ_0. It is seen that for small values of θ_0, the additional complexity needed for prediction results in significantly lower maximum momentum storage requirements. Therefore, the design of the wheel system is affected not only by the magnetic field direction variations, but also by the technique used to take advantage of this variation.

It is also interesting to note the efficiency with which the

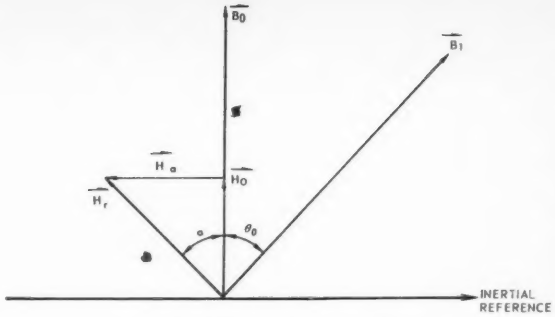

Fig. 2 Momentum removal geometry

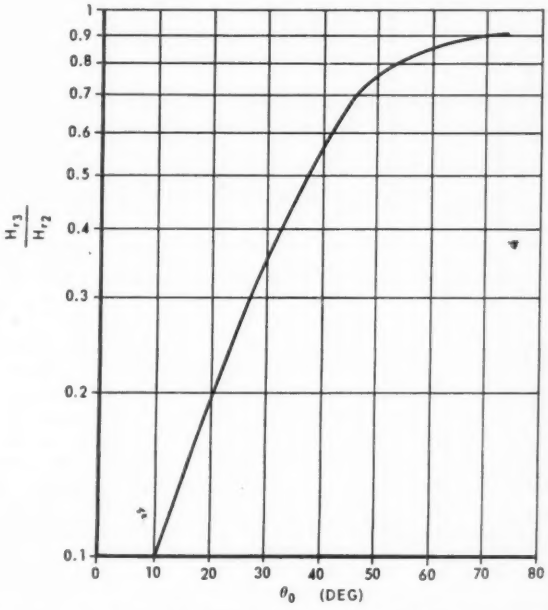

Fig. 3 Ratio of residual momentum with and without prediction vs. field direction variation angle θ_0

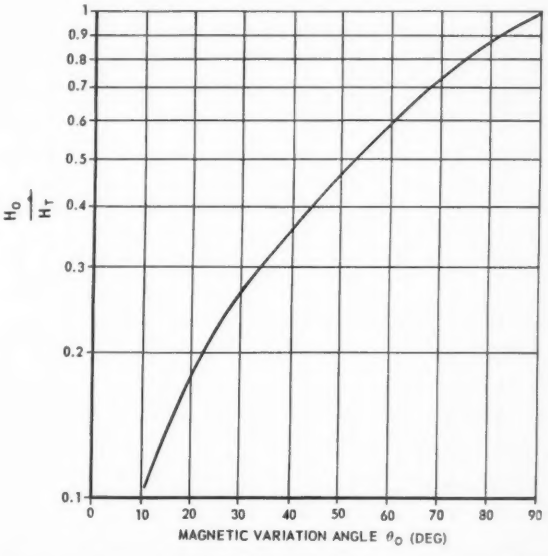

Fig. 4 Momentum disposal efficiency, H_0/H_T vs. magnetic field variation angle θ_0

magnetic torquing system removes momentum. This may be compared with the efficiency of the more conventional gas jet system.

In the case of steady-state torque input, the momentum in the system will go into a limit cycle with a period of half the orbital period. The momentum generated per cycle by the coils may be compared with the momentum input during the cycle. For an ideal gas momentum dump system, the momentum generated by the jets will be the same as the momentum input. Therefore, the ratio of input momentum to coil generated momentum gives a comparison between the efficiency of ideal gas jet and magnetic torquing momentum dumping systems.

This ratio H_0/H_T can be shown to be

$$H_0/H_T = \sin\theta/(1 + \cos\theta)$$

This is illustrated in Fig. 4. It is seen that for small values of the magnetic variation angle θ_0, the magnetic torquing system is quite inefficient in terms of total generated momentum. This ratio may also be used as a measure of the energy required by the dump system in terms of the external torque and magnetic field histories.

Reference

1 Kamm, L. J., "Magnetorquer—A Satellite Orientation Device," ARS JOURNAL, vol. 31, no. 6, June 1961, pp. 813–815.

Approximate Method of Predicting Hypersonic Pressure Distribution on Nonlifting Near Power Law Bodies Using Similar Flow Theory Results

N. R. AUGUSTINE[1]

Douglas Aircraft Co. Inc., Santa Monica, Calif.

BECAUSE of its simplicity, the axisymmetric strong shock similar flow theory (*blast theory*) presents an attractive method for predicting surface pressure coefficients. The applicability of this technique is, however, considerably restricted inasmuch as the form of similarity required by the theory is limited to power law bodies, i.e., bodies of the form $r_b \sim x^m$. An approximate method that enables results of similar flow theory to be applied to an extended class of configurations is described.

The results obtained by Kubota (1)[2] for the second-order approximation to surface pressure coefficient on power law bodies can be written, after slight algebraic manipulation, as

$$\frac{C_p}{(dr_b/dx)^2} = \phi_I^{(\gamma,\, m)} + \phi_{II}^{(\gamma,\, m)} \frac{\bar{x}^{2(1-m)}}{K^2} \qquad [1]$$

for the case where $M_\infty \gg 1$, $M_\infty\delta \gtrsim 1$ and $1/2 < m \leq 1$. Fig. 1 presents the numerical value of the functions ϕ_I and ϕ_{II} from the results given in (1). The functional dependence between pressure coefficient and body reference dimension exhibited by this equation, which in itself precludes rigorous application to nonpower law shapes, becomes insignificant if the following considerations are restricted to near power law bodies.

One possible approach to the problem of modifying the above results so that they can be applied to classes of shapes other than those of the form $r_b \sim x^m$ is to assume the surface pressure coefficient to be that given by similar flow theory for a cone that is locally tangent to the surface in question. That is, the values of ϕ_I (γ, m) and ϕ_{II} (γ, m) in Eq. 1 are replaced by ϕ_I $(\gamma, 1)$ and ϕ_{II} $(\gamma, 1)$ respectively for all m. However, as might be expected from a knowledge of classical tangent cone theory, the resulting surface pressures are overestimated. Nevertheless, this approach does suggest that it might be possible to estimate the surface pressure with the similar flow result (Eq. 1) by using the actual values of M_∞, δ, and (dr_b/dx) for the body in question along with some equivalent value of m (say m_{equiv}), as has been suggested in (1).

The exponent m, which defines the shape of power law bodies, can be interpreted as the ratio of the apex angle of the locally tangent cone to that of the secant cone that connects the body vertex to the point in question. The body shape exponent, defined as the ratio of tangent and secant cone angles (m_{tan}), has been selected as a convenient parameter for extending the similar flow theory results. Thus a general class of bodies of the form $r_b \sim x^{m_{tan}}$ is introduced, of which the power law shapes are a special case possessing the property that m_{tan} is a constant, independent of body station.

A number of analytical approaches to the problem of selecting an equivalent exponent to be used in Eq. 1 for nonpower law bodies have been considered, although a semiempirical method appears to give the best results. This conclusion is based on consideration of the inverse problem of determining the exponent m_{equiv}, which, when used in place of m in Eq. 1, correctly defines the experimentally observed pressures. The results of such a correlation encompassing a number of body shapes are presented in Fig. 2 as a function of m_{tan}, which may also be interpreted as the exponent of the locally tangent power law body that has a common vertex. These results are based on wind-tunnel data, flight test data, and numerical characteristics solutions over a Mach number range of 3.0 to 12.0(2–9). Also presented in Fig. 2 are the tangent cone result and the result given by similar flow theory for

Received Sept. 11, 1961.

[1] Aerodynamics Engineer, Missiles Aerodynamics Section. Member ARS.

[2] Numbers in parentheses indicate References at end of paper.

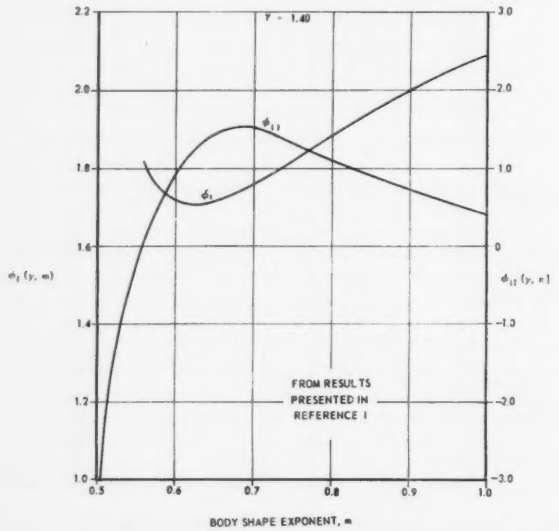

Fig. 1 First-and-second order pressure functions from similar flow solutions

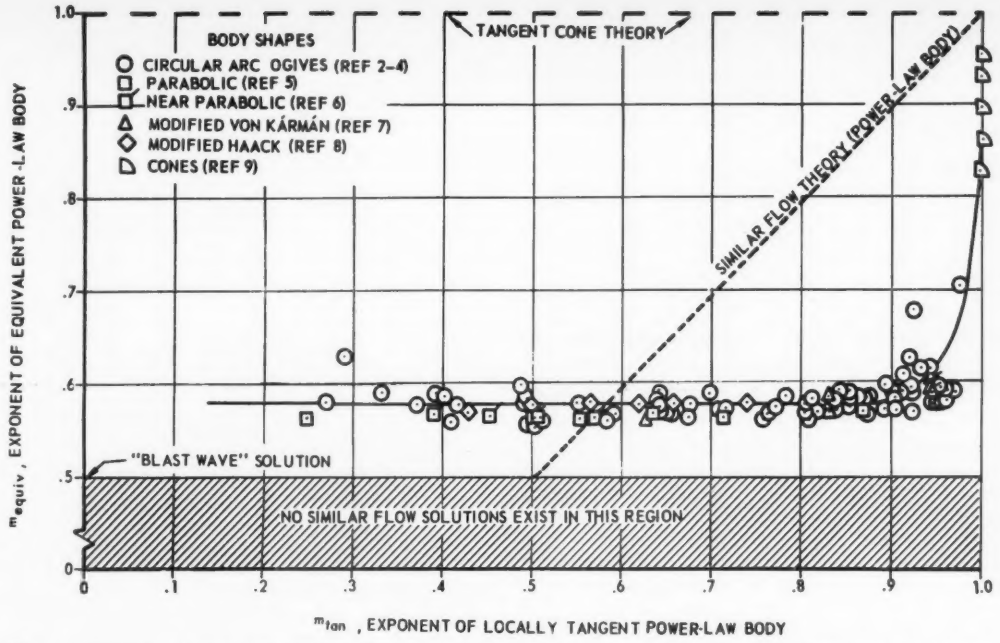

Fig. 2 Exponent of equivalent power law body as determined from correlation of theoretical and experimental results

power law bodies. The close correlation of the data points in this figure indicates that the pressure distribution on the various shapes considered can be predicted simply by using a constant value of m_{equiv} equal to about 0.58 in Eq. 1, although at points very near the nose a somewhat larger value is required, as shown in Fig. 2.

As might be anticipated from consideration of the blast wave case ($m = 0$, shock shape exponent $= {}^1/_2$), the assumption of a constant $m_{equiv} = 0.58$ over most of the body is best justified for bodies characterized by an extensive expansion field downstream of a fairly blunt nose. For bodies having little or no downstream expansion, e.g., power law shapes with $m \to 1$ where the tangent cone and secant cone are nearly identical, the value of m_{equiv} may be expected to be slightly larger than that determined in Fig. 1. It is, however, interesting to note that even for power law bodies the agreement between experiment and theory is frequently enhanced when the reduced value of m_{epuiv} is used rather than the actual body shape exponent, although this result must be regarded as fortuitous.

In conclusion, the hypersonic similar flow theory result for surface pressure coefficient on power law bodies can be extended to more generalized configurations by employing the equivalent body shape exponent shown in Fig. 2. The accuracy of the results thus obtained on the configurations investigated is somewhat better than the accuracy of methods such as Newtonian flow theory and tangent cone theory.

Acknowledgment

The author wishes to acknowledge the assistance of W. W. Tieman of the Douglas Aircraft Co. Inc., Missiles Aerodynamics Section.

Nomenclature

C_p = pressure coefficient, $(p - p_\infty)/q_\infty$
d = body maximum diameter
K = hypersonic similarity parameter, $M_\infty \delta$
L = body length
m = exponent in defining body shape equation for power law bodies
m_{tan} = exponent of power law body tangent to given arbitrary body at specified station
m_{equiv} = equivalent body shape exponent used in Eq. 1 for near power law bodies
M_∞ = freestream Mach number
p = local static pressure
p_∞ = freestream static pressure
q_∞ = freestream dynamic pressure
r_b = body radius
x = axial distance from body nose
$\bar{x}$ = nondimensional distance from body nose, x/L
γ = ratio of specific heats
δ = body thickness parameter, $(d/2)/L$
$\phi_{I,II}$ = first- and second-order pressure functions, respectively

References

1 Kubota, T., "Investigation of the Flow Around Simple Bodies in Hypersonic Flow," *GALCIT HRP Memo. no. 40*, 1957.

2 Lord, D. R. and Ulman, E. F., "Pressure Measurements on an Ogive-Cylinder Body at Mach Number 4.04," *NACA RM L51L20*, February 1952.

3 Savin, R. C., "Application of the Generalized Shock-Expansion Method to Inclined Bodies of Revolution Traveling at High Supersonic Airspeeds," *NACA TN 3349*, 1955.

4 Rossow, V. J., "Applicability of the Hypersonic Similarity Rule to Pressure Distributions which Include the Effects of Rotation for Bodies of Revolution at Zero Angle of Attack," *NACA TN 2399*, June 1951.

5 Lange, R. H. and Wittliff, C. E., "Force and Pressure—Distribution Measurements at a Mach Number of 3.12 on Slender Bodies Having Circular, Elliptical, and Triangular Cross Sections and the Same Longitudinal Distribution of Cross Sectional Area," *NACA RM L56D17*, July 1956.

6 Jack, J. R. and Burgess, W. C., "Aerodynamics of Slender Bodies at a Mach Number of 3.12 and Reynolds Numbers From 2×10^6 to 15×10^6: I—Body of Revolution with Near Parabolic Forebody and Cyindrical Afterbody," *NACA RM E51H13*, November 1951.

7 Bland, W. M., Jr. and Kolenkiewicz, R., "Free Flight Pressure Measurements Over a Flare Stabilized Rocket Model With a Modified Von Kármán Nose for Mach Numbers up to 4.3," *NACA RM L57J24*, 1958.

8 Ehret, D. M., "Accuracy of Approximate Methods for Predicting Pressures on Pointed Nonlifting Bodies of Revolution in Supersonic Flow," *NACA TN 2764*, August 1952.

9 Ames Research Staff, "Equations, Tables, and Charts for Compressible Flow," *NACA TR 1135*, 1953.

Gaseous Detonation Wave Interactions With Nonrigid Boundaries

WILLIAM P. SOMMERS[1]

Martin Co., Division of Martin-Marietta Corp.
Baltimore, Md.

This article reports some experiments in which Chapman-Jouguet detonations in gaseous explosives were subjected to compressible and flexible confinement. Schlieren photographs show that the detonation wave boundary interaction can cause merely a curvature of the wave front or, under other circumstances, quench the combustion process. Both oblique and detached shocks are observed in the boundaries.

EXPERIMENTAL studies[2] on the detonation characteristics of gaseous explosives are usually performed in shock or detonation tubes made of steel or equally rigid materials. This method not only provides the most convenient means of performing such experiments, but it also furnishes the confinement necessary to maintain the one-dimensional flow condition assumed in most theoretical analyses. In a recent study, however, some experiments were made on gaseous detonation waves confined by semiflexible and compressible boundaries (1).[3] Under compressible confinement the properties of the detonation wave are altered considerably, and the theoretical description of the detonation process must include an analysis of the boundary.

The experimental arrangement consisted of a vertically mounted detonation tube approximately 5-ft long and open at the top. Both a round pipe (0.3-in. ID) and a tube of rectangular cross section ($^3/_8 \times {}^1/_2$ in.) were used. The test section was mounted on top of the tube so that the explosive gases, on leaving the tube exit, flowed through a region providing the desired boundary conditions. The gaseous fuel and oxidizer were introduced into the tube base through sonic metering orifices, mixed, and allowed to flow upward through the tube and out the exit. The flow velocities were sufficiently low to maintain a laminar flow of the detonable mixture and were also low enough so that the detonation waves being studied could be assumed to be propagating into quiescent mixtures. (In all cases, the flow velocity was less than 0.3% of the detonation velocity.) Since oxygen and hydrogen were used most frequently as the explosive, the vertical tube arrangement exploited the buoyant forces in maintaining a stable flow from the tube.

Detonations were formed by igniting the explosive at the tube base. The transition process from deflagration to detonation was such that Chapman-Jouguet detonations were formed prior to reaching the test section. In this manner the influences of the various boundaries on fully developed Chapman-Jouguet detonations could be determined. The test sections consisted in turn of the surrounding air, a Saran Wrap[4] tube, and a two-dimensional section that allowed several types of inert gases to be used as a boundary. The first two test sections were used in conjunction with the round detonation tube and the third with the rectangular tube. Fig. 1 is a sketch of the two-dimensional test section.

Spark-schlieren photographs were taken of the detonation wave during its passage through the test region. Because the equipment used allowed only one photograph to be taken per

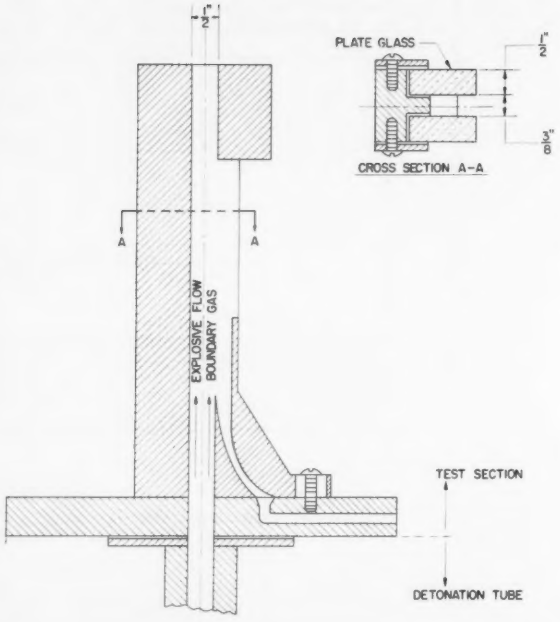

Fig. 1 Cross-sectional sketch of two-dimensional test section

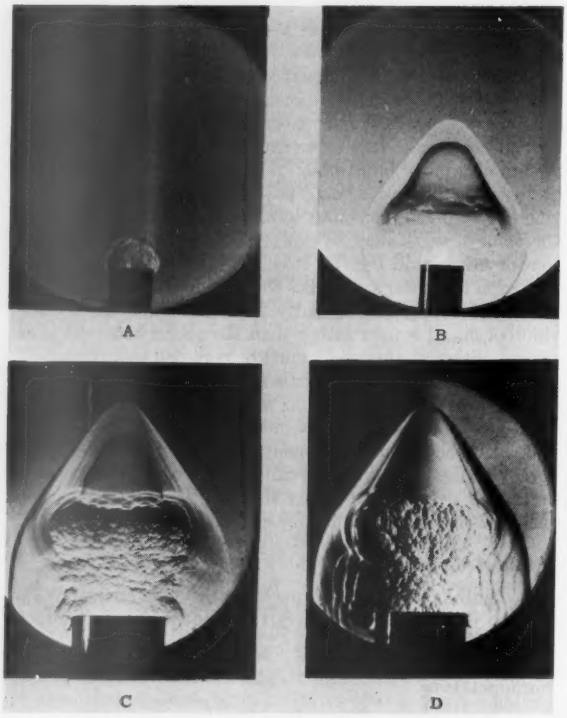

Fig. 2 Failure of detonation to propagate up unconfined column of 80% hydrogen-20% oxygen

Received Sept. 14, 1961.

[1] Chief, Chemical Propulsion, Propulsion and Thermodynamics Dept. Associate Member ARS.

[2] The experiments reported in this paper were performed at the Aircraft Propulsion Laboratory, University of Michigan, Ann Arbor, Mich.

[3] Numbers in parentheses indicate Reference at end of paper.

[4] A clear plastic wrapping material produced by the Dow Chemical Co.

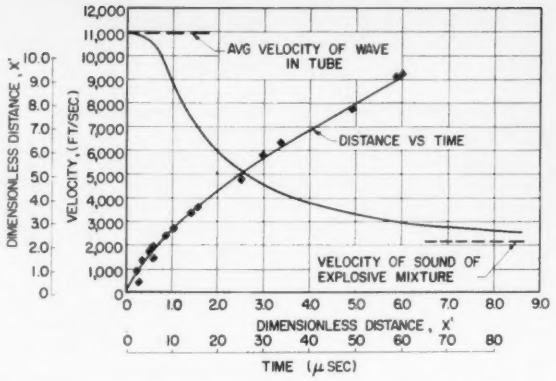

Fig. 3 Progression of shock front up column of 80% hydrogen-20% oxygen

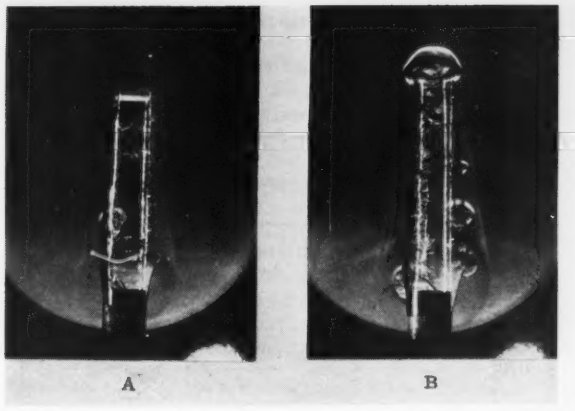

Fig. 4 Detonation of 80% hydrogen-20% oxygen within a Saran Wrap tube

experiment, the experiments were designed to be highly repeatable. A number of checks showed the experiments were repeatable to within ±1% of the detonation velocity. A variable microsecond time-delay unit was used to sequence the photographs so that the influence of a given boundary on a detonation could be constructed from a series of individual photographs. The detonation velocity was measured electronically through the use of two ionization probes and a time interval meter accurate to ±0.1 μsec.

The initial experiments were performed using the round detonation tube and an explosive composed of 80% hydrogen and 20% oxygen by volume. In these experiments a stable jet of the explosive was established in still air, and attempts were made to propagate a detonation up the unconfined column of explosive. Fig. 2 is a sequence of four schlieren photographs that show that the detonation failed to propagate any discernible distance past the tube exit. Instead, the detonation was quenched and thereby deteriorated to a shock wave followed by the combustion products from the tube. Exposures A and D in the sequence were taken with the knife edge parallel to the centerline of the tube, and B and C with it perpendicular. The end of the tube, which is visible at the bottom of the pictures, has a far smaller outside diameter in exposures A and B than in the others, due to machining the tube wall thickness from 0.35 to 0.05 in. prior to these experiments. In frames A and D the explosive jet is well defined. A Mach disk is visible in B. Also visible is the gas interface between the hydrogen-air mixture and the air. The interface is the blunt nose that trails the shock front. Pictures C and D are photographs of identical experiments; this demonstrates their repeatability.

Fig. 3 is a distance vs. time and velocity vs. distance plot of the shock front, which was constructed from photographs such as shown in Fig. 2. The distance X is measured along the tube centerline, starting at the exit, and X' is equal to the distance X divided by the tube's internal diameter, 0.3 in. At $X' = 9.0$, the shock speed is roughly 2500 fps, just slightly higher than the speed of sound in the explosive jet.

Because of the failure to detonate an unconfined column of oxygen and hydrogen, a form of confinement was tried which was thought to be between that provided by air and shock tubes. Fig. 4 shows the results when one layer of Saran Wrap, which is approximately 0.0005-in. thick, was wrapped into a tube. The explosive was 80% hydrogen and 20% oxygen. In the first exposure the detonation wave is approximately at the end of the Saran Wrap tube. The wave is clearly one-dimensional in nature, indicating that an extremely thin material can constitute infinite confinement for a gaseous explosive. Following the passage of the detonation, the tube

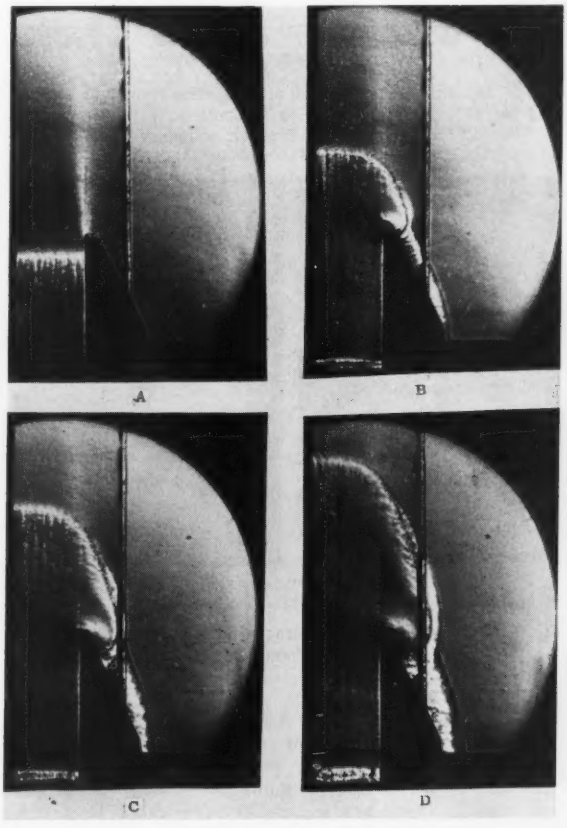

Fig. 5 Detonation of 50% hydrogen-50% oxygen with an air boundry

developed some leaks due to the deteriorating effect of heat on Saran Wrap.

The next set of experiments was performed using the two-dimensional test section shown in Fig. 1. The glass walls maintained the two dimensionality of the detonation, whereas the metal wall was effectively the centerline of an experiment

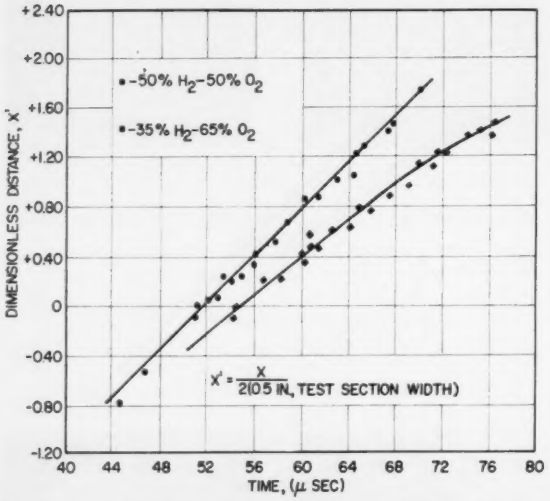

Fig. 6 Dimensionless distance of detonation from tube exit vs. time for 50% hydrogen-50% oxygen and 35% hydrogen-65% oxygen, each with an air boundary

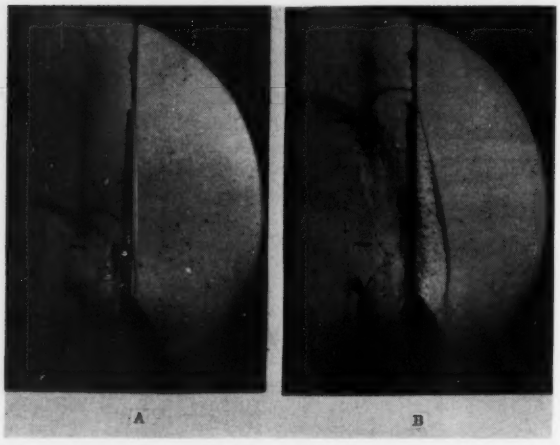

Fig. 7 Detonation of 35% hydrogen-65% oxygen next to a helium boundary

twice as wide. Fig. 5 is a sequence of four photographs showing the propagation of a detonation in a 50-50 mixture of oxygen and hydrogen with an air boundary. Although the wave front becomes curved, the detonation is not quenched by the effect of the compressible boundary. An oblique shock wave and the gas interface between the combustion products and the air are visible below and to the right of the detonation. It was found that stoichiometric oxygen-hydrogen could also be detonated successfully next to an air boundary, while 35% hydrogen and 65% oxygen was quenched. Fig. 6 gives a plot of the results for the 50% and 35% hydrogen by volume mixtures. Some methane, ethane, and propane-oxygen mixtures will also detonate successfully next to air boundaries.

The relative success of the two-dimensional arrangement, compared to the axisymmetric experiments, was attributed to two influences. First, a critical or minimum diameter exists for any detonation. Since the two-dimensional test section was approximately triple in size of the round tube, it is possible that the critical size was exceeded only in the former. Second, two-dimensional shocks are attenuated less rapidly than three-dimensional shocks. Thus, the two-dimensional test section gave effectively better confinement.

A theoretical analysis (1) has shown that the curvature of the wave front, apparent in Fig. 5, is not due to diffusion of the air into the explosive. Instead, it was determined that the wave curvature and quenching are caused by the lateral expansion of the reacting gases between the shock and the Chapman-Jouguet plane. This lateral expansion is the result of the compressibility of the boundary and thus is not observed during the detonation of gaseous explosives with rigid confinement.

In the course of the theoretical analysis it was also noted that different inert gas boundaries could promote different types of interactions between a detonation wave and the boundary. Fig. 7 shows two photographs of the passage of a detonation in 35% hydrogen and 65% oxygen through a two-dimensional region having a helium boundary. Under these circumstances the shock in the boundary is a detached or bow shock. This particular set of experiments clearly demonstrated that the wave front curvature is not due to dilution of the explosive with inert gas along the jet edge, since the dilution of hydrogen-oxygen mixtures with helium increases the detonation velocity. The effect of dilution would therefore require the detonation wave to curve forward, rather than backward, at the jet boundary

Acknowledgment

The help of the staff members of the Aircraft Propulsion Laboratory, especially R. E. Cullen, P. O. Hays, and C. Iott, and the direction of R. B. Morrison, who suggested the study, are gratefully acknowledged.

Reference

1 Sommers, W. P., "The Interaction of a Detonation Wave with an Inert Boundary," University of Michigan Ph. D. thesis, February 1961 (Industry Program Publication, *IP-501*).

Theory of Liquid Atomization in High Velocity Gas Streams

ERNEST MAYER[1]

National Engineering Science Co., Pasadena, Calif.

Liquid atomization by high velocity gas streams is investigated analytically by consideration of gas liquid interface behavior in the regime of capillary wave (ripple) propagation. With given fluid properties (ρ_g, ρ_l, σ, μ_l) and wind velocity relative to the liquid V_g, it is shown that all wavelengths λ exceeding a minimum value λ_{min} will grow at an exponential rate characterized by a time modulus τ dependent on λ and the fluid parameters. It is postulated that when the wind induced wavelength λ has grown to an amplitude comparale to λ, the crest of the wave is shed as a ligament from which droplets of diameter D also proportional to λ are formed. By consideration of the steady-state droplet formation rate on a large liquid surface, an expression is derived for the droplet size distribution function. The latter yields the following formula for the average droplet size obtained on primary atomization $\overline{D} = 9\pi \sqrt[3]{16}B(\mu_l\sqrt{\sigma/\rho_l}/\rho_g V_g^2)^{2/3}$, where B is a numerical factor conceptually of the order of unity. The theoretical result for $\overline{D}$ is in satisfactory agreement with empirical correlations proposed by Weiss and Worsham on the basis of extensive data obtained under conditions corresponding closely to primary atomization.

THE ATOMIZATION of liquid jets by high velocity gas streams is an important process in many technical applications. Owing to the complexity of the physical phenomena involved in the process, the study of liquid atomization in the high velocity gas flow is pursued principally by empirical methods yielding correlations of droplet size with fluid parameters. In particular, a "most serious lack of information is found in the determination of drop-size distributions from the properties of the liquid jet and its surrounding atmosphere" (2).[2]

This note presents a theoretical approach to the problem of atomization in the high velocity regime. In this regime the behavior of the gas-liquid interface appears to govern the atomization process, in accordance with the conclusions reached by Weiss and Worsham (1), quoted in the following paragraph.

> The atomization of liquids by large high velocity airstreams occurs by direct action of the airstream on the exposed liquid surface. Therefore, relative velocity between liquid- and airstreams is of primary importance. Physical properties of the fluids do affect spray fineness, but their net influence is less critical. The exact way in which the liquid is introduced to the air, i.e., the geometry and operation of the injector, is of least importance, particularly at very high air velocities and for customary ranges of the variables.

A fundamental approach to the problem of atomization is made by considering the development of capillary waves (ripples) that are produced by a high velocity gas flow along the liquid surface. Waves of very small wavelength cannot be developed readily because of viscous dissipation. Waves of very long wavelength are slow to develop because of inertial effects, even though in this case viscous dissipation is negligible. Between the extremely short and long (capillary) wavelengths there exists a spectrum of wavelengths which can be excited to appreciable amplitudes during the time of action of the high velocity gas flow. It is reasonable to postulate that if such a wavelength λ with a characteristic excitation time $\tau(\lambda)$ has developed to an amplitude comparable with λ, the gas stream will erode the wave crest as a ligament from which droplets of diameter comparable in size to λ are formed. Thus, by considering a liquid of large surface and great depth, it is possible to assess the fundamental role of fluid properties in the primary atomization of the liquid due to a high velocity gas stream. In particular, kinetic data associated with $\tau(\lambda)$ permit an estimation of the atomization mass flux producing primary droplets derived from capillary wavelengths in the range from λ to $\lambda + d\lambda$, i.e., the primary drop-size spectrum. Furthermore, such kinetic data furnish a basis for assessing the effect of finite liquid boundaries (initial jet configuration) on the primary drop-size distribution and for treating the process of secondary atomization which affects the larger drops in the primary spectrum.

Received Sept. 18, 1961.

[1] Associate Director. Member ARS.

[2] Numbers in parentheses indicate References at end of paper.

Wind-Induced Capillary Waves

An example of wind-generated gravity waves has been analyzed by Jeffreys (quoted in Ref. 3, p. 625). An approximate energy balance for the surface wave of amplitude α is considered by Jeffreys in the form

$$\frac{d\alpha}{dt} = \left\{\frac{\beta\rho_g(V_g - c)^2}{2\rho_l c}\, k^{1/2} - \frac{2\mu_l}{\rho_l}\, k^2\right\} \alpha \qquad [1]$$

In addition to the usual hydrodynamic parameters (see Nomenclature), Eq. 1 contains a *sheltering* parameter $\beta \leq 1$ associated with the portion of the wave crest exposed to the driving effect of the wind. On solving Eq. 1 for gravity waves ($c = \sqrt{g/k}$), Jeffreys obtained good agreement with measured data for the smallest relative wind velocity V_g required to maintain waves, provided the effective value of β is 0.3.

In application to the atomization problem, the solution of Eq. 1 for capillary surface waves (ripples) having the wave velocity c (Ref. 3, p. 457) is considered.

$$c = \sqrt{\sigma k/\rho_l} \qquad [2]$$

where σ is the surface tension.

Substituting c from Eq. 2 into Eq. 1 and neglecting c in comparison with V_g gives

$$\frac{d\alpha}{dt} = \frac{\alpha}{\tau} \qquad [3]$$

where, for convenience, the reciprocal time modulus $1/\tau$ is expressed in terms of the wavelength $\lambda = 2\pi/k$

$$\frac{1}{\tau} = \frac{f}{\lambda^{1/2}} - \frac{v}{\lambda^2} \qquad [4]$$

with

$$f = \sqrt{\frac{\pi}{2}}\,\frac{\beta\rho_g V_g^2}{\sqrt{\sigma\rho_l}} \qquad [5]$$

$$v = \frac{8\pi^2\mu_l}{\rho_l} \qquad [6]$$

A schematic curve of positive τ vs. λ is shown in Fig. 1 for constant values of the forcing parameter f and the viscous damping parameter v. In view of Eq. 3 the capillary waves will grow or diminish according to whether τ is positive or negative. Thus the wind-maintained wavelengths are greater than a minimum value obtained by the condition $1/\tau = 0$ or

$$\lambda \geq \lambda_{min} = \left(\frac{v}{f}\right)^{2/3} = 2\pi\sqrt[3]{16}\left(\frac{\mu_l\sqrt{\sigma/\rho_l}}{\beta\rho_g V_g^2}\right)^{2/3} \qquad [7]$$

Atomization Mechanism

The following mechanism of atomization is postulated. When the wind-induced wave of length λ has grown to an amplitude comparable with λ, the crest of the wave is eroded as a ligament from which droplets of size proportional to λ are

formed

$$D = F\lambda \qquad [8]$$

where F, a dimensionless configuration factor, is independent of λ but possibly dependent on fluid parameters. On conceptual grounds F is anticipated to be of the order of unity. If F were a constant independent of fluid data, the assumption in Eq. 8 would imply a general similarity condition for the crest configuration and ligament formation preceding breakup into droplets. Preliminary comparison of theoretical results based on Eq. 8 with experimental data in (1) suggests that F depends somewhat on liquid viscosity μ_l but is nearly independent of ρ_g, ρ_l, σ, and v_g.

We note that the frequency of ligament formation or crest erosion at the wavelength λ is $1/\tau$ given by Eqs. 4, 5, and 6.

Droplet Size Distribution

Consider now the rate of formation of droplets per unit liquid surface area. Based on the above assumption, the erosion rate in the wavelength range from λ to $\lambda + d\lambda$ is proportional to $\lambda/\tau(\lambda)$. Therefore, the atomization mass flux obtained in the wavelength range from λ to $\lambda + d\lambda$ is given by the proportionality

$$\dot{m}(\lambda)d\lambda \sim \rho_l \frac{\lambda}{\tau(\lambda)}\, d\lambda \qquad [9]$$

The droplet formation rate $\dot{n}(\lambda)$ per unit area of the liquid associated with $\dot{m}(\lambda)$ in accordance with Eq. 8 is given by

$$\rho_l \lambda^3 \dot{n}(\lambda)d\lambda \sim \dot{m}(\lambda)d\lambda \qquad [10]$$

Thus, aside from numerical factors that account for the crest configuration at the instant of erosion, the steady state droplet formation rate is obtained from waves in the range from λ to $\lambda + d\lambda$

$$\dot{n}(\lambda)d\lambda \simeq \frac{d\lambda}{\lambda^2\tau(\lambda)} \qquad [11]$$

In view of the relation between D and λ postulated in Eq. 8, the functional form $1/\lambda^2\tau(\lambda)$ represents the drop-size distribution obtained in primary atomization.

It follows that the mean droplet size

$$\bar{D} = F\bar{\lambda} \qquad [12]$$

is determined from

$$\bar{\lambda} = \int \lambda \dot{n}(\lambda)d\lambda \Big/ \int \dot{n}(\lambda)d\lambda \qquad [13]$$

which yields, upon substitution from Eqs. 4 and 11 and integration

$$\bar{\lambda} = \int_{\lambda_{m\,in}}^{\infty} d\lambda/\lambda\tau(\lambda) \Big/ \int_{\lambda_{m\,in}}^{\infty} d\lambda/\lambda^2\tau(\lambda) = (9/2)\lambda_{min} \qquad [14]$$

Substituting from Eqs. 7 and 14 into Eq. 12, the expression for the mean droplet diameter in terms of fluid parameters is obtained

$$\bar{D} = 9\pi\sqrt[3]{16}B\left(\frac{\mu_l\sqrt{\sigma/\rho_l}}{\rho_g V_g^2}\right)^{2/3} \qquad [15]$$

where

$$B = F/\beta^{2/3} \qquad [16]$$

is a composite numerical factor including the sheltering parameter β and the parameter F associated with the crest configuration at the instant of erosion. Since the latter parameters are of the order of unity, B is also of the order of unity on conceptual grounds.

Comparison With Experimental Data

Comparison of the theoretical result for $\bar{D}$ is made with empirical correlations obtained by Weiss and Worsham (1) in experimental studies of the atomization of molten wax in high velocity gas streams. Both co-stream and contra-stream injections were investigated with nozzles of several orifice sizes, wax and air temperatures being maintained at the same temperature in the range from 300° to 400°F. Because of the low vapor pressure of the wax and the chilling of the droplets in the sampling probe, the collected spherical particles are believed to correspond closely to those produced by primary atomization.

The salient experimental result obtained is the velocity dependence $\bar{D}_{exp} \sim V_g^{-4/3}$ over the range of pressures (P = 1 to 5 atm) and temperature (300° to 400°F) in the experiments, in agreement with the theoretical result in Eq. 15. The proposed correlation with surface tension is $D_{exp} \sim \sigma^{1/4}$ as compared with the theoretical dependence $\bar{D} \sim \sigma^{1/3}$ in Eq. 15. In regard to the influence of air density, the suggested correlation is $\bar{D}_{exp} \sim (1 + 1/P)$, where P is the pressure in atmospheres. However, an effective exponent n based on the relation $\bar{D} \sim \rho_g{}^n$ can be inferred directly from the test data indicated in Fig. 11 of (1). This figure shows that in the high velocity regime ($V_g \sim 600$ fps) an increase of pressure from 1 to 1.5 atm reduces the mean diameter from 36 to 26 micron, implying the value $n \sim -0.7$ in agreement with the theoretical result $n = -2/3$ in Eq. 15.

No definite dependence of $\bar{D}_{exp}$ on ρ_l can be ascertained from the experimental data because of the limited variation of the temperature T in the temperature range from 300° to 400°F. In regard to the influence of liquid viscosity μ_l on $\bar{D}_{exp}$, it may be seen that for the viscosity exponent n' in $\bar{D}_{exp} \sim \mu_l{}^{n'}$, the experimental data of (1) yield $n' = 1/3$ as compared with the theoretical exponent of $2/3$ in Eq. 15. To account for this discrepancy within the framework of the theoretical model, it is suggested that the configuration factor F may contain a viscosity dependence of the form $F \sim \mu^{-1/3}$; i.e., with increasing viscosity a relatively smaller fraction of the wave crest is eroded in ligament shedding. The dependence of F on μ_l and possibly on other fluid parameters can be ascertained directly on the basis of fundamental study of the capillary wave behavior under high velocity gas flow along a large liquid surface.

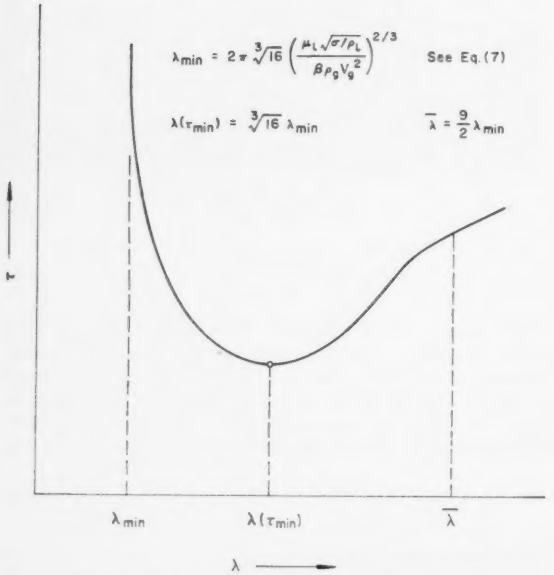

Fig. 1 Sketch of time modulus τ vs. capillary wavelength λ showing the most rapidly growing wavelength $\lambda(\tau_{min})$, and average effective wavelength $\bar{\lambda}$ in capillary mechanism of atomization

Finally, note the numerical value of the factor B required for agreement between the theoretical expression Eq. 15 and the observed data at, say, $V_g = 600$ fps, $P = 1$ atm, $T = 300°F$ in (1), from which the relevant data are quoted below

$$\begin{aligned} \bar{D}_{exp} &= 36 \times 10^{-4} \text{ cm} \\ V_g &= 1.85 \times 10^4 \text{ cm/sec} \\ \rho_g &= 0.80 \times 10^{-3} \text{ gm/cm} \\ \sigma &= 22 \text{ gm/sec}^2 \\ \mu_l &= 0.113 \text{ gm/cm-sec} \\ \rho_l &= 0.828 \text{ gm/cm}^3 \end{aligned}$$

The estimated value of B based on the above data is

$$B \sim 0.30 \qquad [17]$$

This value is of the order of magnitude anticipated for the model considered.

Further resolution of B into the factors indicated in Eq. 16 may be made by assuming the value for the sheltering parameter $\beta \sim 0.3$, determined by Jeffreys, which leads to $F \sim 0.14$. This result implies that a small but significant portion of the wave crest is shed as a ligament at the instant of erosion.

Concluding Remarks

The agreement between the experimental data and the results based on the idealized model of the capillary mechanism of atomization warrants the belief that this mechanism accounts for spray formation produced by high velocity atomization of liquid jets. However, in application to jets of finite size, consideration must be given to the deformation and erosion of the finite liquid element under external aerodynamic forces and internal wave interference effects. In particular, it can be seen that for an initial effective jet diameter D_j large compared with $\bar{\lambda}$, the lifetime of the eroding jet may be estimated from

$$t_j \sim D_j \tau(\bar{\lambda})/\bar{\lambda}$$

The finite lifetime of the jet limits the time interval available for growth of capillary waves, resulting in a modification of the drop-size spectrum with a drop-size cutoff determined by the maximum wavelength λ_{max} that can developed during the lifetime of the eroding liquid element. Thus, the influence of D_j on the atomization in high velocity gases increases in importane as D_j is made smaller, as revealed in the empirical result reported in (1), $\bar{D}_{exp} \sim D_j^{1/6}$.

The preceding concepts are readily extended to the treatment of secondary atomization, which affects the drop-size distribution principally by increasing the small size population at the expense of large size population in the primary spectrum.

Finally, it can be seen that if the liquid and the high velocity gas are at different temperatures, the capillary mechanism of atomization implies that the reference temperature for correlating drop-size data with liquid properties is either the gas temperature or the boiling temperature of the liquid, whichever is smaller.

Nomenclature

g = gravity acceleration, cm/sec²
k = wave number, cm^{-1}
$\dot{m}$ = atomization mass flux per unit wavelength range, (gm/cm)/cm²-sec
$\dot{n}$ = droplet formation rate, (1/cm)/cm²-sec
t = time, sec
μ = dynamic viscosity, gm/cm-sec
ρ = density, gm/cm³
σ = surface tension, dyne/cm

Subscripts

g = gas
j = jet
l = liquid

References

1 Weiss, M. A. and Worsham, C. H., "Atomization in High Velocity Airstreams," ARS JOURNAL, vol. 29, no. 4, April 1959, p. 252.
2 Miesse, C. C., "From Liquid Stream to Vapor Trail," *Proc. of the Gas Dynamics Symposium on Aerothermochemistry*, Northwestern Univ., Chicago, Ill., 1956.
3 Lamb, H., *Hydrodynamics*, 6th ed., Dover Publications, New York, 1945.

Interdependence of Base Pressure and Base Heat Transfer

R. J. DIXON[1]

Aero-Space Division, Boeing Co., Seattle, Wash.

R. H. PAGE[2]

Rutgers University, New Brunswick, N. J.

HEAT transfer from the base wall to the free stream increases the base pressure. One of the consequences of this trend is that increasing the base wall temperature (e.g., by combustion) above the free stream stagnation temperature decreases the drag. However, in the case of high flight Mach numbers, this may lead to base wall temperatures that are much too high for structural purposes. Indeed, in some cases the base heating problem that occurs naturally has already attracted considerable interest. The interaction between base pressure and base heat transfer has been theoretically predicted (1, 2, 3)[3] and experimentally observed (4, 5).

Because of the complexity of the relationship between base pressure and heat transfer, it is convenient to describe this interdependence graphically. A chart has been prepared which directly indicates this effect for airflow over a two-dimensional body with a turbulent wake and a negligible wall boundary layer. This chart is based on the theory of (1, 2, 3) and is presented in Fig. 1.

Fig. 1 shows the theoretical change in the base pressure ratio due to a diabatic wake. Lines of constant value of the heat transfer parameter D are plotted. Positive values of D correspond to heat addition to the wake from the wall. Negative values of D indicate that the direction of heat transfer is from the wake to the wall. For a particular configuration and flow condition, D may be determined from Eq. 1

$$D = \frac{\sigma Q_b}{H c_p p_{0_{1_a}} \sqrt{T_{10_a}}} \left(\frac{R}{k g_c}\right)^{1/2} \left(\frac{k+1}{2}\right)^{(k+1)/2(k-1)} \qquad [1]$$

Received Aug. 17, 1961.

[1] Research Engineer, Flight Technology Dept.
[2] Boeing Co. Consultant, and Chairman, Department of Mechanical Engineering.

[3] Numbers in parentheses indicate References at end of paper.

where

Q_b = heat transfer per unit width from the adjacent walls to the wake
H = base height (height of simple back step or half height of trailing edge)
c_p = specific heat at constant pressure
p_{0_a} = stagnation pressure of the free stream just before the base
T_{0_a} = free stream stagnation temperature
R = gas constant
k = ratio of specific heats
g_c = gravitational constant
σ = similarity parameter for the homogeneous coordinate of the mixing region

Precise numerical values of σ are not yet well defined for high Mach number mixing regions, and so an experimental investigation of σ at high Mach numbers is needed. For the present only limited emperical relationships (6, 7) are available. These data indicate that σ is greater than 12.0 for supersonic mixing, and its value is dependent on the gas and the adjacent Mach number.

In applying Fig. 1, first obtain an estimate of the value of σ and then determine the value of D from Eq. 1. Entering Fig. 1 with D and the approach Mach number[4] (immediately before the base), the percent change in base pressure due to the heat transfer can be directly obtained.

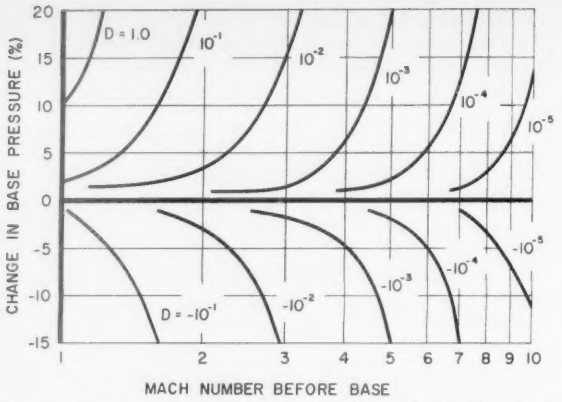

Fig. 1 Base pressure change as influenced by the heat transfer parameter

References

1 Page, R. H. and Korst, H. H., "Nonisoenergetic Compressible Jet Mixing with Consideration of Its Influence on the Base Pressure Problem," *Proceedings of the Fourth Midwestern Conference on Fluid Mechanics*, Purdue Univ., September 1955, pp. 45–68.

2 Page, R. H., "On Turbulent Supersonic Diabatic Wakes," ARS JOURNAL, vol. 29, no. 6, June 1959, pp. 443–445.

3 Korst, H. H., Chow, W. L. and Zumwalt, G. W., "Research on Transonic and Supersonic Flow of a Real Fluid at Abrupt Increases in Cross-Section (With Special Consideration of Base Drag Problems)," *Engng. Experimental Station Rep. no. ME-TR-392-5*, Univ. of Illinois, December 1959.

4 Kurzweg, H. H., "Inter-Relationship Between Boundary Layer and Base Pressure," *J. Aeronaut. Sci.*, vol. 18, 1951, pp. 743–748.

5 Goethert, B. H., "Base Flow Characteristics of Missiles with Cluster-Rocket Exhausts," *IAS paper no. 60-89*, Summer Meeting, Los Angeles, Calif., June 1960.

6 Korst, H. H. and Tripp, W., "The Pressure on a Blunt Trailing Edge Separating Two Supersonic Two-Dimensional Air Streams of Different Mach Numbers and Stagnation Pressures but Identical Stagnation Temperatures," *Proceedings of the Fifth Midwestern Conference on Fluid Mechanics*, Univ. of Michigan, April 1957, pp. 187–199.

7 Vasiliu, J., "Determination of Temperature, Velocity, and Concentration Profiles in the Mixing Layer Between a Rocket Exhaust Jet and the Surrounding Supersonic Air Stream," *Engng. Dept. Rep. no. ERR-AN-005*, Convair-Astronautics, March 1960.

[4] The influence of a boattail or flare can be handled via the reduced Mach number concept (3).

Solutions for Satellite Motion Under Low Acceleration Using the Method of Variation of Parameters

STEPHEN J. CITRON[1]

Purdue University, Lafayette, Ind.

THE PROBLEM of analytically determining the motion of a thrusting satellite has been treated by several authors using different methods. Tsien (1),[2] Dobrowolski (2), and Copeland (3) obtain solutions by using elliptic integrals, whereas Perkins (4) uses linear perturbations. Lass and Lorell (5), using the method of Kryloff and Bogoliuboff, obtain results in agreement with the preceding references which, in certain cases, are arrived at more quickly.

This paper attempts to point out that some of the results previously found can be obtained more easily by using the classical method of variation of parameters. For illustration, the problem of a satellite in an initially circular orbit perturbed by a constant radial acceleration[3] or a constant transverse acceleration is considered. The results are then compared with those found in (5).

The equations for the variation of the perturbed elements of the orbit needed for the comparison are given by (6).

$$\frac{da}{dt} = \frac{2a^2}{\sqrt{\mu p}} \{ea_r \sin \xi + a_t(1 + e \cos \xi)\} \quad [1a]$$

$$\frac{de}{dt} = \frac{1}{e}\sqrt{\frac{p}{\mu}} \left\{ea_r \sin \xi + a_t \left(\frac{p}{r} - \frac{r}{a}\right)\right\} \quad [1b]$$

$$\frac{d\omega}{dt} = \frac{1}{e}\sqrt{\frac{p}{\mu}} \left\{-a_r \cos \xi + \left(1 + \frac{r}{p}\right) a_t \sin \xi\right\} \quad [1c]$$

In the following work cases are considered where e is small, retaining only first-order terms in the expansions used.

To determine the variation of the quantities of interest over one revolution, Eqs. 1a, b, c are integrated over one cycle with the approximation

$$dt = \frac{rd\xi}{v}[1 + 0(e^2)] \simeq \frac{rd\xi}{v} \quad [2]$$

The velocity of a vehicle in a circular orbit is found from

$$v^2 = \mu(2/r - 1/a) \quad [3]$$

where since

$$\frac{r}{a} = \frac{p/a}{1 + e \cos \xi} \simeq 1 - e \cos \xi \quad [4]$$

Received Sept. 25, 1961.

[1] Assistant Professor of Aeronautical and Engineering Sciences.

[2] Numbers in parentheses indicate References at end of paper.

[3] In the case of radial acceleration, the perturbation is assumed to be of a magnitude such that escape does not occur, cf., (2).

Eq. 3 yields

$$v \simeq \sqrt{\mu/r}\ \{1 + e/2 \cos \xi\} \qquad [5]$$

Since it can be expected that the parameters on the right-hand side of Eqs. 1a, b, c will not vary greatly over one cycle, integrations are performed using their initial values. For the eccentricity e, which is initially zero, the average value over the cycle $\bar{e}$ is used.

Constant Radial Acceleration Perturbation

For this case Eqs. 1a, b, c are used with $a_t = 0$. Eq. 1b may be transformed into

$$\frac{de}{d\xi} \simeq \frac{a_0^2}{\mu}\, a_r \sin \xi \qquad [6]$$

which on integration, noting that $e\ (0) = 0$, gives

$$e(\xi) = (a_r a_0^2/\mu)(1 - \cos \xi) \qquad [7]$$

The average eccentricity over the revolution is thus

$$\bar{e} = a_r a_0^2/\mu \qquad [8]$$

Having $\bar{e}$, the rotation of the line of apsides may be determined from Eq. 1c rewritten in the form

$$d\omega/d\xi \simeq -[\cos \xi - 2\bar{e} \cos^2 \xi] \qquad [9]$$

Integrating Eq. 9 over one cycle, the rotation of the line of apsides per revolution is found to be

$$\Delta\omega = 2\pi a_r a_0^2/\mu \qquad [10]$$

The change in the semimajor axis caused by a_r is obtained from Eq. 1a. Writing Eq. 1a as

$$\frac{da}{d\xi} \simeq 2a_r \frac{a_0^3}{\mu}\, \bar{e} \sin \xi \qquad [11]$$

integration yields

$$a/a_0 = 1 + 2[a_r a_0^2/\mu]^2(1 - \cos \xi) \qquad [12]$$

The difference between the maximum and minimum radial distances is found from Eq. 4 with eccentricity given by Eq. 7. Therefore

$$\frac{r_{max} - r_{min}}{r_0} = \frac{2a_r a_0^2}{\mu} \qquad [13]$$

Constant Transverse Acceleration Perturbation

For this case Eq. 1a is used with $a_r = 0$. Rewriting Eq. 1a in the form

$$da/d\xi \simeq 2a_t a_0^3/\mu \qquad [14]$$

the change in the semimajor axis per revolution is found to be

$$\Delta a/a_0 = 4\pi a_t a_0^2/\mu \qquad [15]$$

Summary

The results of the present paper, given by Eqs. 8, 10, 13, 15, are in exact agreement with the equations of (5). Their derivation here, using the already known equations for variation of parameters, is straightforward and simple, emphasizing the usefulness of the method employed.

Nomenclature

- a = semimajor axis of orbit
- a_r = radial acceleration perturbation
- a_t = transverse acceleration perturbation
- Δa = change in the semimajor axis per revolution
- e = orbit eccentricity
- $\bar{e}$ = average eccentricity over one revolution
- p = $a(1 - e^2)$
- r = radial distance from focus of orbit
- t = time
- ξ = true anomaly
- μ = gravitational parameter
- ω = angle between the line of hodes and the line of apsides
- $\Delta\omega$ = rotation of the line of apsides per revolution

References

1 Tsien, H. S., "Take Off From Satellite Orbits," JET PROPULSION, vol. 23, July–August 1953, pp. 233–236.

2 Dobrowolski, A., "Satellite Orbit Perturbations Under a Continuous Radial Thrust of Small Magnitude," JET PROPULSION, vol. 28, October 1958, pp. 687–688.

3 Copeland, J., "Interplanetary Trajectories Under Low Radial Thrust Acceleration," ARS JOURNAL, vol. 29, April 1959, pp. 267–271.

4 Perkins, F. M., "Flight Mechanics of Low-Thrust Spacecraft," *J. Aero/Space Sci.*, vol. 26, May 1959, pp. 291–297.

5 Lass, H. and Lorell, J., "Low Acceleration Takeoff From a Satellite Orbit," ARS JOURNAL, vol. 31, January 1961, pp. 24–28.

6 Ehricke, K. A., "Environment and Celestial Mechanics," *Space Flight*, Vol. 1, D. Van Nostrand Co., Princeton, N. J., January 1960, Chap. 6.

Thrust Vector Determination of an Ion Engine by Differential Comparison With an Unthrusted Orbit

JAMES N. HANSON[1]

Thompson Ramo Wooldridge Inc., Cleveland, Ohio

The mathematics for computing the thrust acceleration vector of a space vehicle continuous propulsion system by purely celestial mechanical means is outlined. The effects of perturbations (Earth oblateness, drag, etc.) are deleted from the total thrust acceleration acting on the center of mass of a thrusted vehicle by the differential orbital comparison with a nearby unthrusted orbiting body. The input information for these computations is a knowledge of the comparison orbit and an accurate record of the vector separation of the comparison object center of mass from the thrusted vehicle center of mass.

DUE TO the problems involved in measuring the effectiveness of neutralizing the charge of an ion engine in an Earth-bound experiment, it becomes apparent that only a space environmental test will yield reliable data (1).[2] The laboratory tests on an ion engine are unreliable and inconclusive due to the presence of a vacuum-chamber wall and residual gases. The method in this discussion presents a celestial mechanical means whereby the effectiveness of charge neutralization can be determined, i.e., by accurately measuring the thrust

Received Sept. 27, 1961.

[1] Research Engineer, New Devices Laboratory. Member ARS.

[2] Numbers in parentheses indicate References at end of paper.

acceleration vector as a function of time. These methods of calculation are designed primarily for an orbiting vehicle. The duration of thrust application may be minutes or hours. This test would be more accurate, though more complicated to instrument, than the test by changes in the vehicles angular motion as proposed by Elliot (2).

Accelerometers in conjunction with this celestial mechanical determination of the thrust vector may be used to obtain the amplitude and frequency of micropulsation of the thrust vector. For these very small thrusts, say $10^{-5}\,g_0$, the accelerometer would be operating near the threshold of sensitivity and therefore would not give absolute acceleration but relative variations.

Let $\mathbf{r}$ and $\mathbf{R}$ be the geocentric radii vectors of the centers of mass of the comparison (unthrusted) and thrusted orbiting objects respectively.

Therefore the vector separation of the center of mass of the thrusted vehicle from the center of mass of the comparison object is defined by

$$\boldsymbol{\varrho} = \mathbf{R} - \mathbf{r} \qquad [1]$$

Let $\mathbf{F}_2$ denote the total force per unit mass acting on the center of mass of the comparison body and $\mathbf{F}_1 + \mathbf{f}$ denote the total force per unit mass acting on the thrusted vehicle, where $\mathbf{f}$ is the thrust acceleration vector.

$$\ddot{\mathbf{r}} = \mathbf{F}_2 \qquad \ddot{\mathbf{R}} = \mathbf{F}_1 + \mathbf{f} \qquad [2]$$

on combining Eqs. 1 and 2

$$\ddot{\boldsymbol{\varrho}} = \mathbf{F}_1 + \mathbf{f} - \mathbf{F}_2$$

and

$$\mathbf{f} = \ddot{\boldsymbol{\varrho}} - (\mathbf{F}_1 - \mathbf{F}_2) = \ddot{\boldsymbol{\varrho}} - \Sigma\Delta\mathbf{F} \qquad [3]$$

Hence $\mathbf{f}$ may be determined from the measured $\ddot{\boldsymbol{\varrho}}$ provided $(\mathbf{F}_1 - \mathbf{F}_2)$ can be suitably determined. The next few sections establish means for determining the various differential perturbations.

Earth Potential

If the Earth is assumed to be an ellipsoid of revolution with a density varying confocally, then its potential function may be represented by an infinite series in Legendre polynomials. If the significant terms of this series are retained, then

$$U = \mu/a_e[a_e/r + J(a_e/r)^3(1/3 - \sin^2\beta) + K(a_e/r)^5(35\sin^4\beta - 30\sin^2\beta + 3)] \qquad [4]$$

Therefore, the differential potential acceleration is given by

$$\Delta\mathbf{F} = \nabla(r, \beta_1) - \nabla(R, \beta_2) = \nabla(r, \beta_1) - \nabla(r + \Delta r, \beta_1 + \Delta\beta_1) \cong -d\nabla(r, \beta_1)|_{dr=\Delta r, d\beta_1=\Delta\beta_1} \qquad [5]$$

where

$$\Delta r = (\mathbf{r}/r)\cdot\boldsymbol{\varrho} \qquad [6a]$$

and

$$\Delta\beta_1 = (\mathbf{r}/r) \times \boldsymbol{\varrho}\cdot\mathbf{r}r^{-1} \qquad [6b]$$

and

$$\nabla = \mathbf{u}_r\frac{\partial}{\partial r} + \mathbf{u}_\phi\, r^{-1}\frac{\partial}{\partial\phi}$$

$$\mathbf{u}_r = \mathbf{r}r^{-1}$$

$$\mathbf{u}_\phi = \mathbf{r}\cos\beta + \sin\beta(\mathbf{i}\cos\lambda + \mathbf{j}\sin\lambda)$$

Solar Radiation Pressure

Let P_R denote the scalar pressure due to solar radiation as received perpendicular on a perfect absorber at 1 a.u. from the sun. Then the differential thrust acceleration due to solar radiation pressure is

$$\Delta\mathbf{F} = \left(-\frac{a_1}{m_1}P_R\frac{\mathbf{r}_{\odot_1}}{r_{\odot_1}}\right) + \left(\frac{a_2}{m_2}P_R\frac{\mathbf{r}_{\odot_2}}{r_{\odot_2}}\right)$$

assuming the pressure exerted on both the comparison object and the thrusted vehicle to be equal and that of a perfect absorber. Because of the sun's great distance in comparison to the orbital diameter, $\mathbf{r}_{\odot_1} = \mathbf{r}_{\odot_2}$. In terms of $\mathbf{D}$ the expression for $\Delta\mathbf{F}$ becomes

$$\Delta\mathbf{F} = P_R\left(\frac{a_2}{m_2} - \frac{a_1}{m_1}\right)\frac{(\mathbf{D} - \mathbf{r})}{|\mathbf{D} - \mathbf{r}|} \cong P_R\left(\frac{a_2}{m_2} - \frac{a_1}{m_1}\right)\frac{\mathbf{D}}{D} \qquad [7]$$

The vector $\mathbf{D}$ is tabulated vs. date in the *American Ephemeris and Nautical Alamanac*. In general a_2 will be known a function of time depending on the vehicle attitude. a_1 can be made independent of time if taken as spherical.

Third Body Perturbation

The only significant third body effects would be those arising from the sun or moon. $\Delta\mathbf{F}$ may be formulated as

$$\Delta\mathbf{F} = \frac{1}{m_1}\left(\frac{Gm_1M}{l_1^2}\frac{\mathbf{l}_1}{l_1}\right) - \frac{1}{m_2}\left(\frac{Gm_2M}{l_2^2}\frac{\mathbf{l}_2}{l_2}\right) \cong G\mu l_2^{-3}\boldsymbol{\varrho} \qquad [8]$$

l_2 may be adequately approximated by the solar or lunar distances.

Aero and Electrodynamical Drags

Let the total drag on the comparison body be denoted by

$$\frac{1}{2}\frac{A_2}{m_2}C_D\sigma v_1^2\mathbf{v}_1/v_1$$

then the differential total drag is given by

$$\Delta\mathbf{F} = \frac{1}{2}C_D\sigma\left(\frac{A_1}{m_1}v_1\mathbf{v}_1 - \frac{A_2}{m_2}v_2\mathbf{v}_2\right)$$

where the atmospheric density σ is taken to be the same for both orbits. Components of electrodynamical drag other than tangential are neglected. A_1 is time, i.e., attitude, dependent, and A_2, from the previous section, is independent of time. By Eq. 1

$$\mathbf{v}_1 = \dot{\mathbf{R}} = \dot{\mathbf{r}} + \dot{\boldsymbol{\varrho}} = \mathbf{v}_2 + \dot{\boldsymbol{\varrho}}$$

and therefore

$$\Delta\mathbf{F} = \frac{1}{2}C_D\sigma\left[\left(\frac{A_1}{m_1}|\mathbf{v}_2 + \dot{\boldsymbol{\varrho}}| - \frac{A_2}{m_2}\mathbf{v}_2\right)\mathbf{v}_2 + \left(\frac{A_1}{m_1}|\mathbf{v}_2 + \dot{\boldsymbol{\varrho}}|\,\dot{\boldsymbol{\varrho}}\right)\right] \qquad [9]$$

The quantity $(1/2)C_D\sigma$ must be determined for the ambient state of the atmosphere during the time of the experiment and for the particular configuration of the thrusted vehicle. Due to the great difficulty in the analytical formulation of $(1/2)\,C_D\sigma$, a celestial mechanical determination of the quantity is chosen.

For an orbiting object in a perfect inverse-square field experiencing only a drag (i.e., tangential) perturbation, it has been shown that the semimajor axis decay in a period is given by

$$\frac{da}{dt} = -4m^{-1}a^2P^{-1}\int_0^\pi\left(\frac{1}{2}C_D\sigma\right)\times(1 + e\cos E)^{3/2}(1 - e\cos E)^{-1/2}dE$$

where the integration has been taken over one sidereal period. For an unperturbed orbit $P_{\text{sideral}} \equiv P = 2\pi\sqrt{a^3/\mu}$. There-

fore in the presence of perturbations

$$\frac{da}{dt} = \frac{3}{2}(2\pi)^{-2/3}\mu^{-1/3}P^{1/2}\frac{dP}{dt}$$

Hence the variation in P is related to $(1/2)C_D\sigma$ as given by the following integral equation:

$$\frac{3}{2}(2\pi)^{-2/3}\mu^{-1/3}P^{1/2}\frac{dP}{dt} = -4m^{-1}a^2 \times \int_0^\pi \left(\frac{1}{2}C_D\sigma\right)(1 + e\cos E)^{3/2}(1 - e\cos E)^{-1/2}dE \quad [10]$$

where it is understood that the variation in P is due only to drag. Therefore before this formula can be applied, the effect of the oblateness must be deleted from that given by drag alone.

$$\left(\frac{dP}{dt}\right)_{\text{observed}} = \left(\frac{dP}{dt}\right)_{\text{drag}} + \left(\frac{dP}{dt}\right)_{\text{oblateness}} \quad [11]$$

From Sterne (4), it can be shown that for small eccentricity, say $e < 0.1$, the variation in P due to oblateness is given by

$$\left(\frac{dP}{dt}\right)_{\text{oblateness}} = -3\mu(2\pi)^{-2}a_e^2Ja_0^{-5} \times (1 - e_0)^{-3}(1 - 3\sin^2 i_0)P^2 \quad [12]$$

Therefore by Eq. 11, $(dP/dt)_{\text{drag}}$ is determined. The observed ΔP/period may be determined by meridian observations of the thrusted vehicle over several successive unthrusted revolutions just before and just after the experiment duration. This integration in Eq. 10 must proceed piecewise over each sidereal period, i.e., the terminal values after one sidereal period are the initial values for the next integration. The accuracy of this integration may be increased by considering the associated change in eccentricity, i.e., (4).

$$\frac{de}{dt} = -4m^{-1}aP(1 - e^2)\int_0^\pi \left(\frac{1}{2}C_D\sigma\right) \times (1 + e\cos E)^{1/2}(1 - e\cos E)^{-1/2}\cos E dE$$

Second-Order Perturbations

For such an experiment conducted over a period of time on the order of days, it was assumed that perturbations due to Earth radiation, atmospheric oblateness, and mass anamolies to the ellipsoid would be negligible. Similarly, the decrease in major axis (i.e., decrease in orbital energy, $-\mu/2a$) due to the kinetic energy of rotation of the orbiting bodies has been neglected. Mutual gravitational attraction between the two bodies has been neglected. No inertial forces will exist, since a nonrotating (inertial) coordinate system placed at Earth's center has been chosen for these calculations.

Observation of the Separation Vector

Attitude control or a knowledge of the attitude of the thrusted vehicle will be assumed, i.e., there is known a rotation matrix Q_{13} such that unit vector $\boldsymbol{\varrho}/\rho$ in a thrusted vehicle body fixed system at the center of mass can be transformed into its inertial components

$$(\rho_X, \rho_Y, \rho_Z)^T = Q_{13}(\rho_1, \rho_2, \rho_3)^T$$

and therefore

$$(\dot\rho_X, \dot\rho_Y, \dot\rho_Z)^T = \dot Q_{13}(\rho_1, \rho_2, \rho_3)^T + Q_{13}(\dot\rho_1, \dot\rho_2, \dot\rho_3)^T$$

The rotational matrix Q_{13} will be the product of two other rotational matrices: the transformation from the body fixed system (by the three Euler angles) to the reference system (the orbital system, i.e., geocentric, circumferential, and orthogonal) and the transformation from the reference system to the inertial system. Let these rotational matrices be denoted by Q_{12} and Q_{13} respectively

$$Q_{13} = Q_{12}Q_{23} = Q_{23}Q_{12}$$

These matrices are given by (5, 6). The Q_{13} matrix contains the orbital elements i, u, and Ω, and Q_{12} contains the modified Euler angles θ_1, θ_2, θ_3 defined in that order to make the final directions of the orbital system axes the same as the vehicle system axes (6).

A simple method for measuring the angular position of the comparison body in the vehicle fixed system would be to observe, photoelectrically, an azimuthal angle and a latitudinal angle with respect to a set of vehicle fixed axes. These measurements may be obtained from a variety of methods, e.g., an automated theodolite-phototube tracking system using a luminescent comparison body or interferometric measurements of radiation emitted from the comparison body. The measurement of $|\boldsymbol{\varrho}|$ may be accomplished by any of the highly accurate electro-optical distance measuring instruments. These devices are of recent development (since 1950) and are completely described in (7).

Case for an Orthogonal Thrust

By a linearization of the time variation of the orbital inclination under an orthogonal thrust acceleration, i.e., perpendicular to the orbital plane, it can be shown that for a circular orbit (8)

$$\Delta i/\text{quadrant} = F_W r^2\mu^{-1}\sin(2\pi T_W/P)$$

If in a 90 min circular orbit, the thrust is applied for 10 min, then there results a change of inclination of $\approx 7 \times 10^{-5}$ rad. After a quarter revolution the angular separation between the thrusted vehicle and the comparison body will correspond to linear separation of $\approx$500 m.

These calculations point out the ability of a thrust not in the orbital plane to give a large effect (namely a large ρ) for very short periods of thrust application. A purely orthogonal thrust has the added advantage of leaving the orbital shape invariant, i.e., e and a are constant.

Nomenclature

a_e	= equatorial Earth radius
a	= orbital semimajor axis
$\mathcal{A}$	= aspect area for solar pressure
A	= aspect area for drag
α	= azimuthal angle in vehicle fixed coordinate system
β	= geocentric latitude = $90° - \phi$
C_D	= drag coefficient
$\mathbf{D}$	= Earth-sun vector
e	= orbital eccentricity
E	= eccentric anomaly
$\mathbf{f}$	= thrust acceleration vector of propulsor engine
$\mathbf{F}$	= disturbing acceleration
$\Delta\mathbf{F}$	= differential disturbing acceleration
G	= gravitational constant
i	= orbital inclination
$(\mathbf{i}, \mathbf{j}, \mathbf{k})$	= unit vectors in inertial system
J, K	= second and third harmonic coefficients in Earth's potential function
$\mathbf{l}$	= third body vehicle vector
m	= vehicle mass
M	= third body mass
μ	= field strength = GM
P_R	= radiation pressure
P	= orbital sidereal period
$\mathbf{r}\odot$	= vehicle-sun vector
$\boldsymbol{\varrho}$	= separation vector = $\mathbf{R} - \mathbf{r}$
$\mathbf{r}$	= geocentric radius vector to comparison body
$\mathbf{R}$	= geocentric radius vector to thrusted vehicle

σ	=	atmospheric density
Q	=	rotational matrix
θ	=	Euler angle
T_W	=	duration of thrust application (orthogonal)
u	=	longitude in orbital plane from the ascending node
U	=	Earth's potential function
(U_r, U_ϕ, U_λ)	=	unit vectors for spherical coordinates
v	=	orbital velocity
Ω	=	longitude of ascending node in inertial space

Subscripts

0	=	initial value
1, 2	=	thrusted body, comparison body
(1, 2, 3)	=	body fixed axes
(X, Y, Z)	=	inertial axes
W	=	a thrust perpendicular to the orbital plane (orthogonal)

References

1 Sellen, J. M., Shelton, H. and Langmuir, D. B., "Electrostatic Propulsion Design Principles and Problems," *11th Internatl. Astronaut. Congress*, Stockholm, 1960, Vol. 1, Paper 10.

2 Elliot, D. G., "Trajectories and Thrust-Measurement Techniques for Space Testing of Ion Rocket Motors," *Electrostatic Propulsion* ("Progress in Astronautics and Rocketry," edited by D. B. Langmuir, E. Stuhlinger, and J. M. Sellen Jr., Vol. 5), Academic Press, New York, 1961, pp. 523–555.

3 Okhocimski, D. Y., Eneyev, T. M., Taratynova, G. P. and Yacunski, J. M., "Orbital Perturbations of Artificial Satellites," Uspekhi Fiz. Nauk 63, translated by Hope, E. R., *Defense Research Board* T270R, Canada, 1957.

4 Sterne, T. E., "The Gravitational Orbit of a Satellite of an Oblate Planet," *Astronom. J.*, vol. 63, no. 1, January 1958.

5 Moulton, F. R., *An Introduction to Celestial Mechanics*, MacMillan Co., New York, 1914, p. 403.

6 Gray, A., *A Treatise on Gyrostatics and Rotational Motion*, Dover Pub., New York, 1918, p. 73.

7 "International Symposium on Electronic Distance-Measuring Techniques," *J. Geophysical Research*, vol. 65, no. 2, February 1960.

8 "Final Report on Mission Analysis for Electric Propulsion Systems," prepared by the New Devices Laboratories of Thompson Ramo Wooldridge Inc., *No. AF 33(616)-5919*, June 1960.

Consumable Case Solid Rocket

A. N. BAXTER

Space Technology Laboratories Inc., Los Angeles, Calif.

For simplicity, the conventional solid rocket pays high performance penalties. A consumable case rocket design is presented which provides high initial and burn-out mass ratios.

IT IS clear from the expression for rocket burnt velocity

$$V^* = g\, I_{sp} \ln (M_0/M_f) \qquad [1]$$

that 1) great performance improvement can be achieved by increasing (effective) I_{sp}; and 2) a significant improvement is possible if mass ratio is greatly increased. This paper concerns a consumable case solid rocket (CCR) having a burnout mass ratio of approximately 30 and the following nominal characteristics: chamber pressure, 700 psi; thrust, 150,000 to 200,000 lb; initial weight, 50,000 lb. A great advantage of the conventional solid rocket is its simplicity, but for simplicity it pays a high performance penalty. Consider the design of the cylindrical case; material thickness t required to resist hoop and axial stress are (t) hoop $= PcD/2S$ and (t) axial $= PcD/4S$. The conventional case is approximately 100% overdesigned for axial stress. The entire case is accelerated throughout its stage's flight. Since the case is designed for pressure peaks (ignition, erosive burning), the rocket operates inefficiently when chamber pressure is below this peak (e.g., during tail-off). If chamber pressure is lowered to reduce weight, performance may be low. Heavy insulation covers the case interior to prevent damage of burn-through at one particular undefined location; insulation is also accelerated during flight.

Conventional nozzles are heavy and heavily insulated, primarily for heat protection. Gimbals or swivels are difficult to make function properly because of high pressure and heating. Roll control requires multiple nozzles or jet vanes (or equivalent); these decrease I_{sp}. The CCR avoids many of these undesirables.

In essence, the CCR consists of a cigarette-burning propellant grain, fore-end dome, converging-diverging nozzle, threaded connecting rods that maintain dome-nozzle spacing, and a drive to advance the nozzle with grain burning surface. The rocket does not have a conventional "case" (Fig. 1); the 5.5-ft diam propellant charge is wrapped with ablative material. Radial stress generated by chamber pressure is resisted by hoop tension in the nozzle only; axial stress is resisted by the rods. (Six "case rods" are shown.) The rods contact neither propellant nor gases.

At ignition, gases flow axially, forward through an insulating blast tube along propellant centerline and aft through the nozzle. The former drives the turbine. The turbine exhausts through ducts to diametrically opposite nozzles situated outside the rocket circumference; nozzle actuation provides roll moment. The turbine powers the rod drive. Combustion gas cooling is achieved by blast tube ablation and coolant spray evaporation. Hydraulic control muscle for throttle and roll comes from the high pressure coolant or turbine inlet gas. The drive keeps the rods in tension; they pull the nozzle forward against the aft-acting chamber-pressure force. The nozzle literally swallows the propellant.

The ablating material slides along the nozzle interior and provides heat protection. Thus, nozzle material may be thin and the diverging section insulation light. Sealing is accomplished at the nozzle-propellant interface by ablating-sleeve to nozzle-seal contact and gas forcing the ablating material against nozzle interior. The rotating, threaded rods are restrained from axial motion by fore-end ball bearings. A low lead Saginaw nut advances the nozzle. Rod exposed aft of the nozzle nut is severed and jettisoned by a small shaped charge located inside the rod.

The three-Curtis-stage turbine operates at 10,000 rpm between the pressure limits of the combustion chamber and 30 psia roll control nozzle inlet. Using a one to one mixture of water-cooled combustion gas at 2000°F, turbine specific is 6 lb/hp-hr. Hollow, threaded cylindrical case-rods were selected because: 1) a high efficiency, Saginaw-ball type of drive could be used; 2) grinding threads into rod exterior produces minimum stress concentration; 3) hollow cylinders offer considerable buckling resistance; and 4) high tensile strength can be achieved in thin wall cylinders. The rods were designed to withstand: 1) the 3×10^6-lb aft, axial force resulting from pressure, plus a 10 g axial acceleration; 2) buckling loads from a 20,000-lb upper stage with the missile standing; and 3) a bending moment of approximately 1,000,000 in.-lb from aerodynamic and control loads.

Because Poisson's ratio is large and the modulus of elasticity low, the propellant tends to expand radially when chamber pressure acts on the aft end and requires circum-

Paper presented at the ARS Solid Propellant Rocket Conference, Salt Lake City, Utah, Feb. 1–3, 1961; revision received Oct. 19, 1961.

[1] Member Technical Staff. Associate Member ARS.

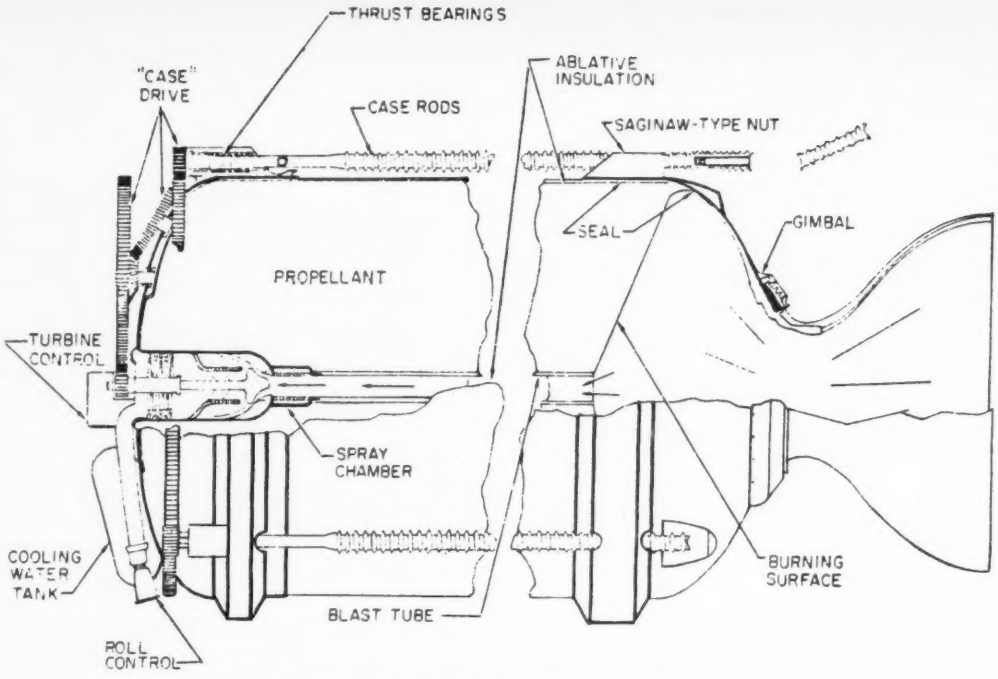

Fig. 1 Consumable case solid rocket; spur gear drive

ferential support to prevent extrusion. A glass-filament resin ablation material of 0.10-in. radial thickness, applied to the propellant exterior, provides this support. The propellant column alone has more capacity for buckling than is required. The 0.10-in. ablating material puckers as it moves aft toward the throat; when it reaches the throat, approximately 0.2 radial inches of material is still present. Considerable gimbal-hardware weight can be saved by using only one nozzle, because the peripheral distance around multiple openings is greater than for a single opening of a given total area.

Sealing the gases at the nozzle-propellant interface promises development difficulties. Several seals were designed. The one shown in Fig. 2 uses a radially thin, lubricant pressurized torus between the nozzle and the grain exterior. As the nozzle moves relative to the ablative insulation, the flexible torus oozes viscous fluid that serves as both seal and lubricant. A combination tongue and groove, plus deformable metal O-ring seal, is provided when the nozzle meets the fore-end dome at burning termination.

Three types of rocket-component heating can occur during missile flight, viz., free-stream convection, and convection and radiant heating from roll-control exhaust. Calculations indicate that no external ablation will occur during a nominal 5500 n mile trajectory and that the case rod temperature rise is approximately 200°F, a rise that would not debilitate physical strength. Each roll-control nozzle uses a plug principle to achieve high C_f at low altitudes. The couple generated is nominally 14,000 in.-lb.

A single-nozzle rocket has the advantage over multiple nozzles of providing greater lateral thrust per unit of angular displacement. However, as the CCR burns, the lever arm between nozzle and missile c.g. may be less than with a conventional rocket. A question arises as to whether the moment of inertia and aerodynamic forces decrease faster than control capability. To determine this, the equations of motion were written for two different types of missiles: 1) a conventional (50,000-lb weight) rocket booster, using a 20,000-lb upper stage; and 2) the same 20,000-lb upper stage with a CCR booster. Typical values of moment of inertia, weights, lengths, etc., were substituted into the equations at burning times shortly after ignition, mid-burn, and near burn out. The calculations showed that at ignition the force require-

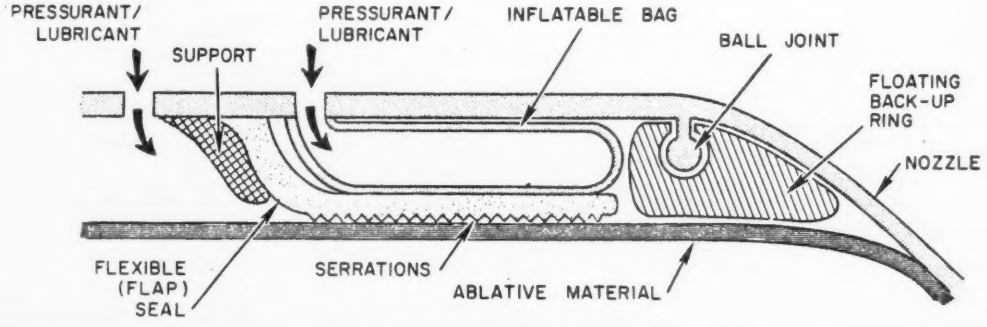

Fig. 2 Nozzle seal

ments for both missiles were essentially identical. At midburn and at burn out, the CCR missile was appreciably less difficult to control.

Three different types of case rod drive systems were designed and weighed, viz., spur-gear, hypoid, and worm; the last two were quite different from the spur drive of Fig. 1. Weights were compared to a typical modern solid; all rockets fit the same basic envelope. Comparisons are shown in Table 1.

Table 1 shows that: 1) considerably more propellant is available for expenditure in the CCR; and 2) the total inert materials before ignition and after burnout are appreciably less for the the CCR.

Two methods were used to calculate the relative performance V^* of the conventional rocket CR and the CCR: 1) gravitationless, drag-free burnt velocity V^* for the rockets only; and 2) V^* for the two types of first-stage rockets (CR and CCR) accelerating identical 20,000-lb upper stages.

The ratio $V^*_{ccr}/V^*_{cr} = 1.41$ was calculated from the following data for the rockets only:

Type	(M_0/M_f)
CCR (worm drive)	31.37
CR	11.62

The CCR produces a (rocket only) burnt-velocity approximately 41% greater than a CR. Calculations (again using Eq. 1) showed that the CCR gave the 20,000-lb upper stage an 11% higher (first stage burnout) velocity. This is equivalent to approximately 700 additional n miles at ICBM ranges. An 11% increase in the V^* provided by a second stage would yield a considerably greater range increase.

As regards fabrication and cost, the CCR appears to offer the following advantages: 1) eliminating manufacture of large diameter, thin wall, easily damaged cases; 2) easier gimbal design; 3) less complex, lighter nozzle, no insulation separation; 4) no madrel to pull, no star point propellant cracking; 5) few metal to grain bonds to inspect; and 6) possibilities for hardware recovery and reuse. On operation and performance: 1) small igniter, no erosive burning; 2) use high I_{sp} propellant because of cooled nozzle; 3) thrust level control by varying burning rate of axial propellant modules; 4) thrust termination and restart by inert separation of axial modules; 5) continually jettisoning the inert; 6) elimination of multiple-nozzle disadvantages; and 7) rocket is nonpropulsive during external fire.

Anticipated development problems include high burning rate propellant, tubeless-tire nozzle seal, and the maintenance of zero relative velocity between nozzle and propellant burning surface.

Table 1

	Typical modern solid	Consumable case rocket Spur*	Hypoid, spiroid, or bevel	Worm
Total weight at ignition	48,360	50,202	50,160	49,942
Material expended during action time	44,200	48,463	48,378	48,351
Inerts at ignition	4,600	3,090	3,144	2,955
Unexpended material at end of action time	4,160	1,739	1,782	1,591

* Type of drive.

Free Flight of a Ballistic Missile

(ARS JOURNAL, Vol. 29, No. 12, 1959, pp. 915–926)

The following typographical errors appear in the paper of the above title:

1) In Eq. 21 on page 918, the factor of $\delta\gamma$ on the right-hand side should read

$$2\frac{\delta V}{V}\ldots = \delta\gamma\left[\frac{\cos(\gamma-\phi)}{\sin\gamma} - \frac{\cos\gamma}{\sin^2\gamma}\sin(\gamma-\phi) - 2\cot\gamma\,\frac{1-\cos\phi}{\lambda\sin^2\gamma}\right] + \ldots$$

2) Expression for $\delta R/\delta\gamma$ above Eq. 25 on page 919 should read

$$\frac{\delta R}{\delta\gamma} = a \times \left[\frac{\cot\gamma\sin(\gamma-\phi) - \cos(\gamma-\phi) + 2\cos\gamma\,\dfrac{1-\cos\phi}{\lambda\sin^2\gamma}}{\dfrac{\sin\phi}{\lambda\sin\gamma} - \cos(\gamma-\phi)}\right]$$

although the final reduced expression for $\delta R/\delta\gamma$ given by Eq. 25 *is* correct as it stands.

3) Eq. 26 on page 920 should read

$$\frac{\delta R}{\delta h} = 2\tan\gamma - \frac{\sin(\gamma-\phi)}{\cos\gamma}$$

although the plotted curves in Fig. 8 are correct.

4) The factors which occur inside the integrands of Eqs. 61 and 62 on page 924 should have plus signs in front of the term $2f(0)$, viz.

$$\int_0^\theta dx\,\sin(\theta-x)[(3\lambda\sin^2\gamma - 2)f(x) + 2f(0)]$$

5) The leading factor in both Eqs. 67 and 68 on page 924 should contain a factor r^4 rather than r^3 in the denominators. For instance, Eq. 67 should read

$$\frac{d^2L}{dt^2} = -2J\,\frac{GMa^2}{r^4}\sin\sigma\cos\sigma(\vec{n}_0\cdot\vec{e}_\sigma)$$

6) The expression for $\vec{n}_0\cdot\vec{e}_\sigma$ at the bottom of the first column of page 924 should have a plus sign rather than a minus

$$\vec{n}\cdot\vec{e}_\sigma = +\frac{\sin\psi\cos\alpha\cos\beta}{\sin\phi\sin\sigma}$$

7) Eq. 69 on page 924 should read

$$\delta L = -\frac{2JGMa^2}{p^2}\,\frac{\sin\psi\cos\alpha\cos\beta}{\sin\phi}\int_0^\phi d\theta' r^2(\theta')\times \int_0^{\theta'} d\theta''\,\frac{A\cos\theta'' + B\sin\theta''}{r^2(\theta'')}$$

8) Eq. 76 on page 925 should read

$$\delta R = \delta a\,\frac{h}{a}\left[2\tan\gamma - \frac{\sin(\gamma-\phi)}{\cos\gamma}\right]$$

New Patents

George F. McLaughlin, *Contributor*

Method of operating a jet propulsion system (2,986,874). P. A. George, Schenectady, N. Y., assignor to General Electric Co. (ARS corporate member).

An inorganic noncombustible residue is deposited as a thermal insulation on walls of system.

Method of minimizing boron oxide deposits (2,986,876). E. Becker, Grand Island, N. Y., assignor to Olin Mathieson Chemical Corp. (ARS corporate member).

Introduction of a normally liquid ether of silicon within combustion, turbine, and exhaust sections of a jet-type engine.

Firewall (2,986,878). S. J. Townsend (ARS member), Dallas, Tex., assignor to Chance Vought Corp. (ARS corporate member).

Openings through a bulkhead surrounding a jet engine, each subdivided into smaller openings too small to allow passage of flame from one compartment to another.

Solid propellant starter (2,986,879). E. A. Volk Jr., Hasbrouck Heights, N. J., assignor to The Bendix Corp. (ARS corporate member).

Breech chamber for a cartridge connected through gas nozzles directed to a bladed turbine wheel for rotating a turbine engine to starting speed.

Low-temperature vessels (2,986,891). H. O. McMahon, Lexington, Mass., assignor to Arthur D. Little Inc. (ARS corporate member).

Gas-permeable barrier between first and second passages enveloping an inner vessel. An outlet is adapted to remove gas from second passage.

Low-recoil variable-range missile projector (2,986,973). A. L. Waxman, Albany, N. Y., assignor to the U. S. Navy.

Venturi port axially extending through rear of an expansion chamber and connected by a valve. Alignment of projector is unaffected by variable venting of burning gases to the atmosphere.

Rocket engine structure (2,987,882). H. W. Nocke (ARS member), Huntsville, Ala., assignor to Thiokol Chemical Corp. (ARS corporate member).

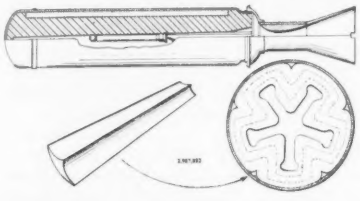

Inert slivers of curved triangular cross-section between star points of hollow propellant charge cast in a casing, aid rapid termination of burning.

EDITOR'S NOTE: Patents listed above were selected from the Official Gazette of the U. S. Patent Office. Printed copies of patents may be obtained from the Commissioner of Patents, Washington 25, D. C., at a cost of 25 cents each; design patents, 10 cents.

Jet ignited tracking flare (2,986,999). W. A. Fiedler, F. L. Haake and E. M. Kane (ARS member), Oxnard, Calif., assignors to the U. S. Navy.

Housing, containing a combustible charge, mounted on a jet-powered missile outside of nozzle exhaust flow. A portion of hot gases from flow ignites charge.

Radar direction of missiles (2,987,269). Dr. R. Weller, Silver Spring, Md.

Method of guiding missiles toward a target area by suspending (as by parachutes) microwave transmitters in successive time intervals above area. Each transmitter projects a beam of different frequency towards target.

Vehicle for testing control systems at subsonic speed (2,987,270). H. H. Porter, Washington, D. C., assignor to the U. S. Navy.

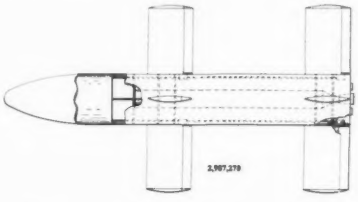

Equipment under test for use in guided missiles is housed in a casing having two sets of four stabilizing airfoils. A sustaining rocket propels vehicle. Auxiliary rockets housed within casing.

Restricted solid propellant grain (2,987,388). W. G. Stanley, Munster, Ind., assignor to Standard Oil Co. (Ind).

Shaped grain consisting of a body composed of an oxidizable thermoplastic binder, an ammonium nitrate combustion catalyst, and ammonium nitrate. Restrictor coating is of cellulose acetate.

Airplane design (190,534). H. A. Smolinski, Santa Susana Heights, Calif.

Four-place, jet-propelled. Deflector ring ahead of passenger compartment, and a deflector ring at either side in swept-back wing panels.

Method for increasing the air specific impulse of a two-stage compressor turbojet (2,987,873). H. M. Fox (ARS member), Bartlesville, Okla., assignor to Phillips Petroleum Co.

Introduction of ammonia into combustion products in primary combustion zone of a ducted fan jet engine to lower temperature of gases to a predetermined value.

Ceramic lined light-weight rocket motor nozzles (2,987,874). K. C. Nicholson, Niagara Falls, N. Y. assignor to the Carborundum Co.

Structure for directional release of high velocity hot gases. Nozzle of refractory material. Main body of bonded silicon carbide. Small volume inlay of zirconium boride molybdenum disilicide, beryllia, thoria, and stabilized zirconia.

Ramjet power plants for missiles (2,987,875). H. M. Fox (ARS member), Bartlesville, Okla., assignor to Phillips Petroleum Co.

Fuel tank near front of housing. Fast burning rocket propellant mounted in combustion chamber. Slow burning propellant between chamber and tank. Fuel in tank is pressured when latter propellant burns.

Exhaust nozzle control for gas turbine engines (2,987,876). H. J. Williams and J. E. Hurtle, South Bend, Ind., assignors to The Bendix Corp. (ARS corporate member).

Variable discharge pump controls a fluid pressure responsive control piston for varying area of exhaust nozzle.

Variable geometry intake duct (2,987,878) R. C. Bogert, Arcadia, Calif., assignor to North American Aviation Inc. (ARS corporate member).

Movable portion within a fixed duct aperture at the front of a jet intake to vary an area of the aperature. Duct throat section varied by an expandable baffle.

Insulation for rocket motors (2,987,880). N. A. Kimmel, Waco, Tex., assignor to Phillips Petroleum Co.

Layer of ceramic fiber paper, layer of aluminum foil, second layer of ceramic fiber paper, layer of resin-impregnated asbestos fiber, and second layer of ceramic fiber paper.

Solid propellant power plant and fuel feed method (2,987,881). L. W. Mullane, Fullerton, Calif.

Grain fed in a direction to continuously advance inwardly through short grain support skirt at end remote from nozzle, toward combustion chamber throughout burning period to assure constant volume engine.

Jet engine noise suppression nozzle (2,987,883). J. W. Lawler, Seattle, Wash., assignor to The Boeing Co. (ARS corporate member).

Discharge duct with peripherally spaced alternate convoluted and involuted portions. Compressed fluid to control nozzles selectively deepens valleys in discharge stream, increasing suppression of noises.

Missile launcher (2,987,964.) A. G. Logan, B. Cain (ARS member), and R. Ginsbert, Norwalk, Conn., assignors to American Machine & Foundry Co. (ARS corporate member).

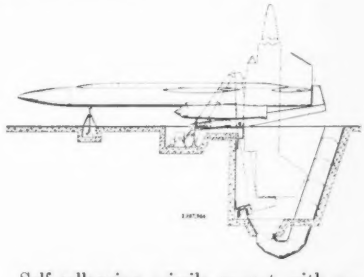

Self-collapsing missile mount with rotatable carriage. A spring returns missile support from an upright firing position to a collapsed servicing position when missile is fired.

Protective cover (2,987,999). R. O. Robinson Jr. and T. W. Sheppard, Silver Spring, Md., assignors to the U. S. Navy.

Groove, in exterior of missile nose, contains low melting point alloy meltable by high velocity air flow occurring after launching. A seal covering nose inlet releases when alloy melts.

Book Notes

Basic Physics of the Solar System, V. M. Blanco and S. W. McCuskey (both in the Department of Astronomy, Case Institute of Technology), Addison-Wesley Publishing Co. Inc., Reading, Mass., 1961, 290 pp. $7.50.

Chapters: 1) Astronomical Coordinate System; 2) Planets and Their Satellites; 3) the Earth-Moon System; 4) Celestial Dynamics I: the Two-Body Problem; 5) Celestial Dynamics II: Three- and n-Body Problems; 6) the Sun and Interplanetary Space. *Appendix:* tables on conversion of arc to time, physical characteristics of the planets, etc (20 pp.)

This book presents some of the basic physical and dynamical aspects of the solar system. It is written for those scientists and engineers, not specialists in astronomy, who are interested in the rapidly expanding area of space technology. It is designed to form a link between elementary books on astronomy and the current specialized literature pertaining to the solar system.

Full-Scale Fatigue Testing of Aircraft Structures, edited by F. J. Plantema and J. Schijve (both of National Aeronautical Research Institute), Pergamon Press, New York, 1961, 426 pp. $15.00.

Contents: 19 technical papers contributed by different authors on such subjects as current trends in fatigue tests of aircraft, endurance under program-fatigue testing, fatigue testing of aircraft structures, and the quantitative statistical approach to the aircraft fatigue problem.

This is the fifth volume of the series of monographs titled "Aeronautics and Astronautics." It contains some of the papers presented in Amsterdam June 9–11, 1959, at a symposium attended by scientists from 11 countries. This book is designed for those engaged in studying the problem of fatigue in aircraft structures and is also intended as a reference work for students.

Nuclear Propulsion, edited by M. W. Thring, Butterworths, London, 1960, 290 pp. $9.50.

Contents: 16 chapters contributed by different authors. 1) Structure of the Nucleus and Nuclear Reactions; 2) Reactor Physics; 3) Thermodynamics of Jet and Rocket Propulsion: the Application of Nuclear Power: 4) Nuclear-Powered Closed-Cycle Gas Turbine; 5) Design of Nuclear Reactors; 6) Metallurgical Problems in Nuclear Reactors; 7) Heat Transfer Problems in Nuclear Engineering; 8) Reactor Control and Instrumentation; 9) Marine Developments in the Nuclear Age; 10) Nuclear Marine Propulsion; 11) Some Observations on the Application of Nuclear Power to Aircraft; 12) Progress in Nuclear Propulsion; 13) Limitations of Chemical Rockets and the Possibility of the Nuclear Rocket; 14) Preparation, Storage, and Properties of Working Fluids; 15) Potential Uses of Ceramics in Nuclear Reactors; 16) Medical and Biological Aspects of Life in Sealed Cabins.

Physical Gas Dynamics, editor-in-chief, A. S. Predvoditelev (Institute of Power Engineering, USSR Academy of Sciences), translated by R. C. Murray and D. R. H. Phillips, Pergamon Press, New York, 1961, 183 pp. $7.50.

Contents: 12 chapters contributed by different authors on such subjects as methods of calculating the kinetic coefficients of air at high temperatures, thermodynamic and gas-dynamic properties of flowing air downstream of a normal shock wave, flow of gas from a nozzle cut in an oblique plane, pressure field occurring in water during an electrical discharge, development of shock waves in water as a result of combination of elementary compression waves, and interaction of a flame with a shock discontinutiy.

This volume contains the proceedings of a symposium devoted to work carried out at the Power Engineering Institute of the Academy of Sciences of the USSR. It is designed to be of interest to scientific workers, teachers, engineers, and students of senior courses in dynamics or combustion physics.

Shock and Vibrations in Linear Systems, Paul A. Crafton (Professor of Mechanical Engineering, George Washington University, and Consultant, Naval Research Laboratory), Harper & Brothers, New York, 1961, 399 pp. $10.00.

Chapters: 1) Complex Variables; 2) Fourier Analysis; 3) Differential Equations of Motion; 4) the Transfer Function; 5) the Frequency Spectrum; 6) Translational Mode of Shock and Vibration; 7) Rotational Mode of Shock and Vibration; 8) Branched Systems; 9) Nonsinusoidal Inputs; 10) Solution of the Frequency Equation; 11) Shock and Vibration Isolation by Feedback Control; 12) Lagrange's Equations of Motion: the Energy Method; 13) Wave Equations for Autonomous Systems; 14) Solutions of the Wave Equations for Autonomous Systems: the Frequency Equation; 15) Force and Motion Inputs.

The purpose of this book is to give the reader an understanding of the fundamental principles of shock and vibration phenonema and the application of these principles to general mechanical and structural systems. It is based on an undergraduate course given over the past several years and is designed to be used as an introductory text.

Temperature Measurement in Engineering, Vol. 2, H. Dean Baker (Professor of Mechanical Engineering, Columbia University), E. A. Ryder (former Consulting Engineer, Pratt & Whitney Aircraft Div., United Aircraft Corp.), and N. H. Baker (former Research Assistant, Department of Mechanical Engineering, Columbia University), John Wiley & Sons Inc., New York, 1961, 465 pp. $13.00.

Chapters: 1) Resistance Thermometers; 2) Resistance-Thermometer Design Calculations; 3) Radiation Detectors; 4) Radiation Pyrometry—Design-Calculation Techniques; 5) Surface Temperatures; 6) Rapidly Changing Temperatures; 7) Moving Bodies; 8) Transparent Bodies; 9) Liquids; 10) Gases; 11) High Temperature Gases; 12) Low Temperatures; 13) Flame Temperatures; 14) Arc, Plasma, Upper Air, Stellar, and Nuclear Reactor Temperatures.

The authors believe that a careful study of this text will usually provide a sufficient introductory grasp of the subject, whereas investigation of the references will yield a more detailed knowledge.

Metallic Fatigue, W. J. Harris Jr. (Chief Physicist, de Havilland Aircraft Co. Ltd., and Thomas Hawksley Medallist, 1957), Pergamon Press, New York, 1961, 323 pp. $12.50.

Chapters: 1) Stress Concentration; 2) Alleviation of Stress Concentration Effects; 3) Frequency; 4) Corrosion; 5) Fretting Fatigue; 6) Crack Propagation; 7) Statistics; 8) Some Standard Aircraft Processes.

This volume is the first of a series of monographs in "Aeronautics and Astronautics," edited by W. J. Harris Jr. and C. Zwikker. It surveys the major factors that affect the fatigue behavior of metals and uses the author's experience in those fields of research associated with flight structures. The researches described to indicate possible solutions to fatigue problems have been selected on the grounds of feasibility with conventional engineering facilities.

Space Astrophysics, edited by William Liller (Professor of Astronomy, Harvard University), McGraw-Hill Book Co. Inc., New York, 1961, 268 pp. $10.00.

The books listed here are those recently received by the ARS from various publishers who wish to announce their current offerings in the field of astronautics. The order of listing does not necessarily indicate the editors' opinion of their relative importance or competence.

Chapters: 1) Ultraviolet Spectroscopy of the Sun; 2) Solar Ultraviolet Research; 3, 4) Telemetering Monochromator Measurements of Extreme Ultraviolet Radiation; 5) Some Plans for Experiments in Space; 6) X-Ray and Ultraviolet Radiation Measurements from Rockets; 7) Ultraviolet Astronomical Photometry from Rockets; 8) Solar Corona and Interplanetary Gas; 9) Solar Wind and the Interplanetary Media; 10) the Solar Wind; 11) the Moon; 12) the Electric Universe; 13) Astrostats for Astrophysical Research in Space; 14) Attitude Control of Artificial Satellites; 15) Choice of Grating Mountings Suitable for a Monochromator in a Space Telescope.

This is a compilation of lectures that were delivered by a number of scientists at the invitation of the University of Michigan. The book is designed as a reference work on the various branches of space astrophysics and as a supplementary text for courses in astrophysics, solar physics, and instrumentation.

The Second International Symposium on Rockets and Astronautics, editor-in-chief, Fumio Tamaki (Institute of Industrial Science, University of Tokyo Yayoi-cho, Chiba City, Japan), Yokendo, Bunkyo-Ku, Tokyo, 1961, 344 pp.

Contents: 56 papers contributed by different authors on such subjects as the spherical solid rocket motor, engineering principles in producing reliable solid rockets, rocket power for manned vehicles, a system for lunar photography and data transmission, and the legal status of outer space.

This volume contains the proceedings of a symposium held in Kanda-Hitotsububashi, Tokyo, May 24–28, 1960. The sessions of the meeting dealt with propellants and propulsion, vehicles, instrumentation, space science, space law, and other subjects in rocket technology.

Miniaturization, edited by Horace D. Gilbert (President, Miniature Precision Bearings Inc.), Reinhold Publishing Corp., New York, 1961, 306 pp. $10.00.

Contents: 16 chapters on miniaturization contributed by different authors on such subjects as military equipment, aircraft electronic equipment, missiles and satellites, medicine, communications equipment, computers, consumer products, facilities planning, problems in manufacturing of microelectronics, and miniaturization for space travel.

The authors present the problems encountered in the design, manufacture, maintenance, and assurance of reliability of miniature devices and describe methods of meeting these problems. The book includes information on the special requirements of miniaturization for space travel.

Technical Literature Digest

M. H. Smith, *Associate Editor*
The James Forrestal Research Center, Princeton University

Propulsion and Power (Combustion Systems)

A Mach 4 Ramjet Propulsion Unit, by W. F. Dankhoff, *General Electric Co., Missile and Space Vehicle Dept.*, T.I.S. R53A0514, May 1953, 55 pp. (ASTIA AD17764.)

Relations of Combustion Dead Time to Engine Variables for a 20,000-Pound-Thrust Gaseous-Hydrogen-Liquid-Oxygen Rocket Engines, by Daniel I. Drain, Harold J. Schum and Charles A. Wasserbauer, *NASA Tech. Note* D-851, June 1961, 23 pp.

Experimental Study of Effects of Geometric Variables on Performance of Conical Rocket-Engine Exhaust Nozzles, by Harry E. Bloomer, Robert J. Antl and Paul E. Renas, *NASA Tech. Note* D-846, June 1961, 61 pp.

Some Problems Encountered in the Design of Large Rocket Engines Test Beds, by R. H. B. Forster and L. Breen, *Brit. Interplanetary Soc., J.*, vol. 18, no. 2, March–April 1961, pp. 55–69.

Propulsion and Power (Noncombustion)

Magnetic Ignition of Pulsed Gas Discharges in Air of Low Pressure in a Coaxial Plasma Gun, by Karlheinz Thom and Joseph Norwood Jr., *NASA Tech. Note* D-910, June 1961, 32 pp.

Energy Conversion for Space Power (a selection of technical papers based mainly on a symposium of the American Rocket Society held at Santa Monica, Calif. Sept. 27–30, 1960), Nathan W. Snyder (ed.), Academic Press, New York, 1961, 779 pp. (Progress in Astronautics and Rocketry, Vol. 3.)

Physics of Thermoelectricity, by A. C. Beer, pp. 3–25, 36 refs.

Thermoelectric Generator Materials, by R. C. Miller and R. W. Ure Jr., pp. 27–53, 31 refs.

High-Temperature Semiconductors for Thermoelectric Conversion, by S. W. Kurnick, R. L. Fitzpatrick and J. F. Leavy, pp. 53–61.

The Use of High Temperature Thermoelectric Materials (Silicides) for Power Generation in Space, by S. E. Mayer and I. M. Ritchie, pp. 63–72.

Irradiation Effects on Thermoelectric Materials, by J. C. Danko, G. R. Kilp and P. V. Mitchell, pp. 73–83.

Thermoelectric Elements in Space Power Systems, by Douglas L. Kerr, pp. 85–109.

Thermoelectric Materials for Space Cooling, by E. E. Gardner and E. Woisard, pp. 111–121, 11 refs.

Review of the Physics of Thermionics, by Wayne B. Nottingham, pp. 125–131.

Plasma Thermionics, by H. W. Lewis, pp. 133–136.

Cesium Converter Studies, by V. C. Wilson, pp. 137–154.

Parametric Optimization of the Emission-Limited Thermionic Converter, by N. S. Rasor, pp. 155–166.

Experimental Research on Plasma Thermionic Energy Converters, by Karl G. Hernqvist, pp. 167–175.

Theory of the Cesium Plasma Energy Converter with Tungsten Cathode, by Howard L. Steele, pp. 177–190, 10 refs.

Chemistry of Fuel Element Cathode Materials, by Melvin G. Bowman, pp. 201–209, 11 refs.

A Nuclear-Thermionic Fuel Element Test, by R. C. Howard, L. Yang, H. L. Garvin and F. D. Carpenter, pp. 211–217.

The Photovoltaic Effect and Solar Energy Conversion, by J. J. Loferski, pp. 221–229, 11 refs.

Advances in Silicon Solar Cell Development, by Martin Wolf, pp. 231–261, 20 refs.

Large Area Solar Cells, by J. F. Elliott, V. F. Meikleham and C. L. Kolbe, pp. 263–273.

Evaporated CdS Film Photovoltaic Cells for Solar Energy Conversion, by A. E. Middleton, D. A. Gorski and F. A. Shirland, pp. 275–299.

Integrally Composed Variable Energy Gas Photo-voltaic Cells, by L. E. Stone, J. E. Powderly and W. E. Medcalf, pp. 299–315.

Some Theoretical Aspects of the Physics of Solar Cells, by Hans J. Queisser and William Shockley, pp. 317–323, 14 refs.

Electron Bombardment of Silicon Solar Cells, by R. G. Downing, pp. 325–344.

Radiation Damage in Satellite Solar

EDITOR'S NOTE: Contributions from Professors E. R. G. Eckert, E. M. Sparrow and W. E. Ibele of the Heat Transfer Laboratory, University of Minnesota, are gratefully acknowledged.

Cell Power Systems, by J. M. Denney, pp. 345–361.

High Energy Proton Radiation Damage, by J. M. Denney, R. G. Downing and A. Grenall, pp. 363–371.

The Use of Vacuum Deposited Coatings to Improve the Conversion Efficiency of Silicon Solar Cells in Space, by Alfred Thelen, pp. 373–383.

General Evaluation of Chemicals for Regenerative Fuel Cells, by James King Jr., Frank A. Ludwig and J. J. Rowlette, pp. 387–410.

Resume of Thermally Regenerative Fuel Cell Systems, by R. E. Henderson, B. Agruss and W. G. Caple, pp. 411–423.

Regenerative Hydrogen-Oxygen Fuel Cell, by Frank A. Ludwig, pp. 425–443.

Fuel Cells with Ion Exchange Membranes, by Walter Juda, Charles E. Tirrell and Robert M. Lurie, pp. 445–459, 12 refs.

Regenerative Ion Exchange Membrane Fuel Cell Developments, by J. S. Bone and M. D. Read, pp. 461–468.

Fuel Cells for Astronautic Application, by Gerald E. Starkey, pp. 469–477.

Secondary Batteries for Energy Storage in Space, by Irwin M. Schulman, pp. 479–496.

Battery Considerations for a Communications Satellite, by U. B. Thomas, pp. 497–514.

Vapor Turbine for Space Power, by Robert O. Bullock, pp. 517–540, 15 refs.

Stirling Engine Development for Space Power, by M. C. Parker and C. L. Smith, pp. 541–564.

Comparative Rating of Positive-Displacement Engines and Turbines for Cryogenic Power Systems, by Homer J. Wood and Normand E. Morgan, pp. 565–592.

Zero Gravity Boiling and Condensing, by Lloyd M. Hedgepeth, pp. 593–611.

An Electro-Mechanical Energy Storage System for Space Application, by John B. Roes, pp. 613–622.

The Prospects for MHD Power Generation, by G. W. Sutton, and L. Steg, pp. 625–661, 11 refs.

Aspects of Magnetohydrodynamic (MHD) Generators for Space, by J. H. Huth, pp. 663–670, 11 refs.

Experiments Relating to Generation of Power by Magnetohydrodynamics, by Stewart Way, pp. 671–691, 13 refs.

A Vortex MHD Power Generator, by R. J. Coerdt, W. C. Davis, R. T. Craig and J. E. McCune, pp. 695–714.

On the Magnetogasdynamics of Compressible Vortices, by James E. McCune and Coleman duP Donaldson, pp. 715–741.

High Voltage Generation in Space: the Parametric Electrostatic Machine, by A. S. Denholm, J. G. Trump and A. J. Gales, pp. 745–766, 13 refs.

Electrostatic Generators in Space Power Systems, by Dominique Gignoux, pp. 767–779.

The Thermoelectric Power of Magnesium-Cadmium Alloys, by Seiichiro Noguchi, *Phys. Soc. of Japan, J.*, vol. 16, no. 6, June 1961, pp. 1145–1140.

Propellants and Combustion

Erosive Combustion of Colloidal Powders, by P. Tavernier and J. Boisson, *Great Britain, Ministry of Aviation, Tech. Info. and Library Services,* T1L, T 4891, Dec. 1959, 10 pp.

Combustion Instability in Liquid Propellant Rocket Motors, Tech. Rep.: An Investigation of Transverse Mode Combustion Instability in Liquid Propellant Rocket Motors, by F. H. Reardon, *Princeton Univ., Dept. Aeron. Engng. Rep.* 550, June 1961, 123 pp. (Thesis, Ph.D.)

Experimental Investigation of Ionization Processes in Flames, by A. Van Tiggelen, *Louvain Univ., Lab. for Inorganic Chem.*, May 1961, 23 pp.

A Technique for Cryopumping Hydrogen, by Jack Grobman, *NASA Tech. Note* D-863, June 1961.

Experimental Investigation of Heat-Transfer Characteristics of Hydrazine and a Mixture of 90% Hydrazine and 10% Ethylenediamine, by M. B. Noel, *Calif. Inst. Tech., Jet Propulsion Lab. Tech. Rep.* 32-109, June 1961, 18 pp.

Free Molecular Heat Transfer in the Ionosphere, by L. M. Gilbert and S. M. Scala, *General Electric Co., Missile and Space Vehicle Dept.* T.I.S. R61SD076, March 1961, 32 pp. 13 figs.

Electrically Exploded Wires; Experiments and Theory, by J. B. Langworthy, R. C. O'Rourke, M. P. Shuler, I. M. Vitkovitsky, C. B. Dobbie, R. J. Veith and D. F. Hansen, *Naval Res. Lab. Rep.* 5489, Prog. Rep. for March 1, 1958 to June 30, 1960, May 1961, 132 pp.

The Thermodynamic and Electrical Properties of Dissociated Combustion Gases, by W. Craig Moffatt, *Proj. Squid Tech. Rep.* MIT-27-P, June 1961, 8 pp.

Bond Dissociation Energies in Small Hydrocarbon Molecules, by Bruce E. Knox and Howard B. Palmer, *Proj. Squid* PSU-6-P. (Reprinted from *Chem. Rev.*, vol. 61, June 1961, pp. 247–255, 64 refs.)

Preliminary Report on the Thermodynamic Properties of Selected Light-Element and Some Related Compounds, by William H. Evans, Thomas W. Mears, George Armstrong, L. A. Krieger, R. F. Walker, Martin L. Reilly, George T. Furnkawa, Thomas B. Douglas and Andrew C. Victor, *National Bur. Standards Rep.* 7093, Jan. 1961, 253 pp.

Rate of Reaction $O + H_2 \rightarrow OH + H$ in Flames, by C. P. Fenimore and G. W. Jones, *J. Phys. Chem.*, vol. 65, no. 6, June 1961, pp. 993–998.

Topologies of B_4 and B_7 Hydrides, by William N. Lipscomb, *J. Phys. Chem.*, vol. 65, no. 6, June 1961, pp. 1064–1070.

Mach Reflection of Detonation Waves in Condensed High Explosives, by B. B. Dunne, *Phys. of Fluids*, vol. 4, no. 7, July 1961, pp. 918–924.

Ignition in a Flow by Hot Bodies, by S. A. Gol'denberg, ARS JOURNAL, vol. 31, May 1961, pp. 691–693.

Proceedings of the 26th Shock and Vibration Symposium, Naval Training Center, San Diego, May 1958, Washington Secretary of Defense, 1958, 326 pp. Shock and Vibration Symposium, 26th San Diego, May 1958 (Shock and Vibration Bull. 26, Pt. II, unclassified papers.) (ASTIA AD-20-0700.)

A Simplified Model of Resonant Burning in Solid Propellants, by W. Nachbar, pp. 209–214.

Materials and Structures

Plasticity and Nonlinear Elastic Strains, by Marvin E. Backman, *Bur. Naval Weapons, NAVWEPS Rep.* 7648, April 1961, 30 pp.

Meteoroids vs. Space Vehicles, by R. L. Bjork, ARS JOURNAL, vol. 31, no. 6, June 1961, pp. 803–807.

Effect Upon Shock Spectra of the Dynamic Reaction of Structures, by G. J. O'Hara, *Experimental Mechanics,* vol. 1, no. 5, May 1961, pp. 145–151.

Stresses of Nozzle Connections of Pressure Vessels, by D. E. Hardenbergh, *Experimental Mechanics,* vol. 1, no. 5, May 1961, pp. 152–158.

Temperature Dependence of Elastic Constants of Some Cermet Specimens, by Sam Spinner, *J. Res. National Bur. of Standards (C. Engng. and Instrumentation),* vol. 65, no. 2, April–June 1961, pp. 89–96.

Progress in Ceramic Science, Vol. 1, J. E. Burke (ed.), Pergamon Press, New York, 1961, 232 pp.

A Review of Glass Strength, by R. J. Charles, pp. 1–38, bibliog. pp. 37–38.

Vaporization of Oxides, by R. J. Ackerman and R. J. Thorn, pp. 39–88, bibliog. pp. 85–88.

Design Problems of Ballistic Missile Tank Structures, by D. S. Houghton and D. J. Johns, *Aircraft Engng.*, vol. 33, no. 389, July 1961, pp. 188–192.

Ignition Characteristics of Metals and Alloys, by L. E. Dean and W. R. Thompson, ARS JOURNAL, vol. 31, no. 7, July 1961, pp. 917–923.

Creep Collapse of Cylindrical Shells, by Thein Wah, *Franklin Inst., J.*, vol. 272, no. 1, July 1961, pp. 45–60.

Compact Apparatus for High Temperature Modulus of Rupture Measurement, by Peter T. B. Shaffer, *Rev. Scien. Instr.*, vol. 32, no. 7, July 1961, pp. 794–795.

Investigation of the Iron-Chromium-Titanium Phase Diagram in a Region of Iron- and Chromium-Rich Alloys, by N. G. Boriskina and I. I. Kornilov, ARS JOURNAL, vol. 31, no. 7, July 1961, pp. 961–966.

The Vaporization of Graphite, TiC, ZrC, and HfC, by G. L. Vidale, *Gen. Electric Co., Missile and Space Vehicle Dept.* T.I.S. R61S D010, Jan. 1961, 47 pp.

Centrifuge Creep Testing of Viscoelastic Materials, by Charles H. Parr, *Rohm & Haas Co., Quar. Prog. Rep. on Engng. Res.*, Dec. 15, 1960 to March 15, 1961, June 1961, 5 pp.

A Boron-Base Refractory, by Perry G. Cotter, *Bureau of Mines, Rep. of Investigations* 5774, 1961, 7 pp.

Axisymmetric Pressure Loading of Thin Shells of Revolution: Approximate Membrane Solution, by H. E. Williams, *Calif. Inst. Tech., Jet Propulsion Lab. Tech. Rep.* 32-52, Feb. 1961, 18 pp.

Axisymmetric Edge Loading of Shells of Revolution, by H. E. Williams, *Calif. Inst. Tech., Jet Propulsion Lab. Tech. Rep.* 32-50, Feb. 1961, 20 pp.

The Effects of Temperature and Time on Aircraft and Missile Structures, by N. J. Hoff, *Stanford Univ., Dept. Aeron. Engng.*, SUDAER No. 99, Jan. 1961, 88 pp. (AFOSR TN 61-646.)

Deformation of Heated Shells, by W. S. Hemp, *Stanford Univ., Dept. Aeron. Engng.*, SUDAER No. 103, April 1961, 94 pp. (AFOSR TN 61-770.)

Analysis of Partly Wrinkled Membranes, by Manuel Stein and John M. Hedgepeth, *NASA Tech. Note* D-813, July 1961, 32 pp.

Stress Concentrations in Filamentary Structures, by John M. Hedgepeth, *NASA Tech. Note* D-882, May 1961, 30 pp.

Stability of Refractory Compounds in Hydrogen Between 4500° and 5000°F, and their Compatibility with Tungsten, by Charles E. May and Paul D. Hoekstra,

NASA Tech. Note D-844, May 1961, 12 pp.

Effect of a Load-Alleviating Structure on the Landing Behavior of a Reentry-Capsule Model, by Edward L. Hoffman, Sandy M. Stubbs and John R. McGehee, *NASA Tech. Note* D-811, May 1961, 29 pp.

Supersonic Panel Flutter Test Results for Flat Fiber-Glass Sandwich Panels with Foamed Cores, by W. J. Tuovila and John G. Presnell Jr., *NASA Tech. Note* D-827, June 1961, 15 pp.

Surface Tension of Refractory Metals, by S. Victor Radcliffe and H. Udin, *Wright Air Dev. Div., WADD TR* 60-566 Dec. 1960, 37 pp., 45 refs.

Investigations of the Deterioration of 22 Refractory Materials in a Mach Number 2 Jet at a Stagnation Temperature of 3,800°F, by B. W. Lewis, *NASA Tech. Note* D-906, June 1961, 17 pp.

The Effect of Axial Constraint on the Instability of Thin Conical Shells Under External Pressure, by Josef Singer, *Israel Inst. Tech., Tech. Note* 2, Dec. 1960. (*AFOSR TN* 60-860.)

Compatibility of Freon 114 Used in Mercury Support Equipment with Various Hose Materials, by W. C. Stormer, *Aerospace Engng.*, vol. 20, no. 6, June 1961, pp. 28–29, 84–86.

Corrosion Problems Encountered in Silo Storage of Missiles, by Leo E. Gatzek, *Aerospace Engng.*, vol. 20, no. 6, June 1961, pp. 34–35, 87–90.

Equations for the Non-Stationary Temperature Fields in Thin Shells in the Presence of Sources of Heat, by V. V. Bolotin, *PMM, J. Appl. Math. and Mech.*, vol. 24, no. 2, 1960, pp. 515–519.

Plasticity Conditions for Thin Shells, by V. I. Rozenblium, *PMM, J. Appl. Math. and Mech.*, vol. 24, no. 2, 1960, pp. 520–524.

Melting Diagram for the Titanium-Vanadium-Molybdenum Ternary System, by I. I. Kornilov and R. S. Poliakova, ARS JOURNAL vol. 31, May 1961, pp. 698–699.

Proceedings of the 26th Shock and Vibration Symposium, Naval Training Center, San Diego, May 1958, Washington Secretary of Defense, 1958, 326 pp. Shock and Vibration Symposium, 26th, San Diego, May 1958, (Shock and Vibration Bull. 26, Pt. II, unclassified papers.) (ASTIA AD-20-0700.)

Vibratory Environment of a Ramjet Vehicle, by R. C. Geiger, pp. 7–15.

Shock and Vibration Data of Corporal Components, by M. M. Yancey, pp. 16–20.

Impulse and Structural Failure at High-Speed Water Entry, by M. Kornhauser, pp. 28–32.

The Response of Missile Components to Water Entry Shock, by J. H. Green, pp. 21–27.

Self-Induced Oscillations of a Cylindrical Cantilever in a Wind for Reynold's Numbers Greater than Critical, by A. A. Ezra, pp. 180–184.

On the Rotationally Symmetric Motion of a Cylindrical Shell Under the Influence of Pressure Front Traveling at Constant Velocity, by J. I. Bluhm and F. I. Baratta, pp. 185–200.

The Theory of Vibration and Noise Isolation in Shells and Housings, by E. J. Skudrzyk, pp. 201–208.

Analysis of Vibration Data, by F. H. Eng, pp. 231–236.

Correlation and Spectral Analysis of Time Varying Data, by J. M. Zimmerman, pp. 237–258.

A Proposed Method for Assessing the Severity of the Vibration Environment, by J. T. Marshall and R. A. Harmen, pp. 259–277.

The Effect of Atmosphere on Creep and Fatigue at Elevated Temperature, by M. R. Achter, pp. 287–294.

Proposal for Acoustical Vibration Tests Using the Redstone and Jupiter Missiles, by R. M. Hunt and J. H. Farrow, pp. 308–314.

Acoustic Fatigue and Damping, by B. J. Lazan and W. J. Trapp, pp. 295–307.

Space Requirements for Equipment Items Subjected to Random Excitation, by J. A. Skoog and G. G. Setterlund, pp. 315–322.

Fluid Dynamics, Heat Transfer, and MHD

Characteristics of Heat Flux Meter for Use in High Temperature Atmospheres, by L. M. Fingerson and P. L. Blackshear, *Project Squid, Tech. Rep.* MIN-1-P, Feb. 1961, 29 pp.

A Method for Determining the Heat Conductivity Coefficient of a Gas with a Single AC Heated Hot Wire, by Herbert J. Bomelburg, *Aberdeen Proving Ground, Ballistic Res. Labs. Rep.* 1107, May 1960, 25 pp.

Experimental Investigations of Laminar Heat Transfer and Transition with Foreign Gas Injection—a 16° Porous Cone at M = 5, by C. J. Scott, *Minnesota Univ., Rosemount Aeron. Labs., Res. Rep.* 174, Oct. 1960, 36 figs., 40 pp., 37 refs. (AFOSR TN 60-1370.)

Inviscid Modes of Instability for Flow in a Curved Channel, by D. A. Lee and W. H. Reid, *Brown Univ., Div. Appl. Math. Tech. Rep.* 140, April 1961, 14 pp.

Compressible Laminar Motion with Fluctuation in a Free Stream Temperature, by S. L. Soo, *Project Squid Tech. Rep.* ILL-1-P, May 1961, 6 pp.

Measurements of Aerodynamic Heat Transfer on a 15° Cone-Cylinder-Flare Configuration in Free Flight at Mach Numbers up to 4.7, by Charles B. Rumsey and Dorothy B. Lee, *NASA Tech. Note* D-824, May 1961, 61 pp.

An Investigation of Laminar Heat Transfer to Slender Cones in the Hypersonic Shock Tunnel, by Charles E. Wittliff and Merle R. Wilson, *Cornell Aeron. Lab. Rep.* AF-1270-A-2, May 1961, 60 pp., 47 refs.

Stagnation Point Fluctuations on Bodies of Revolution with Hemispherical Noses, by A. M. Kuethe, W. W. Willmarth and G. H. Crocker, *Michigan Univ., Dept. Aeron. Astron. Engng.*, June 1960, 26 pp. (AFOSR 60-65.)

Simultaneous Transfer of Momentum, Heat and Mass, Part II: Gas-Vapour Mixtures, by Gianni Jarre, *Torino, Laboratorio di Meccanica Applicata del Politecnico,* Feb. 1961, 15 pp.

Heat Flux Probe for Dynamic Measurements in High Temperature Gases, by L. M. Fingerson and P. L. Blackshear, *Project Squid Tech. Rep.* MIN-2-P, May 1961, 24 pp.

A Frequency Modulation Circuit for the Measurement of Gas Conductivity and Boundary Layer Thickness in a Shock Tube, by P. Savic and G. T. Boult, *Canada, National Res. Council, Div. Mech. Engng.* MT-43, May 1961, 31 pp. 16 figs.

Charts for Conical and Two-Dimensional Oblique-Shock Flow Parameters in Helium at Mach Numbers from about 1 to 100, by Arthur Henderson Jr. and Dorothy O. Braswell, *NASA Tech. Note* D-819, June 1961, 183 pp.

Physical Gas Dynamics (Translated from the Russian by R. C. Murray and D. R. H. Phillips), A. S. Predvoditelev (ed.), Pergamon Press, New York, 1961, 183 pp.

Thermodynamic Properties of Air Between 1000° and 12,000°K and 0.001 and 1000 Atmospheres, by E. V. Stupochenko, et al., pp. 1–40.

Methods of Calculating the Kinetic Coefficients of Air High Temperatures, by E. V. Stupochenko, et al., pp. 41–60.

Effect of Internal Degrees of Freedom of Particles on the Transfer Coefficients in Multi-component Gas Mixtures, by E. V. Samuilov, pp. 61–72.

Thermodynamic and Gas-Dynamic Properties of Flowing Air Downstream of a Normal Shock Wave with Allowance for Ionization and Dissociation, by I. B. Rozhdestvenskii, pp. 73–85.

Determination of Gas-Dynamic Properties of Flow Behind a Normal Shock Wave with Correction for Variable Specific Heats and Dissociation of Air, by N. F. Gorban, pp. 86–95.

Flow of Gas from a Nozzle Cut in an Oblique Plane, by V. P. Motulevich, pp. 96–118.

Unsymmetrical Supersonic Gas Flow Around Edges of Finite Thickness, by V. P. Motulevich, pp. 119–143.

Kinetics, Equilibria and Performance of High Temperature Systems; Proceedings of The First Conference (Combustion Institute Western States Section, 1st Conference, Los Angeles, Nov. 1959) Gilbert S. Bahn and Edward E. Zukoski (eds.), Butterworth & Co., London, 1960, 255 pp.

Approximations to High Temperature Thermodynamics of Air in Closed Form, by A. R. Hochstim, pp. 39–52.

Shock Wave Asymmetry for Cones and Sphere Cones at Angle of Attack, by Robert A. Greenberg and Stephen C. Traugott, ARS JOURNAL, vol. 31, no. 6, June 1961, pp. 821–822.

"Pinhole Camera" for Determination of Plasma Arc Rotational Speed, by E. A. Bunt and H. L. Olson, ARS JOURNAL, vol. 31, no. 6, June 1961, pp. 826.

Contact Surface Tailoring in a Chemical Shock Tube, by Howard B. Palmer and Bruce E. Knox, ARS JOURNAL, vol. 31, no. 6, June 1961, pp. 826–828.

Adiabatic Nozzle Flows, by R. A. A. Bryant, ARS JOURNAL, vol. 31, no. 6, June 1961, pp. 828–830.

Simplified Sudden-Freezing Analysis for Nonequilibrium Nozzle Flows, by K. N. C. Bray, ARS JOURNAL, vol. 31, no. 6, June 1961, pp. 831–834.

Temperature Distribution in Couette Flow With Radiation, by R. Vishanta and R. J. Grosh, ARS JOURNAL, vol. 31, no. 6, June 1961, pp. 839–840.

Estimation of the Critical Viscous Sublayer in Heat Transfer Problems, by Ajit Kumar Ray, *Appl. Sci. Res., Section A,* vol. 10, no. 3–4, 1961, pp. 173–179.

Temperature-Dependent Heat Sources of Sinks in a Stagnation Point Flow, by E. M. Sparrow and R. D. Cess, *Appl. Sci. Res., Section A,* vol. 10, no. 3–4, 1961, pp. 185–197.

Mass Transfer with a Moving Interface, by W. J. Beek and C. A. P. Bakker, *Appl. Sci. Res., Section A,* vol. 10, no. 3–4, 1961, pp. 241–252.

Flow of a Simple Non-Newtonian Fluid Past a Sphere, by John Slattery, *Appl. Sci. Res., Section A*, vol. 10, no. 3–4, 1961, pp. 286–294.

Laminar Stagnation Flow of an Electrically Conducting Fluid Against an Infinite Plate in the Presence of a Transverse Magnetic Field, by A. S Gupta, *Appl. Sci. Res., Section B*, vol. 9, no. 1 1961, pp. 45–50.

Electromagnetic Generation of Vorticity in the Uniform Efflux of a Conducting Fluid from the Surface of a Magnetized Sphere, by J. D. Murray, *Appl. Sci. Res., Section B*, vol. 9, no. 1, 1961, pp. 65–76.

Isentropic One-Dimensional Magnetohydrodynamic Channel Flow, by Boris Podolsky and A. Sherman, *Appl. Sci. Res., Section B*, vol. 9, no. 1, 1961, pp. 77–82.

Relativistic Fluids of Infinite Conductivity, by Yvonne Bruhat, *Astronautica Acta*, vol. 6, no. 6, 1960, pp. 354–365. (In French.)

Linearized Supersonic Flow in an Axisymmetric Jet Issuing in Air at Rest, by Enrico Pistolesi and Marino Marini, *Pisa Univ., Inst. Aeron.*, March 1961, 22 pp. (AFOSR 852.)

Hypersonic Flow-Blast Analogy, by J. Lukasiewicz, *Arnold Engng. Dev. Center*, AEDC TR 61-4, June 1961, 76 pp.

Aerodynamics of Highly Rarefied Gases, by G. N. Patterson, *Toronto Univ., Inst. Aerophys. UTIA Review* 18, March 1961, 74 pp.

Boundary Layer Effects in Magnetohydrodynamic Flows, by W. Craig Moffatt, *Proj. Squid, Tech. Rep.* MIT 26-P, June 1961, 41 pp.

Slip Flow in the Laminar Boundary Layer Over a Flow Plate at Hypersonic Speeds, by Robert E. Street, *Univ. of Washington, Dept. Aeron. Engng.*, April 1961, 44 pp. (AFOSR 558.)

Non-Stationary Boundary Layers Behind Compression Shocks and Expansion Waves, by E. von Becker, *Progress in Aeron. Sciences*, Vol. 1, Pergamon Press, New York, 1961, pp. 105–173, 80 refs. (In German.)

The Downstream Influence of Mass Transfer at the Nose of a Slender Cone, by Robert J. Cresci and Paul A. Libby, *Brooklyn Polytech. Inst., Dept. Aerospace Engng. Appl. Mech. Rep.* 634, May 1961, 46 pp.

One-Dimensional Flow of Dissociated Diatomic Gases, by G. R. Inger, *Douglas Aircraft Co. Rep.* SM-38523, May 1961, 63 pp.

Hypersonic Viscous Shock Layer of Nonequilibrium Dissociating Gas, by Paul M. Chung, *NASA Tech. Rep.* R-109, 1961, 40 pp.

A Flow Model for Hypersonic Rarefied Gasdynamics with Applications to Shock Structure and Sphere Drag, by Nicholas Rott and Clive G. Whittenbury, *Douglas Aircraft Co. Rep.* SM-38524, May 1961, 34 pp.

Laminar Heat-Transfer and Pressure-Distribution Studies on a Series of Reentry Nose Shapes at a Mach Number of 19.4 in Helium, by Richard D. Wagner Jr., W. Clint Pine and Arthur Henderson Jr., *NASA Tech. Note* D-891, June 1961, 39 pp.

Heat Transfer to Cold Electrodes in a Flowing Ionized Gas, by James A. Fay and William T. Hogan, *Mass. Inst. Tech., Magnetogas-dynamics Lab. Rep.* 61-2, April 1961, 14 pp. (AFOSR 595.)

Mass Addition Effects on Hypersonic Heat Transfer to a Two-Dimensional Body, by S. M. Scala and W. F. Ashley, *General Electric Co., Missile and Space Vehicle Dept.* T.I.S. R60SD491, Dec. 1960, 19 pp.

Equations of Transport of Radiant Energy and Similarity of Radiating Systems, by A. S. Nevski, *Purdue Univ. Radiative Transfer Project, Transl.* TT-8, March 1961, 19 pp. (Transl. from *Zhurnal Tekhnicheskoi Fiziki*, vol. 10, no. 18.)

Research on Radiant Energy Transfer in an Absorbing Medium, by I. P. Kolchenogova and S. N. Shorin, *Purdue Univ., Radiative Energy Project, Transl.* TT-7, March 1961, 6 pp. (Transl. from *Izvestiia Akademii Nauk SSSR, Otdel. Tekh. Nauk*, 1956.)

A One-Megawatt Pulsed RF Generator for Plasma Heating, by Homer M. Hill Jr., *Princeton Univ., Plasma Physics Lab.*, MATT-72, May 1961, 11 pp.

The Use of a T-Tube to Produce Shock-Heated Plasmas in an X-Band Waveguide, by J. M. Schecher, *Maryland Univ., Inst. for Fluid Dynamics and Appl. Math., Tech. Note* BN-245, April 1961, 38 pp. (AFOSR 757.)

Investigations of Phenomena Associated with Electrodeless Ring Discharge in Hydrogen, by Gerhard Herzberg, *Cornell Aeron. Lab.*, May 1961, 17 pp. (Transl. by J. Lotsof from *Annalen der Physik*, Fourth Series, vol. 84, no. 21, pp. 553–577, 1927.)

General Theory of Collision-Broadening of Spectral Lines, by Oldwig von Roos, *Calif. Inst. Tech., Jet Propulsion Lab. Tech. Rep.* 32-100, April 1961, 14 pp.

Pressure Shocks in Viscous Heat Conducting Gases, by T. Y. Thomas and C. R. Edstrom, *Proc. National Acad. Sci.*, vol. 47, no. 3, March 1961, pp. 319–325.

Investigation of the Attenuation of Shock Waves Propagated Through an Ionized Gas in the Presence of a Transverse Magnetic Field, by S. P. Carfangno and G. P. Wachtell, *Project Squid, Tech. Rep.* FIL-1-R, June 1961, 80 pp.

Substitution of a Catalytic Probe for a Tube of Infinite Length in Atom Recombination Experiments, by Bernard J. Wood and A. Bruce King, *Project Squid, Tech. Rep.* SRI-10-P, June 1961, 5 pp.

On the Limiting Velocity for a Rotating Plasma, by Shao-Chi Lin, *Avco-Everett Res. Lab. Res. Rep.* 101, April 1961, 51 pp.

The Newtonian Approximation in Magnetic Hypersonic Stagnation-Point Flow, by Paul S. Lykoudis, *J. Aerospace Sci.*, vol. 28, July 1961, pp. 541–546.

Microwave Measurement of Fast Time Varying Plasmas, by Susumu Takeda, *Phys. Soc. of Japan. J.*, vol. 16, no. 6, June 1961, pp. 1267–1268.

Radiation by Charged Particles Passing Through an Electron Plasma in an External Magnetic Field, by S. K. Majumdar, *Phys. Soc., London, Proc.*, vol. 77, Pt. 6, no. 498, June 1961, pp. 1109–1120.

Transport Phenomena in a Fully Ionized Gas Confined in a Strong Magnetic Field, by Tohoki Koga, *Phys. of Fluids*, vol. 4, no. 7, July 1961, pp. 834–841.

Three-Dimensional Hypersonic Gas Flow Past Slender Bodies at High Angles of Attack, by V. V. Sycher, *PMM, J. Appl. Math. and Mech.*, vol. 24, no. 2, 1960, pp. 296–306.

On the Uniqueness of Quasihyperbolic Magnetohydrodynamic Flows, by M. N. Kogan, *PMM, J, Appl. Math. and Mech.*, vol. 24, no. 2, 1960, pp. 530–533.

On the Transition from Subsonic to Supersonic Velocities in Laval Nozzles, by O. S. Ryzkov, *PMM, J. Appl. Math. and Mech.*, vol. 24, no. 2, 1960, pp. 534–540.

One Dimensional Flow of a Compressible Gas in a Pipe in the Presence of a Transverse Magnetic Field, by I. B. Chekmarev, *PMM, J. Appl. Math. and Mech.*, vol. 24, no. 2, 1960, pp. 553–555.

On an Exact Solution of the Equations of Magnetohydrodynamics, by S. A. Regirer, *PMM, J. Appl. Math. and Mech.*, vol. 24, no. 2, 1960, pp. 556–561.

Fall of a Spherical Drop in the Presence of Evaporation of Condensation of Vapors at Its Surface, by V. S. Novoselov, ARS JOURNAL, vol. 31, May 1961, pp. 686–688.

Flight Mechanics

Optimum Maneuvers for Launching Satellites Into Circular Orbits of Arbitrary Radius And Inclination, by J. P. Carstens and T. N. Edelbaum, ARS JOURNAL, vol. 31, no. 7, July 1961, pp. 943–949.

Satellite Life Duration, by Thomas L. Vincent, ARS JOURNAL, vol. 31, no. 7, July 1961, pp. 1015–1018.

Secular Gravitational Torque on a Satellite in a Circular Orbit, by Russel A. Nidey, ARS JOURNAL, vol. 31, no. 7, July 1961, p. 1032.

Dynamic Effects in the Motion of Artificial Earth Satellites, by L. I. Sedov,

CHANGE-OF-ADDRESS NOTICE

In the event of a change of address, it is necessary to include both your old and new addresses, as well as your membership number and coding, when notifying ARS headquarters, in order to insure prompt service. If you are moving or have moved, send the following form to Membership Dept., American Rocket Society, 500 Fifth Ave., New York 36, N. Y.:

Name_____

Membership Card No _____ Coding _____

Old Address_____

_____

New Address _____

_____

Planetary and Space Sci., vol. 5, no. 3, July 1961, pp. 238–243.

Numerical Solutions of Equations of Finite Differences and Their Application to the Calculation of Orbits of Artificial Earth Satellites, by G. P. Taratynova, ARS JOURNAL, vol. 31, no. 7, July 1961, pp. 976–988.

On the Motion of a Slender Rigid Body Caused by a Small Torque, by H. E. Williams, *Calif. Inst. Tech., Jet Propulsion Lab. Tech. Rep.* 32-62, March 1961, 22 pp.

Possible Increase of Base Pressure Behind a Wedge at Hypersonic Velocities, by E. N. Bondarev and M. Ia. Iudelovich, *The Johns Hopkins Univ., Appl. Phys. Lab.* TG 230-T233, April 1961, 2 pp. (Transl. from *Izvestiia Akad. Nauk SSSR, Otdel. Tekh. Nauk. Mekh. i Mashinostroenie*, No. 5, Sept.–Oct. 1960, p. 186.)

Some Experiments at High Supersonic Speeds on the Aerodynamic and Boundary-Layer Transition Characteristics of High-Drag Bodies of Revolution, by Alvin Seiff, Simon C. Sommer and Thomas N. Canning, *NACA Res. Mem.* A56105, Jan. 1957, 91 pp. (Declassified by authority of *NASA TPA* No. 45, June 22, 1961.)

Preliminary Analysis of the Effect of Flow Separation Due to Rocket Jet Pluming on Aircraft Dynamic Stability During Atmospheric Exit, by Murray Dryer and Warren J. North, *NASA Mem.* 4-22-59E, June 1959, 35 pp. (Declassified by authority of *NASA TPA* No. 45, June 22, 1961.)

Non-linear Effects in the Longitudinal Dynamics of a Lifting Vehicle in a Circular Orbit, by R. S. Rangi, *Inst. Aerophysics, Univ. of Toronto Tech. Note* 40, Oct. 1960, 18 pp.

An Investigation of the Aerodynamic Characteristics of Thin Delta Wings with a Symmetrical Double-Wedge Section at a Mach Number of 6.9, by Mitchel H. Bertram and William D. McCauley, *NACA Res. Mem.* L55B14, April 1955, 40 pp. (Declassified by authority of *NASA TPA* No. 45, June 22, 1961.)

Tables of Z Functions for Atmosphere Entry Analyses, by Dean R. Chapman and Arline K. Kapphahn, *NASA Tech. Rep.* R-106, 1961, 277 pp.

The Effect of Radiation Force on Satellites of Convex Shape, by Herbert B. Holl, *NASA Tech. Note* D-604, May 1961, 53 pp.

A Concept of a Manned Satellite Reentry which is Completed with a Glide Landing, by Donald C. Cheatham, *NASA Tech. Mem.* 226*, Dec. 1959, 44 pp. (Declassified by authority of *NASA TPA* No. 45, June 22, 1961.)

Optimum Soft Landing Trajectories, Part I: Analysis, by Lawrence J. Berman, *Mass. Inst. Tech., Dept. Aeron. and Astronautics, Astrodynamics Group,* March 1961. (AFOSR 519.)

On the Dynamics of a Space Vehicle, Equipped with One Main Rocket Motor and Two Vernier Motors, by J. M. J. Kooy, *Astronautica Acta*, vol. 6, no. 6, 1960, pp. 322–341.

Fundamental Analysis of Various Dynamic Stability Problems for Missiles, by T. J. Coakley, E. V. Laitone and W. L. Maas, *Calif. Univ., Berkeley, Inst. Engng. Res. Series* 176, Issue 1, June 1961, 96 pp.

Theory of Artificial Stabilization of Missiles and Space Vehicles with Exposition of Four Control Principles, by R. F. Hoelker, *NASA Tech. Note* D-555, June 1961, 22 pp.

Theoretical Evaluation of the Pressures, Forces, and Moments at Hypersonic Speeds Acting on Arbitrary Bodies of Revolution Undergoing Separate and Combined Angle-of-Attack and Pitching Motions, by Kenneth Margolis, *NASA Tech. Note* D-652, June 1961, 32 pp.

The Flight Environment of Long-Range Ballistic Missiles and Glide Vehicles, by Kurt R. Enkenhus, *Naval Ordnance Lab., NAVORD Rep.* 6745, Oct. 16, 1959, 20 pp.

Proceedings of the 26th Shock and Vibration Symposium, Naval Training Center, San Diego, May 1958, Washington Secretary of Defense, 1958, 326 pp., Shock and Vibration Symposium, 26th, San Diego, May 1958. (Shock and Vibration Bull. 26, pt. II, unclassified papers.) (ASTIA AD-20-0700.)

Karman Vortex Forces on the Vanguard Rocket, by R. L. Goldman, pp. 171–179.

An Experimental Investigation of the Damping of Liquid Oscillations in an Oblate Spheroidal Tank With and Without Baffles, by David G. Stephens, H. Wayne Leonard and Milton A. Silverira, *NASA Tech. Note* D-808, June 1961, 23 pp.

An Investigation of the Natural Frequencies and Mode Shapes of Liquids in Oblate Spheroidal Tanks, by H. Wayne Leonard and William C. Walton Jr., *NASA Tech. Note* D-904, June 1961, 24 pp.

Optimum Trajectory of N-Stage Missiles, by Harry W. Harerow, *Brit. Interplanetary Soc., J.*, vol. 18, no. 2, March–April 1961, pp. 70–73.

Minimum Energy Entry into Planetary Satellite Orbits, by S. W. Greenwood, *Brit. Interplanetary Soc., J.*, vol. 18, no. 2, March–April 1961, pp. 73–75.

Laws of Similitude in the Calculation of Reentry Trajectories and of the Nose Ablation of Vehicles, by L. Broglio, *Astron. Acta*, vol. 7, no. 1, 1961, pp. 21–34. (In French.)

Rigid Body Attitude Stability and Natural Frequencies in a Circular Orbit, by D. B. Debra and R. H. Delp, *J. Astron. Sci.*, vol. 8, no. 1, Spring 1961, pp. 14–17.

On Two Classes of Plane Extremal Motions of a Rocket in Vacuum, by Iu. A. Gorelov, *PMM, J. Appl. Math. and Mech.*, vol. 24, no. 2, 1960, pp. 434–442.

Interplanetary Trajectories for Space Vehicles with Low-Thrust Acceleration, by Gunther Au, *Raketentechnik und Raumfahrtforschung*, vol. 5, no. 2, April–June 1961, pp. 47–55. (In German.)

Space, Time and Astronautics, by J. M. J. Kooy, *Raketentechnik und Raumfahrtforschung*, vol. 5, no. 2, April–June 1961, pp. 37–46. (In German.)

Reconnaissance Orbits Normal to the Ecliptic Plane, by S. W. Greenwood, *Royal Aeron. Soc., J.*, vol. 65, no. 606, June 1961, pp. 437–438.

Vehicle Design, Testing, and Performance

Effects of Boattailing and Nozzle Extension on the Thrust Minus-Drag of a Multiple-Jet Configuration, by William R. Scott, *NASA Tech. Note* D-887, June 1961, 48 pp.

Aerodynamic Characteristics at a Mach Number of 3.10 of Several Fourth-Stage Shapes of the Scout Research Vehicle, by Byron M. Jaquet, *NASA Tech. Note* D-916, June 1961, 17 pp.

Selection of Power Requirements for Nuclear-Electric Spacecraft Missions, by Jerry P. Davis, *Calif. Inst. Tech., Jet Propulsion Lab. Tech. Rep.* 32-114, May 1961, 13 pp.

ENGINEERS & SCIENTISTS in the fields of space vehicle power and propulsion

The Propulsion and Power Systems Department of the Aerospace Vehicles Laboratory has several unusually interesting openings for engineers and scientists who are interested in the fields of space vehicle power and propulsion. The openings are at all levels of experience – from recent graduates to the senior staff level. Most of the positions will involve design and analysis of power and propulsion systems for satellite and space probe application. Specifically, some of the areas of specialization are:

1 SPACE POWER SYSTEMS
The positions will involve analysis and development of such energy sources as: photo voltaic, thermionic, thermoelectric, battery and advanced energy storage systems.

2 SPACE PROPULSION SYSTEMS
The positions will involve the preliminary and conceptual design and comparative analysis of all types of chemical and electric propulsion systems.

3 PROGRAM MANAGEMENT
The positions will be associated with the development of solid and liquid propellent rocket engines. Advanced degrees are preferred and considerable experience in the field will be required.

If you are interested and believe that you can contribute, please mail your resume to:

Robert A. Martin,
Supervisor of Employment
HUGHES
11940 W. Jefferson Blvd.
Culver City, California

We promise you a reply within one week.
An equal opportunity employer.

Creating a new world with Electronics

HUGHES

HUGHES AIRCRAFT COMPANY
AEROSPACE DIVISIONS

The Conceptual Design of a Nuclear-Electric Power Spacecraft for the Exploration of Jupiter, by Robert J. Beale, *Calif. Inst. Tech., Jet Propulsion Lab. Tech. Rep.* 32-115, May 1961, 24 pp.

Development of Hypervelocity Range Techniques at Arnold Engineering Development Center, by J. Lukasiewicz, W. B. Stephenson, P. L. Clemens and D. E. Anderson, *Arnold Engng. Dev. Center,* AEDC-TR-61-0, June 1961, 74 pp.

DOVAP Data Reduction for IGY Grenade Aerobee Rockets, by P. A. Titus, *Michigan Univ., Dept. Aeron. and Astron. Engng. Tech. Rep.* 2387-58-T, March 1960, 15 pp. (Suppl. to *Tech. Rep.* 2387-50-T.)

Interplanetary Trajectories and Payload Capabilities of Advanced Propulsion Vehicles, by W. G. Melbourne, *Calif. Inst. Tech., Jet Propulsion Lab. Tech. Rep.* 32068, March 1961, 79 pp.

The First Titan Hardened Facilities, by Marvin J. Kudroff, *Aerospace Engng.,* vol. 20, no. 6, June 1961, pp. 10–11,41–46.

Vertical Floating Launch of Rocket Vehicles, by J. E. Draim and C. E. Stalzer, *Aerospace Engng.,* vol. 20, no. 6, June 1961, pp. 12–13, 46–53.

Hawk Missile System Electronic Repair Shops, by W. J. Perreault, *Aerospace Engng.,* vol. 20, no. 6, June 1961, pp. 16–17, 66–70.

Range Safety—A Necessary Evil, by Adolf H. Knothe, *Aerospace Engng.,* vol. 20, no. 6, June 1961, pp. 20–21, 70–76.

Minuteman Missile Transportation System, by George T. Drakeley, *Aerospace Engng.,* vol. 20, no. 6, June 1961, pp. 22–23, 78–79.

Hawk Hydraulic and Electromechanical Field Maintenance Equipment, by Theodore Jacobsohn and Henry A. Matarazzo, *Aerospace Engng.,* vol. 20, no. 6, June 1961, pp. 36–37, 90–91.

A Direct Variational Method for the Calculation of Optimum Thrust Programs for Power-Limited Interplanetary Flight, by C. Saltzer and C. W. Fetheroff, *Astronautica Acta,* vol. 7, no. 1, 1961, pp. 8–20.

On a Problem of Minimum Weight Design, by Z. Mroz, *Quar. Appl. Math.,* vol. 19, no. 2, July 1961, pp. 127–136.

What an Astronaut Will See and Encounter When Flying at a Speed Approaching That of Light, by S. M. Rytov, ARS JOURNAL, vol. 31, May 1961, pp. 678–681.

Guidance and Control

Study of an Active Control System for a Spinning Body, by J. J. Adams, *NASA Tech. Note* D-905, June 1961, 30 pp.

Analytical Investigation of an Adaptive Flight-Control System Using a Sinusoidal Test Signal, by Jack E. Harris, *NASA Tech. Note* D-909, June 1961, 64 pp.

Study of a Solar Sensor for Use in Space-Vehicle Orientation Control Systems, by Paul R. Spencer, *NASA Tech. Note* D-885, June 1961, 39 pp.

Analytical Evaluation of a Method of Midcourse Guidance for Rendezvous with Earth Satellites, by John M. Eggleston and Robert S. Dunning, *NASA Tech. Note* D-83, June 1961, 61 pp.

Minimum-Time Steering Programs for Orbital Transfer with Low-Thrust Rockets, by C. R. Foulders, *Astronautica Acta,* vol. 7, no. 1, 1961, pp. 35–49.

Analysis of Error Progression in Terminal Guidance for Lunar Landing, by P. J. deFries, *J. Astron. Sci.,* vol. 8, no. 1, Spring 1961, pp. 18–27.

Approximate Computation of Optimal Control by the Direct Method, by N. N. Krasovskii, *PMM, J. Appl. Math. and Mech.,* vol. 24, no. 2, 1960, pp. 390–397.

A Limiting Process in the Solution of an Optimal Control Problem, F. M. Kirillova, *PMM, J. Appl. Math. and Mech.,* vol. 24, no. 2, 1960, pp. 398–405.

On the Stability of the Equilibrium Positions for Discontinuous Systems, by M. A. Aizerman and F. R. Gantmakher, *PMM, J. Appl. Math. and Mech.,* vol. 24, no. 2, 1960, pp. 406–421.

Optimization in Control Systems with Distributed Parameters, by A. G. Butkowski and A. Ja. Lerner, *Regelungstechnik,* vol. 9, no. 5, May 1961, pp. 185–188. (In German.)

Control Loops with Periodically Applied Instantaneous Value of Controlled Variable, by W. Peinke, *Regelungstechnik,* vol. 9, no. 5, May 1961, pp. 188–194. (In German.)

A Contribution to the Calculating of the Frequency Response of Relay Systems, by J. Tschauner, *Regelungstechnik,* vol. 9, no. 5, May 1961, pp. 200–203. (In German.)

Qualitative Investigation of the Trajectories of Difference Equations Near a Fixed Point, by A. M. Panov, ARS JOURNAL, vol. 31, May 1961, pp. 682–685.

Instrumentation and Communications

Proceedings of the 26th Shock and Vibration Symposium, Naval Training Center, San Diego, May 1958, Washington Secretary of Defense, 1958, 326 pp. Shock and Vibration Symposium, 26th, San Diego, May 1958, (Shock and Vibration Bull. 26, Pt. II, unclassified papers.) (ASTIA AD-20-0700.)

Temperature and Other Extraneous Effects on Piezo-electric Vibration Pickups, by T. A. Peris, pp. 90–95.

Special Considerations in Telemetering Missile Vibration, by M. R. Beckman, pp. 96–101.

A Piezoresistive Semiconductor Accelerometer, by R. G. Barclay, pp. 102–105.

Environmental Effects on Measuring Instruments Causing Errors in Results, by E. L. Kessler, pp. 106–113.

Effects of High-Intensity Acoustic Fields on Crystal Vibration Pickups, by W. Bradley Jr., pp. 114–119.

A Method for Measuring Impact Pressure at High Mach Number without Using a Surface Orifice, by T. R. Wrathall, pp. 147–170.

The Doppler Shift for Accelerating Transmitter, Reflectors and Receivers, by H. Lass and C. B. Solloway, *Calif. Inst. Tech., Jet Propulsion Lab. Tech. Rep.* 32-95, May 1961, 12 pp.

Coding Theory and its Applications to Communications Systems, by Leonard Baumert, Mahlon Esterling, Solomon W. Solomb and Andrew Viterbi, *Calif. Inst. Tech., Jet Propulsion Lab. Tech. Rep.* 32-67, March 1961, 84 pp.

Apparatus and Methods for Measurement of the Radio Transmissions of Artificial Satellites, (Deutsche Bundespost), by H. Fleischer, *Raketentechnik und Raumfahrtforschung,* vol. 5, no. 2, April–June 1961, pp. 56–62. (In German.)

Rapid Response Infrared Spectrometer, by A. Girard and M. Chatanier, *Recherche Aeron.,* no. 81, 1961, pp. 39–44. (In French.)

Ionization Gauge for Transient Gas Pressures, by J. D. Cobine and E. E. Burger, *Rev. Scien. Instr.* vol. 32, no. 6, June 1961, pp. 717–720.

Measurement of the Energy Losses in a Plasma by Means of Bolometers, by L. L. Gorelik and E. A. Lobikov, *Soviet Phys.: Tech. Phys.,* vol. 6, no. 1, July 1961, pp. 90–91.

Influence of Signal at Fluctuational Noise on a Frequency Discriminator, by A. Bol'shakov, *Telecommunications (Transl. of Electrosvyaz'),* no. 10, 1960, pp. 1057–1072.

Spectrum of a Signal Subject to Frequency Conversion, by B. A. Khanov, *Telecommunications (Transl. of Electrosvyaz'),* no. 10, 1960, pp. 1073–1083.

Variation of the Albedo of the First Artificial Earth Satellite as a Result of the Influence of External Factors, by I. M. Yatzunsky and O. V. Gurko, ARS JOURNAL, vol. 31, May 1961, pp. 698–699.

Relation of Frequency of Ultra Short Wave Field Amplitude Decay, Drift Speed of Inhomogeneities in the Troposphere, and Carrier Frequency, by A. A. Semensov and G. A. Karpeyev, ARS JOURNAL, vol. 31, May 1961, pp. 688–691.

An Artificial Comet as a Method for Optical Observation of a Cosmic Rocket, by I. S. Shklovskii, ARS JOURNAL, vol. 31, May 1961, pp. 699–705.

Atmospheric and Space Physics

Certain Computations of the Thermal History of the Moon, by B. Iu. Levin and S. V. Maeva, *Akademiia Nauk SSSR, Doklady,* vol. 133, no. 1, July 1960, pp. 92–94. (In Russian.)

The Origin of the Moon. I. Formation of a Swarm of Bodies Around the Earth, by E. L. Ruskol, *Soviet Astronomy AJ,* vol. 4, no. 4, Jan.–Feb. 1961, pp. 657–668.

Three Theories on the Craters of the Moon, by J. W. MacVey, *Air Force and Space Digest,* vol. 4, no. 3, March 1961, pp. 74–79.

The Origin of the Moon's Surface Features, by T. H. Morrow, *Kentucky Engineer,* vol. 23, no. 2, Jan. 1961, pp. 14–15, 54–55, 57.

The Explicit Expression for First-Order Secular Perturbations in Terms of the Orbit Elements, by M. S. Yarov-Yarovoi, *Soviet Astronomy AJ,* vol. 4, no. 4, Jan.–Feb. 1961, pp. 722–734.

Mirror and Azimuthal Drift Frequencies for Geomagnetically Trapped Particles, by D. A. Hamlin, R. Karplus, R. C. Vik and K. M. Watson, *J. Geophys. Res.,* vol. 66, no. 1, Jan. 1961, pp. 1–4.

Variation of the Equilibrium and Abundances within the Solar and Stellar Photospheres. V - the Abundance of Titanium, by R. Kandel, *Annales d'Astrophys.,* vol. 23, no. 6, 1960, pp. 995–1005. (In French.)

The Cosmic Ray Flare on November 12, 1960, and Solar Activity During the Period November 10–15, 1960 (Staff of the Ionosphere and Radio-Astronomy Sect. of the Netherlands Postal and Telecomm. Services), *Nature,* vol. 189, no. 4763, Feb. 11, 1961, pp. 438–440.

The Mechanism of Formation of Active Regions in the Presence of a Magnetic Field, by S. B. Pikel'ner, *Soviet Astronomy AJ,* vol. 4, no. 4, Jan.–Feb. 1961, pp. 590–594.

The Distance of the Solar Crescent at the Time of a Partial Eclipse of the Sun, by J. Meeus, *Ciel et Terre,* vol. 76, no. 11–12, Nov.–Dec. 1960, pp. 403–406. (In French.)

The Generation of Cosmic Rays in Flares, by A. B. Severnyi and V. P. Shabanskii, *Soviet Astronomy AJ*, vol. 4, no. 4, Jan.–Feb. 1961, pp. 583–589.

Spectra of a Bright Coronal Prominence Associated with a Class 3 Flare, by I. Elliott, M. A. Ellison and J. H. Reid, *Royal Astronom. Soc., Monthly Notices*, vol. 121, 1960, pp. 463–469.

Dynamic Spectra and Polarization of Small Bursts in Solar Radio Emission, by T. deGroot, *Astronom. Inst. of the Netherlands, Bull.*, vol. 15, no. 502, Dec. 30, 1960, pp. 229–236.

Influence of Augmentation of the Continuous Radioelectric Emission on the Emission of Type I Solar Burst, by A. Boischot and P. Simon, *Annales d'Astrophys.*, vol. 23, no. 6, 1960, pp. 1006–1009. (In French.)

Dynamic Spectra and Principal Characteristics of Short-Lived Bursts of Solar Radio Emission, by V. V. Vitkevich and M. V. Gorelova, *Soviet Astronomy AJ*, vol. 4, no. 4, Jan.–Feb. 1961, pp. 595–602.

Theory of X-Ray Emission of the Sun, by G. Elwert, *J. Geophys. Res.*, vol. 66, no. 2, Feb. 1961, pp. 391–401.

Solar Intensity and Limb Darkening Between 8.6 and 13 μ, by F. Saiedy, *Royal Astronom. Soc., Monthly Notices*, vol. 121, no. 5, 1960, pp. 483–495.

The Solar Red-Shift, by L. A. Higgs, *Royal Astronom. Soc., Monthly Notices*, vol. 121, no. 5, 1960, pp. 421–436.

An Estimate of Electron Densities in the Exosphere by Means of Nose Whistlers, by J. H. Pope, *J. Geophys. Res.*, vol. 66, no. 1, Jan. 1961, pp. 67–75.

The 5577 Å Airglow Emission Mechanism, by C. A. Barth and A. F. Hildebrandt, *J. Geophys. Res.*, vol. 66, no. 3, March 1961, pp. 985–986.

Excitation of Green and Red Lines in the Night Airglow, by S. N. Ghosh and A. Sharma, *J. Atmospheric and Terrestrial Phys.*, vol. 20, no. 2–3, March 1961, pp. 110–121.

The Red Line in the Night Sky at the Equator, by A. Delsemme and D. Delsemme, *Annales de geophys.*, vol. 16, no. 4, Oct.–Dec. 1960, pp. 507–524. (In French.)

Study of Variations of the Forbidden Oxygen Lines in the Nightglow, by M. C. Pande and S. S. Varma, *J. Atmospheric and Terrestrial Phys.*, vol. 20, no. 2–3, March 1961, pp. 195–199.

Seasonal Variation and Interpretation of the OH Rotational Temperature of the Airglow, by L. Wallace, *J. Atmospheric and Terrestrial Phys.*, vol. 20, no. 2–3, March 1961, pp. 85–93.

On Antimatter and Cosmology, by C. J. Kevane, *Science*, vol. 133, no. 3452, Feb. 24, 1961, pp. 580–581.

On the Construction of a Model Atmosphere, by A. D. Bolyunova, *Acad. Sci., USSR, Bull. Geophys. Series*, no. 10, March 1961, pp. 1022–1024. (In Russian.)

Temporal Variations of the Auroral Radio-Echo Activity in Subauroral Latitudes, by C. D. Watkins, *J. Atmospheric and Terrestrial Phys.*, vol. 20, no. 2–3, March 1961, pp. 140–148.

On the Excitation of the First Positive N_2 Bands in Aurorae, by A. Omholt, *J. Atmospheric and Terrestrial Phys.*, vol. 20, no. 2–3, March 1961, pp. 217–219.

The Stable Auroral Arc, by D. Barbier, *Annales de geophys.*, vol. 16, no. 4, Oct.–Dec. 1960, pp. 544–549. (In French.)

Correlation of Visual and Subvisual Auroras with Changes in the Outer Van Allen Radiation Zone, *Natl. Acad. Sci., IGY Bull.*, no. 45, March 1961, pp. 1–6.

Spectrographic Study of the Polar Aurorae During the IGY at College, Alaska, by L. Herman, *Annales de geophys.*, vol. 16, no. 4, Oct.–Dec. 1960, pp. 525–543. (In French.)

A Note on 106.1-MC Auroral Echoes Detected at Stanford Following the Solar Event of November 12, 1960, by R. L. Leadabrand, W. E. Jaye and R. B. Dyce, *J. Geophys. Res.*, vol. 66, no. 4, April 1961, pp. 1069–1072.

Auroral Radio-Echoes and Magnetic Disturbances, by C. D. Watkins, *J. Atmospheric and Terrestrial Phys.*, vol. 20, no. 2–3, March 1961, pp. 131–139.

The Relationship Between Unique Geomagnetic and Auroral Events, by Y. Sobouti, *J. Geophys. Res.*, vol. 66, no. 3, March 1961, pp. 725–737.

Comet Observations, by G. Van Biesbroeck, *Astronom. J.*, vol. 66, no. 2, March 1961, pp. 96–102.

Physical and Orbital Behavior of Comets, by R. E. Squires and D. B. Beard, *Astrophys. J.*, vol. 133, no. 2, March 1961, pp. 657–667.

The Motion of Comet Enckebacklund During 1898–1911 and a New Determination of the Mass of Mercury, by S. G. Makover and N. A. Bokhan, *Soviet Physics- Doklady*, vol. 5, no. 5, March–April 1961, pp. 923–925. (In Russian.)

Characteristics of Cosmic Radio Radiation, by H. C. Ko, *Physics Today*, vol. 14, no. 4, April 1961, pp. 35–39.

The High-Energy Cosmic-Ray Flare of May 4, 1960, I. High-Altitude Ionization and Counter Measurements, by J. R. Winckler, A. J. Masley and T. C. May, *J. Geophys. Res.*, vol. 66, no. 4, April 1961, pp. 1023–1027.

Space Radiation Levels, by J. E. Naugle, *Nucleonics*, vol. 19, no. 4, April 1961, pp. 89–91.

Theoretical Calculation of the Solar Diurnal Variation of the Cosmic Ray Intensity, by K. Nagashima, V. R. Potnis and M. A. Pomerantz, *Nuovo Cimento*, vol. 19, no. 2, Jan. 16, 1961, pp. 292–330.

Short-Term Variations in Meson and Nucleon Component of Cosmic Rays, by V. L. Patel and K. Maeda, *J. Geophys. Res.*, vol. 66, no. 4, April 1961, pp. 1286–1287.

The Interpretation of Cosmology, by B. Balazs and Gy Paal, *Nature*, vol. 189, no. 4769, March 25, 1961, pp. 992–993.

Analysis of the Unevenness of the Rotation of the Earth. I The Method and the Annual Term, by A. Danjou, *Comptes Rendus Hebdom. des Seances de l'Academie des Sciences*, vol. 252, no. 14, April 5, 1961, pp. 2039–2044. (In French.)

On the New System of Rotation of the Earth, Established in July 1959, by E. Schatzman, *Annales de geophys.*, vol. 16, no. 4, Oct.–Dec. 1960, pp. 495–506. (In French.)

Satellite Determination of Heavy Primary Cosmic-Ray Spectrum, M. A. Pomerantz, S. P. Agarwal, P. Schwed and H. Hanson, *Phys. Rev. Letters*, vol. 6, no. 7, April 1, 1961, pp. 362–364.

Theoretical World Curves of Maximum F2 Ionization—II, by J. E. C. Gliddon and P. C. Kendall, *J. Atmospheric and Terrestrial Phys.*, vol. 20, no. 2–3, March 1961, pp. 183–188.

The F-Layer at Sunrise, by H. Rishbeth and C. S. G. K. Setty, *J. Atmospheric and Terrestrial Phys.*, vol. 20, no. 4, April 5 1961, pp. 263–276.

Diffusion of Ionization in the Sunrise F-Layer, by H. Rishbeth, *J. Atmospheric and Terrestrial Phys.*, vol. 20, no. 4, April 1961, pp. 277–288.

On the Influence of Horizontal Motion of the Neutral Air on the Diffusion Equation of the F-Region, by J. P. Dougherty, *J. Atmospheric and Terrestrial Phys.*, vol. 20, no. 2–3, March 1961, pp. 167–176.

Solar Wind and the Gegenschein, by E. R. Harrison, *Nature*, vol. 189, no. 4769, March 25, 1961, pp. 993–994.

The Distribution of Hydrogen in the Telluric Hydrogen Corona, by F. S. Johnson, *Astrophys. J.*, vol. 133, no. 2, March 1961, pp. 701–705.

Streaming of Interstellar Hydrogen in the Vicinity of the Sun, by R. X. McGee, J. D. Murray and J. L. Pawsey, *Nature*, vol. 189, no. 4769, March 25, 1961, pp. 957–959.

Interplanetary Gas. III. A Hydrodynamic Model of the Corona, by J. W. Chamberlain, *Astrophys. J.*, vol. 133, no. 2, March 1961, pp. 675–687.

Interplanetary Gas. IV. Neutral Hydrogen in a Model Solar Corona, by J. C. Brandt, *Astrophys. J.*, vol. 133, no. 2, March 1961, pp. 688–700.

Ionosphere Electron Content and Its Variations Deduced from Satellite Observations, by K. C. Yeh and G. W. Swenson Jr., *J. Geophys. Res.*, vol. 66, no. 4, April 1961, pp. 1061–1067.

On the Large Scale Regions of Irregularities Producing Scintillation of Signals Transmitted from Earth Satellites, by J. Frihagen and J. Troim, *J. Atmospheric and Terrestrial Phys.*, vol. 20, no. 2–3, March 1961, pp. 215–216.

Observations of Jupiter at a Wave Length of 10 CM, by R. M. Slaanaker and J. W. Boland, *Astrophys. J.*, vol. 133, no. 2, March 1961, pp. 649–656.

Some Highlights of the 1960 Jupiter Apparition, by P. R. Glaser, *Strolling Astronomer*, vol. 15, no. 3–4, March–April 1961, pp. 37–46.

Low-Latitude and High-Latitude Geomagnetic Agitation, by E. R. Hope, *J. Geophys. Res.*, vol. 66, no. 3, March 1961, pp. 747–776.

Influence of Sunspots on Geomagnetic Disturbances, by F. Ward and R. Shapiro, *J. Geophys. Res.*, vol. 66, no. 3, March 1961, 739–746.

Solar-System Distortion of the Geomagnetic Field and Polar Electrojets, by J. W. Kern, *J. Geophys. Res.*, vol. 66, no. 4, April 1961, pp. 1290–1292.

Effect of the Magnetic Field in Ionospheric Backscatter, by E. E. Salpeter, *J. Geophys. Res.*, vol. 66, no. 3, March 1961, pp. 982–984.

A Theoretical Model of Electron Density Distribution Along a Geomagnetic Line of Force in the Exosphere, by R. L. Dowden, *J. Atmospheric and Terrestrial Phys.*, vol. 20, no. 2–3, March 1961, pp. 122–130.

Geomagnetic-Field Studies Using Earth Satellites, *Natl. Acad. Sci., IGY Bull.*, no. 46, April 1961, pp. 6–12.

The Simultaneity of Geomagnetic Sudden Impulses, by M. Yamamoto and H. Maeda, *J. Atmospheric and Terrestrial Phys.*, vol. 20, no. 2–3, March 1961, pp. 212–215.

Large-Scale Electron Bombardment of the Atmosphere at the Sudden Commencement of a Geomagnetic Storm, by R. R. Brown, T. R. Hartz, B. Landmark, H. Leinbach and J. Ortner, *J. Geophys. Res.*, vol. 66, no. 4, April 1961, pp. 1035–1041.

Second Report on Mars, 1960–1961, by E. E. Both, *Strolling Astronomer*, vol. 15, no. 3–4, March–April 1961, pp. 53–59.

Is Mars Covered with Ice? by W.

Dawydow, *Weltraumfahrt*, vol. 12, no. 1, Feb. 1961, pp. 14–15. (In German.)

Addendum: The Density and Mass Distribution of Meteoritic Bodies in the Neighborhood of the Earth's Orbit, by H. Brown, *J. Geophys. Res.*, vol. 66, no. 4, April 1961, pp. 1316–1317.

Lead and its Isotopic Composition in Iron Meteorites, by I. E. Starik, E. V. Sobotovich, G. P. Lovtsyus, M. M. Shats and A. V. Lovtsyus, *Soviet Physics-Doklady*, vol. 5, no. 5, March–April 1961, pp. 926–928.

The Record in the Meteorites 6. On the Chronology of the Early Solar System, by G. G. Goles and E. Anders, *J. Geophys. Res.*, vol. 66, no. 3, March 1961, pp. 889–898.

Interior of the Moon, by G. J. E. MacDonald, *Science*, vol. 133, no. 3458, April 1961, pp. 1045–1050.

Lunar Brightness Variations with Phase at 4.3-MM Wave Length, by R. J. Coates, *Astrophys. J.*, vol. 133, no. 2, March 1961, pp. 723–725.

Surface Exploration of the Moon, by P. A. E. Stewart, *Spaceflight*, vol. 3, no. 2, March 1961, pp. 34–48.

Some Properties of Radio Waves Reflected from the Moon and their Relation to the Lunar Surface, by T. Hagfors, *J. Geophys. Res.*, vol. 66, no. 3, March 1961, pp. 777–785.

The Glasgow Moonwatch System, by A. E. Roy, *Spaceflight*, vol. 3, no. 2, March 1961, pp. 53–56.

Moonwatch in the United Kingdom, by L. J. Carter, *Spaceflight*, vol. 3, no. 2, March 1961, pp. 49–52.

Report of Conference on Planetary Atmospheres Held by the Space Science Board, National Academy of Sciences, at Arcadia, California, June 24, 1960, by *Am. Geophys. Union, Trans.*, vol. 42, no. 1, March 1961, pp. 9–38.

The Temperatures of Planets, by C. H. Mayer, *Scien. Amer.*, vol. 204, no. 5, May 1961, pp. 58–65.

Absorption of Lyman-Alpha Radiation in the Earth's Atmosphere, by V. V. Katyushina, *Acad. Sci., USSR, Bull.* Geophys. Series, no. 10, March 1961, pp. 1035–1037. (In Russian.)

Cosmological Significance of Angular Measurements of Distant Radio Sources, by W. Davidson, *Nature*, vol. 139, no. 4769, March 25, 1961, pp. 991–992.

Daytime and Nighttime Atmospheric Properties Derived from Rocket and Satellite Observations, by H. K. Kallmann-Bijl, *J. Geophys. Res.*, vol. 66, no. 3, March 1961, pp. 786–795.

The High-Energy Cosmic-Ray Flare on May 4, 1960, 2. Emulsion Measurements, by S. Biswas and P. S. Freier, *J. Geophys. Res.*, vol. 66, no. 4, April 1961, pp. 1020–1033

The Time Variations of Solar Cosmic Rays During July 1959 at Minneapolis, by J. R. Winckler, P. D. Bhavsar and L. Peterson, *J. Geophys. Res.*, vol. 66, no. 4, April 1961, pp. 995–1022.

The Degree to Which Cosmic Dust Influences Certain Actinometric Characteristics of the Atmosphere, by A. A. Dmitriev, M. I. Mishina, A. E. Mikirov and E. P. Cherenkova, *Acad. Sci., USSR, Bull. Geophys. Series*, no. 10, March 1960. pp. 1015–1021. (In Russian.)

Spectral Observations of Solar Radio Burst, I. Receiving Equipment, by A. R. Thompson, *Astrophys. J.*, vol. 133, no. 2, March 1961, pp. 643–648.

The Size of the Solar System, by J. B. McGuire, E. R. Spangler, and L. Wong, *Scien. Amer.*, vol. 204, no. 4, April 1961, pp. 64–72.

The Topology of the Sun's Magnetic Field and the 22-Year Cycle, by H. W. Babcock, *Astrophys. J.*, vol. 133, no. 2, March 1961, pp. 572–587.

Secular Terms and Fluctuations in the Motions of the Sun and the Moon, by B. L. van der Waerden, *Astronom. J.*, vol. 66, no. 3, April 1961, pp. 138–147.

The Solar Lyman-Alpha Emission Line, by D. C. Morton and K. G. Widing, *Astrophys. J.*, vol. 133, no. 2, March 1961, pp. 596–605.

Solar Spectroscopy in the Far Ultraviolet, by R. Tousey, *Optical Soc. of America, J.*, vol. 51, no. 4, April 1961, pp. 384–396.

An Estimate of the Peak Sunspot Number in 1968, by C. M. Minnis, *J. Atmospheric and Terrestrial Phys.*, vol. 20, no. 2–3, March 1961, pp. 94–99.

Distinction Between the Electromagnetic Constants of Tektites and Libyan Desert Glass and their Effect on Lunar Surface Theory, by A. Olte and K. M. Siegel, *Astrophys. J.*, vol. 133, no. 2, March 1961, pp. 706–717.

A Subtropical Convergence Line of the South Pacific—A Case Study Using Meteorological Satellite Data, by L. F. Hubert, *J. Geophys. Res.*, vol. 66, no. 3, March 1961, pp. 797–812.

Rocket Astronomy and Astrophysics Research at the U. S. Naval Research Laboratory March 1959 to October 1960, *Natl. Acad. Sci., IGY Bull.*, no. 45, March 1961, pp. 10–16.

A Local Reduction of F-Region Ionization Due to Missile Transit, by H. G. Booker, *J. Geophys. Res.*, vol. 66, no. 4, April 1961, pp. 1073–1079.

Research on the Magnetic Conjugate Point of Poitiers Nocturnal Variation of the Dispersion of Whistlers, by R. Rivault and Y. Corcuff, *Annales de geophys.*, vol. 16, no. 4, Oct.–Dec. 1960, pp. 550–554. (In French.)

Three-Color Photometry of the Zodiacal Light, by A. W. Peterson, *Astrophys. J.*, vol. 133, no. 2, March 1961, pp. 668–674.

Polarization and Intensity Studies of the Eclipse of October 2, 1959, by E. P. Ney, W. F. Huch, P. J. Kellogg, W. Stein and F. Gillett, *Astrophys. J.*, vol. 133, no. 2, March 1961, pp. 616–642.

The Eclipses of the Sun from 1961 to 1970, by J. Meeus, *Ciel et terre*, vol. 77, no. 1, 2, 3, Jan.–March 1961, pp. 87–92. (In French.)

A Note on Solar Flare Cosmic Rays, by K. Maeda and V. L. Patel, *J. Geophys. Res.*, vol. 66, no. 4, April 1961, pp. 1288–1289.

Photometric Observations of 5577 Å and 6300 Å Airglow During the I.G.Y., by R. A. Duncan, *Australian J. Phys.*, vol. 13, no. 4, Dec. 1960, pp. 633–637.

Magnetic Effects of High-Altitude Nuclear Detonations, by A. M. van Wijk, *Geophys. Res.*, vol. 66, no. 2, Feb. 1961, pp. 647–648.

Relationships Between Auroras in the Northern and Southern Hemispheres, *Natl. Acad. Sci., IGY Bull.*, no. 44, Feb. 1961, pp. 7–14.

The Slant E_s Echo— A High-Frequency Auroral Echo, by H. F. Bates, *J. Geophys. Res.*, vol. 66, no. 2, Feb. 1961, pp. 447–454.

First Observations of the Spectra of the Aurorae by Means of Photoelectric Spectrometers, by O. L. Weissberg, *Acad. Sci., Bull. Geophys. Series*, no. 8, Feb. 1961, pp. 848–849.

A Note on the Dispersion of Daytime Auroral Ionization in Space, by R. L. Leadabrand, *J. Geophys. Res.*, vol. 66, no. 2, Feb. 1961, pp. 421–428.

Comparison of Parameters of Radio Reflections with Variations of Magnetic Field During Aurorae, by V. I. Pogorelov, *Acad. Sci., USSR Bull. Geophys. Series*, no. 7, Jan. 1961, pp. 720–722. (In Russian.)

The World-Wide IGY Cosmic Ray Program, by R. C. Haymes, *New York Acad. Sci., Trans.*, Series II, vol. 22, no. 2, Dec. 1960, pp. 96–103.

Some Geophysical Aspects of Cosmic Rays, by A. E. Sandstrom, *Amer. J. Phys.*, vol. 29, no. 3, March 1960, pp. 187–197.

Distribution of Micrometeorites Near the Earth, by A. R. Hibbs, *J. Geophys. Res.*, vol. 66, no. 2, Feb. 1961, pp. 371–377.

Lunar Tide in the F2 Layer of the Ionosphere Near the Geomagnetic Equator, by R. G. Rostogi, *Nature*, vol. 189, no. 4760, Jan. 21, 1961, pp. 214–215.

Hydromagnetic Waves and the Trapped Radiation. Part 1. Breakdown of the Adiabatic Invariance, by D. G. Wentzel, *J. Geophys. Res.*, vol. 66, no. 2, Feb. 1961, pp. 359–362.

Hydromagnetic Waves and the Trapped Radiation. Part 2. Displacement of the Mirror Point, by D. G. Wentzel, *J. Geophys. Res.*, vol. 66, no. 2, Feb. 1961, pp. 363–369.

The Total Electron Content of the Ionosphere During the Magnetic Disturbance of November 12–13, 1960, by G. N. Taylor, *Nature*, vol. 189, no. 4766, March 4, 1961, pp. 740–741.

Vertical Characteristics of Travelling Ionospheric Disturbances, by L. H. Heisler, *Australian J. Phys.*, vol. 13, no. 4, Dec. 1960, pp. 655–664.

Geomagnetic Micropulsations, by G. R. A. Ellis, *Australian J. Phys.*, vol. 13, no. 4, Dec. 1960, pp. 625–632.

VLF Phase Perturbation Associated with Meteor Shower Ionization, by C. J. Chilton, *J. Geophys. Res.*, vol. 66, no. 2, Feb. 1961, pp. 379–383.

Analysis of a Type of Rough-Trail Meteor Echo, by B. A. McIntosh, *Canadian J. Phys.*, vol. 39, no. 3, March 1961, pp. 437–444.

Atmospheric Phenomena at High Altitudes, by F. L. Bartman and L. M. Jones, *Michigan Univ., Dept. Aeron. and Astron. Engng. Final Rep.*, April 1955 to January 1960, April 1960, 7 pp.

Analysis and Standardization of Astrodynamic Constants, by M. W. Makemson, R. M. L. Baker Jr. and G. B. Westrom, *J. Astron. Sci.*, vol. 8, no. 1, Spring 1961, pp. 1–13.

Upper Atmosphere Density Determination, Based on Flight Observations of the Third Soviet Artificial Earth Satellite, by P. E. El'iasberg and V. D. Yastrebov, ARS JOURNAL, May 1961, vol. 31, no. 5, pp. 706–713.

Human Factors and Bio-Astronautics

A Fixed-Base-Simulator Study of the Ability of a Pilot to Establish Close Orbits Around the Moon, by M. J. Queijo and Donald R. Riley, *NASA Tech. Note* D-917, June 1961, 53 pp.

A Zoometric Study to Determine the Optimum Manual Performance Areas for the Chimpanzee, by Lester M. Zinser, William J. Farley and Frederick H. Rohles Jr., *Air Force Missile Dev. Center, Tech. Rep.* 61-15, May 1961, 25 pp.

Index of Papers Published in ARS JOURNAL

Volume 31—January through December 1961

AUTHORS

ABRAMSON, H. NORMAN, and RANSLEBEN, GUIDO E., JR.
Some Comparisons of Sloshing Behavior in Cylindrical Tanks With Flat and Conical Bottoms (TN).... 542

ABRAMSON, H. NORMAN, and RANSLEBEN, GUIDO E., JR.
Wall Pressure Distributions During Sloshing in Rigid Tanks (TN)..... 545

ABRAMSON, H. N., CHU, W. H., and RANSLEBEN, G. E.
Representation of Fuel Sloshing in Cylindrical Tanks by an Equivalent Mechanical Model..... 1697

ADAMS, K. A., and SEIZEW, M. R.
Notes on Heat Sink Analysis (TN)... 1595

AGALAROV, CH. S.
Transistor Phase-Sensitive Amplifier (RS) 1650

AGAMIROV, V. L., and VOL'MIR, A. S.
Behavior of Cylindrical Shells Under Dynamic Loading by Hydrostatic Pressure or by Axial Compression (RS) 98

AHLBERG, J. H., HAMILTON, S., MIGDAL, D., and NILSON, E. N.
Truncated Perfect Nozzles in Optimum Nozzle Design..... 614

AINTABLIAN, AVEDIS A.
Projected Path of the Longitudinal Axis of Earth-Stabilized Satellites..... 1522

AKASOFU, S.-I., and CHAPMAN, S.
New Theory of the Aurora Polaris.... 775

ALLEN, HARRISON, JR., *see* CIEPLUCH, CARL C.

ALTMAN, SAMUEL P., and PISTINER, JOSEF S.
Hodograph Analysis of the Orbital Transfer Problem for Coplanar Nonaligned Elliptical Orbits..... 1217

ALTMAN, S. P., and PISTINER, J. S.
Polar Hodograph for Ballistic Missile Trajectories (TN)..... 1592

ANDERSON, W. H., and CHAIKEN, R. F.
Detonability of Solid Composite Propellants 1379

ANTHONY, MAURICE L., and FOSDICK, GEORGE E.
Planar Motions About an Oblate Planet 1225

ANTHONY, MAURICE L., and PERKO, LAWRENCE M.
Vehicle Motion in the Equatorial Plane of a Planet: a Second Order Analysis in Ellipticity..... 1413

ARENDT, P. L.
Anomalies of the Geomagnetic Retardation of the Spin of Satellite Vanguard I (1958 Beta)..... 286

ARENS, M.
Staging of Cruising Vehicles (TN)... 824

ARTHUR, PAUL D.
Low Thrust Orbit Penalty (TN)..... 1273

ARTHUR, PAUL D., and LAHDE, REINHARD
Suggested Method for Small Changes in Nodal Longitude for Polar Orbits (TN) 1579

ASHER, GIFFORD W., *see* ASHLEY, HOLT

ASHLEY, HOLT, and ASHER, GIFFORD W.
The Virtual Mass of Clustered Boosters 757

AUFM KAMPE, H. J.
Evolution of Upper Air Meteorology (SA) 1047

AUGENSTEIN, B. W., *see* STEINBERG, M. A.

AUGUSTINE, N. R.
Approximate Method of Predicting Hypersonic Pressure Distribution on Nonlifting Near Power Law Bodies Using Similar Flow Theory Results (TN) 1778

BADE, W. L., MASON, E. A., and YAN, K. S.
Transport Properties of Dissociated Air 1151

Issue	Pages
January	1–169
February	170–285
March	286–468
April	469–587
May	588–750
June	751–862
July	863–1046
August	1047–1181
September	1182–1363
October	1364–1487
November	1488–1668
December	1669–1812

TN, TC, and SA indicate Technical Note, Technical Comment, and Survey Article, respectively. RS indicates supplement of translated Russian articles.

BADE, WILLIAM L., *see also* JOHN, RICHARD R.

BAILEY, W. S., NILSON, E. N., SERRA, R. A., and ZUPNIK, T. F.
Gas Particle Flow in an Axisymmetric Nozzle 793

BALDWIN, G. C.
Electrode Refraction and Ion Beam Collimation 627

BARRY, R. E., and BROTHERS, J. E.
Thrust Termination Transients in Solid Propellant Rockets (TC)..... 848

BASKIN, Y., and SCHELL, D. C.
Rocket Nozzles as Temperature Indicators (TN)..... 1275

BATRAKOV, V. V., *see* PROSKURIN, V. F.

BAUM, ERIC, *see* DENISON, M. RICHARD

BAXTER, A. N.
Consumable Case Solid Rocket (TN) 1790

BEARD, DAVID B.
Meteoritic Impact (TN) 87

BEAUPRE, MERLE A., *see* ETTELSON, BEN L.

BEECHER, NORMAN, and ROSENWEIG, RONALD
Ablation Mechanisms in Plastics With Inorganic Reinforcement..... 532

BEKLEMISHWA, L. A.
Some Properties of a System of Nearly Canonical Differential Equations (RS) 1614

BELL, JAMES E.
Effect of Glass Fiber Geometry on Composite Material Strength..... 1260

BERMAN, K., and CRIMP, F. W., JR.
Performance of Plug-Type Rocket Exhaust Nozzles..... 18

BERRY, EDWIN R.
Effect of Electrical Augmentation on Nuclear Rocket Flight Performance (TN) 92

BERTRAM, MITCHEL H., and HENDERSON, ARTHUR, JR.
Recent Hypersonic Studies of Wings and Bodies..... 1129

BIGELOW, EDWIN C., *see* JOHNSON, ROBERT H.

BILLHEIMER, J. S., *see* ROSSINI, R. A.

BIRD, J. F., *see* MCCLURE, F. T.

BIRNBAUM, S., *see* EZRA, A. A.

BJORK, R. L.
Meteroids vs. Space Vehicles..... 803

BLACK, HAROLD D., and STRUBLE, RAIMOND A.
Useful Correlations of Interior Ballistic Theory and Experimental Data (TN) 90

BLACKMAN, A. W., and KUEHL, D. K.
Use of Binary Light Metal Mixtures and Alloys as Additives for Solid Propellants 1265

BLAZEK, HENRY F., *see* SCHALKOWSKY, SAMUEL

BLECHER, SHELDON, and SALTON, GEORGE W.
Comparison of Some Approximate Methods for Calculating Re-Entry Oblatives of a Subliming Material (TN) 433

BLEEM, G. D., *see* WARFIELD, R. W.

BOLLINGER, LOREN E., and EDSE, RUDOLPH
Thermodynamic Calculations of Hydrogen-Oxygen Detonation Parameters for Various Initial Pressures..... 251

BOLLINGER, LOREN E., FONG, MICHAEL C., and EDSE, RUDOLPH
Experimental Measurements and Theoretical Analysis of Detonation Induction Distances..... 588

BONNELL, J. M., *see* OSBORN, J. R.

BORISKINA, N. G., and KORNILOV, I. I.
Investigation of the Iron-Chromium-Titanium Phase Diagram in a Region of Iron- and Chromium-Rich Alloys (RS) 961

BOURICIUS, G. M. B.
High Temperature Fission Chambers and Ionization Chambers (TN).... 1439

BRADFORD, R. E., *see* SATYENDRA, K. N.

BRAY, K. N. C.
Simplified Sudden-Freezing Analysis for Nonequilibrium Nozzle Flows (TN) 831

BREAKWELL, JOHN V., GILLESPIE, ROLLIN W., and ROSS, STANLEY
Researches in Interplanetary Transfer. 201

BREMNER, G. F., DUKOWICZ, J. K., and GLASS, I. I.
One-Dimensional Overtaking of a Rarefaction Wave by a Shock Wave (TN) 1455

BRERETON, ROY G.
Magnetic Compensation of Satellites (TC) 568

BRERETON, ROY G.
Meteoric Dust on the Surface of the Moon (TC)..... 850

BRESHEARS, ROBERT R., *see* WROBEL, J. RICHARD

BRO, P., and STEINBERG, S.
Entrance Effects in the High Temperature Heat Transfer From Dissociated Gases (TN)..... 375

BRO, P., and STEINBERG, S.
Surface Behavior of Boron Nitride in High Temperature Arc Heated Gases (TN) 1460

BRICK, DONALD B.
An Interesting Observation on the Point Release Into Orbit of a Number of Objects (TC)..... 270

BROCK, FRED H.
Estimation of Specific Heats at Normal Temperatures (TN)..... 265

BROTHERS, J. E., *see* BARRY, R. E.

BROWN, A. H., *see* FREDRICKSON, A. G.

BROWN, DUANE C.
Optical Refraction With Emphasis on Corrections for Points Outside the Atmosphere (TN)..... 549

BRUCE, RICHARD W.
Satellite Orbit Sustaining Techniques. 1237

BRUMFIELD, ROBERT C.
Influences of Solid Propellant Burning Rate Exponents on Performance of Engines With Large Back Pressure Variations (TN)..... 1769

BRUNNER, M. J.
Aerodynamic and Radical Heat Input in Space Vehicles Which Re-Enter at Satellite and Escape Velocity... 1102

BRYANT, R. A. A.
Adiabatic Nozzle Flows (TN)..... 828

BUNT, E. A., and OLSON, H. L.
"Pinhole Camera" for Determination of Plasma Arc Rotational Speed (TN) 826
BURROW, J. W.
Momentum Dumping Using Magnetic Torques (TN) 1776
BURRY, R. V., JORTNER, J., and ROSEMARY, J. K.
High Energy Propellant Comparisons for Space Missions 609
CAMERON, K. E., *see* WING, L. D.
CAMPBELL, GEORGE S.
Analysis of Large Amplitude Re-Entry Oscillations (TN) 1590
CAMPBELL, WILLIAM F., *see* STRUBLE, RAIMOND A.
CARSTENS, J. P., and EDELBAUM, T. N.
Optimum Maneuvers for Launching Satellites Into Circular Orbits of Arbitrary Radius and Inclination 943
CASSUTT, LEON H.
Experimental Investigation of Detonation in Unconfined Gaseous Hydrogen-Oxygen-Nitrogen Mixtures 1122
CHAHINE, M. T., *see* SCHAAF, S. A.
CHAIKEN, R. F., *see* ANDERSEN, W. H.
CHAMBERS, RANDALL M., and NELSON, JOHN G.
Pilot Performance Capabilities During Centrifuge Simulation of Boost and Re-Entry 1534
CHANG, A. L., *see* CHENG, K. H.
CHAPKIS, R. L., *see* WU, JAIN-MING
CHAPMAN, S., *see* AKASOFU, S.-I.
CHENG, K. H., and CHANG, A. L.
On "Numerical Comparison" Between Exact and Approximate Theories of Hypersonic Inviscid Flow Past Slender Blunt-Nosed Bodies (TN) 1024
CHOBOTOV, V.
Dynamic Response of Liquid Fueled Rocket Engines on Flexible Stands 1690
CHU, W. H., *see* ABRAMSON, H. N.
CHUDAKOV, A. E., *see* VERNOV, S. N.
CIEPLUCH, CARL C., ALLEN, HARRISON, JR., and FLETCHER, EDWARD A.
Ignition of Solid Propellant Rocket Motors by Injection of Hypergolic Fluids 514
CIEPLUCH, CARL C.
Effect of Rapid Pressure Decay on Solid Propellant Combustion (TN) 1584
CITRON, STEPHEN J.
Solutions for Satellite Motion Under Low Acceleration Using the Method of Variation of Parameters (TN) 1786
CLARK, FRANK L., *see* JOHNSON, CHARLES B.
COBB, EDGAR R.
Optimum Staging Technique to Maximize Payload Total Energy 342
COHEN, PAULA L., and DEUTSCH, ARMIN J.
Error Analysis for Doppler Determined Satellite Orbits of Other Planets (TN) 1767
COLE, ROY DALE, EKSTRAND, MARY ELIZABETH, and O'NEILL, MICHAEL R.
Attitude Control of Rotating Satellites (TN) 1446
COLEMAN, JOHN J.
Optimum Stage-Weight Distribution of Multistage Rockets (TN) 259
Technical Comment by RICHARD J. WEBER 849
COOK, MELVIN A., and UDY, LEX L.
Calibrations of the Card-Gap Test 52
COOPER, FRANK
Accuracy of Measuring Ballistic Trajectories 523
COOPER, WILFRED M., *see* ETTELSON, BEN L.
CORGAN, JOHN M., *see* WOLFE, ROBERT R.
COURTNEY, WELBY G.
Recent Advances in Condensation and Evaporation (SA) 751
COVERT, EUGENE E., and HALDEMAN, CHARLES W.
The Traveling-Wave Pump 1252
COWAN, W. B., *see* PURCELL, E. W.
CRIMP, F. W., JR., *see* BERMAN, K.
CROCCO, LUIGI, MONTI, RODOLFO, and GREY, JERRY
Verification of Nozzle Admittance Theory by Direct Measurement of the Admittance Parameter 771
CRUMP, J. E., and PRICE, E. W.
Effect of Acoustic Environment on the Burning Rate of Double-Base Solid Propellants (TN) 1026
DAIBER, JOHN W., *see* ESCHENROEDER, ALAN Q.
DAREVSKII, V. M.
Stability of a Console Cylindrical Shell Under Bending by a Transverse Force With Twisting and Internal Pressure (RS) 125
DEAN, L. E., and THOMPSON, W. R.
Ignition Characteristics of Metals and Alloys 917
DEMETRIADES, STERGE T., and ZIEMER RICHARD W.
Direct Thrust and Efficiency Measurements of a Continuous Plasma Accelerator (TN) 1278
DENISON, M. RICHARD, and BAUM, ERIC
A Simplified Model of Unstable Burning in Solid Propellants 1112
DE SOCIO, L., *see* POZZI, A.
DE SOTO, S., and WOLF, H.
Application of the Mangler Transformation in Boundary Layer Flow 553
DETRA, R. W., and HIDALGO, H.
Generalized Heat Transfer Formulas and Graphs for Nose Cone Re-Entry Into the Atmosphere 318
DEUTSCH, ARMIN J., *see* COHEN, PAULA L.
DEWEY, C. FORBES, JR.
Hot Wire Measurements in Low Reynolds Number Hypersonic Flows 1709
DIBELIUS, NORMAN R., *see* MULLANEY, GEORGE J.
DIX, G., *see* HAGIS, W.
DIXON, R. J., and PAGE, R. H.
Interdependence of Base Pressure and Base Heat Transfer (TN) 1785
DOBRY, T., *see* HAGIS, W.
DOEBLER, ROBERT L.
Simple Method for Estimating First-Stage Boost Thrust and Specific Impulse (TN) 550
DOLE, S. H.
Limits for Stable Near-Circular Planetary or Satellite Orbits in the Restricted Three-Body Problem 214
DOLGINOV, S. SH., ZHUZGOV, L. N., and SELIUTIN, V. A.
Magnetometric Equipment of the Third Soviet Artificial Earth Satellite (RS) 1329
DOLGINOV, S. SH., EROSHENKO, E. G., ZHUZGOV, L. N., PUSHKOV, N. V., and LYURMINA, L. O.
Magnetic Measurements on the Second Cosmic Rocket (RS) 1640
DOLLRIES, JOHN F., *see* SARNER, STANLEY F.
DOMINIK, J., *see* IVES, E. K.
DORRANCE, WILLIAM H.
Dissociation Effects Upon Compressible Turbulent Boundary Layer Skin Friction and Heat Transfer 61
DUBOSHIN, G. N.
Rotational Motion of Artificial Bodies in Space (RS) 1345
DUKE, W. M., GOLDBERG, E. A., and PFEFFER, I.
Error Analysis Considerations for a Satellite Rendezvous 505
DUKLER, A. E.
Comparison of Theoretical and Experimental Film Thickness (TN) 86
DUKOWICZ, J. K., *see* BREMNER, G. F.
DUPREE, M. L., *see* ZIEBLAND, H.
EDELBAUM, THEODORE N.
Propulsion Requirements for Controllable Satellites 1079
EDELBAUM, T. N., *see* CARSTENS, J. P.
EDSE, RUDOLPH, *see* BOLLINGER, LOREN E.
EDWARDS, D. K., and TELLEP, D. M.
Heat Transfer in Low Prandtl Number Flows With Variable Thermal Properties (TN) 652
EDWARDS, D. K., and NELSON, K. E.
Maximum Error in Total Emissivity Measurements Due to Non-Grayness of Samples (TN) 1021
EDWARDS, D. K.
Directional Solar Reflectances in the Space Vehicle Temperature Control Problem 1548
EGGERS, ALFRED J., JR., and WONG, THOMAS J.
Motion and Heating of Lifting Vehicles During Atmosphere Entry (SA) 1364
EHLERS, E. EDWARD
Missile Trajectories With Linear Time Variation of the Sine or Tangent of the Thrust Angle 631
EHLERS, F. E.
Linearized Magnetogasdynamic Channel Flow With Axial Symmetry 334
EKSTRAND, MARY ELIZABETH, *see* COLE, ROY DALE
EL'IASBERG, P. E., and YASTREBOV, V. D.
Upper Atmosphere Density Determination, Based on Flight Observations of the Third Soviet Artificial Earth Satellite (RS) 706
EMEL'IANOVA, Q. I., STRAKHOV, B. V., and LEBEDEV, V. P.
Density of Liquid Ozone (RS) 1350
ENGLISH, ROBERT E., and GUENTERT, DONALD
Segmenting of Radiators for Meteoroid Protection (TN) 1162
EROSHENKO, E. G., *see* DOLGINOV, S. SH.
ESCHENROEDER, ALAN Q., and DAIBER, JOHN W.
Nonequilibrium Ionization in a Shock Tunnel Flow (TN) 94
ETTELSON, BEN L., COOPER, WILFRED N., BEAUPRE, MERLE A., FREEDMAN, TOBY, THROSSELL, LAURANCE G., and PINC, BRUCE P.
Internal Animal Telemetry: a Feasibility Test Program 1190
EZRA, A. A., and BIRNBAUM, S.
Design Criteria for Space Vehicles to Resist Wind Induced Oscillations (TN) 1764
FAGG, LAWRENCE W., and FRIEDMAN, RAYMOND
Solid Propellant Source of Cesium Plasma (TN) 157
FAIRWEATHER, STEPHEN H., *see* HANSON, JAMES N.
FAULKNER, FRANK D.
Complete Elementary Solution to Some Optimum Trajectory Problems 33
FISCHELL, ROBERT E.
Magnetic Damping of the Angular Motions of Earth Satellites 1210
FLETCHER, EDWARD A., *see* CIEPLUCH, CARL C.
FLORENCE, DWIGHT E., *see* LEE, VERNON
FONG, MICHAEL C., *see* BOLLINGER, LOREN E.
FOSDICK, GEORGE E., *see* ANTHONY, MAURICE L.
FOSTER, E. L., *see* HUNTER, W. E.
FOX, J. L., *see* STEINBERG, M. A.
FOX, ROBERT H.
Powered Trajectory Studies for Low Thrust Space Vehicles 28
High Energy, Low Thrust Jupiter Missions (TN) 1018
FRANCIS, W. LEON
Irradiation of a Lunar Satellite (TN) 835
FREDRICKSON, A. G., BROWN, A. H., MILLER, R. L., and TSUCHIYA, H. M.
Optimum Conditions for Photosynthesis in Optically Dense Cultures of Algae 1429
FREEDMAN, TOBY, *see* ETTELSON, BEN L.
FRIEDLANDER, S. K.
Particle Impaction Efficiencies for Bodies in a Free Molecule Flow (TN) 96
FRIEDMAN, RAYMOND, *see* FAGG, LAWRENCE W.
GALLANT, R. P., *see* SMEDAL, H. A.
GAWLOWICZ, H. F., *see* HALL, N. S.
GAYLORD, ROBERT S.
Differentiating Gas Jet for Space Attitude Control (TN) 75
GEIGER, R. E., *see* WARREN, W. R.
GILLEO, M. A., *and* KASH, S. W.
Propulsion by Composite Beams of Negative and Positive Ions 621
GILLESPIE, ROLLIN W., *see* BREAKWELL, JOHN V.
GLASS, I. I., HEUCHROTH, L. E., and MOLDER, S.
One-Dimensional Overtaking of a Shock Wave by a Rarefaction Wave (TN) 1453
GLASS, I. I., *see also* BREMNER, G. F.
GLOERSEN, P., GOROWITZ, B., and PALM, W.
Experimental Performance of a Pulsed Gas Entry Coaxial Plasma Accelerator (TN) 1158
GOLDBERG, E. A., *see* DUKE, W. M.
GOL'DENBERG, S. A.
Ignition in a Flow by Hot Bodies (RS) 691
GOLDSTEIN, R. E., *see* MARCINEK, J. J.
GOODMAN, B. D.
Psychological and Social Problems of Man in Space—a Literature Survey (SA) 863

GORDON, L. J.
Calculation of C^* for High Dissociated Propellant Combustion Products (TN) 374
GOROWITZ, B., *see* GLOERSEN, P.
GOURDINE, MEREDITH C.
Recent Advances in Magnetohydrodynamic Propulsion (SA) 1670
GRASSHOFF, L. H.
Eddy Current Torque Compensation in a Spin Stabilized Earth Satellite ... 290
GRASSHOFF, L. H.
A Method for Controlling the Attitude of a Spin-Stabilized Satellite 646
GRANET, IRVING, and MCILROY, WILLIAM
Optimum Radiant Straight Fin With Exponential Sides (TN) 80
GREENBERG, ROBERT A., and TRAUGOTT, STEPHEN C.
Shock Wave Asymmetry for Cones and Sphere Cones at Angle of Attack (TN) 821
GREER, H.
Rapid Method for Plug Nozzle Design (TN) 560
Technical Comment by M. H. SEIDMAN 1292
GRENLESKI, S. E., JR., *see* WALKER, R. E.
GREY, JERRY, *see* CROCCO, LUIGI
GROSH, R. J., *see* VISKANTA, R.
GRUBB, W. T., JR., *see* LIEBHAFSKY, H. A.
GUENTERT, DONALD, *see* ENGLISH, ROBERT E.
GUINN, GERALD R.
Aerodynamic Heating of Plane Bodies of Low Thermal Diffusivity (TN) .. 158
GUMAN, WILLIAM J.
Efficiency Calculations From Thrust Measurements (TC) 676
GUMAN, WILLIAM J.
Measurement of Small Discharge Rate of an Intermittent Exhaust Jet (TN) 1583
GURKO, O. V., *see* YATZUNSKY, I. M.
GURLEY, JOSEPH G.
Propagation of Errors in a Schuler-Type Inertial Navigation System (TC) 269
GUSEV, V. D.
Correlation Method for Analysis of Large Heterogeneities of the Ionosphere (RS) 1323
HAGIS, W., DOBRY, T., and DIX, G.
Nuclear Safety Analysis of Snap III for Space Missions 1744
HAIRE, ALAN M., *see* STEPHENS, CHARLES W.
HALDEMAN, CHARLES W., *see* COVERT, EUGENE E.
HALL, N. S., GAWLOWICZ, H. F., and WALLMAN, E. J.
Choice of Unperturbed Orbit in the Use of Encke's Method for the Effects of Oblateness and Drag (TN) 1436
HAMILTON, S., *see* AHLBERG, J. H.
HANEL, RUDOLF A.
Low Resolution Unchopped Radiometer for Satellites 246
HANSON, JAMES N., and FAIRWEATHER, STEPHEN H.
Nodal Rotation for Continuous Exposure of an Earth Satellite to the Sun 640
HANSON, JAMES N.
Thrust Vector Determination of an Ion Engine by Differential Comparison With an Unthrusted Orbit (TN) .. 1787
HART, R. W., *see* MCCLURE, F. T.
HARTNETT, J. P., *see* KOH, J. C. Y.
HATCH, L. P., REGAN, W. H., and POWELL, J. R.
Fluidized Solids as a Nuclear Fuel for Rocket Propulsion (TN) 547
HENDERSON, ARTHUR J., *see* BERTRAM, MITCHELL H.
HERING, KARL W., and HUFNAGEL, ROBERT E.
Inertial Sphere System for Complete Attitude Control of Earth Satellites 1074
HERSCH, MARTIN
Experimental Method of Measuring Intensity of Turbulence in a Rocket Chamber 39
HERTZBERG, A., *see* WEATHERSTON, R. C.
HESS, T. E.
Stability of Orthotropic Cylindrical Shells Under Combined Loading ... 237
HEUCKROTH, L. E., *see* GLASS, I. I.
HIBBARD, ROBERT R.
Attitude Stabilization Using Focused Radiation Pressure (TN) 844
HILDALGO, H., *see* DETRA, R. W.
HORTON, M. D.
One-Dimensional Solid Propellant Oscillatory Burner (TN) 1596
HSU, CHENG-TING
Nonuniform Deceleration of a Slender Cone in Supersonic, Transonic and Subsonic Flight (TN) 1289
HUFNAGEL, ROBERT E., *see* HERING, KARL W.
HULTQUIST, PAUL F.
Gravitational Torque Impulse on a Stabilized Satellite 1506
HUNTER, W. E., FOSTER, E. T., and MANGUM, G. F.
Binder Crystallization in Polysulfide Propellant (TN) 1573
INGEBO, ROBERT D.
Size Distribution and Velocity of Ethanol Drops in a Rocket Combustor Burning Ethanol and Liquid Oxygen 540
IVES, E. K., DOMINIK, J., and PROELL, W. A.
Heat Sink Strand Bomb for Determining Ballistic Properties of Solid Propellants 783
JACK, JOHN R.
Theoretical Performance of Propellants Suitable for Electrothermal Jet Engines 1685
JACOBS, EDGAR M., MORGENTHALER, GEORGE W., and SEBASTIAN, ROBERT A.
Probability of Satellite Interception by an Air Launched Preguided Missile. 352
JAFFE, IRVING, *see* PRICE, DONNA
JOHN, RICHARD R., and BADE, WILLIAM L.
Recent Advances in Electric Arc Plasma Generation Technology (SA) 4
JOHNSON, CHARLES B., and CLARK, FRANK L.
Measurement of Heat Transfer in a Graphite Rod Heat Exchanger (TN) 1458
JOHNSON, ROBERT H.
Hypersonic Viscous Effects in Wind Tunnels (TN) 1022
JOHNSON, ROBERT H., and BIGELOW, ELWIN C.
Streamlines in Boundary Layers on Flat and Concave Surfaces in Hypersonic Flow (TN) 1452
JORTNER, J., *see* BURRY, R. V.
JUROVICS, STEPHEN
Optimum Steering Program for the Entry of a Multistage Vehicle Into a Circular Orbit 518
KAEGI, E. M., *see* WARREN, W. R.
KALLIS, STEPHEN A., JR.
Proposal for a Simple Visual Tracking Arrangement for Space Probes (TC) 1598
KALT, SHERWIN
Thrust Termination in Solid Rocket Motors—Evaluation of Ballistic Test Data (TN) 84
KAMM, L. J.
Magnetorquer—a Satellite Orientation Device 813
KAPLAN, C. J.
Selection of a Pressurization System for a Storable Liquid Propellant Rocket Engine 786
KARIMOV, M. G., and SHILOVA, N. S.
Connection Between the Motion of Matter in the Corona and the Prominences (RS) 970
KARPEYEV, G. A., *see* SEMENOV, A. A.
KARRENBERG, HANS K., and ROBERSON, ROBERT E.
Celestial Rate Sensing (TN) 440
KASH, C. W., *see* GILLEO, M. A., and STARR, W. L.
KEEGAN, THOMAS J.
Winds and Circulations in the Mesosphere 1060
KELLER, J. A., and RYAN, N. W.
Measurement of Heat Flux From Initiators for Solid Propellants 1375
KENNET, H., and STRACK, S. L.
Stagnation Point Radiative Transfer (TN) 370
KERREBROCK, J. L., *see* ROSENZWEIG, M. L.
KEYES, J. J., JR.
Experimental Study of Flow and Separation in Vortex Tubes With Application to Gaseous Fission Heating .. 1204
KNOX, BRUCE E., *see* PALMER, HOWARD B.
KOH, J. C. Y., and HARTNETT, J. P.
Measured Pressure Distribution and Local Heat Transfer Rates for Flow Over Concave Hemispheres 71
KORNILOV, I. I., and POLIAKOVA, R. S.
Melting Diagram for the Titanium-Vanadium-Molybdenum Ternary System (RS) 694
KORNILOV, I. I., *see also* BORISKINA, N. G.
KOROBEINIKOV, V. P., *see* KVASHINA, S. S.
KORP, E. E., *see* MOE, M. M.
KOWALEWICZ, ANDRZEJ
Stability Problem of the Flow With Combustion in Variable Area Duct (TN) 558
KOZAI, YOSHIHIDE
Comments on Use of Osculating Ellipse in Analysis of Near Circular Orbits (TC) 676
KUEHL, D. K., *see* BLACKMAN, A. W.
KULAKOWSKI, L. J., *see* STANCIL, R. T.
KUMAR, SUDHIR, *see* MURRAY, JAMES J.
KVASHINA S. S., and KOROBEINIKOV, V. P.
Solution of Several Problems of Air Motion in the Presence of Dissociation and Ionization (RS) 997
LADIKOV, YU. P.
Magneto-Vortical Rings (RS) 1635
LAHDE, REINHARD, *see* ARTHUR, PAUL D.
LANDBERG, STANLEY H.
Densities of the Upper Atmosphere Derived From Discoverer Satellites (TN) 155
LANDEL, ROBERT F., and SMITH, THOR L.
Viscoelastic Properties of Rubberlike Composite Propellants and Filled Elastomers 599
LARISH, E.
Aerodynamic Interaction in a Free Molecular Flow (RS) 1630
LASS, H., and LORELL, J.
Low Acceleration Takeoff From a Satellite Orbit 24
LASS, HARRY, and SOLLOWAY, CARLETON B.
Motion of a Satellite of the Moon 220
LAWDEN, D. F.
Optimal Powered Arcs in an Inverse Square Field (TN) 566
LEACH, RICHARD
Nonmatrix Formulation of an Eulerian Angle Vector Transformation (TN) 830
LEBEDOV, V. P., *see* EMEL'IONOVA, T. I.
LEE, VERNON, and FLORENCE, DWIGHT E.
Minimum Time Ballistic Interplanetary Trajectories (TN) 435
LEN'KO, O. N.
Stability of an Orthotropic Cylindrical Shell With Axial Load and External Pressure (RS) 1315
LEVY, RICHARD H.
Radiation Shielding of Space Vehicles by Means of Superconducting Coils (TN) 1568
LEWELLEN, W. S., *see* ROSENZWEIG, M. L.
LI, TING Y.
Recent Advances in Nonequilibrium Dissociating Gasdynamics (SA) 170
LIAKHOV, G. M., and POLIAKOVA, N. I.
Propagation and Interaction of Compression and Rarefaction Waves in Elastic-Plastic Media (RS) 1644
LIBBY, PAUL A.
Preliminary Analysis of the Capabilities of a Composite Slab for an Advanced Heat Sink Design (TN) 658
LIEBHAFSKY, H. A., and GRUBB, W. T., JR.
The Fuel Cell in Space (SA) 1183
LINHART, HANS D., and SILVERN, DAVID H.
Analysis of Partial Admission Axial Impulse Turbines 297
LIPPITT, MAXWELL W., JR., *see* SHARBAUGH, A. HARRY
LOGACHEV, YU. I., *see* VERNOV, S. N.
LORELL, J., *see* LASS, H.
LOWE, ROBERT E., *see* PONSFORD, HENRY T.
LUDERS, R. DAVID
Satellite Networks for Continuous Zonal Coverage 179
MA, CHUK-CHING
Advanced Uncooled Nozzle for Solid Propellant Rocket (TN) 368
MADEWELL, JAMES F., *see* PONSFORD, HENRY T.

MAGER, ARTUR
Approximate Solution of Isentropic Swirling Flow Through a Nozzle.. 1140
MAGER, A., *see* Wu, JAIN-MING
MALAKOFF, JAMES L., and MUELLER, WILLIAM H.
Water Impact of Manned Spacecraft.. 1751
MALDER S., *see* GLASS, I. I.
MANGUM, G. F., *see* HUNTER, W. E.
MARCINEK, J. J., and GOLDSTEIN, R. E.
Impulse Programming for Turbine Boost (TN)..... 1589
MARGERUM, DAVID, *see* PITTS, J. N., JR.
MARKHASHOV, L. M.
Stability of Motion of a Gyroscope With a Cardan Suspension (RS)... 958
MARLOW, RAYMOND
Peltier Cooling of Electrical Components in Telemetering Packages (TN)..... 263
MARMO, F. F., *see* PRESSMAN, J.
MASLACH, G. J., *see* SCHAAF, S. A.
MASON, E. A., *see* BADE, W. L.
MAYER, ERNEST
Analysis of Convective Heat Transfer in Rocket Nozzles..... 911
MAYER, ERNEST
Theory of Liquid Atomization in High Velocity Gas Streams (TN)..... 1783
MCCLURE, F. T., HART, R. W., and BIRD, J. F.
Heat Release Rate, Temperature and Pressure in Solid Rocket Instability (TN)..... 367
MCGRATH, T. F., *see* SHINAULT, L. H.
MCILROY, WILLIAM, *see* GRANET, IRVING
MCKEE, WILLIAM E., *see* PITTS, J. N., JR.
MCMURRAY, L. R.
Alignment of an Inertial Autonavigator 356
MCRUER, D. T., and STAPLEFORD, R. L.
Power and Energy Requirements for a Fixed-Axis Inertia Wheel Attitude Control System (TN)..... 665
MELBOURNE, WILLIAM G.
Three-Dimensional Optimum Thrust Trajectories for Power Limited Propulsion Systems..... 1723
MEYER, A. P., *see* PAGE, R. H.
MIGDAL, D., *see* AHLBERG, J. H.
MILLER, B. P.
Approximate Velocity, Position and Time Relationship for Ballistic Re-Entry (TN)..... 437
MILLER, R. L., *see* FREDRISKSON, A. G.
MOE, M. M., and KARP, E. E.
Effect of Earth's Oblateness on the Anomalistic Period of a Satellite (TN)..... 1462
MOISEYEV, N. D.
Interpolation Averaged Variants of the Canonical Problem of Celestial Mechanics (RS)..... 387
MOISEYEV, N. D.
Complete Averaging of Canonical Problem of Celestial Mechanics With Several Intermediate Elements (RS)..... 390
MOISEYEV, N. D.
Averaged Variants of a Semirestricted Planar Problem of Three Bodies (RS)..... 393
MONTI, RODOLFO, *see* CROCCO, LUIGI
MOORE, JEFFREY A., and ZLOTNICK, MARTIN
Combustion of Carbon in an Air Stream..... 1388
MORAN, JOHN P.
Effects of Plane Liberations on the Orbital Motion of a Dumbbell Satellite..... 1089
MORGAN, T. E., *see* WELCH, B. E., JR.
MORGENTHALER, GEORGE W., *see* JACOBS, EDGAR M.
MORRIS, J. A.
Summary of Solid Propellant Residual Thrust Studies (TN)..... 1283
MORTH, RAYMOND, and SPEYER, JASON L.
Divergence From Equilibrium Glide Path at Supersatellite Velocities (TN)..... 448
MOSKOWITZ, SAMUEL E., and TING, L.
An Approach to Problem of Optimum Rocket Trajectories (TN)..... 551
MOULIC, E. S., *see* SCHAAF, S. A.
MUELLER, WILLIAM H., *see* MALAKOFF, JAMES L.
MULLANEY, G. J., and DIBELIUS, N. R.
Small MHD Power Generator Using Combination Gases as an Energy Source (TN)..... 555
MULLANEY, GEORGE J., and DIBELIUS, NORMAN R.
Determination of Electron Density and Mobility in Slightly Ionized Cesium (TN)..... 1575
MURRAY, BRUCE C.
The Artificial Earth Satellite—a New Geodetic Tool..... 924
MURRAY, JAMES J., and KUMAR, SUDHIR
Vacuum-Air Missile Boost (TN)..... 1443
MYERS, G. H., and THOMPSON, T. H.
Guidance of Tiros I..... 636
NAGAMATSU, H. T., SHEER, R. E., JR., and SCHMID, J. R.
High Temperature Rarefied Hypersonic Flow Over a Flat Plate..... 902
NAZAROVA, T. N.
Results of Investigation of the Meteoric Matter by Means of Instruments Installed on Cosmic Rockets (RS)..... 713
NAZAROVA, T. N.
Investigation of Meteoric Particles by the Third Soviet Satellite (RS).... 1341
NEICE, S. E., and RUTOWSKI, R. W.
Calibration of Hypersonic High Temperature Wind Tunnels (TN)..... 372
NELSON, JOHN G., *see* CHAMBERS, RANDALL M.
NELSON, K. E., *see* EDWARDS, D. K.
NEWTON, ROBERT R.
Variables That are Determinate for Any Orbit..... 364
NICHOLS, M. H., *see* SCHAEFER, E. J.
NIDEY, RUSSEL A.
Unique Cross-Spin Control Concept for Fixed Fin Sounding Rockets (TN) 824
NIDEY, RUSSEL
Secular Gravitational Torque on a Satellite in a Circular Orbit (TN).. 1032
NIKOLAEV, A. G., *see* VERNOV, S. N.
NILSON, E. N., *see* AHLBERG, J. H., and BAILEY, W. S.
NOVOSELOV, V. S.
Fall of a Spherical Drop in the Presence of Evaporation or Condensation of Vapors at Its Surface (RS).... 686
OLIVER, R. C., and STEPHENSON, S. E.
γ Large or Small (TC)..... 1468
OLSON, H. L., *see* BUNT, E. A.
O'NEILL, MICHAEL R., *see* COLE, ROY DALE
ORMSBY, RALPH D., and SMITH, MAHLON C.
Capabilities and Limitations of Reaction Spheres for Attitude Control 808
ORR, J. A.
Determination of Optimum Insulation Weight (TC)..... 269
OSBORN, J. R., and BONNELL, J. M.
Importance of Combustion Chamber Geometry in High Frequency Oscillations in Rocket Motors..... 482
OSBORN, J. R., and BONNELL, J. M.
Effect of Fuel Composition on High Frequency Oscillations in Rocket Motors Burning Premixed Hydrocarbon Gases and Air..... 1397
PAGE, R. H., and MEYER, A. P.
Hydraulic Analog Investigation of a Plug Nozzle (TN)..... 447
PAGE, R. H., *see also* DIXON, R. J.
PALM, W., *see* GLOERSEN, P.
PALMER, HOWARD B., and KNOX, BRUCE E.
Contact Surface Tailoring in a Chemical Shock Tube (TN)..... 826
PALMORE, JULIAN I., III
Lunar Impact Probe..... 1066
PANOV, A. M.
Qualitative Investigation of the Trajectories of Difference Equations Near a Fixed Point (RS)..... 682
PATCH, RICHARD W.
Prediction of Composition Limits for Detonation of Hydrogen-Oxygen-Diluent Mixtures..... 46
PATTERSON, G. B.
Graphical Method for Prediction of Time in Sunlight for a Circular Orbit (TN)..... 441
PATTERSON, PAUL L., *see* RAGSAC, ROBERT V.
PAUSON, WERNER M.
Time Relationships for Interplanetary Trajectories (TN)..... 1281
PENG, T. C., *see* VIEGAS, JOHN R.
PERELMAN, I. I.
Sequential Regression Analysis and Its Application to Some Problems of Automatic Control (RS)..... 1619
PERKO, LAWRENCE M., *see* ANTHONY, MAURICE L.
PETROV, E. A., and TALANTOV, A. V.
Investigation of Basic Characteristics of Combustion of a Homogeneous Mixture of an Open Turbulent Stream (RS)..... 408
PETTY, C. M.
Interplanetary Maneuvers Using Radial Thrust..... 1233
PFEFFER, I., *see* DUKE, W. M.
PFEIFFER, CARL G.
Rudimentary Launch Guidance Methods for Deep Space Missions (TN) 1155
PHILLIPS, RICHARD L.
Effect of Magnetic Drag on Re-Entry Body Heating (TN)..... 672
PIERCE, J. R.
Note on "Pierce Gun Design for an Accelerate-Decelerate Ionic Thrust Device" (TC)..... 368
PINC, BRUCE P., *see* ETTELSON, BEN L.
PISTINER, J. S., *see* ALTMAN, S. P.
PITTS, J. N., JR., MARGERUM, J. DAVID, and MCKEE, WILLIAM E.
Photochemistry and Space Power Generation..... 890
POLIAKOVA, N. I., *see* LEAKHOV, G. M.
POLIAKOVA, R. S., *see* KORNILOV, I. I.
PONSFORD, HENRY T., WOOD, ROBERT M., LOWE, ROBERT E., and MADEWELL, JAMES F.
Thermostructural Design—Entry Vehicles for Mars and Venus..... 474
POSEL, K.
Recording of Pressure Step Functions of Low Amplitude by Means of Composite-Dielectric Capacitance Transducer Placed in Parallel-T Network..... 1242
POTTER, NORMAN S.
Controlled Rendezvous of Orbiting Space Stations..... 1096
POWELL, J. R., *see* HATCH, L. P.
POZZI, A., and DESOCIO, L.
Some Remarks on Solar Sail (TN).. 1164
PRECKEL, R. F.
Plateau Ballistics in Nitrocellulose Propellants (TN)..... 1286
PRESSMAN, J., and MARMO, F. F.
Measurement of Air Density at 430 Km by Sodium Resonance Cloud Techniques (TN)..... 819
PRIAPI, J. J.
Advanced Ignition System for Solid Propellant Rocket Motors (TN)... 1029
PRICE, DONNA, and JAFFE, IRVING
Large Scale Gap Test: Interpretation of Results for Propellants..... 595
PRICE, E. W., *see* CRUMP, J. E.
PROBSTEIN, RONALD F.
Shock Wave and Flow Field Development in Hypersonic Re-Entry..... 185
PROELL, W. A., *see* IVES, E. K.
PROKOF'EV, V. A.
Propagation of Forced Plane Compression Waves of Small Amplitude in a Viscous Gas When Radiation Is Taken Into Account (RS)..... 988
PROSKURIN, V. F.. and BATRAKOV, V. V.
Perturbations in the Motion of Artificial Satellites Due to the Oblateness of the Earth (RS)..... 117
PURCELL, E. W., and COWAN, W. B.
Relating Geodetic Latitude and Altitude to Geocentric Latitude and Radius Vector..... 932
PUSHKOV, N. V., *see* DOLGINOV, S. SH.
PUTNAM, ABBOTT
Integratable Form of Droplet Drag Coefficient (TC)..... 1467
RADCLIFFE, WILLIAM F., and TRANSUE, JOHN R.
Problems Associated With Multiple Engine Starts in Spacecraft..... 1408
RAGSAC, ROBERT V., and PATTERSON, PAUL L.
Multistage Rocket Optimization (TN) 450
RAGUSA, DOMENICO
Radiated Power from 2-In. Sphere of High Temperature Air At Pressures to 50 Atm (TN)..... 445
RANSLEBEN, GUIDO E., JR., *see* ABRAMSON, H. NORMAN
RANSLEBEN, G. E., *see* ABRAMSON, H. N.
RAO, G. V. R.
Recent Developments in Rocket Nozzle Configurations (SA)..... 1488
RAUSHENBACH, B. V., and TOKAR', E. N.
Some Guidance Problems in Interplanetary Space (RS)..... 1624

REEVES, BARRY
Similar Solutions of the Free Convection Boundary Layer Equations for an Electrically Conducting Fluid (TN) 557
REGAN, W. H., *see* HATCH, L. P.
RICHARDS, PAUL B.
Preliminary Orbit Determination of a Nontransmitting Satellite Using the DOPLOC Tracking System..... 1729
RIDER, L.
Characteristic Velocity Requirements for Impulsive Thrust Transfers Between Non Co-Planar Circular Orbits 345
Class of Minimum Altitude Variation Orbits About an Oblate Earth (TN) 1580
ROBERSON, ROBERT E.
Alternate Form of a Result by Nidey (TC) 1292
Gravity Gradient Determination of the Vertical 1509
See also KARRENBERG, HANS K.
ROSA, RICHARD J.
Propulsion System Using a Cavity Reactor and Magnetohydrodynamic Generator 884
ROSEMARY, J. K., *see* BURRY, R. V.
ROSENZWEIG, M. L., LEWELLEN, W. S., and KERREBROCK, J. L.
Feasibility of Turbulent Vortex Containment in the Gaseous Fission Rocket 873
ROSENWEIG, RONALD, *see* BEECHER, NORMAN
ROSNER, DANIEL E.
Application of Heat Flux Potentials to the Calculation of Convective Heat Transfer in Chemically Reacting Gases (TN)..... 816
Surface Temperatures of High Speed, Radiation Cooled Bodies in Dissociating Atmospheres (TN)..... 1013
Correction 1469
ROSS, STANLEY, *see* BREAKWELL, JOHN V.
ROSSINI, R. A., BILLHEIMER, J. S., and THREEWIT, T. R.
Configuration Efficiency: a New Measure of Ballistic Quality for a Grain Design (TN)..... 1761
ROWELL, L. N., and SMITH, M. C.
Effect of Geometrical Libration on the Damped Motion of an Earth Satellite 361
RUBIN, S.
Method for Determining Scale Heights in the Atmosphere (TN)..... 1456
RUDINGER, GEORGE
Interaction of Centered Expansion Waves (TN)..... 1587
RUTOWSKI, R. W., *see* NEICE, S. W.
RYAN, N. W., *see* KELLER, J. A.
RYTOV, S. M.
What an Astronaut Will See and Encounter When Flying at a Speed Approaching That of Light (RS).. 678
Technical Comment by D. T. SWIFT-HOOK 1350
SAMSON, A. M.
Luminosity of Matter Confined Within a Finite Volume and Having Arbitrary Absorption and Emission Bands (RS) 1632
SANDERS, R. W.
Limitations on Space Vehicles Imposed on Communications Requirements (TN) 1450
SANDERS, ROBERT
Geomagnetic and Geoelectric Activity as a Function of Magnetic Latitude (TN) 1438
SANDS, NORMAN
Escape From Planetary Gravitational Fields by Use of Solar Sails..... 527
SARNER, STANLEY F., and DOLLRIES, JOHN F.
An Integrated Propellant Performance Analysis Program (TN)..... 257
SATYENDRA, K. N., and BRADFORD, R. E.
Self-Contained Navigational System for Determination of Orbital Elements of a Satellite..... 949
SCALA, SINCLAIRE M.
Thermal Diffusion Ratio in Dissociated Air (TN)..... 1441
SCHAAF, S. A., MOULIC, E. S., CHALINE, M. T., and MOSLACH, G. J.
Aerodynamic Characteristics of Wedges in Low Density Supersonic Flow... 194
SCHAEFER, E. J., and NICHOLS, M. H.
Mass Spectrometer for Upper Air Measurements (TN)..... 1773
SCHAFFER, ALLEN
Plasma Propulsion With a Pulsed Transmission Line..... 1718
SCHALKOWSKY, SAMUEL, and BLAZEK, HENRY F.
Rotating Pendulum Accelerometer.... 469
SCHELL, D. C., *see* BASKIN, Y.
SCHEUING, RICHARD A.
Outer Inviscid Hypersonic Flow With Attached Shock Waves..... 486
SCHMID, J. R., *see* NAGAMATSU, H. T.
SCHNAPF, A., *see* STERNBERG, S.
SCHRELLO, D. M.
Aerodynamic Influences on Satellite Librations (TN)..... 442
SCHWARTZ, YA. M.
Method of Determining the Electrical Potential of Bodies in Plasma (RS) 1321
SCRUGGS, DAVID M.
Modified Chromium for Unprotected Structures 1527
SEADER, J. D., and WOLF, H.
Theoretical Analysis of Heat Transfer to Gases in Smooth, Round Tubes Under Conditions of Turbulent Flow and High Flux (TN)..... 650
SEBASTIAN, ROBERT A., *see* JACOBS, EDGAR M.
SEGAL, HOWARD M.
Preliminary Thrust-Time Curve for a Spherically Shaped Solid Propellant Rocket Motor (TN)..... 1447
SEIDMAN, M. H.
Comment on "Rapid Method for Plug Nozzle Design" (TC)..... 1292
SEIZEW, M. R., *see* ADAMS, K. A.
SELIUTIN, V. A., *see* DOLGINOV, S. SH.
SELLERS, JOHN P., JR.
Effect of Two-Dimensional Heat Transfer on Wall Temperatures in a Tubular Thrust Chamber (TN).... 445
Effect on Carbon Deposition on Heat Transfer in a LOX/RP-1 Thrust Chamber (TN)..... 662
See also ZUCROW, M. J.
SEMENOV, A. A., and KARPEYEV, G. A.
Relation of Frequency of Ultra Short Wave Field Amplitude Decay, Drift Speed of Inhomogeneities in the Troposphere, and Carrier Frequency (RS) 688
SENTMAN, LEE H.
Comparison of the Exact and Approximate Methods for Predicting Free Molecule Aerodynamic Coefficients (TN) 1576
SERRA, R. A., *see* BAILEY, W. S.
SHAFER, YU., and YARYGIN, A. V.
Measurement of Cosmic Rays by Means of Geophysical Rockets (RS)..... 715
SHAPIRO, M.
Attenuated Intercept Satellite Rendezvous System..... 1733
SHARBAUGH, A. HARRY, and LIPPITT, MAXWELL, W., JR.
A Capacitance Densitometer for Determination of the Transient Densities of Cryogenic Liquids..... 294
SHEER, R. E., JR., *see* NAGAMATSU, H. T.
SHEN, Y. C.
Formulation of the Optimum Rocket Trajectory (TN)..... 89
SHILOVA, N. S., *see* KARIMOV, M. G.
SHINAULT, L. H., and MCGRATH, T. F.
Reactor Core Temperature Measurements 799
SHKLOVSKII, I. S.
An Artificial Comet as a Method for Optical Observation of a Cosmic Rocket (RS)..... 699
SILLA, HARRY
Burning Rates of Composite Solid Propellants at Subatmospheric Pressure (TN) 1277
SILVERN, DAVID H., *see* LINHARDT, HANS D.
SKACHKOV, B. N.
Stability Region of Certain Nonlinear Control Systems (RS)..... 134
SKINNER, G. T.
Calibration of Thin Film Gage Backing Materials (TN)..... 671
SLOCUM, RICHARD W., JR., and ZAPPALA, ALFRED G.
Microwave Rocket Propulsion (TN).. 657
SMEDAL, H. A., VYKUKAL, H. C., GALLANT, R. P., and STINNET, G. W.
Crew Physical Support and Restraint in Advanced Manned Flight Systems 1544
SMITH, F. T.
Optimization of Multistage Orbit Transfer Processes by Dynamic Programming 1553
SMITH, M. C., *see* ROWELL, L. N.
SMITH, MAHLON C., *see* ORMSBY, RALPH D.
SMITH, OLIVER K.
Terminating the Iterative Solution of Kepler's Equation (TN)..... 1598
SMITH, THOR L., *see* LANDEL, ROBERT F.
SOLLOWAY, CARLETON B., *see* LASS, HARRY
SOMMERS, WILLIAM P.
Gaseous Detonation Wave Interactions With Nonrigid Boundaries (TN)... 1780
SPALDING, D. B.
Theory of Mixing and Chemical Reaction in the Opposed-Jet Diffusion Flame 763
SPENCER, ROY C.
Location of Focal Points of Ellipses (TN) 158
SPERLING, HANS
Computation of Keplerian Conic Sections (TN)..... 660
SPEYER, JASON L., *see* MORTH, RAYMOND
STANCIL, R. T., and KULAKOWSKI, L. J.
Rocket Boost Vehicle Mission Optimizations 935
STAPLEFORD, R. L., *see* MCRUER, D. T.
STARK, HAROLD M.
Optimum Trajectories Between Two Terminals in Space (TN)..... 261
STARR, W. L., and KASH, S. W.
Experimental Results With a Collinear Electrode Plasma Accelerator and a Comparison With Ion Accelerators.. 58
STAUFFER, L. H.
Voltage-Current Characteristics of Tungsten Electrodes in Cesium Vapor 322
STEFFAN, KENNETH F.
Satellite Rendezvous Terminal Guidance System..... 1516
STEINBERG, M. A., FOX, J. L., and AUGENSTEIN, B. W.
Proposed Ground and Flight Program to Develop Space Age Materials.... 228
STEINBERG, S., *see* BRO, P.
STEPHANOW, S. E., *see* OLIVER, R. E.
STEPHANS, CHARLES W., and HAIRE, ALAN M.
Internal Design Considerations for Cavity-Type Solar Absorbers..... 896
STERNBERG, S., and SCHNAPF, A.
Performance and Evaluation of Satellites Tiros I and Tiros II..... 1495
STINNETT, G. W., *see* SMEDAL, H. A.
STONE, MAX W.
Slotted Tube Grain Design..... 223
STONE, WILLIAM C.
Practical Methods for Compensation of Erosive Pressure Peaks..... 1288
STRACK, S. L., *see* KENNET, H.
STRAKHOV, B. V., *see* EMEL'IANOVA, Q. I.
STROUD, JOHN F.
Effect of Discontinuity in Wall Curvature on Boundary Layer (TN)..... 664
STRUBLE, RAIMOND A., and CAMPBELL, WILLIAM F.
Theory of Motion of a Near Earth Satellite (TN)..... 154
Technical Comment by YOSHIHIDE KOZAI 676
See also BLACK, HAROLD D.
SUMMERFIELD, MARTIN
ARS Does It Again..... 3
SUTTON, GEORGE W., *see* BLECHER, SHELDON
SWIFT-HOOK, D. T.
Technical Comment (RS)..... 1350
TALANTOV, A. V., *see* PETROV, E. A.
TARATYNOVA, G. P.
Numerical Solution of Equations of Finite Differences and Their Applications to the Calculation of Orbits of Artificial Earth Satellites (RS).. 976
TEETS, PETER B., *see* WOLFE, ROBERT R.
TELLEP, D. M., *see* EDWARDS, D. K.
TEREBUSKO, O. I.
Stability of a Cylindrical Shell Under Twisting, External Pressure and Compression (RS)..... 378
TEWELES, SIDNEY
Meteorological Analysis of Churchill Rocket Sounding Data (TN)..... 841
THOMPSON, T. H., *see* MYERS, G. H.
THOMPSON, W. R., *see* DEAN, L. E.
THREEWIT, T. R., *see* ROSSINI, R. A.
THROSSELL, LAURANCE G., *see* ETTELSON, BEN L.
TING, LU, *see* MOSKOWITZ, SAMUEL E.
TOKAR', E. N., *see* RAUSHENBACH, B. V.

TRANSUE, JOHN R., *see* RADCLIFFE, WILLIAM F.
TRAUGOTT, STEPHEN C., *see* GREENBERG, ROBERT A.
TROSS, CARL
Lunar Landing Sites Selection (TN).. 1153
TSUCHIYA, H. M., *see* FREDRICKSON, A. G.
TSYTOVICH, V. N.
Reflection of a Ring Current by a Plasma (RS)..... 136
TYURMINA, L. O., *see* DOLGINOV, S. SH.
UDY, LEX L., *see* COOK, MELVIN A.
ULVEDAL, F., *see* WELCHM, B. E.
VAKHLOV, P. V., *see* VERNOV, S. N.
VANDENKERCKHOVE, J.
Tentative Explanation of Irregular Burning in Solid Propellant Rockets (TC)..... 1466
VERNOV, S. N.
Cosmic Rays and Outer Space (RS).. 399
VERNOV, S. N., CHUDAKOV, A. E., VAKULOV, P. V., LOGACHEV, YU. I., and NIKOLAEV, A. G.
Radiation Measurements During the Flight of the Second Cosmic Rocket (RS)..... 967
VIEGAS, JOHN R., and PENG, T. C.
Electrical Conductivity of Ionized Air in Thermodynamic Equilibrium (TN)..... 654
VINCENT, THOMAS L.
Satellite Life Duration (TN)..... 1015
VISKANTA, R., and GROSH, R. J.
Temperature Distribution in Couette Flow With Radiation (TN)..... 839
VLACHOS, N. D.
Correction Factor for Annular Nozzles (TN)..... 822
VOL'MIR, A. S., *see* AGAMIROV, V. L.
VON, LI KHEN
Theory of Optimal Signal Filtration in the Presence of Internal Noise in Systems With Variable Parameters (RS)..... 1306
VON KARMAN, THEODORE
Martin Summerfield: Ten Years as Editor..... 1182
VYKUKAL, H. C., *see* SMEDAL, H. A.
WALKER, R. E., and GRENLESKI, S. E., JR.
Instrument for Measuring Total Incident Radiant Heat Transfer to a Jet Engine Surface (TN)..... 77
WALLMAN, E. J., *see* HALL, N. S.
WARDEN, R. V.
Ballistic Re-Entries With a Varying $W/C_D A$..... 208
WARFIELD, R. W., and BLUM, G. D.
Hardening of Plastisol Propellants (TN)..... 674
WARREN, W. R., KAEGI, E. M., and GEIGER, R. E.
Shock Tunnel Experimental Techniques for Force and Moment and Surface Flow Direction Measurements (TN) 82
WATERMEIER, LELAND A.
Experimental Study of Combustion Instability in Solid Rocket Propellants (TN)..... 564
WATSON, RONALD
Effect of Scale Size on a Rocket Engine With Sudden Frozen Nozzle Flow (TN)..... 452
WEATHERSTON, R. C., and HERTZBERG, A.
Investigation of Rocket Flow Problems by Means of Short Duration Flow Devices (TN)..... 1149
WEBER, RICHARD J.
Optimization of Multistage Rockets (TC)..... 849
WEHMER, B. P.
Sputtering Effects on the Moon's Surface (TN)..... 438
WELCH, B. E., MORGAN, T. E., JR., and ULVEDAL, F.
Sealed Cabin Experimentation..... 1541
WHEELON, ALBERT D.
Correction for Free Flight of a Ballistic Missile, ARS JOURNAL, December 1959, vol. 29, pp. 915–926..... 1792
WILSON, HOWARD B., JR.
Stresses Owing to Internal Pressure in Solid Propellant Rocket Grains..... 309
WING, L. D., and CAMERON, K. E.
Solar Collectors for Use in Thermionic Power Supply Systems in Space.... 327
WOLBERS, H. L.
Recent Developments in Bio-Medical Instrumentation..... 1422
WOLF, H., *see* DE SOTO, S., and SEADER, J. D.
WOLFE, ROBERT R., CORGAN, JOHN M., and TEETS, PETER B.
Energy Requirements for Satellite Stabilization of the Gravitational Gradient (TN)..... 836
WONG, THOMAS J., *see* EGGERS, ALFRED J., JR.
WOOD, ROBERT M., *see* PONSFORD, HENRY T.
WOODS, W. A.
Method of Calculating Liquid Flow Fluctuations in Rocket Motor Supply Pipes..... 1560
WOODWARD, E. C.
Combustor Similitude Study..... 1401
WROBEL, J. RICHARD, and BRESHEARS, ROBERT R.
Lunar Landing Vehicles Propulsion Requirements (TN)..... 1570
WU, J. C.
Growth of Magnetohydrodynamic Boundary Layers (TN)..... 562
WU, JAIN-MING, CHAPKIS, R. L., and MAGER, A.
Approximate Analysis of Thrust Vector Control by Fluid Injection..... 1677
YAKUBOVICH, V. A.
Nonlinear Differential Equations of the Automatic Regulation System Having a Single Regulating Member (RS)..... 102
YAO, JOHN C.
Stability of a Cylinder Under Dynamic Radial Pressure..... 1705
YARYGIN, A. V., *see* SHAFER, YU.
YASUI, GEORGE
Reactor Heat Removal Limitations of Nuclear Rockets..... 1195
YATZUNSKY, I. M., and GURKO, O. V.
Variation of the Albedo of the First Artificial Earth Satellite as a Result of the Influence of External Factors (RS)..... 698
YASTREBOV, V. D., *see* EL'IASBERG, P. E.
YUN, K. S., *see* BADE, W. L.
ZAJAC, E. E.
Capture Problem in Gravitational Attitude Control of Satellites (TN).... 1464
ZAPPALA, ALFRED G., *see* SLOCUM, RICHARD W., JR.
ZHUZGOV, L. N., *see* DOLGINOV, S. SH.
ZIEBLAND, H., and DUPREE, M. L.
Thermal Conductivity of Kerosine D. Eng. R.D. 2495 Between 15 and 325C at Pressures Up to 200 Atm. (TN)..... 845
ZIEMER, RICHARD W.
Heat Transfer Gage for Use in Highly Ionized Gases (TN)..... 78
See also DEMETRIADES, STERGE T.
ZLOTNICK, MARTIN, *see* MOORE, JEFFREY A.
ZUCROW, M. J., and SELLERS, JOHN P., JR.
Experimental Investigation of Rocket Motor Film Cooling (TN)..... 668
ZUPNIK, T. F., *see* BAILEY, W. S.

SUBJECTS

PROPULSION AND POWER (Combustion Systems)

RECENT DEVELOPMENTS IN ROCKET NOZZLE CONFIGURATIONS, G. V. R. Rao (SA)..... 1488
PERFORMANCE OF PLUG-TYPE ROCKET EXHAUST NOZZLES, K. Berman and F. W. Crimp, Jr..... 18
EXPERIMENTAL METHOD OF MEASURING INTENSITY OF TURBULANCE IN A ROCKET CHAMBER, Martin Hersch.... 39
ANALYSIS OF PARTIAL ADMISSION AXIAL IMPULSE TURBINES, Hans D. Linhardt and David H. Silvern..... 297
IMPORTANCE OF COMBUSTION CHAMBER GEOMETRY IN HIGH FREQUENCY OSCILLATIONS IN ROCKET MOTORS, J. R. Osborn and J. M. Bonnell..... 482
TRUNCATED PERFECT NOZZLES IN OPTIMUM NOZZLE DESIGN, J. H. Ahlberg and S. Hamilton..... 614
VERIFICATION OF NOZZLE ADMITTANCE THEORY BY DIRECT MEASUREMENT OF THE ADMITTANCE PARAMETER, Luigi Crocco, Rodolfo Monti, and Jerry Grey 771
SELECTION OF A PRESSURIZATION SYSTEM FOR A STORABLE LIQUID PROPELLANT ROCKET ENGINE, C. J. Kaplan..... 786
GAS PARTICLE FLOW IN AN AXISYMMETRIC NOZZLE, W. S. Bailey, E. N. Nilson, R. A. Serra, and T. F. Zupnik 793
APPROXIMATE SOLUTION OF ISENTROPIC SWIRLING FLOW THROUGH A NOZZLE, Artur Mager..... 1140
EFFECT OF FUEL COMPOSITION ON HIGH FREQUENCY OSCILLATIONS IN ROCKET MOTORS BURNING PREMIXED HYDROCARBON GASES AND AIR, J. R. Osborn and J. M. Bonnell..... 1397
METHOD OF CALCULATING LIQUID FLOW FLUCTUATIONS IN ROCKET MOTOR SUPPLY PIPES, W. A. Woods..... 1560
DYNAMIC RESPONSE OF LIQUID FUELED ROCKET ENGINES ON FLEXIBLE STANDS, V. Chobotov..... 1690
THRUST TERMINATION IN SOLID ROCKET MOTORS—EVALUATION OF BALLISTIC TEST DATA, Sherwin Kalt (TN)..... 84
HEAT RELEASE RATE, TEMPERATURE AND PRESSURE IN SOLID ROCKET INSTABILITY, F. T. McClure, R. W. Hart, and J. F. Bird (TN)..... 367
ADVANCED UNCOOLED NOZZLE FOR SOLID PROPELLANT ROCKET, Chuk-Ching Ma (TN)..... 368
HYDRAULIC ANALOG INVESTIGATION OF A PLUG NOZZLE, R. H. Page and A. P. Meyer (TN)..... 447
EFFECT OF SCALE SIZE ON A ROCKET ENGINE WITH SUDDEN FROZEN NOZZLE FLOW, Ronald Watson (TN) 452
RAPID METHOD FOR PLUG NOZZLE DESIGN, H. Greer (TN)..... 560
(Comment by M. H. Seidman).... 1292
EXPERIMENTAL STUDY OF COMBUSTION INSTABILITY IN SOLID ROCKET PROPELLANTS, Leland A. Watermeier (TN)..... 564
CORRECTION FACTOR FOR ANNULAR NOZZLES, N. D. Vlachos (TN)..... 822
ADIABATIC NOZZLE FLOWS, R. A. A. Bryant (TN)..... 828
SIMPLIFIED SUDDEN-FREEZING ANALYSIS FOR NONEQUILIBRIUM NOZZLE FLOWS, K. N. C. Bray (TN)..... 831
INVESTIGATION OF ROCKET FLOW PROBLEMS BY MEANS OF SHORT DURATION FLOW DEVICES, R. C. Weatherston and A. Hertzberg (TN)..... 1149
SUMMARY OF SOLID PROPELLANT RESIDUAL THRUST STUDIES, J. A. Morris (TN)..... 1283
PRELIMINARY THRUST-TIME CURVE FOR A SPHERICALLY SHAPED SOLID PROPELLANT ROCKET MOTOR, Howard M. Segal (TN)..... 1447
IMPULSE PROGRAMMING FOR TURBINE BOOST, J. J. Marcinek and R. E. Goldstein (TN)..... 1589
CONSUMABLE CASE SOLID ROCKET, A. N. Baxter (TN)..... 1790
INFLUENCES OF SOLID PROPELLANT BURNING RATE EXPONENTS ON PERFORMANCE OF ENGINES WITH LARGE BACK PRESSURE VARIATIONS, Robert C. Brumfield (TN)..... 1769
THRUST TERMINATION TRANSIENTS IN SOLID PROPELLANT ROCKETS, R. E. Barry and J. E. Brothers (TC)..... 848
COMMENT ON "RAPID METHOD FOR PLUG NOZZLE DESIGN," M. H. Seidman (TC)..... 1292

PROPULSION AND POWER (Noncombustion)

RECENT ADVANCES IN ELECTRIC ARC PLASMA GENERATION TECHNOLOGY, Richard R. John and William L. Bade (SA)..... 4
THE FUEL CELL IN SPACE, H. A. Liebhafsky and W. T. Grubb, Jr. (SA)... 1183
RECENT ADVANCES IN MAGNETOHYDRODYNAMIC PROPULSION, Meredith C. Gourdine (SA)..... 1670
EXPERIMENTAL RESULTS WITH A COLLINEAR ELECTRODE PLASMA ACCELERATOR AND A COMPARISON WITH ION ACCELERATORS, W. L. Starr and S. W. Kash..... 58
VOLTAGE-CURRENT CHARACTERISTICS OF TUNGSTEN ELECTRODES IN CESIUM VAPOR, L. H. Stauffer..... 322
SOLAR COLLECTORS FOR USE IN THERMIONIC POWER SUPPLY SYSTEMS IN SPACE, L. D. Wing and K. E. Cameron 327

Propulsion by Composite Beams of Negative and Positive Ions, M. A. Gilleo and S. W. Kash 621
Electrode Refraction and Ion Beam Collimation, G. C. Baldwin 627
Reactor Core Temperature Measurements, L. H. Shinault and T. F. McGrath 799
Feasibility of Turbulent Vortex Containment in the Gaseous Fission Rocket, M. L. Rosenzweig, W. S. Lewellen, and J. L. Karrenbrock ... 873
Propulsion System Using a Cavity Reactor and Magnetohydrodynamic Generator 884
Photochemistry and Space Power Generation, J. N. Pitts, Jr., J. Margerum, and Wm. E. McKee 890
Internal Design Considerations for Cavity-Type Solar Absorbers, Charles W. Stephens and Alan M. Haire 896
Reactor Heat Removal Limitations of Nuclear Rockets, George Yasui .. 1195
Theoretical Performance of Propellants Suitable for Electrothermal Jet Engines, John R. Jack 1685
The Traveling-Wave Pump, Eugene E. Covert and Charles W. Haldeman 1252
Effect of Electrical Augmentation on Nuclear Rocket Flight Performance, Edwin R. Berry (TN) 92
Radiated Power from 2-In. Sphere of High Temperature Air at Pressures to 50 Atm, Domenico Ragusa (TN) 445
Fluidized Solids as a Nuclear Fuel for Rocket Propulsion, L. P. Hatch, W. H. Regan, and J. R. Powell (TN) 547
Small MHD Power Generator Using Combination Gases as an Energy Source, S. J. Mullaney and N. R. Dibelius (TN) 555
Microwave Rocket Propulsion, Richard W. Slocum, Jr., and Alfred G. Zappala (TN) 657
Experimental Performance of a Pulsed Gas Entry Coaxial Plasma Accelerator, P. Gloerson, B. Gorowitz, and W. Palm (TN) 1158
Direct Thrust and Efficiency Measurements of a Continuous Plasma Accelerator, Sterge T. Demetriades and Richard W. Ziemer (TN) 1278
High Temperature Fission Chambers and Ionization Chambers, G. M. B. Bouricious (TN) 1439
Thrust Vector Determination of an Ion Engine by Differential Comparison With an Unthrusted Orbit, James N. Hanson (TN) 1787
Plasma Propulsion With a Pulsed Transmission Line, Allan Schaffer ... 1718
Note on "Pierce Gun Design for an Accelerate-Decelerate Ionic Thrust Device," J. R. Pierce (TC) .. 268
Efficiency Calculations From Thrust Measurements, William J. Guman (TC) 676

PROPELLANTS AND COMBUSTION

Prediction of Composition Limits for Detonation of Hydrogen-Oxygen-Diluent Mixtures, Richard W. Patch 46
Calibrations of the Card-Gap Test, Melvin A. Cook and Lex L. Udy 52
Slotted Tube Grain Design, Max W. Stone 223
Thermodynamic Calculations of Hydrogen-Oxygen Detonation Parameters for Various Initial Pressures, Loren E. Bollinger and Rudolph Edse 251
Stresses Owing to Internal Pressure in Solid Propellant Rocket Grains, Howard B. Wilson, Jr. 309
Ignition of Solid Propellant Rocket Motors by Injection of Hypergolic Fluids, Carl C. Ciepluch, Harrison Allen, Jr., and Edward A. Fletcher ... 514
Size Distribution and Velocity of Ethanol Drops in a Rocket Combustor Burning Ethanol and Liquid Oxygen, Robert D. Ingebo 540
Experimental Measurements and Theoretical Analysis of Detonation Induction Distances, Loren E. Bollinger, Michael C. Fong, and Rudolph Edse 588
Large Scale Gap Test: Interpretation of Results for Propellants, Donna Price and Irving Jaffe 595
Viscoelastic Properties of Rubber-like Composite Propellants and Filled Elastomers, Robert F. Landel and Thor L. Smith 599
High Energy Propellant Comparisons for Space Missions, R. V. Burry, J. Jortner, and J. K. Rosemary . 609
Theory of Mixing and Chemical Reaction in the Opposed-Jet Diffusion Flame, D. B. Spalding 763
Heat Sink Strand Bomb for Determining Ballistic Properties of Solid Propellants, E. K. Ives, J. Dominik, and W. A. Proell 783
A Simplified Model of Unstable Burning in Solid Propellants, M. Richard Denison and Eric Baum 1112
Experimental Investigation of Detonation in Unconfined Gaseous Hydrogen-Oxygen-Nitrogen Mixtures, Leon H. Cassutt 1122
Use of Binary Light Metal Mixtures and Alloys as Additions for Solid Propellants, A. W. Blackman and D. K. Kuehl 1265
Practical Methods for Compensation of Erosive Pressure Peaks, William C. Stone 1288
Measurement of Heat Flux From Initiators for Solid Propellants, J. A. Keller and N. W. Ryan 1375
Detonability of Solid Composite Propellants, W. H. Anderson and R. F. Chaiken 1379
Combustion of Carbon in an Air Stream, Jeffrey A. Moore and Martin Zlotnick 1388
Combustion Similitude Study, E. C. Woodward 1401
Investigation of Basic Characteristics of Combustion of a Homogeneous Mixture of an Open Turbulent Stream, E. A. Petrov and A. V. Talantov (RS) 408
Ignition in a Flow by Hot Bodies, S. A. Gol'denberg (RS) 691
Density of Liquid Ozone, T. I. Emel'ianova, B. V. Strakhov, and V. P. Lebedev (RS) 1350
Useful Correlation of Interior Ballistic Theory and Experimental Data, Harold D. Black and Raimond A. Struble (TN) 90
Solid Propellant Source of Cesium Plasma, Lawrence W. Fagg and Raymond Friedman (TN) 157
An Integrated Propellant Performance Analysis Program, Stanley F. Sarner and John F. Dollries (TN) 257
Calculation of C° for High Dissociated Propellant Combustion Products, L. J. Gordon (TN) 374
Stability Program of the Flow With Combustion in Variable Area Duct, Andrezej Kowalewicz (TN) ... 558
Hardening of Plastisol Propellants, R. W. Warfield and G. D. Blum (TN) 674
Thermal Conductivity of Kerosine D. Eng. R.D. 2495 Between 15 and 325 C at Pressures Up to 200 Atm, H. Ziebland and M. T. Dupree (TN) 845
Effect of Acoustic Environment on the Burning Rate of Double-Base Solid Propellants, J. E. Crump and E. W. Price (TN) 1026
Advanced Ignition System for Solid Propellant Rocket Motors, J. J. Priapi (TN) 1029
Burning Rates of Composite Solid Propellants at Subatmospheric Pressure, Harry Silla (TN) 1277
Plateau Ballistics in Nitrocellulose Propellants, R. F. Preckel (TN) ... 1286
Binder Crystallization in Polysulfide Propellant, W. E. Hunter, E. T. Foster, and G. F. Mangum (TN) .. 1573
Effect of Rapid Pressure Decay on Solid Propellant Combustion, Carl C. Ciepluch (TN) 1584
One-Dimensional Solid Propellant Oscillatory Burner, M. D. Horton (TN) 1596
Theory of Liquid Atomization in High Velocity Gas Streams, Ernest Mayer (TN) 1783
Configuration Efficiency: A New Measure of Ballistic Quality for a Grain Design, R. A. Rossini, J. S. Billheimer, and T. R. Threewit (TN). 1761
Gaseous Detonation Wave Interactions With Nonrigid Boundaries, William P. Sommers (TN) 1780
Determination of Optimum Insulation Weight, J. A. Orr (TC) 269
Technical Comment, D. T. Swift-Hook (RS) 1350
Tentative Explanation of Irregular Burning in Solid Propellant Rockets, J. Vandenkerckhove (TC) .. 1466
Integratable Form of Droplet Drag Coefficient, Abbott Putnam (TC) .. 1467
γ Large or Small, R. C. Oliver and S. E. Stephenson (TC) 1468

MATERIALS AND STRUCTURES

Proposed Ground and Flight Program to Develop Space Age Materials, M. A. Steinberg, J. L. Fox, and B. W. Augenstein 228
Stability of Orthotropic Cylindrical Shells Under Combined Loading, T. E. Hess 237
Ablation Mechanisms in Plastics With Inorganic Reinforcement, Norman Beecher and Ronald Rosenweig 532
Meteroids vs. Space Vehicles, R. L. Bjork 803
Ignition Characteristics of Metals and Alloys, L. E. Dean and W. R. Thompson 917
Effect of Glass Fiber Geometry on Composite Material Strength, James E. Bell 1260
Modified Chromium for Unprotected Structures, David M. Scruggs 1527
Directional Solar Reflectances in the Space Vehicle Temperature Control Problem, D. K. Edwards .. 1548
Stability of a Cylinder Under Dynamic Radial Pressure, John C. Yao 1705
Behavior of Cylindrical Shells Under Dynamic Loading by Hydrostatic Pressure or by Axial Compression, V. L. Agamirov and A. S. Vol'mir (RS) 98
Stability of a Console Cylindrical Shell Under Bending by a Transverse Force With Twisting and Internal Pressure, V. M. Darevskii (RS) 125
Stability of a Cylindrical Shell under Twisting, External Pressure and Compression, O. I. Terebusko (RS) 378
Melting Diagram for the Titanium-Molybdenum Ternary System, I. I. Kornilov and R. S. Poliakova (RS) .. 694
Investigation of the Iron-Chromium-Titanium Phase Diagram in a Region of Iron- and Chromium-Rich Alloys, N. G. Boriskina and I. I. Kornilov (RS) 961
Stability of an Orthotropic Cylindrical Shell With Axial Load and External Pressure, O. N. Len'ko (RS) 1315
Propagation and Interaction of Compression and Rarefaction Waves in Elastic-Plastic Media, G. M. Liakhov and N. I. Poliakova (RS) 1644
Meteoritic Impact, David B. Beard (TN) 87
Rocket Nozzles as Temperature Indicators, Y. Baskin and D. C. Schell (TN) 1275
Surface Behavior of Boron Nitride in High Temperature Arc Heated Gases, P. Bro and S. Steinberg (TN) 1460

FLUID DYNAMICS, HEAT TRANSFER, AND MHD

Recent Advances in Nonequilibrium Dissociating Gasdynamics, Ting Y. Li (SA) 170
Recent Advances on Condensation and Evaporation, Welby G. Courtney (SA) 731
Motion and Heating of Lifting Vehicles During Atmosphere Entry, Alfred J. Eggers, Jr., and Thomas J. Wong (SA) 1364

Dissociation Effects Upon Compressible Turbulent Boundary Layer Skin Friction and Heat Transfer, William H. Dorrance 61
Measured Pressure Distribution and Local Heat Transfer Rates for Flow Over Concave Hemispheres, J. C. Y. Koh and J. P. Hartnett 71
Shock Wave and Flow Field Development in Hypersonic Re-Entry, Ronald F. Probstein 185
Aerodynamic Characteristics of Wedges in Low Density Supersonic Flow, S. A. Schaaf, E. S. Moulic, M. T. Chahine, and J. J. Maslach 194
Generalized Heat Transfer Formulas and Graphs for Nose Cone Re-Entry into the Atmosphere, R. W. Detra and H. Hidalgo 318
Linearized Magnetogasdynamic Channel Flow With Axial Symmetry, F. E. Ehlers 334
Outer Inviscid Hypersonic Flow With Attached Shock Waves, Richard A. Scheuing 486
Application of the Mangler Transformation in Boundary Layer Flow, S. de Soto and H. Wolf 553
High Temperature Rarefied Hypersonic Flow Over a Flat Plate, H. T. Nagamatsu, R. E. Sheer, Jr., and J. R. Schmid 902
Analysis of Convective Heat Transfer in Rocket Nozzles, Ernest Mayer 911
Aerodynamic and Radiant Heat Input in Space Vehicles Which Re-Enter at Satellite and Escape Velocity, M. J. Brunner 1102
Recent Hypersonic Studies of Wings and Bodies, Mitchell H. Bertram and Arthur Henderson, Jr. 1129
Transport Properties of Dissociated Air, W. L. Bade, E. A. Mason, and K. S. Yun 1151
Experimental Study of Flow and Separation in Vortex Tubes With Application to Gases Fission Heating, J. J. Keyes, Jr. 1204
Hot Wire Measurements in Low Reynolds Number Hypersonic Flows, C. Forbes Dewey, Jr. 1705
Reflection of a Ring Current by a Plasma, V. N. Tsytovich (RS) 136
Fall of a Spherical Drop in the Presence of Evaporation or Condensation of Vapors at Its Surface, V. S. Novoselov (RS) 686
Propagation of Forced Plane Compression Waves of Small Amplitude in a Viscous Gas When Radiation is Taken Into Account, V. A. Prokof'ev (RS) 988
Solution of Several Problems of Air Motion in the Presence of Dissociation, S. S. Kvashina and V. P. Korobeinikov (RS) 997
Aerodynamic Interaction in a Free Molecular Flow, E. Larish (RS) .. 1630
Magneto-Vortical Rings, Yu. P. Ladikov (RS) 1635
Instrument for Measuring Total Incident Heat Transfer to a Jet Engine Surface, R. E. Walker and S. E. Grenleski, Jr. (TN) 77
Shock Tunnel Experimental Techniques for Force and Moment and Surface Flow Direction Measurements, W. R. Warren, E. M. Kaegi, and R. E. Geiger (TN) 82
Comparison of Theoretical and Experimental Film Thickness, A. E. Dukler (TN) 86
Nonequilibrium Ionization in a Shock Tunnel Flow, Alan Q. Eschenroeder and John W. Daiber (TN) 94
Aerodynamic Heating of Plane Bodies of Low Thermal Diffusivity, Gerald R. Quinn (TN) 158
Estimation of Specific Heats at Normal Temperatures, Fred H. Brock (TN) 265
Stagnation Point Radiative Transfer, H. Kennet and S. L. Strack (TN) 370
Calibration of Hypersonic High Temperature Wind Tunnels, S. E. Neice and R. W. Rutowski (TN) 372
Entrance Effects in the High Temperature Heat Transfer From Dissociated Gases, P. Bro and S. Steinberg (TN) 375
Comparison of Some Approximate Methods for Calculating Re-Entry Ablation of a Subliming Material, Sheldon Blecher and George Salton (TN) 433
Effect of Two-Dimensional Heat Transfer on Wall Temperatures in a Tubular Thrust Chamber, John P. Sellers, Jr. (TN) 445
Similar Solutions of the Free Convection Boundary Layer Equations for an Electrically Conducting Fluid, Barry Reeves (TN) .. 557
Growth of Magnetohydrodynamic Boundary Layers, J. C. Wu (TN) .. 562
Theoretical Analysis of Heat Transfer to Gases in Smooth Round Tubes Under Conditions of Turbulent Flow and High Flux, J. D. Seader and H. Wolf (TN) 650
Heat Transfer in Low Prandtl Number Flows With Variable Thermal Properties, D. K. Edwards and D. M. Tellep (TN) 652
Electrical Conductivity of Ionized Air in Thermodynamic Equilibrium, John R. Viegas and T. C. Peng (TN) 654
Preliminary Analysis of the Capabilities of a Composite Slab for an Advanced Heat Sink Design, Paul A. Libby (TN) 658
Effect of Carbon Deposition on Heat Transfer in a LOX/RP-1 Thrust Chamber, John P. Sellers, Jr. (TN) 662
Effect of Discontinuity in Wall Curvature on Boundary Layer, John T. Stroud (TN) 664
Experimental Investigation of Rocket Motor Film Cooling, M. J. Zucrow and John P. Sellers, Jr. (TN) 668
Effect of Magnetic Drag on Re-Entry Body Heating, Richard L. Phillips (TN) 672
Application of Heat Flux Potentials to the Calculation of Convective Heat Transfer in Chemically Reacting Gases, Daniel C. Rosner (TN) 816
Shock Wave Asymmetry for Cones and Sphere Cones at Angle of Attack, Robert A. Greenberg and Stephen C. Traugott (TN) 821
Contact Surface Tailoring in a Chemical Shock Tube, Howard B. Palmer and Bruce E. Knox (TN) 826
Temperature Distribution in Couette Flow With Radiation, R. Viskanta and R. J. Grosh (TN) 839
Surface Temperatures of High Speed, Radiation Cooled Bodies in Dissociating Atmospheres, Daniel E. Rosner (TN) 1013
(Correction TC) 1469
Maximum Error in Total Emissivity Measurements Due to Non-Grayness of Samples, D. K. Edwards and K. E. Nelson (TN) 1021
Hypersonic Viscous Effects in Wind Tunnels, Robert H. Johnson (TN) .. 1022
On "Numerical Comparison Between Exact and Approximate Theories of Hypersonic Inviscid Flow Past Slender Blunt-Nosed Bodies," K. H. Cheng and A. L. Chang (TN) 1024
Nonuniform Deceleration of a Slender Cone in Supersonic Flight, Chang Ting Hsu (TN) 1289
Thermal Diffusion Ratio in Dissociated Air, Sinclaire M. Scala (TN) .. 1441
Streamlines in Boundary Layers on Flat and Concave Surfaces in Hypersonic Flow, Robert H. Johnson and Elwin C. Bigelow (TN) 1452
One-Dimensional Overtaking of a Shock Wave by a Rarefaction Wave, I. I. Glass, I. E. Heuckroth, and S. Molder (TN) 1453
One-Dimensional Overtaking of a Rarefaction Wave by a Shock Wave, G. F. Bremner, J. K. Dukowicz, and I. I. Glass (TN) 1455
Measurement of Heat Transfer in a Graphite Rod Heat Exchanger, Charles B. Johnson and Frank L. Clark (TN) 1458
Determination of Electron Density and Mobility in Slightly Ionized Cesium, George J. Mullaney and Norman R. Dibelius (TN) 1575
Comparison of the Exact and Approximate Methods for Predicting Free Molecule Aerodynamic Coefficients, Lee H. Sentmen (TN) 1576
Interaction of Centered Expansion Waves, George Rudinger (TN) 1587
Notes on Heat Sink Analysis, K. A. Adams and M. R. Seizew (TN) 1595
Approximate Method of Predicting Hypersonic Pressure Distribution on Nonlifting Near Power Law Bodies Using Similar Flow Theory Results, N. R. Augustine (TN) 1778
Interdependence of Base Pressure and Base Heat Transfer, R. J. Dixon and R. H. Page (TN) 1785

FLIGHT MECHANICS

Low Acceleration Takeoff From a Satellite Orbit, H. Lass and J. Lorell 24
Complete Elementary Solution to Some Optimum Trajectory Problems, Frank D. Faulkner 33
Research in Interplanetary Transfer, John V. Breakwell, Rollin W. Gillespie, and Stanley Ross 201
Ballistic Re-Entries With a Varying W/C_dA, R. V. Warden 208
Limits for Stable Near-Circular Planetary of Satellite Orbits in the Restricted Three-Body Problem, S. H. Dole 214
Motion of a Satellite of the Moon, Harry Lass and Carleton B. Solloway 220
Anomalies of the Geomagnetic Retardation of the Spin of Satellite Vanguard I (1958 Beta), P. L. Arendt 286
Characteristic Velocity Requirements for Impulsive Thrust Transfers Between Non Co-Planar Circular Orbits, L. Rider 345
Probability of Satellite Interception by Air Launched Pre-Guided Missile, Edgar M. Jacobs, George W. Morgenthaler, and Robert A. Sebastian 352
Effect of Geometrical Libration on the Damped Motion of an Earth Satellite, L. N. Rowell and M. C. Smith 361
Variables That Are Determinate for Any Orbit, Robert R. Newton .. 364
Escape From Planetary Gravitational Fields by Use of Solar Sails, Norman Sands 527
Missile Trajectories With Linear Time Variation of the Sine or Tangent of the Thrust Angle, E. Edward Ehlers 631
Nodal Rotation for Continuous Exposure of an Earth Satellite to the Sun, James N. Hanson and Stephen H. Fairweather 640
Rocket Boost Vehicle Mission Optimization, R. T. Stancil and L. J. Kulakowski 935
Optimum Maneuvers for Launching Satellites Into Circular Orbits of Arbitrary Radius and Inclination, J. P. Carstens and T. N. Edelbaum ... 943
Effects of Plane Librations on the Orbital Motion of a Dumbbell Satellite, John P. Moran 1089
Hodograph Analysis of the Orbital Transfer Problem for Coplanar Nonaligned Elliptical Orbits, Samuel P. Altman and Josef S. Pistiner 1217
Planar Motions About an Oblate Planet, Maurice L. Anthony and George E. Fosdick 1225
Satellite Orbit Sustaining Techniques, Richard W. Bruce 1237
Vehicle Motion in the Equatorial Plane of a Planet: A Second Order Analysis in Ellipticity, Maurice L. Anthony and Lawrence M. Perko 1413
Projected Path of the Longitudinal Axis of Earth-Stabilized Satellites, Avedis A. Aintablian 1522
Representation of Fuel Sloshing in Cylindrical Tanks by an Equivalent Mechanical Model, H. N. Abramson, W. H. Chu, and G. E. Ransleben 1697
Water Impact of Manned Spacecraft, James L. Malakoff and William H. Mueller 1751
Three-Dimensional Optimum Thrust Trajectories, William G. Melbourne 1723

Preliminary Orbit Determination of a Nontransmitting Satellite Using the DOPLOC Tracking System, Paul B. Richards 1729
Perturbations in the Motion of Artificial Satellites Due to the Oblateness of the Earth, V. F. Proskurin and V. V. Batrakov (RS) .. 117
Numerical Solution of Equations of Finite Differences and Their Application to the Calculation of Orbits of Artificial Earth Satellites, G. P. Taratynova (RS) 976
Rotational Motion of Artificial Bodies in Space, G. N. Duboshin (RS) 1345
Formulation of the Optimum Rocket Trajectory, Y. C. Shen (TN) 89
Location of Focal Points of Ellipses, Roy C. Spencer (TN) 158
Optimum Trajectories Between Two Terminals in Space, Harold M. Stark (TN) 261
Minimum Time Ballistic Interplanetary Trajectories, Vernon Lee and Dwight E. Florence (TN) 435
Approximate Velocity, Position and Time Relationship for Ballistic Re-Entry, B. P. Miller (TN) 437
Graphical Method for Prediction of Time in Sunlight for a Circular Orbit, G. B. Patterson (TN) ... 441
Aerodynamic Influences on Satellite Librations, D. M. Schrello (TN) 442
Divergence From Equilibrium Glide Path at Supersatellite Velocities, Ramond Morth and Jason L. Speyer (TN) 448
Some Comparisons of Sloshing Behavior in Cylindrical Tanks With Flat and Conical Bottoms, H. Norman Abramson and Guido E. Ransleben, Jr. (TN) 545
Wall Pressure Distributions During Sloshing in Rigid Tanks, H. Norman Abramson and Guido Ransleben, Jr. (TN) 545
An Approach to Problem of Optimum Rocket Trajectories, Samuel E. Moskowitz and Lu Ting (TN) 551
Optimal Powered Arcs in an Inverse Square Field, D. F. Lawden (TN) 566
Computation of Keplerian Conic Sections, Hans Sperling (TN) 660
Theory of Motion of a Near Earth Satellite, Raimond A. Struble and William F. Campbell (TN) 154
(Comment by Yoshihide Kozai) 676
Nonmatrix Formulation of an Eulerian Angle Vector Transformation, Richard Leach (TN) 830
Satellite Life Duration, Thomas L. Vincent (TN) 1015
Some Remarks on Solar Sail, A. Pozzi and L. de Socio (TN) 1164
Low Thrust Orbit Penalty, Paul D. Arthur (TN) 1273
Time Relationships for Interplanetary Trajectories, Werner M. Pauson (TN) 1281
Choice of Unperturbed Orbit in the Use of Encke's Method for the Effects of Oblateness and Drag, N. S. Hall, H. F. Gawlowicz, and E. J. Wallman (TN) 1436
Method for Determining Scale Heights in the Atmosphere, S. Rubin (TN) 1456
Effect of Earth's Oblateness on the Anomalistic Period of a Satellite, M. M. Moe and E. E. Karp (TN) 1462
Suggested Method for Small Changes in Nodal Longitude for Polar Orbits, Paul D. Arthur, and Reinhard Lahde (TN) 1579
Class of Minimum Altitude Variation Orbits About an Oblate Earth, L. Rider (TN) 1580
Analysis of Large Amplitude Re-Entry Oscillations, George S. Campbell (TN) 1590
Polar Hodograph for Ballistic Missle Trajectories, S. P. Altman and J. S. Pistiner (TN) 1592
Terminating the Iterative Solution of Kepler's Equation, Oliver K. Smith (TN) 1598
Solutions for Satellite Motion Under Low Acceleration Using the Method of Variation of Parameters, Stephen J. Citron (TN) .. 1786
Error Analysis for Doppler Determined Satellite Orbits of Other Planets, Paula L. Cohen and Armin J. Deutsch (TN) 1767
An Interesting Observation on the Point Release Into Orbit of a Number of Objects, Donald B. Brick (TC) 270
Comments on Use of Osculating Ellipse in Analysis of Near Circular Orbits, Yoshihide Kozai (TC) .. 676

VEHICLE DESIGN, TESTING, AND PERFORMANCE

Powered Trajectory Studies for Low Thrust Space Vehicles, Robert H. Fox 28
Optimum Staging Technique to Maximize Payload Total Energy, Edgar R. Cobb 342
Thermostructural Design—Energy Vehicles for Mars and Venus, Henry T. Ponsford, Robert M. Wood, Robert E. Lowe, and James F. Madewell 474
Optimum Stage-Weight Distribution of Multistage Rockets, John J. Coleman (TN) 259
(Comment by Richard J. Weber) ... 849
The Virtual Mass of Clustered Boosters, Holt Ashley and Gifford W. Asher 757
The Artificial Earth Satellite—a New Geodetic Tool, Bruce C. Murray 924
Propulsion Requirements for Controllable Satellites, Theodore N. Edelbaum 1079
Problems Associated With Multiple Engine Starts in Spacecraft, William F. Radcliffe and John R. Transue 1408
Performance and Evaluation of Satellites Tiros I and Tiros II, S. Sternberg and A. Schnapf 1495
Sealed Cabin Experimentation, B. E. Welch, L. E. Morgan, Jr., and F. Ulvedal 1541
Optimum Radiant Straight Fin With Exponential Sides, Irving Granet and William McIlroy (TN) 80
Multistage Rocket Optimization, Robert V. Rogsac and Paul L. Patterson (TN) 450
Simple Method for Estimating First-Stage Boost Thrust and Specific Impulse, Robert L. Doebler (TN) ... 550
Staging of Cruising Vehicles, M. Arens (TN) 824
High Energy, Low Thrust Jupiter Missions, Robert H. Fox (TN) 1018
Lunar Landing Sites Selection, Carl Tross (TN) 1153
Segmenting of Radiators for Meteoroid Protection, Robert E. English and Donald Guentert (TN) .. 1162
Vacuum-Air Missile Boost, James J. Murray and Sudhir Kumar (TN) 1443
Radiation Shielding of Space Vehicles by Means of Superconducting Coils, Richard H. Levy (TN) ... 1568
Lunar Landing Vehicles Propulsion Requirements, J. Richard Wrobel and Robert R. Breshears (TN) 1570
Design Criteria for Space Vehicles to Resist Wind Induced Oscillations, A. A. Ezra and S. Birnbaum (TN) 1764
Optimization of Multistage Rockets, Richard J. Weber (TC) 849

GUIDANCE AND CONTROL

Eddy Current Torque Compensation in a Spin Stabilized Earth Satellite, L. H. Grasshoff 290
Alignment of an Inertial Autonavigator, L. R. McMurray 356
Error Analysis Considerations for a Satellite Rendezvous, W. M. Duke, E. A. Goldberg, and I. Pfeffer 505
Optimum Steering Program for the Entry of a Multistage Vehicle Into a Circular Orbit, Stephen Jurovics 518
Accuracy of Measuring Ballistic Missile Trajectories, Frank Cooper. 523
Guidance of Tiros I, G. H. Myers and T. H. Thompson 636
A Method for Controlling the Attitude of a Spin-Stabilized Satellite, L. H. Grasshoff 646
Capabilities and Limitations of Reaction Spheres for Attitude Control, Ralph D. Ormsby and Mahlon C. Smith 808
Magnetorquer—a Satellite Orientation Device, L. J. Kamm 813
Relating Geodetic Latitude and Altitude to Geocentric Latitude and Radius Vector, E. W. Purcell and W. B. Cowan 932
Self-Contained Navigational System for Determination of Orbital Elements of a Satellite, K. N. Satyendra and R. E. Bradford 949
Inertial Sphere System for Complete Attitude Control of Earth Satellites, Karl W. Hering and Robert E. Hufnagel 1074
Controlled Rendezvous of Orbiting Space Stations, Norman S. Potter... 1096
Magnetic Damping of the Angular Motions of Earth Satellites, Robert E. Fischell 1210
Interplanetary Maneuvers Using Radial Thrust, C. M. Petty 1233
Gravitational Torque Impulse on a Stabilized Satellite, Paul F. Hultquist 1506
Gravity Gradient Determination of the Vertical, Robert E. Roberson.. 1509
Satellite Rendezvous Terminal Guidance System, Kenneth F. Steffan 1516
Optimization of Multistage Orbit Transfer Processes by Dynamic Programming, F. T. Smith 1553
Alternate Intercept Satellite Rendezvous System, M. Shapiro.... 1733
Approximate Analysis of Thrust Vector Control by Fluid Injection, Jain-Ming Wu, R. L. Chapkis, and A. Mager 1677
Nonlinear Differential Equations of the Automatic Regulation System Having a Single Regulating Member, V. A. Yakubovich (RS) 102
Stability Region of Certain Nonlinear Control Systems, B. N. Skachkov (RS) 134
Qualitative Investigation of the Trajectories of Difference Equations Near a Fixed Point, A. M. Panov (RS) 682
Stability of Motion of a Gyroscope With a Cardan Suspension, L. M. Markhashov (RS) 958
Some Properties of a System of Nearly Canonical Differential Equations, L. A. Beklemisheva (RS) 1614
Sequential Regression Analysis and Its Application to Some Problems of Automatic Control, I. I. Perelman (RS) 1619
Some Guidance Problems in Interplanetary Space, B. V. Raushenbach and E. R. Tokar (RS) 1624
Differentiating Gas Jet for Space Attitude Control, Robert S. Gaylord (TN) 75
Celestial Rate Sensing, Hans K. Karrenberg and Robert E. Roberson (TN) 440
Power and Energy Requirements for a Fixed-Axis Inertial Wheel Attitude Control System, D. T. McRuer and R. L. Stapleford (TN) 665
Unique Cross-Spin Control Concept for Fixed Fin Sounding Rockets, Russel A. Nidey (TN) 824
Energy Requirements for Satellite Stabilization of the Gravitational Gradient, Robert R. Wolfe, John M. Corgan, and Peter B. Teets (TN) 836
Attitude Stabilization Using Focused Radiation Pressure, Robert R. Hibbard (TN) 844
Slcular Gravitational Torque on a Satellite in a Circular Orbit, Russel Nidey (TN) 1032
Rudimentary Launch Guidance Methods for Deep Space Missions, Carl G. Pfeiffer (TN) 1155
Attitude Control of Rotating Satellites, Roy Dale Cole, Mary Elizabeth Ekstrand, and Michael R. O'Neill (TN) 1446

Capture Problem in Gravitational Attitude Control of Satellites, E. E. Zajac (TN) 1464
Momentum Dumping Using Magnetic Torques, J. W. Burrow (TN) 1776
Alternate Form of a Result by Nidey, Robert E. Roberson (TC) 1292
Free Flight of a Ballistic Missile, Albert D. Wheelon (ARS Journal, December 1959, vol. 29, pp. 915–926), correction 1792

INSTRUMENTATION AND COMMUNICATIONS

Satellite Networks for Continuous Zonal Coverage, R. David Lüders .. 179
Low Resolution Unchopped Radiometer for Satellites, Rudolf A. Hanel 246
A Capacitance Densitometer for Determination of the Transient Densities of Cryogenic Liquids, A. Harry Sharbaugh and Maxwell W. Lippitt, Jr. 294
Rotating Pendulum Accelerometer, Samuel Schalkowsky and Henry F. Blazek 469
Recording of Pressure Step Functions of Low Amplitude by Means of Composite Dielectric Capacitance Transducer Placed in Parallel-T Network, K. Posel 1242
Recent Developments in Bio-Medical Instrumentation, H. L. Wolbers ... 1422
Relation of Frequency of Ultra Short Wave Field Amplitude Decay, Drift Speed of Inhomogeneities in the Troposphere, and Carrier Frequency, A. A. Semenov and G. Karpeyev (RS) 688
Variation of the Albedo of the First Artificial Earth Satellite as a Result of the Influence of External Factors, I. M. Yatzunsky and O. V. Gurko (RS) 698
An Artificial Comet as a Method for Optical Observation of a Cosmic Rocket, I. S. Shklovskii (RS) 699
Theory of Optimal Signal Filtration in the Presence of Internal Noise in Systems With Variable Parameters, Li Khen Von (RS) 1306
Method of Determining the Electrical Potential of Bodies in Plasma, Ya. M. Schwartz (RS) 1321
Magnetometric Equipment of the Third Soviet Artificial Earth Satellite, S. Sh. Dolginov, L. N. Zhuzgov, and V. A. Seliutin (RS) 1329
Magnetic Measurements on the Second Cosmic Rocket, S. Sh. Dolginov, E. G. Eroshenko, L. N. Zhuzgov, N. V. Pashkov, and L. O. Lyurmina (RS) .. 1640
Transistor Phase-Sensitive Amplifier, Ch. S. Agalarov (RS) 1650
Heat Transfer Gage for Use in Highly Ionized Gases, Richard W. Ziemer (TN) 78
Peltier Cooling of Electrical Components in Telemetering Packages, Raymond Marlow (TN) 263
Optical Refraction With Emphasis on Corrections for Points Outside the Atmosphere, Duane C. Brown (TN) 549
Calibration of Thin Film Gage Backing Materials, G. T. Skinner (TN). 671
"Pinhole Camera" for Determination of Plasma Arc Rotational Speed, E. A. Bunt and H. L. Olson (TN) 826
Limitations on Space Vehicles Imposed by Communications Requirements, R. W. Sanders (TN) 1450
Measurement of Small Discharge Rate of an Intermittent Exhaust Jet, William J. Guman (TN) 1583
Mass Spectrometer for Upper Air Measurement, E. J. Schaefer and M. H. Nichols (TN) 1773
Magnetic Compensation of Satellites, Roy G. Brereton (TC) 568
Proposal for a Simple Visual Tracking Arrangement for Space Probes, Stephen A. Kallis, Jr. (TC) .. 1598

AEROPHYSICS AND ASTROPHYSICS

Evolution of Upper Air Meteorology, H. J. aufm Kampe (SA) 1047
New Theory of the Aurora Polaris, S.-I. Akasofu and S. Chapman 775
Winds and Circulations in the Mesosphere, Thomas J. Keegan 1060
Lunar Impact Probe, Julian I. Palmore, III 1066
Correlation Method for Analysis of Large Heterogeneities of the Ionosphere, V. D. Gusev (RS) 1323
Interpolation Averaged Variants of the Canonical Problem of Celestial Mechanics, N. D. Moiseyev (RS) 387
Averaged Variants of a Semirestricted Planar Problem of Three Bodies, N. D. Moiseyev (RS) 393
Complete Averaging of Canonical Problem of Celestial Mechanics With Several Intermediate Elements, N. D. Moiseyev (RS) 390
Cosmic Rays and Outer Space, S. N. Vernov (RS) 399
What an Astronaut Will See and Encounter When Flying at a Speed Approaching That of Light, S. M. Rytov (RS) 678
Technical Comment, D. T. Swift-Hook (RS) 1350
Upper Atmosphere Density Determination, Based on Flight Observations of the Third Soviet Artificial Earth Satellite, P. E. El'iasberg and V. D. Yastrebov (RS). 706
Results of Investigation of the Meteoric Matter by Means of Instruments Installed on Cosmic Rockets, T. N. Nazarova (RS) 713
Measurement of Cosmic Rays by Means of Geophysical Rockets, Yu. Shafer and A. V. Yarygin (RS) 715
Radiation Measurements During the Flight of the Second Cosmic Rocket, S. N. Vernov, A. E. Chudakov, P. V. Vakulov, Yu. I. Logachev, and A. G. Nikolaev (RS) 967
Connection Between the Motion of Matter in the Corona and the Prominences, M. G. Karimov and N. S. Shilova (RS) 970
Investigation of Meteoric Particles by the Third Soviet Satellite, Q. N. Nazarova (RS) 1341
Luminosity of Matter Confined Within a Finite Volume and Having Arbitrary Absorption and Emission Bands, A. M. Samson (RS). 1632
Particle Impaction Efficiencies for Bodies in a Free Molecule Flow, S. K. Friedlander (TN) 96
Densities of the Upper Atmosphere Derived From Discoverer Satellites, Stanley H. Landberg (TN) .. 155
Sputtering Effects on the Moon's Surface, B. P. Wehner (TN) 438
Measurement of Air Density at 430 Km by Sodium Resonance Cloud Techniques, J. Pressman and F. F. Marmo (TN) 819
Irradiation of a Lunar Satellite, W. Leon Francis (TN) 835
Meteorological Analysis of Churchill Rocket Sounding Data, Sidney Teweles (TN) 841
Geomagnetic and Geoelectric Activity as a Function of Magnetic Latitude, Robert Sanders (TN) 1438
Meteoric Dust on the Surface of the Moon, Roy G. Brereton (TC) ... 850

HUMAN FACTORS AND BIOASTRONAUTICS

Psychological and Social Problems of Man in Space—A Literature Survey, B. D. Goodman (SA) 863
Internal Animal Telemetry: A Feasibility Test Program, Ben L. Ettelson, Wilfred N. Cooper, Merle A. Beaupre, Toby Freedman, Laurance G. Throssell, and Bruce P. Pinc 1190
Optimum Conditions for Photosynthesis in Optically Dense Cultures of Algae, A. G. Fredrickson, A. H. Brown, R. L. Miller, and H. M. Tsuchiya 1429
Pilot Performance Capabilities During Centrifuge Simulations of Boost and Re-Entry, Randall M. Chambers and John G. Nelson 1534
Crew Physical Support and Restraint in Advanced Manned Flight Systems, H. A. Smedal, H. C. Vykukal, R. P. Gallant, and G. W. Stinnett 1544
Nuclear Safety Analysis of Snap III for Space Missions, W. Hagis, T. Dobry, and G. Dix 1744

Putting outer space in Pasadena

How will sub-zero cold and intense heat and light from the Sun effect planet-bound spacecraft moving through the void of outer space? The scientists and engineers at Cal Tech's Jet Propulsion Laboratory think they know.

But they're building this giant space simulator at JPL's Pasadena facility just to make sure.

The 80-foot high simulator will soon begin environmental tests on the Mariner — first spacecraft scheduled to fly-by Venus. In a 25-foot-in-diameter chamber, the Mariner may be exposed to a vacuum of 5×10^{-6} millimeters of mercury, a wall temperature of −320°F, and a radiant flux of sun light and heat found as near to the Sun as Venus and as far away as Mars.

Next-to-the-real-thing testing is part of any R & D work. But in JPL's job — exploration of our Moon and planets — the stakes were never higher.

The odds for JPL's (and the nation's) success in space are only as good as our scientists and engineers are good. JPL is looking for good people. The best people. Why not write to us and find out if you can improve the odds.

JET PROPULSION LABORATORY
4806 OAK GROVE DRIVE, PASADENA, CALIFORNIA
Operated by California Institute of Technology for the National Aeronautics & Space Administration

All qualified applicants will receive consideration for employment without regard to race, creed or national origin / U. S. citizenship or current security clearance required.

INPUT FROM OUT THERE
Man's comprehension of the cosmos grows with his ability to assess and control the space environment. This is the task of *astrionics*— the discipline that integrates electronics, optics, mechanics, and the information sciences into unified systems.
Aerojet-General's Astrionics Division, manufacturer of the infrared subsystem of the MIDAS satellite, offers complete capability in research, development, and production of advanced astrionic systems for—
• Guidance and Control
• Target Detection and Identification
• Searching and Tracking
• Electronic Support
• Information Sciences
• Radiometric and Spectral Analysis
ASTRIONICS DIVISION
CORPORATION
Azusa, California
THE GENERAL TIRE
A SUBSIDIARY OF THE GENERAL TIRE AND RUBBER COMPANY

Engineers, scientists—investigate outstanding opportunities at Aerojet

$ 124525